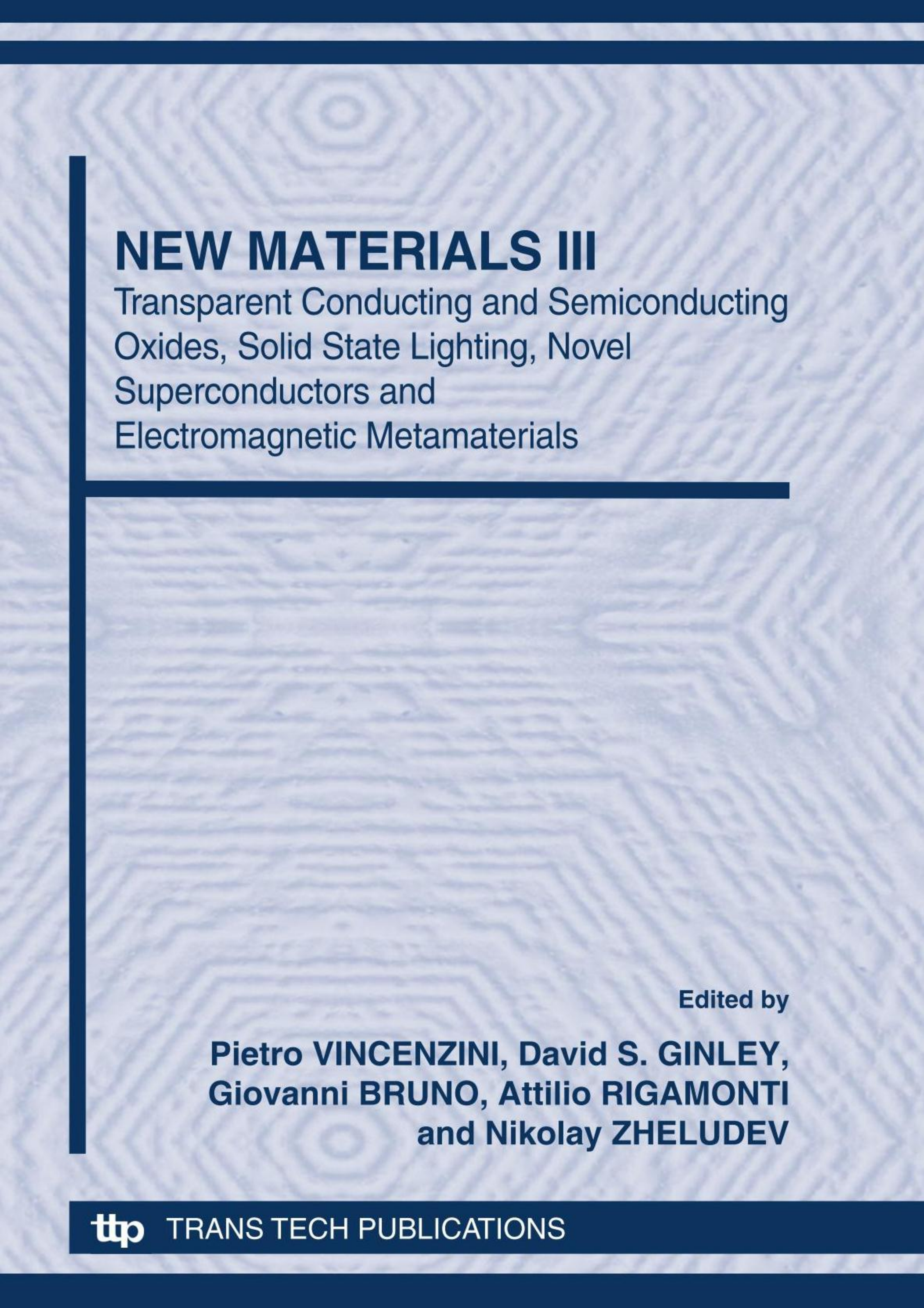

NEW MATERIALS III

Transparent Conducting and Semiconducting Oxides, Solid State Lighting, Novel Superconductors and Electromagnetic Metamaterials

Edited by

Pietro VINCENZINI, David S. GINLEY,
Giovanni BRUNO, Attilio RIGAMONTI
and Nikolay ZHELUDEV

ttp TRANS TECH PUBLICATIONS

5th FORUM ON NEW MATERIALS

PART D

5th FORUM ON NEW MATERIALS

Proceedings of the 5th Forum on New Materials, part of CIMTEC 2010-12 th
International Ceramics Congress and 5th Forum on New Materials
Montecatini Terme, Italy, June 13-18, 2010

PART D *including:*

Symposium FI – Recent Developments in the Research and Application of Transparent Conducting and Semiconducting Oxides

Symposium FJ – Materials for Solid State Lighting

Symposium FK – Science and Engineering of Novel Superconductors

Symposium FM – Electromagnetic Metamaterials

Edited by

Pietro VINCENZINI
World Academy of Ceramics and
National Research Council, Italy

Co-edited by

David S. GINLEY, NREL, USA
Giovanni BRUNO, University of Bari, Italy
Attilio RIGAMONTI, University of Pavia, Italy
Nikolay ZHELUDEV, University of Southampton, UK

TRANS TECH PUBLICATIONS LTD
Switzerland • UK • USA

on behalf of TECHNA GROUP
Faenza • Italy

Published by Trans Tech Publications Ltd., on behalf of Techna Group Srl, Italy

Trans Tech Publications Ltd
Laubisrutistr. 24
CH-8712 Stafa-Zuerich
Switzerland
http://www.ttp.net

EAN: 9783908158424

Volume 75 of
Advances in Science and Technology
ISSN 1661-819X

Full text available online at http://www.scientific.net

The listing of the other Volumes (1-61) of the Series "Advances in Science and Technology" are available at TECHNA GROUP website: http://www.technagroup.it

Distributed worldwide by

Trans Tech Publications Ltd
Laubisrutistr. 24
CH-8712 Stafa-Zuerich
Switzerland

Fax: +41 (44) 922 10 33
e-mail: sales@ttp.net

and in the Americas by

Trans Tech Publications Inc.
PO Box 699, May Street
Enfield, NH 03748
USA

Phone: +1 (603) 632-7377
Fax: +1 (603) 632-5611
e-mail: sales-usa@ttp.net

PREFACE

CIMTEC 2010 was held in Montecatini Terme, Italy on June 6-18, 2010. This high qualitative and comprehensive congressional event, similarly to the previous editions, has been designed to encompass and derive synergism from a broad interdisciplinarity network capable of offering opportunities for identifying and exploring new directions for research and production. The above based on the view that ongoing and future innovations require at an ever increasing extent a complex array of interconnections among scientific research, innovating technology and industrial infrastructure.

CIMTEC 2010 consisted of two major events: the 12th INTERNATIONAL CERAMICS CONGRESS (June 6-11, 2010) and the 5th FORUM ON NEW MATERIALS (June 13-18, 2010). The World Academy of Ceramics and the International Ceramic Federation (ICF) acted as principal endorsers for the first one, and the International Union of Materials Research Societies (IUMRS) for the FORUM.

The 12th INTERNATIONAL CERAMICS CONGRESS included 12 International Symposia, two Focused Sessions and two Serial International Conferences (“Disclosing Materials at Nanoscale” and “Advanced Inorganic Fibre Composites for Structural and Thermal Management Applications”) which covered recent progress in almost all relevant fields of ceramics science and technology. The 5th FORUM ON NEW MATERIALS consisted of 11 International Symposia primarily concerned with energy technologies, one Focused Session and two Serial International Conferences (“Science and Engineering of Novel Superconductors” and “Medical Applications of Novel Biomaterials and Nano-biotechnology”).

A balanced, high quality programme of invited and contributed papers resulted from the over one thousand and seven hundred scientific and technical contributions effectively presented during the working days to a large international audience coming from fifty-seven countries throughout the world.

The 15 volumes which constitute the Official Proceedings of CIMTEC 2010 (10 for the Ceramics Congress, 5 for the Forum) include a selection of the papers presented. Having most of them been written by authors whose mother tongue is not English, considerable revision of the original texts was often required. The partial reworking of several papers and sometimes even complete rewriting was needed to make clear work valid as regards the technical content but difficult to understand because of lack of proficiency in the English language. Even so, in order to allow the scientific and technical community to have access to the proceedings volumes within a reasonable length of time, compromise was necessary in regard to the quality of writing, and papers containing language imperfections were considered acceptable provided that their technical content was adequate and easily understandable.

The Editor, who also acted as the Chairman of CIMTEC 2010, would like to express his sincere appreciation to all the Institutions and Professional Organizations involved in the congress, to the members of the International Advisory Committees, the National Coordinating Committees, the Co-Chairs Prof. Akio Makishima (Japan) for the INTERNATIONAL CERAMICS CONGRESS and Prof. Robert P.H. Chang (USA) for the FORUM ON NEW MATERIALS, the Programme Chairs, the Lecturers, the technical staff of Techna Group, and to the many others who directly or indirectly contributed to the organization. Indeed it was mainly through the involvement of the above bodies and individuals, and the active participation of most internationally qualified experts from major academic and government research institutes and industrial R&D centers that a very valuable scientific programme could be arranged.

It is therefore expected for the Proceedings of CIMTEC 2010-12th INTERNATIONAL CERAMICS CONGRESS & 5th FORUM ON NEW MATERIALS to constitute a further valuable contribution to the literature in the field.

P. VINCENZINI
World Academy of Ceramics
Emeritus Research Manager
National Research Council of Italy

5th FORUM ON NEW MATERIALS

Chairman
Pietro VINCENZINI, *Italy*

Co-Chair
Robert P.H. CHANG, *USA*

Symposium FI – Recent Developments in the Research and Application of Transparent Conducting and Semiconducting Oxides

Programme Chair and Co-Chair
David S. GINLEY, *USA*

Co-Chairs
Claes G. GRANQVIST, *Sweden* Yuzo SHIGESATO, *Japan*

Members
Marcela Bilek, *Australia* Clark Bright, *USA* Klaus Ellmer, *Germany* Norifumi Fujimura, *Japan* Alexander Gaskov, *Russia* Hao Gong, *Singapore* Stuart J.C. Irvine, *UK* Andreas Klein, *Germany* Tobin J. Marks, *USA* Rodrigo Martins, *Portugal* Francis Maury, *France* Julia E. Medvedeva, *USA* Ion N. Mihailescu, *Romania* Tadatsugu Minami, *Japan* Joan Ramon Morante, *Spain* Androula G. Nassiopoulou, *Greece* Bernard Nghiem, *France* Martyn E. Pemble, *Ireland* David Sheel, *UK* Kazushige Ueda, *Japan* M.C.M. Van De Sanden, *The Netherlands* John F. Wager, *USA*

Symposium FJ – Materials and Technologies for Solid State Lighting

Programme Chair
Giovanni BRUNO, *Italy*

Co-Chairs
April S. BROWN, *USA* Chennupati JAGADISH, *Australia* Iain McCULLOCH, *UK*

Members
Hiroshi Amano, *Japan* Herbert Boerner, *Germany* Alberta Bonanni, *Austria* Franco Cacialli, *UK* Luisa De Cola, *Germany* Russell D. Dupuis, *USA* Ian Ferguson, *USA* Bernard Gil, *France* Martin Heeney, *UK* Michael Heuken, *Germany* H.T.J.M. Hintzen, *The Netherlands* Julia W.P. Hsu, *USA* Sheng-Lung Huang, *Taiwan* Dave Irvine-Halliday, *Canada* Masashi Kawasaki, *Japan* Alois Krost, *Germany* Thomas F. Kuech, *USA* Hao-Chung Kuo, *Taiwan* Mike Leszczynski, *Poland* Yung-Sheng Liu, *Taiwan* Michael Lorenz, *Germany* Maria Losurdo, *Italy* Nicola Lovergine, *Italy* Francesco Naso, *Italy* Jeff Nause, *USA* Norbert H. Nickel, *Germany* David P. Norton, *USA* Jamie Phillips, *USA* David Rogers, *France* Timothy D. Sands, *USA* Alan Sellinger, *USA* Franky So, *USA* James S. Speck, *USA* Hongsuk Suh, *Korea* Christian Wetzel, *USA* Magnus Willander, *Sweden* Takafumi Yao, *Japan* Edward T. Yu, *USA*

FK – 6th International Conference "Science and Engineering of Novel Superconductors"

Programme Chair
Attilio RIGAMONTI, *Italy*

Co-Chairs
Donald U. GUBSER, *USA* Hideo HOSONO, *Japan* Davor PAVUNA, *Switzerland*

Members
Marcel Ausloos, *Belgium* Antonio Barone, *Italy* Johann W. Blatter, *Switzerland* Bernd Büchner, *Germany* Alexander I. Buzdin, *France* Paolo Calvani, *Italy* Paul Canfield, *USA* David Caplin, *UK* Tord Claeson, *Sweden* Edward W. Collings, *USA* Guy Deutscher, *Israel* Takeshi Egami, *USA* René Flükiger, *Switzerland* Laszlo Forro, *Switzerland* Hidetoshi Fukuyama, *Japan* Wilfried Goldacker, *Germany* Fedor Gomöry, *Slovakia* Xiao Hu, *Japan* Ienari Iguchi, *Japan* Peter Komarek, *Germany* Igor Mazin, *USA* Masato Murakami, *Japan* Vladimir M. Pan, *Ukraine* Dean E. Peterson, *USA* Justin Schwartz, *USA* Paul Seidel, *Germany* Yuh Shiohara, *Japan* Jozef Spalek, *Poland* Frank Steglich, *Germany* Setsuko Tajima, *Japan* Shoji Tanaka, *Japan* Yasutomo J. Uemura, *USA* Andrei Varlamov, *Italy* Nan Lin Wang, *P.R. China* Harald W. Weber, *Austria* Sergio Zannella, *Italy* Albert Zeller, *USA* Lian Zhou, *P.R. China* *Programme Committee:* Attilio Rigamonti, *Italy (Chair)* Claudio Castellani, *Italy* Andrea Gauzzi, *France* Renato S. Gonnelli, *Italy* Luigi Maritato, *Italy* Marina Putti, *Italy* Laura Romanò, *Italy*

Symposium FM – Electromagnetic Metamaterials

Chair:
Nikolay I. ZHELUDEV, *UK*

Members
Allan D. Boardman, *UK* Tie Jun Cui, *P.R. China* Nader Engheta, *USA* Yuri S. Kivshar, *Australia* Angrey N. Lagarkov, *Russia* Joshua Le-Wei Li, *Singapore* Joan Ferran Martin Antolin, *Spain* Susumu Noda, *Japan* Ekmel Ozbay, *Turkey* John Pendry, *UK* Vladimir M. Shalaev, *USA* Costas M. Soukoulis, *Greece* Sergei A. Tretyakov, *Finland* Lucio Vegni, *Italy* Martin Wegener, *Germany* Xiang Zhang, *USA* Said Zouhdi, *France*

Table of Contents

SECTION I – TRANSPARENT CONDUCTING AND SEMICONDUCTING OXIDES

I-1 Materials Design and Device Development

I-2 Applications

SECTION II – MATERIALS FOR SOLID STATE LIGHTING

SECTION III – SCIENCE AND ENGINEERING OF NOVEL SUPERCONDUCTORS

SECTION IV – ELECTROMAGNETIC METAMATERIALS

doi:10.4028/www.scientific.net/AST.75.1

Fabrication and Magneto-Transport Properties of $Zn_{0.88-x}Mg_xMn_{0.12}O$/ZnO Heterostructures Grown on ZnO Single-Crystal Substrates

Keiichiro Masuko[a], Tatsuru Nakamura[b], Atsushi Ashida[c],
Takeshi Yoshimura[d], and Norifumi Fujimura[e]

Department of Physics and Electronics, Graduate School of Engineering,
Osaka Prefecture University, 1-1 Gakuen-cho, Naka-ku, Sakai, Osaka 599-8531, JAPAN
[a]masuko6@pe.osakafu-u.ac.jp, [b]t.nakamura@pe.osakafu-u.ac.jp,
[c] ashida@pe.osakafu-u.ac.jp, [d]tyoshi@pe.osakafu-u.ac.jp, [e]fujim@pe.osakafu-u.ac.jp

Keyword: Oxide semiconductor, ZnO, ZnMnO, Diluted magnetic semiconductor, Pulsed laser deposition

Abstract

The transport properties of $Zn_{0.88-x}Mg_xMn_{0.12}O$/ZnO modulation-doped heterostructures ($x \leq 0.15$) were investigated. The heterostructures were fabricated on ZnO $\left(000\bar{1}\right)$ single-crystal substrates by a pulsed laser deposition system. Atomic force microscope observation and X-ray diffraction analysis suggested that $Zn_{0.88-x}Mg_xMn_{0.12}O$ layers have atomically flat surface and excellent crystallinity. The results of Hall measurement for $Zn_{0.88-x}Mg_xMn_{0.12}O$/ZnO modulation-doped heterostructure with x=0.075 revealed that the carrier concentration and the electron mobility were 5.1×10^{12}cm^{-2} and 800 cm^2/Vs at 10 K, respectively, suggesting that the carrier confinement effect exits at the heterointerface between $Zn_{0.88-x}Mg_xMn_{0.12}O$ barrier layer and ZnO channel layer. In the magnetoresistance (MR) measurement at 1.85 K, a positive MR behavior was observed below 0.5 T, while a negative MR behavior was recognized above 0.5 T. The slope of the positive MR decreased with increasing the temperature and was well fitted to the Brillouin

function with S=5/2. The electrical and magneto-transport properties were very similar to those of $Zn_{0.88}Mn0_{.12}O$/ZnO heterostructures without doping Mg.

Introduction

II-VI compound semiconductor ZnO has considerable attentions as transparent oxide material for electronics and optics. Furthermore, 3*d* transition-metal doped ZnO is focused as one of transparent spintronics materials [1, 2]. The *n*-type $Zn_{1-x}Mn_xO$ thin films give large magnetoresistance (MR) ratio by a giant spin splitting of conduction band induced *s-d* exchange interaction [3, 4]. Also, *p*-type $Zn_{0.95}Mn_{0.05}O$ is theoretically predicted to be a ferromagnet above room temperature [1].

We have fabricated ZnO-based heterostructures with magnetic barrier using *n*-type $Zn_{1-x}Mn_xO$. The carrier confinement effect and the spin-dependent transport properties in the $Zn_{1-x}Mn_xO$ (x=0.10, 0.12)/ZnO modulation-doped heterostructures grown on *c*-sapphire substrates and ZnO $(000\bar{1})$ single-crystal substrates have been reported [5-9]. It was suggested that the free electrons are induced on the ZnO $(000\bar{1})$ surface by spontaneous and piezoelectric polarizations of the $Zn_{1-x}Mn_xO$ and ZnO layers [7]. Also, we have succeeded in preparing the ZnO layer with step-and-terrace structure using the ZnO $(000\bar{1})$ substrate [13]. To aim for the practical use of spin-LED and spin-FET, the band gap engineering is essential technique. Here, Mg ion was focused as a dopant. Ohtomo *et al.*, reported that $Zn_{1-x}Mg_xO$ ($x \leq 0.33$) epitaxial films with a band gap energy of about 4.0 eV and multiquantum well structures were grown on *c*-sapphire substrate by pulsed laser deposition (PLD) [10,11]. Recently, high quality $Zn_{1-x}Mg_xO$ films were also obtained ZnO (0001) single-crystal substrates by molecular beam epitaxy method [12]. Therefore, for $Zn_{1-x-y}Mg_xMn_yO$/ZnO heterostructures, strong carrier confinement effect and the formation of abrupt interface are expected. However, the structural characteristics and optical properties of $Zn_{1-x-y}Mg_xMn_yO$ films have been unknown so far.

In this paper, we investigated the crystallographic characteristics of the $Zn_{0.88-x}Mg_xMn_{0.12}O$/ZnO heterostructures grown on the ZnO $(000\bar{1})$ single-crystal substrates by PLD. The electrical transport and magneto-transport properties were also studied.

Experimental Procedure

$Zn_{0.88-x}Mg_xMn_{0.12}O$/ZnO heterostructures with x=0, 0.075, 0.15 were deposited on ZnO $(000\bar{1})$ single-crystal substrates by PLD using KrF excimer laser. During deposition, an oxygen pressure was 1×10^{-4} (Torr). After a deposition of the ZnO buffer layers with a thickness in the range of 100 −

300 nm at 670 ˚C, $Zn_{0.88-x}Mg_xMn_{0.12}O$ layers with a thickness d_s of 10 − 80 nm were grown. Al-doped $Zn_{0.88-x}Mg_xMn_{0.12}O$ layers with a thickness d_d of 0 − 60 nm were deposited at 640 ˚C as the doping layer for the modulation-doped heterostructures. Details of substrate preparation and deposition condition have been reported elsewhere [13]. $Zn_{0.90-x}Mg_xMn_{0.10}O$ targets with x= 0.03 and 0.10 were prepared by mixing prescribed amount ZnO (5*N*), MgO (4*N*), and Mn_3O_4 (3*N*) powders. The mixed powder was ground, pressed into a pellet, and sintered at 1000 ˚C for 10 h in air. Also, Al-doped $Zn_{0.88-x}Mg_xMn_{0.12}O$ targets with Al concentration in the range of 0.001%−0.1% were prepared. The concentration of Mn and Mg ions in the heterostructures was estimated using energy dispersive X-ray (EDX) analysis of the $Zn_{1-x-y}Mg_xMn_yO$ thin films grown on sapphire substrates. When x=0.03 and 0.10 in target, x in the film was estimated to be 0.075 and 0.15, respectively. It has already been reported that Mg concentration in the films tends to be larger than that in target, as reported by Ohtomo *et al.*[10]. Also, this slight difference of Mn concentration might be attributed to the fact that the vapor pressure of Zn is larger than that of Mn [14].

Surface morphologies and structural characteristics of $Zn_{0.88-x}Mg_xMn_{0.12}O$/ZnO heterostructures were characterized by means of atomic force microscopy (AFM) (NanoScope E, Toyo Technica, Inc), and high-resolution X-ray diffraction (XRD) (X'pert-MRD, Philips Co.) analysis. Sheet resistivity, electron mobility, and sheet carrier concentration of the heterostructures were measured by the van der Pauw method in the temperature range from 1.85 K to 300 K. As an ohmic electrode, indium was soldered on the sample surface. The magnetoresistance (MR) measurement was carried out below 50 K at a magnetic field applied parallel to the sample surface. The MR was obtained using a standard ac lock-in technique with a current I ranging from 0.01μ to 1 μA. In this paper, the MR measurement was carried out in four-terminal configurations.

Results and Discussion

The surface morphologies of top $Zn_{0.88-x}Mg_xMn_{0.12}O$ layers were observed by AFM. Figure 1 (a) and (b) shows AFM images of the surfaces for the about 80-nm-thick $Zn_{0.88-x}Mg_xMn_{0.12}O$/ZnO heterostructures with x = 0.075, 0.15, respectively. Both heterostructures show a step-and-terrace structure. However, the surface for the layer with x= 0.15 shows irregular step, compared to that for the layer with x= 0.075. We considered that an increase in Mg concentration might lead to a deterioration of crystallographic quality or a precipitation of second phases. To characterize the existence of second phases and the deterioration of crystallographic quality, the X-ray 2θ-ω measurement in the 2θ range of 20−80˚ and the X-ray ω rocking curve measurement of the $Zn_{0.88-x}Mg_xMn_{0.12}O$ 0004 diffraction were performed. The X-ray 2θ-ω profile of the $Zn_{0.73}Mg_{0.15}Mn_{0.12}O$/ZnO heterostructure indicated only a single-phase wurzite structure with

(0001) orientation. Figure 2 (a) shows 2θ-ω profiles near symmetric 0004 diffraction for the $Zn_{0.73}Mg_{0.15}Mn_{0.12}O$/ZnO heterostructure. The peak from the $Zn_{0.88-x}Mg_xMn_{0.12}O$ 0004 diffraction is located at a lower angle than that from the ZnO 0004 diffraction. The full width of half maximum (FWHM) values of the 2θ and ω rocking curve is 0.13° and 0.05°. These are comparable values to the $Zn_{0.88}Mn_{0.12}O$/ZnO heterostructure without Mg doping [8]. Note that high crystallographic quality is maintained even when x=0.15. Therefore, there are no existence of second phases and deterioration of crystallo- graphic quality. Furthermore, by using a reciprocal space mapping (RSM) measurement near $\left(20\bar{2}5\right)$ diffraction for $Zn_{0.73}Mg_{0.15}Mn_{0.12}O$/ZnO heterostructure, we confirmed that the lattice constant along *a* axis for $Zn_{0.73}Mg_{0.15}Mn_{0.12}O$ layer is precisely identical to that of ZnO, as shown in Fig. 2 (b), indicating that the $Zn_{0.73}Mg_{0.15}Mn_{0.12}O$ layer is pseudo-morphically grown on the ZnO buffer layer. The shift of lattice constant along *c* axis (Δc) as a function of Mg concentration (x) was compared with that for $Zn_{1-x}Mg_xO$ thin films grown on ZnO (0001) substrates reported by Nishimoto *et al.*[12], and is shown in Fig. 2 (c). The lattice constant along *c* axis decreases with Mg concentration. The tendency of x dependence on Δc for $Zn_{0.88-x}Mg_xMn_{0.12}O$ is identical to that for their $Zn_{1-x}Mg_xO$ thin films. As described above, the XRD analyses of $Zn_{0.88-x}Mg_xMn_{0.12}O$/ZnO hetero-structures suggested the substitution of Mg^{2+} ions with smaller ionic radius than Zn^{2+} ions at Zn^{2+} sites.

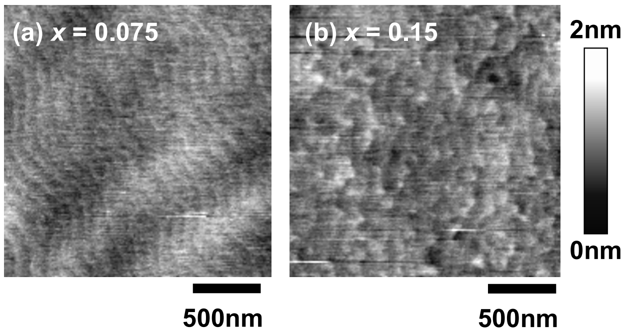

Fig.1 AFM images of the surfaces for $Zn_{0.88-x}Mg_xMn_{0.12}O$/ZnO heterostructures with x= (a) 0.075 and (b) 0.15.

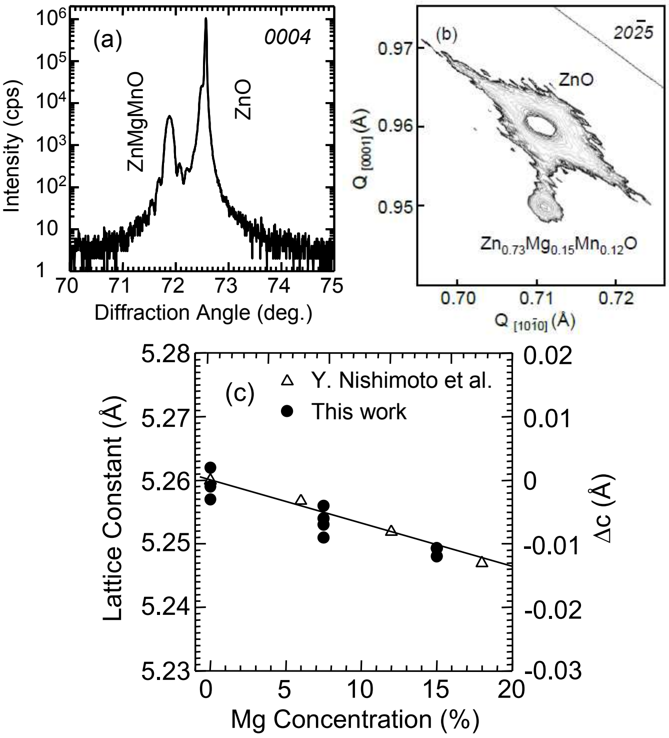

Fig.2 (a) 2θ-ω scanned XRD profiles and (b) RSM for $Zn_{0.88-x}Mg_xMn_{0.12}O$/ZnO heterostructure with x=0.15. (c) Lattice constants along *c* axis (open symbols) as a function of Mg concentration x. Triangle symbols correspond to the shift of lattice constants along *c* axis (Δc) for $Zn_{1-x}Mg_xO$ thin films reported by Nishimoto *et al.*[12].

Secondary, an existence of carrier confinement effect at the $Zn_{0.88-x}Mg_xMn_{0.12}O$ /ZnO heterointerface was discussed using $Zn_{0.88-x}Mg_xMn_{0.12}O$/ ZnO modulation-doped heterostructures. Figure 3 shows the temperature dependence of the sheet carrier concentration (n_s) and electron mobility (μ) for the $Zn_{0.88-x}Mg_xMn_{0.12}O$/ZnO modulation- doped heterostructures with x=0.075 fabricated. A target with Al concentration of 0.05 % was used for a fabrication of the doping layer. Here, d_s and d_d are 11 nm and 49 nm, respectively. The sheet carrier concentration (n_s) decreases with decreasing temperature from 300 to 80 K, suggesting that the parallel conduction in the substrate is involved in the carrier transport in this range, as described in previous paper [7]. Below 80 K, the heterostructure shows very little dependence of n_s. At 10 K, n_s is 5.1×10^{12} cm^{-2}. The electron mobility (μ) increases with decreasing temperature and show 800 cm^2/Vs at 10 K, suggesting that the two-dimensional (2D) electron layer is formed at the $Zn_{0.88-x}Mg_xMn_{0.12}O$/ZnO heterointerface with x=0.075. We have already reported that the carrier confinement effect at the $Zn_{0.88}Mn_{0.12}O$/ ZnO heterointerface [6-8]. It is also expected that the $Zn_{0.88-x}Mg_xMn_{0.12}O$ layer acts as a magnetic barrier and leads the spin-dependent transport in the $Zn_{0.88-x}Mg_xMn_{0.12}O$/ZnO heterostructures.

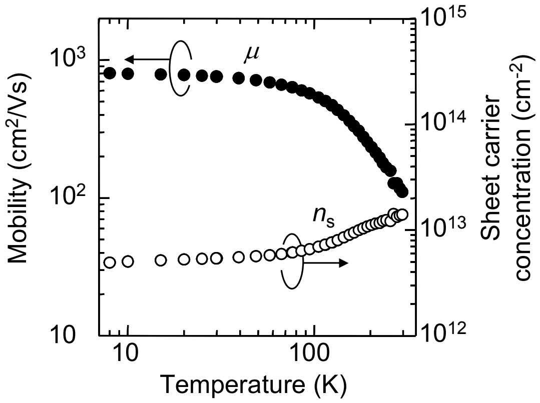

Fig. 3 Temperature dependence of μ and n_s.

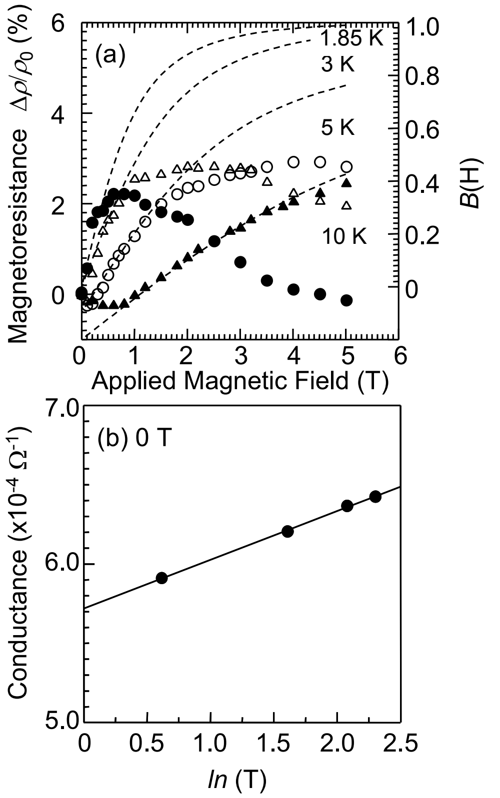

Fig. 4 (a) Parallel-field MR measured at 1.85 K (closed circles), 5 K(open circles), and 10 K (closed triangles). Broken lines represent a Brillouin function. We fitted the Brillouin function to the MR at 10 K, because a large negative MR is not included. (b) Temperature dependence of zero-field conductance. Solid line represents a fitting line using Eq. (2).

Finally, the magneto-transport properties of the $Zn_{0.88-x}Mg_xMn_{0.12}O$/ZnO heterostructure, the MR measurement were investigated. Figure 4 (a) show the MR for the $Zn_{0.88-x}Mg_xMn_{0.12}O$/ZnO modulation-doped heterostructures with x=0.075 at different temperatures. A positive MR is observed in the temperature range from 1.85 K to 10 K. The magnitude of a positive MR below 0.5 T decreases with increasing temperature. Furthermore, the positive MR is well fitted using the Brillouin function for J=5/2 expressed as the following Eq. (1).

$$B(H)=\frac{2J+1}{2J}\coth\left(\frac{2J+1}{2J}x\right)-\frac{1}{2J}\coth\left(\frac{1}{2J}x\right), \tag{1}$$

where x is $g\mu_B JH/k_B T$. We have already reported the mechanism for the Brillouin function-like-positive MR in Ref. [9]. For the $Zn_{0.88-x}Mg_xMn_{0.12}O$/ZnO modulation-doped heterostructures with x=0.075, it is also supposed that the different penetration probability of wave function of up-spin carriers and down-spin carriers in ZnO channel into the magnetic barrier layer leads to the spin splitting in ZnO nonmagnetic layer. Furthermore, a component of negative MR is observed above 0.5 T at 1.85 K. As shown in Fig. 4 (b), we found that the zero-field conductance (σ) over a temperature range of 1.85 − 10 K is proportional to the temperature. Therefore, it is suggested that there does not exist strong localization [16] and the magnetic polaron formation [17] at least above 1.85 K, but a weak localization effect [18] and electron-electron interaction [19] might be responsible for the negative MR. The weak localization effect is expressed by

$$\Delta\sigma=\frac{\alpha e^2}{2\pi^2\hbar}\ln T, \tag{2}$$

where α is a coefficient, which should be one when the spin-orbit and magnetic scatterings. but exist weak localization [20]. Here, α is responsible for the dimensionality of the electron transport. The value of α was evaluated to be 2.5, suggesting the contribution of the weak localization in three-dimensional system.

Conclusions

The $Zn_{0.88-x}Mg_xMn_{0.12}O$/ZnO heterostructures were fabricated on ZnO $(000\bar{1})$ single-crystal substrates by PLD. Their surface morphology, crystallographic quality, and electrical and magneto-transport properties were investigated. The $Zn_{0.88-x}Mg_xMn_{0.12}O$ layer with x=0.15 had a surface with step-and-terrace structure and no existence of second phases. The $Zn_{0.88-x}Mg_xMn_{0.12}O$/ZnO modulation-doped heterostructure with x=0.075 showed the Brillouin function-like-MR behavior, similarly to $Zn_{0.88}Mn_{0.12}O$/ZnO heterostructures without Mg doping.

Acknowledgements

This research was partially supported by a Ministry of Education, Culture, Sports, Science and Technology (MEXT) Grant-in-Aid for Scientific Research on Priority Areas #19033005 and JSPS Fellows #20-5643.

References

[1] T. Dietl, H. Ohno, F. Matsukura, J. Cibert and D. Ferrand: Science Vol. 287 (2000), p. 1019

[2] K. Sato and H. Katayama-Yoshida: Jpn. J. Appl. Phys. Vol. 39 (2000), p. L555

[3] T. Fukumura, Z. Jin, A. Ohtomo, H. Koinuma and M. Kawasaki: Appl. Phys. Lett. Vol. 75 (1999), p. 3366

[4] T. Andrearczyk, J. Jaroszyński, G. Grabecki, T. Dietl, T. Fukumura and M. Kawasaki: Phys. Rev. B Vol. 72 (2006), p. 121309

[5] T. Edahiro, N. Fujimura and T. Ito: J. Appl. Phys. Vol. 93, (2003), p.7673

[6] K. Masuko, A. Ashida, T. Yoshimura and N. Fujimura: J. Appl. Phys. Vol. 103 (2008), p. 07D124

[7] K. Masuko, H. Sakiyama, A. Ashida, T. Yoshimura and N. Fujimura: Phys. Stat. Sol. (c) Vol. 5 (2008), p. 3107

[8] K. Masuko, A. Ashida, T. Yoshimura and N. Fujimura: J. Vac. Sci. Technol. Vol. 27 (2009), p. 1760

[9] K. Masuko, A. Ashida, T. Yoshimura and N. Fujimura: Phys. Rev. B Vol. 80 (2009), p. 125313

[10] A. Ohtomo, M. Kawasaki, T. Koida, K. Masubuchi, H. Koinuma, Y. Sakurai, Y. Yoshida, T. Yasuda and Y. Segawa: Appl. Phys. Lett. Vol. 72 (1998), p. 2466

[11] A. Ohtomo, M. Kawasaki, I. Ohkubo, H. Koinuma, T. Yasuda and Y. Segawa: Appl. Phys. Lett. Vol. 75 (1999), p. 980

[12] Y. Nishimoto, K. Nakahara, D. Takamizu, A. Sasaki, K. Tamura, S. Akasaka, H. Yuji, T. Fujii, T. Tanabe, H. Takasu, A. Tsukazaki, A. Ohtomo, T. Onuma, S. F. Chichibu and M. Kawasaki: Appl. Phys. Express Vol. 1 (2008), p. 091202

[13] K. Masuko, A. Ashida, T. Yoshimura and N. Fujimura: J. Appl. Phys. Vol. 103 (2008), p. 0433714

[14] D.R. Lide : *84th CRC Handbook of Chemistry and Physics*, (CRC Press, United States 2003).

[15] J. A. Gaj, W. Grieshaber, C. Bodin-Deshayes, J. Cibert, G. Feuillet, Y. Merle d'Aubigne and A. Wasiela: Phys. Rev. B Vol. 50 (1994), p. 5512

[16] J. Jaroszyński, T. Andrearczyk, G. Karczewski, J. Wróbel, T. Wojtowicz, D. Popović and T. Dietl: Phys. Rev. B Vol. 76 (2007), p. 045322

[17] M. Sawicki, T. Ditel, J. Kossut, J. Igalson, T. Wojtowicz and W. Plesiewicz: Phys. Rev. Lett. Vol. 56 (1986), p. 508

[18] S. Hikami, A. I. Larkin and Y. Nagaoka: Prog. Theor. Phys. Vol. 63 (1980), p. 707

[19] B. L. Altshulter, A. G. Aronov and P. A. Lee: Phy. Rev. Lett. Vol. 44 (1980), p. 1288

[20] A. Goldenblum, V. Bogatu, T. Stoica, Y. Goldstein and A. Many: Phy. Rev. B 60 (1999), p. 5832

doi:10.4028/www.scientific.net/AST.75.9

Transparent conductors on polymer films

Matthias Fahland[1, a], Tobias Vogt[1,b], Alexander Schoenberger[1c] and Sindy Mosch[2d]

1 Fraunhofer Institute of ElectronBeam and Plasma Technology (FEP) Winterbergstrasse 28, 01277 Dresden, Germany

[2]F Fraunhofer Institute of Ceramic Technology and Systems (IKTS) Winterbergstrasse 28, 01277 Dresden, Germany

[a]matthias.fahland@fep.fraunhofer.de, [b]tobias.vogt@fep.fraunhofer.de, [c]alexander.schoenberger@fep.fraunhofer.de, [d]sindy.mosch@ikts.fraunhofer.de

Keywords: Sputtering, PECVD, web coating, transparent conductors.

Abstract. The paper will present a review of different solutions for transparent conducting electrodes on flexible substrates. The analysis of the present situation reveals a gap for low sheet resistance electrodes.

Two new approaches to the problem will be presented. The first one is a novel technology for the deposition of zinc oxide on polyethylene terephtalate film. The intention for this process is the establishment of a low cost coating in a roll-to-roll machine. Silicon was used as the dopant material with a concentration varying in different samples between 1 and 4 %. The optimum parameters provided a transparent layer with a sheet resistance of 16 Ωsqu. Metal grids are a second promising approach for achieving low sheet resistance electrodes. The combination of these grids with transparent conducting oxides (TCO) will be presented. The TCO were deposited under vacuum in a roll-to-roll coating machine. The grids were applied by aerosol jet printing and subsequent tempering of the film.

Introduction

Transparent conducting electrodes on flexible substrates are a major component for various optoelectronic devices, such as touch screens, e-books, electroluminescent displays or solar cells. The latter have gained significant importance over the last decade. Therefore the needs of these cells will preferably be addressed in this article. A general overview about the requirements to transparent electrodes for different devices is given in [1].

All types of thin film solar cells have already been applied on flexible substrates [2],[3]. In every case a transparent electrode is necessary to open the pathway of the light into the cell. The deposition of a well suited transparent electrode is always a challenge. Besides the conductivity and the transparency the electrode has to fulfill requirements with respect to environmental stability and must have a reasonable price.

Several types of transparent electrodes have been developed in the past. An overview is given in table 1.

Table 1: Overview of different types of transparent electrodes

Type	Conduction principle	Remarks
Single layer ITO	Free electron gas in heavily doped semiconductor with 3.44 eV bandgap	Standard solution for most applications on flexible polymer films;
Single layer doped ZnO	Free electron gas in heavily doped semiconductor with 3.44 eV bandgap	Elevated substrate temperature during deposition required
Dielectric-metal-dielectric-stacks	Conduction is maintained by a thin silver layer (8…14 nm)	Sheet resistance below 10 Ωsqu can easily be achieved, Environmental stability problems
PEDOT:PSS	Charge carrier hopping between localized states	It is difficult to achieve sheet resistance below 50 Ωsqu because of absorption in the red spectral range
CNT blends	Increased conductivity along the CNT axis	Still under investigation for low sheet resistance
Metal network	Conductivity along metal lines	Promising solution, under investigation for low sheet resistance

The approaches are in quite different stage of technological maturity. The most common solution is a single layer of indium tin oxide (In_2O_3 90wt%-SnO_2 10wt%, shortly ITO). This material has become a standard in the flat panel industry. However, on polymer substrates the deposition temperature cannot be set as high as it would be favourable for achieving optimum material properties. Nonetheless, ITO shows a reasonable specific resistance even if it is applied at room temperature on polymer substrates. One can achieve values for the specific resistance ρ in the range between 5×10^{-4} Ωcm and 8×10^{-4} Ωcm. Due to both economic and technological reasons the minimum sheet resistance R_{sh} which can be achieved by single layer ITO is in the range of 25 Ω_{squ}.

The sheet resistance values of single layer TCO on polymer films is still too high for various technical devices. Alternative approaches are silver based multilayer stacks, metal grids and blends based on carbon nanotubes and organic conductors. In the formula (1)

$$\sigma = \frac{\alpha}{R_{sh}\ln(T+R)} \qquad (1)$$

is defined as a figure-of-merit for transparent conducting oxides[4], α representing the absorption coefficient, T and R the total transmittance and reflectance, respectively . However, taking into account different types of transparent electrodes, except single layer TCO, is seems useful to express the performance in a two-dimensional T-R_{sh}-plane (figure1).

A clear picture about the optical performance of the transparent electrodes one can get by redefining the transmittance by

$$T_{sol} = \frac{\int_{300\,nm}^{1200\,nm} EQE(\lambda)T(\lambda)d\lambda}{\int_{300\,nm}^{1200\,nm} EQE(\lambda)d\lambda} \qquad (2)$$

($EQE\ (\lambda)$being the external quantum efficiency of the cell type. In figure 1 a two dimensional representation for transmittance and sheet resistance is presented. The transmittance T_{sol} in figure 1 was determined using a typical external quantum efficiency for organic solar cells [5].

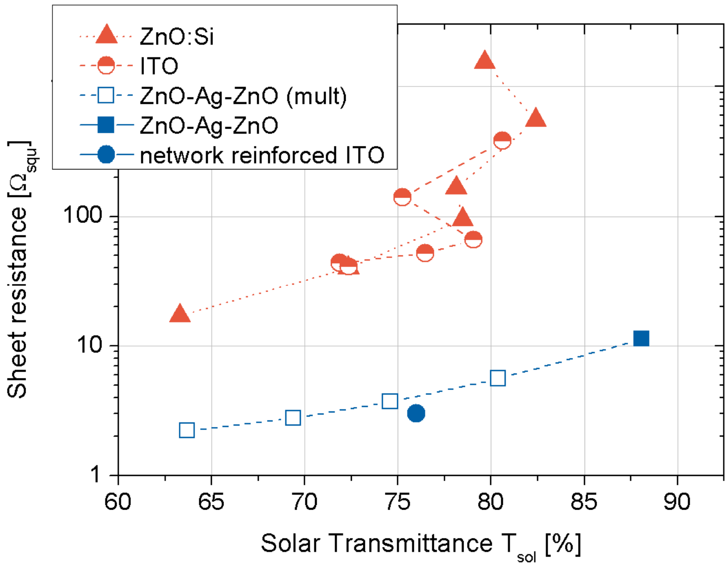

Fig 1: Two dimensional representation of the performance of different types of transparent electrodes, The solar transmittance was determined using the external quantum efficiency taken from [5].

Following figure 1 it becomes evident that there are still limited possibilities to make highly transparent electrodes in the range of 10 Ω_{squ} and below. However, this is exactly the range of interest for potential markets like large scale organic solar cells or OLED based lamps.. One single layer is obviously not sufficient. The best properties exhibit combined approaches like silver based multilayer stacks with one silver layer (ZnO-Ag-ZnO in figure 1). They have the additional advantage that they can be deposited by well known processes in roll-to roll coating machines. The total thickness of the stacks does not exceed 90 nm which allows a large scale production for a low price. This approach was discussed in preceding papers [6].

This paper will focus both on the sputter deposition of ZnO:Si and on the combination of sputtering and aerosol jet printing for making a network reinforced ITO. Both methods are new approaches to the problem. The results presented in this paper are already included in the graph in figure 1.

Experimental

The investigations have been carried out in a laboratory roll-to-roll coating machine (figure 2).

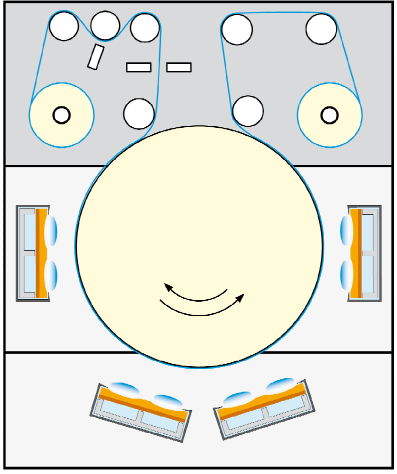

Fig 2: Schematic drawing of roll-to–roll coating machine used for the experiments

The substrate was a film of polyethylenterephalate Melinex 400 (DupontTeijinFilms). The thickness of the film was 75 µm, the coating width 200 mm. Polyethlene naphtalate Teonex Q83 was used for the samples of the network reinforced ITO.

The chilling drum was generally kept at a temperature of 20°C during the deposition. Two magnetrons (Sierra Applied Science) were placed in the lower chamber of the machine. Each had a target surface of $349\text{x}127\text{mm}^2$ oriented towards the surface of the chilling drum.

The vacuum chamber was evacuated to a base pressure of $1\text{x}10^{-3}$ Pa for all experiments. During the coating runs a constant argon flow of 120 sccm was introduced by a mass flow controller, resulting in a partial pressure of 0.4 Pa.

Two ceramic targets were used for the ITO deposition. The powering was done by two DC power supplies (ENI DCG200). The optimum oxygen flow was adjusted by a mass flow controller (MKS Instruments).

The experimental setup was changed for the zinc oxide coatings. A schematic drawing of the lower chamber for these experiments can be seen in figure 3.

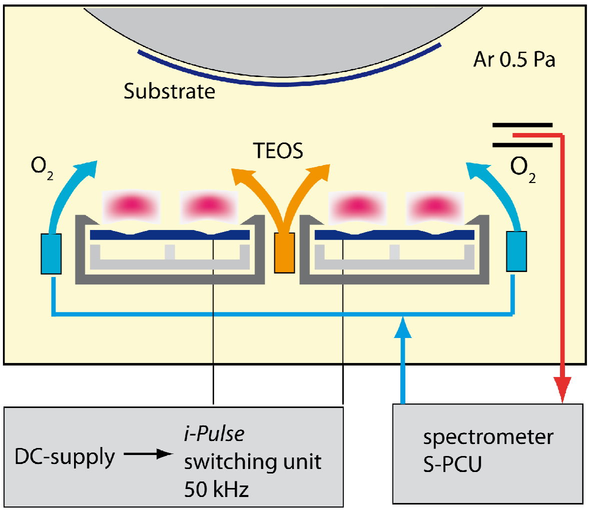

Fig 3: Schematic drawing of the PVC/CVD hybride process used for the ZnO:Si deposition

Metallic zinc targets with 99.995% purity were used. The two magnetrons were connected to a bipolar power supply consisting of two DC channels with a maximum rating of 6 kW (Pinnacle, Advanced Energy) and a UBS-C2 switching unit (Fraunhofer FEP). The total power input for the experiments discussed in that paper was 6 kW. The switching unit realized the bipolar mode, i.e.

each magnetron was acting alternatively as an anode or the cathode. The duty cycle was 9 µs and 1 µs for on-time and off-time, respectively. This resulted into a switching frequency of 50 kHz.

The oxygen flow was regulated by a closed loop control. The optical emission spectrum of the plasma was detected by a spectrophotometer (USB 4000, OceanOptics). The intensities of both the zinc emission line at 636 nm and the argon emission line at 812 nm were used to calculate the ratio of their intensities. The parameter I(636 nm) / I(812 nm) is formed. This value served as the leading value in the closed loop control. The oxygen flow was introduced be a piezoelectric valve. The flow level was adjusted in such a way that the leading value corresponded to the required setpoint.

The doping of the zinc oxide was realized by the introduction of a silicon containing monomer. Conductive layers were achieved by using tetraethylorthosilicate (TEOS). The flow of this monomer was regulated by a combination of a flow meter (Bronkhorst) and a vaporizing valve. This setup allowed the adjustments of the flow levels between 2 sccm and 36 sccm. The monomer was mixed with the argon prior to the introduction into the vacuum chamber. The location of the inlet can be seen in figure 3.

Results

Reactive sputtering of zinc oxide starting from a metallic target shows the typical hysteresis behavior. It is represented by the graph with the squares in figure 4.

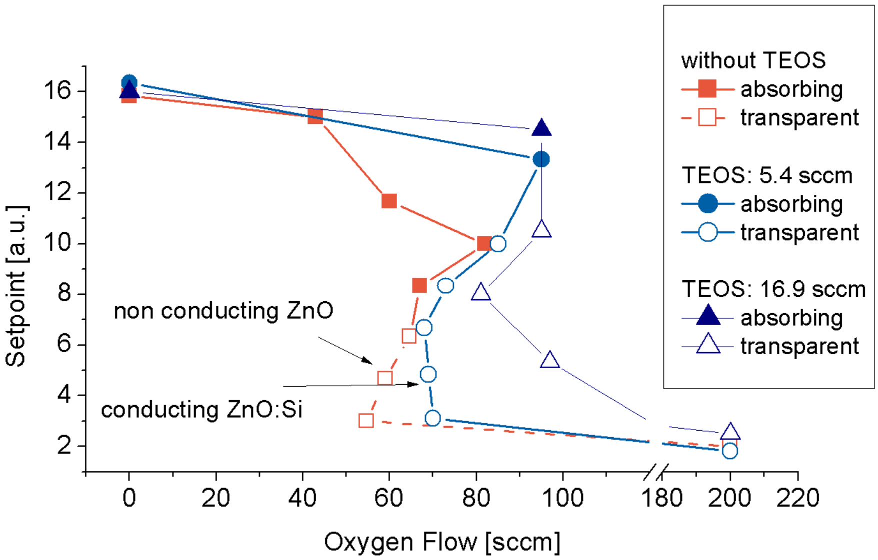

Fig 4: Process characteristic for the ZnO:Si deposition PVD/CVD hybride process. The red graph represents conventional reactive sputtering. The blue graphs represent the hybride process.

The open squares below setpoint 8 denote transparent layers on the polymer substrates. In contrast to that, the closed squares denote either metallic of opaque samples. This characteristic plot is shifted if TEOS is introduced into the chamber. Two characteristic changes can be observed.

First, the range of transparent layers is extended towards higher setpoint values compared to the TEOS-free sample. This can be explained by the fact that the additional TEOS molecules partly contribute the coverage of the zinc target and thus reduce the metallic zinc rate.

Second, the oxygen flow values are shifted to higher values. This can be explained by the assumption that a part of the introduced oxygen is consumed by the oxidation of TEOS fragments which are formed by the plasma.

It was found by EDX analysis that the increase of the TEOS flow increased the silicon content in the layers. The optimum electrical properties have been achieved for the ratio Si/(Zn+Si) = 0.04.

The electrical properties of the material ZnO:Al were compared to conventional ITO. An overview of typical parameters is given in table 2.

Table 2: Comparison between ITO und ZnO:Si; values taken from experiments at the roll coater shown in figure 2..

Property	ITO	ZnO:Si
Minimum sheet resistance	25	17
Mininum specific resistance	5.1x 10^{-4} Ωcm	2.3x 10^{-3} Ωcm
Hall mobility	23 cm^2 V^{-1} s^{-1}	9 cm^2 V^{-1} s^{-1}
Carrier density	5 x 10^{20} cm^3	2.5 x 10^{20} cm^3

The striking difference between the two materials is the fact that ITO has its lowest specific resistance at a thickness of 100 nm. Both for thinner and for thicker layers the specific resistance is rising. This is a special feature of ITO deposited on room temperature substrates.

The situation for ZnO:Si is different. For this material the specific resistance becomes lower with increasing layer thickness. By XRD it was confirmed that this behaviour can be explained by the increase of crystallinity with increasing layer thickness. This leads to a higher carrier mobility and hence to an improved conductivity. The lowest sheet resistance achieved by single layer ZnO:Si was 17 Ω_{squ}.

This value is lower than for ITO, however still much higher than it is needed for several contemporary applications. Therefore a combination between aerosol printing and ITO deposition was investigated. A thin layer of ITO (20nm) was reinforced by a network of silver wires. The single lines had a width of 50 µm and a distance between each other of 500 µm. The baking temperature was approximately 200 °C. These samples achieved a sheet resistance of 3 Ωs_{qu} The result is already shown in figure 1.

The transmittance different vacuum coated transparent electrodes is shown in figure 5.

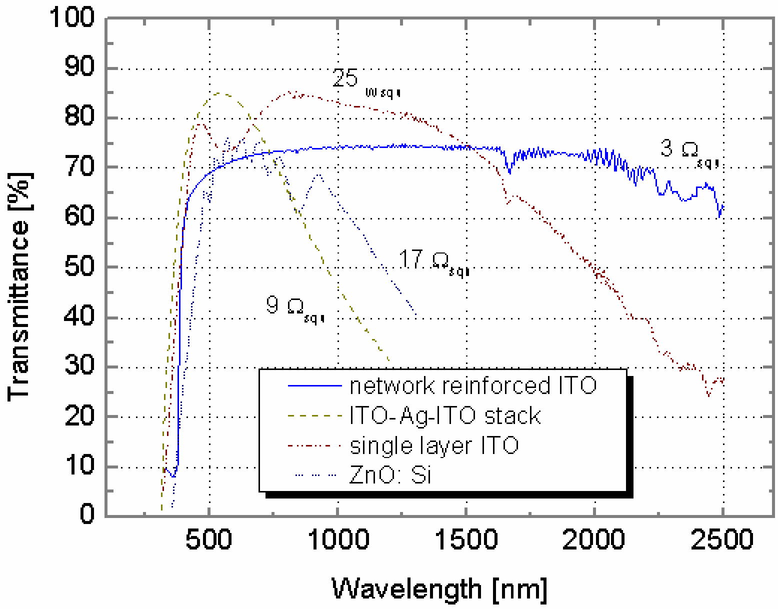

Fig 5: Transmittance spectra of different types of transparent electrodes

It is evident that the network reinforced ITO combines the low sheet resistance with a high transmittance extending far to the infrared. Therefore this approach is ideally suited for solar cell applications harvesting energy in this spectral range.

Summary

Achieving low sheet resistance electrodes on temperature sensitive plastic film is a challenge. The substrates cannot be kept at elevated temperature during the deposition. Two new approaches have been presented. The material ZnO:Si was deposited using a novel PVD/CVD hybride process. The specific resistance of the layers drops with increasing thickness. The minimum sheet resistance achieved with this approach was 17 Ω_{squ}. A combination between ITO sputtering and aerosol jet printing of metal based networks proved to be a more promising way to achieve low sheet resistance values. The best samples showed 75% transmittance for 3 Ω_{squ}.

Literature References

[1] M. Fahland, T. Vogt, W. Schoenberger, N. Schiller, Thin Solid Films 516 (2008) 5777-5780

[2] M. Pagliaro, G. Palmisano, R. Ciriminna: “Flexible Solar Cells” Wiley-VCH, ISBN 978-3-537-32375-3

[3] M. Sibinski, Z. Lisik, A. Iwan, D. Sek Proceedings of 21st European Photovoltaic Solar Energy conference 1878-1880

[4] G.J. Exharhos, X.-D. Zhou, Thin Solid Films 515 (2007) 7025-7052

[5] SPIE 10.1117/2.1200601.0077

[6] M. Fahland, P. Karlsson, C. Charton Thin Solid Films 392 (2001) 334-337

doi:10.4028/www.scientific.net/AST.75.16

Pathways towards p-type oxide layers for optoelectronic applications

Bernd Szyszka[1,a], Christina Polenzky[1,b], Peer Loebmann[2,c],
Stefan Goetzendoerfer [2,d], Christian Elsaesser [3,e], Wolfgang Koerner [3,f]

[1] Fraunhofer Institute for Surface Engineering and Thin Films IST, Bienroder Weg 54e, 38108 Braunschweig, Germany

[2] Fraunhofer Institute for Silicate Research ISC, Neunerplatz 2, 97082 Wuerzburg, Germany

[3] Fraunhofer Institute Fraunhofer Institute for Mechanics of Materials IWM, Woehlerstr. 11, 79108 Freiburg, Germany

[a]bernd.szyszka@ist.fraunhofer.de, [b]christina.polenzky@ist.fraunhofer.de,
[c]peer.loebmann@isc.fraunhofer.de, [d]stefan.goetzendoerfer@isc.fraunhofer.de,
[e]christian.elsaesser@iwm.fraunhofer.de, [f]wolfgang.koerner@iwm.fraunhofer.de

Keywords: p-type oxides, first principles density functional theory, sol-gel route, hollow cathode gas flow sputtering, Seebeck measurements

Abstract. State of the art optoelectronic applications such as thin film solar cells, flat panel displays, and light emitting diodes suffer from the non-availability of p-type oxide materials on the industrial scale. Novel technologies such as transparent electronics, UV light emitting diodes, and improved thin film solar cells using wide band gap p-type oxide layers as front contact will be available once p-type oxide layers with proper layer and interface properties can be obtained on an industrial scale.

In this paper, we report on our progress towards p-type oxide layers for industrial applications. We address the first principles density functional theory modeling of ZnO based layers where a pathway towards p-conductivity is seen taking the nitrogen doping of grain boundaries into account.

The second part of the paper is on the synthesis of p-type Delafossite layers such as $CuCr_{1-x}Al_xO_2$:Mg by Sol-Gel and $CuCrO_2$ by hollow cathodes gas flow sputtering. We report on the deposition processes and film properties obtained. Both methods reveal p-type conductivity by means of Seebeck-coefficient measurements.

Introduction

Transparent and conductive films (TCF) are key components for many electronic and optoelectronic components being relevant for the sustainable growth of our society. The most prominent applications of TCFs are in large area glazing, where the spectral selective properties of transparent conductors are used to provide low emissivity and sun-control-features, and in flat panel displays, where transparent and conductive oxides (TCOs) serve as n-type layers to provide electrical contact to the pixels. Since the last decade, challenging applications for TCFs appear in the emerging fields of (i) thin film photovoltaics, (ii) organic lighting, (iii) printed electronics and (iv) oxide electronics. These new developments open up multiples demands on the development of TCF, since novel layer properties such as amorphous growth, integration of light scattering, control of work function, control of defect states to utilize TCOs as active semiconductive oxides (ASOs) as well as cost driven constraints such as device integration, low cost large area manufacturing and patterned deposition using sustainable materials become important.

The Fraunhofer society addresses these needs via the cooperation of institutes providing expertise in 1st principle material modelling (FhG-IWM), thin film preparation via PVD (FhG-IST) as well as wet chemical techniques (FhG-ISC). Starting from density functional modelling of oxides and oxide metal interfaces including grain boundaries, we develop novel processes such as high power pulse magnetron sputtering (HPPMS), sol gel pad printing and novel materials such as p-type delafossite film processable at low temperature.

Simulation of TCO properties using ab-initio DFT simulations

The doping of wide band gap semiconductors using either cationic or anionic substitution with elements of higher or smaller valence or by oxygen vacancies and interstitials is the essence of the TCO technology.

Understanding the dopant incorporation and its impact on the modification of the electronic structure is a key for new tailored TCFs and improved devices with optimized electronic interfaces.

To understand the doping mechanisms in TCOs such as doped ZnO, we perform band structure simulation using the density functional theory.

We model the electronic band structure of ZnO doped with N, P, Al or Ga and for rutile or anatase TiO2 films doped with Nb and other dopants. Furthermore, we investigate into the defect formation energies for various dopants and grain boundaries.

The first step is to model the pseudo potentials for the free elements Zn, O, Ti and the dopants of interest using the DFT approach for free atoms. Using these pseudo potentials, the model systems ZnO wurtzite phase and TiO2 anatase and rutile have been realized as atomistic single crystal models in the second step. The minimization of the total energy has been performed using the LDA (local density approximation) by relaxation of the structural parameters a, c/a and u of the single crystal unit cell.

An overview on the model systems investigated is given in Table 1. This paper addresses some examples for the DFT modeling of ZnO.

Table 1:TCO systems and grain boundaries chosen for the DFT modeling of the band structure

System	Grain boundary	Symmetry axis	Modeled super cells	γ [J/m^2]	
Wurtzite ZnO	$(10\bar{1}0)[10\bar{1}0]$ $\Sigma 1$	$[10\bar{1}0]$ / 180°	80	0.17	**GB1**
	$(12\bar{3}0)[0001]$ $\Sigma 7$	$[0001]$ / 21.79°	56 / 112	1.81/1.88	**GB2**
	$(23\bar{5}0)[0001]$ $\Sigma 19$	$[0001]$ / 13.17°	152	1.65	**GB3**
Rutile TiO$_2$	$(100)[100]$ $\Sigma 1$	$[100]$ / 180°	72	0.47	
	$(210)[001]$ $\Sigma 5$	$[001]$ / 36.87°	60 / 120	1.86/1.92	
	$(310)[001]$ $\Sigma 5$	$[001]$ / 53.13°	120	2.37	
Anatase TiO$_2$	$(100)[100]$ $\Sigma 1$	$[100]$ / 180°	72	0.64	
	$(120)[001]$ $\Sigma 5$	$[001]$ / 53.13°	120	2.10	
	$(021)[100]$ $\Sigma 5$	$[100]$ / 78.46°	120	0.89	
	$(031)[100]$ $\Sigma 5$	$[100]$ / 101.54°	120	2.36	

The calculation of the defect formation energies is a key point of the doping effect simulation. Figure 1 shows the dependence of defect formation energy on the location of the Fermi energy for different ZnO defects. p-type carriers can be generated via the addition of P or N on oxygen positions. However, when the Fermi energy decreases below a certain value, the generation of the compensating defect, O^{2+}_{vac} becomes energetically more favored which hinders p-conductivity in ZnO [1].

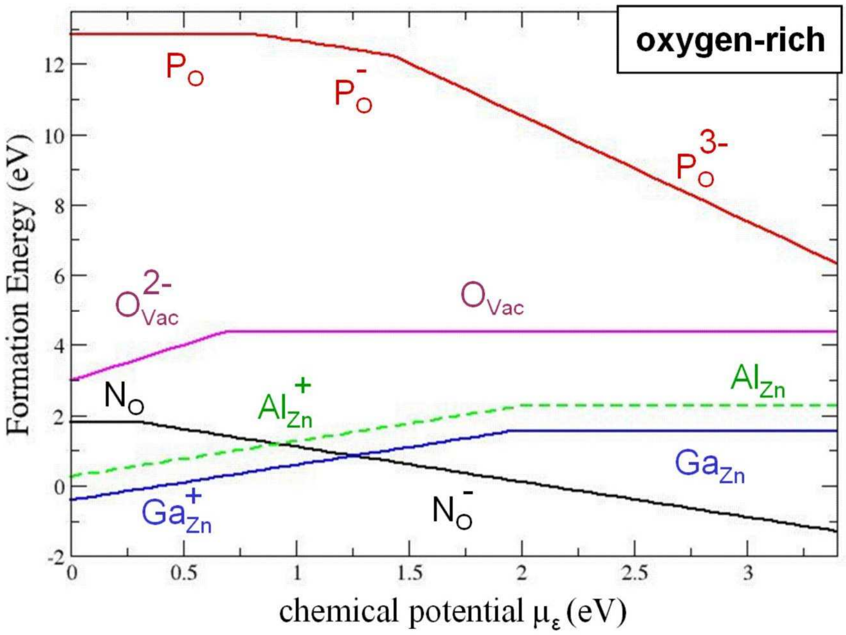

Figure 1: Dependence of defect formation energy on the location of the Fermi energy for different ZnO defects.

To study the effect of dopants in detail, it is necessary to model the band structure quantitatively correct. We have adopted the self interaction correction (SIC) to fit the experimental bandgap energy of $E_g = 3.4$ eV by changing the correction of Zn 3d, O 2s and O 2p orbitals. The former ones are fully corrected, the later one by 80 % to achieve a band gap energy of $E_g = 3.39$ eV.

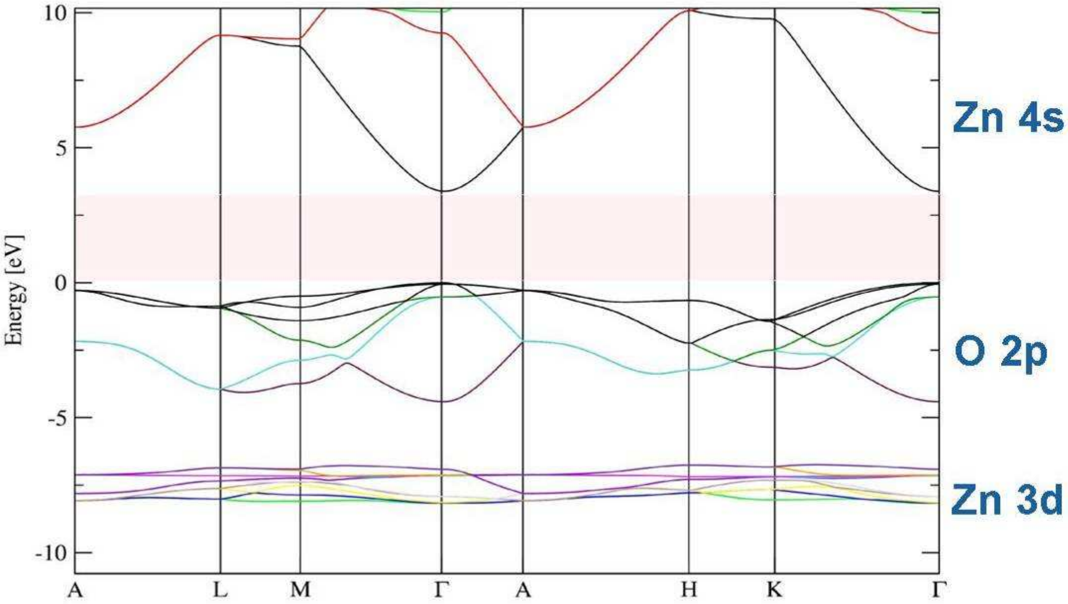

Figure 2: Band structure of ZnO taking the self interaction correction into account.

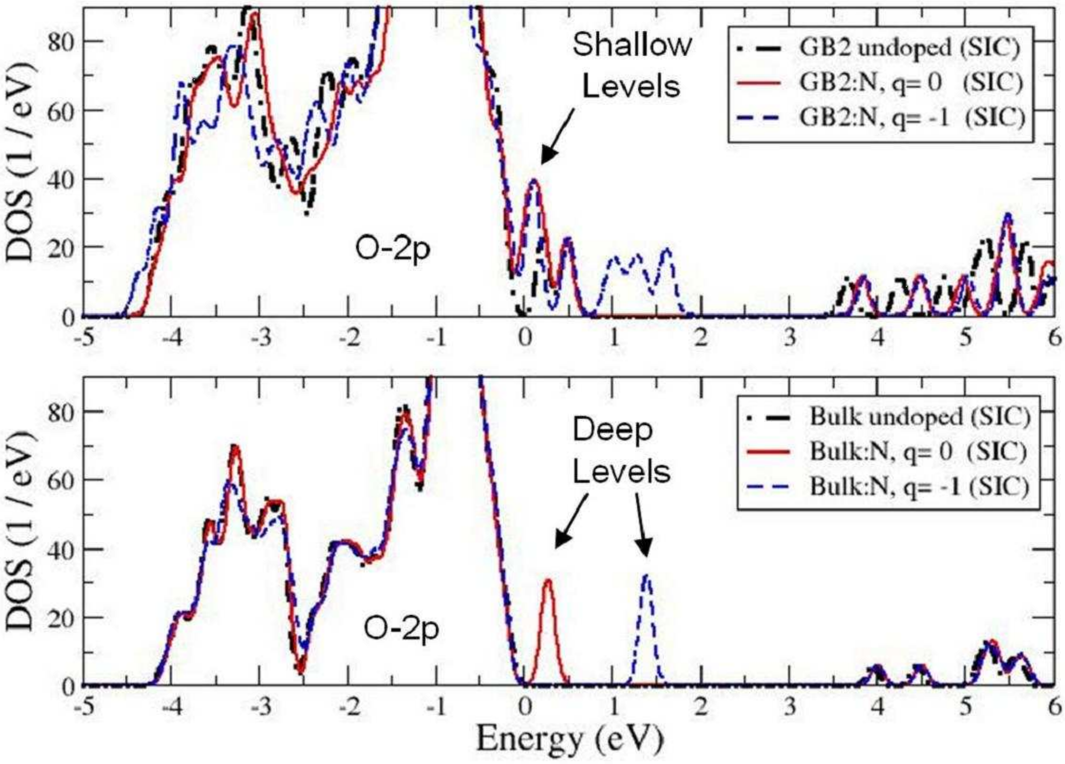

Figure 3: Total densities of states (DOS) for the bulk single crystal (lower panel) and a grain boundary GB2 (upper panel) of ZnO:N with different charge states of the dopant.

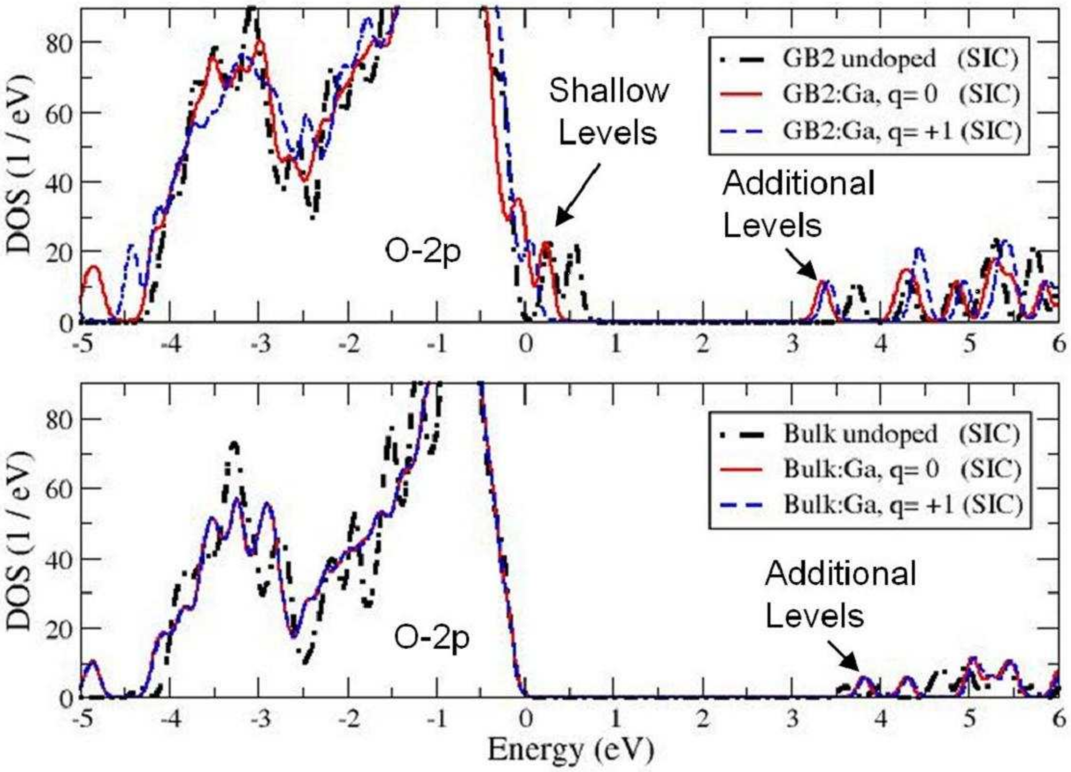

Figure 4: Corresponding total DOS for bulk and GB2 of ZnO:Ga.

The lower panel in Figure 3 shows the electronic-structure results for N doping of a bulk ZnO single crystal in terms of total densities of states (DOS). The doping yields deep states in the band gap which cannot serve as acceptor levels at room temperature. Therefore, the N bulk doping of ZnO is not an option to achieve p-type conductivity in the context of our model. The results for N doping of the ZnO grain boundary GB2 are shown in the upper panel of Figure 3. In this case, the deep insulated dopant levels merge to shallow acceptor levels which might be relevant for p-conductivity at room temperature. This finding reveals the importance of proper grain boundary doping for tailoring the properties of the material. Figure 4 shows corresponding DOS results for Ga doping of the bulk or the GB2 of ZnO. The additional levels indicate n-conductivity for both.

For a detailed report on our ab-initio investigation of dopant elements at grain boundaries in ZnO see Ref. [2].

p-type TCOs by Sol-Gel route

P-type TCOs open up the ability for transparent electronics including transparent diodes and transistors, UV optoelectronics and novel concepts for smart glazing and thin film photovoltaics. Our approach is to develop Delafossite based p-type TCOs compatible to low cost mass production by means of Sol-Gel and PVD coating.

The Sol-Gel routs starts with the synthesis of the appropriate Sol. Film deposition is by dip coating and subsequent pyrolysis and sintering processes. For specific information, see Ref. [3]. An example for the synthesis of $CuCrO_2$ delafossite films is shown in Figure 5. During pyrolysis in air, a transition occurs from cubic to tetragonal Spinel phase. When an appropriate intermediate state is reached, in this case for pyrolysis at 500 °C, the subsequent sintering in Ar allows for the further transition to the Delafossite phase. The phase purity is crucial since Spinel phase coatings are n-type. In the example shown here, optimum performance is achieved for sintering at 700 °C.

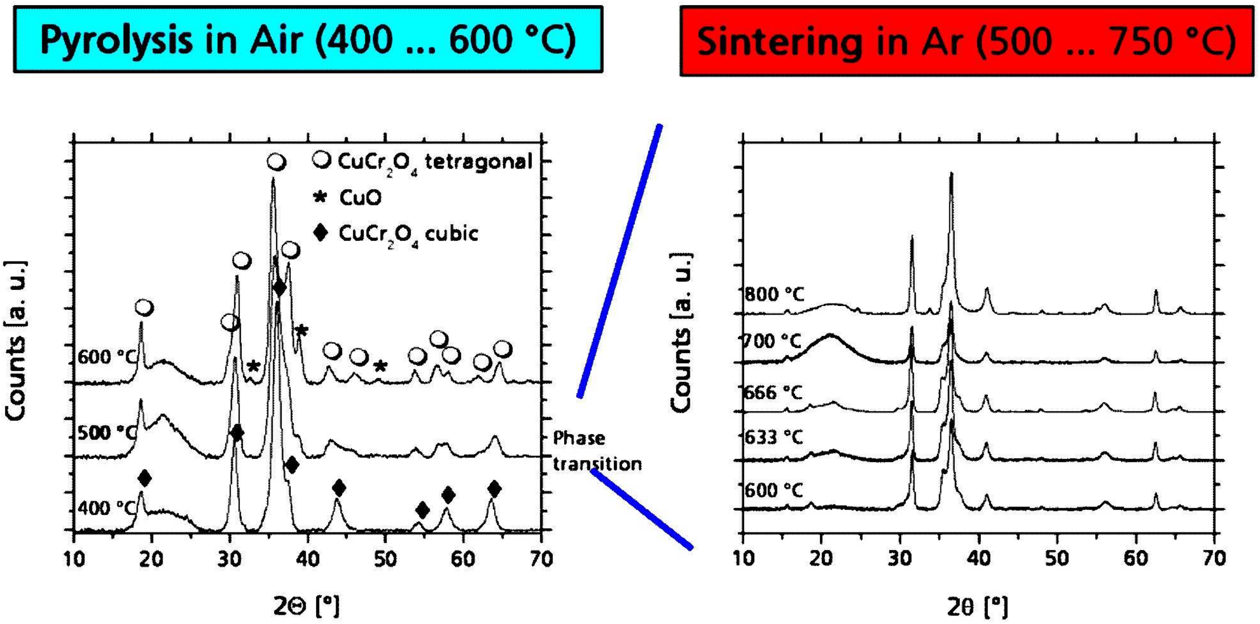

Figure 5: Sol-Gel synthesis of Delafossite p-type $CuCrO_2$ films.

The resistivity of the phase pure Delafossite $CuCrO_2$ films can be decreased via doping. Mg doping has shown to be applicable. The dependence of resistivity and transmittance on Mg content is shown in Figure 6.

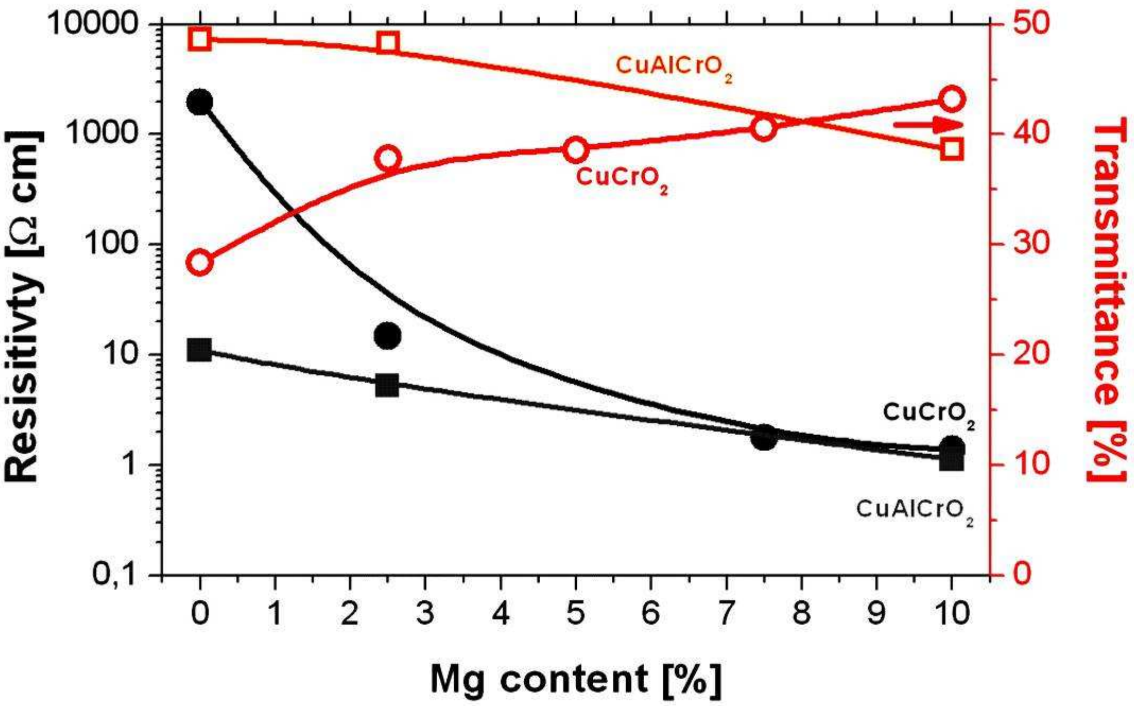

Figure 6: Mg-doping of $CuCrO_2$ and $CuCr_{1-x}Al_xO_2$ films.

The resistivity, optical transmission and Seebeck-coefficient of $CuCrO_2$ and $CuAl_{0.5}Cr_{0.5}O_2$ films oxidized in air at 400 °C and sintered in inert gas atmosphere at 700 °C are summarized in Table 2.

Table 2: Optical and electrical properties of $CuCrO_2$ and $CuAl_{0.5}Cr_{0.5}O_2$ films. The samples were oxidized in air at 400 °C before final sintering under inert gas atmosphere at the temperatures indicated.

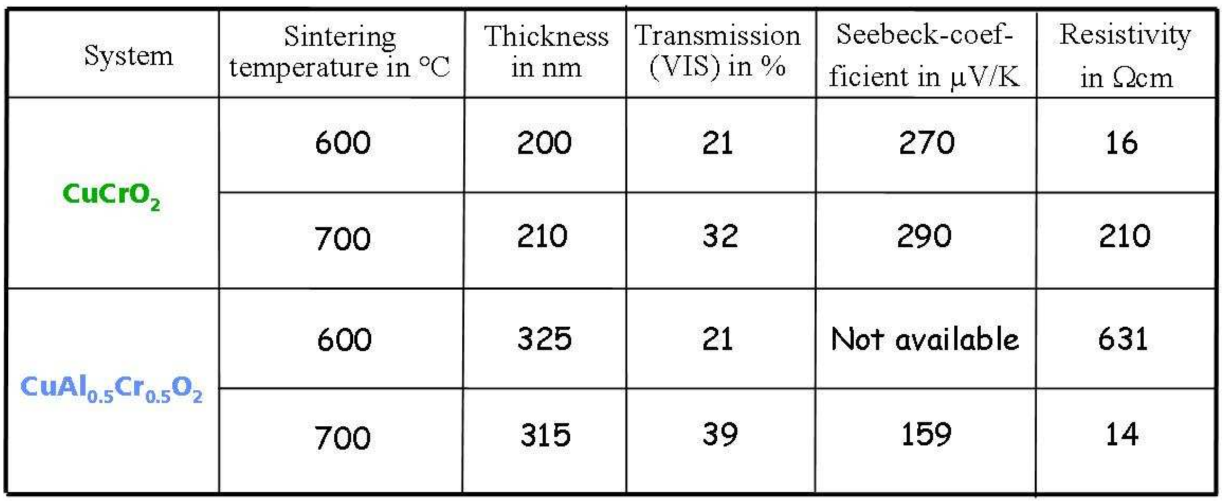

System	Sintering temperature in °C	Thickness in nm	Transmission (VIS) in %	Seebeck-coefficient in µV/K	Resistivity in Ωcm
$CuCrO_2$	600	200	21	270	16
	700	210	32	290	210
$CuAl_{0.5}Cr_{0.5}O_2$	600	325	21	Not available	631
	700	315	39	159	14

By further optimization of the Mg doping the resistivity of the CuCrO2 thin films could even be decreased to values around 1 Ohm cm.

A detailed discussion of all the results can be found in Ref. [4].

p-type TCOs by Hollow Cathode Gas Flow Sputtering

PVD opens up a 2nd pathway for large area deposition of p-type TCOs. We investigated into the deposition of $CuAlO_2$ and $CuCrO_2$ films by hollow cathode gas flow sputtering (GFS).

The main features of this process are a hollow cathode plasma and a particle transport via a gas flow. This process has many free parameters which give you the opportunity in controlling the stoichiometry of the resulting thin films in a wide range.

Fig. 7 shows the scheme of the gas flow sputtering process through a tube formed hollow cathode. The parts of the tube are the targets and consist of copper and aluminium. On the backside of the setup there is an inlet that provides an argon flow of 1 standard liter per minute. Combined with an ordinary pumping unit we have process pressures of around 0.5 mbar. A hollow cathode glow discharge is created in the inner side of the source. The sputtered particles are linked to the gas flow so that the surface of the target always remains clean and free of backscattered particles or reaction products.

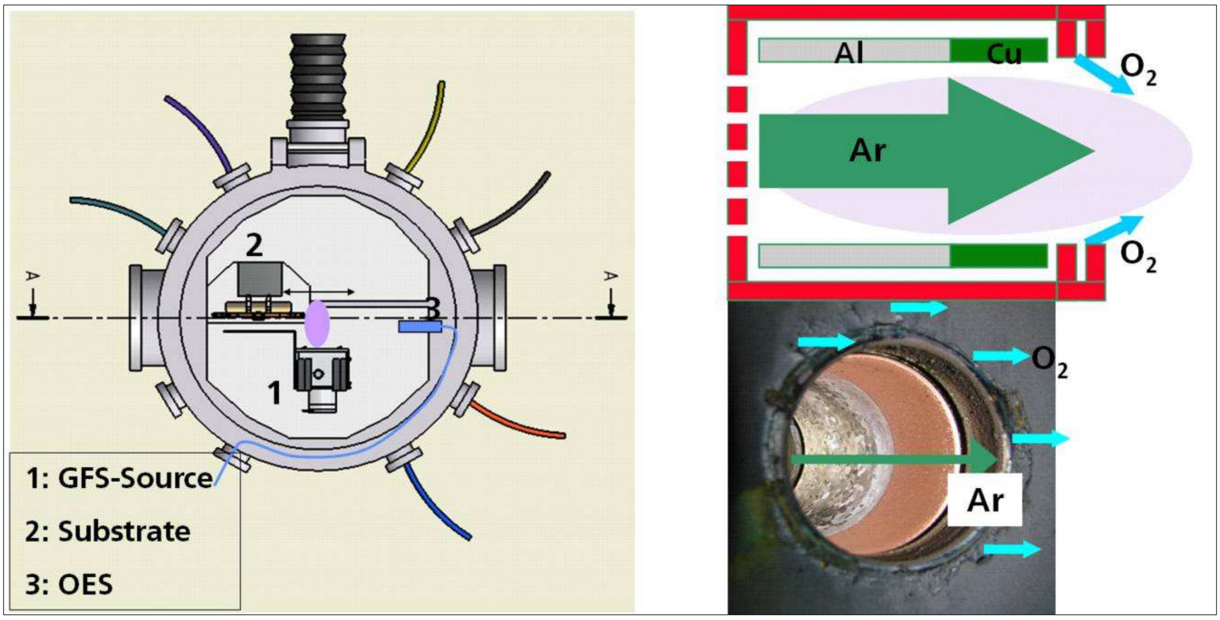

Figure 7: Setup for hollow cathode gas flow sputtering of p-type $CuCrO_2$ films.

Due to the metal surfaces and because of the lack of any products on the surface, the deposition rate of this process is very high. To get oxygen into the film on the substrate, the oxygen inlet is just short before the particles reach the substrate.

By controlling the argon gas flow and the oxygen gas flow one can control the stoichiometry of the resulting films. Furthermore, the ratio of tube segments gives you a third degree of freedom to get influence on film composition. These facts are summarized in the stoichiometric diagram in Figure 8 exemplary for the $CuCrO_2$ system.

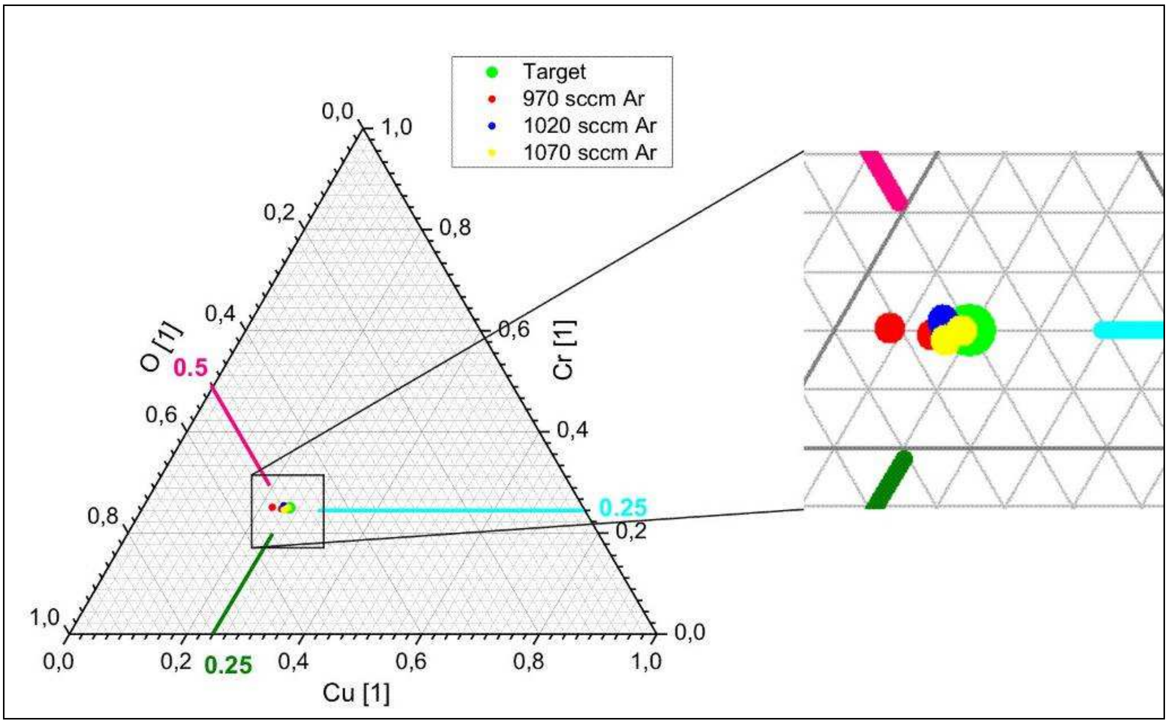

Figure 8: Adjustment of $CuCrO_2$ stoichiometry via control of Ar and O_2 flow for GFS.

For $CuAlO_2$, we found high temperature to be necessary similar to Sol-Gel while $CuCrO_2$ deposition was easier from the viewpoint of post deposition treatment but more difficult from the viewpoint of the handling the Cr^{VI} generation during reactive sputtering.
The impact of annealing on the optical properties is shown in Figure 9. Transparent films with transmittance of ~60 % in the visible range have been obtained.

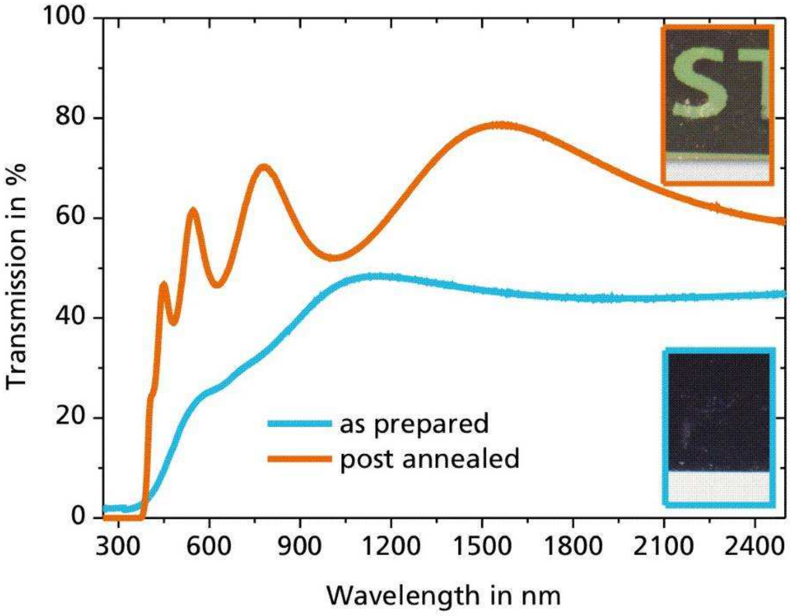

Figure 9: Optical properties of a 500 nm $CuCrO_2$ film prepared by PVD.

The electrical properties of the 500 nm thin films of $CuCrO_2$ are collected by Hall and Seebeck measurements. The results are found to be good enough for electronic applications in transparent electronic junctions and summarized in table 3.

Table 3: Summary of the electrical results of the prepared p-type TCOs.

	Θ_{synth} in °C	ρ in Ωcm	n_H in cm^{-3}	μ_H in cm^2/Vs	α in $\mu V/K$
$CuCrO_2$	700	29	9×10^{18}	3.5×10^{-2}	+320

The Seebeck coefficient α of + 320 µV/K proves holes as the major carrier type. The specific resistivity ρ of about 29 Ωcm for the 500 nm thin films is quite high compared to the results of Li et al. for a PLD process [5] or to the results of Nagarajan et al. [6] for the rf-sputtering process with 4 Ωcm and 1 Ωcm respectively. Despite that, the carrier concentration n_H of $9x10^{18}$ cm^{-3} is similar to the results of the Nagarajan group with $2x10^{19}$ cm^{-3}.
Further results and a detailed discussion of all them will be found in Ref. [7].

Summary

The results of the 3 Fraunhofer Institutes (IWM, ICS and IST) concerning simulation of different kind of TCOs and the preparation of p-type TCOs show new pathways towards layers for optoelectronic applications.
The results of the ab-initio DFT simulation can explain the reported p-type conduction of ZnO under the assumption that nitrogen is built in the grain boundaries of the ZnO matrix.
The Sol-Gel processing of p-type $CuCrO_2$ and $CuAl_{0.5}Cr_{0.5}O_2$ shows a cheap and easy preparation method, especially for doping experiments with Mg.
Hollow-Cathode Gas-Flow Sputtering is a new method for preparation of p-type TCOs and combines the quality advantages of vacuum processes with a cost-effective and robust technique.
From the experimental side, our p-TCOs are found to be good enough for optoelectronic devices considering the optical and electrical results.
So with our work, we are on a good way on the strong emerging field of transparent electronics.

Acknowledgements

This work has been funded within the framework METCO of the Fraunhofer-Gesellschaft.

References

[1] A. Zunger, Applied Physics Letters 83 (2003) 57

[2] W. Körner und C. Elsässer, Phys. Rev. B **81,** 085324 (2010)

[3] S. Götzendörfer, C. Polenzky, S. Ulrich and P. Löbmann, Thin Sold Films, 518 (2009) 1153

[4] S. Götzendörfer, R. Bywalez, P. Löbmann, J. Sol-Gel Sci. Technol. 52 (2009) 113

[5] D. Li, X. Fang, Z. Deng, S. Zhou, R. Tao, W. Dong, T. Wang, Y. Zhao, G. Meng, and X. Zhu, Journal of Physics D: Applied Physics, 40 (2007), pp.4910-4915

[6] R. Nagarajan, A.D. Draeseke, A.W. Sleight, J. Tate, Journal of Applied Physics, 89 (2001), pp. 8022-8025

[7] C. Polenzky, K. Ortner, B. Szyszka, Proceedings of the 8th ICCG, 2010 *(not yet published)*

doi:10.4028/www.scientific.net/AST.75.25

Au-based Transparent Conductors for Window Applications: Effect of Substrate Material

P.C. Lansåker[a], K. Gunnarsson[b], A. Roos[c], G.A. Niklasson[d], and C.G. Granqvist[e]

Department of Engineering Sciences, The Ångström Laboratory, Uppsala University,
P. O. Box 534, SE-75121 Uppsala, Sweden
[a]pia.lansaker@angstrom.uu.se, [b]klas.gunnarsson@angstrom.uu.se, [c]arne.roos@angstrom.uu.se,
[d]gunnar.niklasson@angstrom.uu.se, [e]claes-goran.granqvist@angstrom.uu.se

Keywords: Transparent conductors, gold films, indium doped tin oxide, sputter deposition, optical properties, electrical resistance, thin film growth, large scale coalescence.

Abstract

Thin films of Au were made by sputter deposition onto glass substrates with and without transparent and electrically conducting layers of SnO_2:In. The Au films were up to ~11 nm in thickness and covered the range for thin film growth from discrete islands, via large scale coalescence and formation of a meandering conducting network, to the formation of a more or less "holey" film. Scanning electron microscopy and atomic force microscopy showed that the SnO_2:In films were considerably rougher than the glass itself. This roughness influenced the Au film formation so that large scale coalescence set in at a somewhat larger thickness for films on SnO_2:In than on glass. Measurements of spectral optical transmittance and electrical resistance could be reconciled with impeded Au film formation on the SnO_2:In layer, leading to pronounced "plateaus" in the near infrared optical properties for Au films on SnO_2:In and an accompanying change from such two-layer films having a lower resistance than the single gold film at thicknesses below large scale coalescence to the opposite behavior for larger film thicknesses.

Introduction

Thin films of transparent conductors (TCs) are widely used in modern technology. Within green nanotechnology [1], for example, such films are employed to give low thermal emittance and solar control for architectural windows, and the films can also be used to insert and extract electricity in photovoltaic and electrochromic devices [2].

TCs are of two main types: those based on heavily doped wide band gap oxide semiconductors, such as SnO_2:F, In_2O_3:Sn (ITO), ZnO:Al, and ZnO:Ga, and those based on extremely thin films normally of coinage metals such as Cu, Ag, and Au [2]. The classes have specific pros and cons. For example, Ag-based coatings can be used only in protected environments such as in gas filled spaces of insulated glass units, while Au films are more corrosion resistant and allow applications in laminated electrochromic devices [3]. The oxide-based TCs must be thicker than the metallic ones by at least one order of magnitude to get comparable electrical resistance and thermal emittance, and the associated long thin film deposition times—as well as the frequent use of In-based films—tend to make the oxide-based films cumbersome for large scale applications.

We have recently investigated thin films of TiO_2/Au/TiO_2 with a focus on their use in electrochromic foil technology [3], and in the study reported here we describe recent progress towards the use of Au-based films for such and other applications. A critical issue is the growth of the Au film and how this growth is influenced by, in particular, the nanostructure and electrical properties of the underlying substrate. We therefore report here on the growth of Au films on indium doped tin oxide, SnO_2:In. This oxide has received rather small attention in the past [4-6] but is suitable for two main reasons: (*i*) it can be either *n*-doped or *p*-doped depending on the deposition conditions, especially the substrate temperature, and (*ii*) it serves as an analogue to the much more studied ITO [7] and hence will enable us to compare the growth of Au on SnO_2:In and on In_2O_3:Sn in future work.

Film deposition

Thin films of Au and SnO_2:In were deposited by DC magnetron sputtering onto unheated glass plates at a base pressure of ~2 x 10^{-4} mTorr from targets of 99.99-%-pure $Sn_{0.92}In_{0.08}$ and Au positioned 13 cm above the substrate. Films of SnO_2:In were made by reactive sputtering in Ar and O_2 at an Ar/O_2 mixing ratio of 1.7. The power to the sputter plasma lay in the $78 < P_{SnIn} < 125$ W range, and its pressure was kept at $4.8 < p_{SnIn} < 5.3$ mTorr. The films had thicknesses of $49 < d_{SnIn} < 180$ nm as recorded by scanning electron microscopy (SEM), and controlled optically via point-by-point fitting. Gold films were deposited by sputtering in argon with $P_{Au} \approx 50$ W and $p_{Au} \approx 6.0$ mTorr onto glass substrates with and without SnO_2:In layers. The mass thickness of the Au films, denoted d_{Au}, were measured by Rutherford backscattering spectroscopy (RBS) at the Tandem Laboratory at Uppsala University. In practice we recorded the mass thickness of a thick Au film—made under constant deposition conditions—by RBS and determined smaller d_{Au}s by scaling with time.

Film characterization

Spectral normal transmittance $T(\lambda)$ and near-normal reflectance $R(\lambda)$ were measured for $0.3 < \lambda < 2.5$ μm using a Perkin-Elmer Lambda 900 double-beam spectrophotometer with reflectance attachment and Spectralon reflectance standard. Spectral absorptance was obtained by $A(\lambda) = 1 - T(\lambda) - R(\lambda)$. Electrical sheet resistance $R_\square$ was measured between sputter deposited Au contacts for all samples, and resistivity ρ_{SnIn} was calculated for the SnO_2:In films. Considering the deposition conditions, the conductivity was taken to be of *n*-type [4,5].

Figure 1 shows SEM images for Au films with three d_{Au}s deposited onto a substrate with an SnO_2:In film having $d_{SnIn} \approx 123$ nm and $\rho_{SnIn} \approx 26$ mΩcm and simultaneously onto uncoated glass. Irrespectively of the substrate, the Au films go through the expected growth phases [3,8], starting with discrete Au islands at the smallest thicknesses, then proceding to a large scale coalescence (LSC) phase at $d_{Au} \approx 5.4$ nm where the Au film has a meandering structure and is electrically continuous, and then approaches a uniform film with voids. Figure 1 gives clear evidence that the Au films grow differently on glass and on SnO_2:In. Thus the films with $d_{Au} \approx 5.4$ nm is more continuous for the former case, and the same tendency is found at $d_{Au} \approx 8.1$ nm as evident from the smaller voids for the film on glass.

Thin film growth is influenced by many parameters, with the mean surface roughness r_a being an important one. This property was studied by atomic force microscopy (AFM). Specifically an uncoated glass surface and a SnO_2:In layer with $d_{SnIn} \approx 123$ nm had r_as of ~1 and ~1.5 nm, respectively. Gold deposition tended to gradually smooth the substrate, and r_a was ~1.2 nm for $d_{Au} \approx 8$ nm on glass as well as on SnO_2:In.

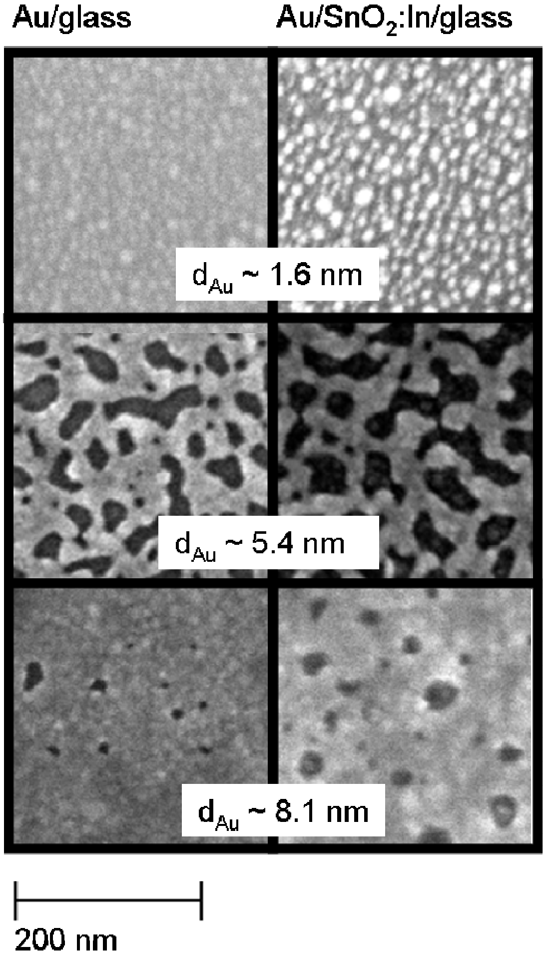

Fig. 1. *Scanning electron micrographs for Au films deposited onto glass and SnO_2:In and having the shown thicknesses. The bright regions represent Au. Data were taken with a LEO 1550 FEG instrument with in-lens detector..*

Electromagnetic properties of gold films growing on SnO_2:In and on glass

Figure 2 shows spectral optical properties for gold films with nine d_{Au}s in the $1.6 < d_{Au} < 10.7$ nm range on SnO_2:In and glass. Each Au film was deposited simultaneously onto a bare glass substrate and a SnO_2:In layer so that the data in Figs. 2(a) and (b) are fully comparable.

The transmittance spectra in Fig. 4(a) are completely consistent with those in earlier work [3,8]. At the lowest d_{Au}s, the films have good transparency in the full wavelength range, which is the expected result. Increased film thickness yields a gradual transformation to a metallic state characterized by a continuous decrease of the transmittance for increasing wavelengths.

At intermediate d_{Au}s—in the range where LSC takes place as apparent from Fig. 1—there are conspicuous plateaus in the transmittance shown in Fig. 2(a). This feature was explained in earlier work [8] as a consequence of plasma oscillations in elongated particles representative of the meandering Au structures. This assignment may not be unique, though, and very recent work has emphasized the role of “metal-in-metal” plasma resonances due to Au particles surrounded by, though unconnected to, more or less continuous gold [9]. However, whatever explanation for the plateaus that is most adequate their existence serves as clear evidence for the LSC stage of thin film growth.

Figure 2(b) shows analogous data for Au films on SnO_2:In with $d_{SnIn} \approx 123$ nm. The overall features of the spectra agree with those for deposition onto glass, but the plateaus in the near-infrared are more pronounced. This can be understood from the fact that the LSC stage of film growth extends to larger d_{Au}s for films on SnO_2:In, as was demonstrated from the SEM images in Fig. 1.

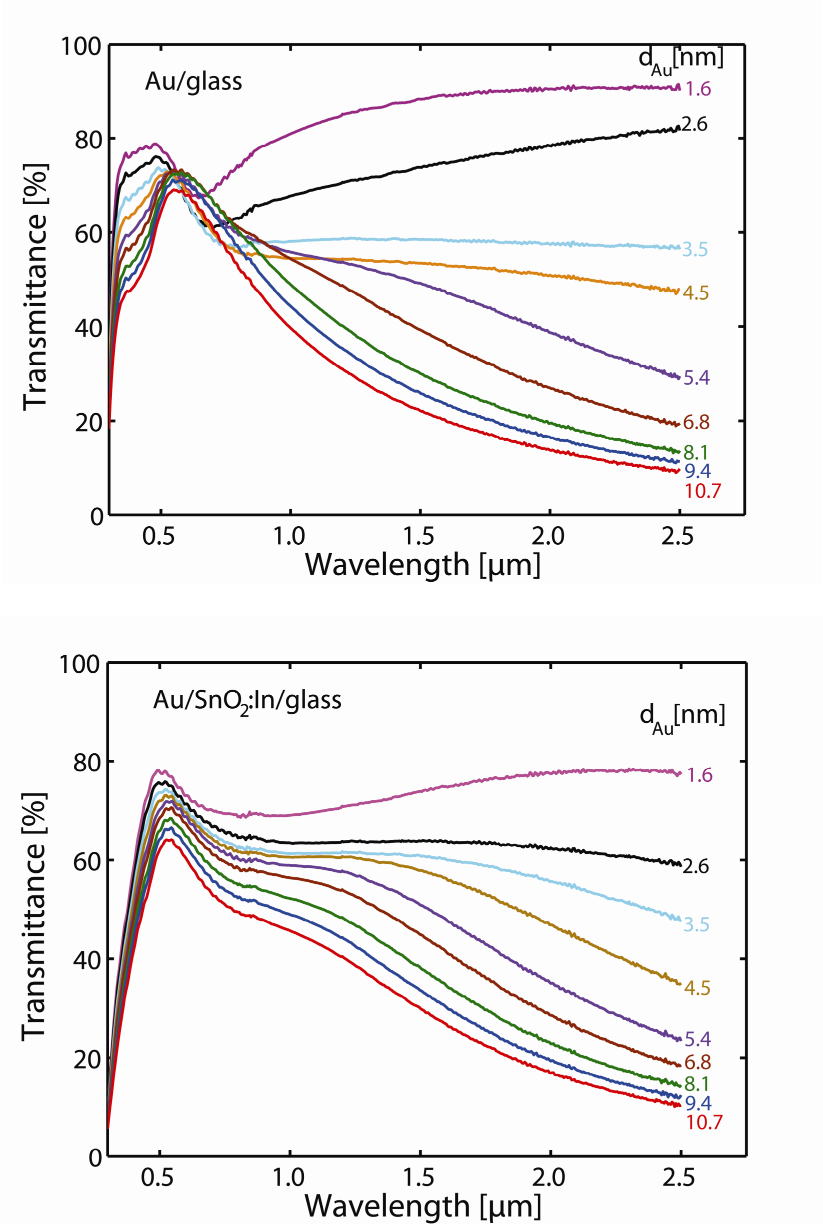

Fig. 2. *Spectral transmittance for Au films deposited on glass (a) and on SnO_2:In. (b). The drop of the transmittance at the approach of the shortest wavelengths in panel (b) is dominated by absorption in SnO_2:In.*

Figure 3 shows data on $R_{\square}$ for films of Au on glass and SnO_2:In. For the former films, resistance was measurable only for $d_{\mathrm{Au}} > 4$ nm. The resistance decreases rapidly as the films pass through LSC and reaches ~11 Ω for $d_{\mathrm{Au}} \approx 10.7$ nm. Films of Au on electrically conducting SnO_2:In naturally displaye a different behavior, and $R_{\square}$ of the two-layer structure goes from 1.5 kΩ for the bare SnO_2:In layer to ~13 Ω at $d_{\mathrm{Au}} \approx 10.7$ nm. Hence the Au film on SnO_2:In has the lower resistance for thicknesses below that corresponding to LSC, whereas the resistivity is lower for the Au film on bare glass above LSC.

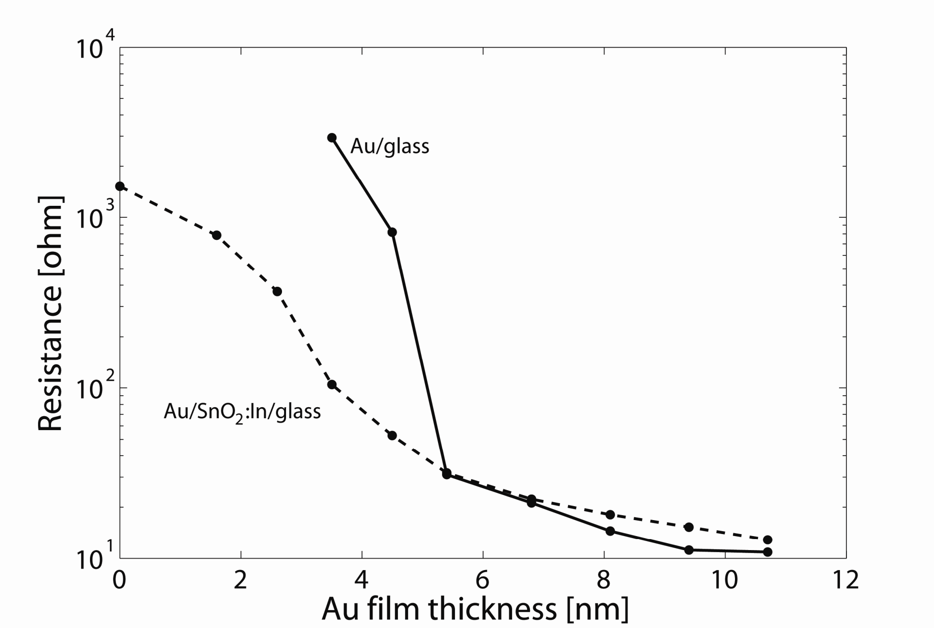

Fig. 3. Sheet resistance for Au films on glass and SnO_2:In. Dots represent data and connecting lines were drawn for convenience.

5. Summary and conclusions

We report initial results on a detailed study on the optical and electrical properties of Au films made by sputter deposition onto glass substrates with and without transparent and electrically conducting layers of SnO_2:In. The Au films had thicknesses up to ~11 nm and hence spanned the range for thin film growth from discrete islands, via large scale coalescence and formation of a meandering conducting network, to the formation of a more or less "holey" film. Measurements showed that the SnO_2:In films were rougher than the glass itself, and this feature influenced the Au film formation so that large scale coalescence set in at a somewhat larger thickness for films on SnO_2:In than on glass.

Measurements of spectral optical transmittance and reflectance gave a consistent pattern that could be understood from impeded Au film formation on the SnO_2:In layer, which led to pronounced plateaus in the near infrared optical properties for Au films on SnO_2:In and a concomitant change from such films having a lower resistance than the single Au film at thicknesses below large scale coalescence to the opposite behavior for larger film thicknesses.

Our work highlights the role of the substrate roughness for TCs of coinage metal films backed by wide band gap transparent conducting oxides. Evidently the oxide film has to be very smooth in order to produce optimum properties of the TC. A more detailed study on the growth on gold on glass and SnO_2:In will be presented in a forthcoming paper [10].

Acknowledgements: We gratefully acknowledge Bengt Götesson for image managements, Patrick Markus at Veeco for some AFM measurements, Malin Johansson and Per Petersson for assistance with RBS measurements and analysis, and Fredric Ericsson for help with SEM analyses. Financial support was received from the Swedish Energy Agency.

References

[1] G.B. Smith and C.G. Granqvist: *Green Nanotechnology: Solutions for Sustainability and Energy in the Built Environment*, CRC Press, Boca Raton, FL, USA, 2010, to be published.

[2] C.G. Granqvist: Solar Energy Mater. Solar Cells Vol. 91 (2007), p. 1529.

[3] P.C. Lansåker, J. Backholm, G.A. Niklasson and C.G. Granqvist, Thin Solid Films Vol. 518 (2009), p. 1225.

[4] Z. Ji, Z. He, Y. Song, K. Liu and Z.-Z. Ye, J. Crystal Growth Vol. 259 (2003), p. 282.

[5] Z. Ji, L. Zhao, Z. He, Q. Zhou and C. Chen, Mater. Lett. Vol. 60 (2006), p. 1387.

[6] G. Qin, D. Li, Z. Feng and S. Liu, Thin Solid Films Vol. 517 (2009), p. 3345.

[7] I. Hamberg and C.G. Granqvist, J. Appl. Phys. Vol. 60 (1986), p. R123.

[8] G.B. Smith, G.A. Niklasson, J.S.E.M. Svensson and C.G. Granqvist, J.Appl. Phys. Vol. 59 (1986), p. 571.

[9] G.B. Smith and A.A. Earp, Nanotechnol. Vol. 21 (2010), p. 015203.

[10] P.C. Lansåker, K.Gunnarsson, A. Roos, G.A. Niklasson and C.G. Granqvist, to be published.

doi:10.4028/www.scientific.net/AST.75.31

The Relationship of electrical and structural properties of synthetic melanin embedded in matrix of thin films zinc oxide, for their use as electrodes in bio-generators

D. C. Altamirano-Juárez[1, a]; J. J. Hernández-Barriga[1] and
C. García-Pacheco[2]

Universidad de la Sierra Sur

[1]Universidad de la Sierra Sur. Guillermo Rojas Mijangos s/n, Col. Ciudad Universitaria.
Miahuatlán de Porfirio Díaz, Oaxaca; México. C. P. 70805

[2]Instituto Tecnológico de Chetumal. Av. Insurgentes Num. 330, Col. David Gustavo Gtz.
Chetumal, Quintana Roo, México. C. P. 77013

[a]E-mail: delcris_1@yahoo.com

Keywords: Zinc_Oxide, Melanine, Electrodes, Bio-generator

Abstract. Melanin doped zinc oxide thin films were obtained using a process of soft chemistry with pH in the basic region. The electric and structural properties of these films were compared with films of un-doped ZnO obtained using the same process. Undoped films show the characteristic diffraction pattern of polycrystalline ZnO wurtzite type, while the doped films also present other signals associated to the melanin or some derived present phase of this. It is relevant because melanin is reported as amorphous material. Differences of grain size were detected and attributed to the presence of at least two existent phases in the films. Resistivity data were analyzed from the obtained values of films of un-doped ZnO and associated to the structural changes. The films have turned out to be stable in bio-generating systems of useful energy.

Introduction

Zinc Oxide thin films (ZnO) has been object of numerous studies for several decades, to be used in assortment of applications as the opto-electronic, the gases sensors or transparent windows in solar cells. Although the electric characteristics of ZnO can be modulated doping appropiately with other elements of the periodic table (metals or non metals), or for a combination of them, until now it is not informed in the literature that has been doped with a bio-polymer to be used as electrode in electric power bio-generators or bio-batteries (bB).

Even though it is certain that from the beginning Zinc has been chosen as an electrode among other metals for batteries, the use of thin films of some ceramic oxide for this type of applications is not known, rather, the typical electrochemical applications produce the oxidation of metallic zinc [1-3]. Of other hand, investigations carried out for the use of the solar energy in type Graetzel cells have achieved multi-layer systems coupled between a polymer and the metallic oxide [4], or, the use of oxides like the ZnO for the production of hydrogen from an impurity that favors the electrical characteristic of acceptor zinc [5], but It is not known as a doping where the oxide and the bio-polymer share the structure.

The polihydroxy-indole is known as the main component nano-aggregate (amorphous and disordered) of the melanin, either natural or synthetic, and it provides the characteristic dark color of the polymer [6 - 8]. Félix et. al [9,10] have reported previously interaction of melanin with ions of metals diamagnetic like Magnesium, Calcium, Cadmium and Zinc, associated to the auto-oxidation of melanin and semiquinone production for photolysis.

The idea of combining melanin with metallic oxides arose of having observed the behavior of bio-batteries designed with wired metallic electrodes of Copper and Aluminum, as well as of the structural characteristics and of the conductivity of thin films of ZnO obtained for technical of soft chemistry [11-15].

Experimental Development

Thin films of ZnO and Melanine doped zinc oxide (ZnO:Hx) were obtained using the Sol-Gel Technique. The synthesis procedure followed the same route of basic pH [12-14] that those obtained in previous works, using acetate of zinc and substituting ethylene-glycol and 1-propanol by methanol like solvent. The purpose of using methanol is to minimize the effect of solvent of diverse structure in the reactions of oxidation into melanin, to avoid the complex interactions inside the precursor solutions and to diminish the treatment temperature and annealed on the films.

Previously Melanin stabilized in water was treated tried to increase its concentration from 4 to 8%, and this way, to avoid that the aging process of precursor solution was fast. Stabilized Melanin at 2% was added in the intermediate phase of preparation maintaining the solution in constant agitation. The films were obtained on glass slides clean and dismineralized, using the immersion process to obtain six coatings, each one with drying treatment at 100° C for 1 h, with later sintering at 400° C for 3 h.

Once obtained, ZnO and ZnO:Hx thin films were selected for i) to establish a reference, ii) to evaluate behavior V-R, immerse in melanin stabilized in absence of metals and iii) to evaluate behavior V-R like electrodes in presence of thin films of other metals, emulating the wired devices battery type. Finally, each film was characterized by X-ray Diffraction before and after of their use.

Results and Discussion

ZnO thin films were transparent with a thickness final average of 0.5 microns, while the ZnO:Hx films presented a thickness average of 0.8 microns, with a marked opacity and low homogeneity (Figure 1).

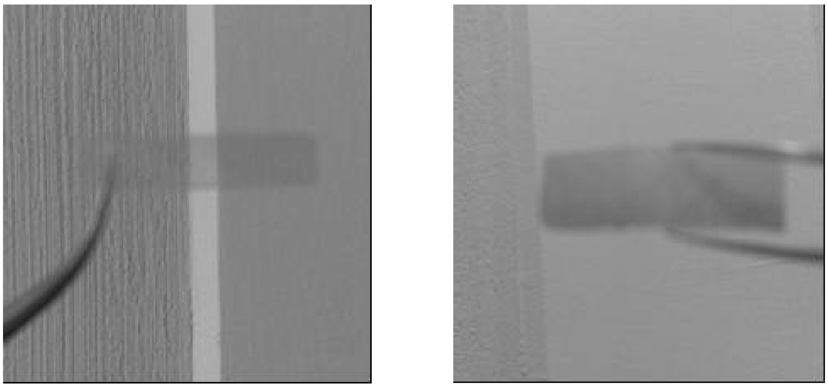

Figure 1. *a) undoped ZnO thin films and b) ZnO:Hx, both obtained by Sol-Gel Technique.*

Regarding the electric behaviour, did the ZnO films show typical fotoconductivity answer of the material (> 10^3 Ω-cm) for steady illumination conditions [13]. While, the ZnO:Hx films showed such a high resistividad as those un-doped, but with absence of photodecay effect. Then, both types of films were submerged in an electrolyte melanimyc, obtaining the V-R response shown in the Table 1.

Table 1. *Response V-R of ZnO and ZnO:Hx thin Films*

Test	ZnO		ZnO:Hx	
	V (volts)	ρ (Ω-cm)	V (volts)	ρ (Ω-cm)
Only air	- - -	5.5×10^2	- - -	$> 10^2$
Only melanin	0.032	1.4×10^2	0.011	4.0×10^0
System battery /Al	0.656	1.8×10^2	0.244	3.6×10^{-2}
System battery /Cu	- - -	- - -	0.101	1.4×10^1

As it is observed, the ZnO thin films submerged in the electrolyte shows a lightly smaller resistance to the measurement obtained in air, without alters this the absence of voltage on the film. When Melanin doped ZnO films were measuring under same conditions, did the resistance vary in at least two orders of magnitude from $>10^2$ a $4.0\text{x}10^0$ Ω-cm. Necessary it is to comment that for itself electrolyte maintains a small difference of potential of 30 mV among the terminals of test of multi-meters, and that that difference is not affected by the presence of the un-doped ZnO film; however, the voltage dropping average registered 20 mV for ZnO:Hx.

The values V-R measured in battery system showed that the variation of voltage was significant among the evaluated systems. For the ZnO/Al system took place a ΔV of 0.101 V and a ΔV of 0.244 V in the ZnO:Hx/Al system, it is to say, a potential dropping of 0.412 V with regard to the system made up with un-doped film. Observe that the difference of potential among the systems should be closely related with the decrease of resistivity over all the system, with a resulting value on the movie of 3.6×10^{-2} Ω-cm. However, happened that in electrode systems ZnO/Cu films, the film of copper was dissolved and it was not possible to register some value in the measure [Figure 2]. For the opposite, the electrode system ZnO:Hx / Cu films was quite stable and an answer significant V-R was obtained, comparable to the ZnO:Hx/Al system.

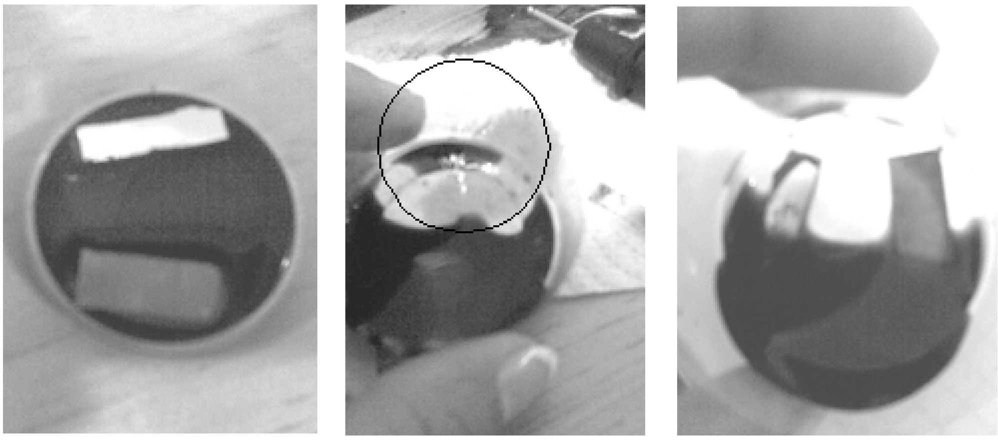

Figure 2. ZnO/Cu electrodes s*ystem were not possible because the film of cupper was dissolved into electrolyte*

Of another hand, XRD patterns were obtained of ZnO and ZnO:Hx films, before and after their use in a system of bio-batteries. The Figure 3a) shows a sequence of diffraction patterns of reference powder ZnO, in contact only with Hx and in contact with the electrode of Al and Cu. Also it is shown for the film of ZnO:Hx in Figure 3b). It is identified that all the XRD of films that had contact with the Hx maintains the first three representative picks of polycrystalline ZnO of wurtzite phase in the positions corresponding to the crystallographies directions (100), (002) and (101), besides presenting other signals of smaller intensity that could not associate to the hexagonal phase of ZnO, and that they were not modified significantly after being exposed to the system of bio-batteries.

It is known that melanin doesn't produce signals of diffraction; however, the outward show of diffraction picks not characteristic of the ZnO does think in a structural joint of the poly-hydroxi-indole as coupled structures to the wurtzite type. Some of the picks suggest the presence of metallic Zn, (that which is probable, but it could not be demonstrated), since the reduction of Zn at Zn^{2+} is possible due to an interaction auto-regulated in the production and recombination of sub-molecules that compose it as the indoles and semiquinones [8, 16]. The dilution of the film of Cu can support this statement.

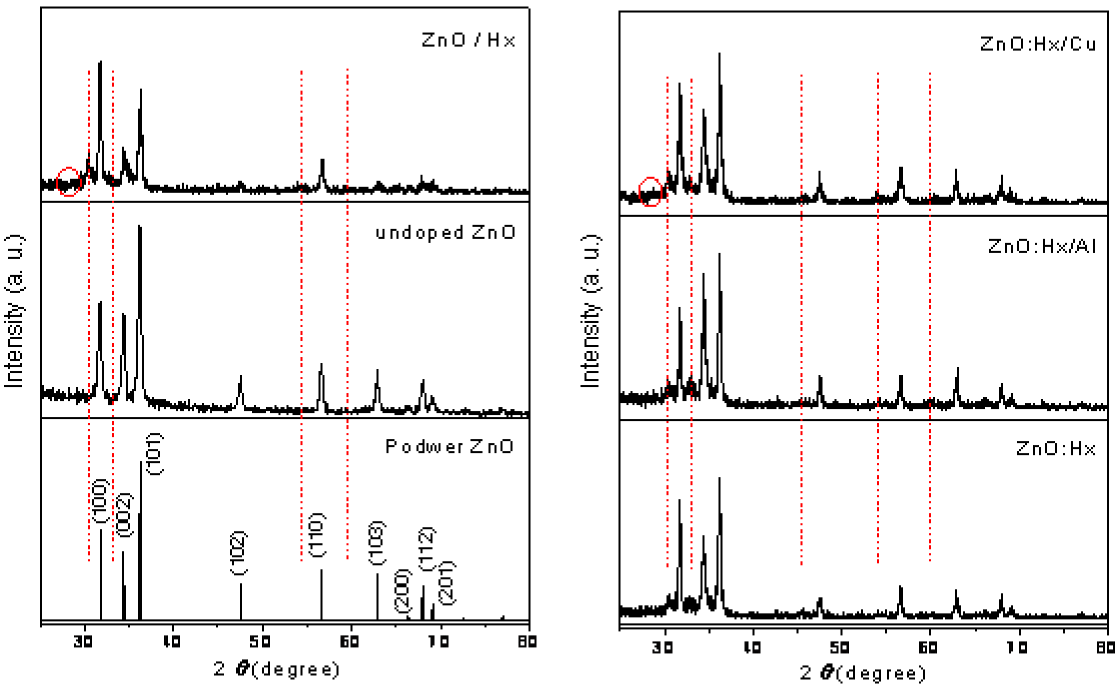

a) b)

Figure 3. *a) ZnO DRx undoped ZnO thin films and b) ZnO:Hx obtained by Sol-Gel Technique.*

The ZnO films studied previously have proven to have a high load density in the grain frontiers due to the oxygen vacancies [12]. In a half oxidizer it is prospective that metallic copper is oxidized and ZnO is electrically stable, but in a half anti-oxidizer, like a melanímic solution, reactions of oxidation are not favored. Apparently, a layer of copper oxide has been developed on the surface of the films, and in contact with the melanin, the reduction process is induced with ZnO like catalyst (as accelerator of the process due to the density of load negative in grain boundary) favoring its "seizure" inside the indolic structure. This effect has not been observed in copper wires used as electrodes, maybe due to its volume.

Conclusions and Considerations

The structural stability observed through the shown diffraction patterns and the relationship V-R measured in systems of bio-batteries indicate that ZnO:Hx is a viable option as cathodes in a ZnO:HX/Al system for generating devices of electric power, of low cost and under environmental impact. However, it is necessary to deepen in the characterization of the products of the experimentation, since many other phenomenons have been observed, as the process of auto-regeneration of the electrolyte and the improvement of the transmission in radiofrecuency.

Acknowledgements.

The authors thank the received technical support of the University Linking Center of the Benemerita Universidad Autónoma de Puebla, of Micro and Nanotechnology Center of the Universidad

Veracruzana and Human Photosynthesis Studies Center; through the work teams of the doctors Efraín Rubio Rosas, Claudia Oliva Mendoza Barrera and Arturo Solís Herrera, respectively.

References

[1] A. Daniels, *Fisicoquímica*. CECSA. 1982.

[2] A. Dassler. *Electroquímica y sus fundamentos electroquímicos*. UTEHA, 1962. Part I: pp. 121-141; Part II: pp. 92-174.

[3] D. Ball. *Physical Chemistry*. 1st Edition. Cengage Learning Publisher, 2004. ISBN 9706863281.

[4] B. O'Regan, M. Graetzel. *Nature*. 353 (24), 737-740. October 1991.

[5] M. Bär, K.-S. Ahn, S. Shet, Y. Yan, L. Weinhardt, O. Fuchs, M. Blum,S. Pookpanratana, K. George, W. Yang, J. D. Denlinger, M. Al-Jassim, and C. Heske1: A*pplied Physics Letters* **94**, 012110 (2009).

[6] V. Capozzi, G. Perna, P. Carmone, A. Gallone, M. Lastella, E. Mezzenga, G. Quartucci, M. Ambrico, V. Augelli, P.F. Biagi, T. Ligonzo, A. Minafra, L. Schiavulli, M. Pallara, R. Cicero. *Thin Solid Films* 511-512 (2006) 362-366.

[7] Y. T. Thathachari, M. S. Blois. Biophysical Journal, Vol. 9, Issue 1, 77-89, 1 January 1969.

[8] T. Sarna, P. M. Plonka. *Biomedical EPR, Part A: Free Radicals, Metals, Medicine, and Physiology*. Spronger US Publisher. ISBN 978-0-306-48506-0.pp. 125-146.

[9] C. C. Felix, R. C. Sealy. *J. Amer. Chem. Soc.* **100** (1978a) p. 3922-3926.

[10] C. C. Felix, J. S. Hyde, T. Sarna, R. C. Sealy. *J. Amer. Chem. Soc.* **103** (1981) p. 2831-2836.

[11] A. Solís, M. E. Lara, L. E. Rendón. *Nature Precedings.* Posted 12 November 2007. http://precedings.nature.com/account/show/1105.

[12] D. C. Altamirano-Juarez. *Advances in Science and Technology.* Trans Tech Publications Ltd. (54) 2008. pp. 337-342.

[13] D. C. Altamirano-Juarez. *Influencia de la variación de parámetros involucrados en la técnica Sol-Gel, en películas delgadas de ZnO impurificadas, para su uso como electrodos transparentes*. Doctoral Tesis. (Library of CINVESTAV-IPN, Unidad Querétaro; México. Agosto 2007)

[14] D. C. Altamirano-Juarez, R. Castanedo-Perez, O. Jimenez-Sandoval, S. Jimenez-Sandoval, J. Marquez-Marin and G. Torres-Delgado. *Modern Physics Letter B*. Vol 15, 17-19 (2001) 730-732. Word Scientific Publishing Company.

[15] S. A. Studenikin, Nickolay Golego and Michael Cocivera. *J. Appl. Phys.* Vol. 87 (5) (2000) p. 2413-2421.

[16] C. A. Bishop, L. K. J. Iong. *Tetrahedron letters* 41, 3043 (1964).

doi:10.4028/www.scientific.net/AST.75.36

Extraordinary stability of structural and electronic properties of tin oxide nanoparticles formed by soft chemistry

M. Rumyantseva[1a], I. Zhurbina[2], E. Varechkina[2], S. Badalyan[3], A. Gaskov[1], V. Timoshenko[4]

[1]Chemistry Department, Moscow State University, 119991 Moscow Russia

[2]Faculty of Material Science, Moscow State University, 119991 Moscow Russia

[3]Institute of General and Inorganic Chemistry, 119991 Moscow Russia

[4]Physics Department, Moscow State University, 119991 Moscow Russia

[a]roum@inorg.chem.msu.ru

Keywords: Tin dioxide, high surface area, photoluminescence, oxygen chemisorption

Abstract. Powders of tin dioxide (SnO_2) have been prepared by two different modifications of wet chemical synthesis, i.e. (i) by conventional hydrolysis of tin chloride dissolved in aqueous ammonia solution and (ii) by precipitation from tin chloride dissolved in aqueous hydrazine monohydrate ($N_2H_4*H_2O$) solution. The prepared gels were dried and then annealed at different temperatures varied from 300 to 700 ^oC in order to form nanocrystals. Structure and optical properties of the samples were investigated by using X-ray diffraction, transmission electron microscopy, thermoprogrammable hydrogen reduction, low temperature nitrogen adsorption method, photoluminescence, infra-red absorption, Raman spectroscopy, and X-ray photoelectron spectroscopy. The samples prepared by hydrazine-based method are characterized by surface area about 127-188 m^2/g with high sintering resistance. The optical spectroscopy data revealed pure crystallinity and high defect concentration for the samples prepared by hydrazine-based method. The experimental results are discussed in view of different states of chemisorbed oxygen on SnO_2 nanocrystal surfaces, which determine electronic and optical properties of the prepared samples.

Introduction

Tin oxide is an important material for various technological applications such as gas sensors and conductive coatings as well as carriers for supported catalysts. For gas sensors and catalytic applications high surface area is one of the most important material's parameters. Different methods of synthesis allowing obtaining high surface area tin oxide were discussed in details in relation with catalytic activity of materials in CO oxidation [1]. The most promising catalytic materials with excellent sintering resistance have been synthesized by the hydrazine method. Physico-chemical properties of this material were extensively characterized by different techniques including FTIR, UV-VIS and EPR spectroscopy [2, 3]. The only explanation of sintering resistance on the base of narrow particle size distribution was proposed [3]. However it seems to be disputable that this narrow particle size distribution can be the reason for low propensity to non-stoichiometry and high electrical resistance of this type of material. In this work we studied in details the microstructure, electrical and optical properties of SnO_2 nanocrystals to discover the features responsible for sintering resistance as well as for extraordinary stability of optical and electrical properties of tin oxide prepared by precipitation with hydrazine.

Experimental

Synthesis. Powders of tin dioxide (SnO_2) have been elaborated by two different modifications of wet chemical synthesis indicated as *g*- and *h*-types. The powder samples of *g*-type were prepared by conventional hydrolysis of tin chloride. $SnCl_4*5H_2O$ was dissolved in deionised water and commercial 25% aqueous ammonia (NH_3*H_2O) was slowly added to the stirred solution to achieve a complete precipitation of α-stannic acid. The resulting gel was centrifuged, washed with deionised water up to complete disappearance of the chloride ions ($AgNO_3$ test), and dried at 80 °C during 24 hours.

Samples of *h*-type were prepared by modifying a literature recipe [2]. 150 ml of 0.6 M solution of $SnCl_4*5H_2O$ were added drop wise to 100 g of commercial 34% aqueous hydrazine monohydrate ($N_2H_4*H_2O$) solution at ambient temperature. A white precipitate formed immediately. After complete addition the mixture was refluxed for 7 days. The precipitate was washed and centrifuged until no more chloride could be detected. The product was dried for 24 h in air at 80 °C. Powders of both types were crushed and annealed in air at 300 °C, 500 °C, and 700 °C for 24 hours.

Characterization. X-ray diffraction (XRD) patterns were recorded using a DRON-3 diffractometer operated at Cu K_α radiation ($\lambda = 1.5406$ Å). The results were processed by using STOE WinXPow software. The average size (diameter) of SnO_2 nanocrystals (d_{XRD}) was estimated from the XRD data using the Scherrer formula applied to the most intense diffraction lines, i.e. (110) and (101).

Specific surface area of the samples was measured by the BET method using N_2-adsorption/desorption isotherms detected with a Micromeritics Chemisorb 2750 unit. Before the measurements the samples were heated at 300 °C in helium flow for 1 hour.

Patterns of the thermoprogrammable hydrogen reduction (TPR-H_2) were obtained using the same device with 90% argon and 10% hydrogen gas mixture. The temperature was increased with a rate of 5°C/min up to 800°C.

Transmission electron microscopy (TEM) was carried out on a Phillips CM30 SuperTwin electron microscope operated at 300 keV with 0.19 nm point resolution. For TEM observations, SnO_2 powders were ultrasonically dispersed in ethanol and deposited on amorphous holey carbon membranes.

In order to perform optical measurements tin oxide powders were deposed from C_2H_5OH suspension on monocrystalline silicon substrates and heated at 220 °C for 10 minutes. IR spectra were obtained using a Bruker 66v/S Fourier-transformed infrared spectrometer. The IR measurements were done in vacuum of 0.002 mBar at room temperature with a spectral resolution of 2 cm^{-1}.

Raman and photoluminescence spectra were measured with MicroRaman spectrometer Horiba Yvon HR800 in the spectral ranges of 200-1200 cm^{-1} and 400-900 nm, respectively. The spectra were excited with 488 nm line of an Ar-laser. The experiments were carried out in air at room temperature.

X-ray photoelectron spectroscopy (XPS) analysis was performed using ESCALAB MK II spectrometer with Mg K_α radiation (1253.6 eV) in high vacuum 10^{-8} torr. Spectra of Sn 3d, O 1s, and C 1s were registered with 0.05 eV resolution and treated using Unifit v. 2006 software.

Results

The XRD spectra demonstrate that all powders are of SnO_2 cassiterite phase. The samples of *g*-type are amorphous before annealing. The average diameter of SnO_2 nanocrystals for *g*-type powders ranges from 4 to 35 nm depending on the annealing temperature while for *h*-type powders this value is about 3 nm and does not increase with the annealing temperature growth (Table 1). Fig. 1 shows typical TEM images of the samples annealed at 300 °C. According to the TEM data the shape of SnO_2 particles is nearly spherical and their average diameter is about 3 nm for the samples of both types. The obtained nanocrystal size is in agreement with the XRD data. Note that *g*-type and *h*-type samples have near the same particle size distribution.

The SnO_2 powders treated at 300 °C are characterized by specific surface area S_{BET} of 120 - 180 m^2g^{-1}. With the annealing temperature growth up to 700 °C specific surface area of *g*-type samples decreases dramatically whereas for *h*-type powders the decrease of S_{BET} does not exceed 33% that indicates high sintering resistance of this kind of material.

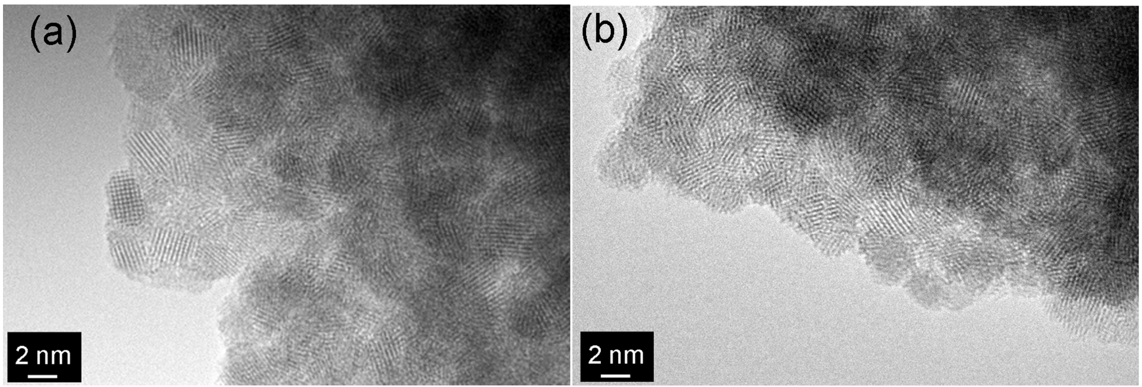

Fig. 1. TEM images of the samples of *g*–type (a) and *h*-type (b) annealed at 300^0C.

Table 1. Annealing temperature T_a, nanocrystal diameter d_{XRD}, and specific surface area S_{BET} of the investigated samples.

	g-type			*h*-type		
T_a [^{o}C]	300	500	700	300	500	700
d_{XRD} [nm]	4	10	22	3	3	3
S_{BET} [m^2g^{-1}]	109	22	10	188	170	127

Fig. 2 shows the TPR-H_2 curves of all the samples. From all diagrams one can distinguish three temperature regions. In low-temperature area (below 400 °C) there is a broad peak, which can be appointed to the hydrogen consumption due to reaction with the oxygen chemisorbed on SnO_2 crystallites surface. The amount of chemisorbed oxygen decreases with annealing temperature for the samples of *g*-type, but is nearly the same for all samples of *h*-type. This may point to unusually strong chemical bounding between crystallite surface and adsorbed oxygen. At higher temperature two features at 450 – 550 °C and 550 – 650 °C are observed. These features are accounted for reduction of Sn^{4+} to Sn^{2+} and Sn^{2+} to Sn^0, respectively. This mechanism was additionally proved by Mössbauer spectroscopy. For the samples of *g*-type the low temperature peak corresponding to Sn^{4+} to Sn^{2+} reduction can be discriminated only for the sample annealed at 300 °C, but both peaks are clearly observed in all the spectra of the samples of *h*-type.

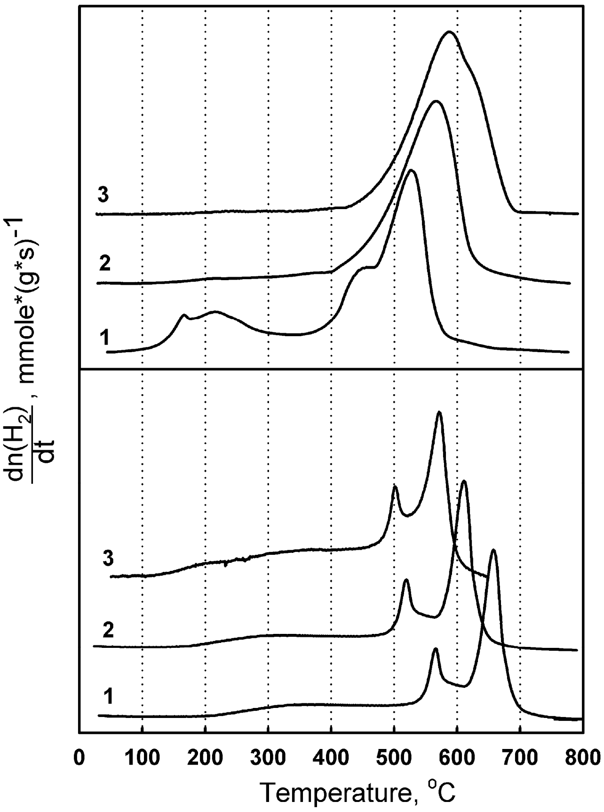

Fig. 2. TPR-H_2 profiles of SnO_2 powders of *g*-type (a) and *h*-type (b), annealed at 300^{o}C (1), 500^{o}C (2), and 700^{o}C (3)

For *g*-type samples the increase of annealing temperature results in the shift of the main peak position in TPR-H_2 profiles to higher temperature area. This responds to impediment of reduction process because of perfecting of crystal lattice and increasing of crystallite size with the growth of the annealing temperature. Surprisingly, the spectra of *h*-type samples demonstrate the inverse dependence on annealing temperature. All consecutive reduction steps, namely reduction of chemisorbed oxygen, reduction of Sn^{4+} to Sn^{2+} and Sn^{2+} to Sn^0, for the *h*-type powder annealed at 300 °C start at higher temperature as compared with the samples annealed at 500 or 700 °C.

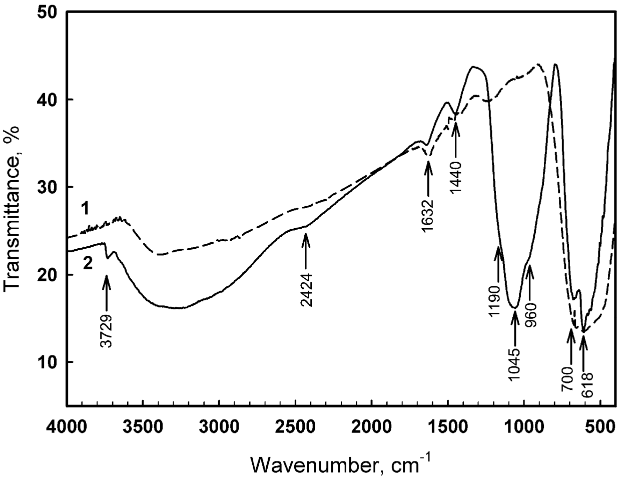

Fig. 3. IR transmittance spectra of *g*-type (1) and *h*-type (2) samples annealed at 300°C.

IR spectra of the samples of *g*-type and *h*-type annealed at 300 °C are shown in fig.3. The main peak in the region 370-770 cm^{-1} corresponds to Sn-O-Sn lattice vibration and includes IR active modes A_{2u} (700 cm^{-1}, νSnO z) and E_u (618 cm^{-1}, νSnO xy) [4, 5]. Stretching vibration modes of hydroxyl groups of water molecules linked to SnO_2 surface are presented in the IR spectra at frequencies 1440, 1632, 2424 and 3729 cm^{-1}. A wide band with in the range 1370 – 3750 cm^{-1} is also arisen due to water molecules absorption. One can note the increased quantity of hydroxyl groups and adsorbed water on the surface of SnO_2 obtained using hydrazine method.

The main feature of IR spectra of *h*-type sample is a strong additional band in the range 800 – 1400 cm^{-1} with a maximum of about 1050 cm^{-1}. The detailed analysis of IR spectra of g-type and h-type samples is present in the in set. According to literature data [6] this peak can be associated with chemisorbed oxygen that is O-O stretching band of O_2^- molecular ions stabilized at fourfold-coordinated tin cations Sn_{4c}, ($\nu_{O\text{-}O}$ = 1045 cm^{-1}) and fivefold-coordinated Sn_{5c} ions ($\nu_{O\text{-}O}$ = 1190 cm^{-1}). These bands were detected by IR spectroscopy on *prereduced* SnO_2 after oxygen adsorption [6]. From fig. 3 one can see that the band with $\nu_{O\text{-}O}$ = 1045 cm^{-1} makes the main contribution into absorbance in this spectrum range while the bands at 1190 and 960 cm^{-1} (attributed to the stretching vibrations of some surface cation – oxygen bonds of the Sn – O or Sn = O type) are presented as a shoulders. An increase of the annealing temperature for *h*-type samples leads to an asymmetrical narrowing of this peak due to reducing of contribution of surface vibration modes at 960 cm^{-1} [6].

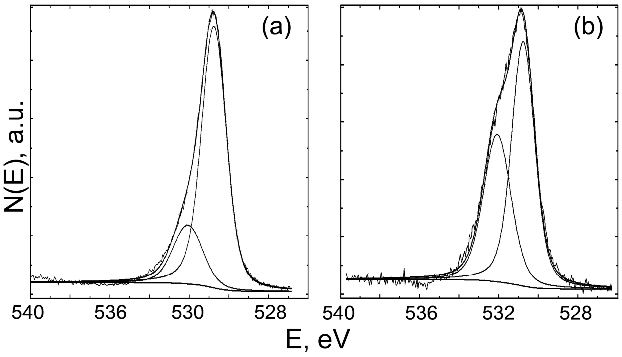

Fig. 4. O 1s X-ray photoelectron spectra of SnO_2 annealed at 300 °C: (a): *g*-type sample, (b): *h*-type sample.

The presence of high quantity of chemisorbed oxygen on the surface of *h*-type samples is confirmed by XPS data (fig. 4). The detailed analysis of O 1s spectra discloses two different peaks with the maxima at 530.6 eV and 532.3 eV. The first peak corresponds to the lattice oxygen on the SnO_2 surface [7], and the second one may be attributed to the different chemisorbed oxygen species [8, 9]: O^- (531.2 – 531.5 eV), O_2^{2-}(532.7 eV), O_2 (532.6 eV). It should be noted that these species are stable in the high vacuum necessary for XPS experiments but can be removed by Ar^+ ion etching. The ratio of peak areas of adsorbed and lattice oxygen for SnO_2 of *g*-type and *h*-type is equal to 0.31 and 0.98 respectively. Even taking in consideration the difference in the specific surface area of samples of *g*-type and *h*-type this result indicates the extremely high concentration of chemisorbed oxygen for *h*-type sample.

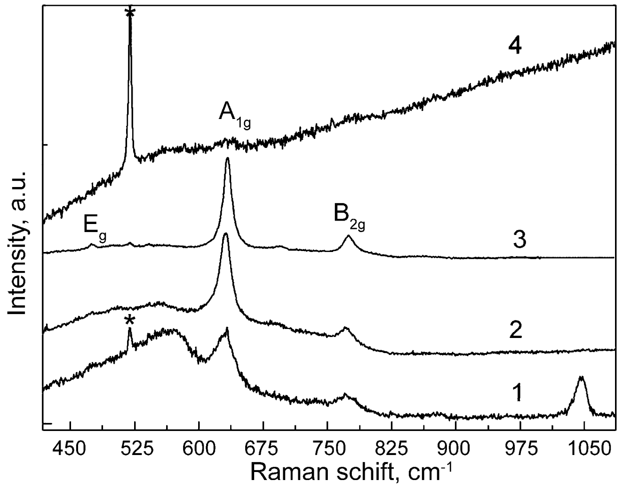

Fig. 5. Raman spectra of the samples of *g*-type annealed at 300^{0}C (1), 500^{0}C (2) and 700^{0}C (3) and of *h*-type annealed at 300^{0}C (4). Asterisks denote the substrate contribution.

Fig. 5 shows Raman spectra of SnO$_2$ samples of both types. In the spectrum of *g*-type sample annealed at 700 ^{o}C (curve 3) three detectable Raman active modes of tin oxide have been observed: E_g (474 cm^{-1}), A_{1g} (631 cm^{-1}) and B_{2g} (773 cm^{-1}). Spectra of of *g*-type samples annealed at lower temperatures exhibit also around A_{1g} mode a broad feature between 400 and 700 cm^{-1}, attributed to the surface modes [10]. The peak broadening and intensity reducing can be explained by crystallite size decreasing. Maximum at 1046 cm^{-1} corresponding to hydroxyl group of water vibrations is risen at the Raman spectrum of the sample with 4 nm particle size what is in a good agreement with the IR data. The Raman spectrum of SnO$_2$ nanocrystals of *h*-type (curve 4) differs greatly from the one of *g*-type with the similar particle size. A continuous increase of the Raman scattering signal of the *h*-type sample in the high-frequency range can be explained by a contribution of the photoluminescence (PL) emission related with high defect concentration.

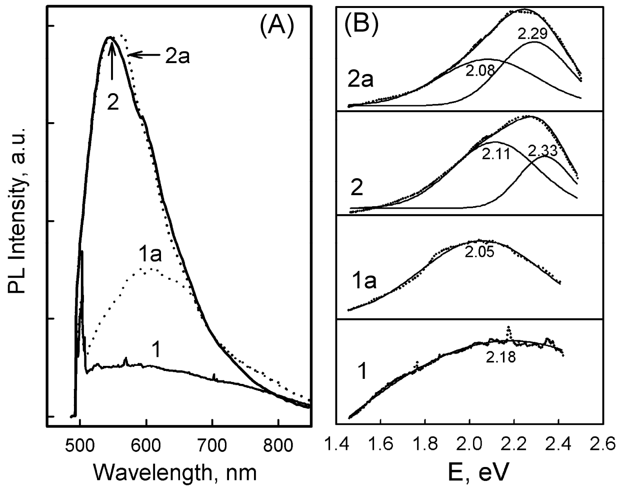

Fig. 6. (A) PL spectra of the samples annealed at 300^{o}C before (solid lines 1 and 2) and after (dash lines 1a and 2a) additional thermal annealing in vacuum. Curves 1, 1a correspond to *g*-type sample, curves 2, 2a correspond to *h*-type sample. (B) PL spectra rebuilt in coordinates $I - E$ with one- or two-peak Gaussian fit.

PL spectra shown in fig. 6a indicate that the samples of *g*-type are low defective. In PL spectrum 1 only low intensive broad peak with maximum at 568 cm^{-1} (2.18 eV) can be detected. An additional annealing in vacuum (10^{-2} torr, T = 300 ^{o}C, t = 2h) leads to the red shift of luminescence maximum to 605 cm^{-1} (1a spectrum) corresponding to photon energy of 2.05 eV with significant increase of PL intensity. For the *h*-type sample a strong asymmetric PL peak centered at around 550 cm^{-1} (spectrum 2) is observed. Figure 6b shows that this spectrum consists of two bands centered at 531 cm^{-1} (*band1*, 2.33 eV) and 587 cm^{-1} (*band2*, 2.11 eV). Therefore, there appear to be two emission centers in *h*-type sample. Analysis of integral intensities of corresponding Gaussian peaks gives the ratio $I_{band1} : I_{band2} = 1 : 2$. Thermal annealing in vacuum leads to slight red shift of the both bands and growth of *band1* intensity $I_{band1} : I_{band2} = 1 : 1$ (figure 6b, spectrum 2a).

In detailed review Comini et al. [11] it is mentioned that nanostructured tin oxide with high surface-to-volume ratio exhibits strong PL emission in visible range 400 – 600 cm^{-1}, which can be attributed to transitions involving defective states within the band gap. The key role is played by oxygen vacancies states. On the base of results obtained for SnO$_2$ nanoribbons by time-resolved X-ray excited optical luminescence (XEOL) and X-ray absorption near edge structures (XANES) Zhou et al. [12] brought out two bands centered at 2.10 and 2.51 eV, which were assigned to the radiative decay of trapped electrons in oxygen vacancies just below the conduction band to intrinsic surface states in the band gap. It is supposed

[12] that these bands are related to the vacancies with one or two adjacent oxygen atoms missing while surface states are due to a large fraction of undercoordinated Sn atoms resulting from oxygen vacancies. The augmentation of intensity of *band1* (2.33 eV) experimentally observed in this work under heating in vacuum is in a good agreement with this conclusion. Since the total quantity of oxygen vacancies seems to be unchanged under heating in vacuum (fig. 6a, spectra 2 and 2a), the removing of oxygen results in increasing of part of vacancies with two adjacent oxygen atoms missing.

Discussion

As it was mentioned in [3] the presence of hydrazine in reaction mixture can lead to formation of neutral oxygen vacancies and consequently undercoordinated Sn atoms. In distinction from thermal annealing in vacuum the reducing action of hydrazine results in oxygen vacancies formation not only on the surface but also in the volume of SnO_2 grains. The low mobility of oxygen in SnO_2 lattice [13] suggests that the annealing in air used in this work (24 h at 300 ^{o}C) would not result in a significant decrease of quantity of oxygen vacancies in the core of SnO_2 crystallites. These undersurface oxygen vacancies are responsible for strong photoluminescence emission of *h*-type sample.

High concentration of oxygen vacancies causes oxygen chemisorption from ambient air (Fig. 5). An *ab initio* study of oxygen adsorption on SnO_2 surface [14] demonstrates that the oxygen molecule coordinated to the Sn centers of low coordination (fourfold-coordinated, Sn_{4c}) is more strongly bonded to the surface and is associated with greater charge transfer from the surface than molecules coordinated to the fivefould-coordinated Sn_{5c} centers. From IR spectra of *h*-type SnO_2 (fig. 5) it is obvious that the band with $\nu_{O\text{-}O}$ = 1045 cm^{-1} attributed to oxygen molecule coordinated on Sn_{4c} makes the main contribution into absorbance in the 800 – 1400 cm^{-1} spectrum range. The presence of great quantity of chemisorbed acceptor–like species should result in the significant decrease of electrical conductivity of *h*-type SnO_2. Indeed, the electrical conductivity of the *h*-type samples measured in DC mode is about 10^{-8} Ohm^{-1}*cm^{-1}. The results of impedance measurements indicate the absence of the difference between electrical characteristics of bulk and surface of SnO_2 grains (flat band conditions).

Conclusions

As a summary we can conclude that tin oxide samples synthesized using hydrazine monohydrate are composed by highly defective nanoparticles, which surface is covered by strongly adsorbed oxygen. The extremely high concentration of chemisorbed oxygen results in full electron depletion of SnO_2 grains, low electron conductivity and flat band structure. In these conditions the surface of SnO_2 nanoparticles has high negative charge, which impedes the intergrain interaction because of Coulomb repulsion. This fact can explain the extraordinary microstructure stability and sintering resistance of such type of material.

Acknowledgements

Authors are grateful to Prof. J. Arbiol (EME and SCT of the University of Barcelona) for the TEM investigations and Dr. L. Yashina (Moscow State University) for XPS experiments. The IR, Raman and PL measurements were performed at User Facility Center of M.V. Lomonosov State University. The work has been supported by FP7-NMP-2009 EU-RU project 247768 S3 and Russian Agency “Rosnauka” project 02.257.11.0008.

References

[1] A. Hagemeyer, Z. Hogan, M. Schlichter, B. Smaka, G. Streukens, H. Turner, A. Jr. Volpe, H. Weinberg, and K. Yaccato: Appl. Catalysis A Vol. 317 (2007), p. 139.

[2] N. Sergent, P. Gelin , L. Perier-Camby, H. Praliaud, and G. Thomas: Sens. Actuators B Vol. 84 (2002), p. 176.

[3] D. Amalric-Popescu, J.M. Herrmann, A. Ensuque, and F. Bozon-Verduraz: Phys. Chem. Chem. Phys. Vol. 3 (2001), p. 2522.

[4] M. Batzill, and U. Diebold: Progr. Surf. Sci. Vol. 79 (2005), p. 147.

[5] S. Monredon, A. Cellot, F.Ribot, C. Sanchez, L. Armelao, L. Gueneauc, and L. Delattre: J. Mater. Chem., Vol. 12 (2002), p. 2396.

[6] A. Davydov, *Molecular spectroscopy of oxide catalysts surfaces* (John Wiley & Sons Ltd, 2003)

[7] C.D. Wagner, W.M. Riggs, L.E. Davis, and G.F. Moulder (Eds.), *Handbook of X-ray Photoelectron Spectroscopy* (Perkin Elmer Co, 1979)

[8] Y. Nagasawa, T. Choso, T. Karasuda, S. Shimomura, F. Ouyang, K. Tabata, and Y. Yamaguchi: Surf. Sci. Vol. 433-435 (1999), p. 226.

[9] Q. Li, X. Yuan, G. Zeng, and S. Xi: Mater. Chem. Phys., Vol. 47 (1997), p. 239.

[10] L. Abello, B. Bochu, A. Gaskov, S. Koudryavtseva, G. Lucazeau, and M. Rumyantseva: J. Solid State Chem. Vol. 135 (1998), p. 78.

[11] E. Comini, C. Baratto, G. Faglia, M. Ferroni, A. Vomiero, and G. Sberveglieri: Progr. Mater. Sci. Vol. 54 (2009), p. 1.

[12] X.T. Zhou, F. Heigl, M.W. Murphy, T.K. Sham, T. Regier, I. Coulthard, and R.I.R. Blyth: Appl. Phys. Lett. Vol. 89 (2006), p. 213109.

[13] J. Maier, and W. Göpel: J. Solid State Chem. Vol. 72 (1988), p. 293.

[14] M. Habgood, and N. Harrison: Surf. Sci. Vol. 602 (2008), p. 1072.

doi:10.4028/www.scientific.net/AST.75.43

Potentiostatic Deposition of Zinc Oxide on Flexible Substrate

ChingHong Wong[a], CheeLeung Mak[b] and KinHung Wong[c]

Department of Applied Physics, The Hong Kong Polytechnic University,
Hung Hom, Hong Kong, People's Republic of China
[a]08901379r@polyu.edu.hk, [b]apaclmak@polyu.edu.hk (corresponding author),
[c]apakhwon@polyu.edu.hk

Keywords: Zinc oxide; thin film; electrodeposition; flexible substrate.

Abstract. Transparent zinc oxide (ZnO) films on flexible copper-coated polyethylene terephthalate (PET) sheet have been grown by a potentiostatic cathodic deposition technique using aqueous zinc nitrate as electrolyte. ZnO films were fabricated using different deposition parameters such as applied potential, electrolyte concentration and bath temperature. Their structural and optical properties were characterized by X-ray diffractometer, scanning electron microscope, diffuse reflectance UV-VIS spectrophotometer and photoluminescence spectrometer. The effects of these deposition parameters on the structural and optical properties of the fabricated ZnO films have been investigated. On the basis of our results, we demonstrate that high quality ZnO films have been successfully grown on flexible polymeric substrates using a low temperature potentiostatic cathodic deposition technique.

Introduction

In recent years, transparent conductive zinc oxide (ZnO) has received much attention. The unique intrinsic properties of large band gap (3.4 eV) as well as high excitonic energy (60 meV), strong resistance to high temperature and being the hardest material in the family of II–VI semiconductors make ZnO to be a potential candidate for devices in areas such as optoelectronics[1], photovoltaics [2], gas sensing [3],field emission [4] and piezoelectrics [5]. Among the various characteristics of ZnO, its tunable electrical conductivity through controlling the doping level and high transparency in visible region are particularly important for photovoltaic devices. Electrodeposition presents a rapid and cost-effective method over most commonly techniques such as pulsed laser deposition (PLD), sputtering , physical vapor deposition [6], chemical vapor deposition [7], etc. This technique also can easily scale up to fabricate large area films which is essential for solar cell applications. The mechanism of electrodospition of ZnO is based on the reduction of a soluble precursor such as nitrate ions, molecular oxygen or hydrogen peroxides to generate hydroxide ions on the conducting substrate which also acts as an electrode. The increased localized pH on the electrode surface helps the zinc ions to precipitate in the form of ZnO. With the increasing need for low cost and flexible electronic devices, flexible conducting substrates play an important role in this field [8]. Recent developed copper coated polyethylene terephthalate (Cu-coated PET) films suit the requirements of low cost, good flexibility and high conductivity. Adhesive copper film makes it capable for many engineering purposes. Since most of the studies on electrodeposited ZnO are those fabricated on ITO-based glasses, utilizing a Cu-coated PET as substrates will demonstrate the possibilities of electrodepositing ZnO on flexible substrates based on a cheap electrode. In this present work, the effects of the major growth parameters of the electrodeposited ZnO films on their morphological as well as optical properties are investigated. On the basis of our results, we demonstrate that, by carefully selecting the growth conditions, high quality ZnO films can be prepared on flexible substrates by electrodeposition methods without any post-annealing.

Experimental Details

Electrodeposition. A conventional three-electrode setup was used to perform the deposition of ZnO films. Graphite rod, Ag/AgCl(sat' KCl) and Cu/PET were employed as the counter electrode (CE), the reference electrode (RE) and the working electrode (WE) respectively. The copper metallization process of PET followed the standard procedures which were reported elsewhere [9]. Aqueous zinc nitrate solution with pH value of 3.6 was employed as the electroplating baths used to synthesis the ZnO films.

The cyclic voltammetry measurement were carried out using an EG&G PAR 2273 potentiosat to analyze the reactions on WE and monitor the deposition process. Through out our experiments, Cu-coated PET films were used as the substrates for all processes. The substrates were first cleaned with acetone, diluted HNO_3 and finally with distilled water. The cyclic voltammetry measurement was carried out at a scan rate of 20mV/s. Six sets of samples (Table 1) with various deposition potential, bath concentration and deposition temperature were fabricated. All the samples had the same deposition time of 16 minutes. All voltages mentioned in this paper were taken against Ag/AgCl (sat' KCl) reference electrode without further specifications.

Table 1. Electrodeposition conditions of ZnO samples on Cu coated PET from zinc nitrate bath.

Sample no.	Deposition potential [mV versus Ag/AgCl]	Bath concecentration [M]	Temperature [°C]
A	-400	0.01	80
B	-550	0.01	80
C	-700	0.01	80
D	-550	0.1	80
E	-550	0.5	80
F	-550	0.1	60
G	-550	0.1	40

Characterization. The phase and the preferential orientation of the ZnO films were determined by a Philips Xpert X-ray diffraction system using CuK_α radiation (λ=1.5418 Å). Surface morphology and grain size of the ZnO films were characterized by a field emission scanning electron microscope (FESEM EOL JSM-6335F). The reflectance properties of the ZnO films were measured by a diffuse UV-VIS reflectance spectrophotometer (Cary 4000 UV-Vis spectrophotometer). Room-temperature photoluminescence spectroscopy was obtained by using a 325nm laser equipped with a spectrometer (Edinburgh Instruments).

Results and Discussion

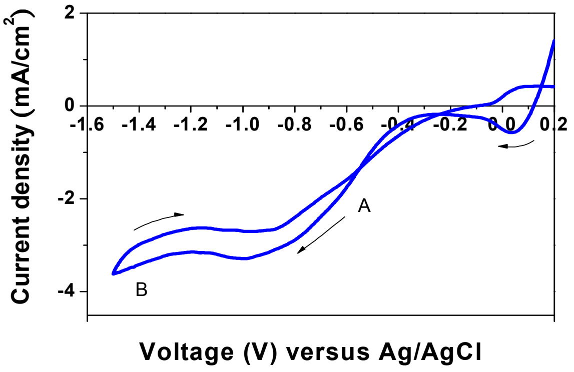

Figure 1. Cyclic voltammogram of a Cu coated PET electrode in 0.01M zinc nitrate solution with bath temperature: 80°C and pH: 3.6 .

The voltammogram in Fig. 1 shows the reactions on the Cu/PET substrate when it is scanned from 0.2V to -1.5V in the zinc nitrate solution. A steep increase of cathodic current occurs at -0.4V and reaches 3.5mA at -0.9mV (curve A). In this region, the reduction of nitrate ions and the reduction of hydrogen ions contribute to the cathodic current as their reducing potential is similar to each other. The reduction of nitrate ions generates the OH^- ions which help the formation of ZnO. When the potential is decreased beyond -0.9V, an slightly increase of the cathodic current is record. It is because a more negative potential favors the reduction of the zinc ions to zinc metal on the surface of substrate and thus results a large current flow around at -1.25V (curve B).

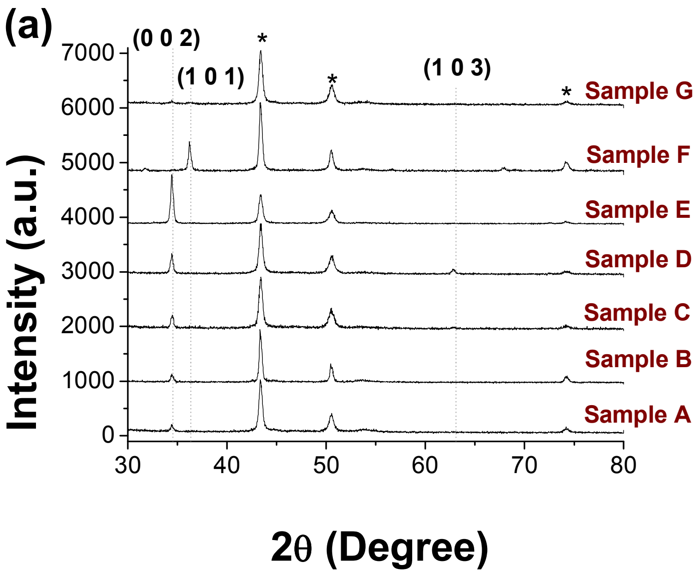

Figure 2. X-ray theta-2 theta scans of the ZnO films prepared. (* represents the diffraction peaks from Cu-coating.)

Structural Analysis. X-ray diffraction patterns of sample A, B and C which were obtained at -0.4V, -0.5V and -0.7V respectively are shown in Fig. 2(a). The depositions temperature and zinc nitrate concentration were maintained at 80°C and 0.01M, respectively. Only (0 0 2) peak is appeared in the XRD over these samples, indicating that the films are possessing good crystalline with highly oriented ZnO crystal in nature. The strong preferential growth habit can be explained by the fast growth kinetics of <0 0 0 1> among all directions [10]. The effect of increasing the concentrations of zinc nitrate solution on the structures is shown in the Fig. 2 (B), Fig. 2 (D) and Fig. 2 (E). Generally speaking, as the bath concentration increases, the relative intensity of the (002) peak increase (as compared to the Cu peaks). Furthermore, the full width at half maximum (FWHM) of the (002) peak remain the same. When decreasing the bath temperature to 60°C, the dominant peak is changed from (002) to (101) as shown in Fig. 2 (F). Further decrease the bath temperature to 40°C, no detectable crystalline ZnO is observed as shown in Fig. 2 (G).

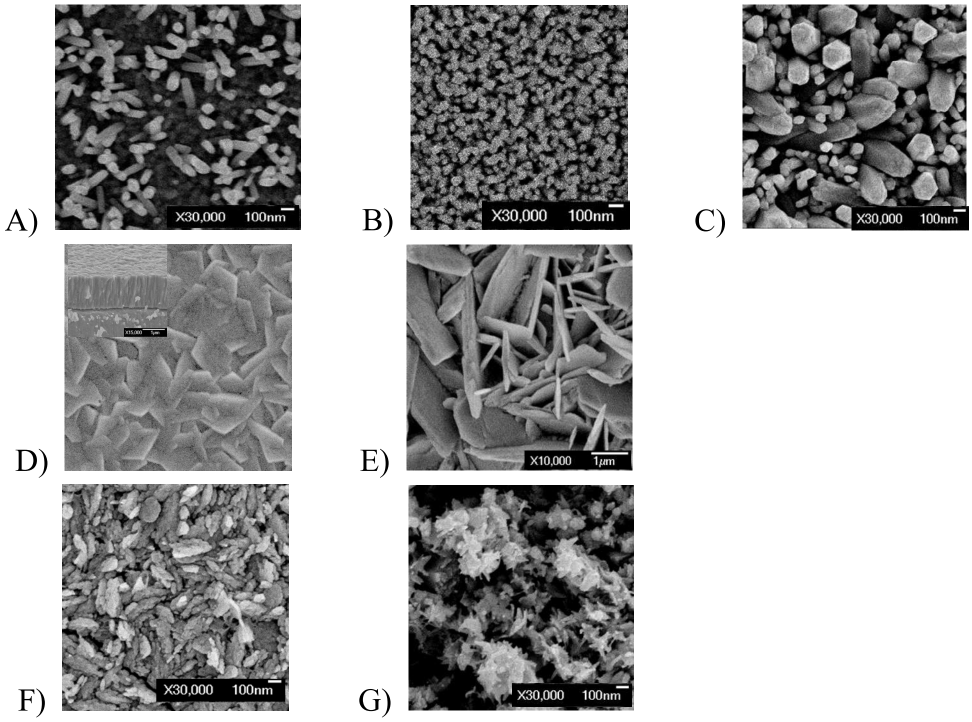

Figure 3. SEM micrographs of the ZnO films prepared by varying deposition potentials, bath concentration and bath temperature (from left to right): sample A to C (first row), sample D and sample E (second row), sample F and sample G (third row).

Surface morphology. Figs. 3 (A) to (G) summarize the effects of applied voltage, bath concentration and deposition temperature on the surface morphology of ZnO films. Generally speaking, ZnO nano-rods of various sizes are deposited on the substrate with different applied potential as shown in Fig. 3 (A). The diameter of the rods enlarges from ~50nm to ~200nm as the deposition potential changed from -0.4V to -0.7V, respectively. Furthermore, a more negative deposition potential results in the increase of rod density resulting a stronger XRD peak. On the other hand, high concentration of zinc nitrate electrolyte produces a denser ZnO films (Figs. 3 (B), (D), (E)). It composes some hexagonal grains but not rods in a smooth surface. Further increase the concentration up to 0.5M, nodular ZnO gains appear in Fig. 3 (E). The plate-like crystals with 3μm in diameter are randomly aligned and their c-axis orient perpendicular to the substrate surface (as shown in XRD results) . Surface morphologies of deposited ZnO at 40°C and 60°C are shown in Figs. 3 (F) and 3 (G). Deposition of ZnO at 60°C (sample F) allows the growth of nano platelet-liked crystals which possess approximately 100nm in size. Further decrease the growth temperature to 40°C, aggregation of ZnO hexagonal slices forms irregular columns and some pores are located between columns. As suggested by XRD, these nano ZnO hexagonal slices are probably amorphous in nature.

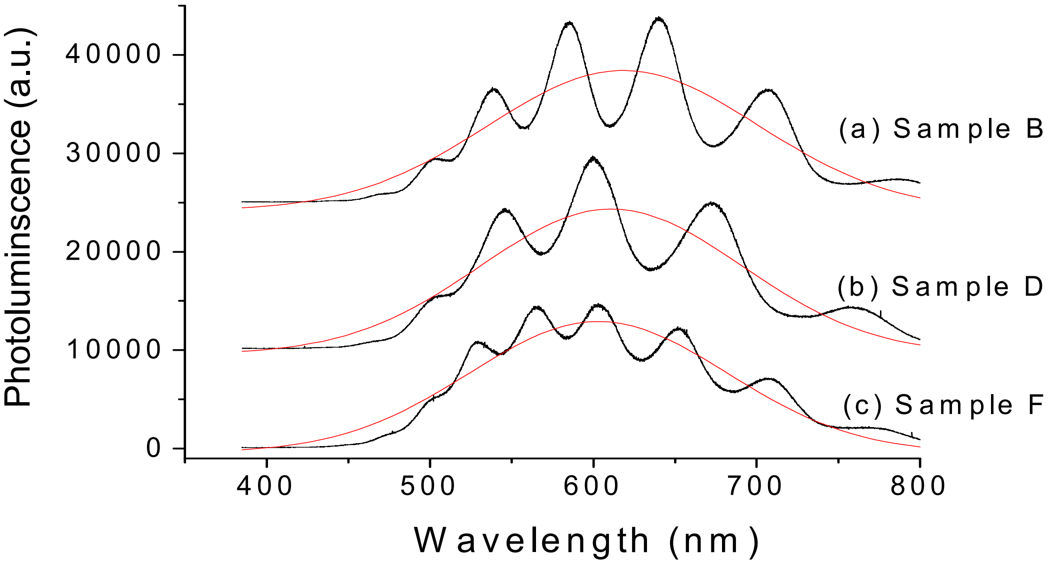

Figure 4. Photoluminescence spectra of (a)sample B, (b) sample D and (c) sample F. Red lines: Gaussian fitting for each curve.

Optical Characterization. Sample B which was electrodeposited from 0.01M zinc electrolyte at 80°C shows a yellow emission with a peak at 618nm as shown by a red line fitting in Fig. 4 (a). It is previously assigned as emission induced by oxygen interstitials [11]. The well structured and smooth oscillations of the photoluminescence profiles indicated that the films have flat surfaces and uniform thicknesses. Fig. 4 (b) shows the effect of 0.1M bath concentration (sample D) on PL, the peak value of this yellow emission is 611nm which show a shift to lower frequency side. Deposition of ZnO film at 60°C (sample F) cause the defect emission shifts from yellow to green peaking at 602nm, which was previously assigned to be arisen from oxygen deficiency [11].

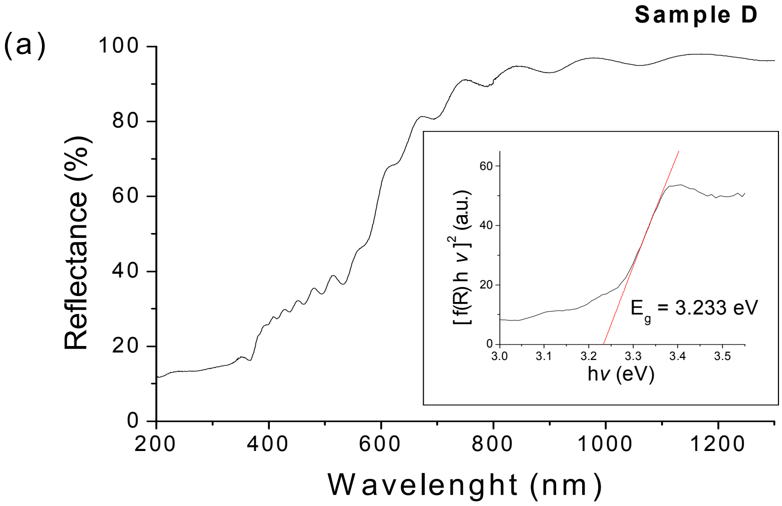

Figure 5. Diffuse UV-Vis reflectance spectrum and Kubelka-Munk transformed reflectance spectrum (inset) of deposited ZnO film on Cu-coated PET (sample D).

Diffuse reflectance spectrum of sample D is shown in Fig. 5. The well structured and the oscillations of the reflectance profile indicates the film have flat surfaces and uniform thickness. A considerable reduction in reflectance starts at about 700 nm. The diffuse reflectance spectrum of sample D after Kubelka-Munk treatment is shown as the inset of Fig. 5. The determination of the bandgap of this sample from the intersection between the linear fit and the photon energy axis gives a value of 3.23eV which is close to 3.3eV obtained in ZnO films [12].

Conclusions

ZnO thin films have been deposited on flexible substrates using potentiostatic cathodic deposition method. XRD patterns revealed that highly c-axis oriented crystalline films are obtained under most fabrication conditions. SEM microstructural studies showed that nanorods, nanoplatelet and dense thin films of ZnO can be obtained. Photoluminescence spectra revealed the presence of oxygen interstitials in films due to the observation of yellow emissions. An absorption edge at 700nm was recorded in the UV-Vis reflectance spectrum, indicating a bandgap energy of 3.23eV. Our results demonstrate that high qualities ZnO films can be easily grown on flexible polymeric surface using potentiostatic cathodic deposition technique.

References

[1] W. I. Park and G. C. Yi: Adv. Mater. Vol. 16 (2004), p. 87

[2] M. Law, L. E. Greene, J. C. Johnson, R. Saykally, and P. Yang: Nature Mater Vol. 4 (2005), p. 455

[3] L. Liao, H. B. Lu, J. C. Li, H. He, D. F. Wang, D. J. Fu, C. Liu, and W. F. Zhang: J. Phys. Chem. C Vol. 111 (2007), p. 1990

[4] X. Wang, J. Zhou, C. Lao, J. Song, N. Xu, and Z. L. Wang: Adv. Mater. Vol. 19 (2007), p. 1627

[5] X. Wang, J. Song, J. Liu, and Z. L. Wang: Science Vol. 316 (2007), p. 102

[6] E.M. Bachari, G. Baud, S. Ben Amor and M. Jacquet: Thin Solid Films Vol. 348 (1999), p. 165

[7] M. Purcia, E. Budianu, E. Rusu, M. Danila and R. Gavrila: Thin Solid Films Vol. 403–404 (2002), p. 485

[8] L. Edman: Advanced Materials & Processes Vol. 167 (2009), p15

[9] C.S. Ng, C.L. Mak and Y.W. Wong: Phys. Stat. Sol. (c) Vol. 5 (2008), p. 3535

[10] W.J. Li, E.W. Shi, W.Z. Zhong and Z.W. Yin: J. Crystal Growth Vol. 203 (1999), p. 186

[11] Y.H. Leung, A.B. Djurisic, Z.T. Liu, D. Li, M.H. Xie and W.K. Chan: J. Phys. Chem. Solids Vol. 69 (2008), p. 353

[12] M. Izaki and T. Omi: J. Electrochem. Soc. Vol. 143 (1996), p. L53

doi:10.4028/www.scientific.net/AST.75.49

Analysis on resistive switching of resistive random access memory using visualization technique of data storage area with secondary electron image

Kentaro Kinoshita[1,2,a], Tatsuya Makino[1], Takatoshi Yoda[1], Kazufumi Dobashi[1], and Satoru Kishida[1,2,b]

[1] Department of Information and Electronics, Graduate School of Engineering, Tottori University, 4-101 Koyama-Minami, Tottori 680-8552, Japan.

[2] Tottori University Electronic Display Research Center, 522-2 Koyama-Kita, Tottori 680-0941, Japan.

[a]kinoshita@ele.tottori-u.ac.jp

[b]kishida@ampere.ele.tottori-u.ac.jp

Keywords: ReRAM, NiO, switching mechanism, C-AFM, SEM, EPMA.

Abstract. Both a low and a high resistance state s which were written by the voltage application in a local region of NiO/Pt films by using conducting atomic force microscopy (C-AFM) were observed by using scanning electron microscope (SEM) and electron probe micro analysis (EPMA). The writing regions are distinguishable as dark areas in a secondary electron image and thus can be specified without using complicated sample fabrication process to narrow down the writing regions such as the photolithography technique. In addition, the writing regions were analyzed by using energy dispersive X-ray spectroscopy (EDS) mapping. No difference between the inside and outside of the writing regions is observed for all the mapped elements including C and Rh. Here, C and Rh are the most probable candidates for contamination which affect the secondary electron image. Therefore, our results suggested that the observed change in the contrast of the secondary electron image is related to the intrinsic change in the electronic state of the NiO film and a secondary electron yield is correlated to the physical properties of the film.

Introduction

Recent years, research and development of resistive random access memory (ReRAM) which utilizes voltage induced resistive change in transition metal oxides (TMOs) as memory media is advancing. ReRAM is a candidate for a substitution for the Flash memory, which is facing a micro-fabrication limit in the near future. Furthermore, a development of a nonvolatile and high-density universal memory with fast switching and high switching endurance is expected in the future. However, the optimization of the performance and the establishment of reliability have been prevented by the facts that switching mechanism of ReRAM has not yet been clarified. Therefore, the elucidation of switching mechanism is urgently required.

ReRAM has a simple structure of a top electrode (TE)/TMO/a bottom electrode (BE). Memory effect develops after a forming process, and it becomes possible to cause a set, which is a resistive switching from a high resistance state (HRS) to a low resistance state (LRS), and a reset, which is a resistive switching from the LRS to the HRS, alternately. Here, the forming is a phenomenon, which is similar to a soft breakdown, and a conductive path called a filament is formed after it. Resistive switching is thought to take place in the filament [1-4]. The reason why the elucidation of resistive switching mechanism is hindered is attributed to the difficulty in applying conventional analytical methods to the resistance switching region due to the facts that the filament is covered with electrodes and that the radius of the filament is very small [5,6].

Recently, it was demonstrated that both the LRS and the HRS can be written over an arbitrary area by applying bias voltage directly to NiO films using conducting atomic force microscopy

(C-AFM) [7,8]. The resistance writing region consists of the aggregation of filaments and can be regarded as the one filament with large radius. Therefore, this technique can provide the filament with arbitrary radius without TE, which allows application of conventional analytical methods, and might be a breakthrough for the switching mechanism elucidation.

In this paper, the LRS and the HRS with the large area of 20 × 20 μm^2 were written in a NiO/Pt film by the voltage application using C-AFM. Taking advantage of the largeness of the target area, the writing regions were analyzed by using the scanning electron microscopy (SEM), electron micro probe (EPMA), and energy dispersive X-ray spectroscopy (EDS) for the elucidation of a physical property of the filament.

Experimental

A 60-nm NiO film was deposited on a Pt(100nm)/Ti(20nm)/SiO$_2$(100nm) substrate by DC reactive magnetron sputtering at 380 °C in the mixture gas of Ar and O$_2$ gases (Ar + O$_2$ gas), and a NiO/Pt/Ti/SiO$_2$ (NiO/Pt) structure was obtained. During the deposition, the pressure of Ar + O$_2$ gas was retained at 0.5 Pa (Ar : O$_2$ = 0.45 Pa : 0.05 Pa).

For the C-AFM measurements, a Rh-coated Si tip was grounded, and a bias voltage was applied to the BE.

HRS or LRS was written in the central 20 × 20 μm^2 area by scanning the tip under a bias voltage of -7 V or +7 V, respectively. Subsequently, the 22 × 22 μm^2 area containing the writing region was scanned with a sensing voltage of +1 V. The HRS was written with a negative bias, whereas LRS with a positive bias as reported in ref. [7].

Analyses with EPMA and SEM on the regions where the HRS and the LRS were written were conducted. EDS mapping analysis on areas containing these writing regions were also performed.

Results and discussion

Resistance states written by using C-AFM. Figures 1(a) and 1(b) show current images before and after performing C-AFM writing under a dc bias voltage of +7 V, respectively. On the other hand, Figs. 1(c) and 1(d) show current images before and after performing C-AFM writing under a dc bias voltage of -7 V, respectively. The bright contrast regions in the current image correspond to the LRS, and the dark contrast regions to the HRS. Therefore, it was confirmed that HRS was written by the application of negative bias voltage, whereas LRS was written by the application of positive bias voltage, which is consistent with ref. [7].

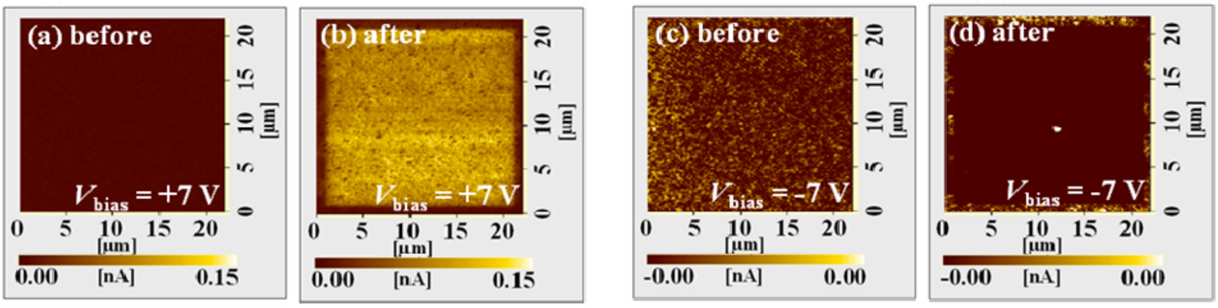

Fig. 1 Current images (a) before and (b) after C-AFM writing by scanning under a dc bias voltage of +7 V. Current images (c) before and (d) after C-AFM writing by scanning under a dc bias voltage of -7 V.

SEM and EPMA analyses. Figure 2(a) shows the locations of four 20 x 20 μm^2 regions on the NiO film to which resistance states were written by using C-AFM. Resistance states of the regions (1), (2), (3), and (4) were written by scanning the AFM-tip under dc bias voltages of +7 V, -7 V, +5 V, and -5V, respectively. Regions (1) and (3) were written to the LRS, whereas regions (2) and (4) were written to the HRS. That is, the resistance decreased by application of positive bias, whereas increased by negative bias, as described above. The scratch in the figure was introduced by a diamond-point pencil to support finding out the same place containing these regions by EPMA and SEM.

Figures 2(b), 2(c), and 2(d) represent a secondary electron (SE), a composition (COMP), and a topographic (TOPO) images of the NiO film containing all the regions (1)-(4), respectively. Here, COMP and TOPO images are obtained by a primary electron emission, which is sensitive to both the composition and surface morphology of the sample. Dark regions in Fig. 2(b), where a secondary electron yield is low compared with the other region, correspond to the regions (1)-(4), whereas no difference in the contrast from the surrounding region is observed in the corresponding region in Figs. 2(c) and 2(d). In addition, the SE image becomes darker with increasing the amplitude of writing voltage.

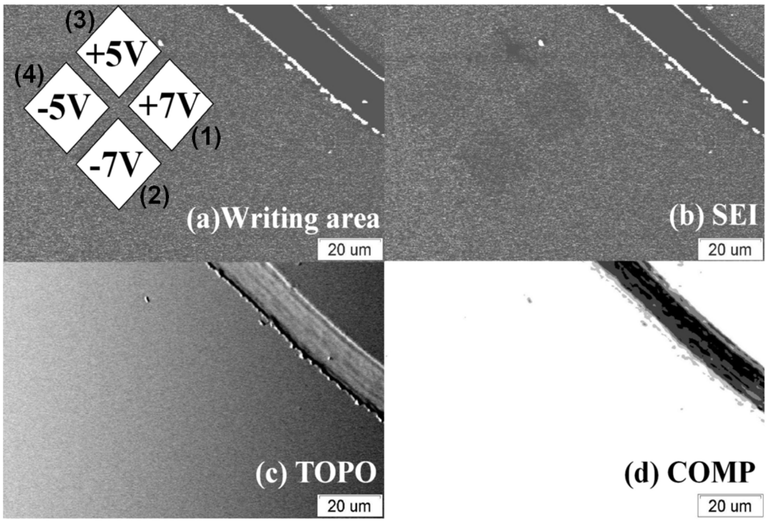

Fig. 2 (a) Schematic that shows location of regions (1)-(4) written by scanning under dc bias voltages of +7, -7, +5, and -5 V using C-AFM, respectively. (b) SE, (c) TOPO, and (d) COMP images of the NiO film in which regions (1)-(4) are included.

Figures 3(a) and 3(b) show SE images before and after C-AFM writing (not the same position). Tetrahedral grain structures are observed on the surface, showing the (111) orientation of the NiO film. No remarkable change in both sizes and shapes of NiO grains were observed. No damage caused by the writing current was also confirmed.

Figure 4 shows applied bias and scanning frequency dependences of a SE image for writing regions. In Fig. 4, regions (1)-(3) were written to the LRS and regions (4)-(6) were written to the HRS under the writing conditions shown in table. 1. The higher the applied bias becomes and/or the lower

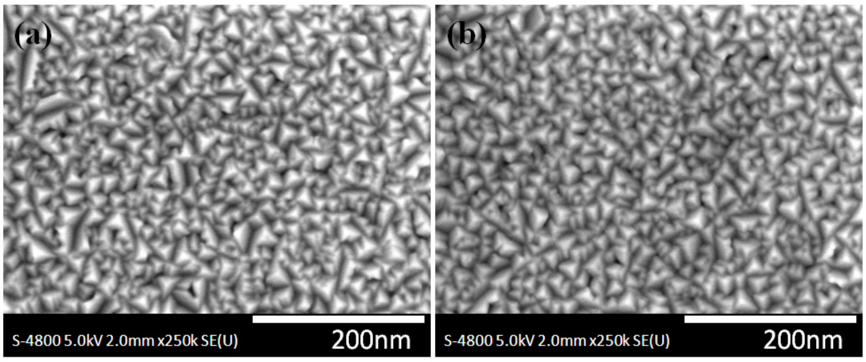

Fig. 3 SE images before and after C-AFM writing under a dc bias voltage of +7V with a scanning frequency of 0.2 Hz.

the scanning frequency becomes, the darker the SE image of the writing regions becomes. Therefore, a darker SE image is obtained by applying a bias voltage with larger amplitude for a longer duration to the unit area.

Table. 1 Conditions under which regions (1)-(6) in Figs. 4 and 5(a) were written to the HRS or the LRS by using C-AFM.

Writing regions	Writing-V V [V]	Frequency ν [Hz]
(1)	+9	1
(2)	+9	0.2
(3)	+5	1
(4)	-9	1
(5)	-9	0.2
(6)	-5	1

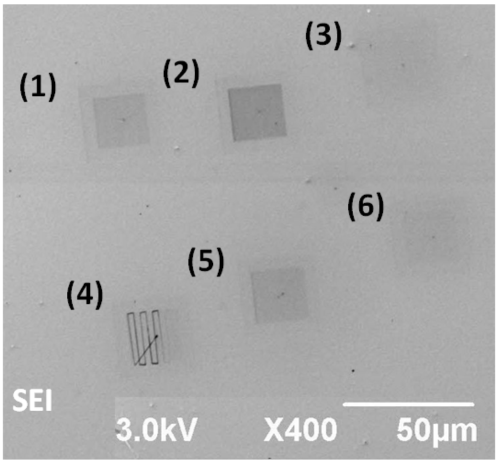

Fig. 4 SE image after C-AFM writing for regions (1)-(6) under the conditions shown in table. 1.

EDS mapping analysis. As possible main factors which cause the change in the contrast of a SE image by the application of a dc bias voltage using C-AFM, the following three factors can be pointed out: (i) The change in the surface morphology has been caused. (ii) Removal/adhesion of contaminations from/to the surface of the NiO film has been caused. (iii) An intrinsic change in electronic state of NiO has been caused. Since no remarkable change in the surface morphology of the sample by the application of C-AFM writing was observed, which denied the factor (i), the possibility of the factor (ii) will be discussed below.

Elements for which EDS mapping analysis were conducted were selected as follows. Hilleret el al. reported that secondary electron yield of an air exposed ZnO film decreased after annealing the film [9]. This is due to a removal of airborne carbonaceous contamination layer formed on the surface of the sample by the annealing process. Analogously, also in the present study, the removal of carbonaceous contamination might be caused by Joule heating generated during C-AFM writing. Therefore, C was selected as a mapping element. In addition, Rh with which the AFM-tip is coated might adhere to the scanned area. By adding the constituent elements of the sample to C and Rh, EDS mapping analyses were performed on C, Rh, Ni, O, and Pt.

Figure 5(a), which is the same figure as Fig. 3, shows the SE image after the C-AFM writing. The square regions surrounded by dotted lines correspond to the writing regions which were written under the conditions shown in Table. 1. Figures 5(b)-5(f) show results of EDS mapping measurements for Rh, C, O, Ni, and Pt, respectively. Here, the square regions surrounded by dotted lines in Fig. 5(b)-5(f) correspond to the writing regions in Fig. 5(a), respectively. The acceleration voltage was 3.0 kV. Energies of C K_α, O K_α, Ni L_α, Pt M_α, and Rh L_α lines are 0.277, 0.525, 0.851, 1.739, 2.048, and 2.696 eV, respectively.

No difference of the intensity distribution in the EDS mappings between inside and outside of the writing regions was observed for all the mapped elements, suggesting the exclusion of the factor (ii). Therefore, as a reason why the SE image becomes dark by the voltage application, it was suggested that the change in the electric conductivity of NiO affected the secondary electron yield.

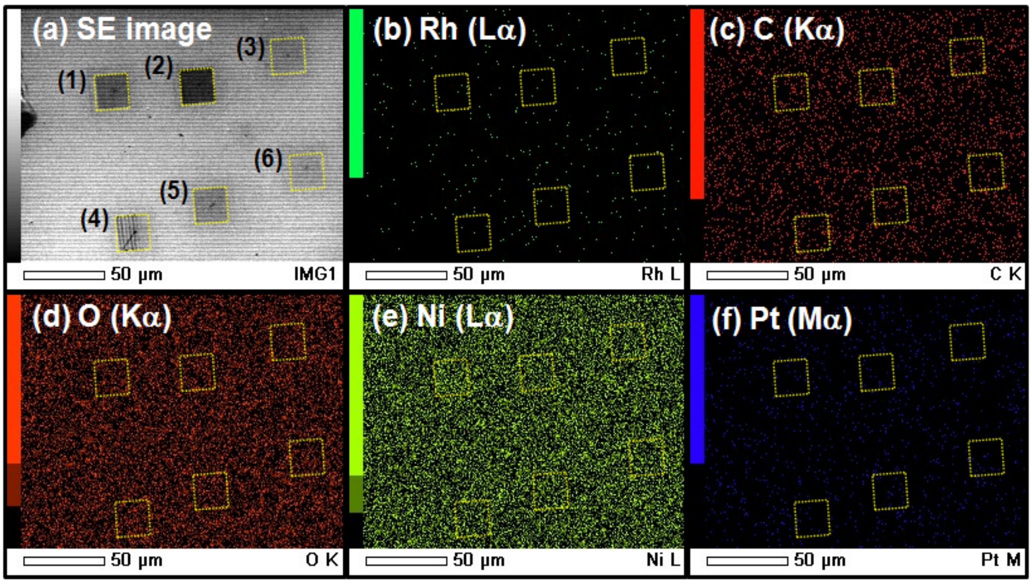

Fig. 5 (a) Secondary electron image after writing under the conditions shown in table. 1, which is the same as Fig. 4. EDS mapping results for (b) Rh, (c) C, (d) O, (e) Ni, and (f) Pt.

It has been widely received that the resistance change effect observed in transition metal oxides is caused by the migration of oxygen ions [2,7,10], which introduces or repairs oxygen vacancies depending on the applied bias condition. It has also been received that the LRS is formed by ranging vacancies through the film, which is the so-called filament, whereas HRS is formed by repairing the vacancies only near the electrode interface [2,11,12]. This means that conductive filaments other than the neighborhood of the electrode interface remain without being repaired even in the HRS. Therefore, this is consistent with the fact that the writing region becomes dark whether it is in the HRS or the LRS in the SE image if assuming that a conductive region becomes dark in the SE image. Shima et al. performed Kelvin probe force microscopy and micro X-ray photoelectron spectroscopy measurements on the LRS of a CoO film which was written by the voltage application using C-AFM [6]. They reported that Fermi energy in CoO is pushed up because of reduction of CoO which causes defect-related energy levels in the band gap. Since it was reported that low secondary electron yield was related to a low work function [13], our result also suggests that the C-AFM writing decreases a work function, which is consistent with ref. [6]. It is worth noting that we obtained the result similar to that reported in ref. [6], in which the photo lithography was used to narrow down the writing regions, without using the photo lithography.

Conclusions

SEM and EPMA analyses on the C-AFM writing region revealed that the writing regions are distinguishable as dark areas in SE images. This enables to specify the writing region without using complicated sample fabrication process to narrow down the writing regions such as the photolithography technique. In addition, EDS mapping analysis on the writing region suggested that the observed change in the contrast of the SE image is related to the intrinsic change in the electronic state of the NiO film, i.e., that the secondary electron yield is correlated to the physical properties of the film.

References

[1] I. G. Baek, M. S. Lee, S. Seo, M. J. Lee, D. H. Seo, D.-S. Suh, J. C. Park, S. O. Park, H. S. Kim, I. K. Yoo, U-In Chung and J. T. Moon, Tech. Digest IEDM 2004, p. 587.

[2] K. M. Kim, B. J. Choi, and C. S. Hwang, Appl. Phys. Letts. **90**, 242906 (2007).

[3] K. Kinoshita, T. Tamura, M. Aoki, Y. Sugiyama, and H. Tanaka, Jpn. J. Appl. Phys. **45**, L991 (2006).

[4] J. F. Gibbons and W. E. Beadle, Solid-State Electron. **7**, 785 (1964).

[5] M.-J. Lee, S. Han, S. H. Jeon, B. H. Park, S. Kang, S-E. Ahn, K. H. Kim, C. B. Lee, C. J. Kim, I.-K. Yoo, D. H. Seo, X.-S. Li, J.-B. Park, J.-H. Lee, and Y. Park, Nano Lett. 9, 1476 (2009).

[6] H. Shima, F. Takano, H. Muramatsu, M. Yamazaki, H. Akinaga, and A Kogure, phys. stat. sol. (RRL) **2**, 99 (2008).

[7] C. Yoshida K. Kinoshita, T. Yamasaki, and Y. Sugiyama, Appl. Phys. Lett. **93**, 042106 (2008).

[8] K. Kinoshita, T. Okutani, H. Tanaka, T. Hinoki, K. Yazawa, K. Ohmi, and S. Kishida, Appl. Phys. Lett. **96**, 143506 (2010).

[9] N. Hilleret, C. scheuerlein, M. taborelli, Appl. Phys. A **76**, 1085 (2003).

[10] Y. B. Nian, J. Strozier, N. J. Wu, X. Chen, and A. Ignatiev, Phys. Rev. Lett. **98**, 146403 (2007).

[11] K. Kinoshita, T. Tamura, M. Aoki, Y. Sugiyama, and H. Tanaka, Appl. Phys. Lett. **89** (2006) 103509.

[12] I. H. Inoue, S. Yasuda, H. Akinaga, and H. Takagi, Phys. Rev. B **77** (2008) 035105.

[13] M. Kudo, Y. Sakai and T. Ichinokawa, Appl. Phys. Lett. **76**, 3475 (2000).

doi:10.4028/www.scientific.net/AST.75.55

Chromogenics for Sustainable Energy: Some Advances in Thermochromics and Electrochromics

C.G. Granqvist[1,a], S.V. Green[1,b], S.-Y. Li[1,c], N.R. Mlyuka[1,d],
G.A. Niklasson[1,e] and E. Avendaño[2,f]

[1]Department of Engineering Sciences, The Ångström Laboratory, Uppsala University,
P. O. Box 534, SE-75121 Uppsala, Sweden
[2]ChromoGenics AB, Märstagatan 4, SE-75323 Uppsala, Sweden
[a]claes-goran.granqvist@angstrom.uu.se, [b]sara.green@angstrom.uu.se, [c]shuyi.li@angstrom.uu.se,
[d]nmlyuka@yahoo.com, [e]gunnar.niklasson@angstrom.uu.se,
[f]esteban.avendano@chromogenics.com

Keywords: Chromogenics, thermochromics, electrochromics, windows, energy efficiency, thin films, nanoparticles, vanadium oxide, tungsten-nickel oxide, sputtering, roll-to-roll coating

Abstract. Chromogenic materials are able to change their optical properties in response to external stimuli such as temperature (in thermochromic materials) and electrical charge insertion (in electrochromic materials). Below we review some recent advances for these types of materials. Specifically we first discuss the limitations of thermochromic VO_2 films for energy efficient fenestration and show from calculations that nanocomposites containing VO_2 can have superior properties and display high luminous transmittance and large temperature-dependent solar transmittance modulation. Even better results may be found for nanoparticles of VO_2:Mg. In the second part of the paper we survey some recent progress for electrochromic devices and show that W oxide films have increased coloration efficiency when some Ni oxide is added. We also present initial results for flexible electrochromic foils produced by roll-to-roll coating and continuous lamination.

Introduction

Worldwide some 30 to 40 % of the primary energy is used in buildings according to a recent study by the United Nations Development Programme (UNDP) [1]. Most of this energy is for heating, cooling, lighting, ventilation and appliances. The percentage for the U.S.A., to take an example, is 39 % [2]. The relative amount of electricity used in buildings is even larger and can reach 70 % for the most industrialized countries. This energy typically comes from fossil fuel, and so it is associated with CO_2 emissions.

The energy savings potential is huge for buildings, and it is largely untapped as a consequence of entrenched and poor building practices. Thus a recent and influential study on how the U.S.A. can reduce global warming and achieve energy security states that [2]

> *"... a large fraction of the energy delivered to buildings is wasted because of inefficient building technologies. How much of this energy can ultimately be saved is an open question – as much as 70 percent by the year 2030 and perhaps more than 90 percent in the long run if there were pressing reasons to go that far. These energy savings can be made not by reducing the standard of living, but by utilizing more efficient technologies to provide the same, or higher, levels of comfort and convenience we have to come to enjoy and appreciate".*

It is important to note the emphasis on the fact that energy savings must be accomplished in conjunction with keeping or increasing the level of human comfort and convenience. In fact the possibility to increase human comfort in buildings—for example by diminishing the use of noisy air conditioning or disturbing glare from windows—can serve as powerful driving forces for the introduction of new energy efficient building technology.

The sense of indoor comfort is a multifaceted and complex issue embracing air quality, temperature, noise pollution, lighting, and the possibility of having visual indoors-outdoors contact. One important aspect on the indoor environment is that—in the industrialized countries—people tend to spend most of their time inside buildings and vehicles; recent evaluations have shown that the fraction of this "indoors" time is often as large as 80 to 90 % [3].

This paper, which is an adaptation of a recent conference report [4], is devoted to one important aspect of energy savings in buildings, *viz.* energy efficient fenestration employing chromogenic materials, *i.e.*, using windows with transmittance levels that can be changed in response to external stimuli [5,6]. Specifically we report on recent progress in *thermochromic* materials which allow the solar energy inflow to be diminished as the temperature goes above a comfort level, and *electrochromic* materials which make it possible to regulate the inflow of visible light and solar energy using electricity. Both types of chromogenic materials—used individually or in conjunction—make it possible to decrease the demand for air cooling. This demand can be very high, and it accounts for ~14 % of the energy used in buildings in the U.S.A. [2].

Thermochromics

General characteristics. Vanadium dioxide has thermochromic properties and has been discussed for temperature-dependent modulation of the solar energy transmittance in windows for many years [7]. VO_2 has a reversible structural transformation at a "critical" temperature τ_c, and it is monoclinic, semiconducting and rather infrared transparent for temperatures $\tau < \tau_c$ while it is tetragonal, metallic and infrared reflecting at $\tau > \tau_c$. The thermochromic switching is highly reversible in thin films. It is not practical to use VO_2 films directly on windows, though, for three reasons as elaborated next.

Firstly, τ_c is ~68 °C, at least in bulk samples, which clearly is too high for buildings-related applications. However doping with transition metal ions having a valency of 6+ and 5+ can decrease τ_c. The most extensively studied dopant is W^{6+}, which can bring τ_c to room temperature without significantly deteriorating the thermochromism [7]; the required amount of tungsten depends on the degree of crystalline order in the VO_2. The addition of some W^{6+} does not have any large effect on the optical properties [8].

A second problem associated with VO_2 is that, in order to display well developed thermochromism, films have to be thick enough that the luminous transmittance T_{lum} is only around 50 % or less, and this is too low for most applications in buildings [7]. Antireflection with high-dielectric coatings can improve the transmittance to some extent as was shown recently for five-layer coatings consisting of $TiO_2/VO_2/TiO_2/VO_2/TiO_2$ [9].

A third problem with VO_2 films is that the thermochromic reflectance modulation is strong primarily in the near-infrared part of the solar irradiance spectrum which corresponds to wavelengths for which the solar radiation is rather weak. Hence the modulation of the solar energy transmittance T_{sol} between a low-temperature and a high-temperature state is undesirably small; typically it is ~5 % for a VO_2 film, but it can be as large as 10 to 15 % in a well-designed $TiO_2/VO_2/TiO_2/VO_2/TiO_2$ multilayer structure [9]. These three limitations of VO_2 have led us to a new study of its potential with regard to windows, as discussed below.

Optical properties of VO_2 films. VO_2 films were made by reactive dc magnetron sputtering onto substrates kept as ~450 °C [9]. Spectral transmittance T and reflectance R were recorded at $\tau < \tau_c$

and $\tau > \tau_c$ for films whose thickness t typically was 0.05 μm. The complex spectral dielectric function, denotes $\varepsilon_f(\lambda)$, was then evaluated by the use of standard formulas of thin film optics. Finally $T(\lambda,\tau,t)$ and $R(\lambda,\tau,t)$ were calculated from $\varepsilon_f(\lambda)$.

Integrated values on the luminous and solar transmittance are of interest for assessing visual and energy-related performance of thermochromic windows. These data were derived from

$$T_{\mathrm{lum,sol}}(\tau,t) = \int d\lambda\ \varphi_{\mathrm{lum,sol}}(\lambda)\ T(\lambda,\tau,t) \,/ \int d\lambda\ \varphi_{\mathrm{lum,sol}}(\lambda)\ , \qquad (1)$$

where φ_{lum} is the spectral sensitivity of the light-adapted eye [10] and φ_{sol} is the solar irradiance spectrum for air mass 1.5 (corresponding to the sun standing 37° above the horizon [11]). Figure 1 shows, as expected, that if one requires a noticeable solar energy modulation then T_{lum} is limited to ~40 %; furthermore the modulation of T_{sol} does not exceed ~10 %.

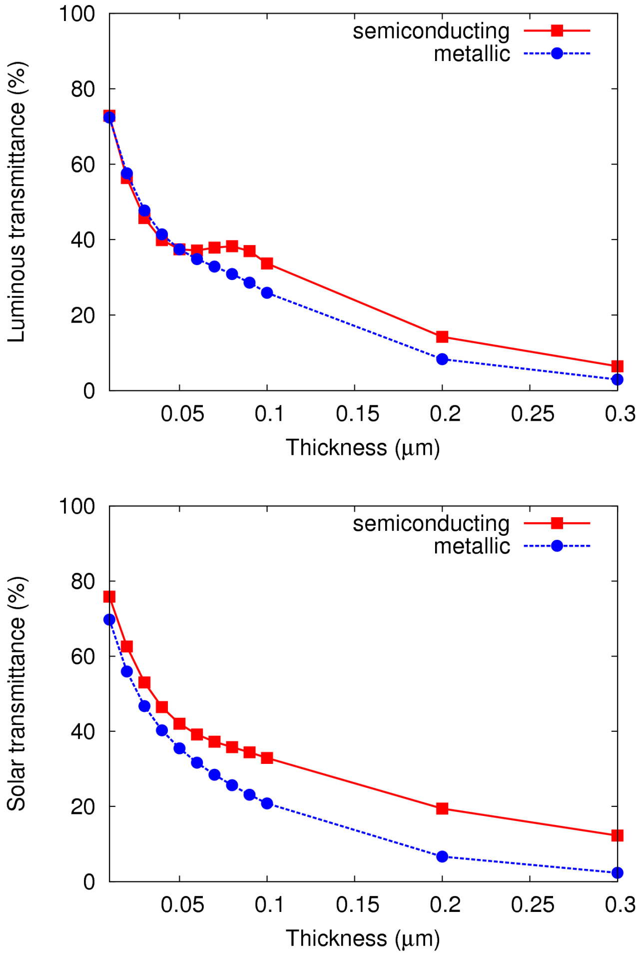

Fig. 1. *Computed luminous (upper panel) and solar (lower panel) transmittance versus thickness of VO_2 films in semiconducting (low-temperature) and metallic (high-temperature) states.*

Optical properties of VO_2 nanoparticle composites. We have very recently shown by computation that materials with VO_2 nanoparticles dispersed in a transparent matrix can increase T_{lum} as well as the modulation of T_{sol} over what is possible in VO_2 films. Hence "nano-thermochromics" appears to give very significant advantages when compared to traditional thin film thermochromics [12].

The nanoparticle composites can be represented as “effective media” with properties intermediate between those of VO_2 and of the embedding matrix. The “effective” dielectric function ε^{MG} can be written [6]

$$\varepsilon^{MG} = \varepsilon_m \frac{1+\frac{2}{3}f\alpha}{1-\frac{1}{3}f\alpha} \quad , \tag{2}$$

where ε_m refers to the matrix and f is the “filling factor”, *i.e.*, the volume fraction occupied by the particles. We make use here of the same terminology as in earlier papers [13]. The calculations presented below used $f = 0.01$ and a thickness of 5 μm (corresponding to a VO_2 mass thickness of 0.05 μm).

Equation (2) is appropriate for the Maxwell-Garnett (*MG*) theory [14], which applies to a topology with nanoparticles dispersed in a continuous matrix [15]. There are numerous other effective medium formulations as well, but they all coincide in the dilute limit so Eq. (2) can be applied here without any loss of generality.

Equation (2) contains a parameter α which can be written

$$\alpha = \frac{\varepsilon_p - \varepsilon_m}{\varepsilon_m + L(\varepsilon_p - \varepsilon_m)} \quad . \tag{3}$$

Here ε_p is the dielectric function of the particles and the L denotes the relevant depolarization factor. Spheres have $L = ⅓$. A random distribution of ellipsoidal particles can be represented by a summation of α over three components pertaining to the symmetry axes [13]. The calculations to be discussed shortly considered prolate and oblate spheroids with depolarization factors obeying $\Sigma L_i = 1$; the L_is are related to the major (a) and minor (c) axes of the spheroidal particles by known formulas [16].

Calculations of $T_{\mathrm{lum}}(\tau,t)$ and $T_{\mathrm{sol}}(\tau,t)$ were performed in the same way as before. We set $\varepsilon_p = \varepsilon_f$ and $\varepsilon_m = 2.25$, where the latter value is appropriate for a matrix of glass or polymer, and assumed randomly oriented spheroids. It is justified to use ε_f without any particle size dependence in the effective medium calculation since free electrons in the high-temperature phase of VO_2 have very short mean free paths [12,17].

The upper panel in Fig. 3 describes the experimental configuration and introduces an aspect ratio $m = a/c$ for prolate spheroids ($m = c/a$ for oblate spheroids). These data can be directly compared with those for a film with a thickness of 0.05 μm in Fig. 1. Such a comparison makes it obvious that the nanoparticle composites have much higher values of T_{lum} and modulation spans for T_{sol} than films. This result is a striking illustration of the superior properties of the nano-termochromic composites. It was found that spherical particles give the highest transmittance.

There are numerous practical techniques for making VO_2 nanoparticles. Thus more or less symmetrical particles have been produced via wet chemical techniques, molten salt synthesis, confined-space combustion, etc. There are also many ways to make nanorods (prolate spheroids with large aspect ratio) and nanosheets (oblate spheroids with high aspect ratio) by wet chemistry, gas phase synthesis, etc. A metastable form denoted VO_2(B) has been prepared by chemical routes and has been widely studied for applications in electrical batteries; this material can be converted to thermochromic VO_2. Furthermore VO_2 can be made by oxidation of metallic vanadium and by reduction of V_2O_5. The literature on nanoparticles based on VO_2 was surveyed recently [12].

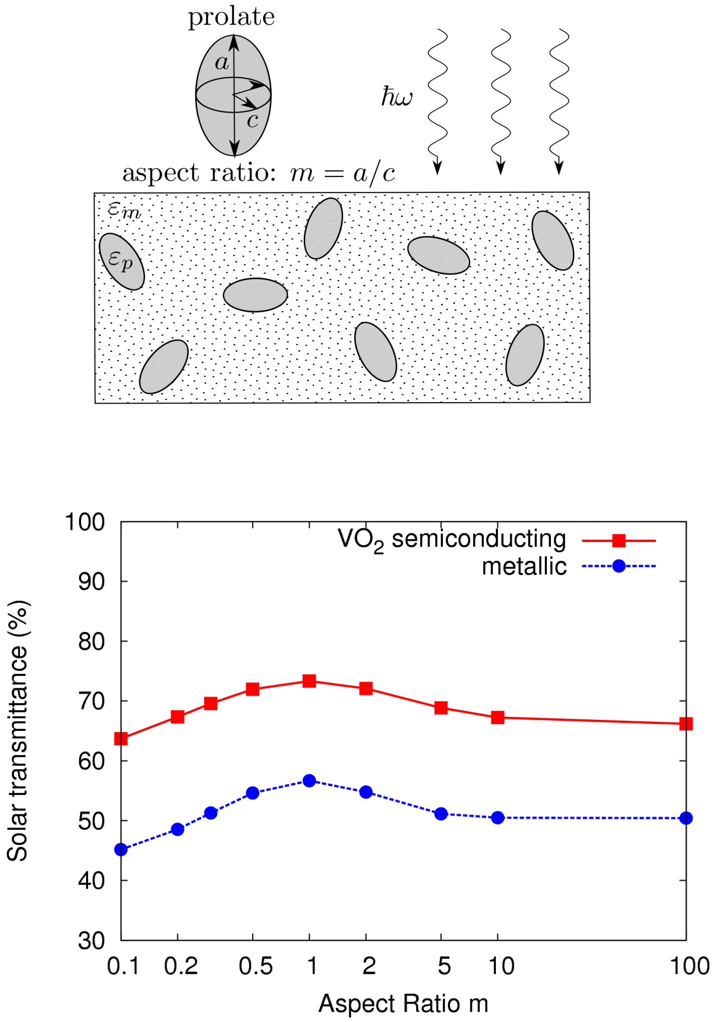

Fig.2. *Structural model for a composite of randomly oriented prolate nanoparticles (upper panel) with dielectric function ε_p embedded in a medium with dielectric function ε_m. Electromagnetic radiation with photon energy $\hbar\omega$ is indicated. Also shown are computed luminous (middle panel) and solar (lower panel) transmittance versus aspect ratio for VO_2-containing composites in semiconducting (lo- temperature) and metallic (high-temperature) states. Prolate and oblate spheroids are characterized by $m > 1$ and $m < 1$, respectively.*

Increased luminous transmittance by Mg doping of VO_2. VO_2 has band-to-band absorption for $\lambda < 0.6$ μm which produces an unwanted decrease of, in particular, T_{lum}. This feature of VO_2 has been an obstacle for windows related applications, but recent work of ours showed that magnesium doping to make VO_2:Mg films led to a widening the band gap and hence an enhancement of T_{lum} [18]. These features are illustrated in Fig. 3, which reports data measured on 0.05-μm-thick films of VO_2 and $Mg_{0.072}V_{0.928}O_2$. Specifically, T_{lum} was significantly enhanced—by more than 10 %—as the Mg content was increased to the level indicated in Fig. 3. There was an accompanying drop of τ_c by ~20 °C, which is advantageous for window applications.

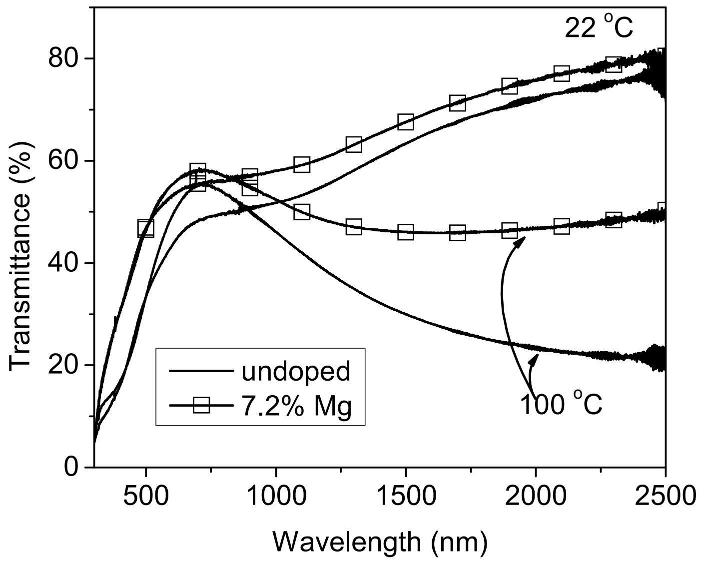

Fig. 3. Spectral transmittance measured at the shown temperatures for 0.05-μm-thick films of VO_2 and $Mg_{0.072}V_{0.928}O_2$. From Ref. [16].

Nanoparticle composites based on VO_2:Mg have not yet been investigated. However, it is obvious that the effect of Mg doping will be both significant and beneficial.

Electrochromics

General characteristics. The standard electrochromic (EC) device has five superimposed layers on a transparent substrate—normally of glass or a polymer such as polyester foil—or positioned between two such substrates in a laminate structure [19,20]. There is a basic similarity to an electrical battery, and EC devices share many of their characteristic features with those of batteries. The outermost layers in the five-layer stack are transparent electrical conductors (typically of In_2O_3:Sn, *i.e.*, Indium Tin Oxide denoted ITO) [7,21]. One of these layers is coated with an EC film (typically based on WO_3) and the other is coated with an ion storage film with or without EC properties (typically based on NiO); both of these layers are nanoporous and able to sustain mixed conduction of ions and electrons. A transparent ion conducting layer (electrolyte) takes the middle position in the device and joins the EC and ion storage films.

When a dc voltage of a few volts is applied to the transparent electrodes, charge is exchanged between the EC and ion storage films, and this leads to a change of the transparency of the device. A voltage with opposite polarity—or, with suitable materials, short circuiting—makes the device regain its original transparency. The charge insertion into the EC film(s) is balanced by electron transport from the transparent conductor(s), and these electrons take part in intervalency transitions leading to optical absorption [22]. The devices display open circuit memory, which is of obvious importance for an energy saving device, and they do not show any visible haze irrespectively of the absorption.

Electrochromism in Ni-containing W oxide films. There are numerous important materials issues for EC devices. They regard the transparent electrodes, the electrolyte and, obviously, the EC films. One of these issues is that the EC effect should be large for a small amount of ion and electron exchange. This property is governed by the coloration efficiency CE defined by [19]

$$\mathrm{CE} = \Delta(\mathrm{OD})/\Delta Q\ . \tag{4}$$

Here Δ(OD) denotes the change in optical density under the exchange of a charge Δ*Q* per area unit. The CE is independent of the charge exchange as long as it is not large enough to produce "site saturation", which is a well known phenomenon at least in WO_3-based films [20,22].

It has been known almost since the discovery of the EC phenomenon that mixed oxides can have modified optical properties and that absorption can extend fairly evenly over the luminous part of the spectrum. Detailed studies have been reported especially for the ternary system WO_3-MoO_3-V_2O_5 [23,24]; this work was once of much interest for EC-based information displays.

Generally speaking there is a severe lack of systematic investigations of CEs in mixed EC oxides. However, we have recently initiated detailed studies on the EC properties of the binary system WO_3-NiO, which goes from cathodic coloration (darkening under ion and electron insertion) at the WO_3-rich end to anodic coloration (darkening under ion and electron extraction) for NiO-rich samples [25,26]. Figure 4 shows recent data for films in the WO_3-rich range. The addition of some Ni obviously yields a significant increase of the CE, while larger amounts of Ni do not have this advantageous effect.

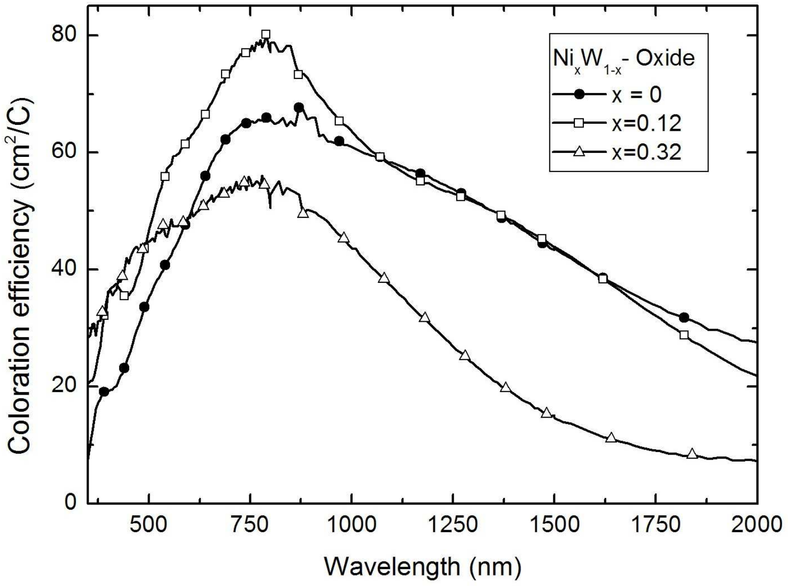

Fig. 4. Spectral coloration efficiency for EC films of Ni-W oxide with the shown compositions.

Roll-to-roll manufacturing of electrochromic foil devices. Low-cost manufacturing is an important issue that has not received due attention in the past, at least not in Academia. The effect has been that EC device technology is often regarded as "expensive". This needs not be the case, though, given appropriate materials and manufacturing strategies.

We have developed a technology with three essential steps: (*i*) roll-to-roll coating of plastic foil with a transparent electrically conducting film and a superimposed EC film of W oxide, (*ii*) roll-to-roll coating of another plastic foil with a transparent electrically conducting film and a superimposed EC film of Ni oxide, followed by (*iii*) continuous lamination with an ion-conducting laminate joining the EC films [20,27]. This manufacturing strategy has recently been demonstrated on a practical scale with thin film deposition onto ~1-km-long and 0.6-m-wide PET foils. Figure 5 shows some initial results of tests on a 240-cm^2-size device prepared from such foils. Despite the highly preliminary nature of the experiment, there is clear evidence that a device with significant EC modulation can be made. The gradual drop in the CE—evident as a loss in the dark-state transmittance—is not an inherent property of the device design since analogous devices prepared by batch technology have demonstrated good cycling durability for tens of thousands of cycles [28].

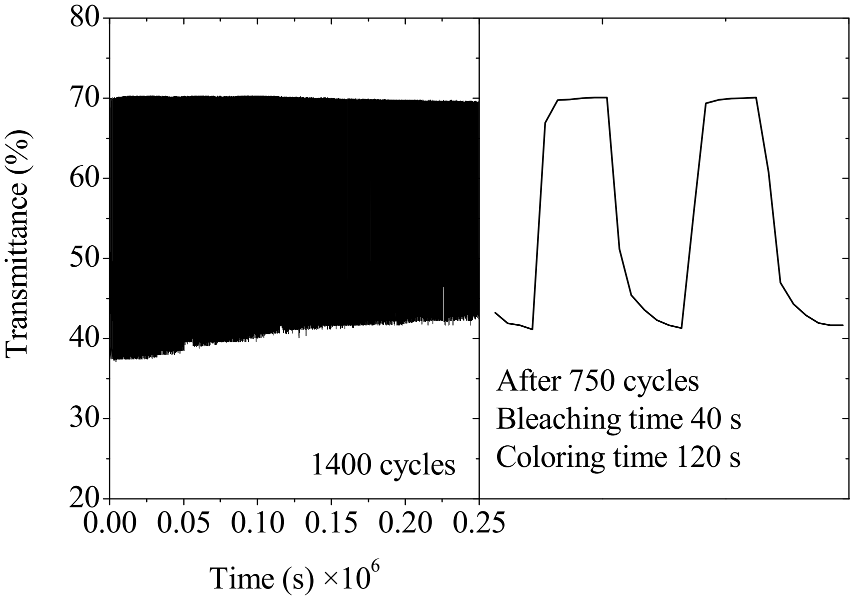

Fig. 5. *Transmittance modulation of luminous radiation in an EC device made by roll-to-roll manufacturing and continuous lamination.*

Conclusions

This paper has summarized some recent advances on thermochromics and electrochromics. We first discussed thermochromic films and nanoparticle composites based on VO_2. Computations appropriate for dilute suspensions of VO_2 nanoparticles in a dielectric host representative of glass or polymer demonstrated that this new nanomaterial would be able to combine high luminous transmittance and large modulation of solar transmittance. Even better results were predicted if the nanoparticles contain a band gap widening additive such as Mg. There are many known techniques for the manufacturing of VO_2-based composites (for example to make VO_2 nanoparticles in glass [29,30]), and hence we believe that “nano-thermochromic” fenestration can become a viable option in the future.

In the second part of this paper we discussed recent advances in electrochromic device technology. Specifically we showed that an addition of Ni to electrochromic W oxide films produced a clear improvement in the coloration efficiency so that a prescribed optical modulation can be achieved for a thinner film. We also showed some initial results of electrochromic foil devices made by roll-to-roll coating and continuous lamination. This work takes a large step towards low-cost electrochromics for energy efficient and comfort enhancing “smart windows”.

By bringing together the two chromogenic technologies discussed in this paper, it may be feasible to construct truly optimized fenestration. Such windows may combine several existing and forthcoming technologies as follows: (*i*) multiple panes, (*ii*) thermochromic nanoparticle composites in thermal contact with the inner pane so as to admit and reject infrared solar radiation according to indoor temperature, (*iii*) electrochromic foil used as lamination material for the outermost pane in order to admit and reject luminous and solar radiation according to user- and energy-based control strategies, (*iv*) low-emittance coating to bring down radiative heat transfer between the panes [6,7,31], and (*v*) vacuum insulation to diminish the conductive and convective heat transfer [6,32].

References

[1] UNEP: *Buildings and Climate Change: Status, Challenges and Opportunities*, United Nations Environment Programme, Paris, France (2007).

[2] B. Richter, D. Goldston, G. Crabtree, L. Glicksman, D. Goldstein, D. Greene, D. Kammen, M. Levine, M. Lubell, M. Sawitz, D. Sperling, F. Schlachter, J. Scofield and D. Dawson: Rev. Mod. Phys. Vol. 80 (2008), p. S1.

[3] J.A. Leech, W.C. Nelson, R.T. Burnett, A. Aaron and M.E. Raizenne: J. Exposure Anal. Environm. Epidem. Vol. 12 (2002), p. 427.

[4] C.G. Granqvist, S.V. Green, S.-Y. Li, N.R. Mlyuka and G.A. Niklasson, in: *Society of Vacuum Coaters 53rd Annual Technical Conference Proceedings*, Society of Vacuum Coaters, Albuquerque, NM (2010), in press.

[5] C.M. Lampert and C.G. Granqvist, editors: *Large-Area Chromogenics: Materials and Devices for Transmittance Control*, SPIE Engineering Press, Bellingham, WA (1990).

[6] G.B. Smith and C.G. Granqvist: *Green Nanotechnology: Solutions for Sustainability & Energy in the Built Environment*, CRC Press, Boca Raton, FL (2010), in press.

[7] C.G. Granqvist: Sol. Energy Mater. Sol. Cells Vol. 91 (2007), p. 1529.

[8] M. Tazawa, P. Jin and S. Tanemura: Appl. Opt. Vol. 37 (1998), p. 1858.

[9] N.R. Mlyuka, G.A. Niklasson and C.G. Granqvist: Phys. Stat. Sol. A Vol. 206 (2009), p. 2155.

[10] G. Wyszecki and W.S. Stiles: *Color Science: Concepts and Methods, Quantitative Data and Formulae*, 2nd ed., Wiley, New York, NY (2000).

[11] ASTM G173-03, in: *Annual Book of ASTM Standards*, Vol. 14.04, American Society for Testing and Materials, Philadelphia, PA (2003).

[12] S.-Y. Li, G.A. Niklasson and C.G. Granqvist: to be published.

[13] C.G. Granqvist and O. Hunderi: Phys. Rev. B Vol. 16 (1977), p. 3513; Vol. 18 (1978), p. 2897.

[14] J.C. Maxwell-Garnett: Philos. Trans. R. Soc. Lond. Vol. 203 (1904), p. 385; Vol. 205 (1906), p. 237.

[15] G.A. Niklasson, C.G. Granqvist and O. Hunderi: Appl. Opt. Vol. 20 (1981), p. 26.

[16] L.D. Landau, E.M. Lifshitz and L.P. Pitaevskii: *Electrodynamics of Continuous Media*, 2nd ed., Butterworth Heinemann, Oxford (1984).

[17] A. Gentle, A.I. Maaroof and G.B. Smith: Nanotechnol. Vol. 18 (2007), p. 025202.

[18] N.R. Mlyuka, G.A. Niklasson and C.G. Granqvist, Appl. Phys. Lett. Vol. 95 (2009), p. 171909.

[19] C.G. Granqvist: *Handbook of Inorganic Electrochromic Materials*, Elsevier, Amsterdam, (1995).

[20] G.A. Niklasson and C.G. Granqvist: J. Mater. Chem. Vol. 17 (2007), p. 127.

[21] I. Hamberg and C.G. Granqvist: J. Appl. Phys. Vol. 60 (1986), p. R123.

[22] L. Berggren, J.C. Jonsson and G.A. Niklasson: J. Appl. Phys. Vol. 102 (2007), p. 083538.

[23] B.W. Crandall and R.S. Faughnan: Appl. Phys. Lett. Vol. 31 (1977), p. 834.

[24] S. Sato and Y. Seino: Trans. Inst. Electronic Commun. Engr. Japan Vol. 65-C (1982), p. 629.

[25] S. Green, J. Backholm, P. Georén, C.G. Granqvist and G.A. Niklasson: Sol. Energy Mater. Sol. Cells Vol. 93 (2009), p. 2050.

[26] S.V. Green, A. Kuzmin, J. Purans, C.G. Granqvist and G.A. Niklasson: to be published.

[27] A. Azens, G. Gustavsson, R. Karmhag and C.G. Granqvist: Solid State Ionics Vol. 165 (2003), p. 1.

[28] C.G. Granqvist, S. Green, G.A. Niklasson, N.R. Mlyuka, S. von Kræmer and P. Georén: Thin Solid Films Vol. 518 (2010), p. 3046.

[29] A.I. Sidorov, O.P. Vinogradova, I.E. Obyknovennaya and T. A. Khrushchova: Pis'ma Zh. Tekh. Fiz. Vol. 33 (13) (2007), p. 85; English translation: Tech. Phys. Lett. Vol. 33 (2007), p. 581.

[30] O.P. Vinogradova, I.E. Obyknovennaya, A.I. Sidorov, V.A. Klimov, E.B. Shadrin, S.D. Khanin and T.A. Khrushcheva: Fiz. Tverd. Tela Vol. 50 (2008), p. 734; English translation: Phys. Solid State Vol. 50 (2008), p. 768.

[31] C.G. Granqvist, in: *Materials Science for Solar Energy Conversion Systems*, edited by C.G. Granqvist, Pergamon, Oxford (1990), p. 106.

[32] R. Baetens, B.P. Jelle, J.V. Thue, M.J. Tenpierik, S. Grynning, S. Uvsløkk and A. Gustavsen: Energy Buildings Vol. 43 (2010), p. 147.

doi:10.4028/www.scientific.net/AST.75.65

High-Performance and High-CRI OLEDs for Lighting and Their Fabrication Processes

Takuya Komoda[1,a], Toshihiro Iwakuma[2,b], Minoru Yamamoto[3,c]
Nobuto Oka[4,d], Yuzo Shigesato[4,e]

[1]Panasonic Electric Works Co., Ltd., 1048 Kadoma, Kadoma-shi, Osaka 571-8686, Japan

[2]Idemitsu Kosan Co., Ltd., 1280 Kami-izumi Sodegaura, Chiba 299-0293, Japan

[3]Tazmo Co., Ltd., 6186 Kinoko-cho, Ibara, Okayama 715-8603

[4]Graduate School of Science and Engineering, Aoyama Gakuin University, 5-10-1 Fuchinobe, Sagamihara, Kanagawa 229-8558, Japan

[a]komoda@panasonic-denko.co.jp, [b]toshihiro.iwakuma@si.idemitsu.co.jp,

[c]minoru.yamamoto@tazmo.co.jp, [d]oka@chem.aoyama.ac.jp, [e]yuzo@chem.aoyama.ac.jp

Keywords: color rendering index, white emission, multi-unit, high-efficiency, large area emission

Abstract. The improvement of the basic performance makes white OLEDs the promising candidate of the next generation, environmental friendly lighting source. However, for the practical application, additional properties of higher color rendering index (CRI), long lifetime at high luminance, large area uniform light emission, and high reliability for long time operation are required. Furthermore, innovative fabrication processes specialized for OLED lighting are required to reduce the cost by improving the material utilization and productivity. We developed various technologies for OLED lighting in the Japanese governmental project "High-efficiency lighting based on the organic light-emitting mechanism" from 2007. In this project, high CRI, highly efficient and long lifetime white OLEDs were realized by optically designed two-unit structure with a fluorescent deep blue emissive unit and a green / red phosphorescent unit. A reliable encapsulation structure with high heat radiation and moisture-proof characteristics realized a stable emission at high luminance as well as long storage stability. Additionally, thermal diffusivities of organic thin films with sub-hundred nanometer thicknesses were analyzed by a "rear heating/front detection type" nanosecond thermo-reflectance method. High speed wet coating process and vacuum deposition process for very thin layers were developed to improve the accuracy, material utilization and productivity.

Introduction

Recently, environmental issues such as global warming caused by CO_2 emission and hazardous materials in wastes (for example, lead, cadmium, hexavalent chromium, bromine compounds and mercury) are extensively discussed. Recent improvement of solid state lightings (SSL) will promise the replacement of the existing lighting sources of energy-consuming incandescent lamps and mercury-containing fluorescent lamps in the near future. In these days, LEDs and OLEDs are most attractive SSLs because of their potentiality for high efficiency and environmental friendliness [1-3]. It is necessary to develop several types of SSLs because "Lighting" emits light in order to illuminate things as well as creates our comfortable lives by producing the circumstances around us. For example, LEDs will be used as directive lighting sources and OLEDs will be applied as diffusive lighting sources, and they will make different atmospheres depending on the situation. Not only the performance but also the quality of light must be strongly required. Actually, the requirements in correlated color temperature (CCT), color rendering index (CRI), color maintenance and spatial uniformity in chromaticity are already determined by "ENERGY STAR® Program Requirements for Solid State Lighting Luminaires, Eligibility Criteria" [4]. However, few studies do mention these characteristics in detail.

We have conducted the Japanese governmental (NEDO) project "High-efficiency lighting based on the organic light-emitting mechanism" from September 2007 to March 2010 to realize the OLED device technologies that targeted the high quality white light and innovative fabrication process technologies to improve the productivity and to reduce the cost of these devices [5].

High Quality White OLED Panels

High-CRI Multi-Unit White Device. "Multi-unit OLED device" contains some emissive units and transparent connecting layer(s) between two electrodes (Figure 1). The well known advantages of this structure are, for example, long lifetime at high luminance and color tunability by stacking emissive units with various colors. Many results have been reported since the publication by Matsumoto and Kido in 2003 [6,7].

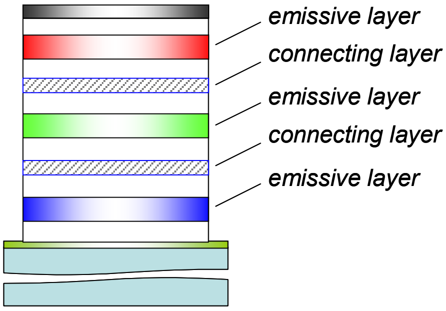

Figure 1. A typical structure of multi-unit device

We chose a two-unit structure with a blue emissive unit and a green and red emissive unit to reduce the difficulty of the optical design described in 2-2 [8]. Additionally, our multi-unit OLEDs employed a wet-coated hole injection layer (HIL) onto the pre-treated patterned anode to improve the stability and durability against morphological defects in the anode. A successive slit coating and drying system developed by TAZMO Co., Ltd. in the NEDO project was used to fabricate this layer [9]. On the HIL, a hole transport layer (HTL), a blue emissive layer and an electron transport layer (ETL) were deposited in vacuum. Optical simulation suggested that the deep blue emission at peak wavelength of less than 460 nm was necessary to achieve high color rendering index, and we used the deep blue fluorescent emitter developed by Idemitsu Kosan also in the NEDO project having an emission peak at about 450 nm and performance to satisfy the required characteristics of efficiency, lifetime and color stability. As a connecting layer, a combination of several layers that enable the injection of both hole and electron to the transport layers was used. As the second emissive unit, HTL, green and red emissive layer(s), ETL, EIL and cathode were deposited. High performance phosphorescent materials and several wide gap & high-T1 carrier transport / host materials with high mobility were carefully chosen in order to realize high efficiency, low driving voltage and long lifetime. The green / red emission ratio was adjusted to obtain the white emission on the black body radiation curve at the desired color temperature as well as excellent efficiency, lifetime and color stability when combined with the deep blue emission. Finally, light out-coupling enhancement structure was implemented on the surface of the substrate. The schematic of our device is shown in Figure 2.

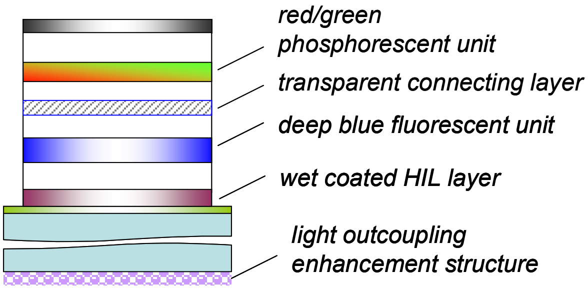

Figure 2. The schematic of our device

Color Spatial Uniformity. From the views of SSL criteria, the improvements of emission properties are strongly desired. ENERGY STAR® defines the desired color spatial uniformity as “the variation of chromaticity in different directions (i.e., with a change in viewing angle) shall be within 0.004 from the weighted average point on the CIE 1976 (u’,v’) diagram” [4]. This variation on (u’,v’) diagram can be converted to the deviation on the CIE 1931 (x,y) color coordinates by formulae 1 [10] and generally the variation of chromaticity on (x,y) coordinates is calculated as within only about 0.01.

$$x = \frac{3u'}{4 + 2u' - \frac{16v'}{3}} \qquad y = \frac{3v'}{9 + \frac{9u'}{2} - 12v'} \tag{1}$$

Formulae 1. Conversion of CIE color coordinates

The optical structure of OLED is generally known that the distance between the emission layer and the cathode (reflective electrode) is (2n+1) λ / 4 (n = 0 or integer, λ is the peak wavelength) to achieve the appropriate optical interference to obtain higher luminance, better emission color and nearly lambertian emission. However, for the multi-unit OLEDs which have at least two emissive units in different positions, the conventional optical design is difficult to be applied, and the multi-unit structure has some issues in the optical properties such as angular dependency in chromaticity and emission color variation derived from the thickness variation.

Some structures to reduce the optical issues are already suggested as follows:

1) extinction of optical interference by using a light-absorbing electrode [11]
2) introduction of light diffusive electrode to reduce the optical interference [11]
3) introduction of thick optical spacer enough to achieve the incoherency [12]

Although these methods would be useful, we applied the modified optical design and light out-coupling enhancement technologies in order to optimize the optical behavior in the device. The emissive layers were carefully designed considering the efficiency and the angular dependences of red, green and blue emission after light out-coupling enhancement by optimizing the order of emissive layers, the regions (positions and widths) of emission sites and optical interferences. Additionally, the diffusive-type light out-coupling structure (e.g., roughened surfaces, scattering layers and microlens arrays) was effectively used to reduce the angular dependence.

Figure 3 shows the color spatial uniformity from 0 deg to 80 deg in CIE (x,y) coordinates and the angular dependence of the relative emission intensity of fabricated devices at the wavelengths of red (600nm), green (520 nm) and blue (460 nm), respectively. Their emission patterns are almost the same as the lambertian and the color spatial uniformity of this OLED fulfills the ENERGY STAR® requirement.

Some of the performance characteristics of our OLEDs are tabulated in Table 1. The size of emission area was 1 cm^2. High CRI of over 90 and high luminous efficacy of over 30 lm/W on the black-body radiation curve were obtained. The half decay lifetime of these devices were over 40,000 h at 1,000 cd/m^2. Additionally, no efficacy decrease was observed even in large area panels (5 x 5 cm^2 and 8 x 8 cm^2).

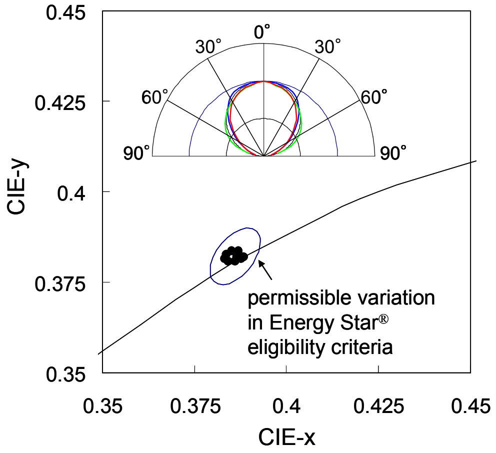

Figure 3. Angular dependence of emission color from 0 deg to 80 deg.
Inset: Emission patterns of Red, Green, and Blue, respectively.

Table 1. Performance of white OLEDs at 1,000 cd/m^2

CRI	95	93
Luminous efficacy	37 lm/W	32 lm/W
Color temperature	4590K	3860K
Color coordinates	(0.36,0.36)	(0.39,0.38)
Color variation (at 0°~80°)	0.013: in (x,y) 0.007: in (u',v')	0.003: in (x,y) 0.002: in (u',v')
Half-decay lifetime	over 40,000 h	over 40,000 h

Highly Reliable Encapsulation for OLED Lighting Panels. The thermally accelerated degradation is one of the significant issues for the large area OLED lighting panels. Sometimes, the thermal break-down of OLED panel was observed [13]. Coping with this phenomenon, the heat radiation structure composed of a heat transfer sheet, a metal plate, and a radiation sheet was effectively applied to our OLED device and the uniform emission at high luminance in large panels was obtained [13]. We improved the encapsulation performance by applying the inorganic / organic passivation layers into this encapsulation structure as shown in Figure 4.

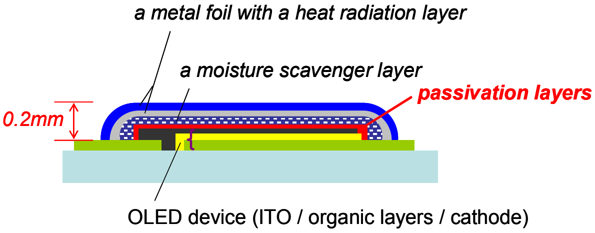

Figure 4. Thin encapsulation structure

This encapsulation structure realized an efficient heat radiation, and as a consequence, uniform and stable emission properties even at a high luminance (up to 5,000 cd/m^2) was obtained. The accelerated storage test at 85 ^{o}C and 85 % RH indicated that the encapsulation performance at room temperature (25 ^{o}C) and 45 % RH was over 80,000 h. Figure 5 is the photograph of the 8 x 8 cm^2 OLED panel uniformly operated at 5,000 cd/m^2. Total thickness of this panel was less than 1 mm and high quality white emission of CRI 94 was realized.

Figure 5. White OLED panel (8 x 8 cm^2) at 5,000 cd/m^2

Thermal diffusivities of organic thin films with sub-hundred nanometer thicknesses. As shown above, the thermal design for OLED devices has received considerable attention. It is because self-heating during operation could damage the OLED device itself and decrease the lifetime of OLED panels. For the effective thermal design, thermo-physical properties, especially thermal diffusivity of the thin organic and inorganic layers, are essential parameters. In this project, as a collaborative academic research with Aoyama Gakuin University, the thermal properties of organic films were quantitatively analyzed. Alq_3 or α-NPD films sandwiched between aluminum (Al) films [Al/(Alq_3 or α-NPD)/Al] were deposited by vacuum evaporation, as commonly used materials in OLED devices. In order to characterize the thermal diffusivity of those thin films quantitatively, a "rear heating/front detection type" nanosecond thermo-reflectance system that can directly observe heat propagation through the film thickness developed by the National Metrology Institute of Japan (NMIJ)/AIST [14-18] was employed. A pulse from the pump laser of the thermo-reflectance system was focused on the rear of the Al/(Alq_3 or α-NPD)/Al specimen, and a fraction of the pulse's energy was absorbed into skin depth of the bottom Al layer and converted into heat. Although Alq_3 and α-NPD films are transparent to the pulse lasers used in the thermo-reflectance system, Al can act as a reflective layer for these lasers. Then, the heat diffused one-dimensionally toward the front side of the specimen. Next, a probe laser pulse detected the temperature change at the front side as change in reflectivity. The normalized temperature rise, i.e., the thermo-reflectance signal, was recorded as a function of the delay time relative to the pump laser pulse. To derive the thermal diffusivities of the Alq_3 and α-NPD films, the thermo-reflectance signals were analyzed using an analytical solution of the one-dimensional heat flow across the three-layered film [14]. Here, the thicknesses of Alq_3 and α-NPD varied roughly from 30 nm to 100 nm equivalent to a practical thickness of actual OLEDs. Figure 6 shows the thermo-reflectance signals of Al/α-NPD/Al three-layered films. The noise signal around the delay time of 150 ns was attributed to the electrical noise emitted by the equipment, which was confirmed not to affect the measurements. Analytic methods and assumed parameters will be shown in reference 19 in detail. The thermal diffusivities of those films were found to be $(1.4–1.6) \times 10^{-7}$ m^2/s for Alq_3 and $(1.1–1.2) \times 10^{-7}$ m^2/s for α-NPD, respectively. These parameters would be helpful to design OLED panels thermally.

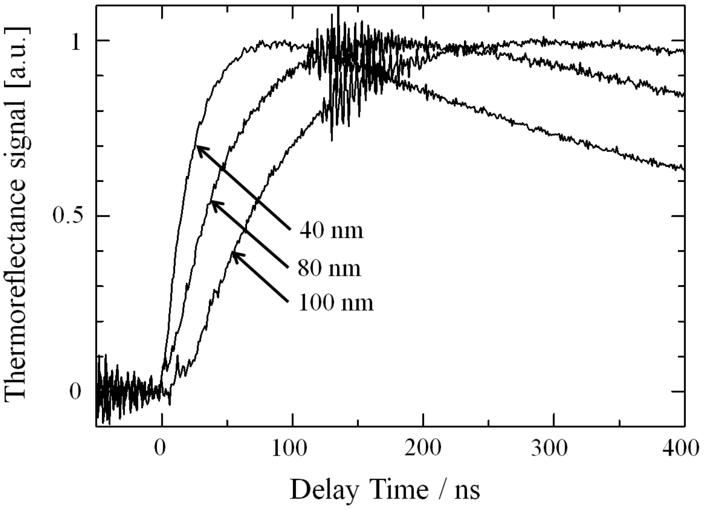

Figure 6. Thermoreflectance signals of Al/α-NPD/Al three-layered films

Resource-saving Fabrication Processes for OLED Lightings

For the prevalence of OLED Lightings, cost competitiveness to other lighting sources is indispensable, thus the dramatic progress of the fabrication processes for OLEDs specialized for lighting application must be desired. A hot-wall deposition source is known as one of the innovative deposition processes that consists of heated cylindrical walls placed between a deposition cell and a substrate [20,21]. Vaporized organic material from the deposition cell is guided to the substrate by heated walls and thanks to this effect, material utilization about 70% and high deposition rate of 2 nm/s were realized already [20].

In the collaborative research with Choshu Industry Co., Ltd., a new hot-wall system composed of reformed heated walls and deposition cells with rate control valves was developed to achieve a better thickness uniformity and deposition rate controllability. Figure 7 shows the schematic configuration of the newly developed hot-wall system.

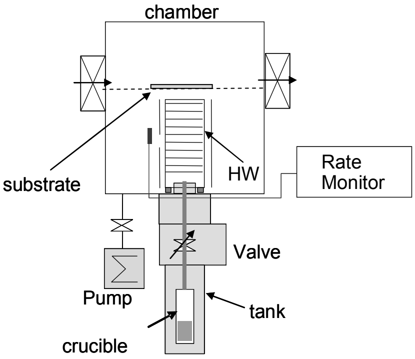

Figure 7. Schematic configuration of the newly developed hot-wall system

The dimensional configuration of heated walls was designed by using molecular dynamics simulation to minimize the distribution of the vaporized organic molecules. For some organic materials, an excellent uniformity within +/- 3 % over the A4 size (300 x 210 mm^2) substrate was obtained even at a high deposition rate of 8 nm/s (about 10 times higher than conventional deposition sources). Furthermore, this system can provide a deposition rate controllability with good linearity within a range up to 20 nm/s as shown in Figure 8. Figure 9 shows the actual deposition rate controllability by regulating the aperture of rate control valve. Only within a few seconds, deposition rate was accurately adjusted to the predetermined value and showed a good repeatability.

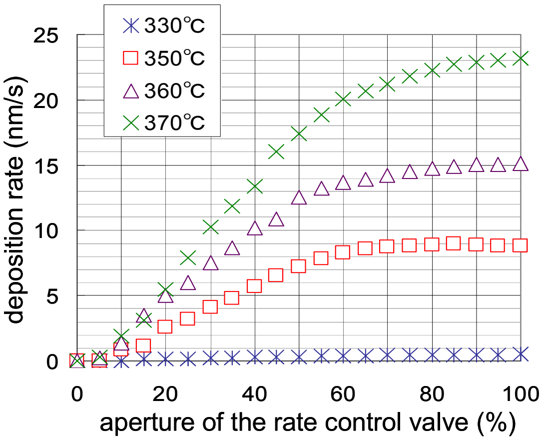

Figure 8. Deposition rate linearity

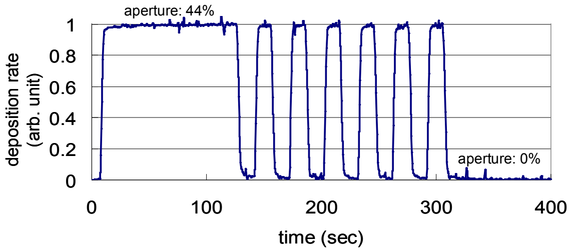

Figure 9. Deposition rate controllability

High deposition temperature sometimes damages the performance of OLED devices due to the thermal degradation of organic materials. To achieve high deposition rate even at a lower temperature, the conductance of vaporized materials in the deposition source was investigated. By applying newly designed rate control valve, the conductance was improved about 4 times higher. Figure 10 shows the change of the deposition temperature of a model organic material in the conventional and developed deposition sources. The deposition temperature in the developed deposition source decreased about 20 °C, and that is still slightly higher than that of open sources (e.g. crucibles) and further improvement of conductance is ongoing. These hot-wall systems were installed into the in-line deposition system and OLED devices with good performance were obtained.

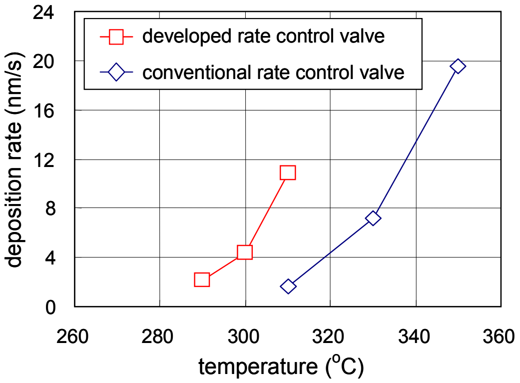

Figure 10. Deposition temperature

Conclusions

High CRI, highly efficient and long lifetime white OLEDs were realized by optically designed two-unit structure with a fluorescent deep blue emissive unit and a green / red phosphorescent unit. Excellent spatial uniformity in chromaticity was achieved by using the optimized optical design and the diffusive-type light out-coupling structure. A reliable encapsulation structure with high heat radiation and moisture-proof characteristics provides a stable emission at high luminance as well as long storage stability. Thermo-physical properties of the thin organic layers are obtained by using the "rear heating/front detection type" nanosecond thermo-reflectance system. These values would be applicable to the thermal design OLED panels. Resource saving and deposition rate controllable vacuum deposition source was developed and the applicability to the in-line process was investigated. The improvement of these technologies will realize the OLED lighting world and will accelerate the spread of them into our daily life.

Acknowledgment

This research was supported by New Energy and Industrial Technology Development Organization (NEDO). We thank to Choshu Industry Co., Ltd. for the collaborative development of vacuum deposition technologies. We also thank to Nippon Steel Chemical Co., Ltd., Universal Display Corporation and Nissan Chemical Industries, Ltd. for their kind provision of their high performance materials.

References

[1] B. D'Andrade, J. Esler, C. Lin, M. Weaver, and J. Brown, "Extremely Long Lived White Phosphorescent Organic Light Emitting Device with Minimum Organic Materials," SID 08 Digest, 940 (2008).

[2] B. W. D'Andrade, J. Esler, C. Lin, V. Adamovich, S. Xia, M. S. Weaver, R. Kwong, and J. J. Brown, "102 lm/W White Phosphorescent OLED," IDW'08, OLED1-4L, 143 (2008).

[3] K. Nishimura, Y. Kawamura, T. Kato, M. Numata, M. Kawamura, T. Ogiwara, H. Yamamoto, T. Iwakuma, Y. Jinde, and C. Hosokawa, "New Green and Red Phosphorescent Host Materials for Highly-efficient and Long-lifetime OLEDs," SID09 Digest, 310 (2009).

[4] Energy Star® Program Requirements for Solid State Lighting Luminaires, Eligibility Criteria – Version 1.1 (2008).

[5] T. Komoda, H. Tsuji, T. Nishimori, N. Ide, T. Iwakuma, and M. Yamamoto, "High-Performance and High-CRI OLEDs for Lighting and Their Fabrication Processes," IDW'09, OLED5-1, 1029 (2009).

[6] J. Kido, T. Matsumoto, T. Nakada, J. Endo, K. Mori, N. Kawamura, and A. Yokoi, "High Efficiency Organic EL Devices having Charge Generation Layers," SID03 Digest, 964 (2003).

[7] T. Matsumoto, T. Nakada, J. Endo, K. Mori, N. Kawamura, A. Yokoi, and J. Kido, "Multiphoton Organic EL device having Charge Generation Layer," SID03 Digest, 979 (2003).

[8] H. Tsuji, N. Ito, Y. Matsuhisa, S. Houzumi, and N. Ide, "High-Performance White OLEDs for Lighting Application," IDW'09, OLED5-2, 1033 (2009).

[9] T. Kawaguchi, Y. Ikagawa, and M. Yamamoto, "Visualization Technique and Evaluation of Meniscus Shape in Slit Coat Method for Uniform Coating of Nano-meter Film under Atmospheric Environment," IDW'09, OLED5-3, 1037 (2009).

[10] CIE, "Colorimetry," Publ. CIE No. 15.2, Central Bureau of the CIE, Vienna (1986).

[11] JP3933591, EP1351558, US2003/189401.

[12] M. Horii, Y. Jinde, S. Tanaka, A. Ogawa, Y. Kawakami, and Y. Naito, "White Multi-Photon Emission OLED without Optical Interference," IDW'04, OLED3-2, 1293 (2004).

[13] A. Oda, "Recent Progress in Organic LEDs," PPS-22, SP7.K1 (2006).

[14] T. Baba, “Analysis of One-dimensional Heat Diffusion after Light Pulse Heating by the Response Function Method,” Jpn. J. Appl. Phys. 48, 05EB04 (2009).

[15] N. Taketoshi, T. Baba, and A. Ono, “Electrical delay technique in the picosecond thermoreflectance method for thermophysical property measurements of thin films,” Rev. Sci. Instrum. 76, 094903 (2005).

[16] T. Yagi, K. Tamano, Y. Sato, N. Taketoshi, T. Baba, and Y. Shigesato, “Analysis on thermal properties of tin doped indium oxide films by picosecond thermoreflectance measurement,” J. Vac. Sci. Technol. A 23, 1180 (2005).

[17] T. Ashida, A. Miyamura, N. Oka, Y. Sato, T. Yagi, N. Taketoshi, T. Baba, and Y. Shigesato, “Thermal transport properties of polycrystalline tin-doped indium oxide films,” J. Appl. Phys. 105, 073709 (2009).

[18] N. Oka, R. Arisawa, A. Miyamura, Y. Sato, T. Yagi, N. Taketoshi, T. Baba, and Y. Shigesato, “Thermophysical properties of aluminum oxide and molybdenum layered films,” Thin Solid Films 518, 3119-3121 (2010).

[19] N. Oka, K. Kato, T. Yagi, N. Taketoshi, T. Baba, N. Ito and Y. Shigesato, “Thermal diffusivities of Alq_3 and α-NPD thin films with sub-hundred nanometer thicknesses,” Submitted (2010).

[20] T. Nishimori, Y. Kondo, Y. Kishi, S. Maki, E. Matsumoto, Y. Yanagi, and J. Kido, “The High Growth Rates and High-Efficiency Materials Vapor Deposition for Organic EL Layers,” Ext. Abst. 63th Autumn Meeting, Jpn. Soc. Appl. Phys., 1166 (2002).

[21] E. Matsumoto, S. Maki, Y. Yanagi, T. Nishimori, Y. Kondo, Y. Kishi, and J. Kido, “The High Growth Rates and High-Efficiency Materials Vapor Deposition for Organic EL Layers,” SID03 Digest, 1423 (2003)

doi:10.4028/www.scientific.net/AST.75.74

Nanostructured metal oxides as cathode interfacial layers for hybrid-polymer electronic devices

M. Vasilopoulou[1, a], L. C. Palilis[1], D. G. Georgiadou[1], P. Argitis[1], I. Kostis[2,3],
G. Papadimitropoulos[1], N. A. Stathopoulos[2], A. Iliadis[3,4], N. Konofaos[3] and
D. Davazoglou[1]

[1]Institute of Microelectronics, NCSR Demokritos, Terma Patriarchou Grigoriou, 15310 Aghia Paraskevi, Greece
[2]Department of Electronics, Technological and Educational Institute of Pireaus, 12244 Aegaleo, Greece
[3]Department of Information and Communication Systems Engineering, University of the Aegean, 83200 Karlovassi, Greece
[4]ECE Department, University of Maryland, College Park, USA

[a]email: mariva@imel.demokritos.gr

Keywords: Transition metal oxides, Hybrid Light Emitting Diodes (Hy-LEDs), Hybrid Photovoltaic Cells (Hy-PVs), Cathode interfacial layer

Abstract

We report the use of nanostructured metal oxides as cathode interfacial layers for improved performance hybrid polymer electronic devices such as light-emitting diodes (PLEDs) and solar cells. In particular, we employ a stoichiometric (WO_3) and a partially reduced tungsten metal oxide (WO_x) ($x<3$), both deposited as very thin layers between an aluminum (Al) cathode and the active polymer layer in hybrid PLEDs and achieve improved PLED device performance reflected as an increase in the current density and luminance and a reduction of the operating voltage. On the other hand, we investigate the use of a stoichiometric tungsten oxide layer as a thin cathode interfacial layer in hybrid polymer photovoltaic cells (Hy-PVs). We demonstrate improved photovoltaic cell performance, primarily as a result of the substantial increase in the short-circuit photocurrent. The improved PLED device characteristics are attributed to enhanced electron injection that primarily results from the lowering of the effective interfacial barrier, as evidenced by photovoltaic open circuit voltage measurements, and improved electron transfer. On the other hand, the observed improvement in the hybrid solar cell performance is primarily attributed to its enhanced internal quantum efficiency, most likely due to the improved electron transport and extraction at the active layer/WO_3/Al interface and the reduction of the corresponding contact series resistance. Correlation between the metal oxide surface morphology and the device performance is also investigated and will be discussed.

Introduction

Since the discovery of organic light-emitting devices (OLEDs), there has been tremendous interest in demonstrating OLEDs with high efficiency and long lifetime for display and lighting applications [1,2]. In order to reduce their operating voltage, thus lowering the power consumption, it is critical to enhance carrier injection from the electrodes and increase charge mobility/bulk conductivity. Generally, in OLEDs based on conjugated polymers (termed as PLEDs), the injection of electrons is more difficult than that of holes due to the large injection barrier present when high work function stable cathode electrodes such as Al or Ag are used. Therefore, there have been many attempts to improve electron injection including the use of low work function metals, such as Ca and Mg [3, 4] and the insertion of thin insulating layers, such as LiF, MgO and MgF_2 at the cathode/polymer interface to enhance electron tunnelling [5,6]. On the other hand, transition metal oxides such as MoO_3, WO_3, and V_2O_5 with high work function have been used to facilitate charge injection from an ITO anode [7,8]. Especially, the high work function of tungsten oxide (WO_3) allows for a simplified high efficiency OLED structure through efficient hole injection directly into a wide-gap organic hole transport material with a low-lying HOMO level [7]. As a result, undoped single or bi-layer OLEDs with high efficiencies, have been demonstrated. The use of transition metal oxides with appropriate workfunction has also found application in organic photovoltaic cells (OPVs) as buffer, interfacial layers at the anode or cathode interface in order to act as optical spacer layers to increase light absorption in the cell [9], to improve hole or electron transport and extraction [10] or to reduce the contact series resistance [11].

In this work, we fabricate Hy-LEDs using very thin stoichiometric (WO_3) and partially reduced nano-crystalline WO_x ($x<3$) films, as cathode interfacial layers in order to facilitate electron injection to the polymer light-emitting layer. The reduction of WO_3 has already been reported to result in the appearance of a narrow density of states band between the Fermi level and the lowest unoccupied molecular orbital (LUMO) (within the band gap) [12]. Here, we explore the increased electronic conductivity of the reduced n-doped WO_x film and this band as a manifold of hopping sites for enhancing electron injection and transfer from the Al cathode to the LUMO of the polymer layer and thus reducing the operating voltage and improving the overall PLED performance. We also investigate the use of thin stoichiometric WO_3 films as cathode interfacial layers in hybrid PVs and demonstrate an increased short-circuit photocurrent in the hybrid cells.

Experimental

Both reference and hybrid PLEDs and PVs with a WO_x and WO_3 modified cathode, respectively, were fabricated on oxygen plasma-cleaned ITO coated glass substrates that have been precoated with a 50 nm thick Poly(3,4-ethylenedioxythiophene):poly(styrenesulfonate) (PEDOT-PSS,obtained from Aldrich) layer. PLEDs were prepared by spin-coating an approximately 70 nm thick layer of a light-emitting copolymer poly[(9,9-dioctylfluorenyl-2,7-diyl)-co-(1,4-benzo-{2,1',3}- thiadiazole)] (YE 233, obtained from ADS) from a chloloform solution with a concentration of 8 mg/ml on top of the PEDOT-PSS film. After spin coating, the YE polymer film was annealed at 80 ºC for 10 min in air. For OPVs, an ~180 nm thick layer of the blend of poly(3-hexylthiophene) (P3HT, obtained from Rieke Metals) and [6,6]-phenyl-C_{70}-butyric acid methyl ester (C_{70}-PCBM) (obtained from Solenne) with a P3HT:PCBM mass ratio of 1:0.8 was spin-cast on PEDOT-PSS from a ~2 wt.% chlorobenzene solution that was first allowed to dry and was then annealed at 150 ºC for 5 min in air. Note that, prior to spin coating, all polymer solutions were filtered using a 0.20 µm PTFE filter. Subsequently, some devices were transferred into a high-vacuum chamber where very thin (~5 nm thickness) layers of WO_3 either fully oxidized ($x=3$) or partially reduced ($x<3$) were deposited to serve as electron injection layers in PLEDs. Thicker (~20 nm) WO_x films were deposited as cathode interfacial layers in hybrid OPVs. The deposition was carried out by heating a W filament at a base pressure of 1 mbar and a filament temperature of 50 ºC, while appropriate gas (Oxygen for the stoichiometric and Hydrogen for the reduced) was flowing through the chamber. Finally, thermal evaporation of a 200 nm thick aluminium (Al) cathode completed device fabrication. Dark and Photo-current density-voltage (J-V) characteristics were measured with a Keithley 2400 source-measure unit while luminance and electroluminescence (EL) spectral characteristics were recorded with an Ocean Optics spectrophotometer equipped with fiber optics, assuming a Lambertian emission profile (for the luminance measurements). Illumination for solar cell characterization was provided by a Hg-Xe lamp equipped with a AM

1.5G filter (light intensity~70 mW/cm^2). Surface morphology and structure were investigated with scanning (SEM) and transmission (TEM) electron microscopy.

Results and Discussion

Nanostructured tungsten oxides as EILs in HyLEDs.

The HyLED device structure is shown in Fig. 1, when WO_3 or WO_x ($x<3$) is used as a cathode interfacial layer.

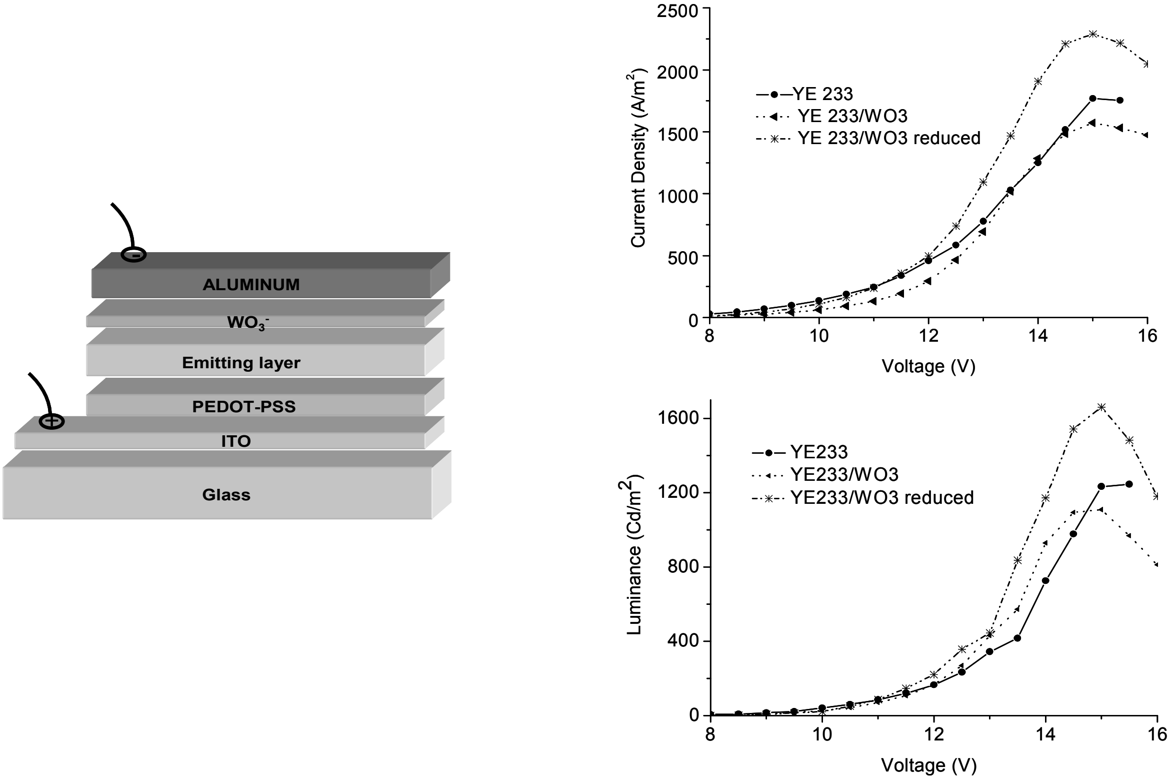

Figure 1. Device structure (left), J-V (right top) and L-V (right bottom) characteristics of the HyLEDs.

In the same Figure, the influence of WO_3 (either fully oxidized or partially reduced) on the J-V and L-V characteristics of the fabricated HyLEDs is also shown. Devices with a thin film of reduced WOx ($x<3$) exhibit a higher current density and luminance compared to both the reference device (without WO_3) and the device with a thin film of oxidized WO_3. Obtained J and L values of ~2300 A/m^2 and 1700 cd/m^2 compared to ~1700 A/m^2 and 1200 cd/m^2, respectively, at 15 V represent an increase of both the current density and the luminance of about 40 %. This improvement is attributed to n-type doping of WO_3 (Fermi level movement towards the conduction band) upon reduction which may contribute in reducing the contact resistance and improving the electron injection characteristics at this interface. Furthermore, the interaction of Al with reduced WO_3 may also be responsible for creating gap states upon electron transfer from Al to WO_3 and filling them with electrons. Improved electron injection and/or transfer results then in increased electron-hole recombination and thus higher luminance. Note that in principle, although these gap states could act as quenching centers for excitons created near this interface, the improved luminance suggests otherwise.

The morphology of thin films of WO_3 with a thickness of 30 nm as grown and after reduction was also investigated by Tunnelling Electron Microscopy. TEM images (Fig. 2) clearly show that the films made of reduced tungsten oxide are smoother and more homogeneous than the ones made in oxygen atmosphere. In the latter ones, several cracks can be observed on the surface that could potentially be disadvantageous for the electrical properties (both injection and conduction might be hindered at the cathode interface).

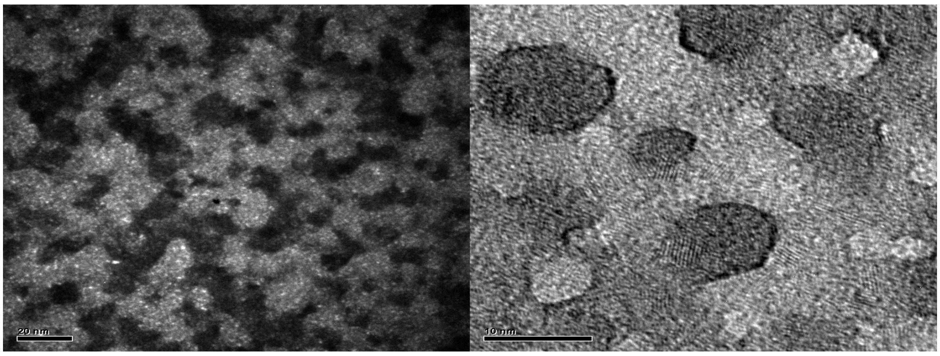

Figure 2. TEM images of 30 nm thick films of WO_3 (up) and reduced WO_x (down).

On the other hand, while TEM images for the reduced tungsten oxide films show some degree of crystallinity, the oxidized films appear to be rather amorphous. Crystallinity is usually desired in metal oxide films, since it results in a decreased density of defect states and grain boundaries that potentially serve as electron traps [12].

Nanostructured tungsten oxides as cathode interfacial layers in HyPVs.

Figure 3 shows a schematic of the Hy-PV cell structure with a thin WO_3 cathode interfacial layer and depicts the influence of this layer on the photocurrent density-voltage characteristics of a P3HT:PCBM based PV.

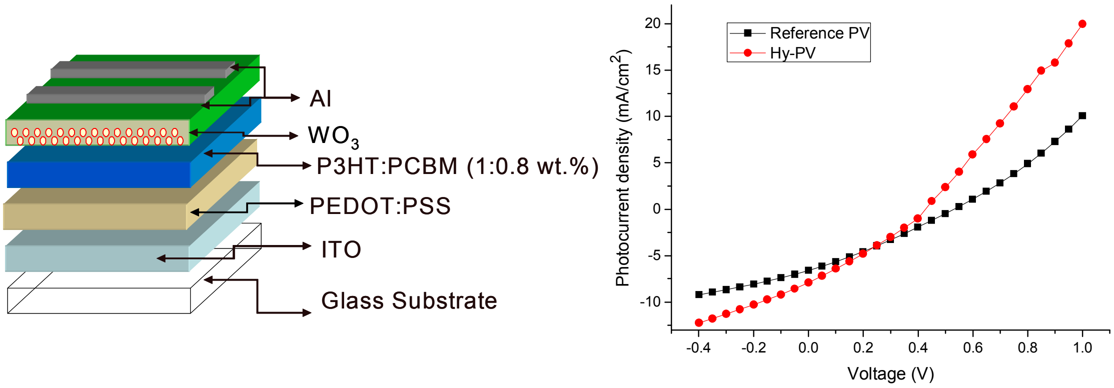

Figure 3. Hy-PV device structure with a WO_3 cathode interfacial layer (left) and photocurrent-voltage characteristics of a reference and a Hy-PV cell (right).

The insertion of a ~20 nm thick stoichiometric WO_3 layer results in a significant increase of the short circuit photocurrent density (J_{sc}). The hybrid-PV exhibits a J_{sc}=7.9 mA/cm^2, compared to 6.6 mA/cm^2 for the reference cell. The "saturation" photocurrent density reaches ~12.5 mA/cm^2 and ~9.5 mA/cm^2 at -0.5 V for the Hy-PV and the reference cell, respectively, suggestive of a field dependent charge separation and collection process that is more pronounced in the Hy-PV. If we apply a "typical" spectral mismatch correction factor of 1.35, as has been reported for a P3HT:PCBM OPV cell [13], the corrected photocurrent density is ~9 mA/cm^2 and ~7 mA/cm^2 for the Hy-PV and the reference cell, respectively. The corrected power conversion efficiency is ~1.1% for both structures due to the slight (~0.1 V) decrease of the open circuit voltage of the Hy-PV, probably due to the formation of shunt paths upon deposition of WO_3. Note, that the use of a similar thickness reduced WO_x layer at the polymer/Al interface results in a shunted device. Detailed optical simulations suggest that the influence of the WO_3 layer in the optical absorption efficiency of the reference cell, by acting for example as an optical spacer layer, is minimal resulting in very similar external quantum efficiencies (EQEs) for both cells [14]. Thus, we attribute the 20-30% photocurrent improvement of the Hy-PV cell to the influence of the WO_3 layer on the cell's internal quantum efficiency (IQE) by reducing the cathode contact series resistance and facilitating electron transport/extraction at the polymer/WO_3/Al interface.

Conclusions

In summary, we have demonstrated that the electron injection in a PLED based on a green emitting yellow copolymer can be significantly improved by inserting a very thin reduced WO_3 layer between the Al cathode and the emitting layer. The presence of an induced density of states below the conduction band (and near the Fermi level) is suggested to contribute to the enhancement of the rate of electron injection from the metallic Al cathode to the LUMO of the polymer as it may create energetically favourable available sites for electron injection. This causes a considerable lowering of the electron injection barrier height (as demonstrated by photovoltaic open circuit voltage measurements), thus improving both injection and recombination, increasing the device luminance and lowering the operating voltage. Furthermore, the use of an appropriate n-type metal oxide cathode interfacial layer, such as WO_3, in hybrid PVs is also demonstrated to result in an increase of the photogenerated current, due to the improved electron transport/extraction at the cathode/WO_3 /polymer interface.

References

[1] C.W. Tang, and S.A. VanSlyke, Appl. Phys. Lett. 51 (1987) 913.
[2] G.E. Jabbour, Y. Kawabe, S.E. Shaheen, J.F.Wang, M.M. Morrell, B. Kippelen and N.Peyghambarian, Appl. Phys. Lett. 71 (1997) 1762.
[3] L.S. Hung, C.W. Tang and M.G. Mason, Appl. Phys. Lett. 70 (1997) 152.
[4] M. Matsumura and Y. Jinde, Appl. Phys. Lett. 73 (1998) 2872.
[5] M. Matsumura, K. Furukawa and Y. Jinde, Thin Solid Films 331 (1998) 96.
[6] G.E. Jabbour, B. Kippelen, N.R. Armstrong and N. Peyghambarian, Appl. Phys. Lett. 73 (1998) 1185.
[7] J. Meyer, S. Hamwi, T. Bülow, H.-H. Johannes, T. Riedl and W. Kowalsky, Appl. Phys. Lett. 91 (2007) 3506.
[8] P.A. Lane, G.P. Kushto and Z.H. Kafafi, Appl. Phys. Lett. 90 (2007) 3511.
[9] J.Y. Kim, S.H. Kim, H.–H. Lee, K. Lee, W. Ma, X. Gong and A. J. Heeger, Adv. Mater. 18 (2006) 572.
[10] D.W. Zhao, P. Liu, X.W. Sun, S.T. Tan, L. Ke and A.K.K. Kyaw, Appl. Phys. Lett. 95 (2009) 3304.
[11] S. Han, W.S. Shin, M. Seo, D. Gupte, S.-J. Moon and S. Yoo, Org. Electr. 10 (2009) 791.
[12] J.J. Kleperis, P.D. Cicmach and A.R. Lusis, Phys. Stat. Sol. (a) 83 (1984) 291.
[13] V. Shrotriya, G. Li, Y. Tao, T. Moriarty, K. Emery and Y. Yang, Adv. Funct. Mater. 16 (2006) 2016.
[14] N.A. Stathopoulos, L.C. Palilis, S.P. Savaidis, S.R. Yesayan, M. Vasilopoulou, G.Papadimitropoulos, D. Davazoglou and P. Argitis, IEEE J. Sel. Top. Quant. Electr. (In Press).

© (2010) Trans Tech Publications, Switzerland
doi:10.4028/www.scientific.net/AST.75.79

Optimisation of Thermochromic Thin Films on Glass; Design of Intelligent Windows

Manfredi Saeli[1 a], Clara Piccirillo [2 b], Ivan P Parkin[2 c *], Russell Binions[2 d] and Ian Ridley[3 e]

[1] Università degli Studi di Palermo, Dipartimento di Progetto e Costruzione Edilizia (DPCE),
Viale delle Scienze, 90128, Palermo, Italy.
[2] Department of Chemistry, University College London, Christopher Ingold Laboratories,
20 Gordon Street, WC1H 0AJ, London, United Kingdom.
[3] Barlett School of Graduate Studies, University College London, Wates House, 22 Gordon Street,
WC1H 0QB, London, United Kingdom.

[a]ing.arch.saeli@hotmail.it, [b]c.piccirillo@ucl.ac.uk, [c]i.p.parkin@ucl.ac.uk, [d]r.binions@ucl.ac.uk,
[e]i.ridley@ucl.ac.uk
*Author to whom correspondence should be addressed:

Keywords: Energy Simulation, Thermochromic Glazing, Chemical Vapor Deposition.

Abstract

Theoretically thermochromic glazing has the potential to reduce energy consumption in buildings by allowing visible light for day lighting, reducing unwanted solar gain during the cooling season, while allowing useful solar gain in the heating season. In this study building simulation is used to predict the savings made by novel thermochromic glazing coatings compared to standard products, for locations with different climates. The results suggest that thermochromic glazing can have a significant energy saving effect compared to current approaches.

Introduction

Thin films of vanadium (IV) oxide have been the subject of intensive research efforts in recent years due to their potential application as an intelligent window coating *[1, 2]*. These technologies are based on the thermochromic metal to semiconductor transition which occurs in the pure material at 68 °C, associated with the structural adjustment from the low temperature monoclinic phase (VO_2 M) to the higher temperature rutile phase (VO_2 R) *[3]*. This structural transformation causes significant changes in electrical conductivity and infrared optical properties. The rutile material is metallic and reflects a wide range of solar radiation, whereas the monoclinic phase is a semiconductor and transmissive. This dynamic behaviour is in contrast to existing commercial approaches which rely on glazing with static behaviour such as heat mirrors, absorbing or Low-E coatings *[4]*.

For vanadium dioxide to be effective as an intelligent window coating it is desirable to lower the transition temperature from 68 °C to nearer room temperature. Doping studies have shown that the transition temperature can be altered by the incorporation of metal ions into the vanadium dioxide lattice *[5, 6]*. It was found that the most effective metal ion dopant was tungsten which lowers the transition temperature by 25 ºC for every atomic percent incorporated of the dopant *[7]*. The transition temperature has also been shown to be affected by film strain *[8]* and it has been demonstrated that strain can be introduced by careful choice of deposition conditions *[9]*.

Tungsten doped vanadium dioxide films have been prepared by a variety of methods including sol-gel *[10]*, sputtering *[11]*, and chemical vapour deposition (CVD) methodologies *[12-14]*. CVD routes to the production of doped VO_2 films are generally considered more attractive because of the compatibility of CVD processes with high volume glass manufacture and the physical properties of CVD produced films which are usually adherent and long lasting.

Recently a new hybrid CVD method has allowed for the easy incorporation of gold nanoparticles into growing films *[15]*. The incorporation of gold nanoparticles leads to significant changes in the optical and thermochromic properties of the film. The film colour can be altered dramatically from an undesirable yellow/brown colour to a range of more aesthetically pleasing greens and blues. The transition temperature is reduced and the film reflectance increased.

It has also been demonstrated that the use of surfactants in hybrid CVD reactions can influence the properties of the grown films. Surfactants are molecules that can change the surface tension of a liquid; within a hybrid CVD process, they can affect the deposition mechanisms and therefore the structure of the films. In the case of vanadium dioxide, they induce strain by templating film growth thus significantly lowering the thermochromic transition temperature *[16, 17]*.

All these data show that significant steps have been made in the production of thermochromic glazing; however the advantages in the use these coating were not investigated conclusively – to our knowledge nothing has been published in the literature regarding the energy saving performance of thermochromic coatings. Several studies have been performed on thermotropic *[18-20]* and electrochromic *[21-24]* systems showing that these can significantly improve building energy performance. However, these are different classes of material in that to work as smart windows they rely on a change in transmission in both the infrared and the visible portion of the spectrum. Thermochromic vanadium dioxide has a constant visible spectrum but a change in the infrared portion of the spectrum *[25]*. We have demonstrated previously through modelling that thermochromic glazing has potential in building energy demand reduction *[26]*.

In this paper we use energy modelling studies to examine the behaviour of a variety of thermochromic vanadium dioxide films and the energy consumptions associated with them. They are assessed with reference to some existing commercial products; a comparison with thermochromic films with "ideal" optical properties based on what is obtainable in practice is also considered. This study, the first of this kind, is crucial to evaluate and quantify the performance of thermochromic glazing.

Glazing and Simulation Model Data

Energy Plus software developed by the Lawrence Berkeley National Laboratory *[27]* and US Department of Energy was used to perform energy simulations and analysis. Energy Plus™ is an energy analysis and thermal load simulation program. Based on a user's description of a building from the perspective of the building's physical make-up, associated mechanical systems etc.

A series of simulations with different configurations and settings were run in order to evaluate the performance of idealised thermochromic coatings. The simulation set period is one year, with data points gathered every hour.

A very simple model of a room in a building was constructed in Energy Plus™. The room has external dimensions 6 x 5 x 3 m (length x width x height) and it is placed so that the axis of every wall is perpendicular to one of the orientation North, South, West and East. We consider the room to represent the façade of a generic building so that just one wall is exposed to the external environment (weather, sun, wind, etc.); the remaining three walls are not affected by external conditions. The building is located in the northern hemisphere and the external wall is supposed to be exposed to the southern side. The modelled zone is a mid-floor office, of a multi-story block, buffered both above and below by air-conditioned spaces. The ground temperature would therefore have no effect on the performance of the studied zone. The choice of ground temperature was set not to reflect the real local ground temperature but rather the temperature of a further buffering, below the modelled spaces, and was taken to be 18 °C throughout the year.

Two different glazing possibilities were considered; one where the window was 1.5 x 2.5 m located in the middle of the southern wall surface (covering 25% of this surface) considered to represent a residential scenario. The other comprised the whole of the southern face (100%) – a glazing wall, representing a modern commercial building. The model is summarised in Figure 1.

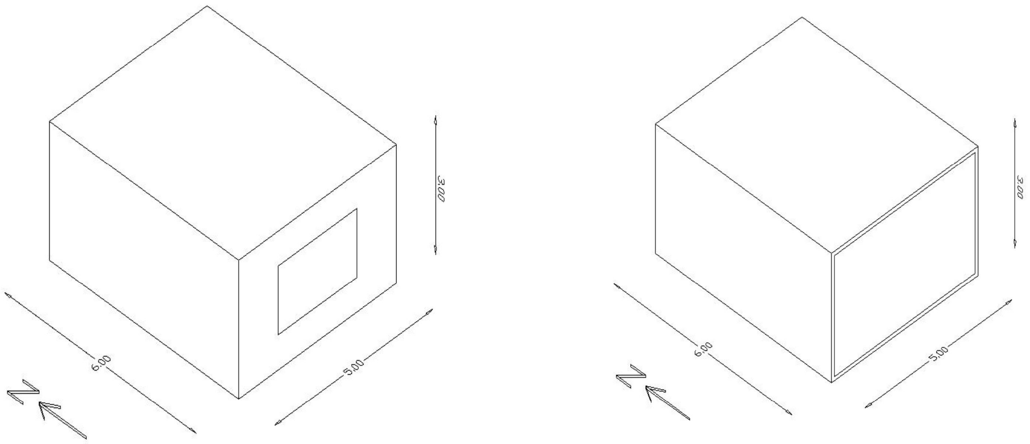

Figure 1. – The two room models: on the left – window 1.5 x 2.5 (25%); on the right - glazing wall (100%).

Further details governing the materials used for walls etc, have been previously reported *[28]*. In both cases the window is double glazed with a 12 mm air cavity, the coating was always modelled on the inside face of the outer pane. The only difference between each simulation was the glazing or coating used.

The internal conditions were chosen to be air-conditioned between 19 – 26 °C to maintain a comfortable working/living environment. The required illuminance level in an office building is taken to be 500 lux, this corresponds to a lighting load of 400 W. The lights are fully dimmable: lowering their output when there is an adequate illuminance from the sun, in order to save energy. It is considered that they can be dimmed in the whole range from 0 to 100 %. The dimming control is automatic and zoned. The casual heat gain (persons + equipment) is taken to be 500 W in total and the ventilation rate used is 0.025 m^3/s. Building occupancy was set as occupied from 8:00 till 18:00, five days a week, as is normal for an office. The simulations were run for Palermo, in southern Italy, as this is an example of a climate where thermochromic glazing would be beneficial *[26]*.

The model is clearly limited because the building is not ideal for all climates. Insulation layers, as well as the materials chosen here, in warmer and cooler climates would be different from that used in the model depending not only on local climate conditions but also on the constructive techniques and materials available in the locality. Likewise the assumption that a constant ground temperature of 18 °C throughout the year is significant. However, by using the results obtained from the plain glass (Optifloat) simulations as a baseline we aim to isolate the change in energy performance caused by the use of different glazings.

The thermochromic properties of the glazing were modelled in version 3.0.0 of Energy Plus by entering the spectral data of the glazing in the hot and cold states. The glazing was switched between the hot and cold states using the shading control feature of EnergyPlus which can "replace" glazing elements in a window, according to environment conditions or set control criteria. The surface temperature of the glazing was correlated against incident solar radiation. The shading control automatically switched the glazing from the cold to hot state when the incident solar radiation exceeded that required for the glazing surface to exceed the transition temperature, switching back to the cold state when solar radiation fell below the trigger value. Note the latest release of Energy Plus, version 3.1.0, now includes a specific thermochromic glazing module, this will facilitate future simulation studies in this area.

Results and Discussion

The aim of this section is to consider the performances of "ideal" thermochromic coatings; this was done to assess what will be the energy savings if a thermochromic film with ideal properties was used. We have decided to consider films with particular spectral characteristics chosen on the basis of the previous sections results and what can be considered to be reasonably achievable in practice. Several values of the thermochromic transition temperature were chosen; we have also selected different values for the change in transmission and reflectance and thus different extents of the thermochromic effect. We chose to run simulations using the weather file for Palermo, in southern Italy, as this provides a hot and sunny environment that thermochromic technology shows most promise for. The simulations were run only for the 100% glazing wall, representing a glass fronted office building.

Spectral characteristics

The spectral characteristics of an ideal thermochromic films were defined as follows: in the cold state (monoclinic, semi-conducting) the maximum transmission in the visible region (300 – 700 nm) of the spectrum is set to 65%, whilst in the infra red (800 – 2500 nm) it is defined as 80%. Conversely the reflectance is set at 17% in the visible and 12 % in the infra-red. In the hot state (rutile, metallic) the optical properties in the visible region remain the same, i.e. 65% transmission and 17% reflectance. In the infra-red they change; it is important that the change covers the range 800-1200 nm; this is the region where the most significant solar heat energy is to be found, so a larger change in this region is expected to have a more profound effect on the energy saving properties of this glass. Spectra with different changes were considered, between 65% and 0%; the example spectra for transmittance and reflectance are shown in Figures 2 & 3 respectively.

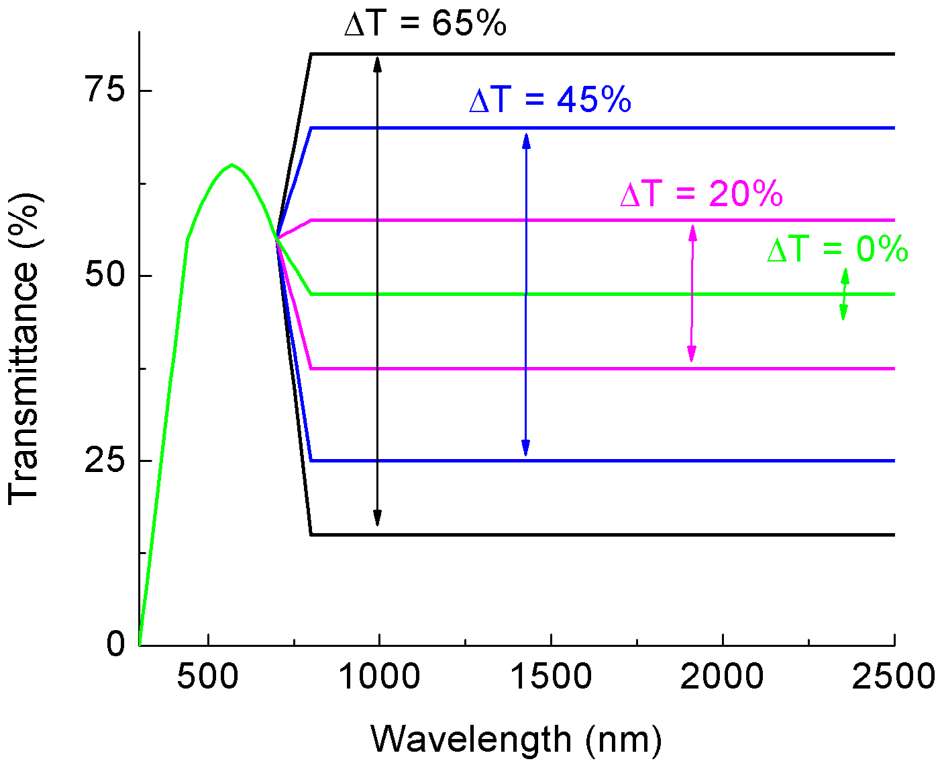

Figure 2. Trasmittance spectra for ideal thermochromic coatings, showing a cold-hot decrease of 65, 45, 20 or 0 %.

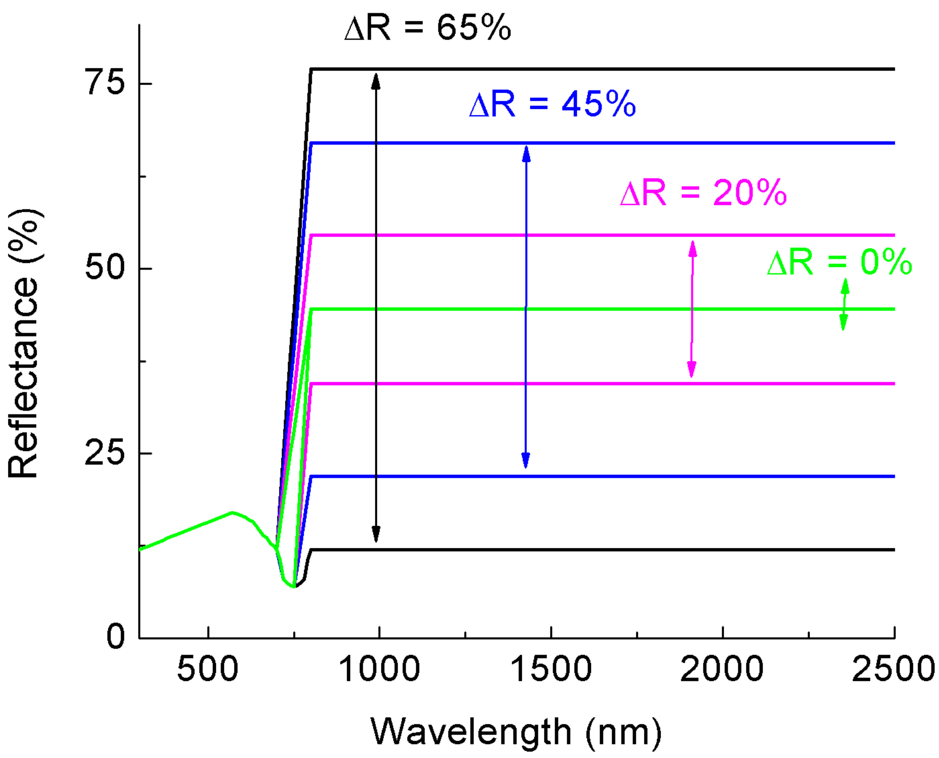

Figure 3. Reflectance spectra for a ideal thermochromic coatings, showing a cold-hot increase of 65, 45, 20 or 0 %.

We have also examined the effect of changing the transition temperature between 20 ºC and 35 ºC. We have not looked at temperatures below 20 ºC as at this temperature the film is always in the cold state. Results of the simulations are shown in Figure 4.

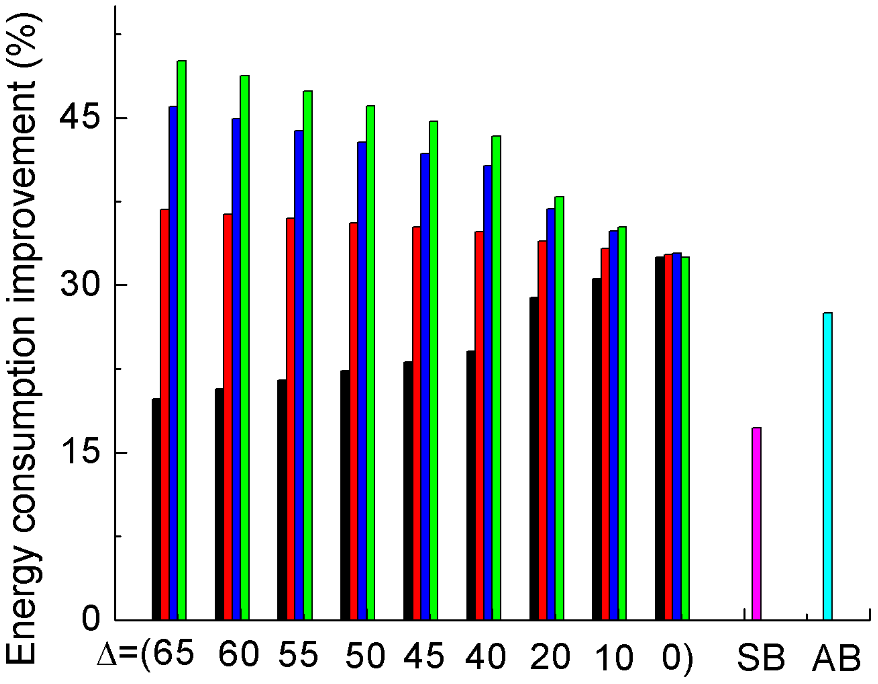

Figure 4. Energy consumption improvement for ideal thermochromic films with different changes in transmittance and reflectance. ■ : T_c = 35°C, 🟥 : T_c = 30°C, 🟦 : T_c = 25°C, 🟩 : T_c = 20°C, 🟪 : Sputtered Silver Coated Glass, ▮ Blue Body Tinted Glass.

Several observations can be made from the results of the simulations. Firstly that all of the ideal products perform better than those standard products they are compared to here. Comparing the spectra of the ideal coatings and the standard products reveals that the ideal coatings have a combination of infrared reflective and absorbing behaviour, whereas the standard products have only one mode of operation. Thus the ideal coatings have a clear advantage. Where there is no change in the optical properties the performance of the coatings is identical. This is expected as the film is behaving in a static manner rather than a dynamic one. The larger the change between hot and cold transmission and hot and cold reflection the higher the percentage improvement versus the clear - clear configuration; this is expected. The higher the difference in infrared reflectivity the more solar energy is reflected, as such the energy benefit derived from it is proportionally larger. The thermochromic transition temperature, T_c, plays an important role in the energy performance of the thermochromic coatings. For the example with the largest change in optical properties (D(T,R) = 65%), a change from T_c = 35°C to T_c = 20°C leads to a change of 30% in the energy performance relative to the clear – clear configuration. In all the cases the lower $T_{c,}$ the lower is the energy consumption and the higher the percentage improvement in energy performance. As seen previously *[26]* the lower T_c the longer the film spends in the hot, metallic state. In warmer climates, such as in Palermo, this significantly enhances the energy performance of the glazing.

The best energy saving performance is calculated to derive from a film with a low transition temperature and a large change in the infrared optical properties above and below this temperature.

Comparison to Real Films

Comparing the results of the ideal coating spectra to those published previously for synthesised coatings *[26]*, several things become clear. Firstly, the ideal spectra have higher values of maximum transmission in the visible region, 65% rather than a minimum of 50%. This means that more light is allowed into the room with the ideal spectra, reducing the lighting cost; also the ideal films are also less absorbing in the near infra-red than the real films. Secondly, the real films do not have such an extreme change in the near infra-red (800 – 1200 nm) as the ideal films; the consequence of this is that the variable heat mirror property inherent in the thermochromism contributes less to the overall energy performance of these films. This is somewhat offset by the fact that there is a resultantly higher absorption character to the film; this means that the real films are less dynamic than they potentially could be.

The ideal coating that performs the best is the one which has the largest change in infra-red reflectivity (a 65% change) and the lowest value for T_c (20 ºC); this leads to a 50% improvement over the clear – clear configuration. The best performance comes from a sample with the lowest T_c subsequently the film is always in the hot state, suggesting that the chromic nature of the films is irrelevant and that the origin of the energy saving effect is a combination of the heat mirror and absorbing properties of the coatings - certainly for warmer climates.

The results of the simulations based on the ideal spectra (Figure 4) suggest that in order to improve the performance of the real thermochromic coatings in building glazing a further two approaches ought to be taken. Firstly we must look to maximise the change in infra-red reflectivity with a particular emphasise on the near infra-red region (800 – 1200 nm). Secondly we must look to lower the transition temperature, T_c, through doping or introducing strain into the film so that the metallic properties of the rutile phase are fully utilised.

Outlook

The use of thermochromic coatings in architectural glazing has been postulated for many years and a great deal of work has been done on film synthesis and characterisation. Little has been published on the energy saving benefit of such films. Here we report that thermochromic films may provide a significant energy benefit when compared with existing approaches (relative to a clear – clear glazing system). This arises through a combination of absorbing and variable heat mirror behaviour and suggests that this system may be optimised by maximising the hours the film spends in the hot state by lowering the transition temperature and by increasing the reflectivity in the near infra-red by doping with metal ions.

Several challenges remain that need to be overcome before thermochromic glazing could be a real product. For instance film emissivity is very poor and this may limit the effectiveness of the film in marginal climates where significant periods are spent below the transition temperature. It is possible that this may be improved by fluorine doping *[29]* although this has not been extensively investigated. A further problem remains the colour of the films. Yellow / brown is a highly undesirable colour for a window even though it provides a desirable absorbative affect. We have previously demonstrated that film colour may be significantly altered by the incorporation of gold nanoparticles into the films *[15, 26, 30]*.

The cost of gold, however, is likely to be a significant stumbling block for this approach. It is likely that any industrial process using gold will be expensive. It is impossible to produce a meaningful figure based on the experiments conducted in our laboratories; but it is likely (at this stage) that the cost outweighs the additional energy benefit that the gold provides. Current approaches to producing coloured glass use body-tinting processes. These can be problematic to produce as the float line may spend a large amount of time off line whilst the melt is bought under control. The hidden benefit that this methodology brings is that it may be incorporated directly onto a float line and started and stopped at will; as such less time would be lost through the float line being unproductive. It may even prove to be possible to change film colour online just by changing the nanoparticle concentration. Additionally the incorporation of these gold nanoparticles contributed to a higher near infrared reflectivity in the cold state, leading to more heat mirror type behaviour. Another approach may be to investigate fluorine doping further, previous reports suggest that the absorption is pushed into the UV region of the spectrum and the doped vanadium oxide films became transparent *[29]*. Whilst this would likely reduce some of the energy benefit which results from absorption in the visible region of the spectrum, it would lead to higher visible transmission and therefore less energy being expended in lighting.

The modelling studies conducted on the ideal spectra are informative; they show that absorbing behaviour is as important as heat mirror behaviour. In the ideal scenario the transition temperature will be as low as possible in order to maximise the number of hours the coating spends in the hot, infrared reflective state and the change in the infrared optical properties will be as large as possible to maximise the benefit of the hot, reflective state.

Conclusion

Simulations based on idealised spectra indicated that the energy saving performance could be optimised by having a large change in optical properties in the near infra-red and by having a low transition temperature to maximise the amount of time the coating spends in its metallic state.

Acknowledgments

Part of this work was supported financially as part of the EU project TERMOGLAZE. Pilkington-NSG are thanked for the provision of glass substrates and the commercial glass examined in this work, in particular Dr. Troy Manning and Mr. Bob Harris are thanked for help with emissivitiy measurements. Mr Kevin Reeves is thanked for his invaluable assistance with electron microscopy. RB thanks the Royal Society for a Dorothy Hodgkin research fellowship. IPP thanks the Wolfson trust for a merit award. MS thanks the University of Palermo for funding.

References

[1] C. G. Granqvist, *Advanced Materials* **2003**, *15*, 1789.
[2] C. G. Granqvist, *Thin Solid Films* **1990**, *193-194*, 730.
[3] K. D. Rogers, *Powder Diffraction* **1993**, *8*, 240.
[4] C. G. Granqvist, *Solar Energy Materials and Solar Cells* **2007**, *91*, 1529.
[5] F. Béteille, R. Morineau, J. Livage, M. Nagano, *Materials Research Bulletin* **1997**, *32*, 1109.
[6] T. E. Phillips, R. A. Murphy, T. O. Poehler, *Materials Research Bulletin* **1987**, *22*, 1113.
[7] T. D. Manning, I. P. Parkin, M. E. Pemble, D. Sheel, D. Vernardou, *Chemistry of Materials* **2004**, *16*, 744.
[8] G. Xu, P. Jin, M. Tazawa, K. Yoshimura, *Applied Surface Science* **2005**, *244*, 449.
[9] R. Binions, G. Hyett, C. Piccirillo, I. P. Parkin, *Journal of Materials Chemistry* **2007**, *17*, 4652.
[10] I. Takahashi, M. Hibino, T. Kudo, *Japanese Journal of Applied Physics* **2001** , *40*, 1391.
[11] W. Burkhardt, T. Christmann, B. K. Meyer, W. Niessner, D. Schalch, A. Scharmann, *Thin Solid Films* **1999**, *345*, 229.
[12] D. Barreca, L. E. Depero, E. Franzato, G. A. Rizzi, L. Sangaletti, E. Tondello, U. Vettori, *Journal of The Electrochemical Society* **1999**, *146*, 551.
[13] I. P. Parkin, R. Binions, C. Piccirillo, C. S. Blackman, T. D. Manning, *Journal of Nano Research* **2008**, *2*, 1.
[14] D. Vernardou, M. E. Pemble, D. W. Sheel, *Surface and Coatings Technology*, *188-189*, 250.
[15] R. Binions, C. Piccirillo, R. G. Palgrave, I. P. Parkin, *Chemical Vapor Deposition* **2008**, *14*, 33.
[16] M. Saeli, R. Binions, C. Piccirillo, G. Hyett, I. P. Parkin, *Polyhedron* **2009**, *28*, 2233.
[17] M. Saeli, R. Binions, C. Piccirillo, I. P. Parkin, *Applied Surface Science* **2009**, *255*, 7291.
[18] H. Feustel, A. de Almeida, C. Blumstein, *Energy and Buildings* **1992**, *18*, 269.
[19] A. Raicu, H. R. Wilson, P. Nitz, W. Platzer, V. Wittwer, E. Jahns, *Solar Energy* **2002**, *72*, 31.
[20] P. Nitz, H. Hartwig, *Solar Energy* **2005**, *79*, 573.
[21] J. A. Clarke, M. Janak, P. Ruyssevelt, *Solar Energy* **1998**, *63*, 231.
[22] C. G. Granqvist, V. Wittwer, *Solar Energy Materials and Solar Cells* **1998**, *54*, 39.

[23] J. H. Klems, *Energy and Buildings* **2001**, *33*, 93.

[24] M. S. Reilly, F. C. Winkelmann, D. K. Arasteh, W. L. Carroll, *Energy and Buildings* **1995**, *22*, 59.

[25] R. Binions, S. S. Kanu, *Proceedings of the Royal Society of London. Series A. Mathematical and Physical Sciences* **2010**, *466*, 19.

[26] M. Saeli, C. Piccirillo, I. P. Parkin, I. Ridley, R. Binions, *Solar Energy Materials and Solar Cells* **2010**, *94*, 141.

[27] http://apps1.eere.energy.gov/buildings/energyplus/.

[28] Saeli. M, in *Dipartimento di Progetto e Costruzione Edilizia (DPCE)*, University of Palermo, Palermo **2008**.

[29] W. Burkhardt, T. Christmann, S. Franke, W. Kriegseis, D. Meister, B. K. Meyer, W. Niessner, D. Schalch, A. Scharmann, *Thin Solid Films* **2002**, *402*, 226.

[30] M. Saeli, C. Piccirillo, I. Parkin, R. Binions, *ECS Transactions* **2009**, *25*, 773.

doi:10.4028/www.scientific.net/AST.75.91

Organic Syntheses and Characteristics of Novel Conjugated Polymers for AMOLEDs

Suhee Song[1,a], Youngeup Jin[2,b], Jooyoung Shim[1,c], Kwanghee Lee[2,d] and Hongsuk Suh[1,e,*]

[1]Department of Chemistry and Chemistry Institute for Functional Materials, Pusan National University, Busan 609-735, Korea

[2]Department of Industrial Chemistry, Pukyong National University, Busan 608-739, Korea

[3]Department of Materials Science and Engineering, Gwangju Institute of Science and Technology, Gwangju 500-712, Korea

[a]songsuhee@pusan.ac.kr, [b]yjin@pknu.ac.kr, [c]jyshim@pusan.ac.kr, [d]klee@gist.ac.kr, [e]hssuh@pusan.ac.kr

Keywords: conjugated polymer, light emitting diodes (LED), luminescence

Abstract. Conjugated polymers with a stabilized blue emission are of importance for the realization of large flat panel AMOLED displays using polymer light-emitting diodes. Several novel conjugated polymers using newly developed templates for the stabilized EL emission are reported. Poly(2,6-(4,4-bis(2-ethylhexyl)-4H-cyclopenta[*def*]phenanthrene)) (PCPP) is a new class of blue-emitting polymers utilizing a new back-bone. This material emits a efficient blue EL without exhibiting any unwanted peak in the long wavelength region (green region) even after prolonged annealing at an elevated temperature of 150°C in air, or operation of the device. New electroluminescent spiro-PCPPs, poly((2,6-(3',6'-bis(2-ethylhexyloxy)-spiro(4*H*-cyclopenta[*def*] phenanthrene-4,9'-[9*H*]fluorene)))-*alt*-(2,6-(4,4-bis(2-ethylhexyl)-4*H*-cyclopenta[*def*]phenanthrene))) (spiro-PCPP-*alt*-PCPP) and poly((2,6-(3',6'-bis(2-ethylhexyloxy)-spiro(4*H*-cyclopenta[*def*] phenanthrene-4,9'-[9*H*]fluorene)))-*alt*-(1,4-phenylene)) (spiro-PCPPP), have been synthesized by the Suzuki polymerization. The PL emission spectra of polymers in THF solution show a same maximum peak at 397 nm. The maximum PL emission spectra of polymers appeared at around 463 and 456 nm in solid state, respectively. The PL spectra in solid thin films show more red-shifted over 60 nm than solution conditions. The blue emissions at 400-409 nm for the π–π^* transitions of conjugated polymer backbone are almost completely quenched or decreased.

Introduction

Since the polymeric light-emitting diodes based on conjugated polymers[1] was reported, various kinds of conjugated polymers have been developed for electroluminescence (EL) because of the potential application in flat panel displays.[2] Among these conjugated polymers, the polyfluorenes (PFs)[1] and polycyclopentaphenanthrenes (PCPPs)[3] for blue[4] and poly(*p*-phenylenevinylene) (PPVs) for green[5] or red[6] color have obtained much attention due to their thermal and chemical stability, and exceptionally high solution and solid-state fluorescence quantum yield.

Blue-emitting polymers are of keen special interest, since they can be used either as a blue light source in full-color displays or as the host material for generating other colors through energy transfer to lower-energy fluorophores.[7] Since PPP was developed for blue color polymer, there has been considerable focused on the development of blue polymers. Especially, polyfluorenes (PFs) have emerged as the most attractive blue emitters due to their high luminescent efficiency and easy functionalization at the 9-position of the fluorene unit with substituting group. However, a major trouble in obtaining blue EL from PFs is the long-range emission (green region) in the emission spectra for the last few years. It was attributed to aggregation,[8] originating from interchain attractions in the π-conjugated systems, and excimer formation by keto defects,[9] inducing an energy transfer of singlet excitons from the main chains. In order to make up for the weak points in blue emitting polymers, synthesis and properties of new EL polymer utilizing a new backbone, poly(2,6-(4,4-bis-(2-ethylhexyl)-4*H*-cyclopenta[*def*]phenanthrene)) (PCPP) with stabilized pure blue emission has been reported in our previous work. Efficient and stabilized blue-light-emitting PLEDs have been demonstrated using a new conjugated polymer (PCPP) with rigid backbone. EL spectrum of PCPP did not show any peak between 500-600 nm, which would correspond to keto defect sites or aggregates/excimers even after annealing the device at 150 °C or operation of the device in air.

Since the distance between the polymer chains is expected to be a crucial governing factor for the formation of aggregates,[10] several researchers have attempted to restrain the green emission by introducing a bulky end group[11] or a cross-linkable group.[12] Especially, spiro-shaped molecules based on 9,9'-spirobifluorene,[13] have been introduced as EL materials to overcome the problem of the low energy emission.[14] A spiro-bifluorene contains two biphenylene units connected by a tetrahedrally bonded carbon atom, where the planes of the biphenylene units lie perpendicular with respect to each other. Once incorporated into the PFs, this three-dimensional structure should prevent the approach of other polymer backbones and, as a result, π-staking of the conjugated polymer backbone could be minimized.[15] More resently, we expected that the presence of spiro moieties onto the phenantherene units would enhance the colar stability, with the alkoxy groups in the main chain improving solubility and processability of aromatic conjugated polymers. By the way, the interchain interaction which leads to quenching of luminescence have been reported in the result of spiro(4*H*-cyclopenta[*def*]phenanthrene-4,9'-[9*H*]fluorene) (spiro-PCPP). The strategy to solve the defect of spiro-PCPP is to introduce comonomer, such as dialkylated-cyclopentaphenanthrene or phenyl, in order to reduce interchain interation.

In this contribution, we report the synthesis and properties of a new EL polymers utilizing new backbone, Poly((2,6-(3',6'-bis(2-ethylhexyloxy)-spiro(4*H*-cyclopenta[*def*]phenanthrene-4,9'-[9*H*] fluorene)))-*alt*-(2,6-(4,4-bis(2-ethylhexyl)-4*H*-cyclopenta[*def*]phenanthrene))) (spiro-PCPP-*alt*-PCPP) and Poly((2,6-(3',6'-bis(2-ethylhexyloxy)-spiro(4*H*-cyclopenta[*def*]phenanthrene -4,9'-[9*H*]fluorene)))-*alt*-(1,4-phenylene)) (spiro-PCPPP) with spiro-structure and cyclopentaphenanthrene backbone.

Synthesis and characterization.

The general synthetic routes toward the monomers and polymers are outlined in Scheme 1 and 2. In the first step, 4*H*-cyclopenta[*def*]phenanthrene (**1**) was hydrogenated using Pd/C to generate 8,9-dihydro-4*H*-cyclopenta[*def*]phenanthrene (**2**). Alumina-supported copper (II) bromide was used for the bromination to provide 2,6-dibromo-8,9-dihydro-4*H*-cyclopenta[*def*]phenanthrene (**3**). Compound **4** was synthesized by the dehydrogenation using bromine and carbon disulfide to provide 2,6-dibromo-4*H*-cyclopenta[*def*]phenanthrene (**4**). Compound **4** is converted into the corresponding 2,6-dibromo-4H-cyclopenta[*def*]phenanthren-4-one (**5**) in good yield by MnO_2. 2-Bromo-5,3'-dimethoxybiphenyl (**7**) was prepared from mono-bromination of 3,3′-dimethoxy biphenyl (**6**). Demethylation of compound **7** gave 6-bromo-biphenyl-3,3′-diol (**8**), and alkylation with 1-octyl bromide gave 2-bromo-3',5-bis[(2-ethylhexyl)oxy]-1,1'-biphenyl (**9**). Compound **9** was treated with *t*-BuLi and 2,6-dibromo-4*H*-cyclopenta[*def*]phenanthren-4-one to generate a tertiary alcohol, which was cyclized to give 2,6-dibromo-(3',6'-bis(2-ethylhexyloxy)-spiro(4*H*-cyclopenta[*def*]phenanthrene-4,9'-[9*H*]fluorene)) (**10**) and its geometric isomer.[21] Separation of geometrical isomers between major compound can be achieved from column chromatography from a mixed solvent of *n*-hexane and dichloromethane. 2,6-Dibromo-4*H*-cyclopenta[*def*]phenanthrene (**4**), which was reacted with 2-ethylhexylbromide, catalytic amounts of triethylbenzyl ammonium chloride in DMSO and 50% aqueous NaOH to obtain 2,6-dibromo-4,4-bis(2-ethylhexyl)-4*H*-cyclopenta[*def*]phenanthrene (**11**). Bis(pinacolato)diboron was reacted with dibromo compound **11** using catalytic amounts of $Pd(dppf)Cl_2$ and potassium acetate in DMF to obtain 2-[4,4-bis(2-ethylhexyl)-6-(4,4,5,5-tetramethyl-1,3,2-dioxaborolan-2-yl)-4*H*-cyclopenta[*def*]phenanthren-2-yl]-4,4,5,5-tetramethyl-1,3,2-dioxaborolane (**12**). The Suzuki coupling reaction were employed for the synthesis of spiro-PCPP-*alt*-PCPP (**14**) and spiro-PCPPP (**15**) using Pd(PPh$_3$)$_4$, K$_2$CO$_3$ and various monomers. The structures of the intermediates, monomers, and the resulting polymers were determined with ^{1}H-, ^{13}C-NMR spectroscopy, mass spectrum.

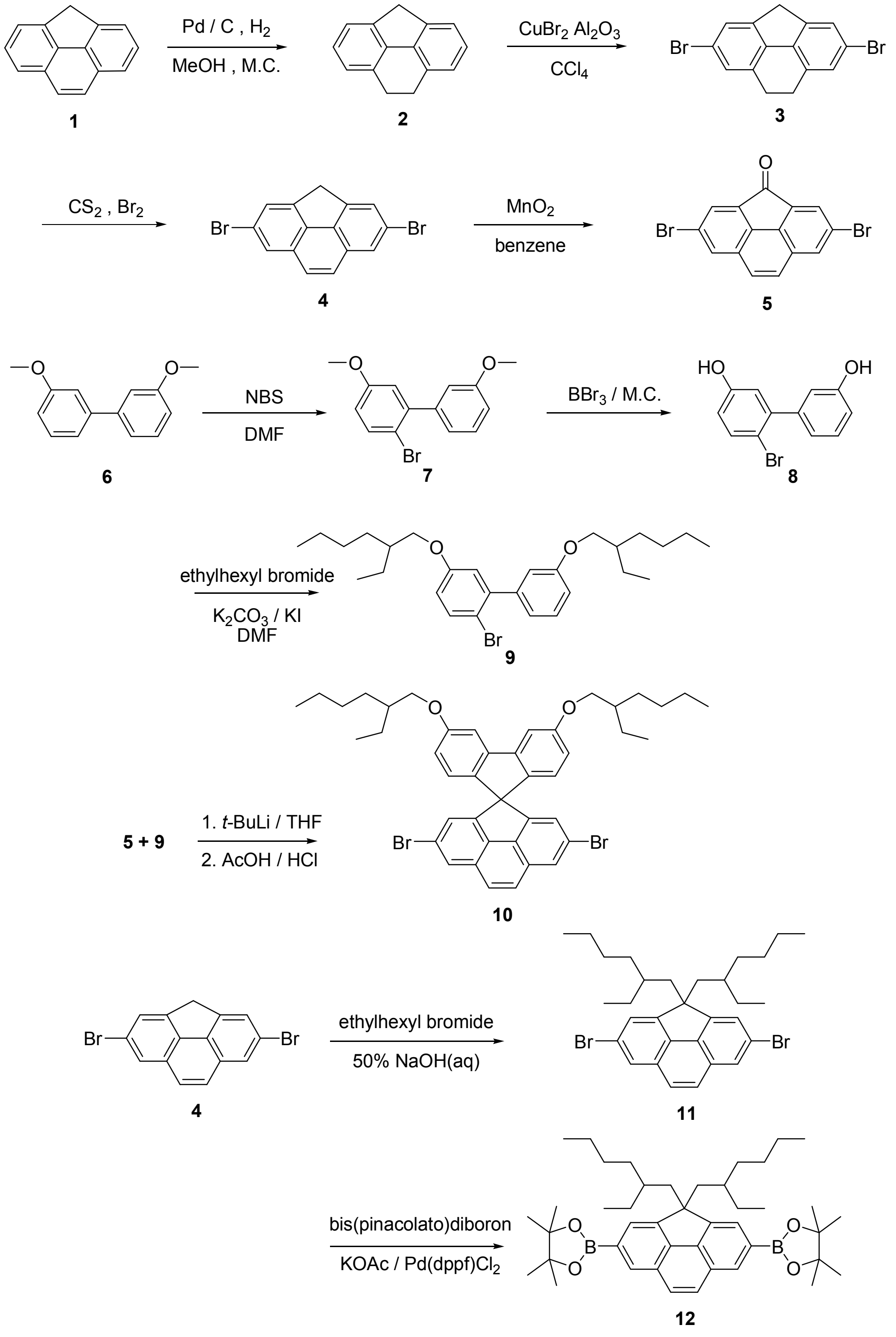

Scheme 1. Synthetic routes for the monomers.

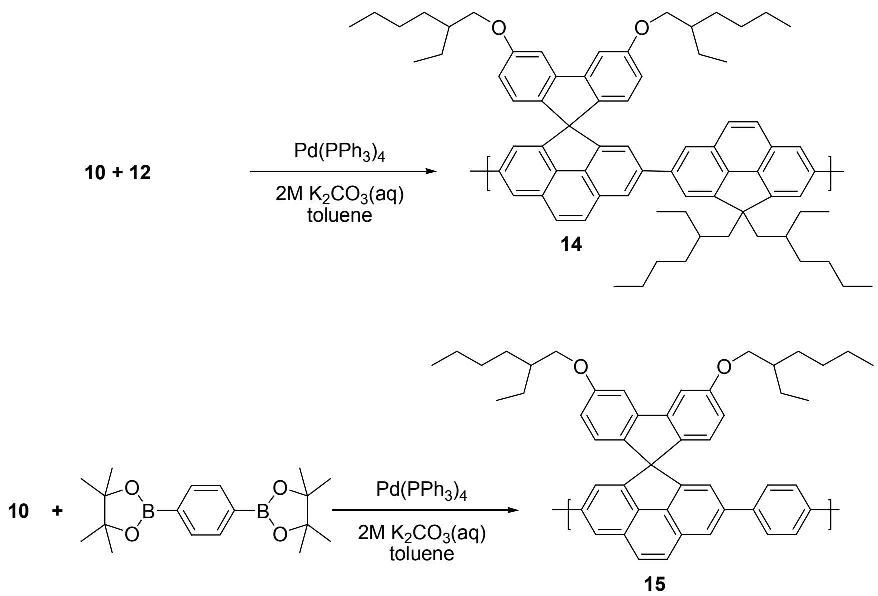

Scheme 2. Synthetic routes for the alternating copolymers

The resulting polymers were soluble in common organic solvents such as chloroform, chlorobenzene, tetrahydrofuran, dichloromethane and *o*-dichlorobenzene. Table 1 summarizes the polymerization results including molecular weights, polydispersity indexes (PDI, M_w/M_n) and thermal stability of the polymers. The number-average molecular weight (M_n) of spiro-PCPP-*alt*-PCPP and spiro-PCPPP, determined by gel permeation chromatography using mono-disperse polystyrene as calibration standard, are 25600 and 22200, respectively, with PDI around 1.7. The thermal properties of the polymers were evaluated by differential scanning calorimetry (DSC) and thermo gravimetric analysis (TGA) under nitrogen atmosphere. All these polymers show good thermal stability, with glass transition temperature (T_g) of polymers at around 89 and 84 °C, respectively, using DSC, performed in the temperature range from 30 to 250 °C. As shown in Figure 1, their decomposition temperatures (T_d), which correspond to a 5% weight loss upon heating during TGA, are 380 and 372 °C for polymers, respectively. The polymers exhibit good thermal stability which is important for the application of these copolymers in flat panel displays.

Table 1. Characterization of the Polymers.

polymers	yield (%)	M_n[a]	M_w[a]	PDI[a]	T_g[b] (℃)	T_d[c] (℃)
spiro-PCPP-*alt*-PCPP	22	25,600	42,900	1.67	89	380
spiro-PCPPP	32	22,200	37,500	1.69	84	372

Photophysical Properties

The linear UV-vis absorption and photoluminescence (PL) emission spectra of polymers as solution and thin film are shown in Figure 2. The solution was prepared using chloroform as solvent and the thin film was prepared by spin-coating on quartz plates from the polymer solutions in chlorobenzene. The maximum absorption peaks appeared at around 363 and 345 nm in the solution of chloroform. The maximum absorption peak of polymers in solid thin film appeared at around 359 and 349nm, respectively. In comparison with the results obtained using dilute solutions, the absorption spectra of the thin films are red-shifted and broadened, while the emission spectra of the thin films are similar. The PL emission spectra of polymers in chloroform solution show a same maximum peak at 397 nm.

The emission peaks in solution nearly correspond with that of PCPP. In solid thin films, the maximum PL emission spectra of spiro-PCPP-*alt*-PCPP and spiro-PCPPP appeared at around 463 and 456 nm, respectively. The PL spectra in solid thin films display a vibronic fine structure, which are also more red-shifted over 60 nm than solution conditions. The blue emissions at 400 and 409 nm for the π–π* transitions of conjugated polymer backbone are almost completely quenched or decreased. This phenomenon can be also explained by the increased inter-chain interaction as happening in the solid thin film state same as reported spiro-PCPP.[16]

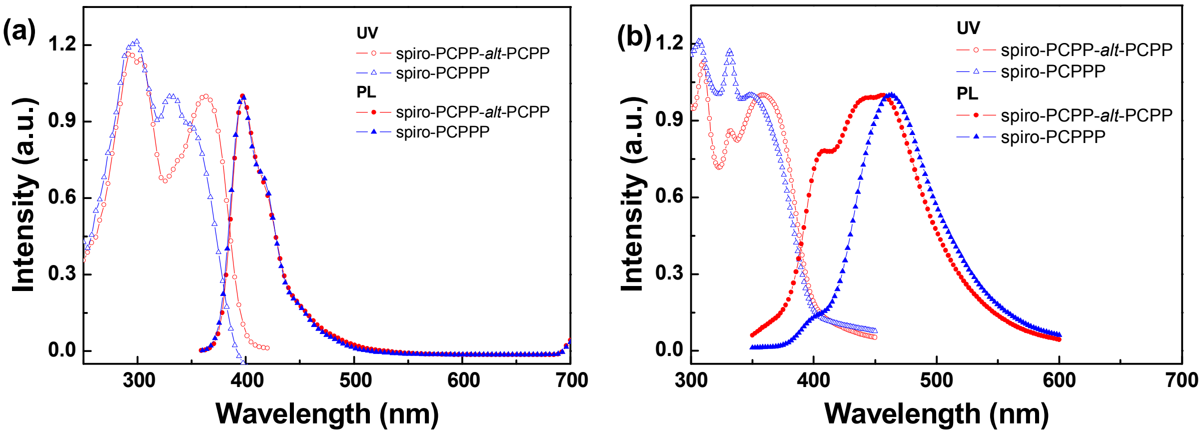

Figure 2. UV-vis absorption and photoluminescence spectra of ploymers in the THF solutions(a), and in the solid state(b).

Listed in Table 2 is the PL efficiency of the polymer in solution. Qauntum yield (Φ_{PL}) in solution determined in chloroform, relative to 9,10-diphenylanthracence as standard (Φ_{PL}=0.91 in ethanol). The efficiencies of the spiro-PCPP-*alt*-PCPP and spiro-PCPP have the maximal efficiency of 70 and 62%, respectively.

Table 2. Characteristics of the UV-vis Absorption, Photoluminescence, and Electroluminescence Spectra.

polymers	solution				film		
	Abs λ_{max} (nm)	PL $\lambda_{max}{}^{a}$ (nm)	fwhm^{b} of PL	QE$_{PL}$ (%)	Abs λ_{max} (nm)	PL $\lambda_{max}{}^{a}$ (nm)	fwhm^{b} of PL
spiro-PCPP -*alt*-PCPP	363	397	39	70.4	359	409, 443, 456	105
spiro-PCPPP	345	397	41	62.0	349	400, 463	78

Conclusion

We present here the synthesis of new conjugated polymers, spiro-PCPP derivatives, by Suzuki reaction. The maximum absorption peaks of the polymers appeared at around 363 and 345 nm in the solution of chloroform and at 359 and 349nm in the solid state, respectively.

The PL emission spectra of polymers in chloroform solution show a same maximum peak at 397 nm. The emission peaks in solution nearly correspond with that of PCPP. The maximum PL emission spectra of polymers appeared at around 463 and 456 nm in solid state, respectively. The blue emissions at 400-409 nm for the π–π* transitions of conjugated polymer backbone are almost completely quenched or decreased. It can be expected that this phenomena exhibit due to increasing inter-chain interaction in solid thin films.

References

[1] G. Gustafasson, Y. Cao, G. M. Treacy, F. Klavetter, N. Colaneri, A. J. Heeger: Nature Vol. 537 (1992) p. 477

[2] Y. Jin, J. Kim, S, Lee, J. Y. Kim, S. H. Park, K. Lee, H. Suh; Macromolecules Vol. 37 (2007) p. 6711

[3] (a) H. Suh, Y. Jin, S. H. Park, D. Kim, J. Kim, C. Kim, J. Y. Kim, K. Lee: Macromolecules Vol. 38 (2005) p. 6285. (b) S. H. Park, Y. Jin,J. Y. Kim, S. H. Kim, J. Kim, H. Suh, K. Lee: Adv. Funct. Mater. Vol. 17 (2007) p. 3063

[4] M. Grell, D. D. C. Bradley, M. Inbasekaran, E. P. Woo, Adv. Mater. Vol. 9 (1997) p. 798

[5] Y. Jin, J. Ju, J. Kim, S. Lee, J. Y. Kim, S. H. Park, S. M. Son, S. H. Jin, K. Lee, H. Suh: Macromolecules Vol. 36 (2003) p. 6970

[6] N. C. Greenham, S. C. Moratti, D. D. C. Bradley, R. H. Friend, A. B. Holmes: Nature Vol. 365 (1993) p. 628

[7] M. D. McGehee, T. Bergstedt, C. Zhang, A. P. Saab, M. B. O'Regan, G. C. Bazan, V. I. Srdanov, A. J. Heeger: Adv. Mater. Vol. 11 (1999) p. 1349

[8] S. A. Bliznyuk, S. A. Carter, J. C. Scott, G. Klärner, R. D. Miller, D. C. Miller: MacromoleculesVol. 32 (1999) p. 361

[9] U. Scherf, E. J. W. List: Adv. Mater. Vol. 14 (2002) p. 4477

[10] Y. Shi, J. Liu, Y. Yang: J. Appl. Phys. Vol. 87 (2000) p. 4254

[11] G. Klärner, R. D. Miller, C. J. Hawker: Polym. Prepr. Vol. 39 (1998) p. 1006

[12] G. Klärner, J. Lee, V. Y. Lee, E. Chan, J. Chen, A. Nelson, D. Markie-wicz, R. Siemens, J. C. Scott, R. D. Miller: Chem. Mater. Vol. 11 (1999) p. 1800

[13] W. L. Yu, J. Pei, W. Huang, A. J. Heeger: Adv. Mater. Vol. 12 (2000) p. 828

[14] H. Y. Lee, J. Y. Oh, H. Y. Chu, J. I. Lee, S. H. Kim, Y. S. Yang, G. H. Kim, L. M. Do, T. H. Zyung, J. H. Lee, Y. S. Park, Tetrahedron: Vol. 59 (2003) p. 2773

[15] D. Vak, S. J. Shin, J. H. Yum, S. S. Kim, D. Y. Kim: J. Lumin.Vol. 115 (2005) p. 109

[16] S. Song, Y. Jin, J. Kim, S. H. Park, S. H. Kim, K. Lee, H. Suh: Polymer Vol. 49 (2008) p. 5643

doi:10.4028/www.scientific.net/AST.75.97

Organic Synthesis and Characteristics of Novel Conjugated Polymers with Cyano Group and Carbazole Unit for AMOLEDs

Suhee Song[1,a], Youngeup Jin[2,b], Jooyoung Shim[1,c], Sun Hee Kim[3,d], Kwanghee Lee[3,e] and Hongsuk Suh[1,f,*]

[1]Department of Chemistry and Chemistry Institute for Functional Materials, Pusan National University, Busan 609-735, Korea

[2]Department of Industrial Chemistry, Pukyong National University, Busan 608-739, Korea

[3]Department of Materials Science and Engineering, Gwangju Institute of Science and Technology, Gwangju 500-712, Korea

[a]songsuhee@pusan.ac.kr, [b]yjin@pknu.ac.kr, [c]jyshim@pusan.ac.kr, [d]shkim@gist.ac.kr, [e]klee@gist.ac.kr, [e]hssuh@pusan.ac.kr

Keywords: conjugated polymer, light emitting diodes (LED), luminescence, polyfluorenevinylene

Abstract. The present investigation deals with the synthesis, characterization and EL of new copolymers, CzCNPFV1, CzCNPFV2 and CzCNPFV3 by Knoevenagel condensation reaction. The CzCNPFVs was synthesized for promoted efficiency of reported CNPFV. The PL emission spectra of the CzCNPFVs in chloroform solution show maximum peaks at 476 ~ 479 nm. In thin films, maximum peaks of the CzCNPFVs appeared at 501 ~ 504 nm, red-shifted around 25 nm as compared to that in solution. The more negative energy of the LUMO of CzCNPFV1 or CzCNPFV2 indicates the electron injection process is easier than in CNPFV. From this result, higher quantum efficiency of CzCNPFV1 or CzCNPFV2 as compared to that of CNPFV can be expected due to its improved electron injection ability from the cathode.

Introduction

Organic light-emitting diodes (OLEDs) have been researched considerably in full color plat panel displays, with several advantages over conventional devices such as a low driving voltage, wide viewing angle, thin film structure, and a simpler manufacturing process for the generation of large area and flexible display.[1] Fluorene based polymers, such as polyfluorenes (PFs), with a well-defined structure have attracted considerable attention because they may function as model compounds which are thought to be promising candidates for blue light-emitting diodes (LEDs) with high photoluminescence (PL) quantum efficiency, good thermal stability and easy functionalization at the 9-position of the fluorene unit.

By the way, the PFs are hole-transport-dominated materials that exhibit low electron mobility in EL devices. Their unbalanced charge injection and transport properties limit the efficient recombination of holes and electrons, resulting in a decrease in the EL efficiency.[3] In order to complement like this disadvantage of PF, many functional groups, such as electron-donating and –withdrawing group, have been introduced in PF backbone. Above all, carbazole units have been chosen as pendants, since carbazole is a well-known hole-transporting group due to the electron-donating capabilities of its nitrogen atom.[4] The polymers derivatives with carbazole units lead to good hole-transporting ability and improved device application in PLED.$_5$ And, carbazole unit can reduce aggregation among polymer backbones with fluorenevinylene units, since the peaks of around 490 nm and the fwhms of the spectra were very stable by protection of aggregation with increase level of the carbazole contents.

The present investigation deals with the synthesis, characterization and EL of new copolymers, CzCNPFV1, CzCNPFV2 and CzCNPFV3. The CzCNPFVs was synthesized for promoted efficiency of reported CNPFV. The new copolymers were synthesized by the Knoevenagel condensation from

9,9'-dihexyl-9*H*-fluorene-2,7-dicarbaldehyde, (7-cyanomethyl-9,9'-dihexyl-9*H*-fluorene-2-yl)-acetonitrile, 9-(6-(9*H*-carbazol-9-yl)hexyl)))-9hexyl-9*H*-fluorene-2,7-dicarbaldehyde and 9,9-bis-(6-carbazol-9-yl-hexyl)-9*H*-fluorene-2,7-dicarbaldehyde. Synthesized CzCNPFVs were incorporated with CN-polydihexylfluorene vinylene (CNPFV), having two cyano groups in a vinylene unit, to investigate the effect of the electron-withdrawing unit on optical and device properties of the copolymers. The incorporation of cyano group as electron acceptor in vinyl unite into the polymer with carbazole pendant group as electron-donor has improved the electroluminescent properties.

Introduction

Synthesis and Characterization

Scheme 1. Synthetic routes for monomers.

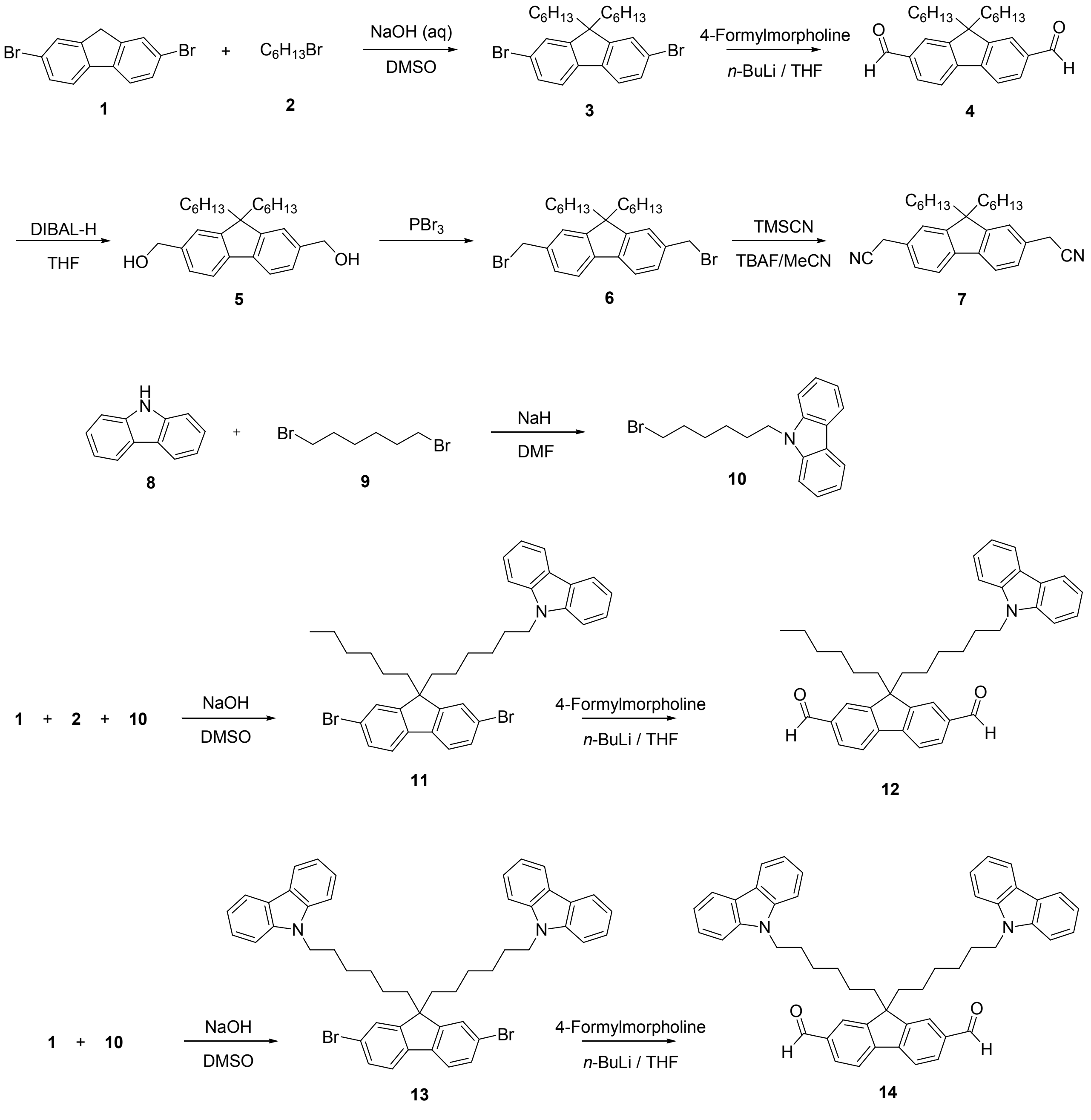

The general synthetic routes toward the monomers and polymers are outlined in scheme 1 and scheme 2. The comonomers, 9,9-dihexyl-9*H*-fluorene-2,7-dicarbaldehyde (**4**) and the (7-cyanomethyl-9,9'-dihexyl-9*H*-fluorene-2-yl)-acetonitrile (**7**), were prepared according to previously reported methods.[6] 2,7-dibromo-9*H*-fluorene (**1**) was coupled with compound **10** and 1-bromohexane (**2**) by using sodium hydroxide in DMSO to generate 9-(6-(2,7-dibromo-9-hexyl-9*H*-fluorene-9-yl)hexyl)-9*H*-carbazole (**11**) and 9,9-bis-(6-carbazol-9-yl-hexyl)-9*H*-fluorene-2,7-dibromide (**13**), which were reacted with formylmorpholine and *n*-BuLi in THF to provide 9-(6-(9*H*-carbazol-9-yl)hexyl)-9-hexyl-9*H*-fluorene-2,7-dicarbaldehyde (**12**) and 9,9-bis-(6-carbazol-9-yl-hexyl)-9*H*-fluorene-2,7-dicarbaldehyde (**14**), respectively. The polymerization reaction was generated by the well-known Knoevenagel condensation reaction, using 1 M tetrabutylammonium hydroxide in methanol and THF. The feed ratios of monomer **14** in CzCNPFV1 and CzCNPFV2 were 0.5 and 0.25 mol %, respectively. CzCNPFV3 was synthesis with monomer **7** and **12** in molar ratio 1:1. The copolymers were purified by dissolving in THF and precipitating into methanol. The copolymers were soluble in various organic solvents such as toluene, chlorobenzene, tetrahydrofuran and *o*-dichlorobenzene (ODCB).

Scheme 2. Synthetic routes for polymers.

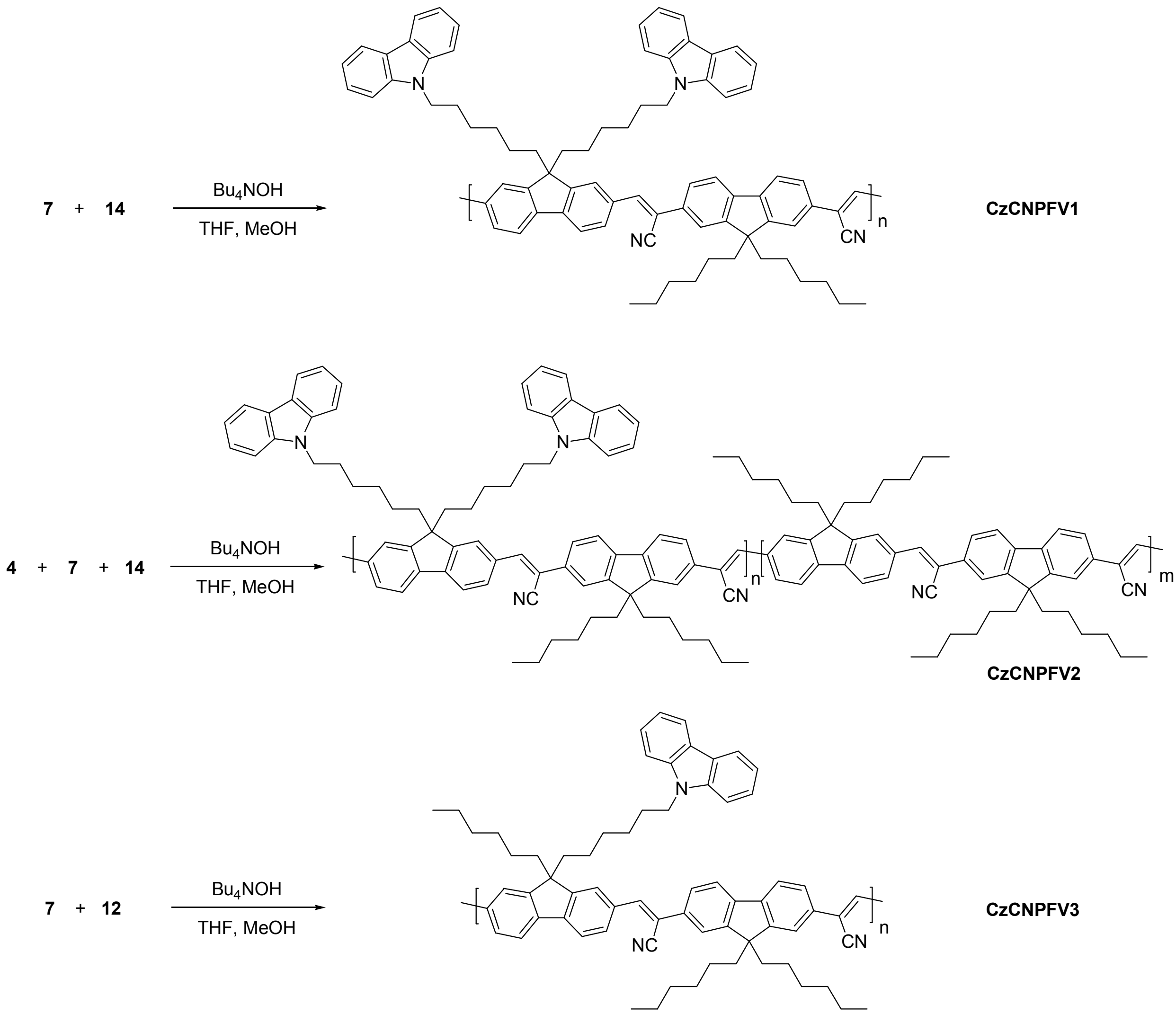

Table 1 summarizes the polymerization results including molecular weights, PDI and thermal stability of the copolymers. These copolymers have weight-average molecular weight (M_w) of 13,000 ~ 94,000 with PDI (poly dispersity index, M_w/M_n) of 1.6 ~ 2.6. The thermal properties of the polymers were evaluated by differential scanning calorimetry (DSC) and thermo gravimetric analysis (TGA) under nitrogen atmosphere. All of the polymers show good thermal stability, with glass transition temperature (T_g) of polymers at around 112 °C for CzCNPFV1, 102 °C for CzCNPFV2 and 95 °C for CzCNPFV3, performed in the temperature range from 30 to 250 °C. Their decomposition temperatures (T_d), which correspond to a 5% weight loss upon heating during TGA, are 416, 408 and 400 °C for polymers, respectively. The polymers exhibit good thermal stability which is important for the application of the copolymers in organic light emitting diodes.

Table 1. Characterization of the CzPFVs.

polymers	M_n[a]	M_w[a]	PDI[a]	T_g[b] (°C)	T_d[c] (°C)
CzCNPFV1	37000	94000	2.6	112	416
CzCNPFV2	34000	56000	1.6	102	408
CzCNPFV3	7700	13000	1.7	95	400

[a] Molecular weight (M_w) and Polydispersity (PDI) of the polymers were determined by gel permeation chromatography (GPC) in THF using polystyrene standards.

[b] Glass temperature was measured by DSC under N_2.

[c] Onset decomposition temperature (5% weight loss) was measured by TGA under N_2.

Optical Properties

Figure 1. UV-vis absorption and photoluminescence spectra of CzCNPFVs in the chloroform solution(a) and in thin film(b).

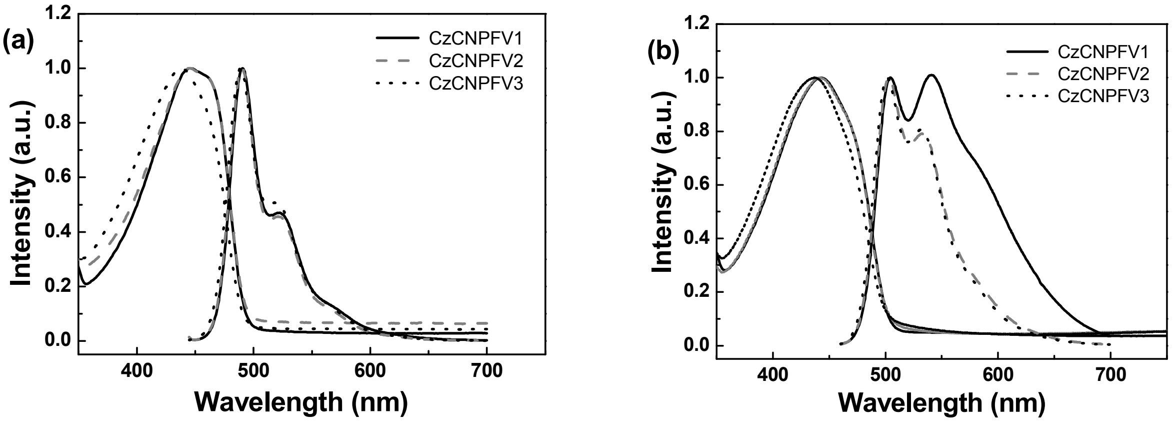

The linear UV-vis absorption and photoluminescence (PL) emission spectra of polymers as solution and thin film are shown in Figure 1. The solution was prepared using chloroform as solvent and the thin film was prepared by spin-coating on quartz plates from the polymer solutions in chlorobenzene. The absorption peaks originating from the conjugated backbone of CzCNPFVs appeared at around 438 ~ 446 nm, in the solution with chloroform as the solvent. The CzCNPFVs exhibited absorption spectra with maximum peaks at around 437 ~ 443 nm in thin films. The film absorption spectra of the polymers were quite similar to their solution ones. The PL emission spectra of the CzCNPFVs in chloroform solution show maximum peaks at 476 ~ 479 nm. In thin films, maximum peaks of the CzCNPFVs appeared at 501 ~ 504 nm, red-shifted around 25 nm as compared to that in solution. It is reported that carbazole unit, which is electron rich moiety, can reduce aggregation among polymer backbones with fluorenevinylene units. Though CzCNPFV1 has two carbazole pendants in one monomer, the PL spectra of CzCNPFV1 reveal a general trend of steadily increased red shift with increasing content of carbazole pendant as compared to CzCNPFV2. Also, side peak of the PL emission was increasing attractively indicating that the introduction of two pendants of monomer can increase the density of carbazole. As shown in Figure 2, the PL spectra of CzCNPFVs films did not show side peak increased, which corresponds to thermal stability, even after annealing for 60 min at 80 °C in air.

Figure 2. Photoluminescence spectra of (a) CzCNPFV1, (b) CzCNPFV2, and (c) CzCNPFV3 in thin film after annealing at 80 °C (from 0 min to 60 min).

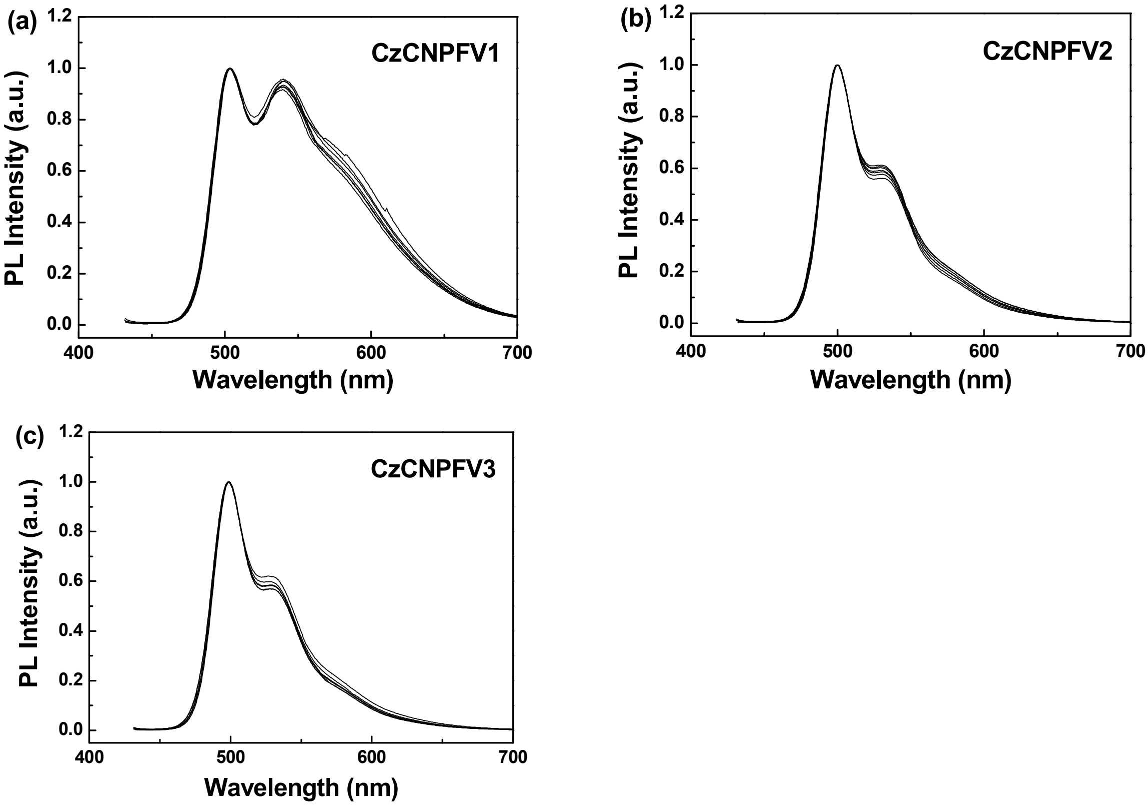

CONCLUSION

The present investigation deals with the synthesis, characterization and EL of new copolymers, CzCNPFV1, CzCNPFV2 and CzCNPFV3 by Knoevenagel condensation reaction. The CzCNPFVs was synthesized for promoted efficiency of reported CNPFV. The absorption peaks originating from the conjugated backbone of CzCNPFVs appeared at around 438 ~ 446 nm, in the solution with chloroform as the solvent. The CzCNPFVs exhibited absorption spectra with maximum peaks at around 437 ~ 443 nm in thin films. The PL emission spectra of the CzCNPFVs in chloroform solution show maximum peaks at 476 ~ 479 nm. In thin films, maximum peaks of the CzCNPFVs appeared at 501 ~ 504 nm, red-shifted around 25 nm as compared to that in solution.

References

[1] M. T. Bernius, M. Inbasekaran, J. O'Brien, W. Wu: Adv. Mater. Vol. 12 (2000), p. 1737.

[2] S. Tang, M. Liu, P. Lu, H. Xia, M. Li, Z. Xie, F. Shen, C. Gu, H. Wang, B. Yang, Y. Ma: Adv. Funct. Mater. Vol. 17 (2007), p. 2869.

[3] T. Tsutsui, S.-B. Lee, K. Fujita: Appl. Phys. Lett. Vol. 85 (2004), p. 2382.

[4] S. Grigalevicius, L. Ma, Z.-Y. Xie, U. Scherf: J. Polym. Sci. Part A: Polym. Chem. Vol. 44 (2006), p. 5987.

[5] Y. Jin, J. Ju, J. Kim, S. Lee, J. Y. Kim, S. H. Park, S.-M. Son, S.-H. Jin, K. Lee, H. Suh: Macromolecules Vol. 36 (2003), p. 6970.

[6] Y. Jin, M. Lee, S. H. Kim, S. Song, Y. Goo, H. Y. Woo, K. Lee, H. Suh: J. Polym. Sci. Part A: Polym. Chem. Vol. 46 (2008), p. 4407.

doi:10.4028/www.scientific.net/AST.75.103

Synthesis, Optical and Electrical Properties of Oligo(phenylenevinylene)s Substituted with Electron-Accepting Sulfonyl Groups

Volker Schmitt[1a] , Stefan Glang[1b], Heiner Detert[1c]*

[1]Institut für Organische Chemie, Johannes Gutenberg-University Mainz Duesbergweg 10 – 14 D-55099 Mainz, Germany
[a]volkerschmitt@aol.com, [b]stglang@gmx.de, [c]detert@uni-mainz.de

Keywords: Oligo(phenylenevinylene), UV-Vis-spectroscopy, fluorescence, Wittig-Horner olefination, cyclic voltammetry.

Abstract. Oligo(phenylenevinylene)s (OPV) composed of five rings and electron donating or withdrawing sulfonyl substituents on the central and lateral rings have been investigated. Two strategies were used for the syntheses of the C_2-symmetrical OPVs both include PO-activated olefinations as central steps. Six flexible side chains guarantee good solubility in toluene or dichloromethane. In solution and in films stabilised by polystyrene (60%), the chromophores are strongly fluorescent, with emissions in the violet-blue domain from solutions and in the green to orange region from solid films. The redox potentials, determined by cyclic voltammetry, and the optical properties are strongly depending on the position of the acceptor groups.

Introduction

Soluble π-conjugated organic materials with a phenylenevinylene backbone are one of the preferred classes of luminescent materials for the use in light emitting diodes (LEDs) and other electro optical and non-linear optical devices [1, 2]. A balanced charge carrier injection is decisive for highly efficient LEDs, but electron injection from aluminum into poly(phenylenevinylen)e (PPV) suffers from high barriers between the molecular frontier orbitals and the work function of the metal. To favor the electron injection low work function metals (Mg or Ca) can be used as electrodes, a more practical approach is to increase the electron affinity of the luminescent material [3 - 5]. Cyano-substitution is very effective in order to increase the electron affinity of PPV, the influence of different substitution pattern on the redox properties has been investigated theoretically [6] and experimentally [7]. As a result, the electron affinity is increased, the band gap reduced, and bathochromic shifts of the absorption and emission spectra are observed. Emitting materials with increased electron affinity of this type are of high interest in order to improve the efficiencies of LEDs [8- 10]. Sulfones are comparable to nitriles regarding the electron accepting power, [11] the second binding site of the sulfone moiety can be used to attach solubility enhancing side chains [12], or to connect conjugated segments in a polymer chain [13]. Recently, the efficiency of photovoltaic cells based on PPV has been strongly enhanced by the introduction of donor (alkoxy) and acceptor (sulfone) groups [14]. Moreover, sulfonyl groups as substituents on conjugated polymers prevent autoxidation [15]. Monodisperse oligomers are not only useful for the systematic study of substituent effects and conjugation length on the electro-optical properties, they are electronic materials in their own right [16, 17]. The combination of side chains with different electronic character allows a tuning of electrical and optical properties. Taking an OPV with five benzene rings as invariable π-system, we studied the influence of sulfones as acceptor groups on different positions and in combination with electron density releasing groups.

Experimental

Synthesis. The syntheses of C_2-symmetrical oligo(phenylenevinylene)s **1** – **6** with side chains of different electronic effects on the terminal and central rings were performed via two twofold

Horner-olefinations. The general strategy is shown in figure **1** using the synthesis of the hexakis-sulfonyl-OPV **6** as an example.

Starting with an alkylation of **7**, the second sulfur was introduced via chlorosulfonation. Reduction to the thiophenol and repeated alkylation led to a bis-thioether **8** that was bromomethylated to give gave an inseparable mixture of mono- and bis-bromomethyl compounds (**8a**, **8b**). Michaelis-Arbusov-reaction of this mixture with an excess of triethyl phosphite transformed the bromomethyl groups into phosphonates (**8c**, **8d**) and the thioethers were oxidized to sulfones using hydrogen peroxide in acetic acid. Due to the large difference in the polarity of the mono- and bisphosphonates (**9**, **10**), the separation of both synthons was easily possible via short-path chromatography. Two routes for the assembly of the chromophore were used. Starting with the central ring, a Horner-olefination of **9** and terephthalaldehyde-monodiethylacetal and subsequent deprotection gave the dialdehyde **11**. Combination of **11** with **10** completed the construction of the chromophore (**6**). Alternatively, **10** was used for the preparation of stilbenecarbaldehyde (**12**) and the condensation of **12** with **11** led to the same chromophore. Both routes gave similar yields.

Figure 1. Synthesis of Hexylsulfonyl-OPVs

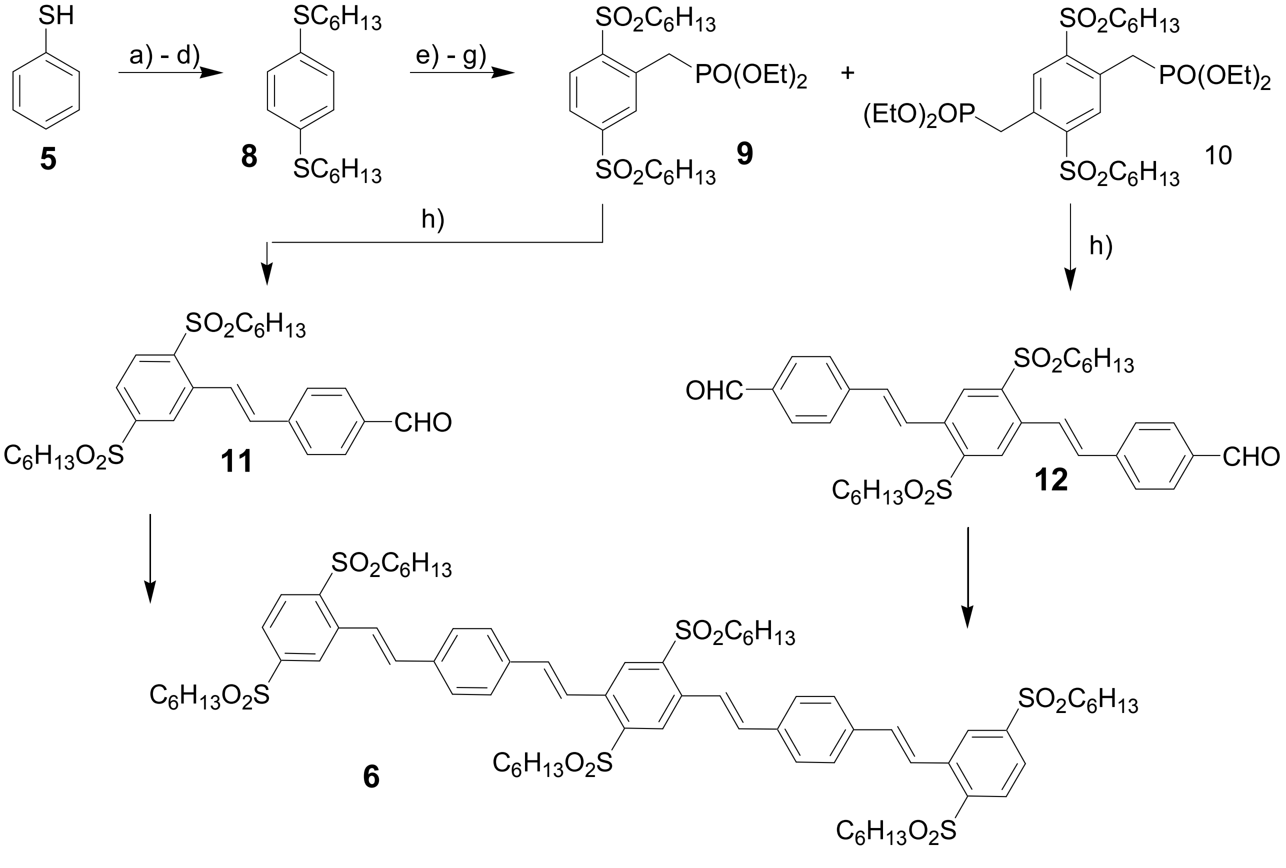

a); **7**, 1-bromohexane, K_2CO_3, 1,4-dioxane, reflux (93% of **7a**);b) **7a**, $ClSO_3H$, $CHCl_3$, 10°C, (63% of **7b**); c) **7b**, P (red), I_2, acetic acid, reflux (81% of **7c**),d) **7c**, 1-bromohexane, K_2CO_3, 1,4-dioxane, reflux (73% of **8**); e) **8**, H_2CO, HBr (48%), 80°C, (82% of (**8a**, **8b** : 3/2); f) **8a**, **8b**, $P(OEt)_3$, 160°C, (94% of **9a**, **9b**); g) **9a**, **9b**, acetic acid, H_2O_2, 70°, (94% of **9** and **10**); h) terephthalaldehyd-monodiethyl acetal, THF, KOtBu, 0°C, 60 min, then HCl (5%), 25°C, 6h, (**11**: 68%, **12**: 68%); i) **12** + **9** or **10** + **11**; KOtBu, THF, 0°C, (58% of **6** from **9** + **12**, 65% from **10** + **11**)

Mono- and bisphosphonates with alkyloxy or alkyl groups were used in combination with the sulfonyl-substituted synthons to prepare OPVs with mixed donor and acceptor substitution(Table 1) [18]. The syntheses of these starting materials have been described earlier [7].

Table 1. Substitution pattern of OPVs **1 – 6**

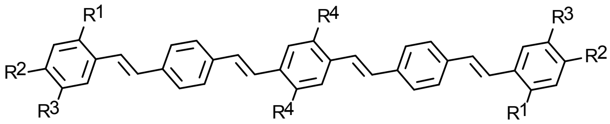

	1	**2**	**3**	**4**	**5**	**6**
R^1	C_6H_{13}	H	OC_8H_{17}	C_6H_{13}	$SO_2C_6H_{13}$	$SO_2C_6H_{13}$
R^2	H	$SO_2C_6H_{13}$	H	H	H	H
R^3	C_6H_{13}	OC_8H_{17}	OC_8H_{17}	C_6H_{13}	$SO_2C_6H_{13}$	$SO_2C_6H_{13}$
R^4	C_6H_{13}	OC_8H_{17}	$SO_2C_6H_{13}$	$SO_2C_6H_{13}$	C_6H_{13}	$SO_2C_6H_{13}$

Electronic spectra. Absorption and emission spectra were recorded from solutions of the OPVs **1** – **6** in toluene and dichloromethane (c = 10^{-5} mol/L for absorption, 10^{-7} mol/L for fluorescence) and from spin-coated films (60% polystyrene) on glass substrates. The absorption and emission maxima are collected in Table 2.

Table 2. Optical and electrochemical data of **1** – **6**

	1	**2**	**3**	**4**	**5**	**6**
Abs (T) [nm]	392	429	434	416	408	415
Abs (D) [nm]	395	427	432	415	410	408
Em (T) [nm]	455 (482)	484 (517)	511	486	477	467
Em (D) [nm]	455 (482)	488 (517)	540-570	504	512	473
Abs (PS) [nm]	391	464	434	413	411	405
Em (PS) [nm]	496	506	528	519	523	586
Exc (PS) [nm]	399	453/462	440	404	399	394/468
1. Ox. [V]	1.12	0.92	1.11	1.41	1.27	1.6§ (1.54)
2. Ox. [V]	1.29	1.24	1.37	-	1.46	1.9§ (1.82)
1. Red. [V]	-2.11§	-1.9§	-1.35	-1.33	-1.50	-1.53
2. Red. [V]	-	-	-1.54	-1.62	(-1.76)	-1.86

Absorption (Abs), emission (Em) and fluorescence excitation (Exc) maxima (λ_{max}) from solutions in toluene (T), dichloromethane (D) and spin-coated films with polystyrene (PS); § irreversible, peak potential given; values in brackets: peak potentials from stair-case voltammetry; ferrocene/ferrocenium: +0.44V.

Electrochemistry. The redox behaviour of the sulfonyl-OPVs was studied using cyclic voltammetry and stair-case voltammetry. A three-electrode setup with a platinum disc (WE), a platinum wire (CE) and a silver wire (RE) was used. The OPVs were dissolved in a 0.1 M solution of tetrabutylhexafluorophosphate in dichloromethane at 25°C. Scan speed was 200 mV/s, each measurement was calibrated using ferrocene as internal standard. The (radical) anions and cations formed during the electrochemical experiments display an intense green colour in solution. The results are summarised in Table 2.

Discussion

All compounds **1** - **6** show strong absorption bands in the blue part of the visible spectrum, the absorption maxima vary over a range of only 42 nm. Relative to **1**, compounds with donor-acceptor interactions (**2**, **3**) show the strongest red shifts ($\Delta\lambda$ = 37 nm, 42 nm). No significant solvatochromism of the absorption spectra was observed. Blue-green fluorescence is emitted from solutions of **1** – **6**. A quadrupolar structure (**3**, **4**, **5)** is the origin of moderate bathochromic shifts of the fluorescence with increasing solvent polarity (e.g. **5**: $\Delta\lambda_{max}$ = 46 nm; **6**: $\Delta\lambda_{max}$ = 11 nm comparing toluene and ethanol). This solvatochromism is accompanied by a reduction of the efficiency of the emission.

Spin-coated films from toluene solutions of the chromophores and polystyrene (40 /60) show broadened absorption spectra with maxima (λ_{max} = 391 – 464 nm) comparable to the dilute solution. But their fluorescence (λ_{max} = 496 – 528 nm) is shifted about 20 – 45 nm to lower energies (**1** – **5**) together with a loss of structure. Hexa-sulfonyl OPV **6** shows a bright and broad fluorescence centred in the orange part of the visible light with a very large shift of $\Delta\lambda$ = 121 nm. These stabilisations of the excited states can be attributed to intermolecular interactions, most obvious for **6**. Aggregation of **6** is favoured due to the six highly polar sulfones in a non-polar PS matrix.

A reduction of the alkyl-OPV **1** is hardly possible; an irreversible wave appears at –2.11 V. A combination of donor and acceptor on the same lateral benzene ring (**2**) slightly improves the electron injection. On the other hand sulfonyl groups on the central rings of OPVs **3** and **4** strongly facilitate the reduction. The reduction appears to be nearly unbiased by substitution on the lateral rings, since the difference between the OPVs with four donor groups (**3**) and four alkyl groups (**4**) is only 0.02 V. The position of the accepting groups is crucial, **5**, carrying two sulfonyl groups on each terminal ring is only reduced at – 1.50 V, comparable to **6** substituted with six electron withdrawing groups.

The first oxidation wave of the alkyl-substituted OPV **1** appears at 1.12 V, similar to **3** with central sulfonyl and lateral alkoxy groups. OPV **2**, with an identical number of donating and accepting groups displays the lowest oxidation potential (+ 0.92 V). The ease of this oxidation may be attributed to the p-dialkoxybenzene unit in the centre of the chromophore. Exchanging the donors in **3** with electronically "neutral" alkyl groups (**4**) shifts the first oxidation wave about 0.3 V to a more positive potential. Though the number of electron accepting groups doubles from **4** to **5**, the first oxidation potential is shifted to significant lower potential (1.27 V). Like **3**, the site of the first oxidation of **5** is the central benzene ring. MO-calculations give a HOMO which is located on the central distyrylbenzene segment. A replacement of the alkyl side chains on the central ring by sulfonyl groups (**6**) inhibits oxidation of the OPV to potentials up to 1.5 V.

Sulfonyl groups as acceptors on a phenylenevinylene chromophore cause pronounced shifts of the redox potentials. Exchange of six alkyl versus six sulfonyl groups shifts both, the first oxidation and reduction steps, about 0.5 V to higher potentials. This lowering of the LUMO level can be important for applications in LEDs, since the barriers for electron injection are reduced. Donor-acceptor interactions reduce the electrochemical window as well as the optical band gap. Materials of this type are less fluorescent and interesting for photo-electronic conversion [19].

Conclusion

The substitution of monodisperse OPVs with alkylsulfonyl groups as electron acceptors results in soluble chromophores with strongly reduced reduction potentials and enhanced resistance towards oxidation. The oxidation potential can be tuned by additional donor groups. A donor-acceptor electronic structure with a sulfonyl-substituted centre strongly reduces the electrochemical window. Correspondingly, their fluorescence is shifted to lower energies. Generally, the emission from the solid state is shifted about 40 nm to the red, only **6** shows a very strong bathochromism ($\Delta\lambda$ = 120 nm). The tuning of the redox potentials is most effective, if the substitution on the centre of the π-system is changed.

References

[1] A. Kraft, A. C. Grimsdale and A. B. Holmes, Angew. Chem. 110 (1998) p. 416

[2] A. Mathy, K. Ueberhofen, R. Schenk, H. Gregorius, R. Garay, K. Müllen and C. Bubeck, Phys. Rev. B 53 (1996) p. 4367

[3] A. R. Brown, D. D. C. Bradley, P. L. Burn, J. H. Burroughes, R. H. Friend, N. C. Greenham, A. Kraft, Appl. Phys. Lett. 61 (1994) p. 2793

[4] T. Yashuda, M. Saito, H. Nakamura and T. Tsutsui, Appl. Phys. Lett. 89 (2006) p. 182108

[5] F. Babudri, G. M. Farinola, M. Gianluca, F. Naso and R. Ragni, Chem. Commun. (2007) p. 1003

[6] J.-L. Brédas, Adv. Mater. 7 (1995) p. 263

[7] H. Detert, D. Schollmeyer and E. Sugiono, Eur. J. Org. Chem. (2001) p. 2917

[8] Z. Peng and M. E. Galvin, Chem. Mater 10 (1998) p. 1785

[9] Z.-K. Chen, H. Meng, Y.-H. Lai and W. Huang, Macromol, 32 (1999) p. 4351

[10] I. I. Perepichka, I. F. Perepichka, M. R. Bryce and L.-O. Pålssson, Chem. Commun. (2005) 3397

[11] O. Manousek, P. Zuman and O. Exner, Collect. Czech. Chem. Commun. 33 (1968) 3979, p. 3988

[12] H. Detert and E. Sugiono, Synth. Metals, 122 (2001) p. 15

[13] H. K. Jung, J. K. Lee, M. S. Kang, S. W. Kim, J. J. Kim and S. Y. Park, Polym. Bull. 43 (1999) p. 13

[14] O. Adebolu, C. E. Bonner jr, C. Zhang and S. Sun, PMSE Preprints 95 (2006) p. 465

[15] J. Y. Li, A. Ziegler and G. Wegner, Chem. Eur. J. 11 (2005) p. 4450

[16] Y. Zhang, G. Cheng, S. Chen, Y. Li, S. Liu, F. He, L. Tian and Y. Ma, Appl. Phys. Lett. 88 (2006) p. 223508

[17] H.-C. Lin, C.-M. Tsai, G.-H. Huang and J.-M. Lin, J. Polym. Sci. A 44 (2005) p. 783

[18] All compounds were characterised by IR-, mass-, ^{1}H-, and ^{13}C-NMR-spectra and gave satisfactory elemental analyses.

[19] S.-S. Sun and C. E. Bonner jr, Synth. Metals 154 (2005) p. 65

doi:10.4028/www.scientific.net/AST.75.108

Synthesis of fluorinated organic and organometallic electroluminescent materials: tuning emission in the blue

Gianluca M. Farinola[1*], Francesco Babudri[1], Antonio Cardone[2], Omar Hassan Omar[2], Carmela Martinelli[1], Francesco Naso[1], Vita Pinto[1], Roberta Ragni[1]

[1]Dipartimento di Chimica, Università degli Studi di Bari, via Orabona,4, I-70125, Bari, Italy

[2]Istituto di Chimica dei Composti OrganoMetallici ICCOM-CNR di Bari, via Orabona,4, I-70125, Bari, Italy

farinola@chimica.uniba.it

Keywords: Organic electroluminescence, electroluminescent polymers, phosphorescent Ir complexes, synthesis of organic semiconductors.

Abstract. Functionalization with fluorine atoms represents a versatile structural modification to finely tune both the emission colour and the electronic properties of organic and organometallic electroluminescent compounds. This paper reports an overview of our systematic investigation on the design and synthesis of the fluorinated version of two important classes of materials for organic light emitting diodes (OLEDs), namely poly(arylenevinylene)s and phosphorescent phenylpyridine Iridium complexes. Synthetic pathways based on organometallic methodologies affording selectively fluorinated molecular structures will be discussed together with a summary of the effect of fluorination on the optical properties of the resulting materials. In particular we will highlight the possibilities offered by the organometallic methodologies as straightforward and resourceful tools to provide a wide series of fluorinated molecular architectures with high regio- and stereoselectivity, mild experimental conditions and good yields.

Introduction

In the last decades growing research efforts have been devoted to the development of new organic and organometallic semiconducting materials, both polymers and small molecules, for applications in electroluminescent devices [1], solar cells [2], thin-film transistors [3], and sensors [4], taking advantage from their good processability and from the tuneability of their electronic and optical properties which can be controlled by manipulating molecular structure and self-assembling behaviour. Functionalization of the molecular structure with substituents having different electronic and steric effects is a valuable strategy for the control of properties, and it largely relies on the development of efficient and selective synthetic methodologies.

Functionalization with fluorine atoms offers several advantages that are mainly related to the special features of the small halogen atom, such as its high electronegativity (in the Pauling scale EN = 4) and the high C-F bond energy (about 480 KJ/ mol). In particular, the electronic effects caused by substitution with fluorine atoms deeply affect the optical and electronic properties of the materials, and the strength of the C-F bond can significantly improve the thermal and oxidative stability of the fluorinated organic materials. As far as organic electroluminescent materials are concerned, fluorination represents a structural modification that may contribute to improve some characteristics of the materials relevant to their applications in display and lighting technologies. While efficient yellow, red and green electroluminescent (both singlet and triplet emitters) materials have been developed, the search for efficient and stable blue emitters is still an open issue. Moreover, high LUMO energy levels of many organic emitters makes them poor electron acceptors form stable metal electrodes, such as aluminium, thus reducing the device performances. Both blue-shifted emission colour and improved electron accepting properties can be expected by fluorination of the molecular backbone of various classes of electroluminescent organic and organometallic materials. In particular, theoretical calculations [5] indicate that the introduction of electron-withdrawing substituents can cause a blue-shift of the emission in some conjugated polymers by widening the HOMO-LUMO gap, lowering at the same time both the HOMO and LUMO energy levels. The low polarizability and small size of the fluorine atom and the strength of the C–F bond [6] also determine the intriguing properties of the fluorinated systems. Besides, in fluorinated organic compounds, F…H–C interactions occur, that are similar to the hydrogen bond, but with a much lower energy, which may play an important role in the solid state organization of fluorine compounds bearing both C–F and C–H bonds.

In the light of all the above mentioned consideration, functionalization with fluorine atoms has been explored as a chemical modification of several classes of organic materials for electroluminescent devices [7] and we describe herein our contribution in this research field dealing, in particular, with the synthesis of fluorinated arylenevinylene polymers and phosphorescent Iridium complexes.

Fluorinated poly(arylenevinylene)s

The protocols that we have developed for the synthesis of fluorinated poly(arylenevinylene)s are based upon the Stille cross coupling reaction between bis-stannylated vinylic monomers and functionalized aryl bis-iodides [8]. This methodology had been already exploited to obtain several alkoxy-substituted PPV polymers [9]. First, we have extended the methodology to the preparation of a poly(*p*-phenylenevinylene) PPV polymer with fully fluorinated aromatic rings, namely poly(*p*-tetrafluorophenylenevinylene) **PTFPV**. The synthesis of such polymer had been previously unsuccessfully attempted *via* both water-soluble and organic solvent-soluble precursor routes by Brooke and Mawson in 1990 [10]. Our polymerization was carried out by reacting the commercial 1,4-diiodotetrafluorobenzene **1** with (*E*)-1,2-bis(tributylstannyl)ethene **2** [11] in the presence of $Pd(AsPh_3)_4$ as the catalyst (generated *in situ* from $Pd_2(dba)_3$ and $AsPh_3$), in refluxing benzene (Scheme1) [12].

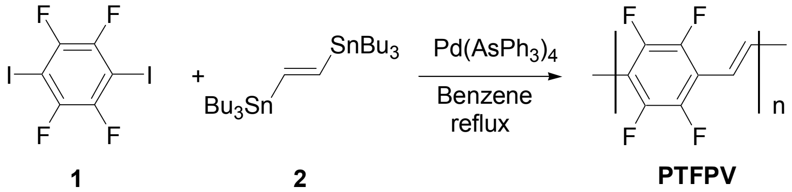

Scheme 1

The polymer **PTFPV** was insoluble in common organic solvent and in several perfluorinated solvents, therefore its structure and molecular weight were determined by MALDI-TOF mass analysis, applied for the first time to the characterization of an insoluble conjugated polymer. The MALDI-TOF analysis protocol was developed starting from the method used to analyze insoluble polyamides [13]. The average polymerization degree was calculated to be approximately 17-20 arylenevinylene units. Fourier Transformed Infrared Spectroscopy (FTIR) confirmed the *trans* configuration of the double bonds of the polymer.

Subsequently, the Stille cross-coupling reaction protocol was extended to the preparation of soluble random copolymers of 2,3,5,6-tetrafluorophenylenevinylene and 2,5-dialkoxyphenylenevinylene, **co(TFPV-DFPV)s,** by reacting (*E*)-1,2-bis(tributylstannyl)ethene **2** with different ratios of the two aromatic diiodo monomers 1,4-diiodo-2,3,5,6-tetrafluorobenzene **1** and 1,4-diiodo-2,5-bis(octyloxy)benzene **3**, using $Pd(PPh_3)_4$ as the catalyst in the presence of copper iodide (Scheme 2) [14].

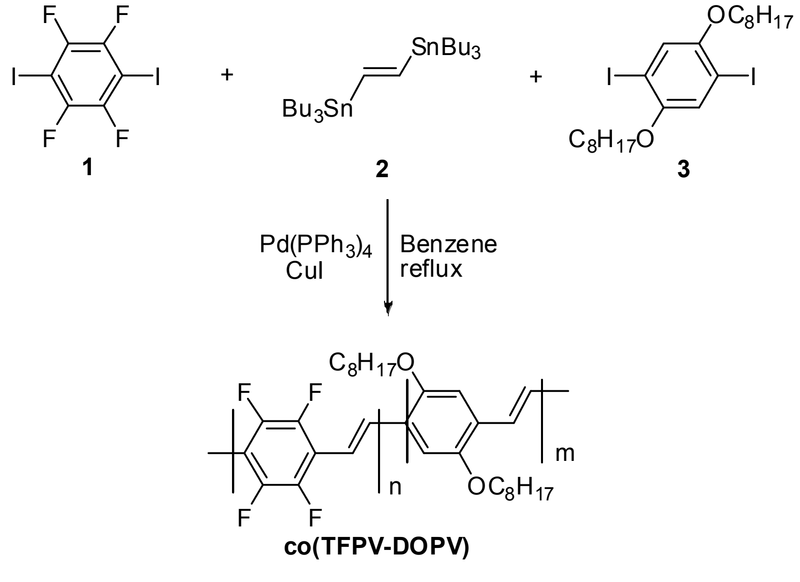

Scheme 2

Three different copolymers **co(TFPV-DOPV)s** were obtained changing the feed ratio of the two monomers **1** and **3** (20:80; 50:50; 65:35). A detailed ^{1}H NMR investigation revealed a preferential incorporation of the tetrafluoro-substituted unit (63:37 percent ratio of fluorinated aromatic *vs.* the alkoxy-substituted units) when an equimolar feed ratio of the two aromatic monomers (50:50) was used, likely due to the higher reactivity of the fluorinated monomer with respect to the non-fluorinated counterpart. The introduction of fluorine atoms on the double bonds of arylenevinylene systems is more challenging than the synthesis of polymers with fluorinated aromatic rings. However, we have recently reported that the Stille reaction - based protocol can be conveniently extended to the synthesis of such systems. In fact, before our work only two PPV polymers with fluorinated double bonds had been prepared by Suh and co-workers [15]. The Gilch route described in their paper for the preparation of the two polymers requires the treatment of the monomers with strong bases, thus preventing the extension of their methodology to base-sensitive functionalized substrates. In addition, incomplete elimination of halogen atoms and coupling in a head-to-head and tail-to-tail fashion, that are common drawbacks of the Gilch approach, can lead to structural defects that negatively affect the optical and electrical properties of the polymers.

The availability of (*E*)-(1,2-difluoro-1,2-ethenediyl)bis(tributylstannane) **4**, as reported by Burton *et al.* [16], prompted us to extend the Stille cross-coupling reaction to the synthesis of soluble poly(arylenevinylene) with *all-trans* fluorinated double bonds (Scheme 3). To explore the potentiality of this polymerization protocol, we synthesized not only PPVs with fluorinated double bonds and alkoxy-substituted aromatic rings (**11-12**), but also different poly(arylenevinylene)s such as the poly(fluorenedifluorovinylene) **13** and the poly(thienylenedifluorovinylene) **14** [17].

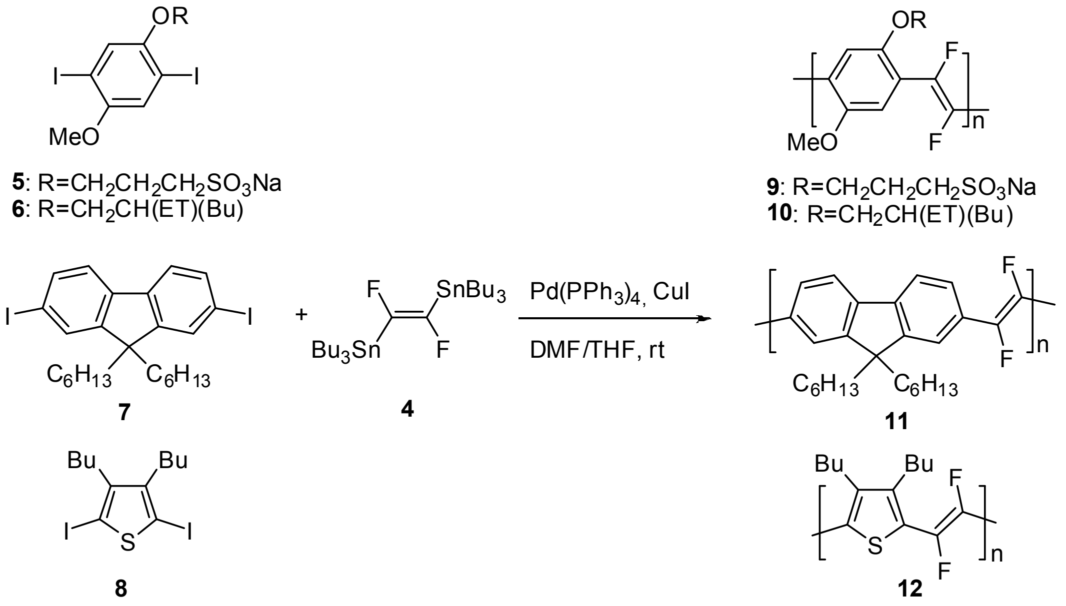

Scheme3

All reactions were carried out using Pd(PPh$_3$)$_4$ as the catalyst, CuI in stoichiometric amount, a THF/DMF mixture as solvent, at room temperature. By the same approach, we have recently obtained the first fully fluorinated poly(arylenevinylene)s, namely poly(1,4-tetrafluorophenylene-difluorovinylene) **6F-PPV** and poly(2,5-difluorothienylene-difluorovinylene) **4F-PTV,** by reacting the (*E*)-(1,2-difluoro-ethenediyl)bis[tributylstannane] **4** with 1,4-diiodotetrafluorobenzene **1** and 3,4-difluoro-2,5-diiodothiophene **13**, respectively (Scheme 4) [18].

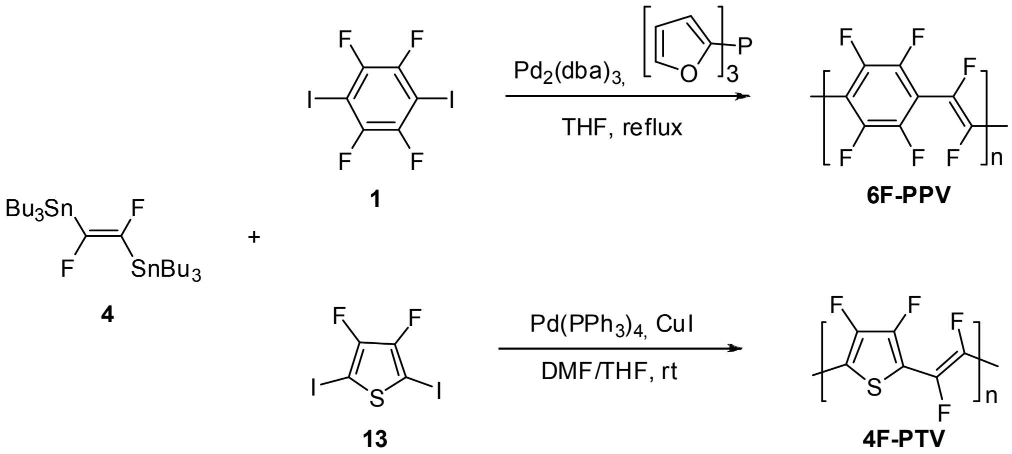

Scheme 4

The **6F-PPV** was obtained in the presence of Pd$_2$(dba)$_3$ and tri(2-furyl)phosphine as the catalytic system, in THF at reflux for one week while to synthesize polymer **4F-P** the same conditions summarized in the scheme 3 were described. Both the polymers **6F-PPV** and **4F-PTV** are insoluble in the most common organic and perfluorinated solvents, and they were characterized by FT-IR spectroscopy and MALDI-TOF mass spectrometry. The IR spectra show the presence of the two significant absorbance bands related to the C-F stretching vibration of the conjugated vinylene units and the C-F stretching vibration of the aromatic rings. The MALDI-TOF analysis shows polymeric chains length ranging approximately from 3 to 9 repeating units for **6F-PPV** and from 6 to 12 for

4F-PTV. Even though mass discrimination phenomena in favor of low molecular weight components occur in MALDI-TOF mass spectrometry of polydisperse polymers [19], we think these results can be considered a good approximation of the real mass distribution of the two polymers, because the scarce solubility should cause a precipitation of the growing polymer chains in the reaction medium. Moreover, the low molecular weight of the materials does not represent a drawback to their application as semiconductors. In fact, oligomeric materials can exhibit electrical and optical properties suitable for device application with the advantage, in some cases, to be be easily processable by thermal evaporation. This is also the case for the polymers **6F-PPV** and **4F-PTV**, that can be thermally evaporated in thin film under reduced pressure (about 10^{-5} mbar).

The availability of a series of PPVs differing for the number and position of fluorine substituents on the conjugated backbone enabled to study the effect of fluorination on the absorption and emission spectra of phenylenevinylene systems. The maximum of the absorption bands of **PDOPV** and **PTFPV** falls at λ_{max} = 460 nm and λ_{max} = 350 nm, respectively. The blue shift observed for **PTFPV** compared to **PDOPV** can be attributed to the inductive electron-withdrawing effect of the fluorine atoms on the aromatic rings of the conjugated backbone [12], which is opposite to the electron donating effect of the alkoxy substituents on the **PDOPV** main chain. The absorption spectrum of the copolymer **co(TFPV-DOPV)** synthesized using and equimolar amount of the two aromatic co-monomers shows two resonances at λ = 440 nm and λ = 360 nm, which are close in energy to the main absorption bands of the parent homopolymers. This structure of the spectrum suggests the presence of two differently substituted phenylenevinylene segments, randomly arranged in the copolymer. The comparison of the photoluminescence spectra maxima of the three polymers in thin film **PDOPV** (λmax = 580), **TFPV** (λ max = 520) and **co(TFPV-DOPV)** (λ max = 645 nm) shows a strong red shift for the copolymer compared with the parent homopolymers. Moreover a Stokes' shifts of 190 nm is observed for **co(TFPV-DOPV**), higher than the 110 nm Stokes' shifts measured for **PDOPV**. The strong red-shift and the large value of the Stokes' shift measured for **co(TFPV-DOPV)** can be attributed to the more effective formation of interchain species in the copolymer in the solid state, due to the simultaneous presence of electron deficient **TFPV** and electron rich **PDOPV** segments [14]. The comparison of the absorption and emission spectra in chloroform solution of **MEH-PPV** (λmax abs = 360 nm, λmax PL = 466 nm) with that of **MEH-PPDFV** (λmax abs = 480 nm, λmax PL = 555 nm) shows the effect of the introduction of fluorine atoms on the double bonds of alkoxy-substituted PPV polymers: a blue shift of 120 nm of the absorption maximum is measured for the polymer with the fluorinated double bonds **MEH-PPDFV** compared with the non fluorinated **MEH-PPV**, and a corresponding 89 nm blue shift is observed in the PL spectrum maxima in solution. Based on theoretical modeling and spectroscopic measurements of oligomeric model systems, the observed increase in absorption energy can be attributed to a steric effect rather than to the electron-withdrawing character of the fluorine atoms on the double bonds [20]. The **MEH-PPDFV** polymeric film shows strong blue photoluminescence (PL) at room temperature, with a maximum at 458 nm, which is slightly blue-shifted also with respect to the photoluminescence of the polymer in chloroform solution (PL λmax = 466 nm) [17], contrarily to the red-shift of the emission spectrum of **MEH-PPV** from solution to thin film. This blue-shift of the emission in the solid state with respect to the solution indicates that no strong inter-chain aggregation occurs for the **MEH-PPDFV** in thin films. Moreover, the PL λmax of the **MEH-PPDFV** thin film is blue-shifted of about 110 nm compared to that of similar thin film of **MEH-PPV** obtained by the same synthetic methodology (λmax = 568 nm) and this represents the most blue shifted emission reported so far for a poly(*p*-phenylenevinylene) polymer.

Complete substitution of hydrogen atoms with fluorine atoms on the conjugated backbone of the poly(arylenevinylene)s results in a strong increase of the band gap as revealed by the study of spectroscopic properties of **6F-PPV** [18]. Actually, the HOMO-LUMO transition value is about 4.18 eV while the value for the corresponding hydrogenated polymers poly(*p*-phenylenevinylene) (**PPV**) is Eg = 2.4 eV. Interestingly, the **6F-PPV** has a band gap even larger than that of **MEH-PPDFV** [17]. Several structural factors can be responsible for this strong blue-shift, including the reduced polymer chains length, the electron-withdrawing effect of the fluorine atoms and the steric repulsion between the fluorine atoms ortho to the vinylene units on the aromatic rings and those on the double bonds. The EL spectra of **MEH-PPDFV** is about 100 nm blue-shifted with respect to that of **MEH-PPV**. In fact the EL spectra of **MEH-PPDFV** and **MEH-PPV** obtained from from a ITO/PEDOT:PSS/MEH-PPDFV/Ba/Al devices exhibit maxima at approximately 2.4 (*circa* 520 nm) and 1.98 eV (*circa* 625 nm), respectively, corresponding to greenish-blue and red light [21].

Fluorinated phosphorescent phenylpyridine Iridium complexes

Fluoro-functionalization represents a strategy to shift the emission colour of electrophosphoresent Ir complexes in the blue region of the visible spectrum and eventually to increase their chemical stability. Aiming to obtain blue-emitting electrophosphoresent Ir complexes, we prepared phenylpyridine cyclometalating ligands functionalized with three or four fluorine atoms on the phenyl ring, as shown in scheme 5 [22].

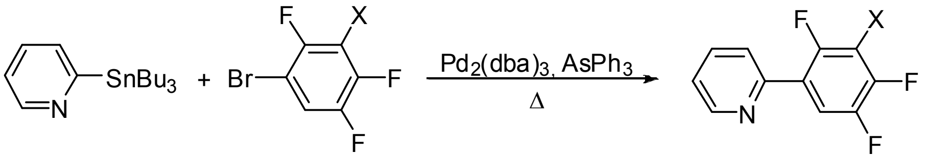

14

15a, X=H
15b, X=F

16a, X=H
16b, X=F

Scheme 5

The ligands **16a** and **16b**, obtained by reacting 2-tributylstannyl pyridine **14** (prepared by metallation of the 2-bromo pyridine) with reagents **15a** and **15b** respectively, in the Stille reaction conditions, were used to complex Iridium(III) ion yielding both the homoleptic and heteroleptic complexes (schemes 6 and 7).

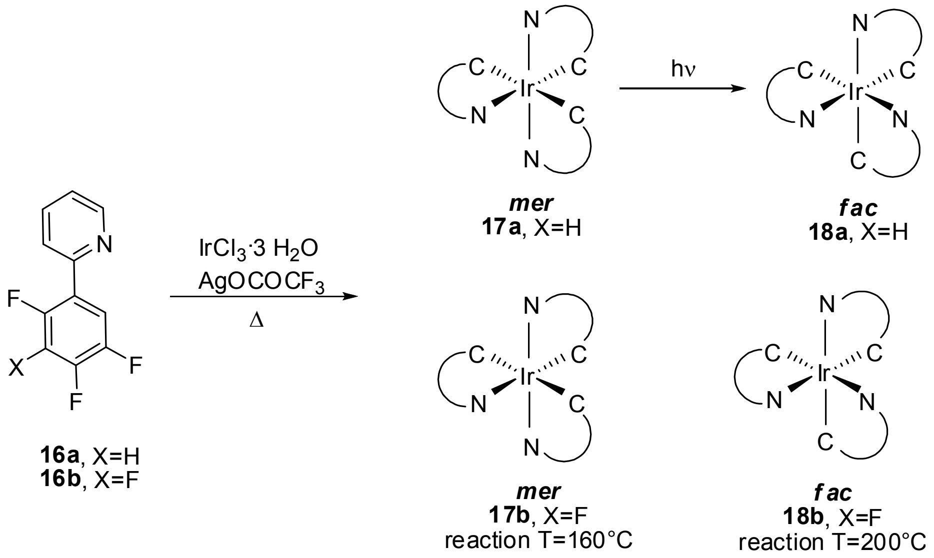

Scheme 6

The homoleptic complexes were synthesized in a single-step using a procedure reported in the literature [23], involving the reaction of $IrCl_3 \cdot 3H_2O$ with a slight excess of fluorinated ligand in the presence of silver trifluoroacetate. Contrary to the results reported in the literature, where only the *facial* stereoisomers are obtained by this protocol, in our case, when the tetrafluoro-substituted ligand **16b** was used, we obtained both the *meridianal* (***mer,*** **17b**) and the *facial* (***fac,*** **18*b***) stereoisomers, depending on the reaction temperature (Scheme 6). In the case of the trifluorosubstituted ligand, the complexation reaction afforded only the ***mer*** **17a** isomer, and a photochemical isomerization process was necessary to convert it into the corresponding ***fac*** **18a** complex (Scheme 6). Heteroleptic acetylacetonate complexes **20a** and **20b** were also obtained by a double-step procedure [24] carried out by cleavage of dichloro-bridged dimer complexes **19a** and **19b** with acetylacetonate in the presence of sodium carbonate (Scheme 7).

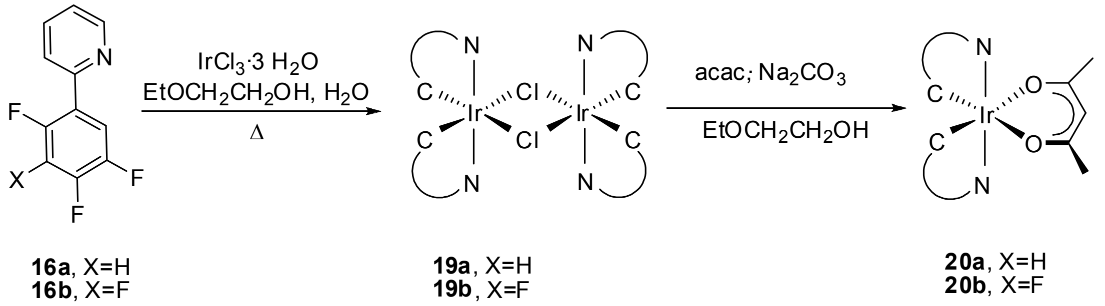

16a, X=H
16b, X=F

19a, X=H
19b, X=F

20a, X=H
20b, X=F

Scheme 7

All the fluorinated homoleptic and heteroleptic complexes obtained exhibit broad emission in the ‘‘light blue’’ region, and their photoluminescence appears significantly affected by the number of fluorine atoms bonded to the ligands. Indeed, under the same stereochemical configuration, the emission is 10 nm blue shifted for complexes bearing three fluorine atoms on each phenylpyridine with respect to the corresponding complexes bearing four fluorine substituents. Furthermore, the ***mer*** homoleptic complexes show a 5 nm blue shift in the photoluminescence with respect to the corresponding ***fac*** stereoisomers. Moreover, the replacement of one of the three phenylpyridine ligands with acetylacetonate bathochromically shifts the emission of complexes of about 10 nm, regardless of the number of fluorine atoms.

Electroluminescent devices were fabricated using the Ir complexes dispersed (9% concentration) in a poly(9-vinylcarbazole) (PVK) host matrix, in the presence of an electron carrier molecular material (Bu-PBD) and a hole-blocking layer. All the complexes emitted with potentials between 5.0 and 6.5 V, showing emission maxima in the blue region and shapes and energies similar to those found in solution. The maximum external quantum efficiency (5.5%) was observed for the device made with the ***fac*** iridium complex bearing tetra fluorinated phenylpyridines while the devices made with the heteroleptic complexes showed reduced efficiencies with respect to the homoleptic ***fac*** complexes. Furthermore, electroluminescence data showed a critical difference in the stability of the devices fabricated with the ***fac*** and the ***mer*** isomers: in fact, the ***mer*** complex based devices exhibit a fast spectral change of the emission from the blue to the green region of the spectrum, most likely due to low stability of the *meridianal* complex.

Recently, we also synthesized and investigated heteroleptic iridium complexes functionalized with sulfonyl groups and fluorine atoms in order to evaluate the combined effect of these electron-withdrawing substituents on the properties of the phosphorescent materials (Figure 1) [25].

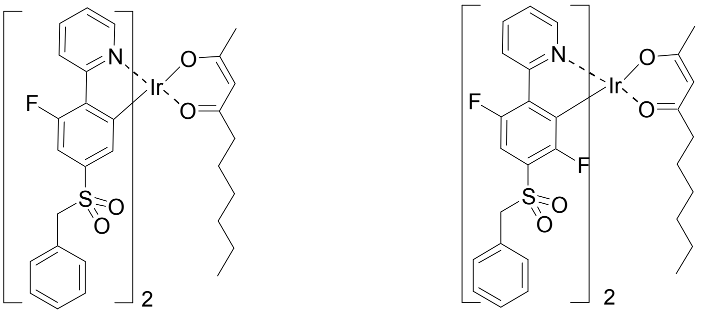

Figure 1

In this case, the third ancillary 2,4-decandionate ligand was introduced instead of the more common acetylacetonate to increase the solubility of iridium complexes in common organic solvents. In particular, we developed a straightforward synthetic protocol for the preparation of fluorinated and sulfonyl functionalized phenylpyridines, as shown in Scheme 8.

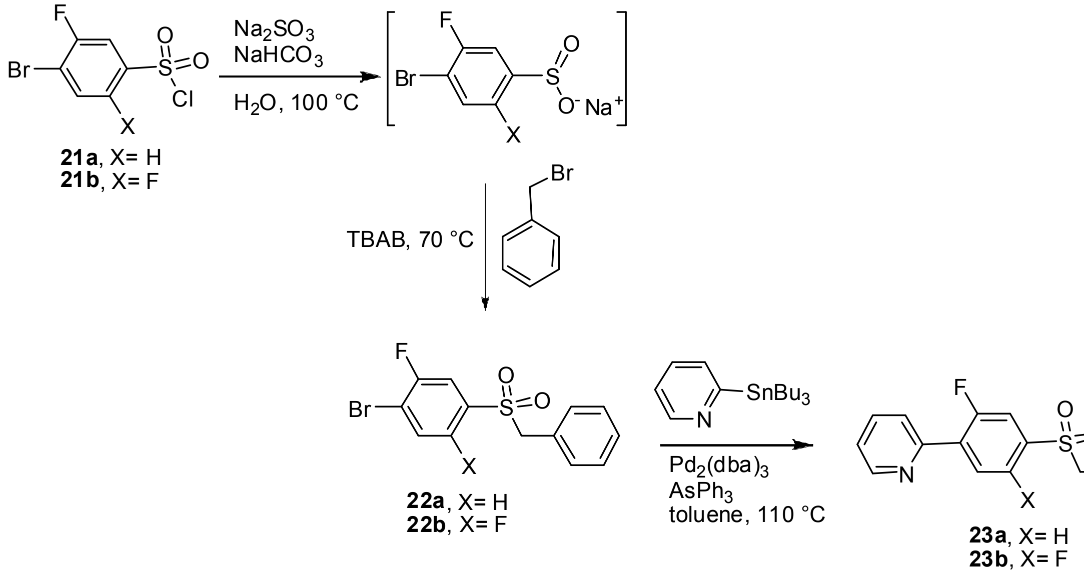

Scheme 8

The protocol involves the preliminary synthesis of bromophenyl benzyl sulfones **22a** and **22b**, by a one-pot procedure based on the reaction of commercially available sulfonyl chlorides **21a** and **21b** with sodium sulfite and sodium hydrogen carbonate followed by the nucleophilic substitution of the resulting sulfinate intermediates salts with benzylbromide in the presence of tetra-*N*-butyl ammonium bromide TBAB, as the phase transfer catalyst. The bromophenyl benzyl sulfones **22a** and **22b** were then submitted to the palladium catalyzed Stille cross-coupling reaction with 2-tributylstannyl pyridine **14**, to yield the final ligands **23a** and **23b**, used to complex Iridium

We found that the presence of one and two fluorine atoms in the sulfonyl-substituted ppy ligands leads to a blue shift of photoluminescence (λmax = 533 nm and 516 nm respectively) when compared to the non-fluorinated analogue complex (λmax = 546 nm). The complexes also exhibit very high quantum yield values in deareated conditions, (Φ = 62% and 65% respectively). Interestingly, emission quantum yields measured for air-equilibrated solutions also show values remarkably higher than those reported in the literature, which are typically below 5% [26]. In particular, the complex bearing two fluorine atoms on phenylpyridines has a quantum yield of 16% in aerated conditions, a value almost three times higher than expected, and, to the best of our knowledge, the highest reported in the literature for iridium complexes in the presence of dioxygen. We believe that this unexpected behaviour could be related to the combination of several factors which more efficiently prevent oxygen quenching, such as steric hindrance around the iridium core, the presence of two F atoms known to have a hydrophobic character [6], the electronic effects due to the simultaneous presence of two F atoms and a sulfonyl group, the position of the substituents on the ppy ligand or, more important, the lack of a thermally activated state responsible for the quenching, at room temperature, of the emission.

Summary

This paper has reported an overview of our studies dealing with fluorinated organic and organometallic materials for electroluminescent devices.

Our work demonstrates the versatility of the Stille cross-coupling reaction as a synthetic tool to selectively access a wide variety of fluorinated polyconjugated organic systems. By applying this methodology we have prepared different poly(arylenevinylene)s selectively functionalized with fluorine atoms on the aromatic rings or on the double bonds. We have also synthesized two poly(arylenevinylene)s completely fluorinated, that are insoluble in common organic solvents, but can be easily evaporated in thin film at reduced pressure. At the same time the Stille reaction has been demonstrated to be suitable to synthesize fluoro-functionalized phenylpyridine ligands used to prepare phosphorescent Iridium complexes.

The study on the impact of the fluorination on optical and electrooptical properties of poly(arylenevinylene)s reveals that electronic and steric effects caused by the fluorine atoms bonded to the main polymeric backbone deeply affect the characteristics of the conjugated system, enabling to achieve efficient blue emission from polymers with phenylenevinylene conjugated backbone.

Homoleptic and heteroleptic iridium complexes with the fluorine substituents have been used as effective phosphorescent blue-emitters in phosphorescent organic light emitting devices (PHOLEDs).

All the results discussed demonstrate that the fluoro-functionalization is a useful structural modification to finely modulate the emission colour in the blue part of the visible spectrum.

Acknowledgements

This work was financially supported by Ministero dell’Istruzione, dell’Università e della Ricerca (MIUR), ‘‘Progetto PRIN 2007 PBWN44’’ and by Università degli Studi di Bari.

References

[1] J. Liu, Q. G. Zhou, Y. X. Cheng, Y. H. Geng, L. X. Wang, D. G.Ma, X. B. Jing, F. S. Wang: Adv. Funct. Mater. Vol. 16 (2006), p. 957.

[2] S. Neyshtadt, M. Kalina, G. L. Frey: Adv. Mater. Vol. 20 (2008), p. 2541. Y. Kim, S. Cook, S. M. Tuladhar, S. A. Choulis, J. Nelson, J. R. Durrant, D. D. C. Bradley, M. Giles, I. McCulloch, C. S. Ha, M. Ree: Nat. Mater. Vol. 5 (2006), p.197.

[3] R. Zhang, B. Li, M. C. Iovu, M. Jeffries-El, G. Sauve`, J. Cooper, S. Jia, S. Tristram-Nagle, D. M. Smilgies, D. N. Lambeth, R. D. McCullough, T. Kowalewski: J. Am. Chem. Soc. Vol. 128 (2006), p. 3480.

[4] D. H. Charych, J. O. Nagy, W. Spevak, M. D. Bednarski: Science Vol. 261 (1993), p. 585.

[5] J. L.Bredas, A. Heeger: J Chem Phys Lett Vol. 217 (1994), p. 507.

[6] Reichenbacher, H. I. Suss and J. Hulliger: Chem. Soc. Rev. Vol. 34 (2005), p. 22.

[7] F. Babudri, G. M. Farinola, F. Naso, R. Ragni: Chem Commun (2007), p. 1003.K.

[8] F. Babudri, G. M. Farinola, Naso: J. Mater. Chem. Vol. 14 (2004), p. 11.

[9] F. Babudri, S. R. Cicco, L. Chiavarone, G. M. Farinola, L. C. Lopez, F. Naso, G.Scamarcio: J. Mater. Chem. Vol. 10 (2000), p. 1573.

[10] G. H. Brooke, S. D. Mawson, J. Fluorine Chem., Vol. 50 (1990), p. 101.

[11] A. F. Renaldo, J. W. Labadie, J. K. Stille, Org. Synth., Vol. 67 (1989), p. 86.

[12] F. Babudri, A. Cardone, L. Chiavarone, G. Ciccarella, G. M. Farinola, F. Naso, G. Scamarcio: Chem. Commun. (2001), p. 1940.

[13] R. Skelton, F. Dubois, R. A. Zenobi: Anal. Chem. Vol. 72 (2000), p. 1707.

[14] F. Babudri, A. Cardone, G. M. Farinola, F. Naso, T. Cassano, L. Chiavarone, R. Tommasi: Macromol. Chem. Phys. Vol. 204 (2003), p. 1621.

[15] Y. Jin, J. Kim, S. Lee, J. Y. Kim, S. H. Park, K. Lee, H. Suh: Macromolecules Vol. 37 (2004), p. 6711.
[16] D. J. Burton, Q. Liu: Org. Lett. Vol. 4 (2002), p. 1483.
[17] F. Babudri, A. Cardone, G. M. Farinola, C. Martinelli, R. Mendichi, F. Naso, M. Striccoli: Eur. J. Org. Chem. (2008), p. 1977.
[18] A. Cardone, C. Martinelli, V. Pinto, F. Babudri, M. Losurdo, G. Bruno, C. Pinalysa, F. Naso, G. M. Farinola: J. Poly. Sci.: Part A: Polym. Chem. Vol. 48 (2010), p. 285.
[19] Nielsen, M. W. F. Mass Spectrom Rev. Vol.18 (1999), p. 309 and references therein.
[20] M. Piacenza, F. Della Sala, G.M. Farinola, C. Martinelli, G. Gigli: J. Phys.Chem. B vol. 112 (2008), p. 2996.
[21] M. Losurdo, M.M. Giangregorio, P. Capezzuto, A. Cardone, C. Martinelli, G.M. Farinola, F. Babudri, F. Naso, M. Büchel, G. Bruno: Adv. Mater. Vol. 21 (2009), p. 1115.
[22] R. Ragni, E. A. Plummer, K. Brunner, J. W. Hofstraat, F. Babudri, G. M. Farinola, F. Naso, L. De Cola: J. Mater. Chem. Vol. 16 (2006), p. 1161.
[23] V. V. Grushin, N. Herron, D. D. LeCloux, W. J. Marshall, V. A. Petrov, Y. Wang: Chem. Commun. (2001), p. 1494.
[24] S. Lamansky, P. Djurovich, D. Murphy, F. Abdel-Razzaq, R. Kwong, I. Tsyba, M. Bortz, B. Muy, R. Bau, M. E. Thompson: Inorg. Chem. Vol. 40 (2001), p. 1704.
[25] R. Ragni, E. Orselli, G. S. Kottas, O. Hassan Omar, F. Babudri, A. Pedone, F. Naso, G.M. Farinola, L. De Cola: Chem.: A Eur. J. Vol. 15 (2009), p. 132.
[26] L. Flamigni, A. Barbieri, C. Sabatini, B. Ventura, F. Barigelletti: Top. Curr. Chem. Vol. 281 (2007), p. 143.

doi:10.4028/www.scientific.net/AST.75.118

Tailoring optical properties of Blue-Gap Poly(p-phenylene vinylene)s for LEDs applications

Elena Dilonardo[1,3,a], Maria M. Giangregorio[1], Maria Losurdo[1] ,
Pio Capezzuto[1], Giovanni Bruno[1], Antonio Cardone[2], Carmela Martinelli[3],
Gianluca M. Farinola[3], Francesco Babudri[3], Francesco Naso[3]

[1]Istituto di Metodologie Inorganiche e Plasmi, IMIP-CNR, Via E. Orabona 4, 70126 Bari, Italy

[2]Istituto di Chimica dei Composti Organometallici, ICCOM-CNR di Bari, Via E. Orabona 4, 70126 Bari, Italy

[3]Dipartimento di Chimica, Università degli studi di Bari,Via E. Orabona 4, 70126 Bari, Italy

[a]elena.dilonardo@chimica.uniba.it

Keywords: Conjugated polymer thin films, MEH-PPDFV, Optical properties.

Abstract. There has been growing interest in developing new semiconducting polymers for applications in optoelectronics (OLEDs) due to their exceptional processability and appealing characteristic of manipulating electronic and optical properties by tuning of molecular structure and self-assembling.

This study is an investigation on the interplay among supermolecular organization and optical properties of thin films of the poly[2-(2-ethylhexyloxy)-5-methoxy]-1, 4-phenylenedifluorovinylene (MEH-PPDFV) conjugated polymer, which has fluorinated vinylene units. This interplay is elucidated exploiting atomic force microscopy, spectroscopy ellipsometry, photoluminescence and electroluminescence. Thin films of MEH-PPDFV have been deposited by drop casting on indium-tin-oxide (ITO), quartz and glass substrates. The dependence of polymer chains self-organization and morphology on substrate surface is presented. Furthermore, it is demonstrated that the presence of F-atoms in the vinylene units of the MEH-PPDFV yields a blue optical band gap with the maximum of the fundamental HOMO-LUMO transition at 331 nm and photoluminescence at 458 nm. The OLED built with the above polymer shows a very stable blue-greenish electroluminescence that is also achieved at 504 nm.

Introduction

Nowadays, the development of new polymeric semiconductors for applications in optoelectronics (i.e., organic light-emitting diodes (OLEDs)), photovoltaics, thin film transistors and sensors has attracted great interest due to their exceptional processability and appealing characteristics of manipulating electronic and optical properties by tuning of molecular structure and self-assembling [1]. For applications based on optical emission, the ability to tune the colour of emission is essential. In this frame, there is interest in stable deep-blue emitting polymers. Various approaches are being investigated for addressing colour tuning [2]. Among the various approaches reported in literature aimed at blue-emission, polymers like poly(phenylene)s [3], polyfluorenes [2], which have no vinylene linkage and have good chain rigidity, are good blue-light emitters. Although polyfluorenes and their copolymers are widely used for blue-light emission, OLEDs based on these polymers suffer from poor stability and from the appearance of a green emission after a short operation time, due to keto-defects caused by photo-oxidative degradation [4,5]. PPV polymers with fluorinated vinylene units have been proposed [6, 7] as a class of polymers with increased stability to double bond photo-oxidation, blue–shifted photoluminescence [7] and improved OLEDs performance [8].

It is well known that the optical properties and anisotropy [9] of conjugated polymeric films strictly depend on the polymer chains organization in the film, which ultimately depends on deposition conditions [10].

In this contribution, we investigate the optical properties of poly[2-(2-ethylhexyloxy)-5-methoxy]-1,4-phenylenedifluorovinylene (MEH-PPDFV) thin films as an example of poly(p-phenylenedifluorovinylene)s (PPDFVs) with two fluorine atoms in the vinylene units. In particular, we report the correlation existing between the solid state organization of polymeric chains and the optical functionality of MEH-PPDFV thin films. We demonstrate that these polymeric thin films have the largest HOMO-LUMO transition energy (above 3.75 eV) ever reported for organic films and intense room temperature blue photoluminescence at 450 nm and electroluminescence at 504 nm. Since the performances of organic materials used in optoelectronic devices strongly depend on the polymer self-assembling process in the solid state, which induces a modulation of polymer morphological and optical properties, we discuss the effects of the substrate on the aggregation structure of the polymer in the solid state, the structural order and the anisotropy, and the subsequent impact on the electronic and optical properties of the polymer film.

Experimental

Polymer-Film Preparation. The MEH-PPDV polymer was synthesized by the Stille cross-coupling reaction [11]. The non-fluorinated MEH-PPV was also prepared by the same way, as comparison material. Polymer films were deposited on ITO, Corning glass and quartz by drop casting a dichlorobenzene (ODCB) solution containing 11 mg l^{-1} of polymer by very slow solvent evaporation while the whole system was kept inside a small box saturated by the vapour solvent.

Before analyses, all films were annealed for 30 min at 130°C in UHV to remove any solvent residual and to stabilize film microstructure.

Characterization. The surface morphology of films was analyzed by AFM (Autoprobe CP-VEECO) in intermittent mode (IC-AFM).

The optical properties and anisotropy were investigated in non destructive mode by spectroscopic ellipsometry (SE) [12]. Measurements at multiple angles of incidentnin the range 55°-70° were carried out using a phase modulated spectroscopic ellipsometer in the energy photon range 0.75-6.5 eV (UVISEL, Jobin Yvon) with a resolution of 0.01 eV. To derive the spectral dependence of (n + ik) from the measured variable angle, the experimental SE spectra of the pseudo-refractive index, <N>, and/or pseudo-dielectric function, $<\varepsilon> = <\varepsilon_1> + i<\varepsilon_2> = <N>^2$, where analyzed using a two-layer model consisting in substrate/polymer film/surface roughness. The energy dispersion of the polymer optical constants was modelled using an ensemble of four Lorentzian oscillators

$$\boldsymbol{N}^2 = (\boldsymbol{n} + \boldsymbol{ik})^2 = \varepsilon = \varepsilon_1 + \boldsymbol{i}\varepsilon_2 = \varepsilon_\infty + \sum_j \frac{\boldsymbol{A}_j \omega_j^2}{\omega_j^2 - \omega^2 - \boldsymbol{i}\gamma_j \omega} \tag{1}$$

where ε_∞ is the high-frequency dielectric constant, ω_j, γ_j and Aj are the frequency width and strength of the j oscillator. The first oscillator describes the fundamental π- π* optical transition, and the other oscillators are for taking into account bands II due to an exciton associated with the interband transition yielding, the band III at 4.7 ev, and the absorption band IV at approximately 6.2 eV, due to the electron and hole states of a Frankel exciton localized on the phenyl ring (L-L* transitions) according to the band structure reported in ref. [13].

Photoluminescence (PL) and electroluminescence (EL) corroborate the results. Details on the conditions used for PL and EL measurements are reported elsewhere [14].

Results and discussion

Self-organization of polymer chains in thin films and, hence, morphology and surface roughness are important parameters because they might hinder the movement of charge carriers; the surface roughness can lead to the formation of voids or non-interconnectivity between grains, which act as electrical traps. Fig. 1 shows AFM images of ITO film as received and after O_2 plasma treatment. A better morphology with a significant decrease of the surface roughness is found on ITO film after O_2 plasma treatment. The smoothing of ITO morphology is important to enhance OLEDs operation, since a better interface between the ITO film and the holes transport layer has been reported to improve OLEDs performance [15]. Consistently, Fig. 1 shows a better adhesion, a smoother and more uniform morphology of MEH-PPDFV polymer films deposited on ITO substrate pre-treated with O_2 plasma. For comparison, the morphology of MEH-PPDFV films deposited on glass and quartz, substrates typically used for running optical characterization like UV-vis transmittance measurements, are also reported in Fig. 1; the corresponding values of surface roughness (root mean square RMS) are also indicated. AFM analysis clearly puts in evidence that the morphology of films deposited on substrates used in technological device (e.g. ITO) is quite different from that characterized by non-interconnected poly-grains in films deposited on quartz and glass. This difference can be explained by the different surface tension of the substrates and, hence, the wettability by the polymer chains. In particular, an increase of surface tension to 64.5 mJ m^{-2} for ITO film treated by O_2 plasma results in a lower contact angle and improves the wetting by polymer [16]; while a lower surface tension in the range 57.6-59 mJ m^{-2} for quartz-glass, depending on the amount of the silanol groups and adsorbed water on the surface [17], results in lower wettability on those substrates.

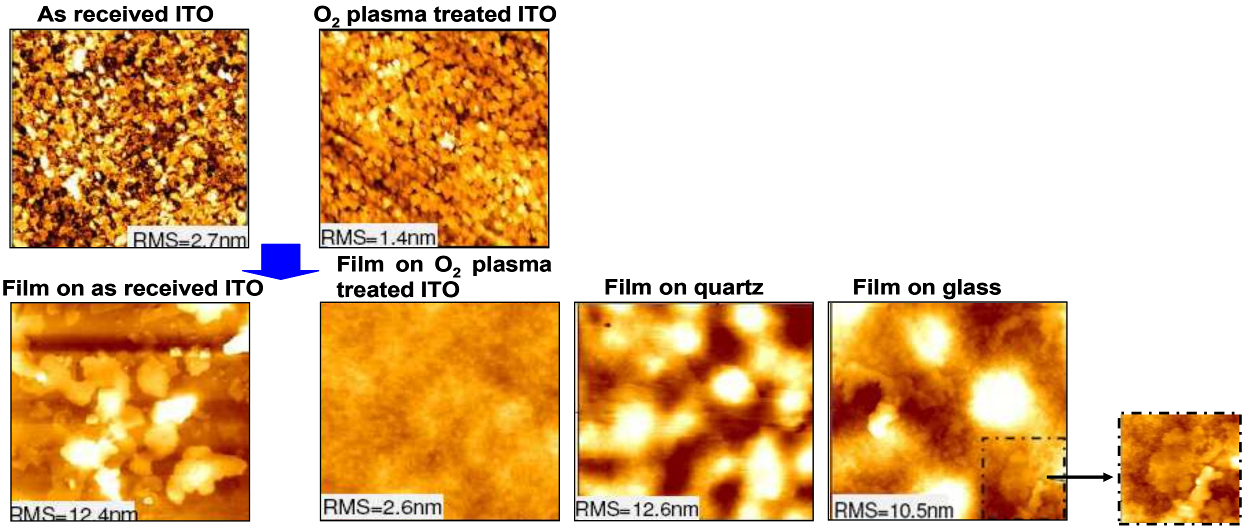

Figure 1. AFM images (5 μm x 5 μm) of ITO film before and after O_2 plasma surface treatment and of 80 nm thick MEH-PPDFV film drop casted on both substrates are shown. For comparison, morphologies of films deposited under the same experimental conditions on both quartz and glass substrates are also reported. Corresponding RMS values are indicated.

The different self-organization of polymer chains on different substrates also impacts on the resulting optical properties. Fig. 2 shows the experimental spectra of the pseudo-extinction coefficient, <k>, for MEH-PPDFV films deposited on the various substrates.

The fundamental π- π* transition is in the range 3.5-3.7 eV, depending on polymer chains organization and film morphology. Below this fundamental transition, interference fringes due to multiple reflection at the substrate/film interface appear(from which ellipsometry analysis calculates the film thickness). Above the fundamental π- π* transition, the higher energy bands, II, III and IV, as defined in ref. [13], appear. The relative position and intensity of absorption bands clearly depend on polymer chains self-organization and film morphology, which depends on the interaction with the substrate. This is an indication that the different chain organization on the various substrate also results in a different optical anisotropy which reflects the different structural order. In order to analyze the interplay between anisotropy and solid-state organization, ellipsometric measurements at various angles of incidence have been performed to drive the in-plane and out-of-plane components of the optical properties.

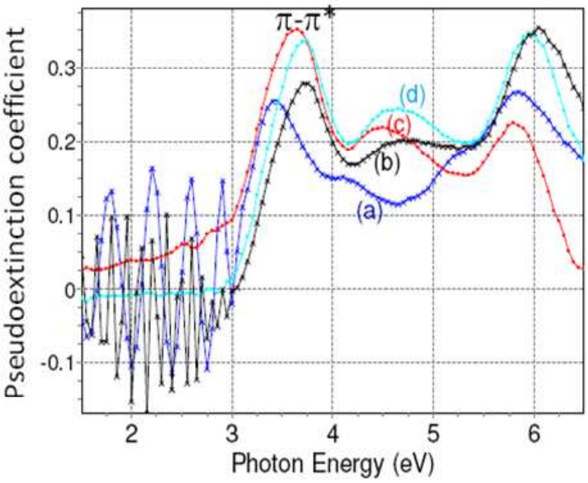

Figure 2. Experimental spectra of the pseudo extinction coefficient for MEH-PPDFV films deposited on (a) plasma treated ITO, (b) as received commercial ITO, (c) quartz, and (d) glass substrates.

In Fig. 3 typical experimental SE spectra at various angles of incidence for MEH-PPDFV film deposited on O_2 plasma treated ITO substrate are shown. A simple two-layer model (presented in the same figure), including film and surface roughness, was considered in the analysis. The surface roughness was modelled using a mixture of 50% of polymer and 50% of voids dielectric functions. The films were uniaxial anisotropic and two set of four oscillators were used to describe in-plane and out-plane optical constants.

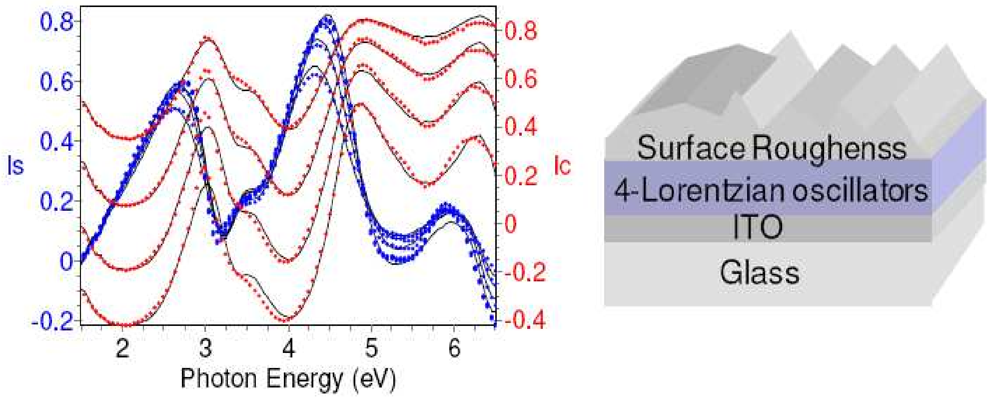

Figure 3. Typical ellipsometric spectra of Is=sin2Ψsin∆ and Ic=sin2Ψcos∆ (Ψ, ∆ are the measured ellipsometric angles) at various incidence angle in the range 55°-70° for 80 nm thick MEH-PPDFV film deposited on ITO substrate treated by O_2 plasma. Dots are the experimental points and black lines are the fit results according to the model sketched on the right.

Fig. 4 shows the anisotropic optical constants for typical films deposited on O_2 plasma treated ITO and on glass. The π- π*, II and IV transitions are strongly polarized along polymer chain, while the band III has a substantial strength perpendicularly to the chain direction. It is also observed that bands I and IV have a weak perpendicular contribution, some of which comes form the vinyl groups and some form the order of the film.

The main π- π* transition is slightly red-shifted for films deposited on glass, consistently with aggregation in grains, as also demonstrated by AFM images in Fig. 1. Furthermore, from Fig. 4 it can be inferred a larger anisotropy (measured by the ration between the amplitude of the π- π* transition in-plane and out-of-plane), consistently with the better structural order of the film deposited on O_2 plasma treated ITO substrate.

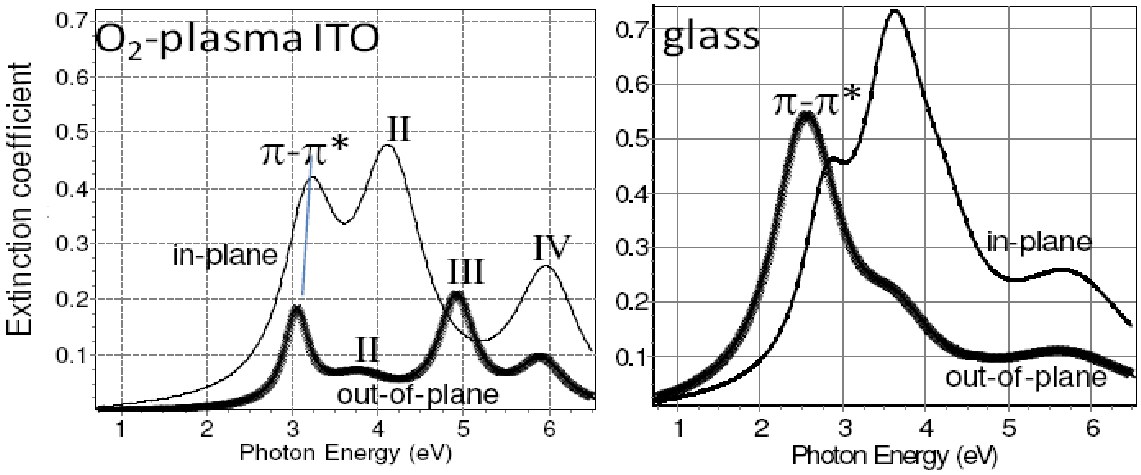

Figure 4. Spectra of the in-plane and out-of-plane extinction coefficient derived for MEH-PPDVF films deposited on O_2 plasma treated ITO and on glass substrates.

Devices have been fabricated using the structure sketched in Fig. 5. In the same Fig. 5 EL and PL spectra, recorded under identical experimental conditions, of devices including 80 nm thick films of MEH-PPV and of its fluorinated analogous MEH-PDDFV are reported. MEH-PPDFV polymeric film shows strong PL at room temperature with a maximum at 27.1 eV (458 nm). Furthermore, the MEH-PDDFV PL λ_{max} is also blue-shifted of about 110 nm relative to that of respective un-fluorinated polymer (MEH-PPV). The EL spectra of MEH-PDDFV and MEH-PPV exhibit the maximum of peaks at 2.46 (504 nm) and 1.98 eV (625 nm), respectively, which correspond to blue-greenish and red light, showing a blue-shift of 120 nm for the fluorinated polymer. Indeed, the blue-greenish electroluminescence of the fluorinated MEH-PPDFV has been found to be stable after hours of operation.

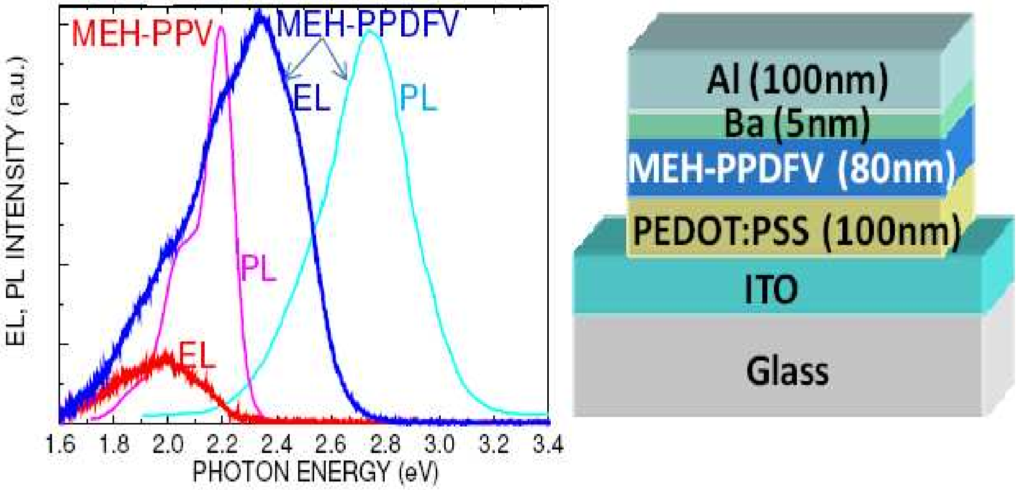

Figure 5. Room temperature PL spectra of 80 nm thick drop casted MEH-PPV (magenta line) and MEH-PPDFV (cyan line) films. The corresponding EL spectra of MEH-PPV (red line) and MEH-PPDFV (blue line), measured in the device configuration reported on the right, are also shown. EL spectra of the two polymers are in the same scale to make a relative comparison of intensities.

Conclusions

Exploiting ellipsometry, AFM, PL and EL, it has been demonstrated that MEH-PPDFV represents a valuable way to blue-shift the optical absorption and emission of conjugated polymeric thin films. Specifically, MEH-PPDFV film show blue-shifted π- π* transition at 3.74 eV (331 nm), and blue PL at 2.71 eV (458 nm) in the solid state, which is blue-shifted of 200 nm with respect to the non-fluorinated MEH-PPV polymer. MEH-PPDFV films have also a stable blue-greenish EL at 2.46 eV (504 nm), which is also blue shifted from that at 1.98 eV of the analogous hydrogenated MEH-PPV polymer. Furthermore, it has been demonstrated that π- π*transition as well as of all other optical transitions and properties are affected by electronic structural changes associated with changes in the self-organization in the solid state.

Acknowledments

This work was supported by Ministero dell'Università e della Ricerca (MIUR), project FIRB 2003 SYNERGY (Prot. N. RBNE03S7XZ), and by the University of Bari.
The 7FP Coordination Action "NanoCharM" (Multifunctional NanoMaterials Characterization exploiting Ellipsometry and Polarimetry) (NMP3-CA-2007-218570) is also acknowledged.
Authors are grateful to Mr Alberto Sacchetti at IMIP-CNR for the assistance in film preparation.

References

[1] S. Neyshatadt, M. Kalina and G.L. Frey: Adv. Mater. Vol. 1 (2008), p. 9999.

[2] H. Plank, R. Guntner, U. Scherf and E.J.W. List: Adv. Funct. Mater Vol. 17 (2007), p. 1093.

[3] G. Grem, G. Leditzky, B. Ullrich and G. Leising: Adv. Mater. Vol. 4 (1992), p. 36.

[4] U. Scherf and E.J.W. List: Adv. Mater. Vol. 14 (2007), p. 477.

[5] X.H. Yang, F. Jaiser, D. Neher, P.V. Lawson, J.L. Bredas, E. Zojer, R. Guntner, P. Scanduicci de Freitas, M. Forster and U. Scherf: Adv. Funct. Mater. Vol. 14 (2004), p. 1097.

[6] F. Babudri, G.M. Farinola, F. Naso and R. Ragni: Chem. Comm. Vol. 1005 (2007), p. 1003.

[7] M. Losurdo, M.M. Giangregorio, P. Capezzuto, G. Bruno, F. Babudri, D. Colangiuli, G.M. Farinola, F. Naso and M. Buchel: Polymer Vol. 49 (2008), p. 4133.

[8] Y. Jin, J. Lee, K. Kim, J. Kim, S. Song, S.H. Park, K. lee and H. Suh: Polymer Vol.48 (2007), p. 1541.

[9] M. Losurdo, M.M. Giangregorio, P. Capezzuto, G. Bruno, F. babudri, D. Colangiuli, G.M. Farinola and F. Naso: Macromolecules Vol. 36 (2003), p. 4492.

[10] C.R. Ramsdale and N.C. Greenham, Adv. Mat. Vol. 14 (2002), p. 212.

[11] F. Babudri, A. Cardone, G.M. Farinola, C. Martinelli, R. Mendichi, F. Naso and m. Striccoli: Eu. J. Org. Chem. (2008), p. 1977.

[12] M. Losurdo, G. Bruno and E.A. Irene: J. Appl. Phys. Vol. 94 (2003), p. 4923.

[13] N. Kirova, S. Brazovskii and A.R. Bishop: Synthetic Metals Vol. 100 (1999), p. 29.

[14] M. Losurdo, M.M. Giangregorio, P. Capezzuto, A. Cardone, C. Martinelli, G.M. Farinola, F. Babudri, F. Naso, M. Buchel and G. Bruno: Adv. Mater. Vol. 21 (2009), p. 1115.

[15] T. Kawai, Y. Maekawa and M. Kusabiraki: Surf. Sci. Vol. 601 (2007), p. 5276.

[16] J.S. Kim, R.H. Friend and F. Cacialli: J. Appl. Phys. Vol. 86 (1999), p. 2774.

[17] B. Janczuck and A. Zdziennicka: J. Mater. Sci. Vol. 29 (1994), p. 3559.

doi:10.4028/www.scientific.net/AST.75.124

Advanced real time metrology of AlGaN/GaN and InGaN/GaN epitaxy

Tong-Ho Kim[1,a] , Soojeong Choi,[1,b] April S. Brown[1],
Maria Losurdo,[2c] Giuseppe V. Bianco[2] Maria M. Giangregorio[2],
Giovanni Bruno[2]

[1] Department of Electrical and Computer Engineering, Duke University, 128 Hudson Hall, Durham, NC, USA

[2] Institute of Inorganic Methodologies and of Plasmas, IMIP-CNR, Bari, via Orabona, 4, 70126 Bari, Italy

[a]thkim@duke.edu, [b]maria.losurdo@ba.imip.cnr.it

Keywords: GaN; AlGaN; InGaN; Epitaxy; Spectroscopic ellipsometry.

Abstract. Nitride materials are critical for a range of applications, including UV-visible light emitting diodes (LEDs). Advancing the performance, reliability and synthesis of AlGaN/GaN and InGaN/GaN heterojunction devices requires a systematic methodology enabling characterization of key metric like alloy composition, thickness and quality possibly in real time.

This contribution reports on the real time characterization of the plasma assisted molecular beam epitaxy of AlGaN/GaN and InGaN/GaN heterostructures. Spectroscopic ellipsometry real time monitoring has revealed a number of key process and material iusses, such as the roughening of the GaN templates depending on plasma exposure during the substrate cleaning step, the composition of the alloy and the growth mode. Parameters like the plasma conditions, the surface temperature and the atomic flow ratio are investigated to understand the interplay process-material composition-structure-optical properties.

Introduction

III-Nitride materials are important for a range of applications, including blue UV-to-visible light-emitting diodes (LEDs) [1], laser diodes (LDs) [2], ultraviolet photodetectors [3], as well as microwave and millimeter wave electronics [4,5]. The peculiarity of these materials is that they are grown epitaxially on substrates with lattice and thermal mismatch, requiring a multi-step approach including substrate pre-treatments, nucleation and epitaxial growth. Lattice-matched substrate development remains a key barrier to advances in the technology; however, intermediate technologies to high quality, large area bulk substrates exist, such as the GaN "template" substrate that consists of GaN grown by halide vapor phase epitaxy (HVPE) or metalorganic vapor phase epitaxy (MOVPE) on sapphire. The study of growth on these surfaces is of fundamental importance, and will be a great benefit for applications and future synthesis exploiting these substrates.

Herein, we exploit *in-situ* spectroscopic ellipsometry (SE) to better understand GaN, AlGaN and InGaN epitaxy on GaN template substrates. Our primary motivation is to develop and exploit a range of important measurements achievable with spectroscopic ellipsometry. SE is used for *in situ* real time monitoring of all the critical steps involved in the GaN growth process, from the substrate preparation to the epitaxial growth [6]. Our demonstration shows that the GaN template surface can be optimized for overgrowth by understanding the interplay of substrate cleaning (removal of the oxide overlayer and contaminants) and GaN surface decomposition arising from high temperature exposure. In addition, we use SE for controlling and assessing material quality and film thickness, as well as the growth kinetics and growth mode.

(b) S.Choi present address: Materials Department, University of California. Santa Barbara, CA 93106

Finally, we show the efficacy of the *in situ* determination of alloys composition and its characterization being of critical importance to device structure synthesis.

The explored III-nitride materials optical properties, such as the fundamental exciton transition, the dielectric function, refractive index, and extinction coefficient are determined.

Experimental

Epitaxial GaN, AlGaN and InGaN are grown on commercial GaN templates (4-5 μm thickness grown on c-axis sapphire by HVPE) by using an r.f. (13.56 MHz) plasma-assisted molecular beam epitaxy (VEECO) Gen II system equipped with an in situ phase modulated spectroscopic ellipsometer (UVISEL-Horiba-JY).

The following growth sequence was applied. Following solvent degreasing, the template was etched in sulphuric acid (H_2SO_4:H_2O = 4:1) for 10min. After coating titanium of 1.2 μm thickness on the substrate backside, the substrate was loaded and degassed at 500°C for 1hr in a buffer chamber. In order to remove the native oxide prior to starting growth, the substrate was annealed at 710°C for 10 min in the growth chamber without plasma operation. The GaN growth was performed at temperatures of 710-780°C with, while temperatures of 600-650°C and T=730°C were adopted for InGaN and AlGaN, respectively, varying Ga/N flux ratio under a constant nitrogen plasma condition (rf power of 350W and nitrogen flow rate of 0.5sccm),

Spectroscopic ellipsometry (SE) was exploited for the real time monitoring of the growth process. Ellipsometry measures the ratio, ρ, of the Fresnel reflection coefficient of the p-polarized (parallel to the plane of incidence of the linearly polarized light beam) and s-polarized (perpendicular to the plane of incidence) light reflected from the surface through the ellipsometric angles Ψ and Δ defined by the equation:

$$\rho = \tan\Psi \exp(i\Delta)$$

where $\tan\Psi = |Ep| / |Es|$ and $\Delta = \delta p - \delta s$ represent the amplitude and phase variation of the electric field vector associated with the light electromagnetic wave. ρ and, hence, Ψ and Δ, are related to the film pseudodielectric function, $\langle\varepsilon\rangle = \langle\varepsilon_1\rangle + i\langle\varepsilon_2\rangle = \langle N^2\rangle = (n+ik)^2$ (where n is the refractive index and k is the extinction coefficient) through the equation

$$\langle\varepsilon\rangle = \sin^2\phi[1+\tan^2\phi\,(1-\rho)^2/(1+\rho)^2]$$

where ϕ is the angle of incidence [7]. For the present *in situ* real time measurement, the ellipsometer is assembled on the MBE reactor with ϕ=70.68°, using strain-free windows. Real-time ellipsometric data were acquired with a time resolution of 1 sec and reported as spectra of the pseudodielectric function <ε> as a function of time.

Results and discussion

GaN surface preparation for GaN homoepitaxy

The thermal removal process of the native oxide from the GaN template surface, before the initiation of growth, is a critical step in the III-nitride materials growth, since it competes with thermal roughening when the substrate is heated up to 700°C. SE is sensitive to removal of contaminant and native oxide from the substrate surfaces, through measurement of the residual absorption in the GaN dielectric function; the properties of the substrate and surface were monitored through the variation of the GaN dielectric function prior to the initiation of growth. The pseudodieletric function at energy higher than the GaN band gap is sensitive to modification at atomic scale. Specifically, Figure 1(a) demonstrates surface roughening causing a decrease in <ε_1> and an increase in <ε_2> of GaN spectra. Thus, the time variation of the GaN pseudodielectric function allows us determining the surface roughening rate and its dependence on the process conditions. Figure 1(b) shows the time derivatives of the pseudodielectric functions, d<ε_2>/dt, of two GaN template substrates with different GaN layer thickness. Above 800°C, we clearly see the relatively abrupt onset of significant roughening regime which should be avoided prior to growth. This is also confirmed by the atomic force microscopy images (see Fig. 2) showing the initial GaN surface and the roughening induced at temperatures above 800°C. Thus SE significantly improves our ability to characterize the surface and understand the origin of surface roughening.

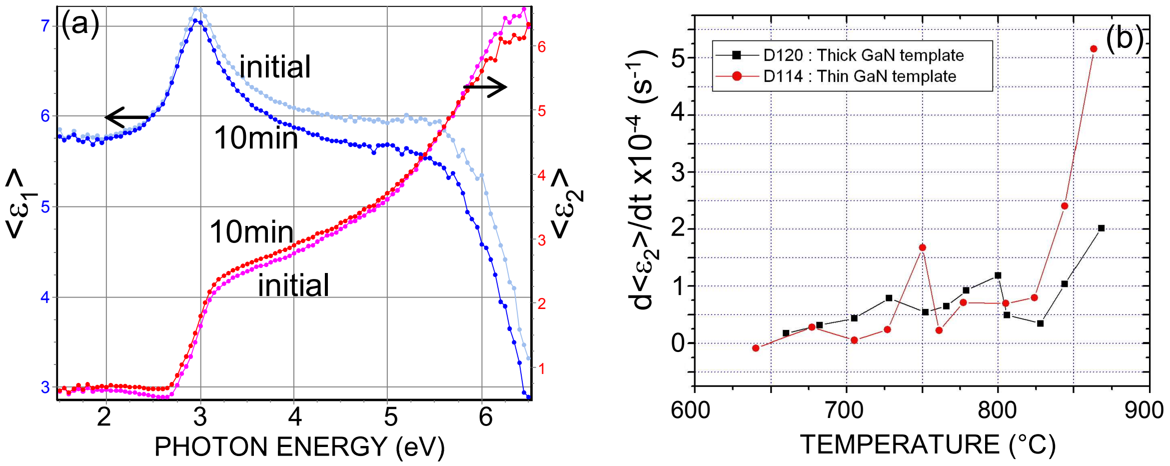

Figure 1. (a) SE spectra of the real, <ε_1>, and imaginary, <ε_2>, parts of the GaN template pseudodielectric function before and after 10min at T=850°C; (b) Derivatives of the imaginary part of pseudodielectric functions of two GaN template substrates with different GaN layer thickness versus substrate temperature (measured at the photon energy of 4eV).

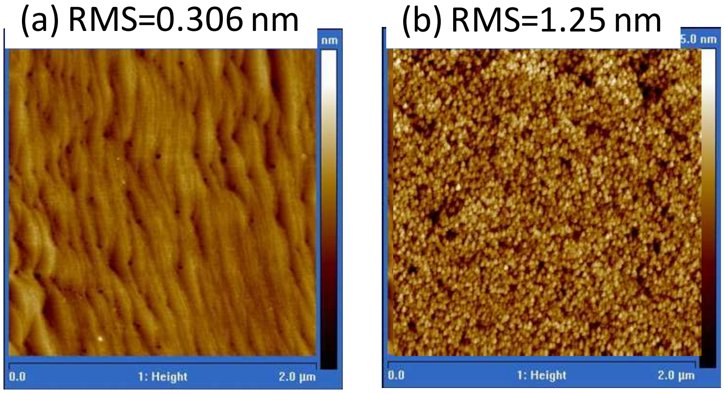
(a) RMS=0.306 nm
(b) RMS=1.25 nm

Figure 2. 2µmx2µm AFM images of (a) GaN template and (b) after cleaning treatments at temperatures above 800°C

GaN homoepitaxy: growth and characterization of film quality

SE results a sensitive tool to determining appropriate growth experimental conditions and in assessing growth reproducibility. In situ monitoring of the real or the imaginary part of the pseudodielectric function allows growth regime being controlled.

A 0.23µm thick GaN film was overgrown on the HVPE GaN template at 710°C under Ga droplet boundary conditions. The quality of the homoepitaxial layer can be assessed by the analysis of the ellipsometric spectra. Figure 3 shows the in situ SE spectra of MBE grown GaN epitaxial layer and of the GaN template and the corresponding AFM images. The improvement of the GaN homoepitaxial layer with respect to the GaN template can be read in the higher amplitude of the $<\varepsilon_1>$ spectrum, in the lower amplitude of the $<\varepsilon_2>$ spectrum and in the narrower and higher excitonic peak at 3.43eV. Similar RMS AFM surface roughness values (≈0.3nm) were found for the GaN template and the GaN epitaxial layer.

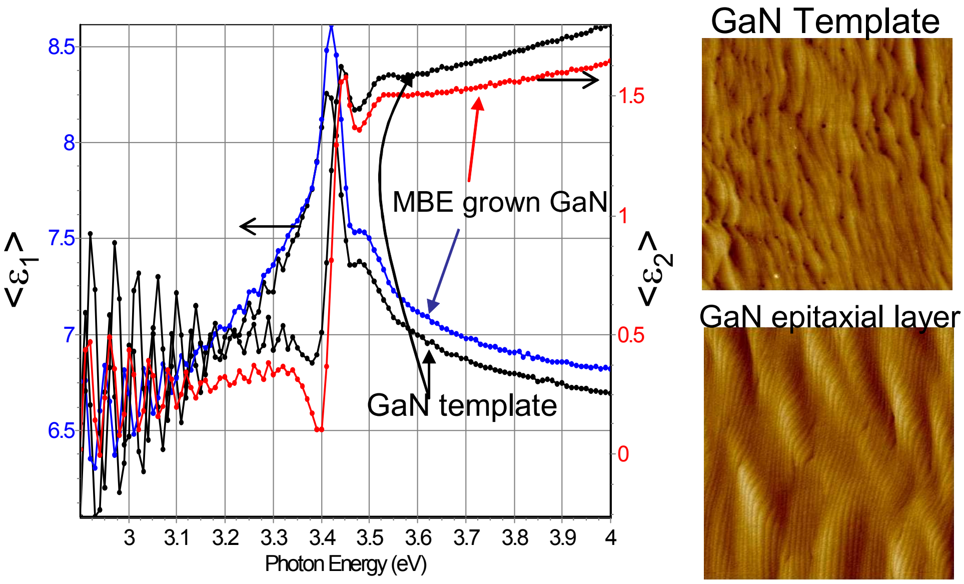

Figure 3. Ellipsometry spectra of the refractive index and extinction coefficient of the GaN template and of the GaN homopitaxial layer overgrown at 710°C under Ga droplet boundary conditions. Sample AFM images, before and after the GaN growth, are also reported in the figure.

AlGaN growth and characterization

Figure 4 shows a typical real time trajectory in the Ψ-Δ ellipsometric plane at a photon energy of 4eV (which is below the bandgap of AlGaN where both materials are expected to be transparent). The shape and position are related to refractive index and absorption coefficient of the GaN layer. The closed and cyclical loop indicates that the growing AlGaN is transparent and homogeneous in composition. Variation of stoichiometry and, hence, of the refractive index, residual absorption because of defects, and roughening of the growing layer would yield a variation and shift in the Ψ-Δ plane of the trajectory. This trajectory can be simulated by assuming a layer-by-layer growth mode for the $Al_xGa_{1-x}N$ layer. Furthermore, the position and amplitude in the Ψ-Δ plane depends on the refractive index of the growing $Al_xGa_{1-x}N$ and, hence, can be used to infer its stoichiometry.

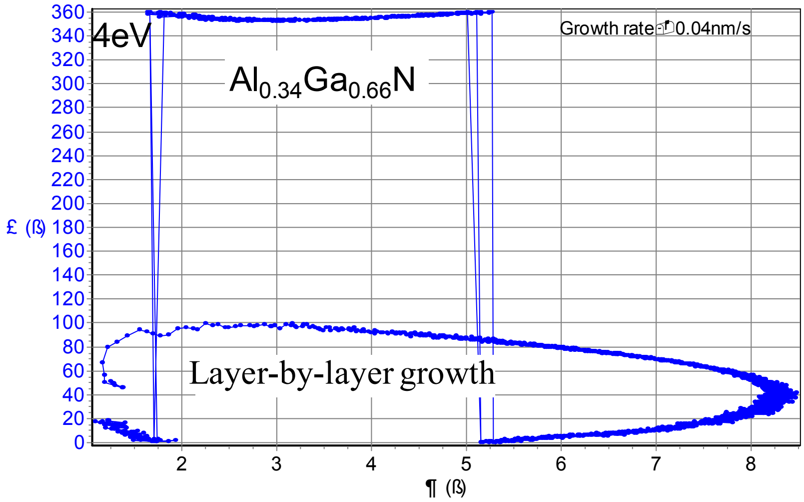

Figure 4. Real time trajectory in the Ψ-Δ plane at the photon energy of 4eV for AlGaN layer-by-layer growth at the substrate temperature of 730°C. The total AlGaN growth time is 2h.

Therefore, the trajectory can be used from run to run to check the reproducibility of growth under nominally identical conditions, as well as to monitor AlGaN properties.

Figure 5 shows the SE spectra of the refractive index and extinction coefficient for the GaN, AlN, and of a $Al_xGa_{1-x}N$ alloy grown on the GaN template by PA-MBE at 730°C. The major feature is the E_0 optical band gap (which is seen as a peak in the real part of the pseudodielectric function and as onset of the absorption in the spectrum of the imaginary part), which shifts from that of GaN to higher energies towards that of AlN depending on $Al_xGa_{1-x}N$ stoichiometry. This peculiarity can be used for monitoring multilayer structure for HFET applications: an initial corroboration of SE spectra with SIMS measurements for the exact determination of the layer compositions allows in situ real time determination of Al compositions from the analysis of the position of the E_0.

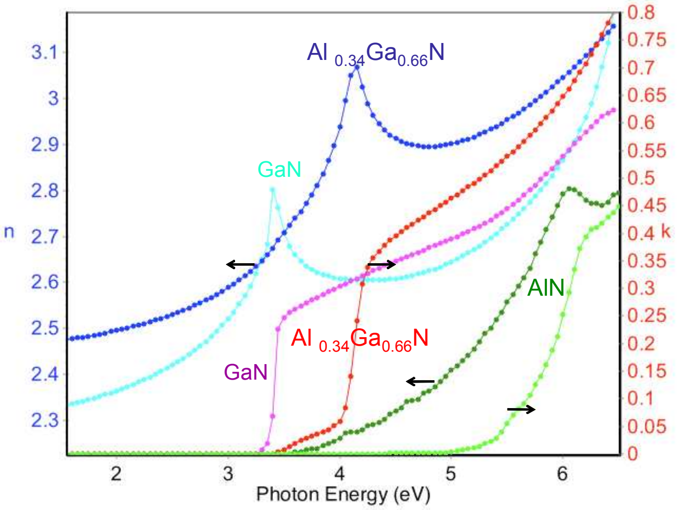

Figure 5. Ellipsometry spectra of the refractive index and the extinction coefficient of AlN, GaN and of an $Al_xGa_{1-x}N$ alloy grown on the GaN template by PA-MBE at 730°C. The stoichiometry of the alloy, determined from the analysis of the position of the E_0, is reported.

InGaN growth and characterization

Figures 6a and 6b show the spectra of the real and imaginary part of the pseudielectric function of 50 nm thick $In_xGa_{1-x}N$ layers grown on GaN template with different Ga and In flux ratio. The real part of the pseudodielectric function, $<\varepsilon_1>$, exhibits a clear maximum at the fundamental gap energy of the $In_xGa_{1-x}N$, and as onset of the absorption in the spectrum of the imaginary part, $<\varepsilon_2>$, which allows a determination of the In content via the composition dependence of that gap energy.. Two distinct bandgap energies can be clearly seen which are due to the different In composition of x=0.15 and x=0.26. The higher the indium amount, the lower value of the E_0. Another major feature of the spectra consists on the band gap of the GaN template at 3.43eV.

For evaluating appropriately the band gap as a function of the Indium content, the bowing parameter, b, should be duly considered, being the bandgap energy E_0 as a function of composition represented by

$$E_0(x) = xE_0(\mathrm{InN}) + (1-x)E_0(\mathrm{GaN}) - bx(1-x)$$

A critical discussion on the bowing parameter b for InGaN and on the band gap dependence on composition can be found in ref. [8].

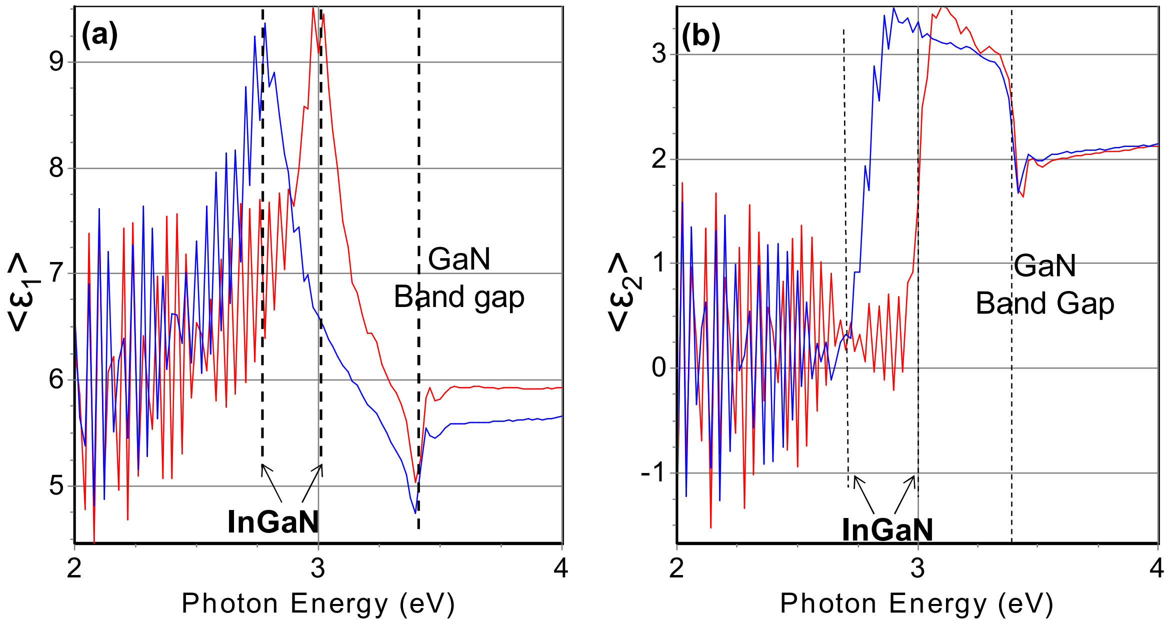

Figure 6. Spectra of the real (a) and imaginary part (b) of the pseudielectric function of InGaN alloys grown on GaN template with different Ga and In flux ratio.

Conclusions

We have explored the use of real time, in situ spectroscopic ellipsometry for monitoring the growth and material properties of GaN, AlGaN and InGaN on GaN template. In order to optimize the GaN template surface for overgrowth, we have shown that ellipsometry can detect the rate of thermal roughening that could occur during removal of the native oxide before the initiation of GaN growth. Second we have studied and controlled the III-Nitride materials growth by in situ real time SE monitoring. Finally, we have exploited ellipsometry for the in situ determination of ternary alloy composition and on the relative optical properties depending on various growth parameters.

References

[1] J. M. Moison, C. Guille, and M. Bensoussan: Phys. Rev. Lett., Vol. 58 (1997), 2555.

[2] S. Nakamura, M. Senoh, S. Nagahama, N. Iwasa, T. Yamada, T. Matsushita, H. Kiyoku and Y. Sugimoto: Jpn. J. Appl. Phys., Vol. 35 (1996), L74.

[3] J.L. Pau, C. Rivera, E. Muñoz, E. Calleja, U. Schülle, E. Frayssinet, B. Beaumont, : Journal of Applied Physics, Vol. 95 (2004), 8275-8279.

[4] P. Waltereit, O. Brandt, A. Trampert, M. Ramsteiner, M. Reiche, M. Qi, K.H. Ploog, Appl. Phys. Lett., Vol. 74 (1999), 3660.

[5] K. Jeganathan, M. Shimizu, H. Okumura, S. Nishizawa, F. Hirose, Surf. Sci., Vol. 527 (2003), L197.

[6] G. Bruno, M. Losurdo, M. M. Giangregorio, P. Capezzuto, A. S. Brown, Tong-Ho Kim, Soojeong Choi, Applied Surface Science, Vol. 253 (2006), 219–223.

[7] H.G. Tompkins, E.A. Irene, in “Handbook of Ellipsometry”, William Andrei Publishing, NY (2004).

[8] P. Schley, R. Goldhahn,* A. T. Winzer, G. Gobsch, V. Cimalla, O. Ambacher, H. Lu, W. J. Schaff, M. Kurouchi, Y. Nanishi, M. Rakel, C. Cobet, N. Esser, Phys. Rev. B **75**, 205204 (2007)

© (2010) Trans Tech Publications, Switzerland
doi:10.4028/www.scientific.net/AST.75.130

Interface and surface modification of ZnO induced by hydrogen and nitrogen and their impact on optical properties

Maria M.Giangregorio[1, a], Giuseppe V.Bianco[1] Alberto Sacchetti[1] ,
Pio Capezzuto[1], Maria Losurdo[1b], and GiovanniBruno[1c]

[1]IMIP-CNR University of Bari, Italy

[a]michelaria.giangregorio@ba.imip.cnr.it, [b]maria.losurdo@ba.imip.cnr.it,
[c]giovanni.bruno@ba.imip.cnr.ir

Keywords: ZnO; Atomic hydrogen; atomic nitrogen; polarity, temperature

Abstract. In this contribution, we address two critical and interesting aspects from both fundamental and technological point of views, which are the polarity of ZnO and the interface reactivity and stability to hydrogen and nitrogen. The effects of atomic hydrogen and nitrogen produced by radiofrequency (r.f. ,13.56 MHz) H_2 and N_2 plasmas and of temperature on the optical, compositional and structural properties of Zn- and O-polar ZnO have been studied. It is found that Zn-polar ZnO is highly reactive with atomic hydrogen while O-polar ZnO is almost inert. Conversely, both polarities react with nitrogen, with the O-polar ZnO showing a larger reactivity toward N-atoms than the Zn-polarity.

1. Introduction

ZnO is a direct wide band gap (Eg = 3.37 eV) semiconductor that, in its various forms including epitaxial layers, polycrystalline thin films and nanostructures, is attracting interest to its high photocatalytic activity, excellent chemical andmechanical stability, for potential applications in optoelectronic devices [1] such as short wavelength lasers and light-emitting diodes (LEDs), due to its strong excitonic feature (exciton binding energy of 60 meV) and lasing properties, even at room temperature, and for piezoelectric transducers, sensors and transparent conducting electrodes.

For all the applications, it is of interest to study the interaction of ZnO with atomic hydrogen and nitrogen. Atomic hydrogen improves ZnO conductivity, passivates the green emission enhancing the band edge luminescence [2] and modifies the ZnO catalytic activity and adsorption of gases [3]. Nitrogen has been has been used as dopant in one of the first ZnO homojunction diode devices [4], although a recent study has reported that nitrogen cannot lead to p-type doping in ZnO [5]. Atomic nitrogen can interact with ZnO during the epitaxial growth of III-nitrides, e.g. GaN, InGaN, AlGaN, on ZnO substrates to produce white light emitting devices (LEDs) [6]. Understanding the modification of ZnO by nitrogen is helpful to control the interface reactivity in ZnO/nitrides, which affects the light emission properties of LEDs.

The interaction of ZnO with atomic hydrogen and nitrogen depends on the ZnO polarity and on temperature [7]. It is well known that the Zn-polar and O-polar faces of ZnO are structurally and chemically different [8], and it has been reported that optical [9] and electrical properties [10], thermal stability [11], impurity incorporation, doping efficiency [12] and the adsorption and reactivity of gases are influenced by polarity.

This contribution presents a study of the optical, chemical and structural modifications of Zn- and O-polar ZnO single crystals upon interaction with atomic hydrogen and nitrogen produced by remote radiofrequency (r.f. 13.56 MHz) plasmas of H_2 and N_2, respectively. It is shown that the reactivity and consequent ZnO modifications strongly depend on the polarity and on temperature. The Zn-polar surface results more reactive toward atomic hydrogen, while O-polar ZnO is almost inert. Conversely, both polarities react with nitrogen, with the O-polar ZnO showing a larger reactivity toward N-atoms than the Zn-polarity.

The impact of hydrogen and nitrogen remote plasma processing at different temperatures from room temperature (RT) to 600°C on chemical, morphological and optical properties of Zn- and O-polar ZnO is also discussed.

2. Experimental

O-polar *(*000-1*)* and Zn-polar (0001) ZnO *n*-type crystals (provided by CERMET Inc.) were used for this study. The polar crystals of ZnO were exposed to atomic hydrogen and nitrogen produced, respectively, by remote H_2 and N_2 r.f. 13.56 (MHz) plasma sources [7]. The H_2 plasma was operated at 60W, 1 Torr and 800 sccm of H_2, while the N_2 plasma was operated at 140 W, 0.2 Torr and 100 sccm of N_2. Exposures of the ZnO surface to atomic hydrogen and nitrogen were performed at different temperatures from RT to 600°C.

Spectroscopic ellipsometric (SE) spectra of the pseudodielectric function, $<\varepsilon> = <\varepsilon_1> + i<\varepsilon_2>$, were acquired from 0.75 to 6.5 eV (UVISEL-Jobin-Yvon) [13] before and after exposure of the ZnO surfaces to atomic hydrogen and nitrogen. Variation of the pseudodielectric function was monitored in real time at the photon energy of the excitonic transition, 3eV, during the atomic hydrogen treatment to monitor the ZnO surface modifications.

Ex-situ x-ray photoelectron spectroscopy (XPS) analysis was performed using a Mg Kα source to evaluate the surface chemical state upon the hydrogen and nitrogen treatment.

The surface morphologies of ZnO films were examined by atomic force microscopy (AFM) (Autopre CP-VEECO) in intermittent contact mode.

3. Results and Discussion

3.1 Optical modification by Ellipsometry

Figure 1 shows the real, $<\varepsilon_1>$, and imaginary, $<\varepsilon_2>$, parts of the pseudodielectric function, recorded at room temperature, before and after exposure to atomic hydrogen and nitrogen of the (a) O- and (b) Zn-polar ZnO single crystals. The excitonic transition dominates the spectra at approximately 3.4 eV.

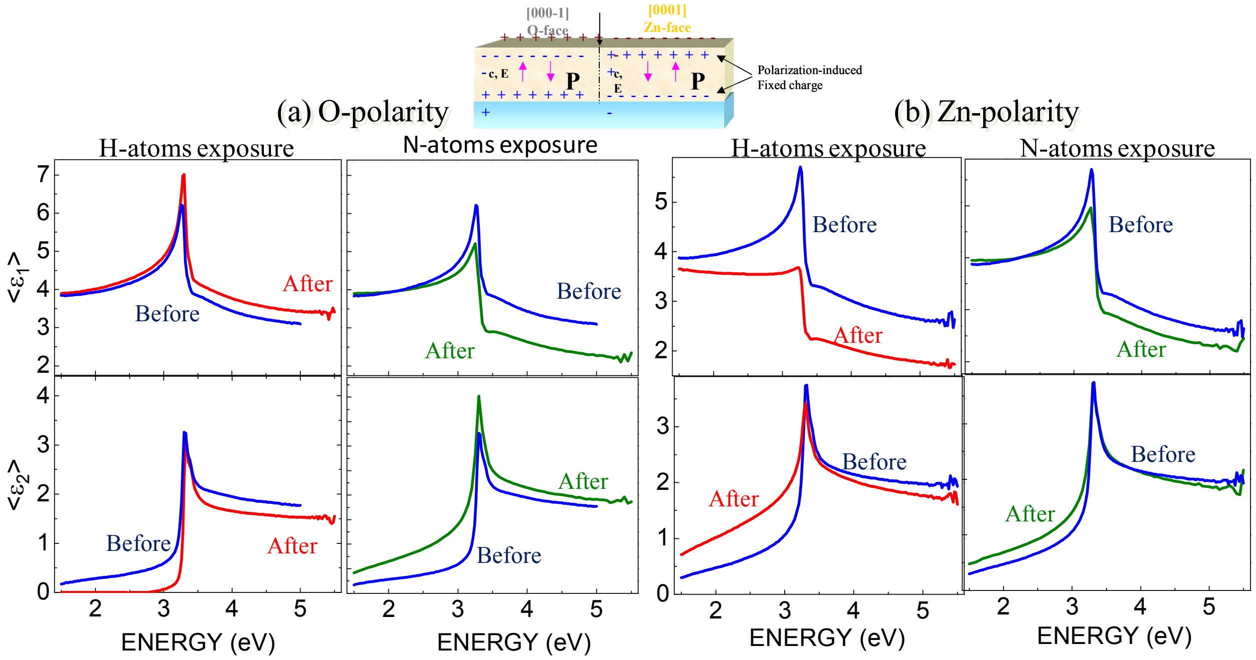

Figure 1: Real, $<\varepsilon_1>$, and imaginary, $<\varepsilon_2>$, parts of the pseudodielectric function recorded before (blue line) and after exposure to atomic hydrogen (red line) and nitrogen (green line) of the (a) O- and (b) Zn-polar ZnO crystal.

A different reactivity to atomic hydrogen and nitrogen can be read in Fig. 1. In particular, after exposure to atomic hydrogen, the strong decrease of <ε_1>, and the increase of <ε_2>, i.e., an increase of the ZnO absorption, in the region below the 3.4 eV gap of ZnO, indicate damage of the ZnO surface for the Zn polar ZnO (0001) crystal. Conversely, smaller changes and reactivity are seen for the O polar ZnO *(*000-1*)* crystal; in this case the small increase of <ε_1> and the decrease of <ε_2> can be explained by cleaning of the O-polar ZnO surface. In fact, the best ZnO surface is that with maximized <ε_1> and minimized <ε_2>.

After exposure to atomic nitrogen, <ε_1> decreases while <ε_2> increases for both the Zn- and O-polar ZnO. Larger variations in <ε_1> and <ε_2> are observed in the SE spectra of the O-polar ZnO than the Zn-polar ZnO. This observation indicates that both polarities react with atomic nitrogen, being the O-polar although through different chemical reactions giving reason of the larger reactivity suspected for the O-poalr ZnO.

Figure 2 shows the kinetic profiles of the <ε_2> variation acquired at 3eV during exposure to (a) atomic hydrogen and (b) atomic nitrogen of Zn- and O-polar ZnO at different temperatures. The kinetic profiles show that the ZnO reactivity depends on the temperature as well. In particular, during the exposure to atomic hydrogen, the higher the temperature, the larger the modifications of the Zn-polar ZnO. Conversely, the flat profiles measured for the O-polar ZnO at room temperature, 200°C and 300°C are evidence of absence of reactivity to hydrogen atoms. And the interaction of O-polar ZnO with hydrogen atoms is not thermally activated since no changes were observed increasing the temperature up to 400°C.

During exposure to atomic nitrogen, both the Zn- and O-polar ZnO reactivity increases with temperature, indicating a thermal activated process for both polarities.

(a) H-atoms exposure

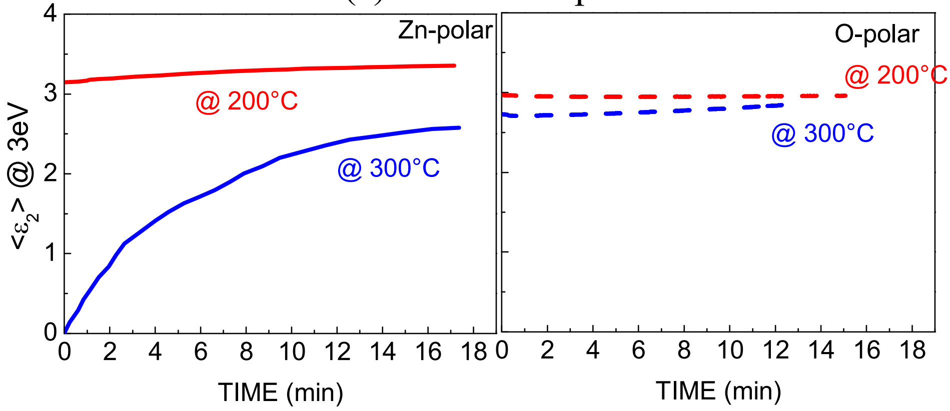

(b) N-atoms exposure

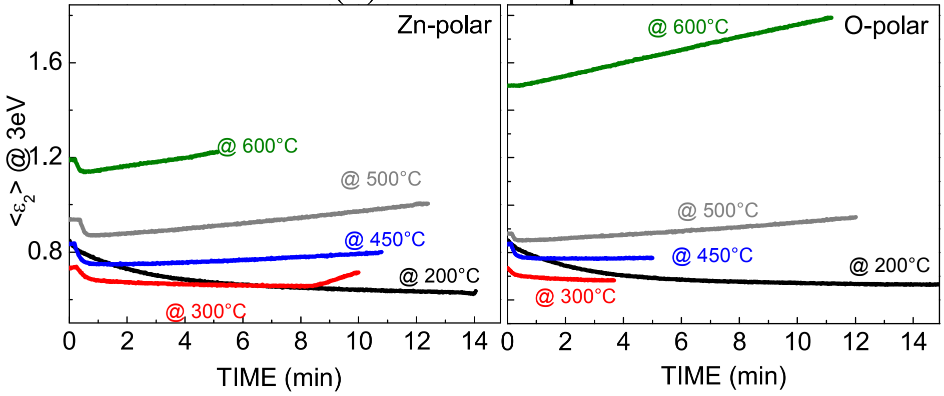

Figure 2: Kinetic profiles of the imaginary, <ε_2>, part of the pseudodielectric function acquired at 3eV during exposure at different temperatures to (a) atomic hydrogen and (b) nitrogen of Zn- and O-polar ZnO.

3.2 Chemical modifications by XPS

Figure 3 shows typical high-resolution XPS N1s and Zn2p photoelectron spectra of the Zn- and O-polar after exposure to atomic nitrogen. A detailed fit analysis shows intermixing with formation of Zn-N and N-O bonds. While Zn_3N_2 is the main component for the Zn-polar ZnO, a larger contribution of NO characterizes the O-polar ZnO.

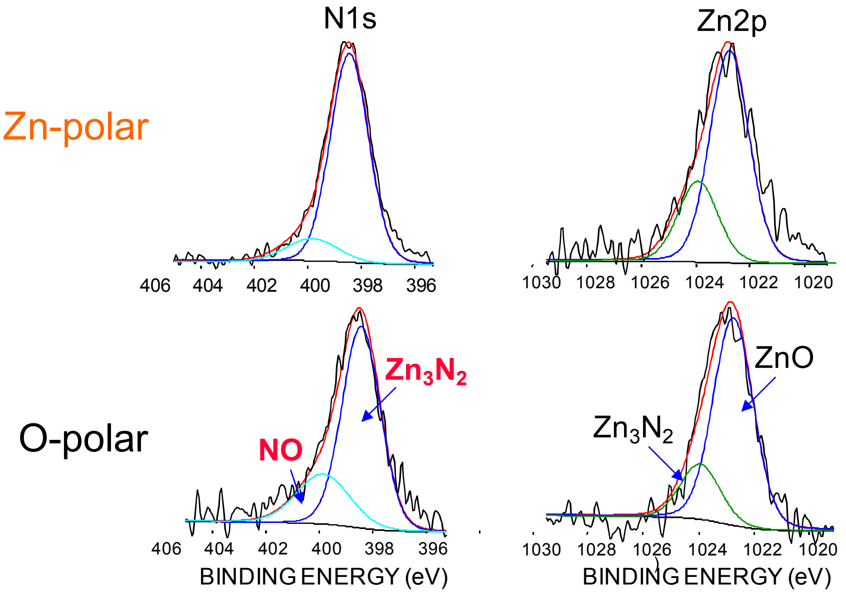

Figure 3: XPS spectra of the N1s and Zn2p peaks for the Zn-polar and O-polar ZnO after exposure to nitrogen-atoms.

3.3 Morphological modification by AFM

The different reactivity observed by SE and XPS is also corroborated by AFM measurements. Figure 4 shows 5μm×5μm AFM images before and after exposure to atomic hydrogen and nitrogen of the (a) Zn- and (b) O-polar ZnO single crystals.

(a) Zn-polar

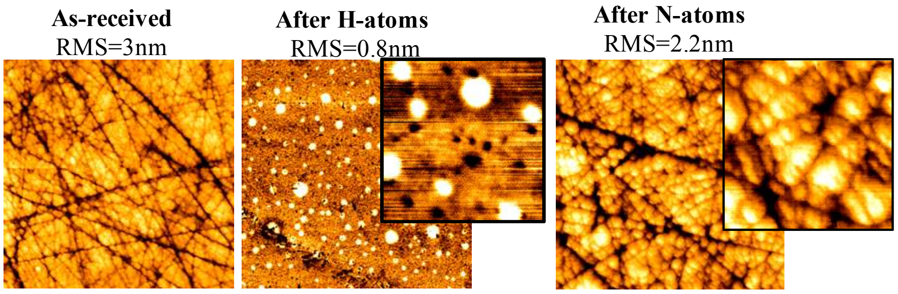

(b) O-polar

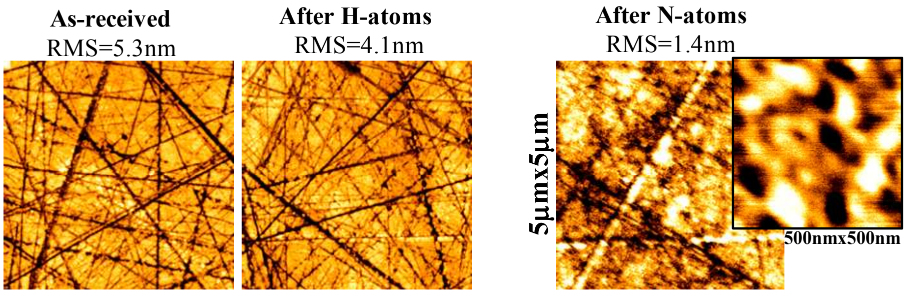

Figure 4: 5μm×5μm AFM images (the inset are 500nmx500nm) before and after exposure to atomic hydrogen and nitrogen of the (a) Zn- and (b) O-polar ZnO single crystals

Before any treatment the surfaces of the ZnO wafers showed on a large scale AFM scan *(*>5 μm*)* many scratches and pits. The morphology of the O-polar ZnO surface is almost unchanged after the atomic hydrogen exposure consistently with the absence of reactivity highlighted by the ellipsometry. In contrast, the morphology of the Zn-polar surface drastically changes upon interaction with atomic hydrogen and shows submicron pits and bumps/clusters that surface potential mapping of the surface has revealed to be chemically different from ZnO, being Zn metallic clusters.

Upon exposure to atomic nitrogen, the surface morphology of both the O-polar and Zn-polar ZnO changes, and although there is an overall decrease in the surface roughness (maybe just because of the scratches attenuation) a bumpy morphology appears. Those surface changes are consistent with the $<\varepsilon_1>$ and $<\varepsilon_2>$ variations observed by ellipsometry.

3.4 Chemical model

The different reactivity of the two polarities can be explained on the basis of the different polarizations and surface charges of the O- and Zn-polar crystals and the effect of the reaction product, O–H, on the stability of the crystal/surface. The surface charge, by changing the surface band bending and position of the surface Fermi level, changes the adsorptivity of the ZnO surface [15]. In relation to the adsorption of atomic hydrogen, which is known to act as a donor, it increases on a positively charge surface (Zn-polarity), while it decreases on a negatively charged surface (O-polarity).

Schematizing the reactivity as follows:

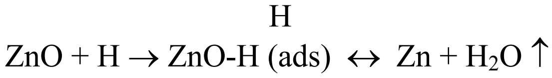

$$\mathrm{ZnO} + \mathrm{H} \rightarrow \overset{\mathrm{H}}{\mathrm{ZnO\text{-}H\ (ads)}} \leftrightarrow \mathrm{Zn} + \mathrm{H_2O}\uparrow \qquad (1)$$

(where –O-H simply denotes the reactive site, which can be for both the Zn-polar and O-polar surfaces), the last step with desorption of H_2O has a high activation energy and, hence, is inhibited for the O-polar ZnO because of the lower hydrogen chemisorption and also by the fact that −OH formation stabilizes the O-polar ZnO surface [14]. Conversely, the larger chemisorption of atomic hydrogen on the Zn-polar surface and the lower activation energy for H_2O desorption makes the Zn-polar ZnO(0001) surface highly unstable and for larger exposure to hydrogen it undergoes structural changes that destroy the lateral order of the ZnO crystal [16]. Therefore, hydrogen adsorbed on the Zn-polar surface is so reactive that it is capable of reducing bulk ZnO units to metallic Zn.

The reactivity to N-atoms of both Zn- and O-polar ZnO can be explained considering the nitrogen has been reported to be substitutional for oxygen, (NO), yielding simultaneous formation of N-O and Zn-N bonds as shown in the scheme below:

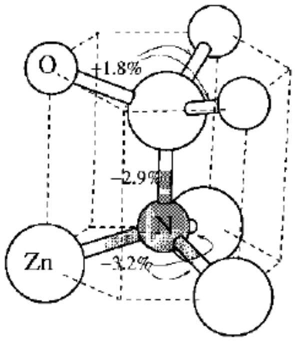

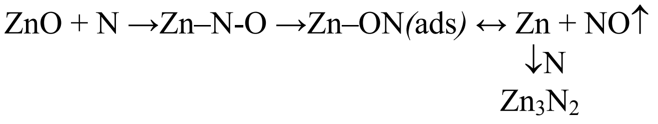

$$\begin{array}{ll} \mathrm{ZnO} + \mathrm{N} \rightarrow \mathrm{Zn{-}N{-}O} \rightarrow \mathrm{Zn{-}ON}(ads) \leftrightarrow & \mathrm{Zn} + \mathrm{NO}\uparrow \\ & \downarrow \mathrm{N} \\ & \mathrm{Zn_3N_2} \end{array}$$

which might also form volatile NO, leaving a modified surface rich in Zn-nitrides as detected by XPS.

4. Conclusion

We have investigated the interaction of O- and Zn-polar ZnO single crystals with atomic hydrogen and nitrogen produced by remote r.f. H_2 and N_2 plasmas, respectively. It is found that the Zn-polar form is highly reactive to atomic hydrogen, while the O-polar form is almost inert. In contrast, the atomic nitrogen reacts with both O- and Zn-polar ZnO, yielding modification of the morphological and optical properties. This reactivity should be duly considered in the technological process of growth of III-Nitrides on ZnO substrates for blue LEDs applications.

References

[1] S.F. Yu, Y. Clement, S.P. Lau and H.W. Lee: Appl. Phys. Lett. Vol. 84 (2004), p. 3244

[2] Y.M. Strzhemechny, J. Nemergut, P.E. Smith, J. Bae, D.C. Look and L.J. Brillson: J. Appl. Phys. Vol. 94 (2003), p. 4256

[3] B. Meyer and D. Marx: J. Phys. Condens. Matter Vol. 15 (2003), p. L89

[4] A. Tsukazaki, M. Kubota, A. Othomo, T. Onuma, K. Ohtani, H. Ohno, S. F. Chichibu, and M. Kawasaki: Jpn. J. Appl. Phys. Vol. 44 (2005), p. L643

[5] J.L. Lyons, A Janotti, C.G. Van de Walle, Appl. Phys. Lett. 95, 252105 (2009).

[6] J. Soohwan, J.J. Chen, F. Ren, H.S. Yang, S. Y. Han, D. P. Norton, S. J. Pearton, J. Vac. Sci. Technol. B 24, 690 (2006).

[7] G. Bruno, M. M. Giangregorio, G. Malandrino, P. Capezzuto, I. L. Fragala`, M. Losurdo, Adv. Mater. 21, 1700-1706 (2009).

[8] Y. Segawa, A. Ohtomo, M. Kawasaki, Z.K. Tang, P. Yu and G.K.L. Wong: Phys. Stat. Sol. B Vol. 202 (1997), p. 669

[9] V. Kirilyuk, A.R.A. Zauner, P.C.M. Christianen, J.L. Weyher, P.R. Hageman and P.K. Larsen: Appl. Phys. Lett. Vol. 76 (2000), p. 2355

[10] R. Dimitrov, M. Murphy, J. Smart, W. Schaff, J.R. Shealy, L.F. Eastman, O. Ambacher, M. Stutzman: J. Appl. Phys. Vol. 87 (2000), p. 3375

[11] C.J. Sun, P. Kung, A. Saxler, H. Ohsato, E. Bigan, M. Razeghi, D.K. Gaskill: J. Appl. Phys. Vol. 76 (1994), p. 236

[12] L.K. Li, M.J. Jurkovic, W.I. Wang, J.M. Van Hove,P.P. Chow: Appl. Phys. Lett. Vol. 76 (2000), p. 1740

[13] M. Losurdo, M. Bergmair, G. Bruno, D. Cattelan, C. Cobet, et al., J Nanopart Res 11, 1521-1554 (2009)

[14] T. Wolkenstein, Electronic Processes on Semiconductor Surfaces during Chemisorption, Consultant Bureau-Plenum Publishing Corporation, New York, 1991

[15] M. Kunat, S.G. Girol, T. Becker, U. Burghaus and C. Woll: Phys. Rev. B Vol. 66 (2002), p. 081402

[16] G. Kresse, O. Dulub and U. Diebold: Phys. Rev. B Vol. 68 (2003), p. 245409

doi:10.4028/www.scientific.net/AST.75.136

Iron pnictide thin film hybrid Josephson junctions

P. Seidel[1,a], F. Schmidl[1], V. Grosse[1], S. Döring[1], S. Schmidt[1], M. Kidszun[2], S. Haindl[2], I. Mönch[3], L. Schultz[2], and B. Holzapfel[2,b]

[1]Friedrich-Schiller-University Jena, Institute of Solid State Physics, Helmholtzweg 5, 07743 Jena, Germany

[2] IFW Dresden, Institute for Metallic Materials, Helmholtzstrasse 20, 01069 Dresden, Germany

[3] IFW Dresden, Institute for Integrative Nanosciences, Helmholtzstrasse 20, 01069 Dresden,Germany

[a]Paul.Seidel@uni-jena.de, [b]B.Holzapfel@ifw-dresden.de

Keywords: iron pnictides, thin films, tunneling junctions, Josephson junctions

Abstract. Thin films of iron pnictides open the way for fundamental experiments on superconductivity in this material. Thus we started to develop tunneling and Josephson junctions with pnictide film electrodes. Different preparation methods for Josephson junctions were investigated and the first results are presented. Resistive measurements show a high superconductive transition temperature of about 20 K even for the La-1111 electrode after patterning and preparation of the tunneling window. The hybrid junctions were completed with a PbIn counter electrode and normal conducting gold layers as barriers.

Introduction

The experimental investigation of the electronic properties of the iron-based superconductors (iron pnictides) is a helpful tool to investigate the nature of superconductivity in these materials. Tunneling and Josephson junctions offer ways to measure the energy gap and the symmetry of the order parameter as fundamental properties. If the symmetry of pairing differs from conventional s-wave, the behavior of these junctions will change. There exist some theoretical works comparing different types of symmetry and the resulting properties like density of states of the quasiparticles, Andreev bound state or the magnetic field dependence of Josephson current [1-9]. Some new experiments with tunneling and Josephson junctions to test the pairing symmetry were proposed, e.g. asymmetrical corner junctions [2], hybrid single or tri-junctions [4, 6, 8], measurements of the Riedel peak [7] or new corner-SQUIDs [9].

Status of iron pnictide Josephson junctions

The first observations of Josephson effects were reported for doped $BaFe_2As_2$ (122-phase). Zhang et al. [10] fabricated hybrid Josephson junctions with a conventional s-wave counter-electrode (lead) and $Ba_{1-x}K_xFe_2As_2$ single crystals (T_c about 20 K) in c-direction. The Pb electrode was used in two geometries, point contact tip and planar thin film of PbIn, respectively. They reported rather conventional Josephson behavior which seems to rule out d-wave or p-wave pairing symmetry. Another experiment on a hybrid junction was realized by Zhou et al. [11] where a $BaFe_{1.8}Co_{0.2}As_2$ single crystal (T_c=22K) was used. To test the order parameter symmetry a phase-sensitive corner junction coupling the a- and the b-direction via a conventional s-wave superconductor (Pb) was measured. The Fraunhofer-like pattern for the critical Josephson current on external magnetic field with a maximum at zero field suggests in that there is no phase shift between the a- and b-direction. This excludes d-wave symmetry in contrast to the cuprate superconductors. Meanwhile it was shown theoretically by Parker and Mazin [2] that for an

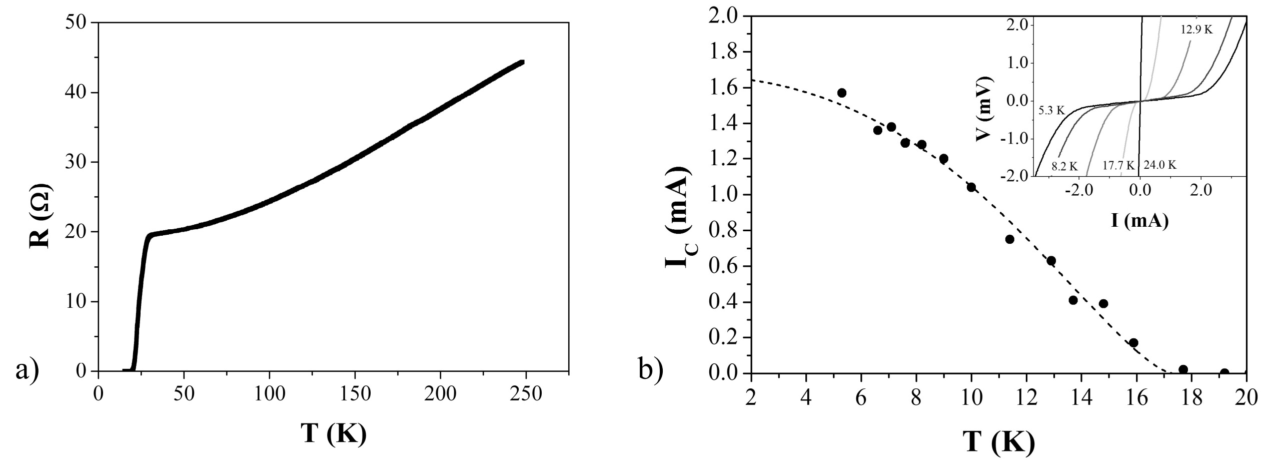

Fig.1 a) $R(T)$ and b) temperature dependence of the critical current of the patterned La-1111 base electrode with the dotted line representing a fit according to the Ginzburg-Landau theory. The inset in b) shows the I-V characteristics at different temperatures.

extended s-wave superconductor this simple corner junction geometry in general can not provide exact information on the symmetry.

Zhang et al. [12] just demonstrate an all pnictide Josephson junction produced by crossing two differently doped 122 single crystals. They observed RSJ-like I-V characteristics with I_cR_n of about 10 μV, Fraunhofer-like $I_c(H)$-pattern and Shapiro steps for 2.5 as well as 4 GHz. The first thin film Josephson junctions with Ba-122 were realized on (La,Sr)(Al,Ta)O_3 bicrystals by Katase et al. [13]. They observed RSJ-like I-V characteristics up to 17 K but I_cR_n of only 60 μV at 4 K with a quite linear temperature dependence and unusual $I_c(H)$-patterns.

Because corner junctions are hard to realize using $RO_{1-x}F_xFeAs$ (1111-phase) with R denoting La or a rare earth, Chen et al. [14] introduced a new symmetry test with controlled point contact junctions. A conventional s-wave superconductor (Nb) forms a loop. Both ends of this loop were formed as sharp tips and contacted a polycrystalline sample of $NdO_{0.88}F_{0.12}FeAs$ with a T_c of 43 K. The observation of flux and the persistent currents in the now closed loop was done by a pick-up coil of a standard DC-SQUID system. The SQUID signal shows the entry of single flux quanta. By changing the position of the contacts across the polycrystalline pnictide sample sometimes half-integer flux quantum jumps in time appear. This supports spin-singlet state of superconductivity in the Nd-1111 but also a sign change in the order parameter thus an extended s-wave symmetry.

Scanning SQUID microscopy of polycrystalline Nd-1111 samples with T_c of 48 K by Hicks et al. [15] did not show spontaneous currents resulting from π phase shifts thus excluding p- and d-wave orders but the resolution is not high enough to decide on extended s-wave or s+id symmetry.

For the 1111-material there exist first measurements of c-axis transport by Müller et al. [16]. They prepared mesa structures from single crystals and polycrystalline samples of $LaO_{0.9}F_{0.1}FeAs$ (La-1111) and observed I-V characteristics of overdamped Josephson junctions with I_cR_n products of about 10 μV. The Josephson current density was in the order of 10^5 A/cm^2 and temperature dependence of critical Josephson current follows the Ambegaokar-Baratoff relation for SIS junctions. They also see Josephson emission at 11 GHz and a resistive memory switching effect. Sm-1111 single crystal mesas show similar behavior.

Preparation and electrical properties of the base electrode

We fabricated hybrid Josephson junctions with La-1111 thin films. The oxypnictide thin films were prepared by pulsed laser deposition at room temperature and an additional heat treatment at 950°C in evacuated quartz tubes as first reported in [17]. A more detailed description of the growth process can be found elsewhere [18]. By transmission electron microscopy (TEM) we found a polycrystalline LaOF impurity phase on top of the La-1111 superconducting phase. A θ-2θ Bragg-Brentano diffractogram shows that a large fraction of grains are oriented with the c-axis perpendicular to the film plane, however, the La-1111 film itself is polycrystalline with a total thickness of about 700 nm [19].

The pnictide film was covered by a 120 nm gold film, then patterned by photolithography and dry etched with Ar ion beam etching (rate 30 nm per minute). In the resulting base electrode a window for the junction was realized using sputtered SiO_2 insulation. The measurement of the resistive transition showed no depression of the T_c~20 K of the pnictide, fig.1a. We also measured the temperature dependence of the critical current through the base electrode. The characteristic for untreated films (fig. 1b) shows a Ginzburg-Landau type behavior, see e.g. [20]. The low critical current density in the order of 10^4 A/cm^2 is related to the polycrystalline structure of the film. Both experiments show that superconducting properties of the pnictide film is not being altered by the processes necessary to fabricate Josephson junctions.

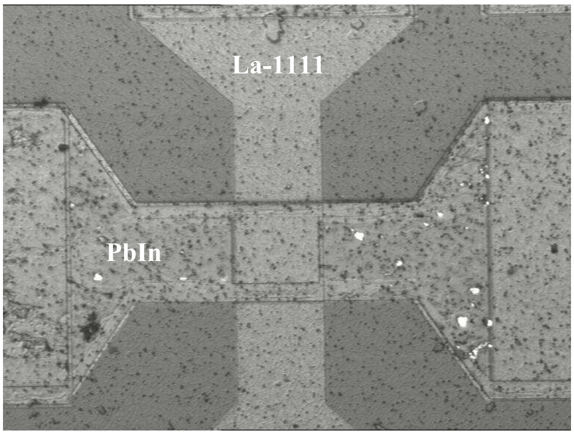

Fig.2 Microscope picture of a La-1111 bottom electrode crossed by a PbIn counter-electrode. The size of the crossing bridges is 100 μm.

Electrical characteristics of the junction

In the next step a PbIn counter-electrode (T_c~7 K) was prepared by thermal evaporation through a mask in crossed geometry. A photograph of the junction is given in fig.2. The Au layer deposited after the pnictide growth now acts as the barrier forming a SNS junction. Fig.3 shows typical

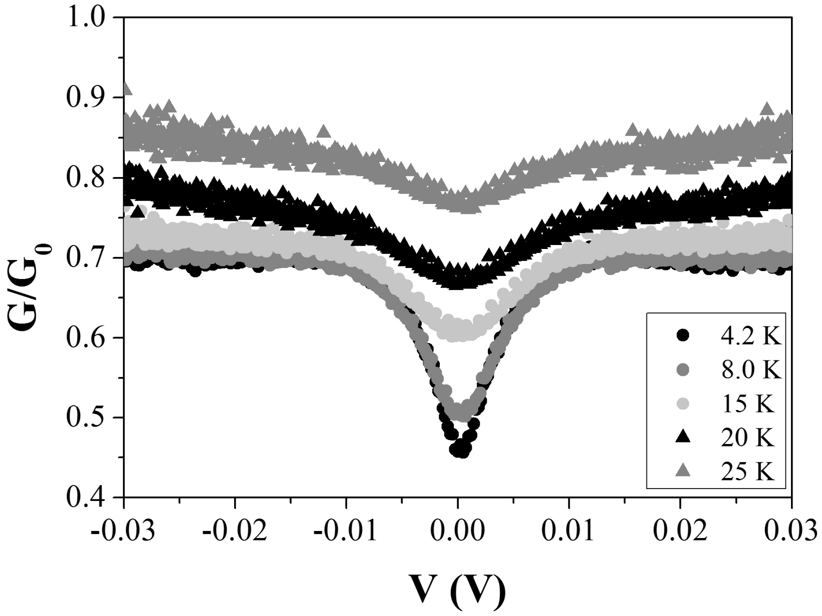

Fig.3 Normalized conductivity on voltage at different temperatures for a La-1111/Au/PbIn junction. Normalization has been accomplished by dividing the conductivity by the corresponding value at 35 K.

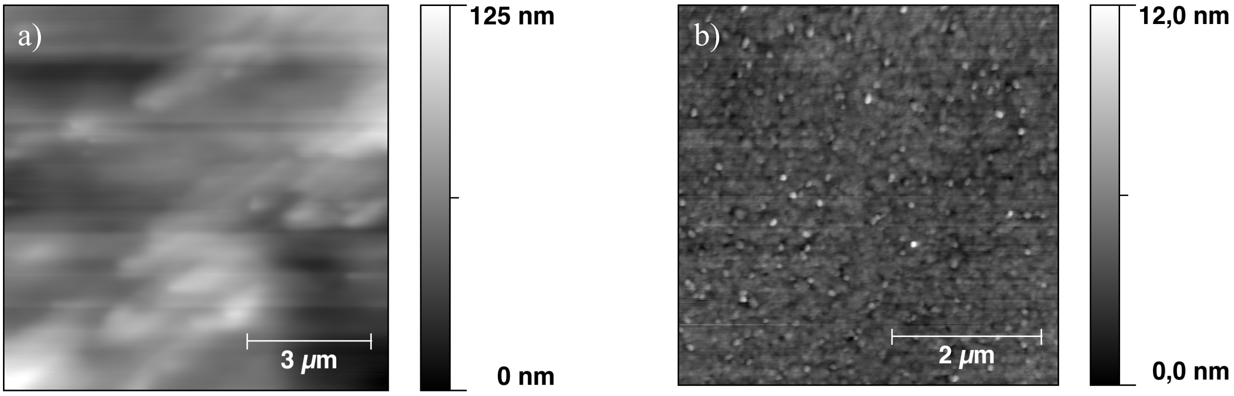

Fig.4 AFM images of the surface a) of a typical La-1111 phase film showing a rms-roughness of 19 nm and b) a doped Ba-122 phase film with a surface roughness of 0.8 nm.

normalized conductance on voltage characteristics at different temperatures close to T_c of the involved superconductors. We observed tunnel-like behavior, but with no occurrence of a supercurrent through the junction. At this stage of experimental investigations the gold barrier is yet too thick to allow Josephson effects. Thinner and well-defined barriers, however, are only obtainable if surface roughness is reduced significantly. Fig. 4 shows that the roughness of the La-1111 surface is about an order of magnitude higher compared to that of the Ba-122 phase. Additionally, the LaOF impurity phase at the surface of the La-1111 appears not to be superconductive which opens the possibility to use it as a natural barrier. However, there is not much knowledge about this material concerning conductivity, thickness and temporal evolution under different conditions. Without this knowledge theoretical evaluation of tunneling characteristics is arbitrary. Therefore, further technological improvements on film growth and sample preparation are necessary. In this regard, we will evaluate techniques such as polishing [21] for suitability to overcome above mentioned challenges.

To further characterize the electrical properties of the La-1111/Au/PbIn junction we measured the temperature dependence of the resistance in a four-probe geometry. The characteristics are

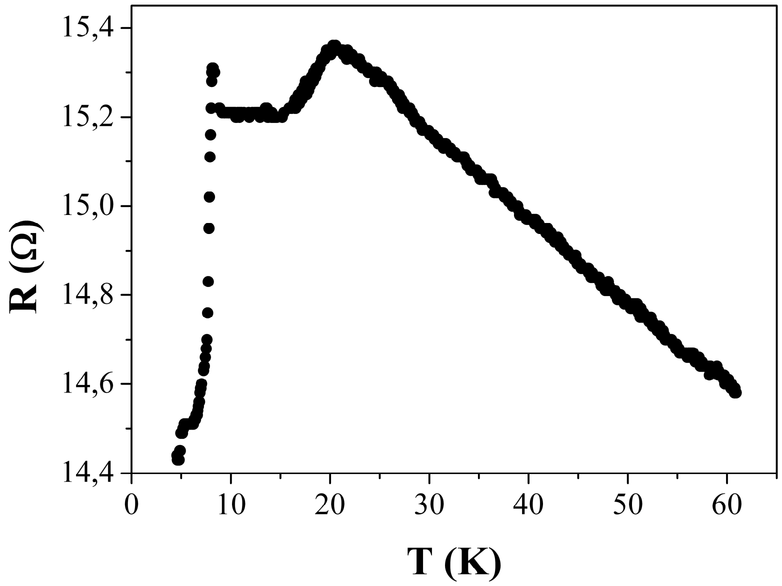

Fig.5 Temperature dependence of the resistance of a La-1111/Au/PbIn junction.

presented in fig.5. Above T_c of the La-1111 film the resistance increases monotonously with decreasing temperatures. At the superconducting transition of the base and again of the counter electrode the resistance drops steeply. The electrical behavior of the junction can thus be described in terms of a series connection of the two superconductors, the gold film and the interfacial LaOF layer. From the temperature dependence at high temperatures and the small relative change of the resistance at T_c we conclude that the conductance of the present junction is dominated by the LaOF layer which mainly shows semiconducting behavior.

Summary

We fabricated and measured La-1111/Au/PbIn thin film junctions as a step towards hybrid Josephson junctions. We found that the preparation process is not depressing the superconducting properties. The thick gold barrier together with the interface roughness as well as additional native impurity layers result in a reduced transmission of the barrier. Quasiparticle tunneling was possible, but no Cooper pair transfer. Thus the barrier and interface properties have to be improved to get high quality Josephson junctions.

References

[1] M. M. Parish, J. Hu, A. B. Bernevig, Phys. Rev. B, 78 (2008) 144514.
[2] D. Parker and I.I. Mazin, Phys. Rev. Lett., 102 (2009) 227007
[3] S. Onari, Y. Tanaka, Phys. Rev. B 79 (2009) 174526 .
[4] W. F. Tsai, D.X. Yao, B. A. Bernevig, J. P. Hu, Phys. Rev. B 80 (2009) 012511.
[5] P. Ghaemi, F. Wang, A. Vishwanath, Phys. Rev. Lett. 102 (2009) 157002.
[6] Y. Ota, M. Machida, T. Koyama, H. Matsumoto, Phys. Rev. Lett., 102(2009) 237003.
[7] D. Inotani, Y. Ohashi, arXiv: 0901.1718 (2009), unpublished.
[8] C. T. Chen, C. C.Tsuei, M. B. Ketchen , Z. A. Ren, Z. X. Zhao, Nature Physics 6 (2010) 260.
[9] J. Wu, P. Phillips, Phys. Rev. B 79 (2009) 092502.
[10] X.H. Zhang, Y.S. Oh, Y. Liu, L. Yan, K.H. Kim, R.L. Greene, and I. Takeuchi: Phys.Rev.Lett. 102 (2009) 147002
[11] Zhou YR, Li YR, Zuo JW, Liu RY, Su SK, Chen GF, Lu JL, Wang NL, and Wang YP, arXiv: 0812.3295 (2009), unpublished
[12] X.H. Zhang, S.R. Saha, N.P. Butch, K. Kirshenbaum, J.P. Paglione, R.L. Greene, Y. Liu, L.Q. Yan, Y.S. Oh, K.H. Kim, I. Takeuchi, Appl. Phys. Lett. 95 (2009) 062510
[13] T. Katase, Y. Ishimaru, A. Tsukamoto, H. Hiramatsu, T. Kamiya, K. Tanabe, H. Hosono, Appl. Phys. Lett. 96 (2010) 142507
[14] W.Q. Chen, F. Ma, Z.Y. Lu, F.C. Zhang, Phys. Rev. Lett. 103 (2009) 207001.
[15] C.W. Hicks, T.M. Lippman, M.E. Huber, Z.A. Ren, Z.X. Zhao, K.A. Moler, J. Phys. Soc. Jpn. 78 (2009) 013708.
[16] P. Müller, Y. Koval, G. Behr, B. Büchner, Verhandl. DPG, Dresden, TT36.7 (2009)
[17] E. Backen, S. Haindl, T. Niemeier, R. Huehne, T. Freudenberg, J. Werner, G. Behr, L. Schultz, B. Holzapfel, Supercond. Sci. Technol. 21 (2008) 122001
[18] M. Kidszun, S. Haindl, E. Reich, J. Hänisch, K. Iida, L. Schultz, B. Holzapfel, Supercond. Sci. Technol. (2010) 23, 022002
[19] S. Haindl, M. Kidszun, A. Kauffmann, K. Nenkov, N. Kozlova, J. Freudenberger, T. Thersleff, J. Hänisch, J. Werner, E. Reich, L. Schultz, B. Holzapfel., Phys. Rev. Lett. 104 (2010) 077001
[20] W. J. Skocpol, M. R. Beasley, M. Tinkham, J. Appl. Phys. 45 (1974) 4054.
[21] T. Shapoval, S. Engel, M. Gründlich, D. Meier, E. Backen, V. Neu, B. Holzapfel, L. Schultz, Supercond. Sci. Technol. 21 (2008) 105015.

doi:10.4028/www.scientific.net/AST.75.141

Investigation of fluctuating diamagnetism and spin dynamics in $SmFeAsO_{1-x}F_x$ superconductors

Giacomo Prando[1,2,a], Pietro Carretta[1,b], Alessandro Lascialfari[1,3,c],
Attilio Rigamonti[1,d], Samuele Sanna[1,e], Laura Romanò[4,f],
Andrea Palenzona[5,g], Marina Putti[5,h], Matteo Tropeano[5,i]
[1]Dip. di Fisica "A. Volta", Università di Pavia – CNISM, I-27100 Pavia, Italia
[2]Dip. di Fisica "E. Amaldi", Università di Roma Tre – CNISM, I-00146 Roma, Italia
[3]Dip. di Scienze Molecolari Applicate ai Biosistemi, Università di Milano, I-20134 Milano, Italia
[4]Dip. di Fisica, Università di Parma – CNISM, I-43100 Parma, Italia
[5]Dip. di Fisica, Università di Genova – CNR/INFM-LAMIA, I-16146 Genova, Italia
[a]giacomo.prando@unipv.it, [b]pietro.carretta@unipv.it, [c]alessandro.lascialfari@unipv.it,
[d] attilio.rigamonti@unipv.it, [e]samuele.sanna@unipv.it, [f]laura.romano@fis.unipr.it,
[g]metalli@chimica.unige.it, [h]putti@fisica.unige.it, [i]tropeano@fisica.unige.it

Keywords: superconducting iron-pnictides, NMR spectra and relaxation, SQUID magnetometry, spin dynamics.

Abstract. The superconducting iron-pnictides $SmFeAsO_{1-x}F_x$ (x = 0.15 and x = 0.2) are studied by means of ^{19}F-NMR spectroscopy and SQUID magnetometry. Fluctuating diamagnetism above T_c is briefly examined, stressing the analogy with the phenomenology in underdoped cuprates. The ^{19}F relaxation rate allows us to infer an indirect magnetic coupling between Sm^{3+} moments, possibly involving conduction electrons in FeAs bands, with no appreciable effects on crossing the superconducting transition temperature. A comparison between the superconducting samples and the insulating SmOF, often present as spurious phase in $SmFeAsO_{1-x}F_x$ pnictides, is also carried out. Relevant differences in the spin dynamics features are found.

Introduction. The widely spread attention devoted to the iron-pnictide superconductors along the last two years, with a variety of experimental studies [1], has not led until now to a full understanding of the interplay between the microscopic mechanism underlying superconductivity and the low-energy magnetic excitations involving strongly correlated electrons. Thus the situation about basic properties is somewhat similar to the one already met in cuprates and rutheno-cuprates, especially in the underdoped compounds. In the light of the experimental approaches carried out in those materials [2], in this report we discuss the interplay between rare-earth (RE) magnetism and superconductivity in $SmFeAsO_{1-x}F_x$ (Sm-1111 from now on) on the basis of ^{19}F-NMR spectra and relaxation rate as well as of SQUID magnetometry. Phase diagrams of Sm-1111 have already been devised from a variety of measurements of spectroscopic character [3]. The possible role of spurious phases is taken into account by comparison with SmOF, where Sm^{3+} ions are characterized by a similar coordination.

Experimental results and discussion. The experimental studies have been focussed on powder samples of the (nominally) optimally doped compound $SmFeAsO_{0.8}F_{0.2}$ (Sm20% from now on) and of the slightly underdoped $SmFeAsO_{0.85}F_{0.15}$ (Sm15%). The characterization of the samples was carried out by means of SQUID magnetometry and it indicated 52.7 K and 46.8 K (respectively) as superconducting transition temperatures T_c. A small amount of magnetic impurities was found to be present in both samples (a μ^+SR study of typical magnetic impurities in Sm-1111 has been reported in [4]), causing a slight difference between the field-cooled (FC) and zero-field-cooled (ZFC) magnetization (M) already above T_c (see Fig. 1). SQUID measurements also allowed us to study the diamagnetic effects linked to superconducting fluctuations in the Sm20% sample. Isothermal M vs. magnetic field (H) curves displaying the fluctuating contribution M_{FLUCT} were obtained through the subtraction procedure described elsewhere [5]. The temperature dependence of the upturn field H_{UP}, namely the field at which M_{FLUCT} starts to decrease in modulus on increasing field, was found to be highly reminiscent of the phenomenology already observed in underdoped cuprate materials (see Fig. 2). Isothermal magnetization curves on those compounds have evidenced a non-conventional fluctuating diamagnetism, on approaching T_c from above [5]. The M_{FLUCT} vs. H data were found to fit within the framework of the phase-fluctuation theory [6] that was already successfully used to describe similar effects in underdoped cuprates [5].

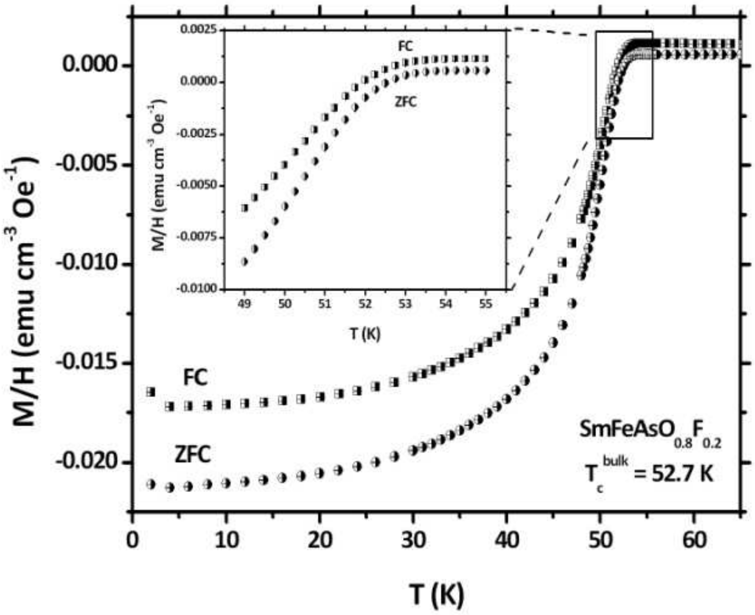

Fig. 1. ZFC and FC curves displaying the static susceptibility M/H of Sm20% (H = 5 Oe). Inset: blow-up of the transition region, showing a slight difference between ZFC and FC curves.

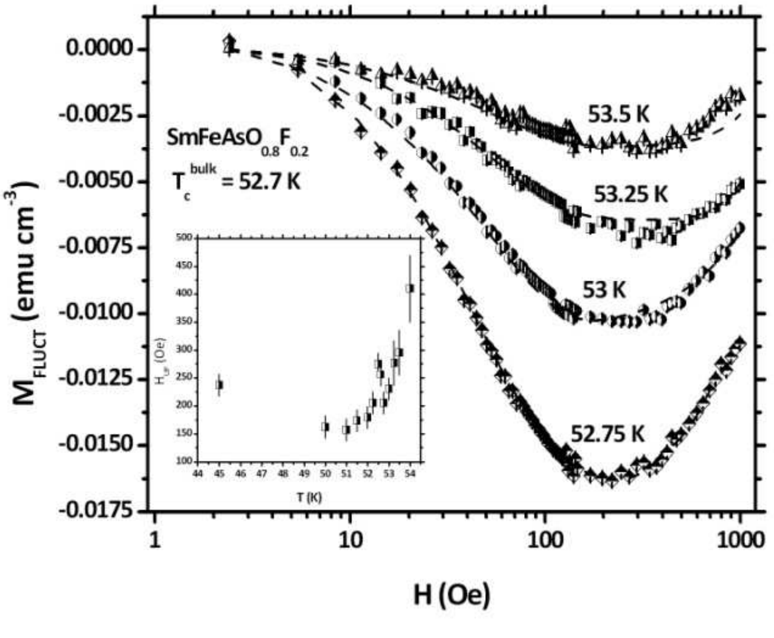

Fig. 2. Isothermal curves for the diamagnetic contribution M_{FLUCT} to the static magnetization M above T_c due to superconducting fluctuations in Sm20%. Dashed curves are best fits obtained from the phase-fluctuations model. Inset: temperature dependence of the minimum of the isothermal curves (upturn field H_{UP}).

The Sm^{3+} spin dynamics and the related low-frequency excitations were probed in Sm20% and Sm15% by means of ^{19}F-NMR spectroscopy. In order to ensure that the results can be univocally associated with the intrinsic properties of the superconducting phase, similar studies were also performed on a powder sample of SmOF, a compound known to be easily formed as spurious phase during the Sm-1111 synthesis [7]. From the temperature dependence of the shift K of the resonance frequency ν

$$K = \frac{\nu - \nu_0}{\nu_0} = \frac{A\,\chi_S}{g\,\mu_B\,N_A} \tag{1}$$

with respect to the reference frequency ν_0 (at room temperature), the scalar hyperfine coupling constant A between the ^{19}F nuclei and the magnetic ions can be obtained from the temperature dependence of the spin susceptibility χ_S (N_A is the Avogadro's number). In the examined samples, the shift was found to follow a Curie-Weiss behaviour dependent on the field H_0, suggesting a sizeable dependence of the spin susceptibility on the applied magnetic field. It is observed that the shifts between Sm15% and SmOF at $H_0 \approx 1$ T ÷ 1.5 T are safely different (Fig. 3). From the data of M/H at high field (H = 5 T) it was possible to estimate $A \approx -3.7 \pm 0.4$ kOe for Sm15% [8] while, from H = 1 kOe data, $A \approx -9.15$ kOe was found for SmOF.

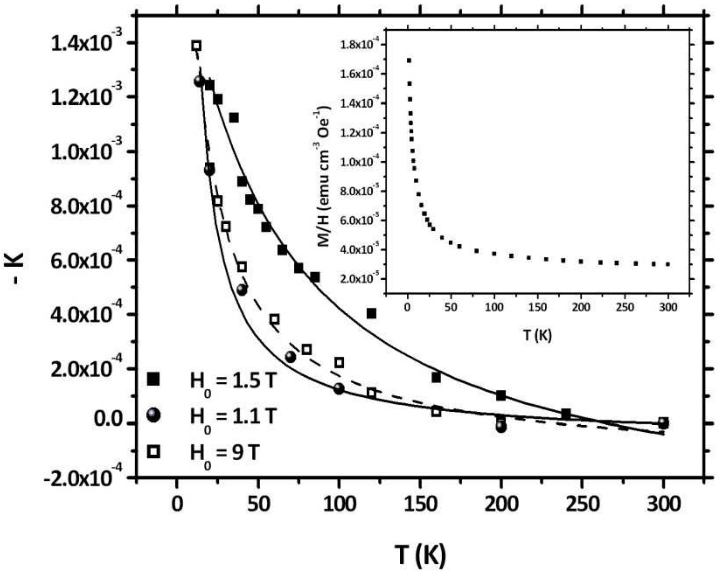

Fig. 3. Temperature dependence of the (negative) shift K at different values of the magnetic field H_0 for Sm15% (open and full squares) and SmOF (full circles). The lines are best fits obtained with Curie-Weiss functions. Inset: temperature dependence of the static susceptibility M/H (H = 1kOe) of SmOF.

At the same time, a sizeable difference between the ^{19}F-NMR signals of Sm15% and SmOF appears in the temperature dependence of the line-width Δν (Fig. 4). Following a standard solid-echo sequence $\pi/2 - \tau_{echo} - \pi/2$, the Fourier transform of the second half of the echo signal gives a typically Lorentzian line-shape. Starting from a common field-independent background of about 25 kHz above T_c, the increase in Δν below T ≈ 40 K is much sharper in Sm15% than in SmOF. The extra-broadening of the NMR lines are different in origin for the two systems, being related in Sm15% mostly to the field modulation due to the flux-line lattice typical of type II superconductors while in SmOF it should be associated only with the increase in static magnetic susceptibility (see Fig. 3, inset).

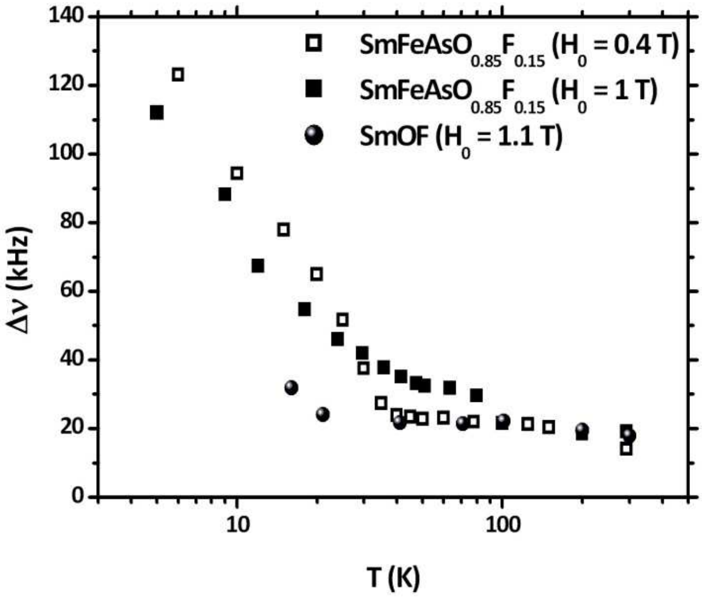

Fig. 4. Comparison of the ^{19}F -NMR line-width (FWHI) in Sm15% (open and full squares) and in SmOF (full circles) for different external fields H_0.

Interesting insights into the spin dynamics can be obtained from the analysis of the temperature dependence of the spin-lattice relaxation time T_1, as deduced by a standard ^{19}F-NMR inversion sequence $\pi - \tau - \pi/2 - \tau_{echo} - \pi/2$. The recovery laws obtained at all temperatures can be fit by single-exponential relaxation functions. It is noted that for ^{19}F nuclei (nuclear spin I = ½) a single-exponential is expected in microscopically homogeneous samples. A plot of $1/T_1$ vs. T (for T > 10 K) evidenced a sample- and field-independent power-law behaviour of the form

$$^{1}/_{T_1} \propto T^{\nu} \tag{2}$$

with an exponent $\nu \approx -0.6$ for the Sm-1111 samples, with no modification on crossing the superconducting transition temperature [8] (see Fig. 5). A similar behaviour has been reported for the isostructural non-superconducting heavy-fermion compound CeFePO [9]. This result can be compared with the trend of the relaxation rate in LaFeAsO$_{1-x}$F$_x$ (La-1111), characterized by a steady decreas on cooling and by a sudden steep change at T_c [10, 11, 12]. The absence of localized magnetic moments (associated with RE ions) in La-1111 allows one to conclude that the observed behaviour in Sm-1111 can be associated with the progressive slowing down of the antiferromagnetically correlated Sm^{3+} spin fluctuations [13]. Since the correlations already arise at 300 K, one can deduce that the magnetic interactions must be much stronger than the dipolar or the direct exchange ones. In this respect, it is pointed out that a certain degree of hybridization between RE ions and the metallic FeAs tri-layers has been found from ^{75}As-NMR measurements in the similar compounds NdFeAsO$_{1-x}$F$_x$ [14]. This suggests that the magnetic interaction between Sm^{3+} ions is of indirect nature (RKKY-like) and is possibly mediated by the conduction electrons on the metallic tri-layers [8]. The comparison between $1/T_1$ vs. T in Sm20% and SmOF shows that the two behaviours are rather different on a wide temperature range (see Fig. 5).

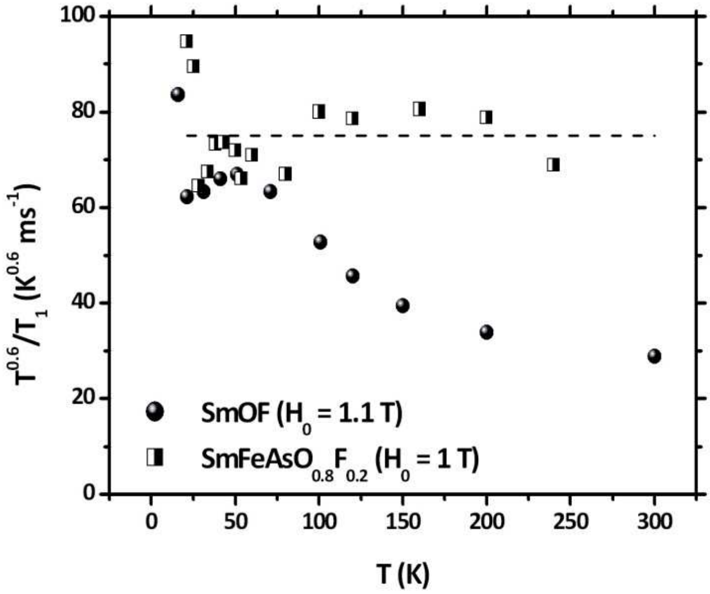

Fig. 5. Temperature dependence of the ratio $T^{0.6}/T_1$ in Sm20% and in SmOF sample at similar values of the external field H_0. The dashed line tracks the power-law function (2).

Summarizing remarks. From SQUID magnetometry measurements it is noted that the pnictide superconductors $SmFeAsO_{0.8}F_{0.2}$ and $SmFeAsO_{0.85}F_{0.15}$ show a fluctuating diamagnetism above T_c reminiscent of the underdoped cuprates. In other words, local non-percolating regions at non-zero order parameter modulus exhibiting strong phase fluctuations are present above the bulk T_c. The ^{19}F-NMR relaxation rate $1/T_1$ has a temperature behaviour typical of antiferromagnetically correlated weakly itinerant electrons and cross the superconducting transition temperature with no modification. This indicates that the low-energy spin excitations involving Sm^{3+} magnetic ions (in indirect interaction via delocalized hybrid electrons) are not directly involved in the mechanism underlying the superconductivity. Only a slight increase in the NMR line width is noted below T_c, consistent with the raise of the fluxoids lattice. The comparison of the magnetic properties in $SmFeAsO_{0.8}F_{0.2}$ and $SmFeAsO_{0.85}F_{0.15}$ with SmOF, often generated as spurious phase in $SmFeAsO_{1-x}F_x$, shows that only a little (if any) of this phase should be present in our samples.

References

[1] Special issue, Physica C 468 (9 – 12) (2009).

[2] A. Rigamonti, F. Borsa and P. Carretta: Rep. Prog. Phys. 61 (1998), p. 1367.

[3] S. Sanna, R. De Renzi, G. Lamura, C. Ferdeghini, A. Palenzona, M. Putti, M. Tropeano and T. Shiroka: Phys. Rev. B 80 (2009), p. 052503; A. J. Drew, C. Niedermayer, P. J. Baker, F. L. Pratt, S. J. Blundell, T. Lancaster, R. H. Liu, G.Wu, X. H. Chen, I. Watanabe, V. K. Malik, A. Dubroka, M. Rössle, K. W. Kim, C. Baines and C. Bernhard: Nature Mater. 8 (2009), p. 310; C. Hess, A. Kondrat, A. Narduzzo, J. E. Hamann-Borrero, R. Klingeler, J. Werner, G. Behr and B. Büchner: Europhys. Lett. 87 (2009), p. 60007; Y. Kamihara, T. Nomura, M. Hirano, J. E. Kim, K. Kato, M. Takata, Y. Kobayashi, S. Kitao, S. Higashitaniguchi, Y. Yoda, M. Seto and H. Hosono: New Journ. Phys. 12 (2010), p. 033005.

[4] S. Sanna, R. De Renzi, G. Lamura, C. Ferdeghini, A. Martinelli, A. Palenzona, M. Putti and M. Tropeano: J. Supercond. Nov. Magn. 22 (2009), p. 585.

[5] E. Bernardi, A. Lascialfari, A. Rigamonti, L. Romanò, M. Scavini and C. Oliva: Phys. Rev. B 81 (2010), p. 064502 and references therein.

[6] G. Prando, A. Lascialfari, A. Rigamonti, L. Romanò and S. Sanna (to be published).

[7] J. Hölsä, E. Säilynoja, P. Ylhä, P. Porcher, P. Dereń and W. Stręk: J. Phys. Chem. 100 (1996), p. 14736.
[8] G. Prando, P. Carretta, A. Rigamonti, S. Sanna, A. Palenzona, M. Putti and M. Tropeano: Phys. Rev. B 81 (2010), p. 100508(R).
[9] E. M. Brüning, C. Krellner, M. Baenitz, A. Jesche, F. Steglich and C. Geibel: Phys. Rev. Lett. 101 (2008), p. 117206.
[10] K. Ahilan, F. L. Ning, T. Imai, A. S. Sefat, R. Jin, M. A. McGuire, B. C. Sales and D. Mandrus: Phys. Rev. B 78 (2008), p. 100501(R).
[11] Y. Nakai, K. Ishida, Y. Kamihara, M. Hirano and H. Hosono: J. Phys. Soc. Jpn. 77 (2008), p. 073701.
[12] M. Sato, Y. Kobayashi, S. C. Lee, H. Takahashi, E. Satomi and Y. Miura: J. Phys. Soc. Jpn. 79 (2010), p. 014710.
[13] D. H. Ryan, J. M. Cadogan, C. Ritter, F. Canepa, A. Palenzona and M. Putti: Phys. Rev. B 80 (2009), p. 220503(R).
[14] P. Jeglič, J.-W. G. Bos, A. Zorko, M. Brunelli, K. Koch, H. Rosner, S. Margadonna and D. Arčon: Phys. Rev. B 79 (2009), p. 094515.

doi:10.4028/www.scientific.net/AST.75.147

Terahertz Spectroscopy of Superconductors

Stefano Lupi' [1,a], Leonetta Baldassarre [2,b], P. Calvani [3,c]
P. Dore [3,d], C. Mirri [3,e], M. Ortolani[4,f] and A. Perucchi [2,g],

[1]CNR-IOM and Department of Physics, University of Rome La Sapienza, P.le A. Moro 2, 00185 Rome (Italy)

[2]Sincrotrone Trieste, Strada Statale 14, Basovizza, Trieste (Italy)

[3]CNR-SPIN and Department of Physics, University of Rome La Sapienza, P.le A. Moro 2, 00185 Rome (Italy)

[4]CNR–Institute of Photonics and Nanotecnology, Via Cineto Romano 42, I-00156 Rome, Italy

[a]stefano.lupi@roma1.infn.it, [b]leonetta.baldassarre@elettra.trieste.it, [c]paolo.calvani@roma1.infn.it
[d]paolo.dore@roma1.infn.it, [e]chiara.mirri@roma1.infn.it, [f]michele.ortolani@ifn.cnr.it,
[g]andrea.perucchi@elettra.trieste.it,

Keywords: Terahertz Spectroscopy, Superconductivity.

Abstract.

We show how synchrotron radiation (SR) in the terahertz (THz) region provides the possibility to measure the properties of conventional and exotic superconductors in their superconducting state. Indeed, through the coupling of SR and a conventional Michelson interferometer, one can obtain in the THz range a signal-to-noise ratio up to 10^3. We review the application of this technique to superconductors with a different degree of complexity: the single-gap boron-doped diamond BCS isotropic material; CaAlSi, a superconductor isostructural to MgB_2 with a slight anisotropy between the gap in the hexagonal planes and that along the orthogonal c axis; and isotropic V_3Si, where superconductivity opens two gaps at the Fermi energy.

Introduction

The discovery of high-T_c cuprates in 1986 has renewed the interest on superconducting materials. Many new superconductors have been found, among them one may cite K-doped C_{60}, Na_xCoO_2 co-doped with H_2O, MgB_2, Boron-doped diamond [1], CaAlSi [2], and the new Iron pnictides.

The main question about a new superconductor concerns whether it can be describe by a conventional Bardeen-Cooper-Schrieffer (BCS) theory, or it presents exotic properties. For instance, strongly covalent bonds, high concentration of impurities, and high phonon frequencies make B-doped diamond much different from the conventional metals where the BCS model holds. Instead CaAlSi, with its hexagonal planes stacked along the c axis, has anisotropic properties that are not considered by the conventional models of superconductivity. Finally, after the discovery of MgB_2, multiple bands superconductivity has been put forward and the properties of known materials like V_3Si with a T_c of about 20 K, have been rediscussed in this new scenario.
Infrared spectroscopy is a powerful tool to characterize both the normal and the superconducting state in such solids, as it probes directly, and with the highest spectral resolution, their low-energy electrodynamics. In particular, when $T < T_c$ a gap appears in the electronic density of states at the Fermi level. This gap opens along all directions of the Brillouin zone, if the Cooper pairs are in a spherically symmetric *s* state. When more symmetric bands cross the Fermi energy, they can be characterized by different gaps if a low interband scattering is present. If a *p* or *d* type bands define the electronic properties of the system near its Fermi energy the gap (gaps) opens only along particular ***k*** directions (where ***k*** is the lattice momentum) and this is the case for high-Tc cuprates.

The optical properties of a material can be described through the reflectivity *R* and/or the trasmittance *T*. In an isotropic superconductor and below T_c, *R* reaches (and for T = 0 becomes equal to) the value 1 for any frequency $\omega < 2\Delta(T)$ where $\Delta(T)$ is the superconducting gap at a temperature T. Above T_c and in the same low-frequency range, the reflectivity (transmittance) follows a Drude behavior characterized by the plasma frequency ω_p and the scattering rate $\Gamma(T)$. Therefore, if the metal is in the "dirty" regime defined by $\Gamma(T_c) > 2\Delta(0)$, the ratio $R_s(T<T_c)/R_n$ ($T_s(T<T_c)/T_n$) exhibits a peak [3] at $2\Delta(T)$. Both the value of $2\Delta(T)$ and its temperature dependence can be easily compared with the BCS predictions. For example, in the weak coupling limit of the original BCS model, $2\Delta(0) = 3.53\ T_c$.

In real experiments, however, one may encounter serious difficulties to measure the small difference between R_s (T_s) and R_n (T_n), as R_n in a good metal may be as high as 0.99 in the range of frequencies of the gap. Therefore, a signal-to-noise ratio on the order of 10^3 is often needed in the Terahertz region (1 THz = 33 cm^{-1} = 4 meV) to measure the gap. Nowadays, this strong requirement can be fulfilled with a conventional Michelson interferometric apparatus, when it is coupled to Terahertz Synchrotron Radiation (SR) [4]. A SR source with these characteristics is routinely open to users in Europe at the infrared beamlines IRIS [5] and SISSI [6] of the storage rings BESSY and ELETTRA, respectively.

Section 1: The optical gap of superconducting diamond

Previous studies indicate that B-doped diamond films are in the dirty limit and display a highly symmetric wave function [7]. The optical gap can therefore be measured, and compared with the BCS prediction $2\Delta(0)/k_BT_c = 3.53$. The sample was a film about 3 μm thick, 2.5x2.5 mm wide, grown by CVD and deposited on pure CVD diamond [1]. X-ray diffraction patterns collected just after the growth showed that the whole film surface had a (111) orientation, with no appreciable spurious contributions, as already reported for similar samples [1]. The boron concentration was estimated to be nearly $6\text{x}10^{21}$ cm^{-3}. The sample magnetic moment M(T), reported in the inset of Fig. 1 shows the superconducting transition with an onset at T_c = 6 K. Below 6.3 K the zero-resistance regime is already established by a sharp transition, which confirms the good homogeneity of the film (see the dc resistance R_{dc} in the inset). However we assume here T_c = 6 K, by considering that the magnetization is a bulk quantity like the THz conductivity. In order to measure the gap, the sample was illuminated by the terahertz radiation extracted from BESSY. Nothing else in the optical apparatus was moved while the sample temperature decreased below T_c, driving it to the superconducting phase. By this procedure we obtained in the sub-THz range an error $\delta = I_{Rs}/I_{Rn} \sim 0.2$ %, where I_{Rs} (I_{Rn}) is the intensity reflected by the sample in the superconducting (normal) state.

The ratio $I_{Rs(T)}/I_{Rn(10\ K)} = R(T)/R(10\ K)$ is reported in Fig. 1. The three curves at $T < T_c$ show a strong frequency dependence in the sub-THz region, with the predicted BCS peak at $\omega \sim 2\Delta(T)$. As a cross-check, the data for $T > T_c$ do not show any peak and are equal to 1 within the noise. A first inspection to our sub-THz data at T = 2.6 K provides a peak value at ~12 cm^{-1}, which gives the value $2\Delta(2.6\ K)/k_BT_c \sim 3$. Therefore we fit the data using a BCS approach [8], which indeed well describes the data. The main output of the fit, however, is the superconducting gap value, which at 4.6, 3.4, and 2.6 K is found to be 2Δ= 9.5, 10.5, and 11.5 cm^{-1}, respectively. This furnishes an extrapolated value $2\Delta(0)$= 12.5 cm^{-1}, or $2\Delta(0)/k_BT_c = 3.0 \pm 0.5$, in satisfactory agreement with the BCS prediction of 3.53.

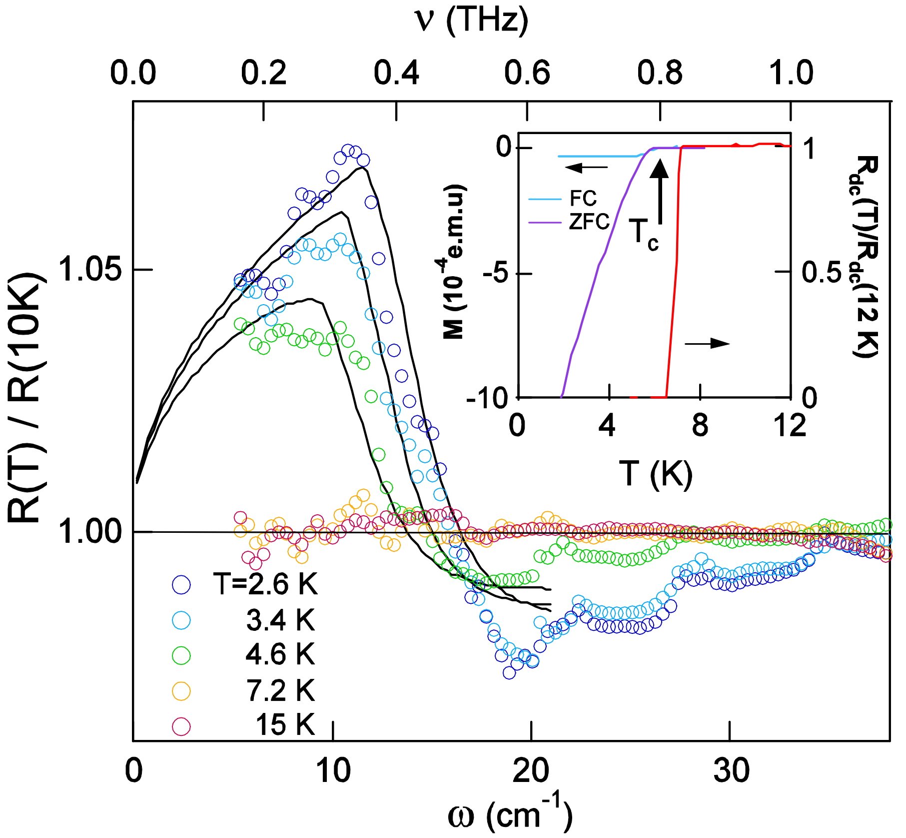

Fig.1. Reflectivity of a strongly B-doped diamond film in the sub-THz region, normalized to its values at 10 K. The lines are fits obtained by assuming a BCS reflectivity below T_c and a Hagen-Rubens model at 10 K. The inset shows on the left scale the magnetic moment of the sample, as cooled either in a 10 Oe field (FC) or in zero field (ZFC), on the right scale its resistance normalized to its value at 12 K. The FC values are multiplied by 10.

Section 2: The anisotropic gap of CaAlSi.

CaAlSi is a novel superconductor characterized by a maximum value of T_c of 7.7 K and hole transport [2]. It has attracted wide interest for its properties including the hexagonal crystal structure similar to that of MgB_2, where however the carriers are electrons. Like MgB_2, CaAlSi has two Fermi-surface sheets. However, it is not clear if one should expect one SC gap or two gaps like in MgB_2. In any case it is reported to have an s-wave anisotropic symmetry [9], but the available experimental data are not clear. Angle resolved photoemission (ARPES) [10], within the energy resolution, distinguished in CaAlSi one isotropic gap of about 1.2 meV = 4.2 k_BT_c. Muon spin relaxation (μR) data [11] indicated a highly anisotropic gap, or possibly two distinct gaps like in MgB_2. Finally penetration depth measurements [9] support weakly anisotropic s-wave gap, but not two distinct gaps. THz spectroscopy, which allows one to measure the gap directly and with a resolution in energy higher than in ARPES, may help to solve this issue, provided that one attains a suitable signal-to-noise ratio. The present sample of CaAlSi was a single crystal with a 2x4.5x3 mm^3 [2]. Its magnetic moment M(T) (see the inset of Fig. 2) shows the SC transition with an onset at 6.7 K. The ratio $R_{ab}(T)/R_{ab}(10K)$ is reported in Fig.2 for the radiation polarized in the hexagonal sheets at T, both below and above T_c. The curves at $T < T_c$ exhibit the expected peak at $2\Delta_{ab}(T)$, while for $T > T_c$ (12 K), the above ratio is equal to 1 at any ωwithin the noise. We modeled the optical conductivity, for the hexagonal planes in the normal state, by a Hagen-Rubens model with a plasma frequency $\omega_p(ab)$ and a scattering rate Γ_{ab}. In the SC state we used the Mattis-Bardeen model with a fixed T_c = 6.7 K and $\Delta_{ab}(T)$ as a free parameter. The curves $R_{ab}(T)/R_{ab}(10\ K)$ calculated in this way are also reported in Fig. 2. The fit is good at the three temperatures and provides $2\Delta_{ab}$= 15 and 17.5 cm^{-1} at 4.5 and 3.3 K, respectively. This leads to an extrapolated value $2\Delta_{ab}(0)$= 19.0 ± 1.5 cm^{-1}, or $2\Delta_{ab}(0)/k_BT_c$ = 4.1 ± 0.4, a value which confirms - with the higher resolution provided by infrared spectroscopy - a previous determination by ARPES [10]. The $2\Delta_{ab}(0)/k_BT_c$ ratio suggests that CaAlSi is a BCS superconductor with moderately strong electron-phonon coupling. On the basis of our fits, a single gap well describes the superconducting transition in the hexagonal planes.

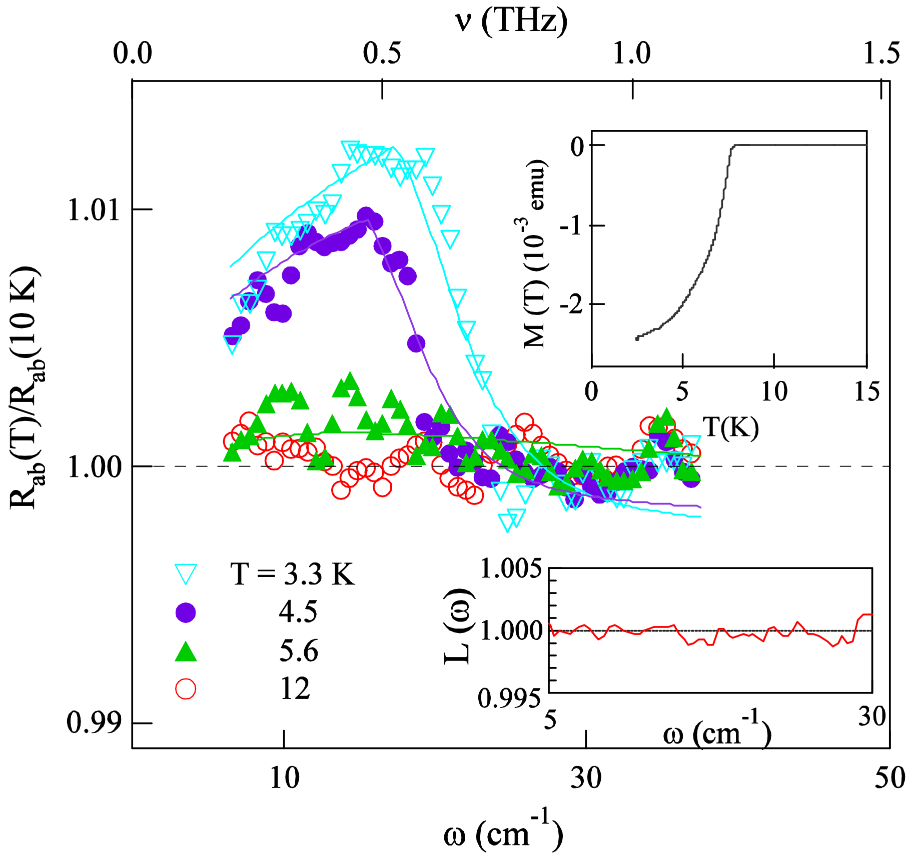

Fig.2. Ratio between the sub-THz reflectivity of the *ab* planes below T_c and in the normal phase at 10 K. The lines are fits based on a BCS reflectivity below T_c and on a Hagen-Rubens model at 10 K. The upper inset shows the magnetic moment measured by cooling the sample in a field of 10 Oe, showing the superconducting transition at T_c = 6.7 K. The lower inset shows a check on data reproducibility, performed by dividing two subsequent spectra of 256 scans.

Let us now consider the optical response of CaAlSi along the c-axis. Fig.3 shows the ratio $R_c(T)/R_c(10\ K)$, as measured with the radiation polarized along the c direction. A peak appears below T_c, but its different shape with respect to those in Fig.2.

Such a shape suggests that either only a fraction of the carriers contribute to the optical conductivity of the SC phase or there are two distinct gaps. The former case is observed, for example, in high-T_c cuprates, where the order parameter has nodes in the *k* space due to its *d*-wave symmetry, but this should be excluded in CaAlSi. The second situation corresponds to MgB_2, where a two-gap model well accounts for the reflectivity data below T_c. In CaAlSi, the two gaps should come out from different regions of the Fermi surface, which are topologically disconnected along the k_z direction. A two gap model well fit the $R_c(T<T_c)\ /R_c(10\ K)$ data of Fig. 3 (solid lines) and the results for the two gaps are $2\Delta_{c,1}$=22 cm^{-1} at 4.5 K, 26 cm^{-1} at 3.3 K, and 28 cm^{-1} extrapolated to 0 K; in turn,

$2\Delta_{c,2}$=2, 6, and 8 cm^{-1} at 4.5, 3.3 and 0 K, respectively. It is reasonable to associate the two gaps to the bands which cross the Fermi level.

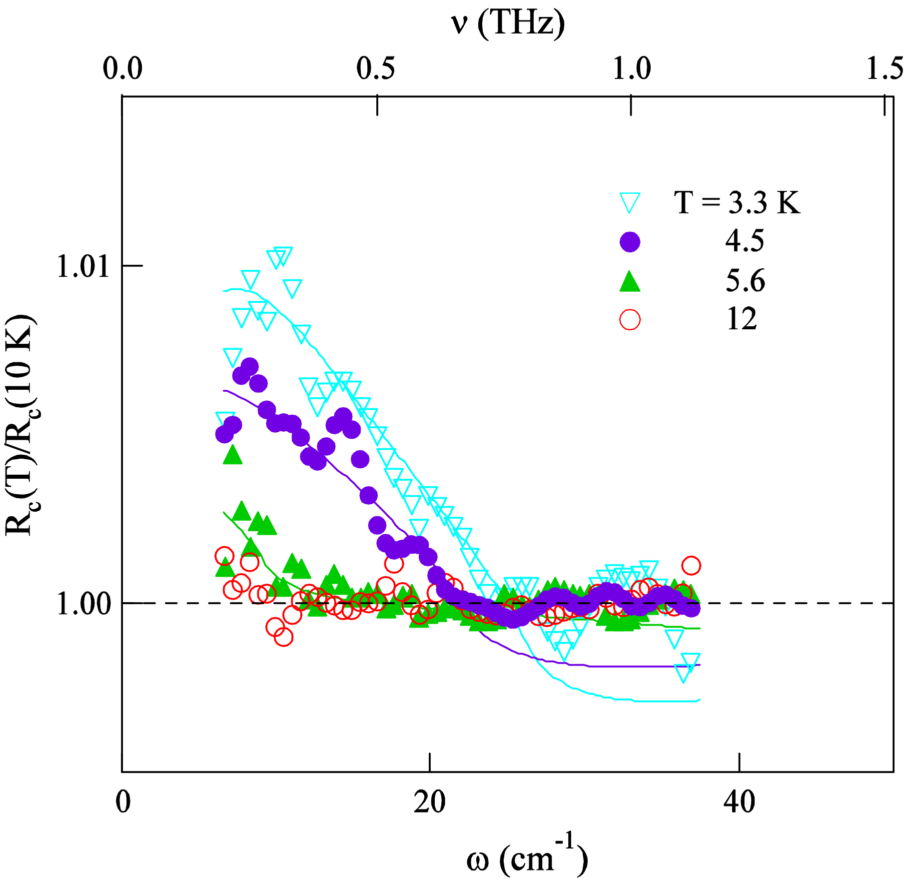

Fig.3. Ratio between the sub-THz reflectivity along the c-axis below T_c and in the normal phase at 10 K. The lines are fits based on a BCS reflectivity below T_c and on a Hagen-Rubens model at 10 K.

Section 3: The two gap scenario in V_3Si.

Large experimental and theoretical efforts have been devoted to multi-band superconductivity [12] after the discovery of the MgB_2 superconductor, since several of the unique properties of this system are based on the presence of two bands with two distinct superconducting gaps [13]. In the case of the A15 V_3Si system, a spread in the $2\Delta/k_BT_c$ value extending from 1.0 to 3.8 has been reported while a number of papers report gap values corresponding to $2\Delta/k_BT_c$ ranging from 3.4 to 3.9 [14]. Recently, contradictory results have been reported: the study of the electrodynamic response in the microwave region gave evidence of two gaps [15] while muon spin rotation measurements were shown to be consistent with a single-gap model [16]. THz spectroscopy may help to solve this issue. In particular we performed both reflectivity and transmittance measurements on high-quality V_3Si textured films. Details on the film growth by pulsed laser deposition and on their properties are reported elsewhere [17]. We studied two films deposited on $LaAlO_3$ (LAO) (001) 0.5 mm thick substrates, which exhibit preferential (210) orientation along the out-of-plane direction. The first film of thickness d=180 nm (film d180), measured in reflectivity, has good transport properties (resistivity at 300 K close to 200 μΩ cm, residual resistivity ratio RRR=8) and T_c=16.1 K. The second film, 33 nm thick (film d033) used for transmittance measurements, has worst transport properties (RRR=4.5) and a slightly lower T_c value (T_c=15.3 K) probably due to the strain induced by the substrate on the film structure.

The $R(\mathrm{T})/R_N(20\ \mathrm{K})$ ratios for the d180 film is reported in Fig. 4.

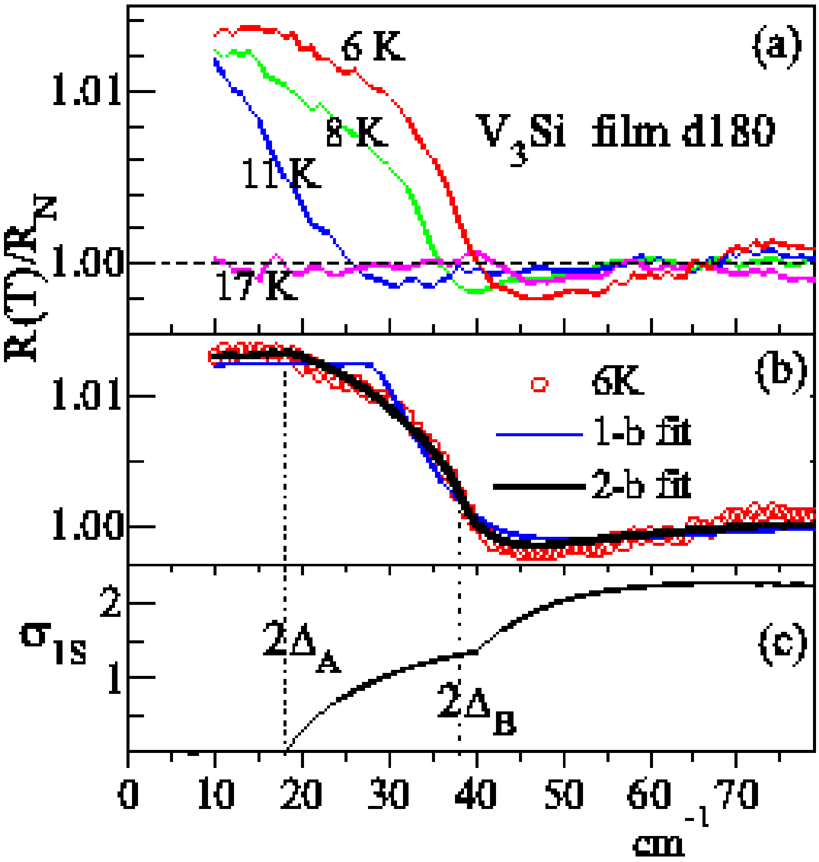

Fig. 4. (a) $R(\mathrm{T})/R_N(20\mathrm{K})$ spectra of the film d180 at selected temperatures in the THz region. (b) $R(6\mathrm{K})/R_N(20\mathrm{K})$ spectrum compared with the two-band (2-b) and one-band (1-b) best fit curves. (c) Real part of the optical conductivity in the superconducting state σ_{1s} (in units $10^4\ \Omega^{-1}\ \mathrm{cm}^{-1}$) of V_3Si from 2-b model.

These measurements were made by cycling the temperature in the 6-20 K range, without collecting reference spectra. In this way one avoids any variation in the sample position and orientation, which may yield frequency-dependent systematic errors both in reflectivity $R(\omega)$ and transmittance $T(\omega)$. We first notice that the $R(\mathrm{T})/R_N$ ratio (Fig. 4a) increases on decreasing temperature until it reaches a maximum and becomes nearly constant below 20 cm^{-1}. This indicates the presence of a superconducting gap Δ close to 10 cm^{-1}. Indeed, for $\omega \rightarrow 0$ the reflectance R_N of a conducting system tends to 1 in the case of a bulk system, and to a slightly lower value for a thin film. Therefore, as discussed in the introduction, when R_s approaches 1 at $\omega = 2\Delta$ R_s/R_N exhibits a maximum around 2Δ in the case of a bulk sample, while it remains nearly constant below 2Δ in the film case. Instead in the $T(\mathrm{T})/T_N(20\ \mathrm{K})]$data (see Fig.5a), a maximum develops on decreasing T until $T(\mathrm{T})/T_N$ exhibits a well defined peak around 40 cm^{-1}, which indicates the presence of a superconducting gap around 20 cm^{-1}. The $R(\mathrm{T})/R_N$ and the $T(\mathrm{T})/T_N$ ratios agree only with a two gaps scenario. A one gap description cannot take into account neither the shape nor the T-dependence of both ratios (see Fig. 4b and 5b, fit 1-b model).

For reflectivity ratio at T = 0 one obtains, from the two-gaps fit, $\Delta_a(0) = 10 \pm 1\ \mathrm{cm}^{-1}$, and $\Delta_b(0) = 19 \pm 2\ \mathrm{cm}^{-1}$, while for trasmittance measurements $\Delta_a(0)$ ranging from 11 to 16 cm^{-1} and $\Delta_b = 21.0 \pm 0.5\ \mathrm{cm}^{-1}$. These data correspond to BCS ratios of $2\Delta_b(0)/k_BT_c=3.8\pm0.3$ and $2\Delta_a(0)/k_BT_c=1.8\pm0.2$ respectively. While the former ratio agrees with a standard BCS weak coupling, the latter indicates an anomalous superconducting weak coupling that may be related to the specific electronic density of states in which this small gap opens [17].

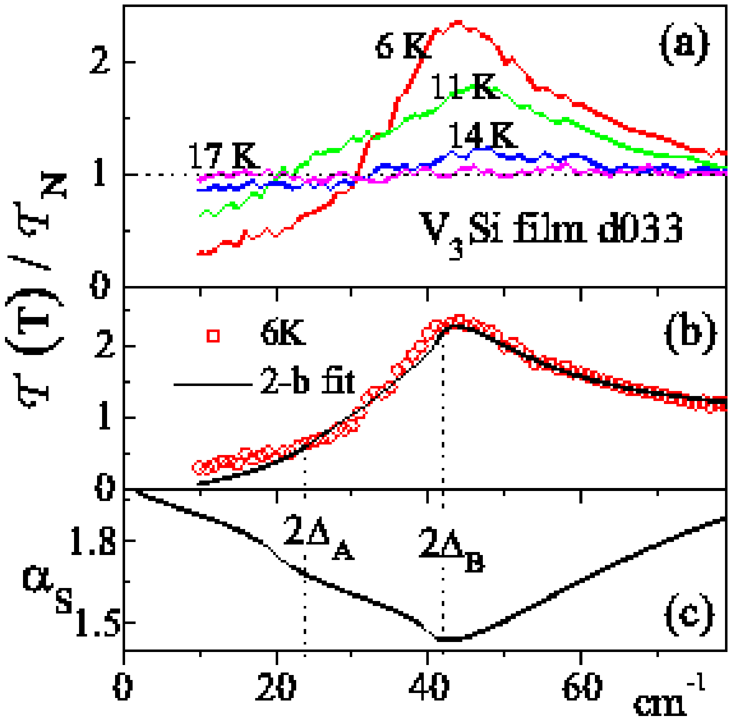

Fig. 5. (a) $\mathcal{T}(\mathrm{T})/\mathcal{T}_N(20\mathrm{K})$ spectra of the film d33 at selected temperatures in the THz region. (b) $\mathcal{T}(6\mathrm{K})/\mathcal{T}_N(20\mathrm{K})$ spectrum compared with the two-band (2-b) and one-band (1-b) best fit curves. (c) Absorption coefficient in the superconducting state α_s (in units 10^4 Ω^{-1} cm^{-1}) of V_3Si from 2-b model.

Summary

In conclusion, in the experiments reported here we have determined the superconducting gap for the B-doped diamond, CaAlSi and V_3Si superconductors, by exploiting the high intensity of terahertz synchrotron radiation. This technique provides a signal-to-noise ratio of the order of 10^3, which is needed to appreciate the weak increase (decrease) in the reflectivity (transmittance) across the critical temperature T_c. We have shown that B-doped diamond is an isotropic superconductor characterized by a BCS ratio $2\Delta(0)/k_BT_c = 3.0 \pm 0.5$, in satisfactory agreement with the theoretical prediction of 3.53. In CaAlSi, which has a crystal structure similar to that of MgB_2, we have determined the superconducting gap both in the hexagonal *ab* sheets and along the orthogonal c axis showing that CaAlSi is a BCS anisotropic s-wave superconductor. Finally we have addressed the debated problem of multi-band, multi-gap nature of V_3Si by means of reflectance and transmittance measurements in the THz region. Our experimental results indicate that in the two main electronic bands crossing the Fermi energy two gaps of different magnitude open below T_c. This result is of general interest, especially after the discovery of the Fe-As based superconductors, since it allows to address multi-gap superconductivity in a system where complications coming from magnetism and nodal gap symmetries do not arise.

References

[1] Y. Takano, M. Nagao, I. Sakaguchi, M. Tachiki, T. Hatano, K. Kobayashi, H. Umezawa and H. Kawarada, Appl. Phys. Lett. 85 (2004) p. 2851. [2] A. K. Ghosh, M. Tokunaga, and T. Tamegai, Phys. Rev. B68 (2003) p. 054507.

[3] D.N. Basov, S.V. Dordevic, E.J. Singley, W.J. Padilla, K. Burch, J.E. Elenewski, L.H. Greene, J.Morris and R. Schickling, Rev. Sci. Instrum. 74 (2003) p. 4703.

[4] M. Ortolani, P. Calvani, S. Lupi, U. Schade, A. Perla, M. Fujita, and K. Yamada, Phys. Rev. B.73 (2006) p. 184508.

[5] M. Abo-Bakr, J. Feikes, K. Holldack, P. Kuske, W.B. Peatman, U. Schade, G. Wustefeld and H.-W. Hubers , Phys. Rev. Lett. 90 (2003) p. 094801 .

[6] S. Lupi, A. Nucara, A. Perucchi, P. Calvani, M. Ortolani, L. Quaroni, and M. Kiskinova,

JOSA B24, (2007) p. 959.

[7] T. Yokoya, T. Nakamura, T. Matsushita, T. Muro, Y. Takano, M. Nagao, T. Takenouchi, H. Kawarada and T. Oguchi, Nature 438, (2005) p. 647.

[8] W. Zimmermann, E.H. Brandt, M. Bauer, E. Seider and L. Genzel, Physica C 183, (1991) p. 99.

[9] R. Prozorov, T. A. Olheiser, R. W. Giannetta, K. Uozato, and T. Tamegai, Phys. Rev. B 73, (2006) p.184523.

[10] S. Tsuda, T. Yokoya, S. Shin, M. Imai, and I. Hase, Phys. Rev. B69, (2004) p.100506(R).

[11] S. Kuroiwa, H. Takagiwa, M. Yamazawa, J. Akimitsu, K. Ohishi1, A. Koda, W.Higemoto and R. Kadono, J. Phys. Soc. Japan.73, (2004) p. 2631.

[12] I.I. Mazin, and V.P. Antropov, Physica C 385, (2003) p.49.

[13] J. Kortus, I.I. Mazin, K.D. Belashchenko, V.P. Antropov, and L.L. Boyer, Phys. Rev. Lett. 86, (2001) p.4656.

[14] A. Perucchi, D. Nicoletti, M. Ortolani, C. Marini, R. Sopracase, S. Lupi, U. Schade, M. Putti, I. Pallecchi, C. Tarantini, M. Ferretti, C. Ferdeghini, M. Monni, F. Bernardini, S. Massidda, P. Dore, Phys. Rev. B 81, (2010) p.092509.

[15] Y. A. Nefyodov, A. M. Shuvaev, and M. R. Trunin, EPL **72**, 638_(2005)

[16] J. E. Sonier, F. D. Callaghan, R. I. Miller, E. Boaknin, L. Taillefer, R. F. Kiefl, J. H. Brewer, K. F. Poon, and J. D. Brewer, Phys. Rev. Lett. **93**, 017002 _(2004)

[17] C. Ferdeghini, E. Bellingeri, C. Fanciulli, M. Ferretti, P. Manfrinetti, I. Pallecchi, M. Putti, C. Tarantini, M. Tropeano, A. Andreone, G. Lamura, and R. Vaglio, IEEE Trans. on Appl. Supercond.19, (2009) p. 2849.

© (2010) Trans Tech Publications, Switzerland
doi:10.4028/www.scientific.net/AST.75.155

Reentrance of Macroscopic Quantum Tunneling in Cuprate Superconductors

Jens Michelsen[1, a],Vitaly. S. Shumeiko[1, b]

[1]Department of Nanotechnology and Nanoscience, MC2

Chalmers University of Technology

SE-41296 Gothenburg, Sweden

[a]jens.michelsen@chalmers.se, [b]vitaly.shumeiko@chalmers.se

Keywords: Macroscopic Quantum Tunneling, Cuprate Superconductors, Josephson Effect

Abstract. We present a theoretical analysis of the transition from thermal activation (TA) regime to the macroscopic quantum tunneling (MQT) regime of the decay from a metastable persistent current state in grain boundary junctions of cuprate superconductors. This transition is conventionally characterized by a single crossover temperature determined by the potential profile and dissipative mechanisms. It is shown that due to the existence of low energy bound states (mid-gap states) for various relative orientations of the crystal axes, there exists a window of parameters where one finds, with lowering temperature, an inverse crossover from MQT to TA, followed by a subsequent reentrance of MQT. It is shown that these predictions are in reasonable agreement with recent experiments.

Introduction

Coherent quantum dynamics of the superconducting phase difference, φ, in Josephson tunnel junctions is the textbook example of macroscopic quantum coherence. Since being suggested in theory [1]it has been experimentally verified in a variety of setups [2,3,4] and has made superconducting circuits one of the most promising arenas for developing qubit applications [5,6,7]. The superconducting qubits developed so far are based on Josephson tunnel junctions with conventional superconductors. A question of both conceptual and practical importance is whether junctions made out of unconventional superconductors, such as the high temperature cuprate superconductors, can exhibit macroscopic quantum coherence.

The central issue is the intrinsic source of dissipation and decoherence originating from the interaction of the superconducting phase difference with the microscopic quasiparticles in the superconductors. In Josephson tunnel junctions composed of conventional superconductors these effects are, at low temperatures, exponentially suppressed due to a large isotropic gap $\sim 2\Delta$, in the quasiparticle energy spectrum. By contrast, the unconventional, anisotropic order parameter, $\Delta(k)$, in cuprate superconductors admits low energy quasiparticles which can be categorized into two species originating from two different features of the d-wave symmetry of the order parameter: (i) the gapless dispersion of itinerant quasiparticles implies low energy states close to the four nodal lines on the cylindrical Fermi surface, and, (ii) the sign variation of the order parameter admits the formation of surface bound states situated at zero energy in the middle of the quasiparticle gap known as midgap states (MGS) [8].

The effect of the nodal quasiparticles has been extensively analyzed in literature [9,10] and was found to have a less dramatic effect than one might anticipate due to the low phase space volume associated with these states. Furthermore due to its continuous dispersion the dissipation associated with these states is only weakly temperature dependent.

The effect of the MGS is more profound and interesting: they exist for a large volume of phase space where electronic trajectories connect wave-vectors corresponding to order parameters of opposite sign (See Figure 1). In grain boundary junctions the degenerate zero energy surface states split into a narrow band under the effect of tunneling and anisotropy of the order parameter [11,12]. The MGS band situated in the middle of the superconducting gap produces a strong temperature dependence of the dissipation that underlines the reentrance effect discussed in this article; at temperatures exceeding the MGS bandwidth, ε_m, the states become saturated and effectively unable to absorb energy from the phase degree of freedom, while at temperatures well below the MGS bandwidth the distribution of occupied/unoccupied states becomes sharp thus activating the MGS induced dissipation.

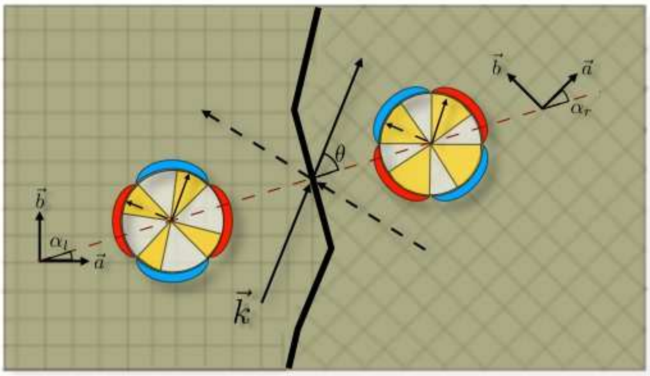

Figure1: Sketch of planarartificialgrainboundaryjunctionwith 0-π/4 misorientation of thecrystallographicaxes of theelectrodes. Boldlineindicates an interfacewithrandomlyorientedfacets, thefacetorientationisdefinedbyanglesα_l, α_r, betweencrystallographicaxes and normal to thefacet (red dashedline). Circlesdepictanisotropy of the order parameter in themomentumspace, $\Delta(k_F)=\Delta_0\cos(2\theta- 2\alpha_{l/r})$, positive (negative) lobesareshownwith red (blue) colors. Bold and dashedarrowsindicateelectrontrajectorieswithincidentalanglesθ and $\pi-\theta$involved in theformation of hybridized MGS pairs, yellowsectorswithinthecirclesindicateincidentalangleswhere MGS areformed, $\pm\pi/4-\alpha_{l/r}<\theta<\pm\pi/4+\alpha_{l/r}$, wheretheincident and reflectedmomenta (thinarrows) hitthelobeswith different signs. MGS pairsareformedbytrajectoriesbelonging to theyellowsectors at bothsides of theinterface.

The observation of macroscopic quantum tunneling (MQT) represents an important indication of the ability of Josephson junctions to exhibit quantum coherent dynamics. Experimentally macroscopic quantum tunneling is observed as the saturation with temperature of the width of the distribution of switching events from a metastable persistent current state to the dissipative running state. At higher temperatures the switching is dominated by thermal activation (TA) over the potential barrier separating the metastable minimum from the running state, in this regime the width of the distribution as a function of temperature is determined by Arrhenius law. Below a crossover temperature T* quantum tunneling of the macroscopic variable becomes the dominating source for switching events and the width of the distribution becomes temperature independent. Such an experiment was performed in [13] with tilted YBCO grain boundary junctions. The temperature dependence of the switching distribution revealed an anomalous feature associated with the crossover from TA to MQT, characterized by a “hump-structure” around 50-150 mK (for illustration see Figure 2). In this article we interpret this feature in the terms of a reentrance effect caused by the MGS. In the following section we shall present the general outline of our argument along with a short presentation of the method used to extract the crossover temperature(s). The section is followed by a microscopic derivation and quantitative analysis of the effect in terms of a simplified model depending only on a small number of facet-averaged microscopic parameters, suitable for comparison with experiments. We conclude the analysis by extracting valuable microscopic characteristics from the experimental data.

MQT-TA Crossover

According to the method developed in [14] the crossover temperature in a dissipative system can be extracted from an analysis of the phase fluctuations in imaginary time around the top of the barrier, φ_b, determined by the condition $I_J(\varphi_b)=I_e$, where $I_J(\varphi)$ denotes the Josephson current as a function of the superconducting phase difference and $I_e$denotes the external biasing current. The crossover is manifested by an instability of the phase fluctuations governed by an effective action

$$S[\varphi]=S[\varphi_b]+\sum_n \Lambda(\nu_n)\,|\delta\varphi_n|^2,\ \Lambda(\nu_n)=(\nu_n^2-\omega_b^2+i\nu_n\gamma(i\nu_n)), \quad (1)$$

where $\hbar\nu_n=2\pi n/k_BT$ is the bosonic Matsubara frequency, $\delta\varphi_n$ is the corresponding frequency component of the fluctuations $\delta\varphi(\tau)=\varphi(\tau)-\varphi_b$, and $\gamma(i\nu_n)$ is a dissipation kernel to be evaluated from the microscopic model. The instability is characterized by the sign change of the fluctuation kernel $\Lambda(\nu_1)$ and the crossover temperatures are found from the equation $\Lambda(\nu_1)=0$.

In the absence of dissipation the crossover temperature is given by $k_BT=\hbar\omega_b/2\pi$where $(\hbar\omega_b)^2=-(2e/\hbar C)\partial_\varphi I_J(\varphi_b)$ is the barrier frequency, i.e. the plasma frequency of the flipped Josephson potential. The presence of a temperature independent dissipation lowers the crossover temperature, while a strongly temperature dependent dissipation can potentially result in the far more interesting reentrance effect discussed in this article. In d-wave grain boundary junctions the strong temperature dependence is provided by the narrow band of low energy mid-gap states.

The reentrance effect proposed in this article can be understood in the following sense: If the crossover temperature, T_1, determined by the barrier frequency and the weakly temperature dependent dissipation from the nodal quasiparticles, is larger than the MGS bandwidth the system will crossover to the MQT dominated regime as the temperature goes below this first crossover temperature. Upon further lowering the temperature the dissipation of the MGS will become activated due to the desaturation of MGS band. If the dissipation is sufficiently strong it will cause the system to undergo an inverse transition into the thermally activated regime at a temperature T_2. The dissipation approaches a maximum value at temperatures well below the MGS bandwidth, and eventually the MQT will once again dominate over TA and the system undergoes a reentrance into the MQT regime at temperature T_3.

Microscopic description of reentrance effect in d-wave grain boundary Josephson junctions

Our microscopic analysis follows the seminal work [15] by presenting the imaginary time path integral representation of the partition function

$$Z=\int D\varphi D\psi^* D\psi\, Exp\{-S[\varphi,\psi^*,\psi]\}, \quad (2)$$

where the action, S, is given by

$$S[\varphi,\psi^*,\psi]=\int_0^{\hbar\beta} d\tau\left(\frac{C}{2}\left(\frac{\hbar\dot\varphi}{2e}\right)^2-\frac{\hbar\varphi}{2e}I_e+\int d^2r\,\psi^\dagger\left(\hbar\partial_\tau+H+i\frac{\hbar\dot\chi}{2}\right)\psi\right). \quad (3)$$

Here I_e is the applied bias current and the quasiparticle Hamiltonian is given by

$$H=\left(\frac{p^2}{2m}-\mu+V(r)\right)\sigma_z+\hat\Delta e^{i\chi}\sigma_+ +\hat\Delta e^{-i\chi}\sigma_-, \quad (4)$$

where $V(r)$ represents the interface potential and $\chi(r,t)=\mathrm{sign}(x)\varphi(t)$ is the superconducting phase within the electrodes. The last term in the brackets represents the electronic potential needed to maintain electro-neutrality in the superconducting electrodes.

In reference [15] the junction was described by a tunnel model, an approach also adopted in references [9,10], for d-wave Josephson junctions. Unfortunately, this model fails to give accurate results in systems where the surface density of states is dramatically different from the bulk density of states [16]. This is the case for grain boundary junctions between d-wave superconductors where zero energy surface states (MGS) are present [17].

In this article we shall use a different approach more suitable for extracting the physics involving the low energy MGS. By expanding the Nambu-fields in terms of instantaneous eigen states of the

Hamiltonian,$\psi(r,t)=\sum_i \phi_i(r)a_i(t)$, and performing the integration over the quasiparticle degrees of freedom we find

$$S_{eff}[\varphi] = \int_0^{\hbar\beta} d\tau \left[\frac{C}{2}\left(\frac{\hbar\dot{\varphi}}{2e}\right)^2 - \frac{\hbar\varphi}{2e} I_e\right] - \mathrm{Sp}\ln[G^{-1}]. \tag{5}$$

Where $G^{-1}=\hbar\partial_\tau+H$ is the inverse of the Matsubara Greens function with the Hamiltonian in the instantaneous eigen basis given by

$$\hat{H} = \hat{E} - \hbar\dot{\varphi}\hat{A}. \tag{6}$$

Here E is a diagonal matrix with elements corresponding to the instantaneous eigen energies E_i, and the elements $A_{ij}=(\phi_i,i\partial_\varphi\phi_j)-(1/4)(\phi_i,\mathrm{sign}(x)\sigma_z\phi_j)$ denote the transition matrix elements between states i,j due to temporal variation of the phase.

After expanding the effective action to include the quadratic fluctuations of the small deviation $\delta\varphi=\varphi-\varphi_b$, we get an effective action of the form Eq. (1) with the dissipation kernel given by

$$\gamma(\nu_n) = \frac{2}{C}\left(\frac{2e}{\hbar}\right)^2 \sum_{ij} \frac{\varepsilon_{ij}|A_{ij}|^2(n_i - n_j)}{\varepsilon_{ij} - i\hbar\nu_n}, \tag{7}$$

where $n_i=n_F(E_i)$ represents the Fermi filling factors and $\varepsilon_{ij}=E_i-E_j$ represents the level spacing between two quasiparticle states i,j.

Focusing on the effect of the MGS we truncate Eq. (7) to the MGS subspace. The matrix elements only couple MGS pairs within the same electronic trajectory while transitions between trajectories is forbidden due to preserved translational invariance along the interface. The dissipative contribution can then be written

$$\gamma(i\nu_n) = -i\nu_n \frac{8e^2 S}{\hbar C}\left\langle \frac{\varepsilon A^2 (n_1 - n_2)}{\varepsilon^2 + (\hbar\nu_n)^2}\right\rangle, \tag{8}$$

where S denotes the surface area, $\varepsilon=E_1-E_2$ and $A=iA_{12}$ denote the level spacing and transition matrix elements for a pair of MGS associated with one trajectory, and the brackets indicate an average over the Fermi surface. In general the anisotropy of the functions $\varepsilon(k_F)$ and $A(k_F)$ over the Fermi surface is strongly dependent on the relative orientation of the crystal axes of the cuprate superconductors to the junction interface, which for grain boundary junctions typically consists of several micrometer sized facets [18,19,20]. This makes any detailed realistic model complicated and strongly dependent on the particular realization of junction geometry. Nevertheless we can extract some universal behavior by making some drastic simplifications which, nevertheless retain the qualitative features of the temperature dependence: The temperature dispersion of the MGS dissipation is primarily defined by the Fermi filling factors and the resonant denominator, while the particular dependence of the functions $\varepsilon(k_F)$ and $A(k_F)$ play a secondary role. From the general scaling relations at small transparency [11,12] $D<<1$, $A \sim\sqrt{D}$ and $\varepsilon\sim\sqrt{D}\Delta_0$ we can formulate an analytical model independent of the particular junction orientation by neglecting the anisotropic form of the functions and, for the sake of simplicity, assuming nearly symmetric orientation. The resulting equation determining the crossover temperatures is then given by

$$\Lambda(T) = (2\pi k_B T/\hbar)^2\left(1 + \varepsilon_0\gamma_0 \int d\varepsilon \frac{\tanh(\varepsilon/4k_B T)}{\varepsilon^2 + (2\pi k_B T)^2}\right) - \omega_p^2 = 0, \tag{9}$$

where $\eta=8a\pi\hbar/R_nC\varepsilon_m$ represents a dimensionless coupling parameter, $1/R_n=(2e^2/h)S\langle D\rangle$ denotes the normal state resistance and a ~ 1 denotes a dimensionless geometry specific constant.

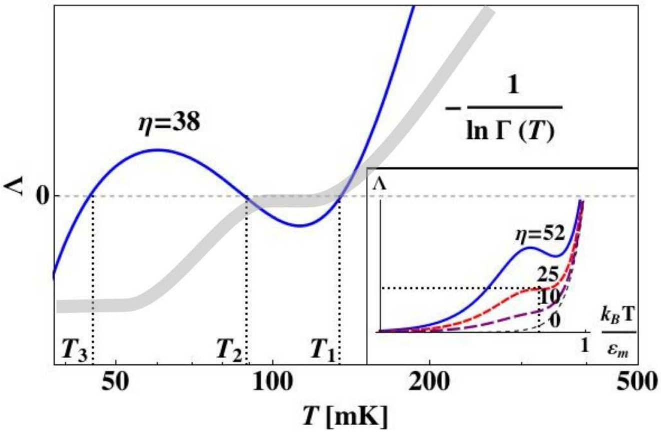

Figure2: Reentranceeffect in MQT. Sketch of temperaturedependence of decay rate (wideshadowline) illustratestheeffectfeaturingthreetransitionsbetween thermal activation and MQT regimes. Experimental transitiontemperaturesaregivenbytheroots, Λ(T)=0, forη= 38. Insetshowsdevelopment of non monotonicfeature of functionΛ(T) withincreasingcouplingstrength.

When η=0 the function Λ(T) has a monotonic quadratic form crossing the zero line at $k_BT=\hbar\omega_b/2\pi$. Numerical analysis shows (see inset Figure 2.) that this qualitative behavior remains for small coupling strength until it becomes a non-monotonic function of temperature at coupling strengths exceeding η≈25. The condition that this critical coupling corresponds to a transition temperature is given by $\omega_b\approx3.45\varepsilon_m$. At this bifurcation point the single crossover temperature then splits into three crossover temperatures representing the onset of the reentrance effect. These findings constitute the central result of this article.

In the experiment with a tilt YBCO junction [13] the anomalous temperature dependence of the decay rate (see main figure 2.) can be interpreted in terms of this reentrance effect: the first transition to MQT regime at T_1=150 mK is interrupted at T_2=90 mK by an inverse transition into the thermal activation regime and eventually undergoes a second MQT transition at T_3=50 mK. To make a quantitative comparison we fit the three experimental transition temperatures by adjusting the average model parameters η, ω_b and ε_m. Including a stray LC-oscillator present in the experimental setup [21] does not make any qualitative difference but rather insignificantly changes the parameter values. The best fit is eventually achieved for the values η=45, ε_m=320 mK and ω_b= 1.7 K and C=36 fF. Given the experimental junction critical current I_C=1.4 μA, transparency D ~ 10^{-4} , and switching current $I_e=0.9I_C$, we are able to evaluate the zero bias plasma frequency ω_p=2.5 K and the maximum energy gap Δ_0=16 K. The geometrical constant in the equation for η is estimated for the experimental value R_n=500 Ω to be a=1.5 as expected.

Conclusions

Consistency of our theory with the experimental observations strongly indicates an involvement of the MGS pairs in the macroscopic dynamics moreover it provides us with valuable information about the microscopic MGS parameters. Since the MGS bandwidth is lower than the plasma frequency by about a factor of 8 we would expect the real time dynamics to be unaffected by MGS.

Acknowledgement

We are thankful to J. Clark, M. Fogelström, T. Löfwander, and C. Tsuei for useful discussions; illuminative discussion of experiment with Th. Bauch and F. Lombardi are gratefully acknowledged. The work was supported by the Swedish Research Council (VR), and the European FP7-ICT Project MIDAS.

References

[1] A. J. Leggett, and A. J. Garg: Phys. Rev. Lett. Vol. 54, p. 857 (1985)

[2] Y. Nakamura, C. D. Chen and J. S. Tsai: Phys. Rev. Lett. Vol. 79, p. 2328 (1997)

[3] V. Bouchiat, et al.: Phys. Scr. T76, p. 165 (1998)

[4] J. R. Friedman, et al.: Nature, Vol. 406, p. 43 (2000)

[5] Y. Makhlin, G. Schön, and A. Shnirman: Rev. Mod. Phys. Vol. 73, p. 357 (2001).

[6] G. Wendin and V. S. Shumeiko: Low Temp. Phys. Vol. 33, p 724 (2007).

[7] J. Clarke, and F. K. Wilhelm: Nature Vol. 453, p. 1031 (2008).

[8] C.–R. Hu: Phys. Rev. Lett. Vol. 72, p. 1526 (1994).

[9] C. Bruder, A. van Otterlo, and G. T. Zimanyi: Phys. Rev. B. Vol. 51, p. 12904 (1995).

[10] S. Kawabata, et al: Phys. Rev. B, Vol. 72, p. 052506 (2005).

[11] T. Löfwander, et al: Supercond. Sci. Technol. Vol. 14, R53 (2001).

[12] S. Kashiwaya and Y. Tanaka: Rep. Prog. Phys. Vol. 63, p. 1641 (2000).

[13] Th. Bauch, et al.: Phys. Rev. Lett. Vol. 94, p. 087003 (2005).

[14] H. Grabert and U. Weiss: Phys. Rev. Lett. Vol. 53, p. 1787 (1984).

[15] V. Ambegaokar, U. Eckern, and G. Schön: Phys. Rev. Lett. Vol. 48, p. 1745 (1982).

[16] J. Cuevas and M. Fogelström: Phys. Rev. B. Vol. 64, p. 104502 (2001)

[17] M. Matsumoto, and H. Shiba: J. Phys. Soc. Jap., Vol. 64, p. 1703 (1995).

[18] H. Hilgenkamp and J. Mannhart: Rev. Mod. Phys. Vol. 74, p. 485 (2002).

[19] D. J. Van Harlingen: Rev. Mod. Phys. Vol. 67, p. 515 (1995).

[20] C. C. Tsuei and J. R. Kirtley: Rev. Mod. Phys. Vol. 72, p. 969 (2000).

[21] Th. Bauch, et al.: Science, Vol. 311, p. 57 (2006).

doi:10.4028/www.scientific.net/AST.75.161

The effect of oxygen distribution inhomogeneity and presence of higher borides on the critical current density improvement of nanostructural MgB_2

PRIKHNA Tetiana[1,a], GAWALEK Wolfgang[2,b], SAVCHUK Yaroslav [1,a],
SERGA Maxim[1,a], HABISREUTHER Tobias' [2,b], SOLDATOV Alexander [3,c],
YOU Shujie [3,c] EISTERER Michael [4,d], WEBER Harald W.[4,e],
NOUDEM Jacques[5,f], SOKOLOVSKY Vladimir[6,g], KARAU Friedrich[7,h], ,
DELLITH Jan[2,b], WENDT Michael[2,b], TOMPSIC Mikhael[8,i] TKACH Vasiliy [1,a],
DANILENKO Nikolay[9,a], FESENKO Igor [1,a], DUB Sergey[1,a],
MOSHCHIL Vladimir[1,a], SERGIENKO Nina[1,a], SCHMIDT Christa[2,b],
LITZKENDORF Doris [2,b], NAGORNY Peter[1,a] and SVERDUN Vladimir [1,a]

VAJDA Istvan[10,j], KÓSA János[10,j]

[1] Institute for Superhard Materials of the National Academy of Sciences of Ukraine, Kiev 04074, Ukraine

[2] Institut für Photonische Technologien, Jena, D-07745,Germany

[3] Luleå University of Technology, Department of Applied Physics &Mechanical Engineering, SE-971 87 Luleå, Sweden

[4] Vienna University of Technology, Atominstitut, 1020 Vienna, Austria

[5] CNRS/CRISMAT, 6, Bd du Maréchal Juin, CNRS UMR 6508, 14050, Caen, France

[6] Ben-Gurion University of the Negev, P.O.B. 653, Beer-Sheva 8410,5 Israel

[7] H.C. Starck GmbH, Goslar 38642, Germany

[8] Hyper Tech Research, Inc. 1275 Kinnear Road Columbus, OH 43212, USA

[9] Institute for Problems in Material Science of the National Academy of Sciences of Ukraine, 3 Krzhizhanovsky Street, Kiev, 03680, Ukraine

[10] Budapest University of Technology and Economics, Budapest, Hungary 1111 Budapest, Egry Jozsef u. 18. Hungary

[a] **prikhna@mail.ru, prikhna@iptelecom.net.ua**, [b] wolfgang.gawalek@ipht-jena.de,
[c] Alexander.Soldatov@ltu.se, [d] eisterer@ati.ac.at, [e] weber@ati.ac.at,
[f] jacques.noudem@ensicaen.fr, [g] sokolovv@bgu.ac.il, [h] Friedrich.Karau@hcstarck.com,
, [i] mtomsic@hypertechresearch.com, [j] vajda.istvan@vet.bme.hu

Keywords: MgB_2-based nanostructural materials, superconducting characteristics, Raman spectroscopy

Abstract. MgB_2-based nanostructural materials with rather high oxygen concentration (5-14 wt.%) and dispersed grains of higher borides (MgB_{12}, MgB_7) high-pressure (2 GPa or 30 MPa) synthesized (*in-situ*) or sintered (*ex-situ*) demonstrated high superconducting characteristics (critical current density, j_c, up to $1.8\text{-}1.0\cdot 10^6$ A/cm^2 in the self magnetic field and 10^3 in 8 T field at 20 K, $3\text{-}1.5\cdot 10^5$ A/cm^2 in the self field at 35 K, upper critical field up to H_{C2} = 15 T at 22 K, field of irreversibility H_{irr} =13 T at 20 K). The additives (Ti, SiC) and synthesis or sintering temperature can affect the segregation of oxygen and formation of oxygen-enriched Mg-B-O inclusions in the material structure, thus reducing the amount of oxygen in the material matrix as well as the formation of higher borides grains, which affects an increase of the critical current density. The record high H_{C2} and H_{irr} have been registered for the material high-pressure (2 GPa) synthesized from Mg and B at

600 °C having 17% porosity and more than 7 wt.% of oxygen. The attained values of the critical current, AC losses and thermal conductivity make the materials promising for application for fault current limiters and electromotors. The structural and superconducting (SC) characteristics of the material with matrix close to MgB_{12} in stoichiometry has been studied and the SC transition T_c=37 K as well as j_c= 5×10^4 A/cm^2 at 20 K in the self field were registered, its Raman spectrum demonstrated metal-like behavior.

Introduction

The high critical current density, j_c and upper critical field, H_{c2} , the fields of irreversibility, H_{irr}, can be attained in a polycrystalline MgB_2- based material, in which the grain boundaries are not the obstacles for tunneling of coupled electrical charges as in the case of high-temperature superconductors, for example, Y-Ba-Cu-O-based. Pinning centers in the material can be the grain boundaries and nanostructural inclusions of other phases. The admixture of oxygen in the MgB_2 material structure has been considered to be harmful for SC properties of MgB_2 because of the formation of MgO, leads to appearance of “dirty” boundaries between grains, which results in a decrease of effective cross-sectional area, through which a current can flow, or reduction of the “connectivity”. It has been expected that the critical current density will decrease. However the recent investigation has shown that the SC properties can be improved by the distribution of oxygen in the MgB_2 structure in a certain way. Eom et al. [1] have shown that substitution of oxygen for boron in the boron layers in films (the films with a c-axis parameter of 0.3547 nm, which is larger than that for bulk material: 0.3521 nm have been formed) leads to a lower T_c but to a steeper slope of dH_{c2}/dT both in the parallel and perpendicular magnetic field higher than that for films with normal parameters. Also, the authors have supposed that additional co-pinning by the non-superconducting MgO particles can contribute to the total pinning force. Using high-resolution transmission electron microscopy (HREM) Liao et al. [2] have shown that the oxygen substitution in the bulk of MgB_2 grains forms coherently ordered $MgB_{2-x}O_x$ precipitates in sizes from about 5 to 100 nm and that these precipitates can act as pinning centers, thus increasing the critical current density. These precipitates are formed due to the ordered replacement of boron atoms by atoms of oxygen and are of the same basic structure as the MgB_2 matrix but with composition modulations. No difference in the lattice parameters between the precipitates and the matrix can be detected in conventional electron diffraction patterns. However, extra satellite diffraction spots are seen in some directions implying the structural modulation nature of the precipitates. The precipitates have the same orientation as the MgB_2 crystallites and the replacement of boron by oxygen makes the precipitates stronger in electron scattering. The periodicity of oxygen atom ordering depends on the concentration of oxygen atoms in the precipitate and first of all occurs in the (010) plane [2].

In our previous studies [3, 4] it have been shown that the presence of higher amount of fine dispersed grains of higher borides (MgB_{12}, MgB_{6-7}) in magnesium-diboride-based materials obtained under high (2 GPa) and moderate pressures (30 MPa) correlates with higher critical current densities in magnetic fields. The additions of Ti, Ta, Zr, and SiC may increase the critical current density, in particular, of high pressure synthesized materials. However, the exact mechanism of their influence is not clear up to now. It has been observed that additions of Ti and Ta can promote the increase of the amount of MgB_{12} inclusions in high pressure synthesized MgB_2-based materials [4].

The paper presents new data, which allows hypothesizing that the SC characteristics of MgB_2-based materials depends to a large extent on the character of oxygen distribution in the material structure, which in turn is defined by the interrelations between the synthesis temperature, above mentioned additions, and higher borides formation. a transport critical current and AC losses have been determined, when testing rings from MgB_2 –based material as elements of inductive fault current limiter model. The high pressure and hot pressure synthesized MgB_2 –based materials are perspective for the application in inductive fault current limiters, electromotors, and for high magnetic fields creation.

Experimental

Samples were prepared using (1) high pressures, HP, in recessed-anvil high-pressure apparatuses (under 2 GPa) [3] and (2) hot pressing, Hot-P, (under 30 MPa) techniques. To produce MgB_2-based materials, metal Mg turnings or powder and amorphous boron were taken in the stoichiometric ratio of MgB_2. To study the influence of Ti, Zr or SiC, the powders were added to the stoichiometric MgB_2 mixture in the amount of 10 wt%. The components were mixed and milled in a high-speed activator with steel balls for 1-3 min. To study the processes of the higher borides formation, Mg and B were taken in the MgB_4-MgB_{20} ratio and heated up to 1200 °C at 2 GPa for 1h.

The structure of the materials was analyzed using TEM, SEM, and X-ray diffraction. For Raman studies, we used a WiTec CRM-200 confocal imaging system with the HeNe laser excitation (a photon energy of 1.96 eV). The spectra were collected in back scattering geometry with a resolution of 2 cm^{-1}. Incident laser power was measured directly on the sample stage and did not exceed 2 mW in order to avoid a sample heating.

The values of j_c were estimated by an Oxford Instruments 3001 vibrating sample magnetometer (VSM) using Bean's model; Hc_2 and Hirr were estimated using Quantum Design PPMS equipped with vibrating sample magnetometer. The transport critical current and AC losses were measured by the inductive method. A thermal conductivity coefficient was measured by a nonstationary method using a IT3-MXTI special device. The hardness, H_V (using a Vickers indenter), was measured by a Mod. MXT-70 Matsuzawa microhardness tester, and a nanohardness, H_B (using a Berkovich indenter) by a Nano-Indenter II.

Results and discussions.

Figure 1 demonstrates the structure and critical current density, j_c, vs. magnetic field at 10-35 K of the high pressure-synthesized materials from Mg chips and two types of amorphous B taken into MgB_2 stoichiometry without and with additions of Ti and SiC synthesized at 800 °C and 1050 °C (two temperatures were chosen because at 1050 °C the highest j_c were attained in low and medium magnetic fields and at 800 °C in the high ones). As SEM EDX (by INCA 450) study has shown (using electronic probes less than 500 nm and 2 nm in diameter), the material matrices contain Mg and B in nearly MgB_2 ratio and 5-14 wt.% of oxygen. No correlations between the amount of oxygen and j_c have been found. But there are some correlation between the oxygen distribution and j_c. The synthesis temperature increase promotes the oxygen segregation into oxygen–enriched areas or inclusions, besides the addition of Ti promotes the oxygen segregation as well (compare Figs. 1a and 1b, 1d and 1e, where a brighter color corresponds to a higher amount of oxygen, in Figs. 1d and 1e the big white spots are inclusions of a Ti-containing phase). The amount of oxygen in the matrix (where Mg-B-O oxygen-enriched inclusions are absent) of the material with Ti additions synthesized at 1050 °C was 1.5 – 5 %, while it was 8 % in the matrix of the material (with Ti) synthesized at 800 °C. At a lower synthesis temperature there is a higher amount of higher borides inclusions with mainly near MgB_{12} stoichiometry of the matrix in the case of a material high-pressure (at 2 GPa) synthesized or mainly MgB_7 in the hot-pressed (at 30 MPa) one. Higher borides inclusions are relevant pinning centers in MgB_2, but they cannot be revealed by X-ray (Figs. 2c, d). In the case of SiC additions the j_c have been increased when there were no notable (which can be detected by X-ray analysis) interaction between MgB_2 and SiC (Figs. 2 a, b). For a SiC-doped material, we also observed the segregation of oxygen (in the places of the matrix where SiC inclusions were absent marked by "A".). However, the structure is much dispersed and rather complicated for analysis. As a synthesis temperature increases, the higher borides content decreases but the segregation of oxygen becomes more pronounced. This could be the reasons for high critical current densities in high and low magnetic fields (see Figs. 1c, f, i, l) and for the existence of two types of optimal technology conditions. The porosity of the materials did not exceed 1 – 3.5 %. The thermal conductivity of HP–synthesized MgB_2–based material with Ti additions was 53 ±2 W/(m×K) at 300 K.

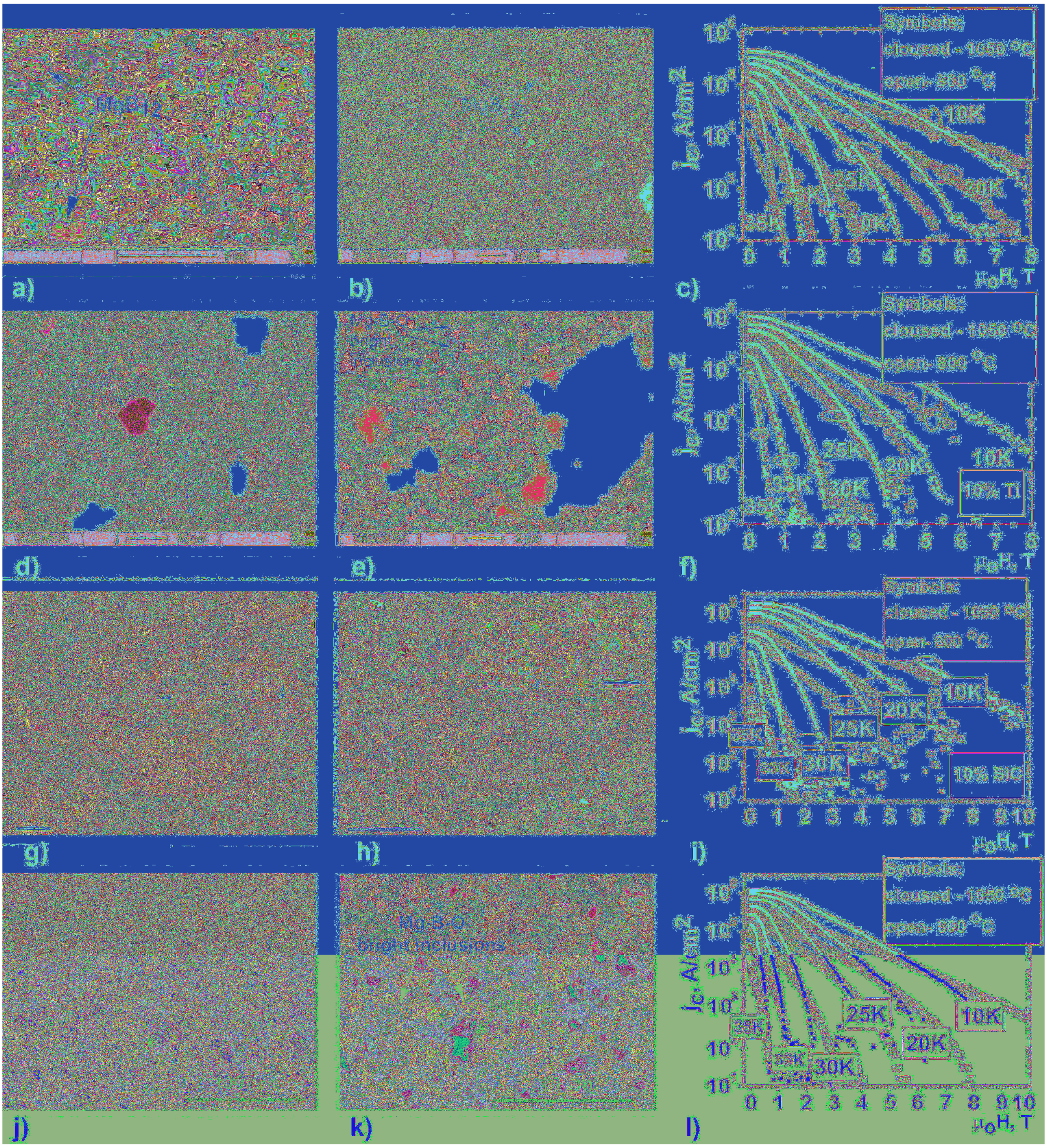

Figure 1. Structures (backscattering electron images – BEI) of samples HP-synthesized under 2 GPa for 1 h from Mg chips and two types of B (H.C. Starck) taken into MgB_2 ratio (a, b, d, e, g, h, j,k) and corresponding dependences of critical current density j_c, on magnetic field, μ_0H (e, f, i, l): from boron type I of average grain size 4 μm and 1.5 % O (a-f, j, k) and (II) <5 μm and 0.66 % O(g, h, i, l);
(a, b) without additions synthesized at 800 °C and 1050 °C, respectively and their j_c (c);
(d, e) with 10 wt.% of Ti additions synthesized at 800 °C and 1050 °C, respectively, and (f) their j_c;
(g, h, j, k) with addition of 10 wt.% of SiC synthesized at 1050 °C from different boron: type I – j, k, type II – g, h; Figs. 1h and 1k show enlarged places of the same samples where SiC is absent in each sample, respectively;
(i, l) dependences of j_c, on μ_0H for the samples (synthesized from type II boron) at 800 °C and 1050 °C with SiC additions (i) and without (l).

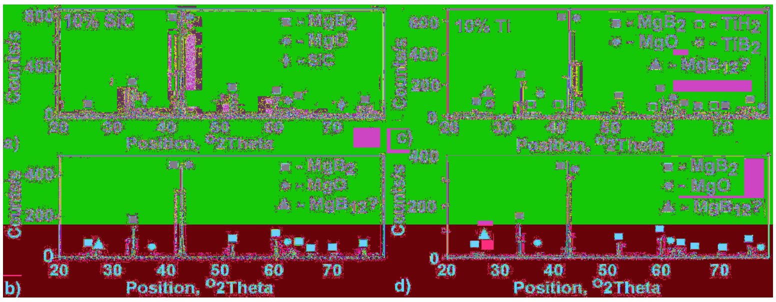

Figure 2. X-ray patterns of the samples synthesized at 2 GPa, 1050 °C, 1 h from Mg chips and amorphous boron (a, b) –from B (II) (<5 μm and 0.66 % O, H.C. Starck) with 10 wt % of SiC (200-800 μm) (a) and without (b); (c, d) – from B(I) (4 μm and 1.5 % O, H.C. Starck) with 10 wt % of Ti (0.8 – 3.3 μm)(c) and without (d).

Figure 3. (a) Upper critical field, H_{c2}, and the field of irreversibility, H_{irr}, as a function of temperature, T, of the synthesized MgB_2- based materials : curves 1-4 – from Mg chips and B(III) (95-97% , 0.8 μm, 1.7 % of O, MaTecK) at 2GPa, 800 °C, 1 h with additions of 10 wt.% Ti (curves 1, 3) and 10 wt.% Zr (curves 2,4) before irradiation (curves 1, 2) and after irradiation by fast neutron fluence of 10^{22} m^{-2} (E > 0.1 MeV) (curves 3,4); curve 5 – from powdered Mg and B (HyperTech) 2GPa, 600 °C, 1 h; **(b, c)** SEM BEI image X-ray pattern of the high-pressure synthesized at 2 GPa, 600 °C, 1 h material from Mg(HyperTech):B(HyperTech)=1:2; where in BEI image(b): D-admixtures of SiC or $CaCO_3$ trapped in material's pores from polishing. The average composition of the area inside square "A" had near the $MgB_{3.1}O_{0.3}$ stoichiometry, (c) Reflexes marked "x" at the X-ray pattern may be assigned to higher borides.

Recently material with extremely high upper critical field, H_{c2}, (Fig. 3, curve 5) and field of irreversibility, H_{irr}, has been high-pressure-synthesized at 600 °C from powders of Mg and B (HyperTech) (Figs. 3 b, c): H_{c2}=15 T at 22 K and H_{irr}=15 T at 18.5 K, which are the highest values ever mentioned in literature (even for the carbon-doped materials). The material contained about 7 wt.% of oxygen, its porosity being 17%.

From response of the transformer devices (in which the secondary winding was fabricated as a SC ring from hot pressed (30 MPa) material) the quenching current of 24000 A and transport j_c of 63200 A/cm^2 at 4.2 K have been determined. The transport j_c was about an order of magnitude lower than the critical value obtained from magnetization experiment ($6 \cdot 10^5$ A/cm^2 at 10 K). This can be explained by the granular structure of the superconductor, when the j_c measured from magnetization is mainly determined by this density in granules but the transport j_c is determined by the properties of intergranular area. At an induced current of ~95% of the critical value the AC loses were about 17 J and power of the losses was about 200 W.

The samples synthesized by us from the boron-enriched compositions (MgB_4 up to MgB_{20}) at 2GPa, 1200 °C, 1 h were superconducting [4], but the highest j_c and transition temperature, T_c near 37 K were demonstrated by the materials (Figs. 4a-e) with near MgB_{12} composition of matrix, which as was shown by TEM-EDX and SEM-EDX (with microprobes of 0.7 nm and 2 nm in diameter, respectively). The Raman spectra of the materials (Fig. 4 f) demonstrated the metal-like behavior, the same as superconductors. We did not reveal an MgB_2 network or greed in these materials, and only areas of about 200 nm in diameter with MgB_2 composition were founded.

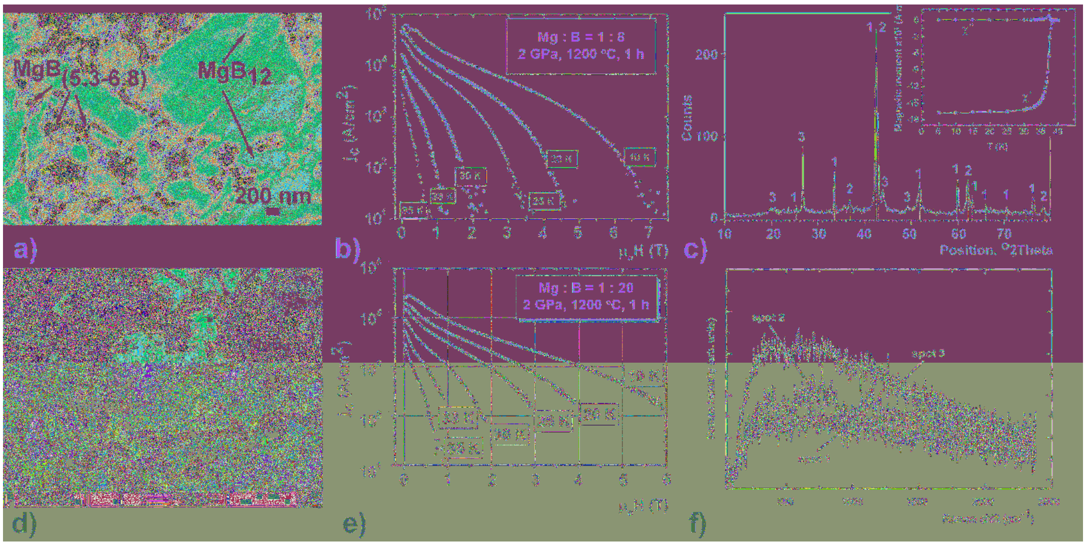

Figure 4. (a, d) structures in BEI and (b, e) dependences of j_c, on μ_0H of the materials high pressure synthesized (2 GPa, 1200 ^oC for 1 h) from Mg chips and B type I (4 μm and 1.5 % O, H.C. Starck) taken in 1:8 (a, b) and 1:20 (d, e) ratios; (c) X-ray pattern of the sample synthesized from 1:8 mixture of the sample shown in Fig.2a (reflexes marked “1” and “2” coincide with those of MgB_2 and MgO, respectively, reflex marked “3” at $2\Theta=26.7^o$ coincides with that of BN), in the upper right corner the dependences of real (χ') and imagined (χ'') parts of resistance on temperature are shown; it should be mentioned that X-ray of the material prepared from the Mg:B=1:20 mixture (shown in Fig. 2d) has the X-ray pattern very similar to that in the case of 1:8 mixture (Fig. 2c); (f) Raman spectrum (at room temperature) of the material synthesized from Mg:B=1:20 mixture.

The Vickers microhardness (H_v) of the material with near MgB_{12} composition was twice as high as that of MgB_2 (25±1.1 GPa and 12.1±0.8 GPa, respectively, at a load of 4.9 N). The inclusions with near MgB_{12} composition in MgB_2 matrix had 35.6±0.9 GPa nanohardness at a 60 mN-load and Young modulus 385±14 GPa.

Conclusions

The effect of oxygen distribution inhomogeneity and presence of higher borides on the critical current density improvement of nanostructural MgB_2 has been revealed. The synthesis temperature and additions can effect the oxygen segregation as well as higher boride formation.

References

[1] C. B. Eom, M.K. Lee, J. H. Choi, L. J. Belenky, X. Song, L.D. Cooley, M.T. Naus, S. Patnaik, J. Jiang, M. Rikel, A. Polyanskii, A. Gurevich, X.Y. Cai, S.D. Bu, S.E. Babcock, E.E. Hellstrom, D.C. Larbalestier, N. Rogado, K.A. Regan, M.A. Hayward, T. He, J.S. Slusky, K. Inumaru, M.K. Haas and R.J. Cava: Nature Vol. 411 (2001), p. 558

[2] X.Z. Liao, A.C. Serquis, Y.T. Zhu, J.Y. Huang, L. Civale, D.E. Peterson, F.M. Mueller and H. Xu: Journal of Applied Physics Vol. 93 (2003), p. 6208

[3] T. A. Prikhna, W. Gawalek, Ya. M. Savchuk, T. Habisreuther, M. Wendt, N. V. Sergienko, V. E. Moshchil, P. Nagorny, Ch. Schmidt, J. Dellith, U. Dittrich, D. Litzkendorf, V. S. Melnikov and V. B. Sverdun: Supercond. Sci. Technol. Vol. 20 (2007), p. S257

[4] T. A. Prikhna, W. Gawalek, Ya. M. Savchuk, A. V. Kozyrev, M. Wendt, V. S. Melnikov, V. Z. Turkevich, N. V. Sergienko, V. E. Moshchil, J. Dellith, Ch. Shmidt, S. N. Dub, T. Habisreuther, D. Litzkendorf, P. A. Nagorny, V. B. Sverdun, H. W. Weber, M. Eisterer, J. Noudem and U. Dittrich: IEEE Transactions on Applied Superconductivity Vol. 19 (2009) p. 2780

doi:10.4028/www.scientific.net/AST.75.167

A Multiband Model for $LaO_{1-x}F_xFeAs$

Gabriela Murguía[a], S. Orozco[b], M. A. Ortiz[c],
R. M. Méndez-Moreno[d] and P. de la Mora[e]
Departamento de Física, Facultad de Ciencias, Universidad Nacional Autónoma de México,
Apartado Postal 21-092, 04021 México, D.F., México
[a]murguia@ciencias.unam.mx, [b]sos@fciencias.unam.mx, [c]maof@fciencias.unam.mx,
[d]rmmv@fciencias.unam.mx, [e]delamora@servidor.unam.mx

Keywords: High Tc Superconductivity, Iron-based Oxypnictide Superconductors, LaOFeAs, Band Overlap.

Abstract. Based on electronic structure calculations using WIEN2k code for the iron oxypnictide $LaO_{1-x}F_xFeAs$ a multi-band model is proposed. Within the BCS framework a generalized Fermi surface with overlapping bands is introduced. s-wave pairing symmetry and different doping values are considered. This model is used to describe some properties of iron-based oxypnictide superconductors as function of the coupling parameter as well as other relevant parameters of the model. In order to get numerical results the experimental data of $LaO_{1-x}F_xFeAs$ with several doping concentrations provide the input of this work.

Introduction

The discovery by Hosono et al [1] of high transition temperature superconductivity (HTSC) in $LaO_{1-x}F_xFeAs$ has triggered interest in the development of transition-metal superconductors. F doping strongly affects the electronic properties of $LaO_{1-x}F_xFeAs$ [2]. The replacement of O^{2-} by F^- in the layered iron-based LaOFeAs (La1111) originates a superconducting transition. In fact it was found that the Fe-As-based compounds become superconductors by electron doping. Some of these materials have transition temperatures up to 55K. The high-temperature superconductivity had been limited to the cuprates, where the charge carriers in these materials are confined to the two dimensional (2D) CuO_2 layers [3]. These layered structures of high-T_c materials suggest that two-dimensional physics is important in the study of HTSC. In the oxypnictides the conduction is also two dimensionally confined to the Fe-As layers. The (La1111) contains a large concentration of magnetic Fe, given the opportunity to study the connexion between magnetism and high critical temperature T_c superconductivity.

Understanding of the electronic structure at the Fermi level can give some useful clues to unravel the fundamental ingredients responsible for the high transition temperature T_c [4]. However, to present the underlying physical process remains unknown. In this context, it seems crucial to study new ideas that use simplified schematic models to isolate the mechanism(s) that generate HTSC.

Pairing symmetry is an important element toward understanding the mechanism of high-T_c superconductivity. From optical measurements it was found that Fe-based superconductors have s-wave symmetry superconductivity [5].

Numerous indications point to the multiband nature of the superconductivity in $LaO_{1-x}F_xFeAs$. Electronic structure calculations using WIEN2k code [6] for the iron oxypnictide $LaO_{1-x}F_xFeAs$ have been done. This code is an all electron full potential-linearized augmented plane wave (FP-LAPW) method based on density functional theory, showing overlapping energy bands at the Fermi level. The agreement of the multiband model with experimental findings, suggests that Fe-based superconductors are multiband systems [5].

Based on the WIEN2k code calculations mentioned, a simple model with generalized Fermi surface topologies via band overlapping is proposed in this work. This model was successfully employed to describe cuprate superconductors [7]. It confirms the idea that the tendency toward superconductivity can be enhanced when the Fermi level lies at, or close to, the energy of a singularity in the density of states (DOS).

Two-dimensional generalized Fermi surface topologies via band overlapping are used as a model for HTSC in this work. As a prototype of multiband superconductors a two overlapping band model is considered. This model, within the BCS framework, can lead to higher T_c values than those expected from the traditional phonon barrier. The energy band overlapping modifies (increases) the DOS near the Fermi level allowing the high T_c values observed. For physical consistency, an important requirement of the proposed model is that the band overlapping parameter is not larger than the cutoff Debye energy, E_D. The model here proposed will be used to describe some properties of iron-based oxypnictide superconductors in terms of the doping and the parameters of the model.

The Model

We begin with the famous gap equation

$$\Delta(k') = \sum_k V(k,k')\Delta(k)\frac{\tanh(E_k/2k_BT)}{2E_k}, \tag{1}$$

in the weak coupling limit, with $V(k,k')$ the pairing interaction, k_B is the Boltzman constant, and $E_k^2 = \varepsilon_k^2 + \Delta_k^2$, where $\varepsilon_k = \hbar^2k^2/2m$ are the self-consistent single-particle energies.

In the s-wave approximation, for the electron-phonon interaction, we have considered $V(k,k') = V_0$, with V_0 a constant when $|\varepsilon_k|$ and $|\varepsilon_{k'}| \le E_D = k_BT_D$ and 0 elsewhere. As usual the attractive BCS interaction is nonzero only for unoccupied orbitals in the neighborhood of the Fermi level E_F. The superconducting order parameter, $\Delta(k) = \Delta(T)$, nulls for $T = T_c$.

With these considerations we propose a generalized Fermi surface, such that the Fermi sea consists of two overlapping bands. As a particular distribution with anomalous occupancy in momentum space the following form for the proposed Fermi sea has been considered

$$n_k = \Theta(\gamma k_F - k) + \Theta(\gamma k_F - k)\Theta(k - \beta k_F), \tag{2}$$

with k_F the Fermi momentum and $0 < \beta < \gamma < 1$. In order to keep the average number of electron states constant, the parameters are related in the 2D system by the equation $2\gamma^2 - \beta^2 = 1$, then only one of the parameters is independent, say γ. The distribution in momentum induces one in energy, $E_\beta < E_\gamma$ where $E_\beta = \beta^2E_F$ and $E_\gamma = \gamma^2E_F$. We require that the band overlapping be of the order or smaller than the cutoff (Debye) energy, which means $(1-\gamma^2)E_F \le E_D$. The minimum γ^2 value consistent with our model is $\gamma_D^2 = 1 - E_D/E_F$. While $E_F - E_\gamma \le E_D$, implies that the energy difference between the anomalously occupied states must be provided by the material itself.

In the last framework the summation in Eq. 1 is changed to an integration which is done over the (symmetric) generalized Fermi surface defined above. One gets

$$1 = \frac{\lambda}{2}\int_{E_\gamma - E_D}^{E_\gamma + E_D} \tanh\left(\frac{\sqrt{\Xi_k}}{2k_BT}\right)\frac{d\varepsilon_k}{\sqrt{\Xi_k}} + \frac{\lambda}{2}\int_{E_\beta}^{E_F} \tanh\left(\frac{\sqrt{\Xi_k}}{2k_BT}\right)\frac{d\varepsilon_k}{\sqrt{\Xi_k}}. \tag{3}$$

In this equation $\Xi_k = (\varepsilon_k - E_F)^2 + \Delta(T)^2$, the coupling parameter is $\lambda = V_0 D(E)$, with $D(E)$ the electronic density of states, which will be taken as a constant for the $2D$ system in the integration range.

The two integrals correspond to the bands proposed by Eq. 2. The integration over the surface at E_γ in the first band, is restricted to states in the interval $E_\gamma - E_D \le E_k \le E_\gamma + E_D$. In the second band, in order to conserve the particle number, the integration is restricted to the interval $E_\beta \le E_k \le E_F$, if $E_\gamma + E_D > E_F$, with $E_\beta = (2\gamma^2 - 1)E_F$.

The critical temperature is introduced via the Eq. 3 at $T = T_c$, where the gap becomes $\Delta(T_c) = 0$. At this temperature Eq. 3 is reduced to

$$1 = \frac{\lambda}{2}\int_{E_\gamma - E_D}^{E_\gamma + E_D} \tanh\left(\frac{\varepsilon_k - E_F}{2k_B T_c}\right)\frac{d\varepsilon_k}{\varepsilon_k - E_F} + \frac{\lambda}{2}\int_{E_\beta}^{E_F} \tanh\left(\frac{\varepsilon_k - E_F}{2k_B T_c}\right)\frac{d\varepsilon_k}{\varepsilon_k - E_F}, \tag{4}$$

which will be numerically evaluated. The last equation relates T_c to the coupling constant λ and to the anomalous occupancy parameter γ^2. This relationship determines the γ^2 values which reproduces the critical temperature, in the weak coupling region, of some materials, like the ones of the oxypnictide family.

At $T = 0K$, Eq. 3 will also be evaluated:

$$1 = \frac{\lambda}{2}\left[\sinh^{-1}\frac{E_D - (1-\gamma^2)E_F}{\Delta_0} + \sinh^{-1}\frac{(1-\gamma^2)E_F + E_D}{\Delta_0} + \sinh^{-1}\frac{2E_F(1-\gamma^2)}{\Delta_0}\right], \tag{5}$$

where $\Delta(0) = \Delta_0$.

The model presented in this section can be used to describe high-T_c iron oxypnictide superconductors. In any case a specific material must be selected to introduce the available experimental data. Ranges for the coupling parameter λ in the weak coupling region, and the overlapping parameter γ^2, consistent with the model and the experimental values of Δ_0 and E_F, can be obtained for each material. The relationship between the characteristic parameters will be obtained for Fe-As-based compounds at several doping concentrations x. In order to get numerical results the model will be used to describe the iron oxypnictide $LaO_{1-x}F_xFeAs$.

Results and discussion

We have done electronic structure calculations for the iron oxypnictide $LaO_{1-x}F_xFeAs$ using the WIEN2k code [6] which is an all electron full potential-linearized augmented plane wave (FP-LAPW) method based on density functional theory (DFT). The generalized gradient approximation of Perdew et al [8] was used for the treatment of the exchange-correlation interactions. For the number of plane waves the used criterion was R_{MT}^{min} (muffin tin radius) × K_{max} (for the plane waves) = 9. The number or k-points used was $12 \times 12 \times 25$. The charge density criterion with a threshold of 10^{-4} was used for convergence.

Fig. 1 shows the energy band structure calculated for $LaO_{1-x}F_xFeAs$ for $x = 0$ and $x = 0.10$, which is near the value of the optimally doped case ($x = 0.11$). It shows that there are five bands at the Fermi level. The density of states calculations indicate that they have almost no contribution from La, O and As, that is they have almost total Fe character. They have almost no dispersion in the c-direction (the corresponding Fermi surfaces (FS) are vertical tubes), thus electrically the material is 2D. The 3 bands at right hand side (near Γ), are almost full (hole like) and their corresponding FS are at the centre of the reciprocal cell (Γ-Z). The other two bands, the left hand side bands near M, are almost empty (electron like), their FS are at the corners of the cell (M-A), these bands become degenerate at the sides of the cell (X=1/2), along the M-Γ direction. The hole like bands have DOS at the Fermi level that diminish with energy, while the electron like are mainly constant. Substituting O for F adds electrons and the Fermi level rises. Notice how the bands overlap near the Fermi level. For the doped case, the Fermi level has been risen as compared with the undoped case.

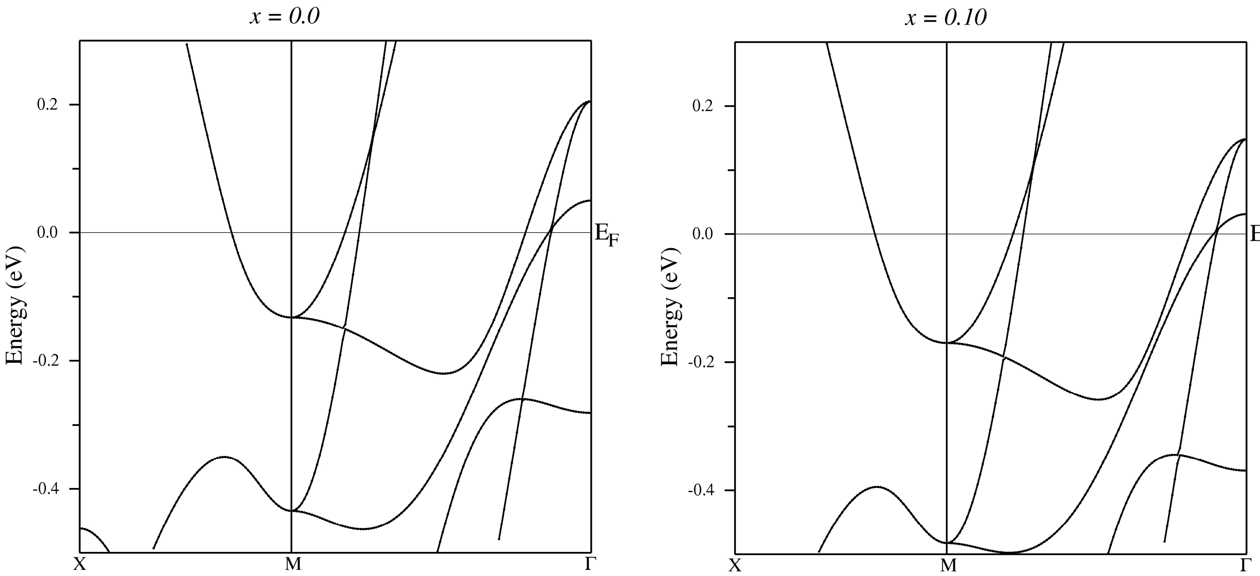

Fig. 1. The energy band structure for $LaO_{1-x}F_xFeAs$ for $x = 0$ (left) and $x = 0.10$ (right). Along the vertical axis, the energy is measured respect to the Fermi level E_F. It can be noticed how the bands overlap near the Fermi level, which rises for the doped case in comparison with the undoped one.

Within the BCS framework, based on the band structure obtained at the Fermi level, we presented an overlapping band model with s-wave symmetry to describe high-T_c oxypnictide superconductors. We have used anomalous Fermi occupancy in the 2D fermion gas. The anomaly is introduced via a generalized Fermi surface with two bands as a prototype of bands overlapping. Experimental values of T_c for different doping values x and Eq. 4 of our model were used to obtain numerical results of the coupling parameter λ as function of the overlapping parameter γ^2. Evaluating numerically Eq. 5 we got λ as function of γ^2 considering an specific gap value Δ_0. In order to get these numerical results, the Fermi energy value was taken from the reported data in reference [9], while for the Debye energy we used the reported value in [10]. The used gap value was calculated for $T_c = 26\text{K}$ in order to have $2\Delta_0 / k_B T_c \approx 4.41$, which is in the range of the experimental reported data [10].

In Fig. 2, the coupling parameter λ as function of γ^2 obtained from Eq. 4 for the optimal doped case $x = 0.11$ (upper plot) and for the overdoped case $x = 0.14$ (lower plot), is depicted. In each case the input for the critical temperature were the experimental values of $T_c = 26.8\text{K}$ and $T_c = 14.0\text{K}$ respectively. In both, optimal dopping and overdoped cases, the values of the coupling parameter λ are in the weak coupling region for the γ^2 values which satisfy the conditions of our model. The minimum overlapping parameter γ^2 for the optimal dopping corresponds to $\gamma_D^2 = 0.705$. The minimum values obtained of the coupling parameter are $\lambda_{\min} = 0.27$ at $\gamma^2 = 0.845$ for optimal dopping, and $\lambda_{\min} = 0.20$ at $\gamma^2 = 0.85$ for the overdoped case, being consistent with the value of $\lambda = 0.21$ reported using density functional perturbation theory [11].

Fig. 3 shows the coupling parameter λ as function of the overlapping parameter γ^2 obtained through Eq. 5 for the gap value $\Delta_0 = 4.94\text{meV}$. It shows that consistently, for several band overlapping parameter values, it is possible to ensure a weak coupling near the optimal doping. The minimum coupling parameter obtained in this case is $\lambda_{\min} = 0.285$, which corresponds to an overlapping parameter $\gamma^2 = 0.91$. Notice that the values obtained for the coupling parameter λ are consistent with those shown in Fig. 2 for the optimal doped case, within the range of values of γ^2 shown in Fig. 3.

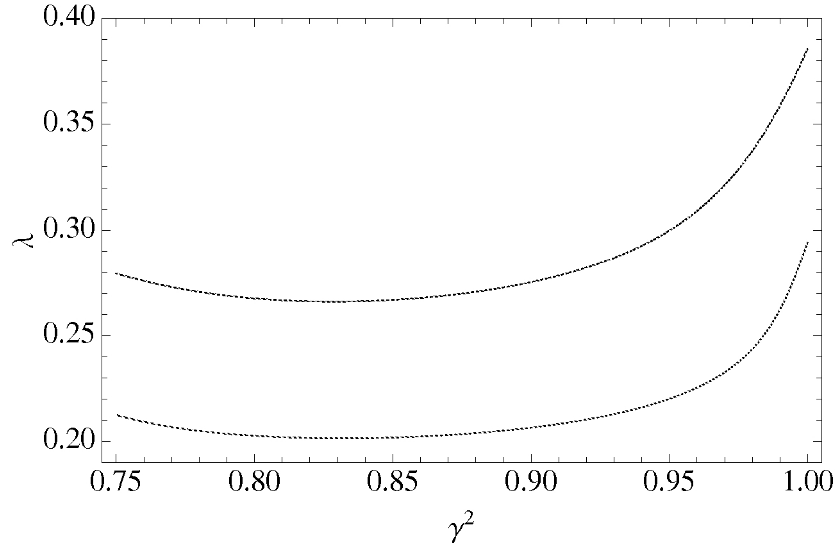

Fig. 2. The coupling parameter λ as function of the overlapping parameter γ^2. The upper plot corresponds to the optimally doped case of $x = 0.11$ for the experimental value of T_c=26.8K. The lower plot corresponds to the overdoped case $x = 0.14$ for the experimental value of T_c=14.0K.

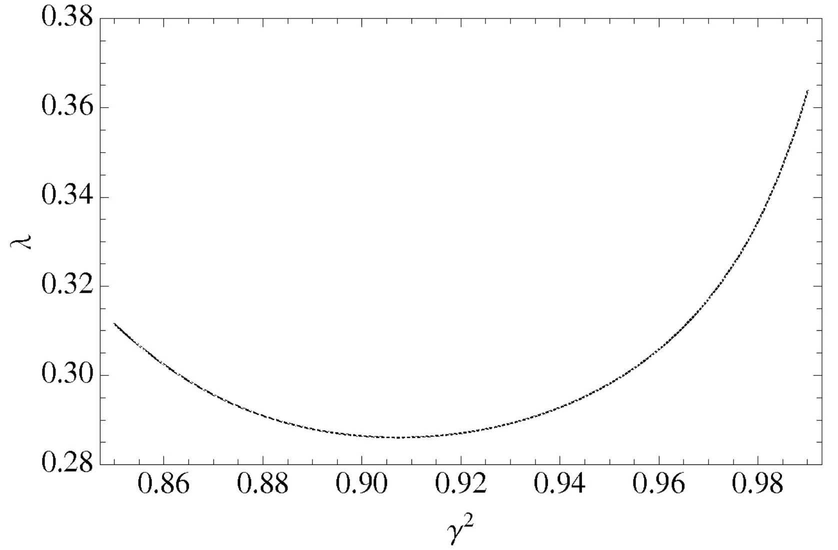

Fig. 3. The coupling parameter λ as a function of the overlapping parameter γ^2. The gap value of $\Delta_0 = 4.94\text{meV}$ for the optimal doped case was used. Notice that for several γ^2 values it is possible to ensure a weak coupling near the optimal doping $x = 0.11$.

In conclusion, we presented an overlapping band model with s-wave symmetry to describe high-T_c oxypicnitide superconductors within the BCS framework. With the available experimental data, we presented numerical results for $LaO_{1-x}F_xFeAs$. We have used a model with anomalous Fermi occupancy and s-wave pairing in the 2D fermion gas. The anomaly is introduced via a generalized Fermi surface with two bands as a prototype of bands overlapping. The band overlapping allows the improvement of the results obtained within BCS theory, overcoming the phonon barrier for T_c and the $R = 2\Delta_0 / k_B T_c = 3.52$ value. The experimental values of T_c and Δ_0 are consistent with our results in the weak coupling regime, in a scheme in which the electron-phonon interaction is the relevant high-T_c mechanism i.e., the energy scale of the anomaly $(1-\gamma^2)E_F$ is of the order of the Debye energy. The Debye energy is then the overall scale that determines the highest T_c and gives credibility to the model because it requires an energy scale accessible to the lattice.

References

[1] Y. Kamihara, T. Watanabe, M. Hirano and H. Hosono: J. Am. Chem. Soc. 130, 3296 (2008).

[2] L. Wang et. al.: Phys. Rev. B 80, 094512 (2009).

[3] D.R. Harshman and A.P. Mills: Phys. Rev. B 45, 10684 (1992).

[4] D.J. Singh: Physica C 469, 418 (2009).

[5] W.Z. Hu, Q.M. Zhang and N.L. Wang: Physica C 469, 545 (2009).

[6] P. Blaha, K. Schwarz, G.K.H. Madsen, D. Kvasnicka, and J. Luitz, *WIEN2K, An Augmented Plane Wave + Local Orbitals Program for Calculating Crystal Properties*, edited by K. Schwarz, Techn. Universität Wien, Austria (2001), ISBN 3-9501031-1-2.

[7] M. Moreno, R.M. Méndez-Moreno, M.A. Ortiz and S. Orozco: Mod. Phys. Lett. B 10, 1483 (1996).

[8] J.P. Perdew, S. Bruke and M. Ernzerhof: Phys. Rev. Lett. 77, 3865 (1996).

[9] D.J. Singh and M.-H. Du: Phys. Rev. Lett. 100, 237003 (2008).

[10] G. Mu, X. Zhu, L. Fang, L. Shan, C. Ren and H.-H. Wen: Chin. Phys. Lett. 25, 2221 (2008).

[11] L. Boeri, O.V. Dolgov and A.A. Golubov: Phys. Rev. Lett. 101, 026403 (2008).

doi:10.4028/www.scientific.net/AST.75.173

Stabilization of Superconductivity in Pure and C-Intercalated 1T-TaS$_2$ Synthesised Under High Pressure

SELLAM A.[1], GILIOLI E.[2], ROUSSE G.[1], KLEIN Y.[1], PORCHER, F. [3], LE GODEC Y.[1], MEZOUAR M. [4], D'ASTUTO M.[1], TAVERNA D.[1], LOUPIAS G.[1], SHUKLA A.[1], and GAUZZI A.[1]

[1] Institut de Minéralogie et de Physique des Milieux Condensés, Université Pierre et Marie Curie-Paris 6 and CNRS, Paris, France

[2] Istituto Materiali per Elettronica e Magnetismo, CNR, Parma, Italy

[3] Laboratoire Léon Brillouin, CEA and CNRS, Saclay, France

[4] European Synchrotron Radiation Facility, Grenoble, France

[a]amine.sellam@upmc.fr, [b]andrea.gauzzi@upmc.fr

Keywords: superconductivity, charge density wave, transition metal dichalcogenides, pressure effects.

Abstract. In order to elucidate the origin of the interplay between charge density wave (CDW) and superconductivity in 1T-TaS$_2$, we have synthesized powder samples of pure and C-intercalated 1T-C$_x$TaS$_2$ by means of a multi-anvil high-pressure synthesis method. We have found that single-phase samples are obtained in the 2-6 GPa range at 400 °C and for x=0-0.3. The structural, magnetic and transport properties of all samples have been investigated by means of neutron and x-ray diffraction, dc magnetization and dc electrical resistivity. For all x values including x=0, the data show that the CDW phase is suppressed concomitant to an abrupt onset of superconductivity, with T_c=3.2 K for x=0. The T_c value turns out to be weakly dependent on x, with a maximum T_c=3.8 K for x=0.2. This onset is accompanied by a crossover of magnetic behavior from paramagnetic Pauli-like to paramagnetic Curie-Weiss-like with effective moment $\mu \approx 1.2\ \mu_B$/Ta, which suggests that a ionic picture is suitable for the superconducting phase, but not for the CDW phase. The analysis of the dependence of the *a* and *c* lattice parameters upon *x* as well as upon the synthesis conditions shows that the onset of superconductivity is mainly ascribed to unusual changes of the unit cell induced by the high-pressure synthesis. Specifically, the *ex-situ* lattice parameters exhibit a significantly larger *c*-axis parameter and a shrinking of the *a*-axis parameter stabilized by the high-pressure synthesis route. We argue that the above suppression of the CDW phase is induced by a broadening of the relevant $5d(t_{2g})$ band which stabilizes the metallic and superconducting phases. This scenario suggests that the strength of the electronic correlations are the main control parameter of the CDW-superconductivity competition in 1T-TaS$_2$.

Introduction

A large number of experimental studies show that several Transition Metal Dichalcogenides (TMD) MX_2 (M=Ti, Nb or Ta, X=S or Se) exhibit an interesting interplay between superconductivity (SC) and charge density wave (CDW) [1,2]. This feature typically concerns the so called 1T and 2H polytypes characterised by a stacking of triangular layers of MX_6 octahedra or trigonal prisms, respectively [3,4]. This issue has recently attracted a great deal of interest following recent experimental reports showing that the two ground states may coexist, e.g. in intercalated 1T-Cu$_x$TiSe$_2$ [5] and 1T-TaS$_2$ under high pressure [6]. This suggests that the microscopic mechanism of both states may be the same but this mechanism remains controversial. Two competing electron-phonon and excitonic scenarios have been proposed by some authors [6,7]. The latter scenario traces back to early proposals by Little [8] and Ginzburg [9] in the '60. It was suggested that TMDs would be the prototype systems for hosting excitonic superconductivity by virtue of their layered structures made of metallic layers adjacent to highly polarisable van der Waals gaps [10]. This scenario would be relevant to the search for new superconductors with high critical temperatures T_c. However, despite intense research, no conclusive studies have been hitherto reported. In the case of $TiSe_2$, both excitonic and phonon softening mechanisms have been invoked [7,11]. On the other hand, in the case of $NbSe_2$, recent *ab initio* calculations [12] suggest that the CDW mechanism is of electron-phonon type and the CDW is triggered when the wave vector of a given soft phonon is commensurate with the Brillouin zone. In order to elucidate the above points, high pressure and chemical intercalation have been employed recently as control parameters of the interplay between SC and CDW. Notable is the discovery of the CDW suppression and concomitant enhancement of SC induced by Cu intercalation in Cu_xTiSe_2 [5]. A similar behaviour induced by pressure has been reported on 1T-TaS_2 [6]. In view of these results, it would be important to establish the structure-property relationships that may account for the stabilisation of superconductivity induced by both intercalation and pressure. In order to address this point, in this work we have employed high-pressure synthesis to stabilise new intercalated 1T-TaS_2 phases. Specifically, we have succeeded in the synthesis of C-intercalated 1T-C_xTaS_2 with x=0-0.2. Contrary to our expectations, we have found that the main control parameter of the CDW-superconductivity competition is not the intercalant concentration x but the changes of lattice parameters induced by the high-pressure synthesis methods.

Experimental

The samples studied in this work have been prepared using a two-step route. First, high-purity precursors of 1T-TaS_2 powders were prepared using a standard solid state synthesis method as described in detail elsewhere [13]. In summary, stoichiometry amounts of high-purity powders of metallic Ta (99.99%, Alfa Aesar) and of S (99.98 %, Sigma Aldrich) in excess of 0.15g/mole [14] were thoroughly grinded in an agate mortar, pressed into pellets and introduced into sealed quartz tube under a vacuum better than 5×10^{-5} mbar. The pellets were thermally treated at 950 °C for several days and then at 750 °C for 3 days. Typical X-ray diffractograms taken using a commercial Philips X'pert Cu K_α diffractometer in the Bragg-Brentano geometry show that the as-prepared samples typically are single-phase and no significant amounts of impurity phases were detected.

These precursors were subsequently used for the high-pressure synthesis step using two types of multi-anvil high-pressure apparatus in both Walker-type [15] and Paris-Edinburgh [16] anvil configurations. Both configurations enable to achieve quasi-hydrostatic pressure and uniform temperature conditions up to 16 or 25 GPa, respectively, and up to 1500 °C and comparable results were obtained. The main difference between the two configurations is the much larger sample volume ~500 mm^3 obtained using the former configuration as compared to the volume of ~20 mm^3 obtained using the latter. Such larger sample volume is required for the neutron diffraction measurements described below. In our case, high pressure synthesis presents the advantage of stabilising new intercalated phases [17] not stable at ambient pressure conditions and of ensuring a good control of the sulphur stoichiometry thanks to the use of sealed high-pressure cells.

In order to achieve C intercalation, the above precursor powders were thoroughly mixed and grinded with stoichiometric amounts of very fine powder (grain size ~27-30 μm) of high-purity graphite (Polysciences, 99.9%). Such mixed powder was used for the high pressure synthesis at 2, 4 or 6 GPa and at 400 °C during 90 min followed by a quenching of the temperature and by a slow release of pressure. For the HP synthesis, the samples we used a large volume multi-anvil press.

The nuclear structure of the samples was studied in detail by means of high resolution neutron powder diffraction at the high-resolution powder diffractometer 3T2 beamline of the LLB (λ=1.54 Å). The samples were studied at room temperature, 140 K, i.e. below the CDW transition temperature, T_{CDW}=180-230 K, and at low temperature (8 K). dc magnetisation and dc electrical resistivity were measured as a function of temperature using a commercial Quantum Design SQUID magnetometer and by a commercial Quantum Design Physical Property Measurement System, respectively, in the 2-300 K range.

In order to compare the *ex-situ* structural properties of the samples synthesized under high pressure with the structural changes induced at equilibrium under high pressure, the precursor powder of 1T-TaS_2 was measured at room temperature by means of *in situ* high pressure x-ray diffraction in the Debye-Scherrer geometry using synchrotron x-ray radiation at the ID27 beamline of the ESRF. For this experiment, we employed a Paris-Edinburg press at pressure ranging from 1 to 9 GPa.

Results

Synthesis and magnetic properties of the 1T-TaS_2 precursors

In the left panel of Fig. 1 we report a typical x-ray diffractogram of the 1T-TaS_2 precursor synthesised using the standard solid state synthesis method described above. One notes than no sizable amounts of secondary phases are detected. The *a* and *c* lattice parameters were determined using Le Bail fit of the experimental spectrum as described in detail elsewhere [18]. The good quality of these diffractograms enabled us to obtain an uncertainty better than ±0.001 Å.

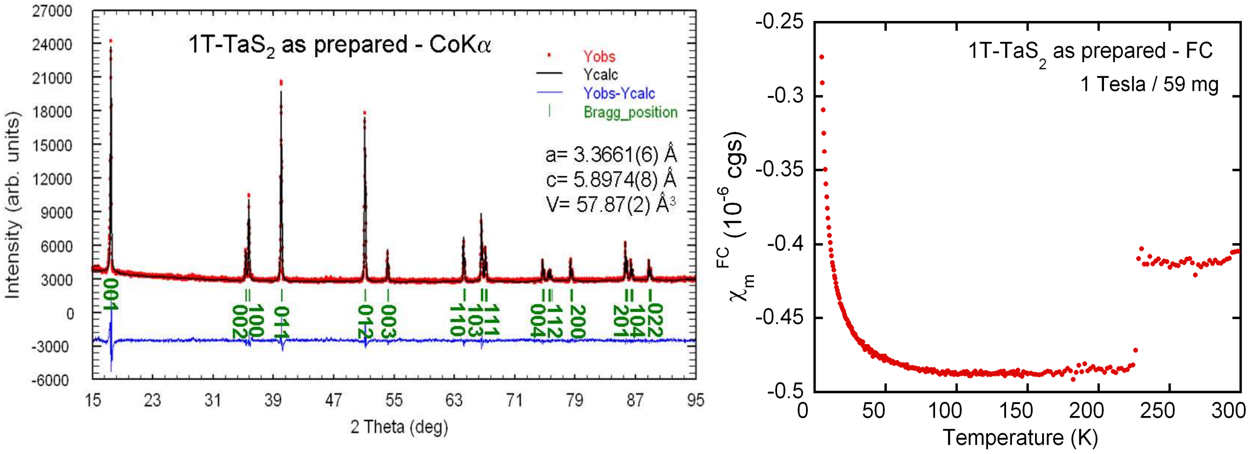

Figure1. Left: Experimental and calculated x-ray diffraction spectrograms of the as-prepared precursor of 1T-TaS_2 used for the high-pressure synthesis of the pure and C-intercalated samples. Right: field-cooling (FC) magnetic susceptibility of the above sample in a field of 1 T. Note the drop of the susceptibility corresponding to the non-commensurate to commensurate charge density wave transition at about 230 K.

In the left panel of Figure 1, we report of the T-dependent magnetic susceptibility of the as-prepared precursor samples. This measurement is in a very good agreement with previously reported results [13], thus confirming the high-quality of the precursors used for the high pressure synthesis. Notable is the small value of the susceptibility of 0.1x10^{-6} emu/ œrsted mole below the critical temperature corresponding to the non-commensurate to commensurate CDW transition. Its value is T_{CDW}~225 K for the field-cooling curve, to be compared to the value T_{CDW}~180 K reported previously for the zero-field curve [13]. The hysteresis corresponding to this difference confirms the first-order nature of the transition.

Structural and magnetic properties of the C-intercalated 1T-C_xTaS_2 samples synthesized under high-pressure

We shall now present the results obtained on the C-intercalated samples synthesized under high pressure. In the left panel of Figure 2, we report the *ex situ* a and c lattice parameters obtained using the Le Bail fit of the x-ray diffractograms mentioned above. Notable are the abrupt changes of both parameters as compared to those of the precursor sample even without intercalation, i.e. for $x = 0$. Specifically, the c-axis undergoes an unusual expansion whilst the a axis shrinks. As a result, the unit cell volume of the HP sample is smaller than that of the pristine sample. Second, we observe a monotonic increase of the c axis with x in the whole range studied up to x=0.3, whilst the a axis displays a negligible dependence. Both trends confirm the effectiveness of the intercalation process, which tends to increase the interlayer distance, as expected and consistently with previous results reported by Morosan *et al.* [5] on the Cu intercalation of the isostructural compound $TiSe_2$.

In the right panel of Figure 2, we report a summary of the superconducting properties measured *ex-situ* on the above series of samples. In agreement with the previous effects of high-pressure synthesis on the lattice parameters, it is noted that all samples synthesised under high pressure included the pristine (x=0) sample are superconductors. Superconductivity is found at T_c=3.0 K for x=0 and then slightly increases with x up to a maximum of T_c=3.8 K for x=0.2 and then decreases again down to 3.0 K for higher x values. This clearly shows that the main effect on the competition between CDW and superconductivity is caused by the structural changes stabilised by the high-pressure synthesis rather than by C intercalation. Though the effects of intercalation observed in our C-intercalated samples are very similar to those observed in Cu-intercalated $TiSe_2$ and the T_c values are also similar.

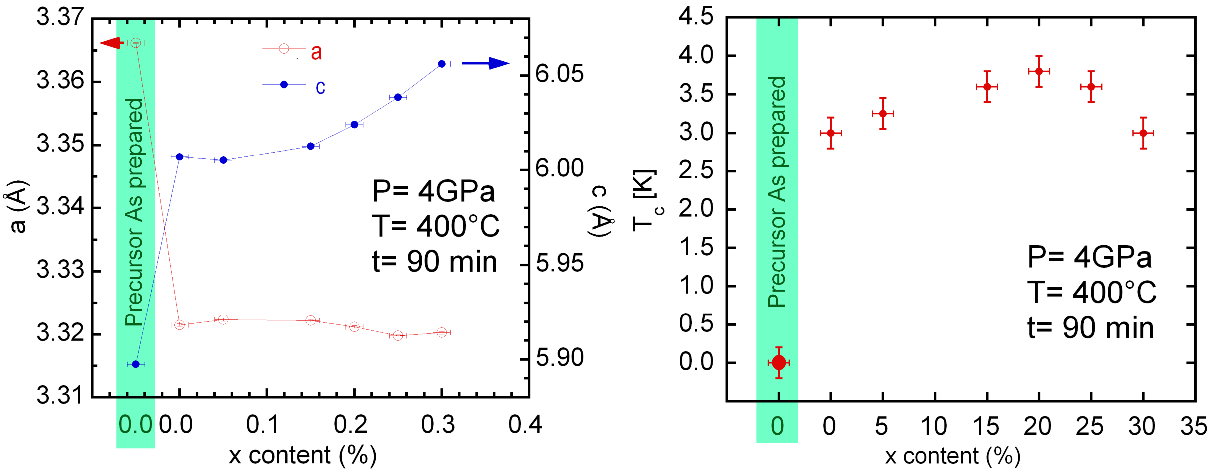

Figure 2. Left panel: Dependence of the *ex situ* cell parameters of the 1T-C_xTaS_2 samples synthesised under high-pressure as compared to those of the precursor. Right panel: dependence of the superconducting critical temperature T_c on x for the same samples as before.

Structural properties of pristine 1T-TaS_2 synthesized under high pressure

In order to investigate in detail the structural changes induced by the high-pressure synthesis, we have measured both the pure 1T-TaS_2 sample before and after the high-pressure synthesis step at 2, 4 and 6 GPa at different temperatures. Figure 3 summarizes the changes of the lattice parameters induced by the high pressure synthesis. From this figure, one notes that high pressure synthesis at 2 GPa is sufficient to stabilise the aforementioned expansion and shrinking of the c and a lattice parameters, respectively, whilst higher pressures do not modify the lattice parameters further. We then expect than even lower pressures may be sufficient to stabilize these changes. As to the effects of temperature, we notice a conventional [19] temperature dependence of such elongated unit cell at low temperatures. Thus, we conclude that this unit cell corresponds to a metastable 1T-TaS_2 phase stabilised by high pressure synthesis at 2 GPa or higher. This metastable phase is characterised by an elongated *c* axis parameter and by a shrinked *a* axis parameter as compared to the pristine phase synthesized under ambient pressure conditions.

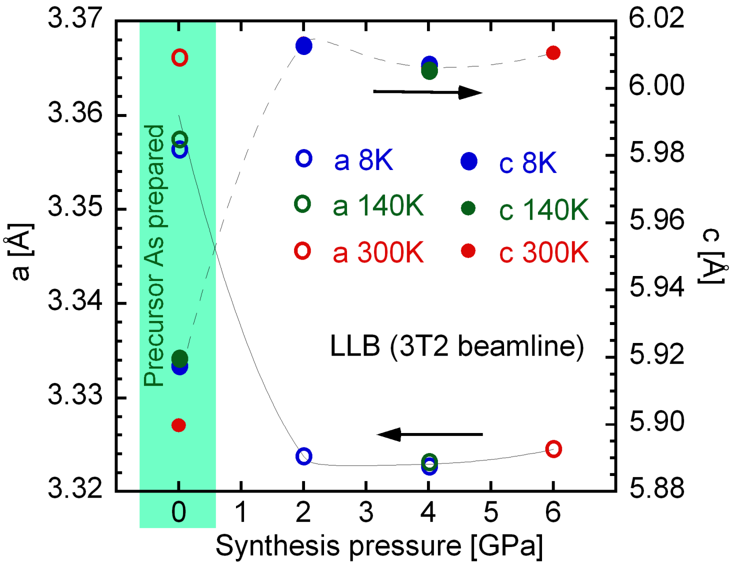

Figure 3. *Ex situ a* and *c* axis cell parameters of pure 1T-TaS_2 before and after high pressure synthesis as a function of pressure during the synthesis. Data are taken at different temperatures. Error bars are smaller than symbols.

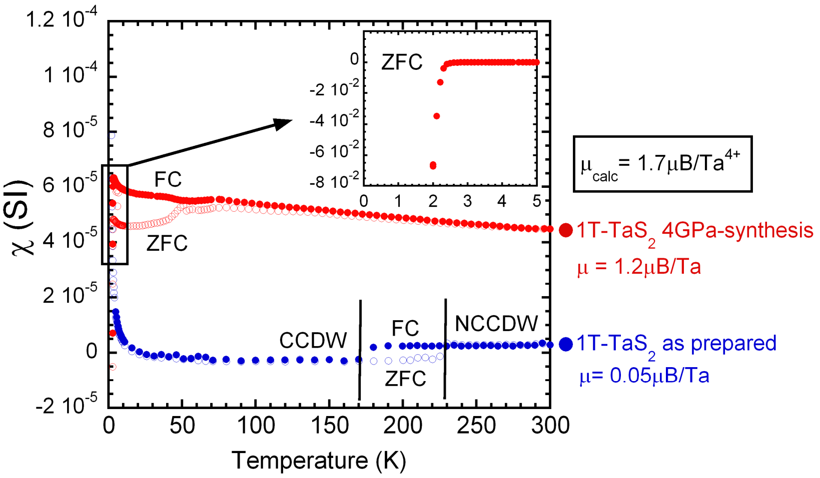

Figure 4. Ex-situ magnetic response of 1T-TaS_2 before (blue) and after (red) high pressure synthesis. ZFC and FC denote zero-field- and field-cooling curves.

These structural changes are accompanied by a suppression of the CDW phase concomitant to a stabilisation of the superconducting phase. A further characteristic feature of such metastable phase is a radically different magnetic response as compared to that of the pristine phase stable at ambient pressure conditions. As shown in Fig. 4, the metastable superconducting phase displays a paramagnetic Curie-Weiss-like behaviour in the whole temperature range 2-300 K studied with negligible Weiss constant ($\theta \approx 0$) and a sizable effective moment $\mu \approx 1.2\ \mu_B$/Ta, comparable to the value μ □$\approx 1.76\ \mu_B$/Ta, expected for a free Ta^{4+} ion within a purely ionic picture. This contrasts the paramagnetic behavior reported previously charcaterised by a much lower susceptibility value, which is rather consistent with a Pauli-like model for free carriers. A support of a picture of localized carriers for the superconducting metastable phase synthesized under high pressure is provided by dc resistivity measurements. Representative results of this study for the sample synthesized at 4 GPa are reported in Figure 5. In this figure, one notes an upturn of the resistivity at low temperatures preceding the superconducting transition in agreement with a picture of localized carriers. Further studies on single crystals synthesized under high pressure would be required to confirm this scenario.

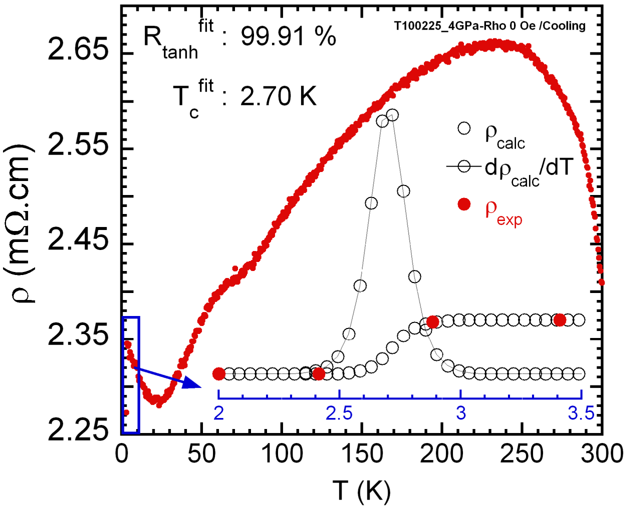

Figure 5. dc electrical resistivity curve of the ex-situ ample of 1T-TaS_2 synthesised at 4GPa. Inset: detail of the transition region and of the derivative of this curve which put into evidence the narrow transition. Dots indicate experimental points, while the solid line is an interpolation of the experimental points.

High-pressure in-situ X-ray diffraction study of pristine 1T-TaS2:

The above results raise the question of whether the superconducting properties observed *ex situ* in the 1T-TaS_2 samples synthesised under high pressure are the same as those observed *in situ* by Sipos *et al.* under high pressure on 1T-TaS_2 single crystls grown at ambient pressure conditions In order to address this question, we have carried out an *in situ* x-ray diffraction study under high pressure on the precursor sample of 1T-TaS_2 using synchrotron radiation. Figure 8 summarizes the dependence of the *a* and *c* lattice parameters in the 1-9 GPa range. This dependence shows a conventional decrease of both parameters with pressure. This contrasts our previous observation of *c*-axis expansion in the *ex situ* samples synthesised under high pressure, thus confirming our conclusion on the stabilisation of a metastable phase with elongated unit cell along the *c*-axis.

Conclusions

In conclusion, we have studied the competition between CDW and superconductivity in 1T-TaS_2 by investigating the structural, magnetic and transport properties of pure and C intercalated powder samples synthesised under high pressure. The main results of our work is the observation of a metastable phase of 1T-TaS_2 with elongated *c*-axis parameter stabilised by high pressure synthesis at 2 GPa or higher. The structural changes stabilised by high pressure synthesised are concomitant to the suppression of the CDW phase and to the abrupt onset of superconductivity with T_c=3.0 K. The appearance of superconductivity is accompanied by a crossover from a paramagnetic Pauli-like behaviour to a Curie-Weiss-like with an effective moment per Ta ion comparable with the value expected for the free Ta^{4+} ion. This supports a ionic picture for the 5d electron of the metastable superconducting phase which is corroborated by the evidence of incipient carrier localisation at low temperature preceding the superconducting transition given by electrical resistivity measurements. In addition, we have succeeded in synthesising C-intercalated samples under high pressures with x up to 0.3. We have found that C intercalation slightly enhances T_c up to a maximum of 3.8 K for x=0.2. The resulting dome-shaped T_c-x phase diagram is similar to that previously reported for Cu intercalated $TiSe_2$. Finally, our *in situ* x-ray diffraction study of pure 1T-TaS_2 under high pressure up to 9 GPa shows a conventional monotonic decrease of both a and c axis lattice parameters with pressure. This contrasts the anomalous c axis expansion observed *ex situ* in the samples synthesised under high pressure. This difference suggests that the superconducting properties observed *in situ* under high pressure may reflect a different superconducting phase. In order to elucidate this point, further studies on single crystals synthesised under high pressure would be required to unveil the intrinsic transport properties of the metastable superconducting phase stabilised using high pressure synthesis.

We thank M. Calandra and F. Mauri for useful discussions and acknowledge C. Petit and I. Lisiecki for their collaboration in the dc electrical resistivity measurements.

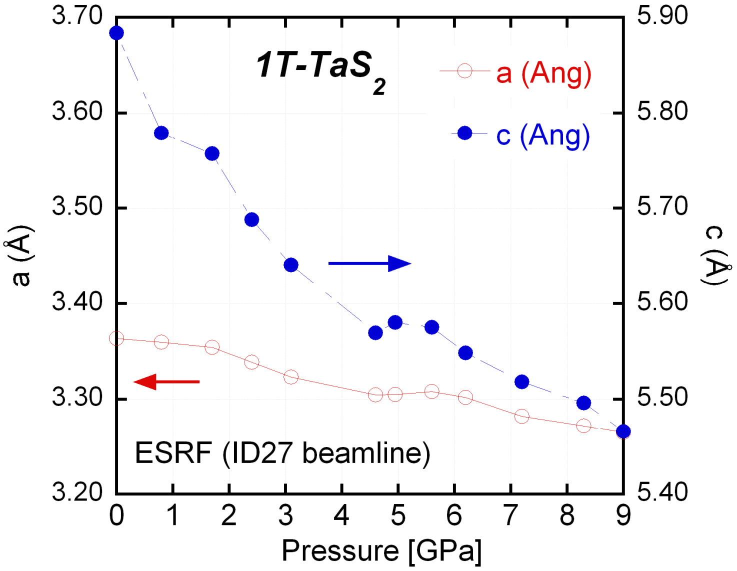

Figure 6. *In situ* dependence of the a and c-axis cell parameters of pristine 1T-TaS_2 upon pressure at ambient temperature measured at the ID27 beamline of the ESRF synchrotron facility.

References

[1] J. A. Wilson and A. D. Yoffe: Adv. Phys. Vol. 28 (1969), p. 193

[2] J. A. Wilson, F. J. Di Salvo and S. Mahajan: Adv. Phys. Vol. 24 (1975), p. 117

[3] F. Jellinek: J. less-Common Metals Vol. 4 (1962), p. 9

[4] M. Kertesz and R. Hoffmann: J. Am. Chem. Soc. Vol. 106 (1984), p. 3453

[5] E. Morosan, H. W. Zandbergen, B. S. Dennis, J. W. G. Bos, Y. Onose, T. Klimczuk, A. P. Ramirez, N. P. Ong and R. J. Cava: Nat. Phys. Vol. 2, (2006), p. 544

[6] B. Sipos, A. F. Kusmartseva, A. Akrap, H. Berger, L. Forró and E. Tutiš: Nature Mater. Vol. 7 (2008), p. 960

[7] H. Cercellier, C. Monney, F. Clerc, C. Battaglia, L. Despont, M. G. Garnier, H. Beck, and P. Aebi: Phys. Rev. Lett. Vol. 99 (2007), p. 146403-1

[8] W. A. Little: Phys. Rev. Vol. 134 (1964), p. A1416.

[9] V. L. Ginzburg: Contemp. Phys. Vol. 9 (1968), p. 355

[10] J. Rouxel: Physica B Vol. 99 (1980), p. 3

[11] T. E. Kidd, T. Miller, M.Y. Chou, and T.-C. Chiang: Phys. Rev Lett. Vol. 88 (2002), p. 226402-1

[12] M. Calandra, I. I. Mazin, and F. Mauri: Phys. Rev. B Vol. 80 (2009), p. 241108-1

[13] F.J. DiSalvo and J.V. Waszczak: Phy. Rev. B Vol. 22 (1980), p. 4241

[14] T. Endo, S. Nakao, W. Yamaguchi, T. Hasegawa and K. Kitazawa: Solid State Commun. Vol. 116 (2000), p. 47

[15] D. Walker, M.A. Carpenter, C.M. Hitch: Am. Mineralogist Vol. 75 (1990), p. 1020

[16] S. Klotz, G. Hamel and J. Frelat: High Press. Res. Vol. 24 (2004), p. 219

[17] V. A. Nalimova: Mol. Cryst. Liq. Cryst. Vol. 310 (1998), p. 5

[18] Le Bail, H. Duroy, and J.L. Fourquet: Mat. Res. Bull. Vol. 23 (1988), p. 447

[19] F. L. Givens and G. E. Fredericks: J. Phys. Chem. Solids Vol. 38 (1977), p. 1363

doi:10.4028/www.scientific.net/AST.75.181

Development of Low-Loss (Bi,Pb)-2223 Tapes with Interfilamentary Resistive Barriers

Ryoji Inada[1, a], Akio Oota[1, b], Chengshan Li[2, c] and Pingxiang Zhang[2, d]

[1]Toyohashi University of Technology, 1-1 Tempaku-cho, Toyohashi, Aichi 4418580, Japan

[2]Northwest Institute for Nonferrous Metal Research, P.O. Box 51, Xi'an, Shaanxi 710016, P.R. China

[a]inada@ee.tut.ac.jp, [b]oota@ee.tut.ac.jp, [c]csli@c-nin.com, [d]pxzhang@c-nin.com

Keywords: (Bi,Pb)-2223 tapes, filament coupling, resistive barriers, AC losses, coupling frequency

Abstract. This paper presents our recent activities for the development of low-loss (Bi,Pb)-2223 tapes with interfilamentary resistive barriers. To suppress the side effect on the phase formation in the filaments during sintering, $SrZrO_3$ were selected as barrier materials. Moreover, small amount of Bi-2212 was mixed with $SrZrO_3$ to improve their ductility for cold working. For non-twisted barrier tapes, transport critical current densities J_c at 77 K and self-field were ranged between 18 and 21 kA/cm^2 and its uniformity within 4% along a 1 m length. By combining the barrier introduction, reducing the tape width (< 3 mm) and twisting the filaments tightly, coupling frequency f_c exceeded 250 Hz even in an AC perpendicular field at 77 K. Transport J_c of the barrier tapes with tightly twisted filaments were in the range of 12−14 kA/cm^2 at 77 K and self-field. In our knowledge, this is the first result to achieve both $J_c > 12$ kA/cm^2 and $f_c > 250$ Hz simultaneously in an isolated (Bi,Pb)-2223 tape. At 50 mT and 50 Hz, our twisted barrier tapes showed 60-70% lower perpendicular field losses than a conventional 4 mm-width tape with fully coupled filaments.

Introduction

Powder-in-tube (PIT) processed (Bi,Pb)-2223 tapes with high critical current densities J_c of 40–50 kA/cm^2 over their lengths of 1 km are commercially available at present [1]. However, due to the strong electromagnetic coupling among the superconducting filaments via Ag matrix with low electric resistivity, their AC losses are still too large for practical AC applications such as cables and transformers. Particularly, because of the anisotropic geometry of (Bi,Pb)-2223 tape, both the hysteresis loss (Q_h) in superconductor and the coupling loss (Q_c) in matrix under a perpendicular field becomes much larger than in a parallel field case, and the conditions for filament decoupling become more restrictive [2–4]. To reduce the interfilamentary coupling in an AC perpendicular field, it is necessary – in addition to twisting the filaments with a suitable pitch length – to increase the matrix resistivity by introducing oxide layers between the filaments as highly resistive barriers [5−11].

For the composite multifilamentary wire with normal metal matrix, it is widely known that the coupling loss Q_c per-cycle in the matrix part has the maximum at a coupling frequency f_c, which is related to the decay time constant of a coupling current τ_c as follows:

$$f_c = 1/2\pi\tau_c \propto L_t^2/\rho_{t\perp} \quad (1)$$

where $\rho_{t\perp}$ is a effective transverse resistivity of the composite and L_t is a twist pitch length, respectively. When operating frequency f_{op} is higher than f_c, the filaments are electromagnetically coupled among them and their hysteresis loss Q_h becomes much larger than that for completely decoupled filaments, at field well above the full penetration field B_p. Therefore, f_c should at least be higher than f_{op} to achieve a significant loss reduction by decoupling the filaments.

In the early stage of the fundamental research for the development of (Bi,Pb)-2223 tapes with oxide barriers, f_c under an AC perpendicular field was increased to 80–180 Hz by introducing $BaZrO_3$ or $SrZrO_3$ barriers combined with filament twisting [6, 8]. The higher f_c of 300–500 Hz was achieved in twisted tape using $SrZrO_3$ with mixing some amount of $SrCO_3$ [9, 10] or Bi2212 [11] as barriers. However, J_c of those barrier tapes with f_c above several 100 Hz are limited to only 4–6 kA/cm^2. Such serious J_c drops are caused by not only the reduction of conversion ratio from Bi-2212 to Bi-2223 phases during sintering [7] but also the distortion of filament flatness [11]. Poor J_c property also results into much larger total magnetization losses around 50–60 Hz than completely decoupled case [8−11]. The simultaneous achievement of both J_c well above 10^4 A/cm^2 and f_c higher than several 100 Hz are urgently required for widening the applicability of (Bi,Pb)-2223 tapes for AC devices.

In this paper, we report our recent activities for the development of low-loss (Bi,Pb)-2223 tapes with interfilamentary oxide barriers. To suppress the side effect on the phase formation in the filaments during sintering, $SrZrO_3$ were selected as barrier materials. The coating thickness of oxide barrier around each filament are controlled to maintain the composite deformability and suppress the J_c degradation. The longitudinal uniformity of barrier tape were investigated on the order of 1 m length. The geometrical parameters of barrier tapes such as tape width and twist pitch length were also optimized to decouple the filaments under an AC perpendicular field. The loss reduction effect under a perpendicular field was examined systematically at 77 K.

Experimental

(Bi,Pb)-2223 tapes with oxide barriers among the twisted filaments were prepared by a conventional PIT method. $SrZrO_3$ powders with a mean grain size below 1 μm were used as barrier materials, and additional Bi-2212 powder corresponding to 20wt% was mixed with $SrZrO_3$ powder to improve their ductility for cold working [11].

The precursor powders with a nominal composition of $Bi_{1.76}Pb_{0.34}Sr_{1.93}Ca_{2.02}Cu_{3.1}O_x$ were packed into pure Ag tube with an outer diameter of 9.6 mm and a wall thickness of 0.7 mm. Then, the composite was deformed into a hexagonal cross-sectional shape by drawing, with a diagonal length of 1.8 mm. In order to suppress the deterioration of workablity for composite, the outside surface of the monocore wire was coated by $SrZrO_3$ + Bi-2212 pastes with a thickness of 50–60 μm, which is approximately one half the coating thickness for our previous barrier tape fabrication [11]. After a heat treatment at 550°C in air to avoid the organic binder in the pastes, 19-pieces of coated monocore wire were stacked and packed into Ag-Mg alloy tube with an outer diameter of 15.6 mm and wall thickness of 0.7 mm. The composite was drawn to the diameter and then twisted very carefully with intermediate heat treatments at 400°C in vacuum. Finally, the twisted round wires were formed into tape shapes by flat rolling, and sintered at 830–840°C with an intermediate rolling. For comparison, non-twisted barrier tape was also fabricated by using the same fabrication process.

The critical current (I_c) was measured in all tapes with conventional DC four-probe method at 77 K in a self-field, with an electric field criterion of 1 μV/cm. The critical current density (J_c) was determined from the I_c value using the transverse cross-sectional area of all superconducting filaments. The AC losses (Q_m) at 77 K in an AC perpendicular field were measured by a saddle shaped pick-up coil and a conventional lock-in technique [12].

Results and Discussion

The transverse cross sectional view of non-twisted tape with $SrZrO_3$ + Bi-2212 barriers is shown in Fig. 1. The size of a tape section and the volume fraction of filaments are 3.6 mm × 0.25 mm and 23%, respectively. The length of this barrier tape set to approximately 1 m for measuring the longitudinal uniformity of transport J_c. As can be seen, the filament flatness is reasonably good and $SrZrO_3$ + Bi-2212 barrier seems to be introduced around each filament. Fig. 2 shows the longitudinal distribution of transport J_c at 77 K and self-fields for non-twisted barrier tape with length of 1 m. The measurements were carried out at every 10 mm section along a tape length, using a contact-type voltage taps. Although the structure of a barrier tape becomes very complex, the J_c values uniformly

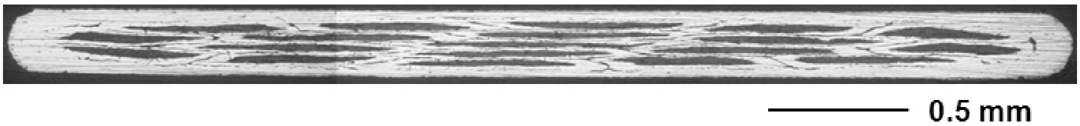

Fig. 1. Transverse cross sectional view of non-twisted tape with $SrZrO_3$ + Bi-2212 barriers. The size of tape section and fraction of the filaments are 3.6 mm × 0.25 mm and 23%, respectively.

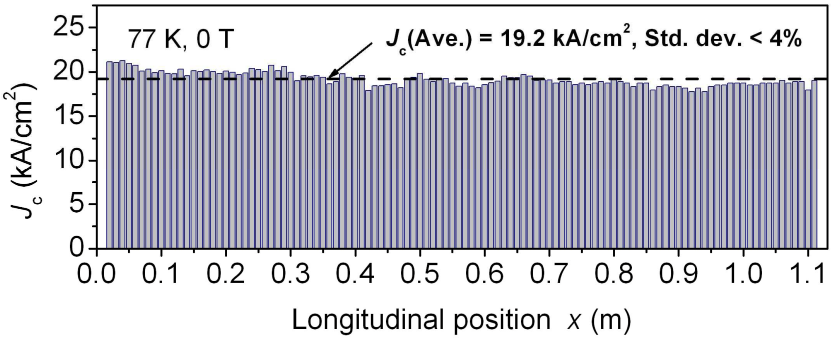

Fig. 2. Longitudinal J_c distributions at 77 K and self-field for non-twisted $SrZrO_3$ + Bi-2212 barrier tape. The measurements were continuously made at every 10 mm section along a tape length.

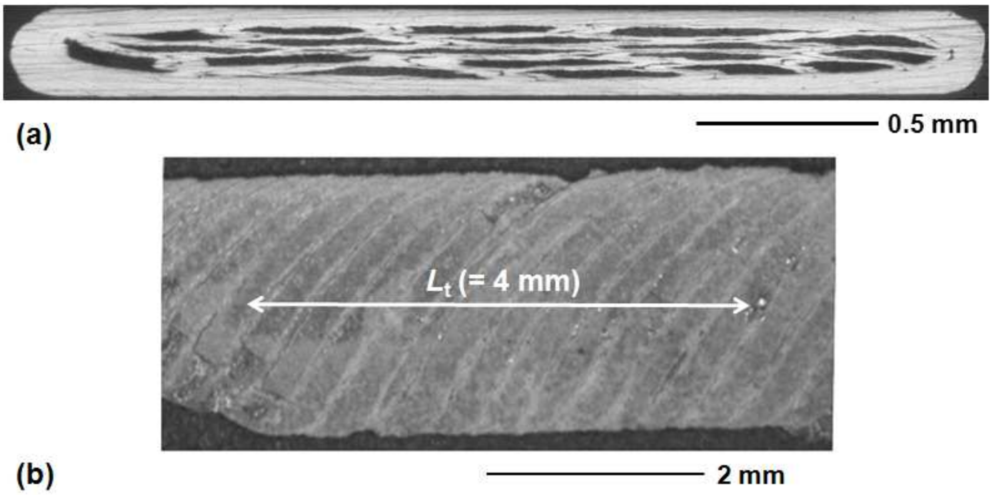

Fig. 3. Transverse cross sectional view and plan view (after removing sheath part by chemical etching) for twisted $SrZrO_3$ + Bi-2212 barrier tape. The size of tape section and twist pitch length are 2.7 mm × 0.24 mm and 4 mm, respectively.

distributed around a whole part of a tape length. Average value and standard deviation of J_c are estimated to be 19.2 kA/cm^2 and 4%, respectively. Since the tape without barriers prepared by same fabrication process showed J_c = 23 kA/cm^2, the degradation caused by introducing $SrZrO_3$ + Bi-2212 barrier is suppressed within 15–20%.

Fig. 3 shows the transverse cross sectional view and plan view (after removing sheath part by chemical etching) of twisted $SrZrO_3$ + Bi-2212 barrier tape with twist pitch length L_t = 4 mm. In order to suppress the serious J_c drops caused by tight filament twisting, the widths of final tapes (w_{tape}) are reduced to 2.7 mm. In our previous study [11], it was confirmed that in $SrZrO_3$ + Bi-2212 barrier tapes with L_t < 10 mm, the filaments positioned at an inner part of a tape section are deformed irregularly and physically connected each other. On the other hand, the filament flatness for newly prepared barrier tape with tightly twisted filaments (L_t = 4 mm) is good and physical connections among the filaments were not observed. Such fine structure would be attributed to improvements for deformability of a composite by controlling oxide barrier thickness and twisting very carefully with intermediate heat treatments.

Transport critical current density J_c at 77 K and self-field for $SrZrO_3$ + Bi2212 barrier tape with narrow w_{tape} (= 2.7 mm) are shown in Fig. 4, as a function of inverse of twist pitch lengths L_t. For comparison, our previous data for the tapes with thicker $SrZrO_3$ + Bi-2212 barriers and w_{tape} = 3.1 mm are also plotted [11]. As can be seen, J_c of both non-twisted and twisted barrier tapes with different L_t were improved remarkably compared with previous ones. For twisted barrier tapes with $L_t < 7$ mm, their J_c values were maintained in the range of 12–14 kA/cm^2, which was 20–30% lower than non-twisted one (= 18 kA/cm^2). We consider that avoidance of irregularly deformed filaments as shown in Fig. 3(a) strongly contributes to the improvement of transport J_c in twisted barrier tapes.

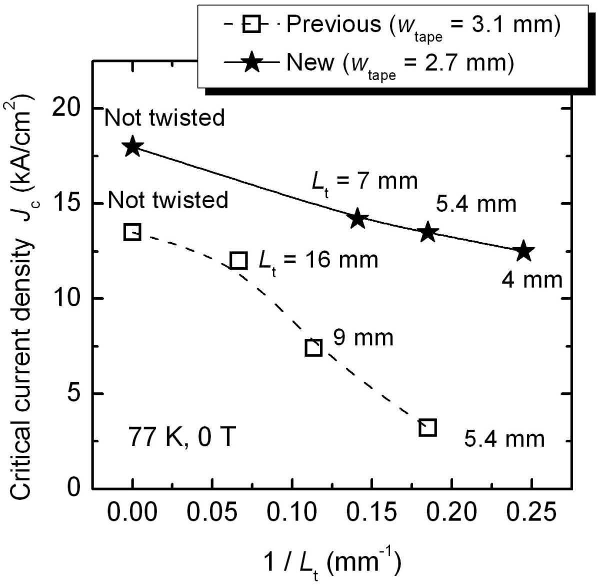

Fig. 4. Transport J_c at 77 K and self-field for $SrZrO_3$ + Bi-2212 barrier tapes plotted against the inverse of twist pitch lengths L_t. Our previous data for barrier tapes are also shown for comparison [11].

For the tape with shortest L_t = 4 mm, we investigated the AC loss properties at 77 K in an AC perpendicular field. Fig. 5(a) shows the frequency dependence of AC losses Q_m per-cycle at 77 K. As can be seen, Q_m data show the maximum around operating frequency f_{op} = 260 Hz. This specific frequency corresponds to coupling frequency f_c at which coupling loss Q_c per-cycle included in measured Q_m show the maximum. Although the achievement for f_c well above 300 Hz in twisted barrier tapes was already reported [10, 11, 13], transport J_c of barrier tapes with such high f_c were limited to only several kA/cm^2. In our knowledge, this is the first report to achieve both $J_c > 12$ kA/cm^2 and $f_c > 250$ Hz simultaneously in a single (Bi.Pb)-2223 tape. In preliminary study, we also confirmed that twisted tape with L_t = 4 mm and resistive Ag-8%Au alloy matrix showed lower f_c = 160 Hz [14]. Since Ag-8%Au alloy has 7–8 times higher resistivity than pure Ag at 77 K, the effective transverse resistivity $\rho_{t\perp}$ of our $SrZrO_3$ + Bi-2212 barrier tapes is suggested to be 12 times higher than a tape with pure Ag matrix.

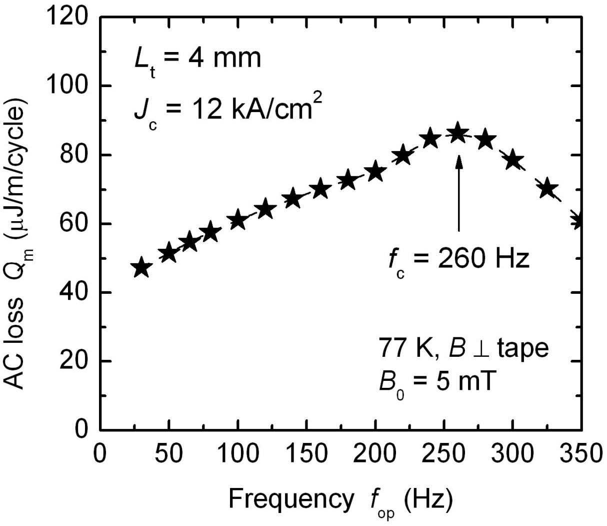

Fig. 5. Frequency dependence of AC losses Q_m per-cycle at 77 K and B_0 = 5 mT for $SrZrO_3$ + Bi-2212 barrier tape with L_t = 4 mm under an AC perpendicular field.

To confirm the loss reduction effect for the twisted barrier tape around power-grid frequency, field amplitude dependence of losses at 77 K and 45 Hz are shown in Fig. 6. The data for non-twisted tapes with their tape widths (w_{tape}) of 2.7 mm and 4 mm are also plotted. For these two reference tapes, all filaments are electromagnetically coupled among them and behave as a single superconductor under a perpendicular field at 45 Hz. In addition, the loss values for each tape are normalized by its critical current I_c at 77 K and self-field for direct comparison among the tapes. As can be seen, the loss values for twisted barrier tapes and L_t = 4 mm are reduced by 45~55%, compared with the reference tape with same w_{tape} = 2.7 mm at B_0 from 5 to 50 mT. Such remarkable loss reduction

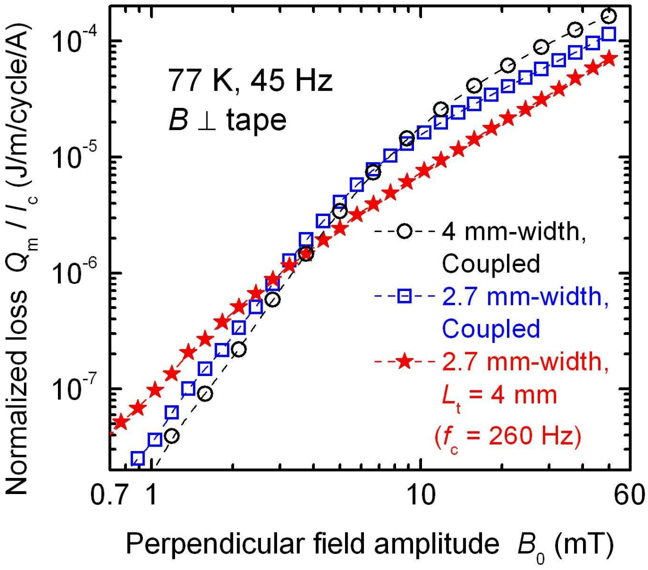

Fig. 6. Field amplitude dependence of normalized AC losses Q_m/I_c at 77 K and 45 Hz for twisted Bi2223 tape with $SrZrO_3$ + Bi-2212 barriers ($L_t = 4$ mm). The data for non-twisted tapes with same tape width (= 2.7 mm) and wider one (= 3.7 mm) are also plotted as references. The filaments in these two reference tapes are fully coupled at 45 Hz.

around power-grid frequency range is attributed to achieve both $f_c > 250$ Hz and $J_c > 10^4$ A/cm^2. It is also confirmed that the loss values for the twisted barrier tapes are 60–70% lower than those for the reference tape with wider $w_{tape} = 4$ mm.

From the systematical analysis for frequency dependence of losses Q_m in this twisted barrier tape with $f_c = 260$ Hz, it has been confirmed that the magnitude of coupling loss Q_c around 50 Hz is nearly the same as hysteresis loss component Q_h in filaments above 30 mT [15]. This indicates that Q_m reduction of this barrier tape around power-grid frequency range is still limited by large Q_c contribution. In order to obtain more remarkable loss reduction and maintain the effect towards higher perpendicular field range, both increasing coupling frequency f_c to reduce Q_c and improving J_c to enhance Q_h contribution in total Q_m should be necessary. The optimization of both fabrication process and geometrical structure to improve the performance (f_c and J_c) for twisted barrier tapes is currently being studied.

Summary

Our recent activities for the development of low-loss (Bi,Pb)-2223 tapes with interfilamentary resistive barriers were reported. To suppress the side effect on the phase formation in the filaments during sintering, $SrZrO_3$ were selected as barrier materials. Moreover, small amount of Bi-2212 was mixed with $SrZrO_3$ to improve their ductility for cold working. For non-twisted barrier tapes, transport J_c at 77 K and self-field was attained to 19 kA/cm^2 in average and its uniformity within 4% along a 1 m length. By controlling coating thickness of $SrZrO_3$ + Bi-2212 barriers before stacking, reducing a tape width below 3 mm and careful filament twisting with its length below 5 mm in a final tape, coupling frequency f_c exceeded 250 Hz even in an AC perpendicular magnetic field. Critical current densities J_c of tightly twisted barrier tapes were ranged in 12-14 kA/cm^2 at 77 K and self-field, which was 25% lower than non-twisted barrier tape. In our knowledge, this is the first result to achieve both $J_c > 12$ kA/cm^2 and $f_c > 250$ Hz simultaneously in an isolated (Bi,Pb)-2223. Our twisted barrier tapes with $L_t < 5$ mm showed 60-70% lower perpendicular field losses than a conventional 4 mm-width tape with fully coupled filaments at 50 mT and 50 Hz. Although J_c in our barrier tapes are still lower than commercial one, these achievements are promising for remarkable improvement for AC performance of (Bi,Pb)-2223 tapes in near future.

Acknowledgements

This work was partially supported by Grant-in-Aids for Scientific Research from MEXT (No.20686020) and JSPS (No.22560270) of Japan. It was also supported in part by TEPCO Research Foundation, Research Foundation for the Electrotechnology of Chubu (No.R-20302), and also by the grant for young researchers' project of Research Center for Future Technology, Toyohashi University of Technology. The authors would like to thank Messrs. Y. Okumura and T. Makihara in Toyohashi University of Technology for their technical support in all experimental.

References

[1] N. Ayai, S. Kobayashi, M. Kikuchi, T. Ishida, J. Fujikami, K. Yamazaki, S. Yamade, K. Tatamidani, K. Hayashi, K. Sato, H. Kitaguchi, H. Kumakura, K. Osamura, J. Shimoyama, H. Kamijyo, Y. Fukumoto: Physica C 468 (2008) p. 1747.

[2] H.G. Knoopers, J.J. Rabbers, B. ten Haken, H.H.J. then Kate: Physica C 372-376 (2002) p. 1784.

[3] K. Funaki, Y. Sasashige, H. Yanagida, S. Yamasaki, M. Iwakuma, N. Ayai, T. Ishida, Y. Fukumoto, and Y. Kamijo: IEEE Trans. Appl. Supercond. 19 (2009) p. 3053.

[4] E. Martínez, Y. Yang, C. Beduz, and Y.B. Huang: Physica C 331 (2000) p. 216.

[5] K. Kwasnitza, St. Clerk, R. Flükiger, and Y.B. Huang: Physica C 299 (1998) p. 113.

[6] M. Dhallé, A. Polcari, F. Marti, G. Witz, Y.B. Huang, R. Flükiger, St. Clerc, and K. Kwasnitza: Physica C 310 (1998) p. 127.

[7] W. Goldacker, M. Quilitz, B. Obst, H. and Eckelmann: Physica C 310 (1998) p. 182.

[8] K. Kwasnitza, St. Clerk, R. Flükiger, and Y.B. Huang: Cryogenics 39 (1999) p .829.

[9] H. Eckelmann, J. Krelaus, R. Nast, and W. Goldacker: Physica C 355 (2001) p. 278.

[10] R. Nast, H. Eckelmann, O. Zabara, S. Schlachter, and W. Goldacker: Physica C 372-376 (2002) p. 1778.

[11] R. Inada, Y. Nakamura, A. Oota, C.S. Li, and P.X. Zhang: Supercond. Sci. Technol. 22 (2009) p. 035014.

[12] R. Inada, K. Tateyama, Y. Nakamura, A. Oota, C.S. Li, and P.X. Zhang: Supercond. Sci. Technol. 20 (2007) p. 138.

[13] B. ten Haken, J.J. Robbers, and H.H.J. ten Kate: Physica C 377 (2002) p. 156.

[14] R. Inada, Y. Tanaka, Y. Nakamura, A. Oota, C.S. Li and P.X. Zhang: Abstracts of CSJ conference Vol. 81 (2008) p. 4 (in Japanese).

[15] R. Inada, Y. Okumura, A. Oota, C.S. Li and P.X. Zhang: Submitted to J. Supercond. Novel Magn.

doi:10.4028/www.scientific.net/AST.75.187

Grain Morphology for $Bi_2Sr_2CaCu_2O_8$ Tapes Heat-Treated in High Magnetic Fields

K. Watanabe[a], T. Inoue and S. Awaji

High Field Laboratory for Superconducting Materials, Institute for Materials Research,
Tohoku University, Sendai 980-8577, Japan
[a]kwata@imr.tohoku.ac.jp

Keywords: Ag-sheathed $Bi_2Sr_2CaCu_2O_8$, magnetic field alignment, differential thermal analysis, n-value, E-J properties.

Abstract. We prepared Ag-sheathed $Bi_2Sr_2CaCu_2O_8$ (Bi2212) tapes heat-treated in high fields (in-field heat-treatment Bi2212) and heat-treated without magnetic fields (out-of-field heat-treatment Bi2212), in order to examine the magnetic field effect on the microstructure of Bi2212. The differential thermal analysis (DTA) was performed at 10 T using Bi2212 powders. The DTA suggests that the in-field heat-treatment changes the grain morphology of Bi2212. It was found that the critical current density J_c for the in-field heat-treatment Bi2212 tape is largely improved at 10 K in fields. In addition, the in-field heat-treatment Bi2212 tape has also a large n-value in the form of $E=E_c(J/J_c)^n$, which is related to the microstructure change.

Introduction

Ag-sheathed $Bi_2Sr_2CaCu_2O_8$ (Bi2212) wires are expected for a high field superconducting magnet from a splendid critical current density viewpoint in high fields at low temperatures below 20 K [1]. However, one of problems for Bi2212 wires lies in having a small n-value in the form of $E=E_c(J/J_c)^n$, compared with $Bi_2Sr_2Ca_2Cu_3O_{10}$ (Bi2223) [2]. Here, E_c is the electric field criterion to determine the critical current density J_c. Such a small n-value will become a serious issue, when the persistent current mode is adopted in an NMR superconducting magnet. On the other hand, there is a crystal growth method in magnetic fields to enhance J_c by improving the crystal orientation [3]. The anisotropy of the crystallographic structure is large in the copper-oxide superconductor. This results in an outstanding difference in the magnetic susceptibility along the c-axis and the ab-plane. Especially, the Bi2212 superconductor has a very large anisotropy of the crystallographic structure [4]. Since the Bi2212 superconductor is usually heat-treated by the partial melting and slow-cooling method in the coexistence state with a liquid phase, it is a suitable material for the preferred alignment effect in magnetic fields.

In this paper, we describe the superconducting properties for Ag-sheathed mono-core Bi2212 tapes heat-treated in high magnetic fields. The microstructure change of Bi2212 due to the heat-treatment in high magnetic fields is investigated using the differential thermal analysis (DTA) in high fields.

Experimental

As-rolled and unreacted Bi2212 mono-core tapes with 3 mm wide and 0.23 mm thick size were prepared. It was heat-treated using the electric furnace combined with a cryogenfree superconducting magnet. The heat-treatment was carried out in fields perpendicular to the Bi2212 tape surface, and the tape samples heat-treated in fields (in-field heat-treatment Bi2212) and heat-treated without magnetic fields (out-of-field heat-treatment Bi2212) were prepared at B_{HT} = 5 T and B_{HT} =0 T, respectively. When the magnetic field is applied perpendicular to the tape surface, the c-axis of the crystallographic structure in plate-like Bi2212 grains is strongly aligned vertically to the tape surface. The in-field heat-treatment was performed in an oxygen atmosphere and, after the magnetic field was increased to a desired magnetic field.

The four-terminal method was used for the resistance measurement of the E-J characteristics, and the tape sample was set in the temperature-variable cryostat conductively cooled by a GM-cryocooler [5]. This cryostat was combined with a 15 T cryogenfree superconducting magnet, and external magnetic fields up to 14 T were applied in parallel to the c-axis direction of each sample. The maximum current was assumed to be 200 A by using the pulsed current source to reduce Joule's heating due to the large current to the sample. J_c was determined by the electric field criterion of 1 μV/cm, and the n-values were decided from the E-J characteristics ranging from 10^{-6} to 10^{-5} V/cm.

In order to examine the influence of the in-field heat-treatment that will exert on the Bi2212 crystal growth process, DTA was obtained in magnetic fields. The experiment was carried out using a 10 T cryogenfree superconducting magnet. Bi2212 powders as an investigated sample and Al_2O_3 powders as a reference sample were utilized. They were set in the DTA measurement furnace shown in Fig. 1. This DTA measurement system consists of Pt crucibles and an alumina support equipped with two pairs of Pt-PtRh thermocouples, and the temperature difference is measured [6]. The maximum temperature was assumed to be 1000 ºC when the temperature increases in the oxygen atmosphere, and the temperature increasing and decreasing rate was set at 200ºC/h.

Results and discussion

The DTA signals for Bi2212 at B=0 T and 10 T were obtained in the temperature increasing process in Fig. 2(a) and in the temperature decreasing process in Fig. 2(b). In the temperature increasing process, the melting temperature of Bi2212 at 0 T, which corresponds to T_{p1} in the figure, is about

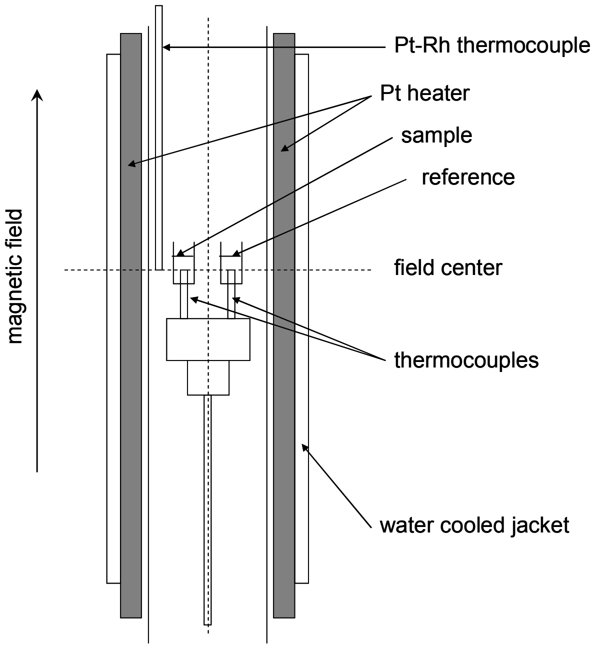

Fig.1. DTA measurement system with a 50 mm outer diameter furnace at temperatures up to 1200 ºC in fields up to 10 T.

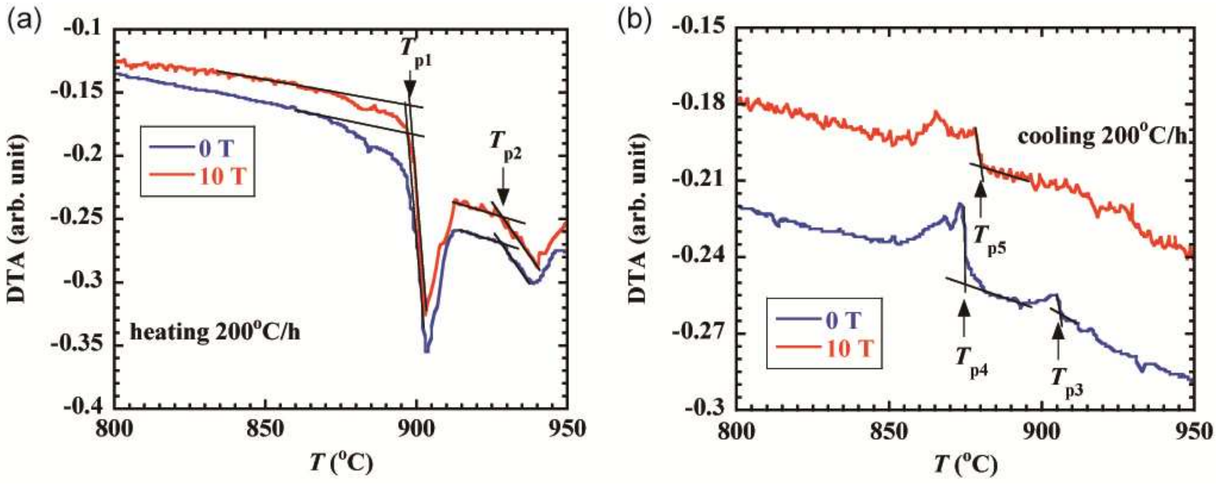

Fig.2. DTA signals for Bi2212 powders (a) in heating process and (b) in cooling process.

897 ºC, and does not change regardless of the magnetic field at 10 T. It is well known that the Bi2212 phase is decomposed at about 900ºC into the Bi-rich liquid phase and the $(Sr,Ca)_2CuO_3$ (21 phase) and $(Sr,Ca) CuO_2$ (11 phase) solid phases. An endothermic peak of about 897 ºC corresponds to this decomposition temperature. Moreover, another endothermic peak corresponding to T_{p2} was seen at 930 ºC and at 0 T and 10 T. It means that the 21 phase is decomposed at 930 ºC into the liquid phase and the CaO solid phase, and that the magnetic field at 10 T does not affect to such decomposition temperature.

In the cooling process, it was found that the solidification temperature (T_{p5}) of the Bi2212 phase at 10 T, which was derived from the onset method, shifts to the high temperature in comparison with T_{p4} at 0 T. It was 875 ºC for the out-of-field heat-treatment Bi2212 at 0 T and 880 ºC for the in-field heat-treatment Bi2212 at 10 T. We understand that the solidification temperature of the 21 phase is T_{p3} at 0 T, although it reveals a broad behavior at 10 T. The solidification process with crystallization is strongly related to the crystal nucleation condition and the rate of a crystal growth. The solidification temperature rise means the increase in the degree of supersaturation. Since the crystal nucleation increases with increasing the degree of supersaturation, the magnetic field effect in the Bi2212 crystal growth process leads to increasing the crystal nucleation. As for the atom movement, it means the

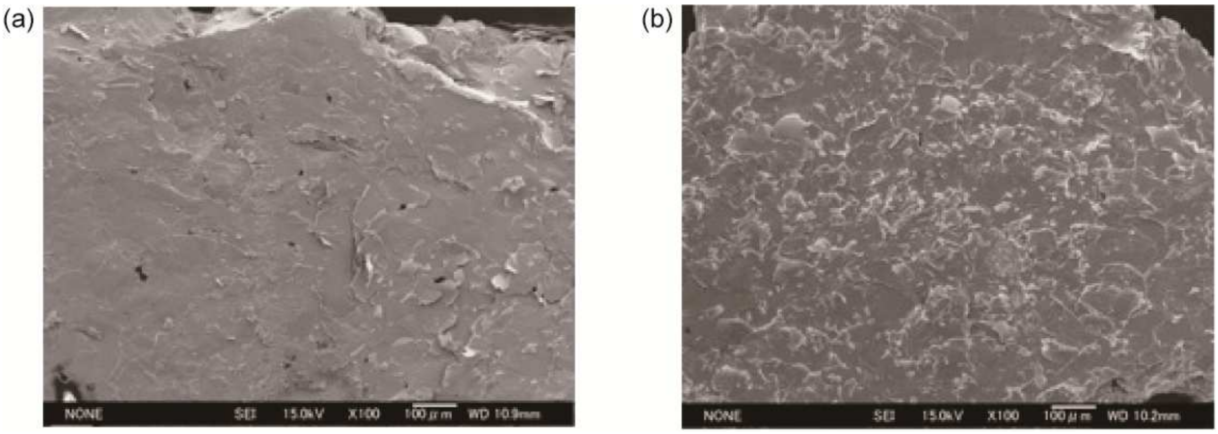

Fig.3. SEM observation for Bi2212 mono-core tapes heat-treated at (a) B_{HT} = 0 T and (b) B_{HT} = 5 T.

movement of the charge. This results in decreasing the crystal growth rate in magnetic fields due to the in-field diffusion suppressed by Lorentz force. This viewpoint also suggests that the decrease of the growth rate causes the small crystal grain by the heat-treatment process in magnetic fields. The microstructure of Bi2212 with and without the in-field heat treatment was investigated by scanning electron microscope (SEM), as shown in Fig. 3. We observed the microstructure difference between out-of-field heat-treatment Bi2212 and in-field heat-treatment one, which indicates the very small grains of the in-field heat-treatment Bi2212. This is consistent with the DTA results related with the reduction of a Bi2212 grain size due to the heat-treatment in magnetic fields.

The magnetic field dependences of J_c and n-value at 10 K are shown in Figs. 4 and 5, respectively. One notes that J_c for Bi2212 was improved by the in-field heat-treatment. Further, the n-value of the in-field heat-treatment Bi2212 improved more greatly than that of the out-of-field heat-treatment sample. We found that the heat-treatment in high fields for Bi2212 is effective in not only the J_c improvement due to the c-axis-preferred orientation but also the n-value enhancement. These results also may be related to the Bi2212 microstructure change from plate-like large grains to sintered-like small grains.

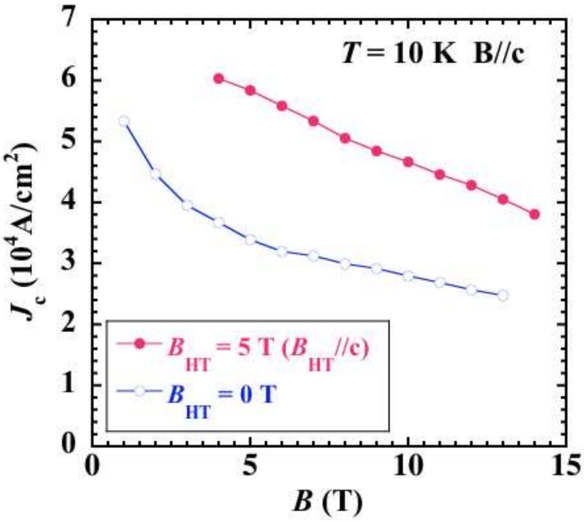

Fig.4. J_c properties at 10 K in fields for Bi2212 mono-core tapes heat-treated at B_{HT} = 0 T and B_{HT} = 5 T.

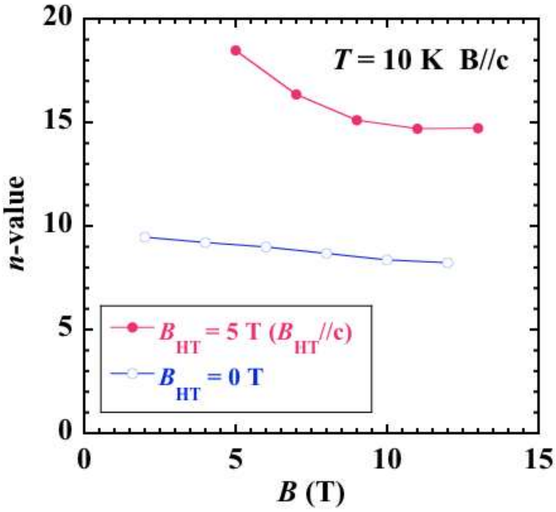

Fig.5. n-values at 10 K in fields for Bi222 mono-core tapes heat-treated at B_{HT} = 0 T and B_{HT} = 5 T.

Conclusion

We carried out the DTA experiments at 10 T using Bi2212 powders, in order to investigate the effect on the heat-treatment in high fields for Ag- sheathed Bi2212 tapes. It was found that in the cooling process the solidification temperature of the Bi2212 phase shifts to the high temperature at 10 T. This means that the magnetic field in the Bi2212 crystal growth process has the effect of increasing the crystal nucleation. As a result, the microstructure of Bi2212 heat-treated in high fields seems to change from plate-like large grains to sintered-like small grains. The J_c characteristic for Bi2212 heat-treated in high fields was improved largely at 10 K in fields. The Bi2212 tape heat-treated in high fields has a large n-value in the form of $E=E_c(J/J_c)^n$, which comes from the microstructure change.

Acknowledgment

We would like to thank Dr. K. Takahashi and Dr. H. Kumakura of NIMS for helping the sample preparation.

References

[1] K. Watanabe, S. Awaji and T. Fukase: Synthetic Metals Vol. 71 (1995), p.1585
[2] H. Kumakura, H. Kitaguchi, H. Miao, K. Togano, T. Koizumi, and T. Hasegawa: Physica C Vol. 335 (2000), p. 31
[3] Y. W. Ma, K. Watanabe, S. Awaji, and M. Motokawa: Appl. Phys. Lett. Vol. 77 (2000), p. 3633
[4] D.C. Johnston, and J.H. Cho: Phys. Rev. B Vol. 42 (1990), p. 8710
[5] K. Takahashi, S. Awaji, G. Nishijima, K. Watanabe and K. Togano: Supercond. Sci. Technol. Vol. 17 (2004), p. S568
[6] S. Awaji, K. Watanabe, and M. Motokawa: J. Crys. Growth Vol. 226 (2001), p. 83

© (2010) Trans Tech Publications, Switzerland
doi:10.4028/www.scientific.net/AST.75.192

Synthesis and Precise Analysis of $Bi_2Sr_2Ca_{n-1}Cu_nO_y$ Superconducting Whiskers

Hiromi Tanaka[1,a], Hideki Yoshikawa[2], Masahiro Kimura[2], Chusei Tsuruta[3], Sei Fukushima[2], Yoshio Matsui[3], Shingo Nakagawa[4], Kentaro Kinoshita[4], Satoru Kishida[4]

[1]Department of Electrical and Computer Engineering, Yonago National College of Technology,
Tottori 683-8502, Japan

[2]Department of Materials Infrastructure, National Institute for Materials Science,
Hyogo 679-5148, Japan

[3]Advanced Nano-Characterization Center, National Institute for Materials Science,
Tsukuba 305-0044, Japan

[4]Graduate school of Electrical and Electronic Engineering, Tottori University,
Tottori 680-8552, Japan

[a]E- mail: hitanaka@yonago-k.ac.jp

Keywords: high-temperature superconductor, critical current density, whisker

Abstract. We synthesized Ca-rich Bi-based superconducting whiskers by an Al_2O_3-seeded glassy quenched platelet method. The grown whiskers were precisely characterized by synchrotron radiation X-ray photoemission spectroscopy and high-resolution transmission electron microscopy. The Ca-rich Bi-based superconducting whiskers show a high critical current density of 2×10^5A/cm^2 at 40K in self-field. We found that excess Ca^{2+} ions substitute for the Sr^{2+} sites and cause nano crystalline domains with shorter-period modulation embedded in the base crystalline. The embedded nano crystalline domains can result in structural distorted defects which work as strong pinning center.

Introduction

Since high-temperature superconductors (HTSCs) attain high critical current density (J_c), HTSCs are the most promising materials for the application of high-electric-current equipment such as electric power cables and magnets of superhigh magnetic field. Recent studies on the process of HTSC wires show an increase of J_c [1,2]. In particular, the J_c of $Bi_2Sr_2Ca_{n-1}Cu_nO_y$ (Bi-based) superconducting wires was improved by a powder-in-tube method using Ag-sheath [3]. Further challenges to high J_c are needed for widespread applications. To achieve a high J_c, the growing of strong pinning centers is required. A neutron irradiation or a heavy-fast ion irradiation to Bi-based HTSCs is known as one of the most effective methods to introduce strong pinning centers which contribute to enhancement of the intragrain J_c, but these methods have practical issues on their residual radiation and economic efficiency [4,5].

To understand an strong pinning center in a Bi-based superconductor, we focused on a Bi-based superconducting whisker (hereafter, Bi-based whisker), because Bi-based whiskers are known to have a very high J_c of 7.3×10^4A/cm^2 at 77K in self-field [6]. We have synthesized the high-quality and large-size single crystal of Bi-based whisker [7]. Empirically, we know that excess of Ca in raw materials enhances the growth rate and J_c of Bi-based whisker. However, the mechanism of the high J_c in the Ca-rich Bi-based whisker has not been clarified so far. In this paper, we investigate the high J_c mechanism of the Ca-rich Bi-based whisker by the analysis of Bi-based whiskers with different J_c and Ca compositions. We then show that J_c has an relationship with the substitution ratio of Ca^{2+} ions for Sr^{2+} sites (hereafter, Ca/Sr substitution ratio). Since the whisker is known as a single crystal with good crystallinity, it is proper to study pinning centers which enhance an intragrain J_c of HTSCs.

Experimental

We prepared Bi-based whiskers using the glassy quenched platelet with Bi:Sr:Ca:Cu = 2:2:u:v (u = 1-2, v = 2-4). We adopted an Al_2O_3-seeded glassy quenched platelet (ASGQP) method for the sample preparation [7]. The grown whiskers' J_c were evaluated by current-voltage (I-V) characteristic measurements using a conventional four-probe method. The chemical compositions of the Bi-based whiskers were checked by electron probe microanalysis (EPMA) measurements. Chemical states of constituent elements in Bi-based whiskers were studied by X-ray photoemission spectroscopy using synchrotron radiation (SR-XPS). The SR-XPS measurements were carried out using X-rays of 4.75 keV at BL15XU (NIMS) of SPring-8. The total energy resolution was set to about 700 meV [8]. Local structures of Bi-based whiskers were observed by high-resolution transmission electron microscopy (HR-TEM). The spatial resolution was about 0.14 nm with the electron acceleration voltage of 800 kV.

Results and discussion

Fig. 1 shows the optical photograph of the grown Bi-based whiskers. We can see that the Bi-based whiskers grow from Al_2O_3 particles, where Al_2O_3 particles are scattered on the surface of the glassy-quenched platelet for the purpose of catalyser. High-growth-rate of Bi-based whiskers needs both excess Ca and Al_2O_3 catalytic particles.

The excess Ca has another great benefit which attains a high J_c as follows. Fig. 2 shows the effect of the various Ca/Sr substitution ratios on the Bi-based whisker's J_c at 40 K in self-field. In this paper, we define the Ca/Sr substitution ratio as $(x/2)\times100$ % in the nominal composition of $Bi_2Sr_{2-x}Ca_{1+x}Cu_2O_y$. As seen in the Fig. 2, the J_c exponentially increases with increasing of the Ca/Sr substitution ratio. The Bi-based whisker with the Ca/Sr substitution ratio of about 25 % shows the highest J_c of 2×10^5 A/cm^2. This J_c is much greater than the previously-reported J_c in the Bi-2212 single crystals (5×10^3 A/cm^2) [9]. We found that the Ca/Sr substitution ratio is closely correlated with the J_c of Bi-based whiskers. The J_c increases by a factor of 200 when the Ca/Sr substitution ratio increases from 5 to 25 %. Although higher J_c is expected by further improvement of the Ca/Sr ratio, it is actually difficult to prepare a whisker with higher Ca/Sr ratio because of its solid solubility limit.

Fig. 3 shows the XPS spectrum of Sr 3p and C 1s core levels from the surface of the as-grown whisker.

Fig. 1. Optical photograph of the grown Bi-based whiskers.

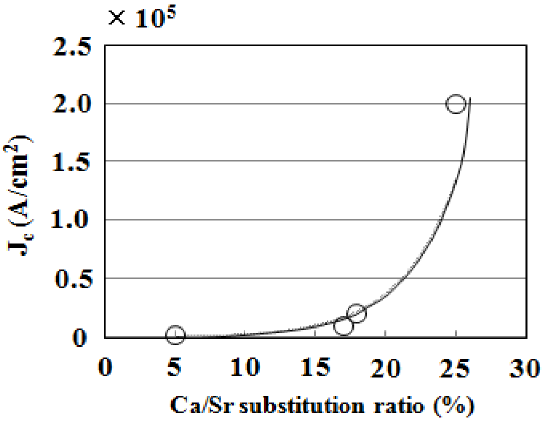

Fig. 2. Effect of Ca^{2+}substitution for Sr^{2+} sites on the whisker's J_c.

The spectrum is taken at hν= 1253.6 eV which the X-ray source for the measurements is MgK$_{\alpha}$. As shown in the figure, lots of carbon impurities are adsorbed or absorbed on the surface of the as-grown whisker. In the C 1s spectrum, the peak observed at the binding energy of around 289eV seems to come from the carbonates which are produced by the absorption of hydroxyl. Here, the Bi-based whisker was measured without any surface cleaning, since the cleaving of tiny Bi-based whisker is difficult. To overcome surface contamination of Bi-based whisker, we performed XPS measurement with hard X-ray of 4.75 keV, which has a large probing depth.

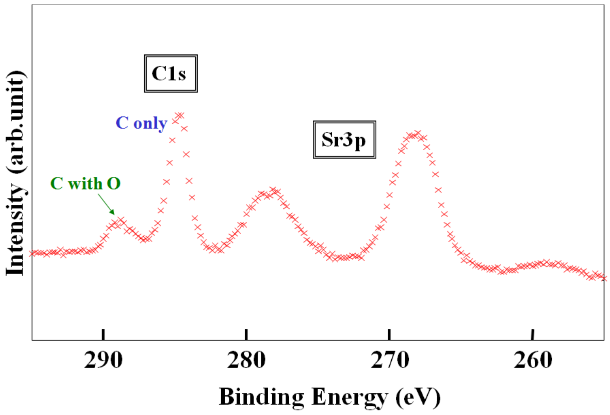

Fig. 3. C 1s and Sr 3p XPS spectrum observed from the surface of as-grown Bi-based whisker. The spectrum is taken at hν = 1253.6 eV.

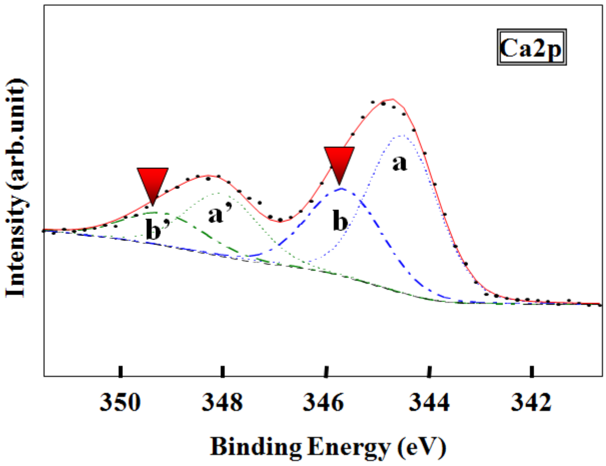

Fig. 4. Ca 2p XPS spectrum observed form the as-grown Bi-based whisker with the Ca/Sr substitution ratio of about 25 %. The spectrum is taken at hν= 4750 eV.

Fig. 4 shows Ca 2p XPS spectrum of the Bi-based whisker with the Ca/Sr substitution ratio of about 25 %. In the Bi-based whisker, the Ca 2p spectrum showed broad asymmetric doublet peaks. In general, the Ca 2p spectrum of the Bi-2212 single crystal is known to show much sharper doublet peaks [10]. To understand the broad asymmetric doublet peaks in the Bi-based whisker, we attempted to decompose the Ca 2p spectrum. For the decomposition, we referred the binding energy and full width at half maximum of the Ca 2p spectrum of the Bi-2212 single crystal. The Ca 2p spectrum of the Bi-based whisker was separated into spin-orbit doublets of two components, aa' and bb', as shown in Fig. 4. The aa' component appears at the binding energy of 344.5 eV and 348 eV. The bb' component appears at the binding energy of 345.7 eV and 349.2 eV. Considering the results reported by Tanaka et al., the aa' component is assigned to the Ca^{2+} ions that occupy the native Ca^{2+} site in the typical Bi-based HTSCs, while the bb' component is assigned to the Ca^{2+} ions that occupy the Sr^{2+} sites [11]. In the Ca 2p spectrum of the Bi-based whisker, the intensity ratio between the aa' component and the bb' component is about 7:3. Considering the intensity ratio between Sr 2p XPS spectrum and Ca 2p XPS spectrum, the x in the nominal composition of $Bi_2Sr_{2-x}Ca_{1+x}Cu_2O_y$ is estimated to be about 0.5, which means 25 % of original Sr^{2+} sites are substituted by Ca^{2+} ions. The value of x, which corresponds to excess Ca, is consistent with the bb' component ratio in Ca 2p XPS spectrum. It is also consistent with the EPMA results. This result indicates that the excess Ca^{2+} ions occupy the Sr^{2+} sites in the Bi-based whisker.

We performed HR-TEM observation of local structural for the Bi-based whiskers, of which Ca/Sr substitution ratio is about 25 %. The observation is carried out in the bc-plane of the Bi-based whisker of which face was measured by XPS. We noticed that there exists short structural modulation, which we have never seen in usual Bi-based HTSCs. It is known that the Bi-based HTSCs intrinsically have the structural modulation along the b-axis direction. The period of the structural modulation is conventionally about five times of the a-axis lattice constant (b = 4.8a = 2.6 nm) [12]. We found the period of the structural modulation is shortened by about 23 % in some rows of unit cells along the c-axis. The period of the short structural modulation is about four times of the a-axis lattice constant (b = 3.7a = 2.0 nm).

We found that the volume fraction of the short modulation is about 25 % within the HR-TEM image of 30 nm×40 nm. The volume fraction (~25 %) is same as the Ca/Sr substitution ratio estimated by EPMA and SR-XPS results. This indicates that Ca/Sr substitution causes unique short structural modulation. In the conventional Bi-based HTSCs, it is known that the structural modulation intrinsically exists to release the lattice mismatch between Bi-O layer and CuO_2 layer through the mediation of Sr-O buffer layer. The ion radius of Ca^{2+} (0.099 nm) is smaller than that of Sr^{2+} (0.113 nm). Therefore, it can be suggested that Ca/Sr substitution shortens the lattice parameter of Sr-O buffer layer and changes the periodicity of structural modulation of Bi-based whisker.

Considering that J_c drastically increases with increasing of the Ca/Sr substitution ratio, mixture of the shorter-period and longer-period structural modulations in the Bi-based whisker can play a role of a defect which works as a strong pinning center. Hu et al. recently reported that nano-pins introduced in RE123 by compositional modulation lead to the spatial fluctuation of local T_c, which works as a strong pinning center [13]. Scenario of this strong pinning center gives us a clue to understand our new pinning center. Both pinning centers include not only compositional modulation but also structural strain. The size of strains is nano-scale in the both pinning centers. The hypothesis that nano-sized shorter-period structural modulations embedded in the base crystal works as strong pinning centers is very interesting point to promote further research and development of higher J_c Bi-based HTSCs.

Summary

In summary, we have studied the J_c properties of the Bi-based whiskers. The Bi-based whisker with the Ca/Sr substitution ratio of about 25 % showed the high J_c of 2×10^5 A/cm^2 at 40 K in self-field. We investigated the Bi-based whisker with the Ca/Sr substitution ratio of about 25 % by SR-XPS and HR-TEM. The origin of the high J_c was found to be the Ca^{2+} substitution for the Sr^{2+} site. The HR-TEM result indicates that the substitution leads to the short structural modulations in some unit cells. The nano-sized shorter-period structural modulations embedded in the matrix crystal can play an important role of a strong pinning center, and enhances J_c.

Acknowledgment

This work was partly supported by Nanotechnology Support Project of the Ministry of Education, Culture, Sports, Science and Technology (MEXT), Japan, and a Grant-in-Aid for Scientific Research from the Japan Society for the Promotion of Science.

References

[1] S. Cho, Y. T. Yao, J. B. Ketterson and K. L. Teischow: Appl. Phys. Lett. Vol. 67 (1995), p.851.

[2] D. T. Verebelyi, D. K. Christen, R. Feenstra, C. Cantoni, A. Goyal, D. F. Lee, M. Paranthaman, P. N. Arendt, R. F. DePaula, J. R. Groves and C. Prouteau: Appl. Phys. Lett. Vol. 76 (2000), p.1755.

[3] K. Heine, J. Tenbrink and M. Thoner: Appl. Phys. Lett. Vol. 55 (1989), p.2441.

[4] Q. Y. Hu, H. W. Weber, F. W. Sauerzopt, G. W. Schulz, R. M. Schalk, H. W. Neumuller and S. X. Dou: Appl. Phys. Lett. Vol. 65 (1994), p.3008.

[5] L. Civale, A. D. Marwick, T. K. Worthington, M. A. Kirk, J. R. Thompson, L. Krusin-Elbaum, Y. Sun, J. R. Clem and F. Holtzberg: Phys. Rev. Lett. Vol. 67 (1991), p.648.

[6] I. Matsubara, H. Tanigawa, T. Ogura, H. Yamashita, M. Kinoshita and T. Kawai: Appl. Phys. Lett. Vol. 57 (1990), p.2490.

[7] H. Uemoto, M. Mizutani, S. Kishida and T. Yamashita: Physica C Vol. 392-396 (2003), p.512.

[8] H.Yoshikawa, Y. Kita, K.Watanabe, A. Tanaka, M. Kimura, A. Nisawa, A. M. Vlaicu, M. Kitamura, N. Yagi, M. Okui, M. Taguchi, R. Oiwa and S. Fukushima: J. Surf. Anal. Vol. 9 (2002), p.374.

[9] T. Terai, T. Kobayashi, Y. Ito. K. Kishio and J. Shimoyama: Physica C Vol. 282-287 (1997), p.2285.

[10] H. Tanaka, S. Kishida, H. Yoshikawa, M. Kimura, A. Tanaka and S. Fukushima: Physica C Vol. 392-396 (2003), p. 153.

[11] K. Tanaka, H. Takaki and S. Mizuno: Jpn. J. Appl. Phys., Part 1 Vol. 31 (1992), p.2692.

[12] Y. Matsui, H. Maeda, Y. Tanaka and S. Horiuchi: Jpn. J. Appl. Phys., Part 2 Vol. 27 (1988), p.L372.

[13] A. Hu, I. Hirabayashi, M. Winter, M. R. Koblischka, U. Hartmann and H. Zhou: Appl. Phys. Lett. Vol. 86 (2005), p.92505.

© (2010) Trans Tech Publications, Switzerland
doi:10.4028/www.scientific.net/AST.75.197

Synthesis and structural characterization of Hg(Re)-Pb-Ca-Ba-Cu-O superconducting thin films grown by spray pyrolysis

Concepción Mejía-García[1, a], José Luis López-López[1, b], Elvia Díaz-Valdés[1, c]
and Claudia Verónica Vázquez-Vera[1, d]

[1]Escuela Superior de Física y Matemáticas, IPN, Edif. 9 UPALM, México D. F. C. P. 07738, México.

[a]concepcionmejia@gmail.com, [b]joseluisl@gmail.com, [c]ediazva@gmail.com, [d]claus300487@gmail.com

Keywords: Hg-based precursor films, Rietveld refinement, spray pyrolysis technique, superconductor.

Abstract. We present a statistical study of the crystalline phase distribution in Pb-Ca-Ba-Cu-O precursor films grown by spray pyrolysis technique, with thickness and composition suitable to incorporate Hg by the sealed quartz tube technique in a subsequent treatment. A series of 9 precursor thin films were deposited on MgO substrates. Interdependence among deposition temperature, solution concentration, annealing temperature and annealed time and the effect in the relative percentage of each precursor phases was studied, applying a fractional factorial design 3IV-II. Chemical composition was obtained from atomic absorption measurements. Crystalline phase identification was performed by X-ray diffraction technique (XRD) and the quantification of each one was carried out by Rietveld method. The $BaPbO_3$, $Ba_4Pb_3O_{10}$ ternary phases were obtained at 810ºC, and the $BaCuO_2$ phase was got between 835ºC and 860ºC. Deposition temperature and molarity of the solution have clear influence on the thickness of the film. The effect of deposition temperature on the film composition was observed.

Introduction

The superconductor system $HgBa_2Ca_{n-1}Cu_nO_d$ (n = 1, 2, 3,…) has been extensively studied since its discovery in 1993 [1], because of their highest T_c among the superconducting cuprates. The n = 3 compound of this series has the T_c record of 135 K at atmospheric pressure [2]. On account of the difficulty for obtaining high-quality samples in this system and the complex reaction in the preparation, it is important for both fundamental and application fields to study and to understand the dynamics in the preparation of precursor phases applied in the growing of thin films [3, 4]. In order to determine optimal methods of preparation by controlling the deposition and annealing parameters we have done a systematic study in precursor films for the preparation of Hg-based thin films. In order to observe the effect on the composition and film thickness, values of preparation parameters were varied, as molarity of the solution, deposition temperature, time and temperature of thermal treatment.

Methodology

A series of 9 precursor thin films were deposited on MgO substrates, at different temperatures, with the spray pyrolysis technique from an aqueous nitrate solution with different concentrations. Subsequently, the films were processed under different thermal treatments. Samples were prepared according to an experimental design (Table 1), in order to observe the effect on the variation of these parameters in composition and thickness of the thin films obtained.

An aerosol atomized ultrasonically from an aqueous nitrate solution of Ba, Ca, Cu and Pb, with 2.00:1.70:4.90:1.40 nominal cation ratios, was sprayed on a MgO substrate. The volume used for each sample was 21 ml. It was deposited in equal parts in three cycles. After each cycle, a thermal treatment in situ, of 5 minutes at 500°C and heating rate of 21°C/min was carried out. After deposition, samples were annealed as follows: From room temperature (T_{room}) to 700°C at 5°C/min and from 700°C to T_a at 2°C/min; annealing during t_a hours at T_a according to Table 1; cooling from T_a to 700°C at 10°C/min and from 700°C to T_{room} at 2°C/min.

Table 1 Design N2: Fractional factorial design 3^{4-2} for the determination of the influence of T_D, T_a, t_a , and molarity on the thickness of the precursor film

Sample	Parameters			
	T_D [°C]	M	T_a [°C]	t_a [h]
ra1	150	0.005	810	3
ra2	250	0.005	835	21
ra3	350	0.005	860	12
rb1	250	0.010	860	3
rb2	350	0.010	810	21
rb3	150	0.010	835	12
rc1	250	0.015	810	12
rc2	350	0.015	835	3

Were T_D is the deposition temperature, M is the concentration in moles of the deposition solution, T_a is the annealing temperature, and t_a is the annealing time in the thermal treatment.

Samples were characterized by XRD with CuKα radiation using a Siemens D500 diffractometer. Chemical composition for both, solutions and thin films were determined by atomic absorption spectroscopy. We report DRX, thickness and atomic absorption measurements of Ba-Ca-Cu-Pb-O precursor thin films.

Results

X Ray diffraction. Fig. 1 shows the pattern diffractogram of sample rc3. All samples show the following compounds: $BaPbO_3$, $Ba_4Pb_3O_{10}$, $BaCuO_2$, CuO, Cu_2O and Ca_2CuO_3.

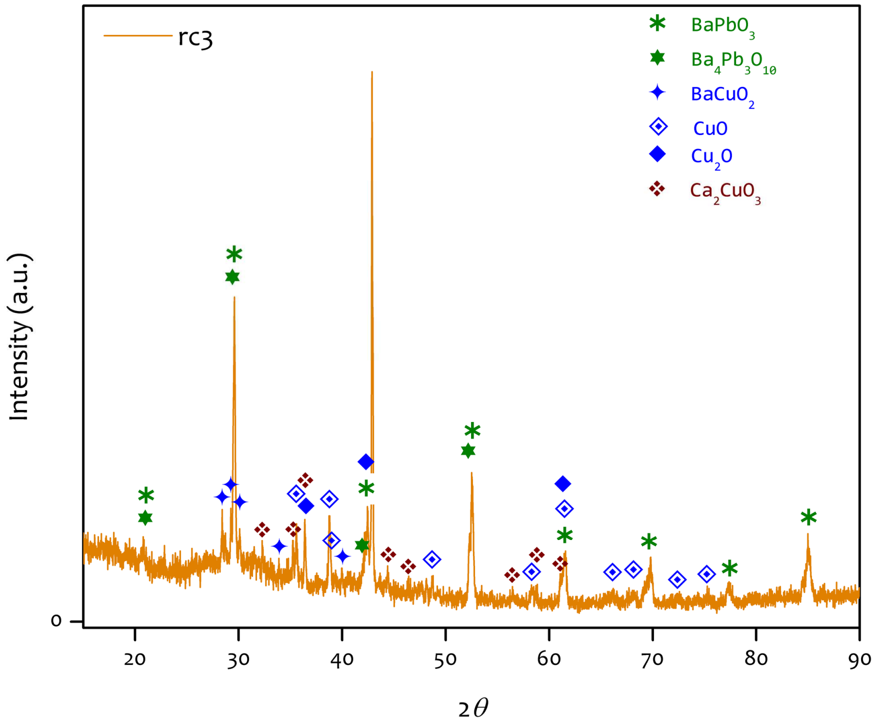

Fig. 1 X-ray pattern from sample rc3.

Rietveld method. Fig. 2 shows the relative content of the compounds, where we can observe that the samples contain five measurable phases and their variation in percentage. Quantitative determination of the precursor films was performed by means of the Rietveld method using Rietveld refinement data and the Fullprof program [5]. A typical Rietveld refinement is shown in Fig. 3.

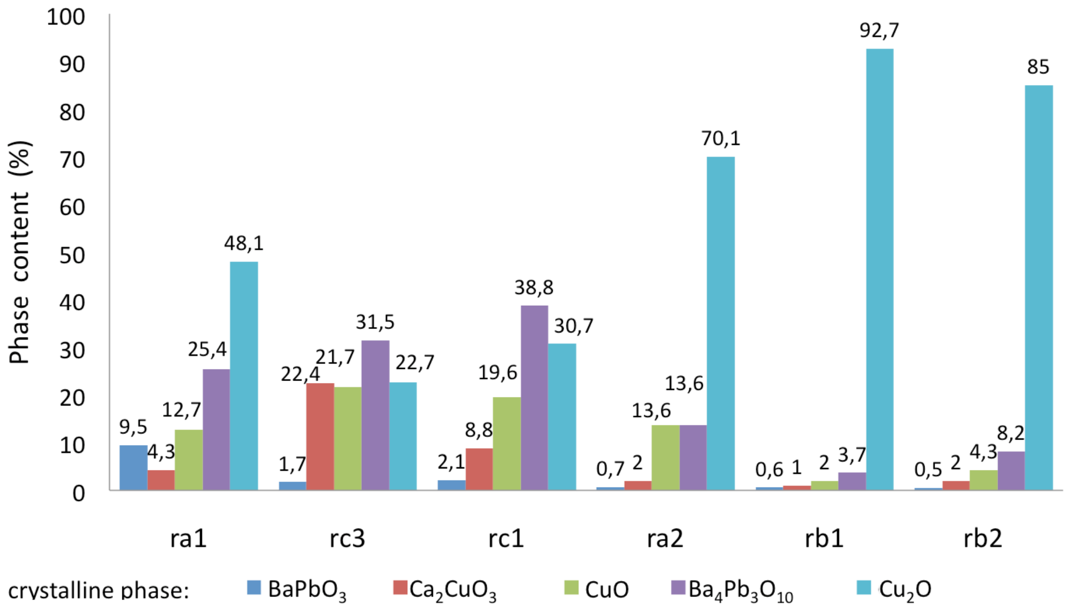

Fig. 2 Variation of $BaPbO_3$, Ca_2CuO_3, CuO, $Ba_4Pb_3O_{10}$ y Cu_2O on samples ra1, ra2, rb1, rb2, rc1 and rc3.

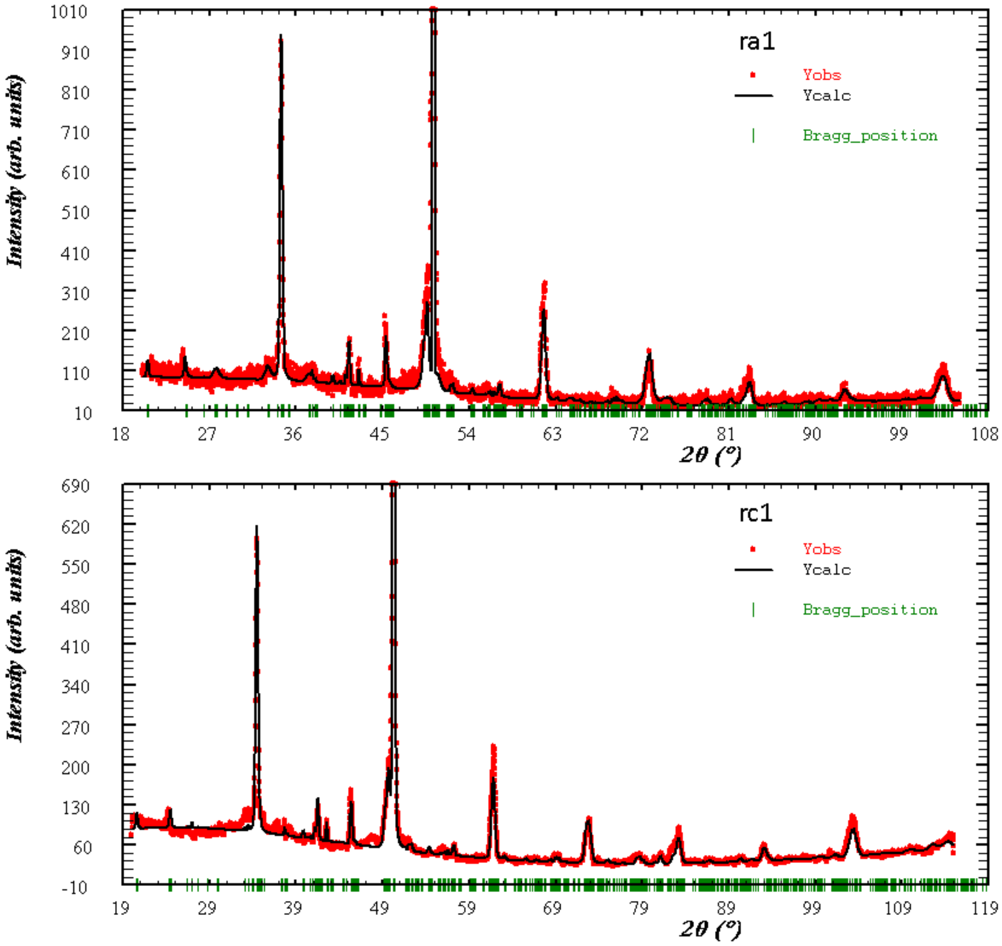

Fig. 3 Rietveld refinement. Samples ra1 and rc1.

Atomic absorption. Chemical composition of thin films was determined by atomic absorption spectroscopy. Fig. 4 shows the composition relating to one of the elements fixed as constant in order to observe the behavior of the relative content in each of the samples.

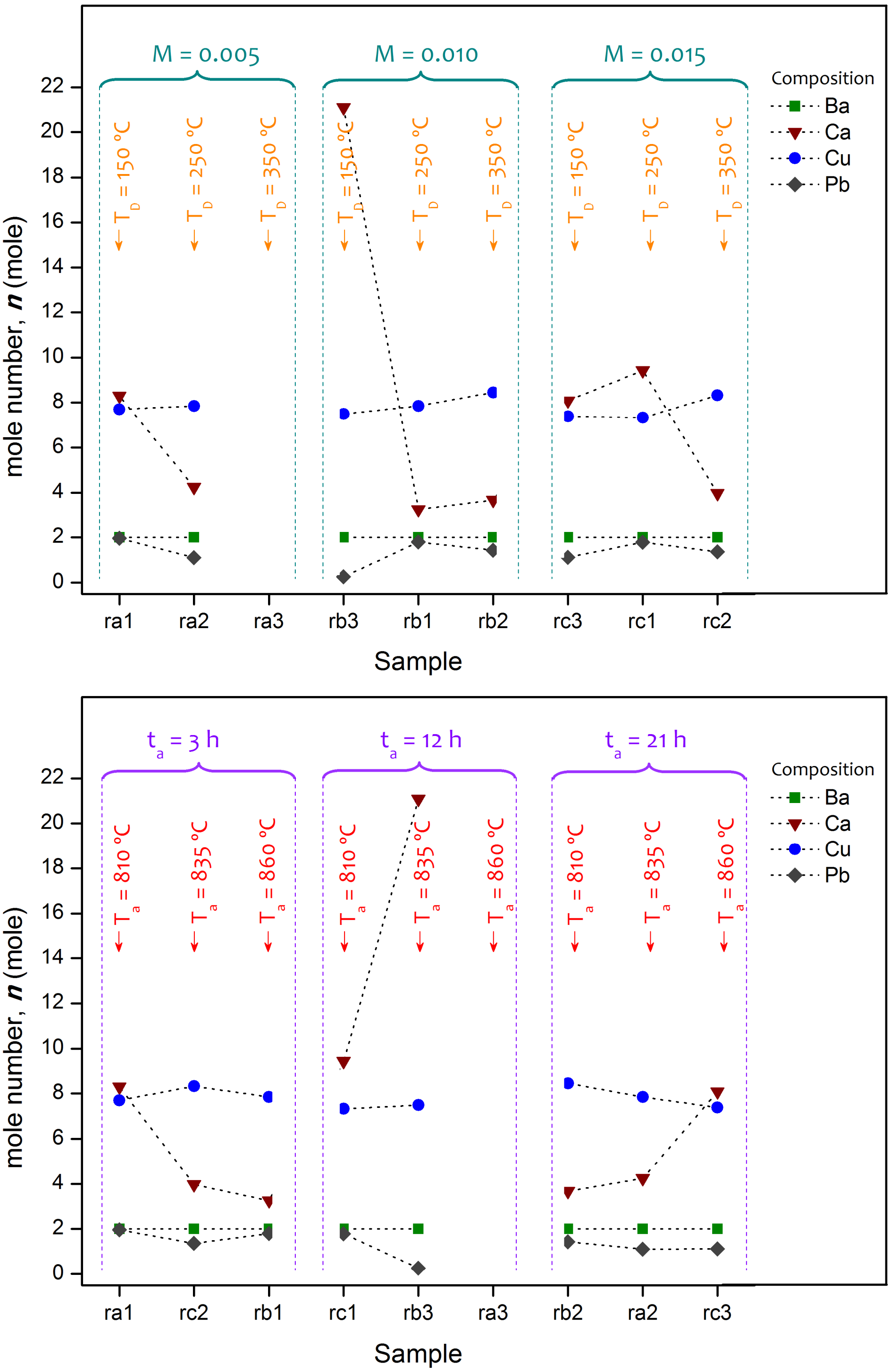

Fig. 4 Variation of Ba-Pb-Ca-Cu composition on samples ra1 - rc3. Comparison of the samples behavior according to moles number in function of the T_D, M, T_a and t_a values used in their preparation

Thickness. Measurements of thickness and roughness along of 3mm from border to center of annealed samples were performed. Samples showing minor roughness were ra1, rb2 and rc1. These samples were annealed at 810°C. Thickness behavior is shown in Fig. 5.

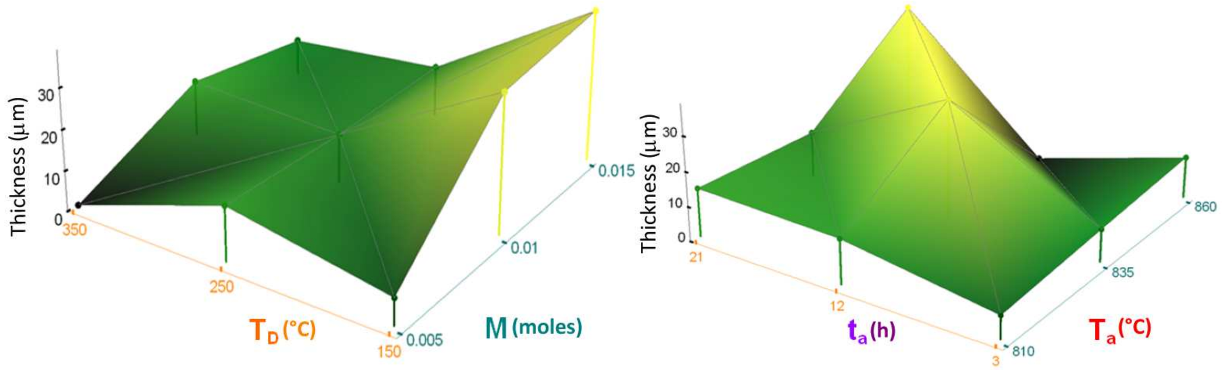

Fig. 5 Thickness curves on samples ra1 – rc3, taking values T_D and M, and T_a and t_a, in order to compare the influence in the thickness, simultaneously.

Discussion

The $BaPbO_3$ compound presents several crystalline phases, mainly orthorhombic and cubic. This last is observed in higher quantity on samples ra1 and rb2. The compound $Ba_4Pb_3O_{10}$ was grown in its tetragonal phase in greater quantity on samples ra1, ra2, rb1 and rb2 than in the others. Formation of compounds where Ba, Pb and O took part was favorable at annealing temperatures of 810°C or higher and with annealing times of 3 hours. The $BaCuO_2$ cubic phase appears in higher quantities on samples ra2 and rc3 than in the rest of samples but this quantity is not enough for Rietveld refinement. XRD results show that for the rest of samples the $BaPbO_3$ and $Ba_4Pb_3O_{10}$ phases are in a higher quantity. Therefore it means that Ba is associated preferably with Pb. The CuO monoclinic phase appears in a higher quantity on samples ra2 and rc3. On the other hand, Ca_2CuO_3 is present in the same quantity in all samples, although its content is in competition with Cu_2O. Traces of phases which inhibit the incorporation of Hg, as for example Ba_2CuO_{3+d} and $BaCO_3$ phases, were not observed.

Deposition temperature and solution molarity have more influence on the thickness than thermal treatment parameters as annealing temperature and annealing time.

Conclusions

It was possible to determine the conditions in which each precursor phase was formed. In order to obtain ternary compounds of Ba-Pb-O, a temperature of 810°C is suitable and to grow ternary compounds of Ba-Cu-O, higher temperatures between 835°C and 860°C are required.

Increasing deposition temperature, Pb and Cu content are maintained approximately constant, while Ca content diminishes notably.

Acknowledgements

This work was supported by Project SIP-IPN 20091030 and 20091066.

References

[1] S.N. Putilin, E.V. Antipov, O. Chmaissen and M. Marezio: Nature 362 (1993), p. 226

[2] A. Schilling, O. Jeandupeux, J.D. Guo and H.R. Ott: Physica C 216 (1993), p. 6

[3] M. E. Yakinci, M.A. Aksan and Y. Balci: Supercond. Sci. Technol. 18 (2005), p. 494

[4] S. Kumari, A.K. Singh and O.N. Srivastava: Supercond. Sci. Technol. 10 (1997), p. 235

[5] J. Rodriguez-Carvajal: Physica B. 192 (1993), p. 55

doi:10.4028/www.scientific.net/AST.75.202

Processing by pulsed laser deposition and structural, morphological and chemical characterization of Bi-Pb-Sr-Ca-Cu-O and Bi-Pb-Sb-Sr-Ca-Cu-O thin films

V. Ríos[1, a], E. Díaz[1, b], J. R. Aguilar[1, c], T. Kryshtab[1, d], C. Falcony[2, e]

[1]ESFM-IPN, Edificio 9 UPALM, Col. San Pedro Zacatenco, Delegación G.A.M., México 07738 México.
[2]Centro de Investigación y de Estudios Avanzados del IPN, Departamento de Física, Av. IPN 2508, Apdo. Postal 14-740, Mexico 07000 México.
[a]rivers@hotmail.com, [b]elviadv@esfm.ipn.mx, [c]jaguilar@esfm.ipn.mx, tkrysh@esfm.ipn.mx[d], cfalcony@fis.cinvestav.mx[e]

Keywords: BPSCCO, pulsed laser deposition, superconducting films, structural characterization.

Abstract. Bi-Pb-Sr-Ca-Cu-O (BPSCCO) and Bi-Pb-Sb-Sr-Ca-Cu-O (BPSSCCO) thin films were grown on MgO single crystal substrates by pulsed laser deposition. The deposition was carried out at room temperature during 90 minutes. A Nd:YAG excimer laser (λ = 355 nm) with a 2 J/pulse energy density operated at 30 Hz was used. The distance between the target and substrate was kept constant at 4,5 cm. Nominal composition of the targets was $Bi_{1,6}Pb_{0,4}Sr_2Ca_2Cu_3O_\delta$ and $Bi_{1,6}Pb_{0,4}Sb_{0,1}Sr_2Ca_2Cu_3O_\delta$. Superconducting targets were prepared following a state solid reaction. As-grown films were annealed at different conditions. As-grown and annealed films were characterized by XRD, FTIR, and SEM. The films were prepared applying an experimental design. The relationship among deposition parameters and their effect on the formation of superconducting Bi-system crystalline phases was studied.

Introduction

Actually one of the principal targets in solid-state physics is the discovery of novel materials and other one is to increase possibilities of application in fields as optoelectronics and nanotechnology. As size continues diminishing below micron dimensions and heterogeneous materials are integrated in a single solid state device, it becomes of paramount importance to understand the fundamental processes and microscopic mechanisms in order to control film deposition. In the processing of thin films of Bi-Sr-Ca-Cu-O system it has been too much effort to stabilize the high-temperature superconducting phase. It has been reported that the formation temperatures of $Bi_2Sr_2CuO_6$ (2201) and $Bi_2Sr_2CaCu_2O_8$ (2212) phases are about 600 and 800°C respectively and that the transformation between the 2201 and 2122 phases depend upon the annealing time and temperature range. This last has been reported from 800°C to 880°C [1]. Other results suggest that BSCCO films are highly sensitive to growth conditions, as those ones mentioned above, as well as, incident atomic fluxes, and film growth rate [1- 3]. PLD has become a standard technique for the production of thin films of complicated stoichiometry as the $Bi_2Sr_2Ca_{n-1}Cu_nO_{2n+4}$ (BSCCO) system that has several competing phases coexisting, e.g., stable n = 1, 2, 3 phases with zero-resistance T_{c0} = 20 K, 85 K, and 110 K, respectively, as well as metastable phases with higher n. The most studied compounds of the family are those of n = 1 and n = 2. The compound with n = 3 is difficult to obtain because of the stabilization of the phase [4]. In order to obtain epitaxial BSCCO films by pulsed laser deposition (PLD) it is necessary to prepare them in two stages: deposition and annealing of the as-deposited films, but it is important to consider that the physical processes in PLD are highly complex and it is interrelated, and dependent on the laser pulse parameters and the properties of the target material [2, 5-7]. It seems likely that BSCCO films grown by PLD would contain variations in stacking along the growth (c-axis) direction, as well as an increased defect density, both of which can affect superconducting properties. In order to obtain high quality films for many applications and fundamental studies, the growth of films must be done on suitable substrates. The production of BSCCO thin films has been reported on SrTiO3, ZrO and MgO [8, 9]. The exact mechanism by which crystallization and superconductivity are improved is not yet known. Therefore, in order to improve the quality of PLD BSCCO films, it is important to systematically study changes in phase-content, microstructure, and superconducting properties, as deposition conditions are varied. One of the applications of main interest on these superconducting films is the development of optoelectronic devices due to two phases of high critical temperature in the Bi-based system. Furthermore the compounds of the system are no toxic. With the high intensity pulsed laser ablation technique uniform and thin films can be obtained, these two characteristics are important in the development of optoelectronic devices. It has been reported that Sb doping enhances the stabilization of the Bi high-T_c phases [9]. In this work, we study BSCCO films grown on single crystal MgO using polycrystalline Bi-Pb-2223 and Bi-Pb-Sb-2223 targets, following an experimental design 2^3.

Experimental

Experimental work was developed as follows: Targets preparation (superconducting pellets), targets characterization, laser ablation deposition of precursor films, precursor films characterization, thermal treatment of precursor films and finally characterization of annealed films.

Targets for ablation laser deposition were superconducting pellets of one inch diameter, which were prepared by solid state reaction from stoiquiometric quantities of Bi_2O_3, PbO, $SrCO_3$, $CaCO_3$, CuO y Sb_2O_3. These were calculated in order to obtain $Bi_{1.6}Pb_{0.4}Sb_xSr_2Ca_2Cu_3O_\delta$ nominal composition, where x took values of 0 and 0,1. The preparation procedure to obtain the targets that consists on several mills and thermal treatments is presented in Table 1. In order to study the relationship between deposition parameters and their effect on the formation of superconducting Bi-system crystalline phases, an experimental design 2^3 that is shown in Table 2 was applied. The studied parameters were content of Sb, annealing temperature (T_a), and annealing time (t_a). Deposition parameters were established constant as well as type of substrate. From the experimental design, 8 runs were carried out. Precursor films were deposited by pulsed laser ablation on single crystal MgO of 1 cm^2. A laser of Nd: YAG was used. Deposition was performed with 150,000 pulses by one and a half hour in a vacuum of 1,6*10-6 torr and a substrate-target distance of 4,5 cm. After deposition, each precursor film was subjected to thermal treatment in the plane zone of a quartz tube furnace and according to the experimental design, table 2. For annealing, each precursor film was covered with a clean substrate in order to avoid the loss of material by evaporation. Precursor and annealed films were characterized by XRD, SEM and electrical measurements. XRD profiles were obtained in the Bragg-Brentano geometry using a K_α source operated at 45 KV and 40 mA, in an X`Pert Panalytical diffractometer with a hybrid monochromator and a triple axis/HR rocking curve detector. The film thickness was taken by the reflectivity technique in the same diffractometer. The film morphology was observed at different magnifications by scanning electron microscopy in a Sirion-FEI equipment with Everhart-Thornley (ET) and TTL detectors and using secondary electrons. Electrical measurements of annealed films were performed with the 4-probe method from room temperature to 20 K.

Results and discussion

Fig. 1 shows the XRD profiles of the B6L-1 and BS6L-1 targets. The B6L-1 target shows a mixture of $Bi_{1.6}Pb_{0.4}Sr_2Ca_2Cu_3O_x$ and $Bi_{1.6}Pb_{0.4}Sr_2CaCu_2O_x$ phases while the BS6L-1 target that was doped with Sb shows only the $(BiPb)_2Sr_2Ca_2Cu_3O_x$ phase. This indicates that Sb stabilizes the Bi-2223 phase. Fig. 2 shows the XRD profiles of the films ALR1 to ALR8. The film ALR1 presents the growth of the $Bi_3Pb_{0.6}Sr_2CaCu_3O_x$ phase and Bi_2SrO_4 as main phase. The films ALR2 to ALR8 present mixtures of $Bi_3Pb_{0.6}Sr_2CaCu_3O_x$, $Bi_2Sr_2CaCu_3O_x$ and $BiSrCaCu_2O_x$ phases with different relative contents among them and with the least relative quantity of the $Bi_3Pb_{0.6}Sr_2CaCu_3O_x$ phase. The $BiSrCaCu_2O_x$ phase has a tetragonal crystal lattice and the $Bi_2Sr_2CaCu_3O_x$ phase has an orthorhombic one. In connection with preparation conditions (table 2),

Table 1 Target preparation procedure.

Sample as	T_a **[°C]**	t_a **[h]**
Powder	*400-600*	*10-100*
Powder	*700*	*10*
Powder	*750*	*10*
Powder	*800*	*10*
Pellet	*830*	*10*
Pellet	*860*	*720*

Table 2 Matrix arrangement of the 2^3 experimental design with the studied parameters values, where x = Sb content in the nominal composition of the target; T_a = annealing temperature and t_a = annealing time.

Sample	***x***	T_a ***[°C]***	t_a ***[h]***
ALR1	0	820	1
ALR2	0,1	820	1
ALR3	0	840	1
ALR4	0,1	840	1
ALR5	0	820	2
ALR6	0,1	820	2
ALR7	0	840	2
ALR8	0,1	840	2

XRD results show that at T_a = 840°C and t_a = 1 h, the film prepared with the B6L-1 target (ALR3) shows as majority phase the tetragonal one because of the high intensity of the (008) reflection, whereas the film prepared with the BS6L-1 target (ALR4) shows as majority phase the orthorhombic one as it can be observed in the highest intensity of the (0 0 10) reflection. When the preparation conditions change to T_a = 820°C and t_a = 2 h, the tetragonal phase increases in the film prepared with BS6L-1 target (ALR6) and the orthorhombic one increases in the film prepared with B6L-1 target (ALR5). When the T_a is set constant and the t_a increases from 1 h to 2 h, we can observe a change in phases growing from the orthorhombic to tetragonal phase in films prepared with the B6L-1 target (ALR3 and ALR7) and the opposite in films prepared with the BS6L-1 target (ALR4 and ALR8). This makes clear that the formation of superconducting phases is independent of targets composition used here or rather it is up to thermal treatment conditions, that is, the conditions of the solid state reaction.

Fig. 3 shows the electrical measurements of the films. The film ALR1 did not present superconducting behavior that is according with the XRD results. Before the superconducting transition, the most resistive film was the ALR3 one and the least resistive was the ALR6 one. All films presented two or three transitions that can be related with the presence of several

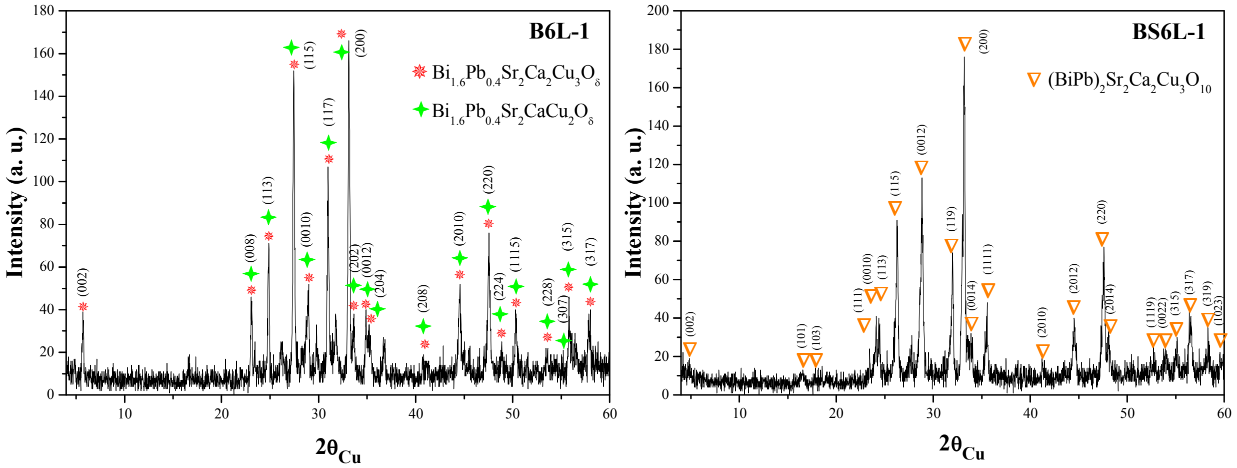

Fig. 1 XRD profiles of Bi-Pb-Sr-Ca-Cu-O targets prepared according to the conditions shown in table 1, from $Bi_{1.6}Pb_{0.4}Sb_ySr_2Ca_2Cu_3O_\delta$ nominal composition, where *y* took values of 0 and 0,1.

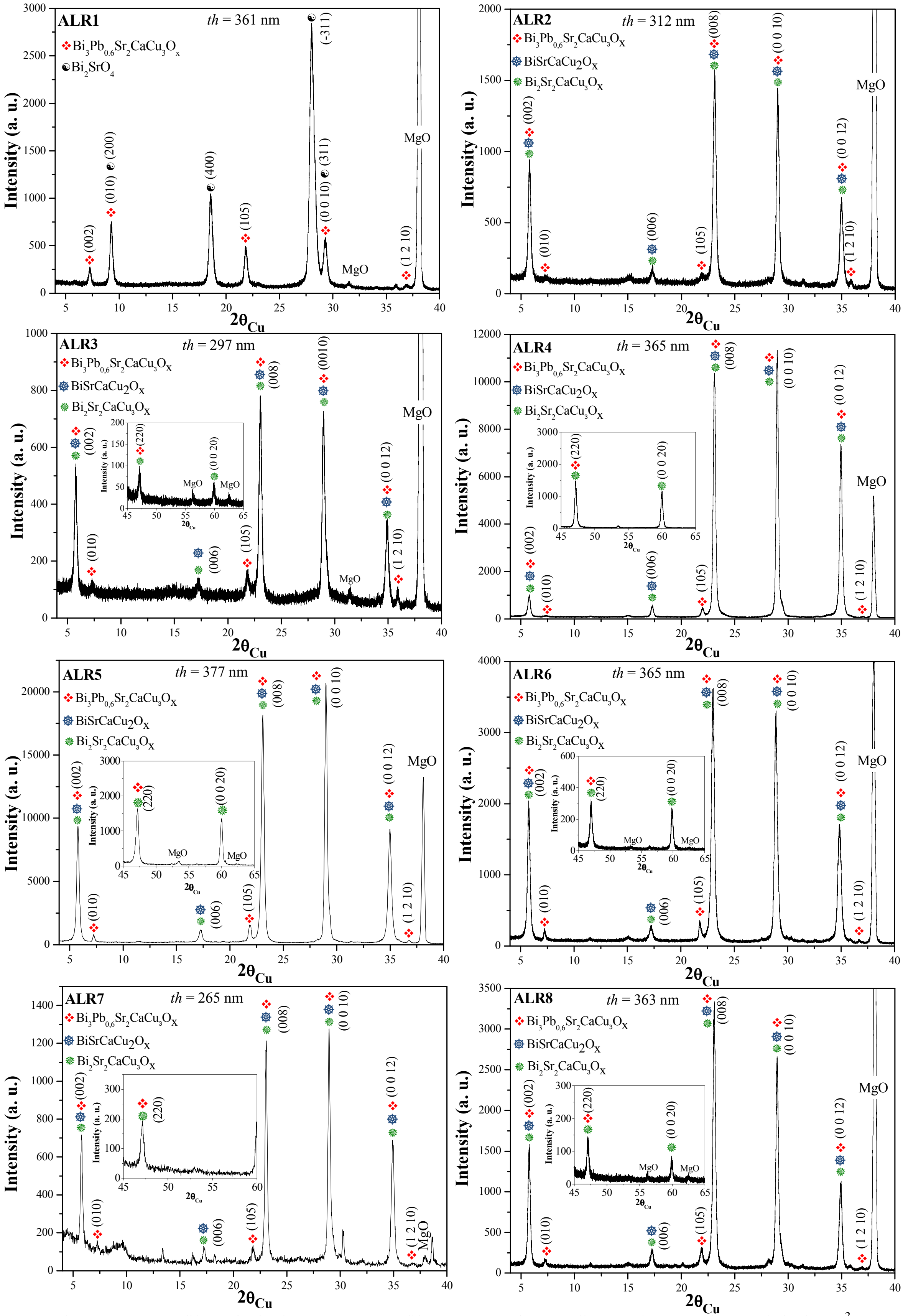

Fig. 2 XRD profiles of Bi-Pb-Sr-Ca-Cu-O films prepared according to the experimental design 2^3 that is showed in table 2. In all the diffractograms the film thickness (*th*) is shown.

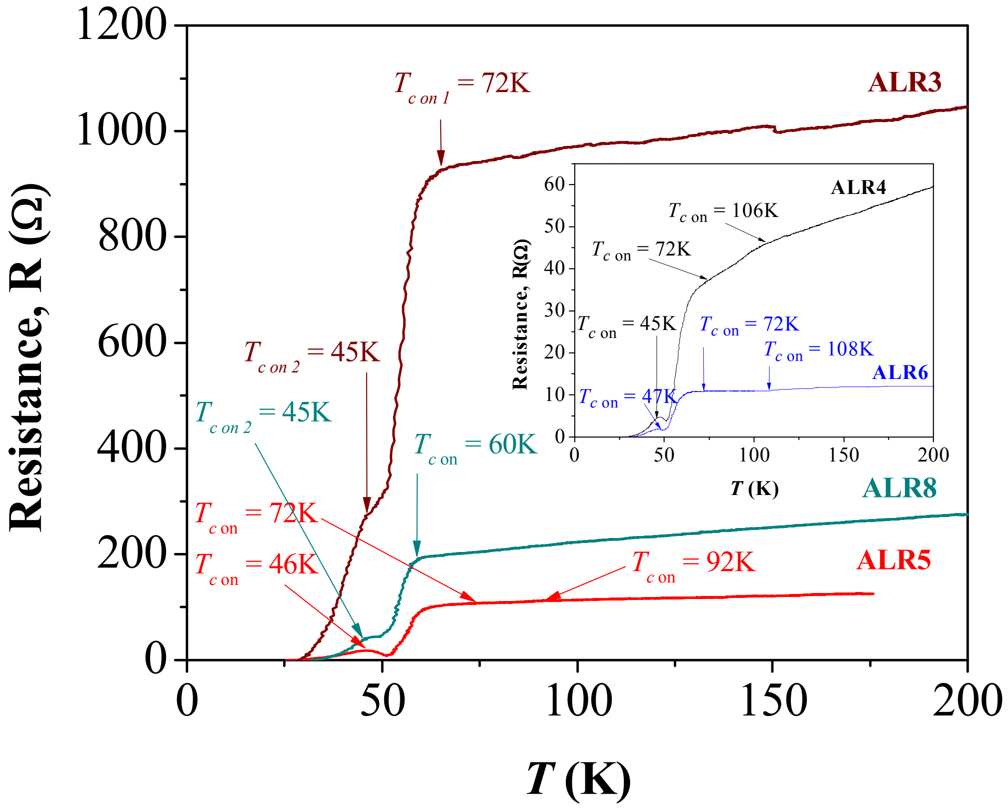

Fig. 3 Electrical behavior of Bi-Pb-Sr-Ca-Cu-O prepared according to the experimental design 2^3 that is showed in table 2.

superconducting phases. The film ALR4 showed the highest $T_{c\ on}$ at 106 K. Several films presented $T_{c\ on}$ at 72 K and transitions around 45 K. All superconducting films got the superconductivity at resistance zero below 35 K. Films ALR4 and ALR6 showed the best electrical behavior because of their resistance as normal conductors and their $T_{c\ on}$.

From XRD and electrical measurements results related to the preparation conditions we can observe that at conditions of $T_a = 840^{o}$C and $t_a = 1$ h, the orthorhombic phase increases and improve the electrical behavior of the film (Comparison between ALR3 and ALR4 films). When the preparation conditions change to $T_a = 820^{o}$C and $t_a = 2$ h, the tetragonal phase increases and also the electrical behavior of the film is improved (Comparison between films ALR5 and ALR6). When T_a is setting constant and t_a is increased the electrical behavior is degraded as we can observe making a comparison between films ALR4 and ALR8.

In Fig. 4 are presented typical micrographs of precursor and annealed films.

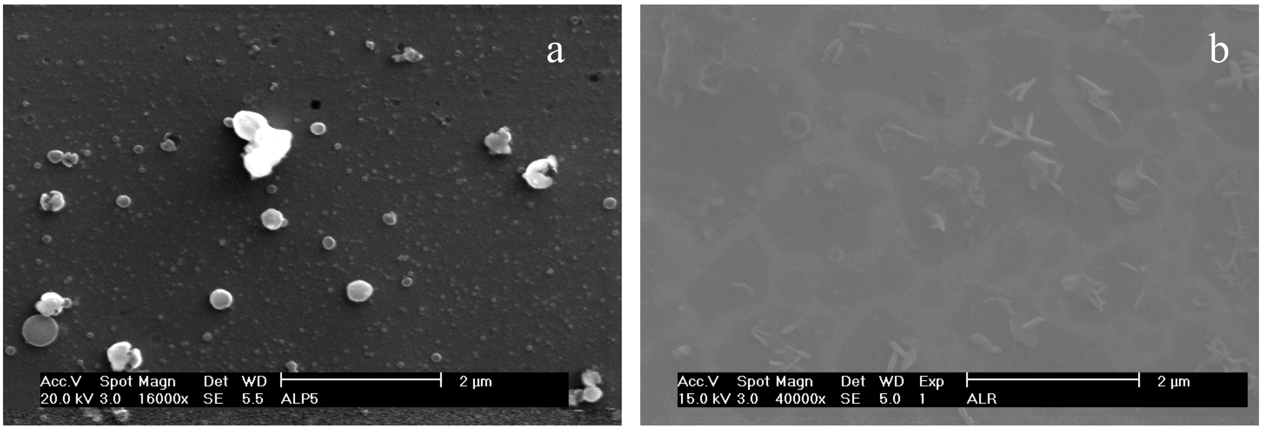

Fig. 4 Scanning electron micrographs obtained with secondary electrons from film ALR5. a) Precursor film, b) annealed film

In Fig. 4a droplets and precipitates from the laser ablation production are observed over a surface with smaller droplets. Fig. 4b shows the morphology of the annealed film showing particles with flake form over a plane surface. From the micrographs obtained with secondary electrons, we can observe that some technological obstacles need to be resolved in the pulsed laser deposition of films. By far the most important of these is the laser droplet production and impurity levels from droplets and precipitates. It means that it is necessary filtration of plasma particles.

Conclusions

Targets with a mixture of $Bi_{1.6}Pb_{0.4}Sr_2Ca_2Cu_3O_x$ and $Bi_{1.6}Pb_{0.4}Sr_2CaCu_2O_x$ phases and targets with a single $(BiPb)_2Sr_2Ca_2Cu_3O_x$ phase produce the growth of superconducting phases but the relative content of each one and the film electrical behavior are up to the conditions of the solid state reaction. On the other hand, in order to avoid droplets and precipitates as a product of the laser ablation production it is necessary elimination of plasma particles.

Acknowledgements

The authors gratefully acknowledge financial support to the SIP-IPN and to Centro de Nanociencias - IPN for its support in the XRD measurements. Special thanks go to the Ph.D Alicia Rodríguez P. and Dr. Gabriela Gazga for XRD measurements, Gerardo Ortega C. and J. I. Guzmán Castañeda for SEM measurements and Zacarías Rivera Alvarez for R-T measurements.

References

[1] T. Matsumoto, T. Kawai, K. Kitahama, S. Kawai, l. Shigaki and Y. Kawate: *Layer-by-layer epitaxial growth of a* $Bi_2Sr_2Cu0_6$ *thin film on a* $Bi_2Sr_2CaCu_20_8$ *single crystal*, Appl. Phys. Lett. Vol. 58 No.18 (1991) p. 2039-2041

[2] M. Yavuz, M. S. Boybay, C. Elbuken, M. J. Andrews, C. R. Hu and J. H. Ross: *Bi-Sr-Ca-Cu-O superconducting thin films: theory and experiment*, Journal of Physics: Conference Series Vol. 43 (2006) p. 277–280

[3] S. Zhu, D. H. Lowndes, B. C. Chakoumakos, J. D. Budai, D. K. Christen, X. Y. Zheng, E. Jones and B. Warmack: *In situ growth of epitaxial* $Bi_2Sr_2CaCu_20_{8-x}$, *and* $Bi_2Sr_2Cu0_{6-x}$ *films by pulsed laser ablation*, Appl. Phys. Lett. Vol. 63 No.3 (1993) p. 409-411

[4] L. Rano, D. Martínez-García, J. Perrière and P. Barboux : *Phase intergrowth in* $Bi_2Sr_2Ca_{n-1}Cu_nO_y$ *thin films*, Phys. Rev. B Vol. 48, No. 18 (1993) 13945-13948

[5] R. K. Singh and J. Narayan: *Pulsed-laser evaporation technique for deposition of thin films: Physics and theoretical model*, Phys. Rev. B, Vol. 41 No. 13 (1990) p. 8843-8859

[6] J. Shou: *Physical aspects of the pulsed laser deposition technique: The stoichiometric transfer of material from target to film*, Appl. Surf. Sc. Vol 255 (2009) p. 5191‑5198

[7] P. R. Willmott and J. R. Huber: *Pulsed laser vaporization and deposition*, Reviews of Modern Physics Vol. 72, No. 1, (2000) p. 315-328

[8] D. K. Fork, J. B. Boyce, F. A. Ponce, R. I. Johnson, G. B. Anderson, G. A. N. Connell, C. B. Eom and T. H. Geballe: *Preparation or oriented Bi-Ca-Sr-Cu-O thin films using pulsed laser deposition*, Appl. Phys. Lett., Vol. 53, No. 4 (1988), p. 337-339

[9] 328K. L. Mao, R. E. Russo, H. B. Liu and J. C. Ho: *As-deposited Sb-doped Bi-Pb-Sr-Ca-Cu-O thin films prepared by pulsed laser deposition*, Appl. Phys. Lett. Vol. 57, No. 24 (1990) p. 2591-2593

doi:10.4028/www.scientific.net/AST.75.208

Seawater Magnetohydrodynamics Power Generator / Hydrogen Generator

Minoru TAKEDA

Graduate School of Maritime Sciences, Kobe University, Kobe 658-0022, Japan

takeda@maritime.kobe-u.ac.jp

Keywords: MHD generator, Superconducting technology, Helical flow, Seawater, Hydrogen

Abstract

A seawater magnetohydrodynamics (MHD) power generator / hydrogen generator is expected to become popular with the development of superconducting technology because of low loss and high efficiency. We have designed a new helical-type seawater MHD generator using a solenoid superconducting magnet, by considering the experimental results for a helical-type MHD ship. The experimental and computational results for the helical-type generator including the results of a recent study on hydraulic characteristics are discussed.

Introduction

A seawater magnetohydrodynamics (MHD) power generator / hydrogen generator is a unique system that not only directly transforms the kinetic energy of an ocean current / tidal current into electric energy but also generates hydrogen gas as a by-product. The energy of the ocean current / tidal current is expected to be effective as a sustainable energy source because of its independence of both weather and season in comparison with solar energy and wind power energy. It is great importance for an oceanic country such as Japan to develop the seawater MHD generator based on the sustainable ocean current / tidal current energy. In our work, experimental and computational studies on a seawater MHD generator using a superconducting magnet have been performed to investigate the application of superconductivity to maritime sciences. So far, a linear-type seawater MHD generator with a dipole superconducting magnet was constructed and experiments on power generation were successfully accomplished [1].

In seawater MHD generation, the applied magnetic field is an important factor determining the generator output and efficiency. A linear-type generator has the problem of requiring a large and strong superconducting magnet. To solve this problem, we designed a new helical-type seawater MHD generator using a solenoid superconducting magnet, by considering the experimental results for a helical-type MHD ship [2]. Preliminary experiments on generator output using the helical-type generator were carried out in a magnetic field of 7 T [3]. A numerical simulation was carried out continuously using a three-dimensional model [4], assuming its size to be equal to that of the generator. In this paper, experimental and computational studies on the helical-type seawater MHD power generator / hydrogen generator including our recent study on its hydraulic characteristics [5,6] are reported.

Preliminary Study

Principle of Helical-Type MHD Generator. Fig. 1 shows the principle of the helical-type MHD generator. The helical-type generator consists of double-cylindrical coaxial electrodes, a helical insulation wall (a helical partition board) and a solenoid superconducting magnet. When seawater rotates around an anode in the presence of a magnetic field B parallel to the coaxial direction, an electromotive force V_e is generated in accordance with the law of electromagnetic induction. V_e is proportional to B, the flow velocity U, the distance between the electrodes D and $\sin\theta$, where θ is the

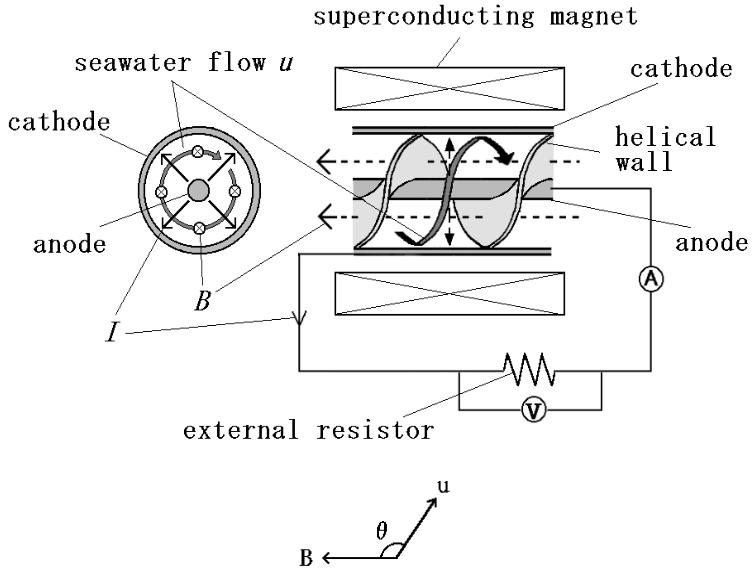

Fig. 1 Principle of the helical-type seawater MHD generator.

angle between the directions of B and U. When V_e exceeds the electrolysis voltage V_d, electric power P and also hydrogen gas as a by-product are generated by the electric current I.

Experimental Apparatus. Fig. 2 shows a schematic diagram of the helical-type MHD generator [3]. The helical wall is made of polyvinyl chloride and has a spiral shape with a rotation number of 2.5 and a length of 140 mm. The anode is a cylindrical rod 10 mm in diameter and 1350 mm long. The cathode is a cylindrical pipe 100 mm in outer diameter, 1.5 mm in thickness and 260 mm long. The electrodes are made of SUS316, which is nonmagnetic and corrosion-resistant. Fig. 3 shows a schematic diagram of the experimental system for the MHD generator. The system mainly consists of the generator, a cryostat with a 7 T solenoid superconducting magnet, a seawater tank, a seawater circulation pump, a flow meter, a pressure gauge and a thermometer.

Experimental Results. Experiments on the electromotive force and generator output were carried out to elucidate the fundamental characteristics of the helical-type generator using NaCl aqueous solution (3.4%) [3]. The electromotive force was measured at various sample flows from 0 to 45 m^3/h and magnetic fields from 0 to 7 T. The generator output was also measured similarly using an external load of 1 Ω.

Fig. 4 represents the dependence of the electromotive force on the average flow velocity in a magnetic field of 7 T. The electromotive force increased linearly with increasing average flow

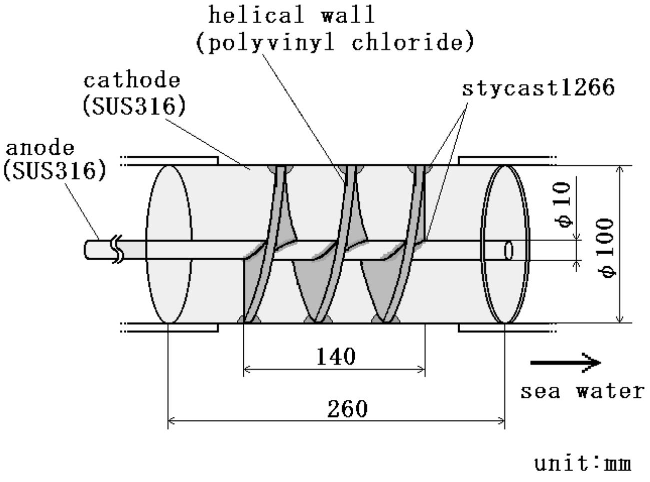

Fig. 2 Schematic diagram of the helical-type seawater MHD generator.

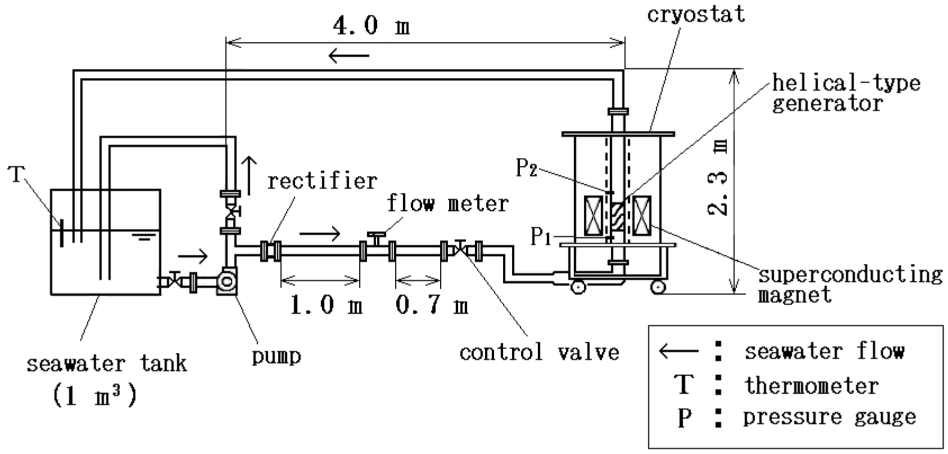

Fig. 3 Schematic diagram of the experimental setup.

velocity in a constant magnetic field. The dependence of the generator output on the average flow velocity in a magnetic field of 7 T is shown in Fig. 5. The generator output increased quadratically to average flow velocity over certain points. When the average flow velocity was kept at the maximum value (5.6 m/s), a generator output of 0.05 W was attained. In this experiment, the electromotive force and generator output were small owing to the large flow loss of the generator.

Numerical Simulation

Simulation Model. To simulate the MHD generation system, we set up a three-dimensional model [4] and assumed its size to be equal to that of the generator used in the preliminary experiment. The simulation was carried out by the finite element method (FEM) on ANSYS multiphysics software (ANSYS Inc., version 8.0), which can perform a combined structural, thermal, fluid and electromagnetic simulation. The simulation includes two parts: fluid numerical analysis and electromagnetic numerical analysis.

Fluid Numerical Analysis. In this analysis, the values of flow loss, i.e., the pressure drop ΔP between the entrance and exit of the helical flow obtained in the experiment, were used. To confirm the validity of the numerical analysis of the generation system, we compared the flow rates Q obtained experimentally with the numerical calculation for various pressure drops. The results were in good agreement for all pressure drops. Fig. 6 shows an example of the flow velocity distribution in the generation system at a flow rate of 45 m^3/h. In this figure, because a large number of nodes were used in the analysis, the vectors at selected nodes are distinguished by length as well as color. In addition,

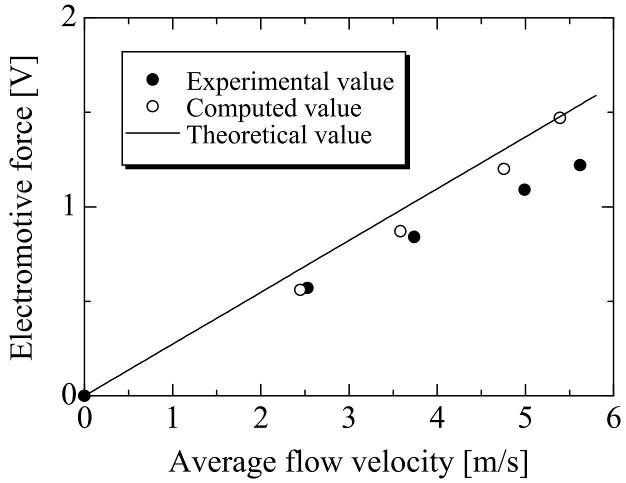

Fig. 4 Relationship between electromotive force and average flow velocity with $B = 7$ T.

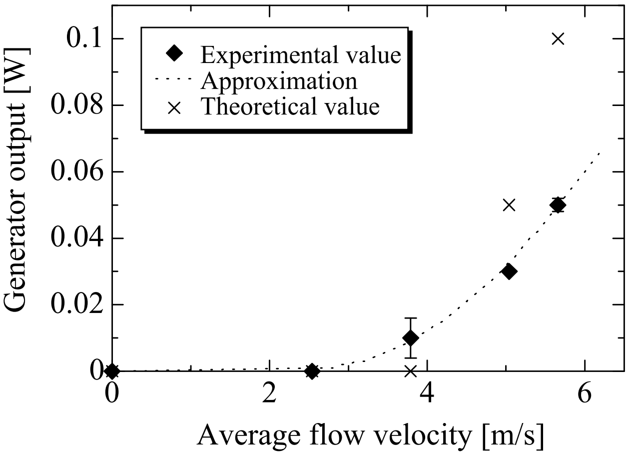

Fig. 5 Relationship between generator output and average flow velocity with $B = 7$ T. Dotted line shows an approximation of experimental values.

to illustrate the directions of the velocity vectors clearly, a few of them are shown as thick black lines on the right side in Fig. 6.

Electromagnetic Numerical Analysis. The electromagnetic numerical analysis was carried out after the flow velocity distribution was obtained from the fluid numerical analysis. The helical wall acts as an insulator, and the magnetic permeability of each part in the generator was assumed to be equal to the value μ_0 in a vacuum. The magnetic field was assumed to be homogeneous, and this analysis was performed by a technique of harmonic magnetic field analysis in ANSYS. Fig. 7 shows the electric current distribution at a flow rate of 45 m^3/h and a magnetic field of 7 T.

It is possible to obtain the potential difference between electrodes, i.e., the electromotive force, by Ohm's law. Fig. 8 shows calculated values of electromotive force at magnetic fields of 6 and 7 T, comparing with the experimental and theoretical values. The theoretical values were calculated taking account of the average flow velocity (flow rate / cross section of helical flow) and the average external field of 90% of the maximum value. As can be seen in this figure, the calculated values agreed with the experimental values at a low flow rate but the experimental values were lower at a high flow rate.

Recent Study on Hydraulic and Other Characteristics

Effect of Flow Rectifier. To reduce the flow loss, and also to increase the electromotive force, experiments on the fundamental characteristics of the MHD generator were carried out using flow

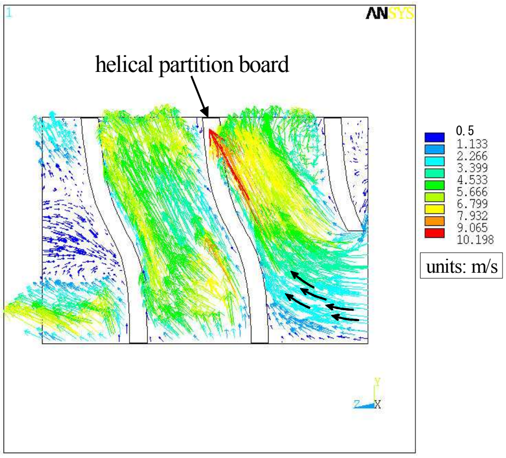

Fig. 6 Flow velocity distribution.

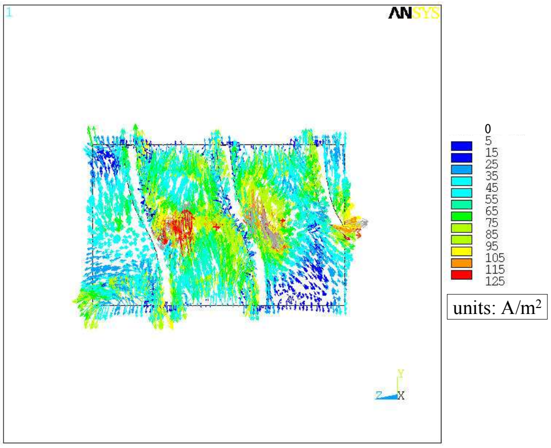

Fig. 7 An electric current density distribution. ($B = 7$ T, $\Delta P = 88.664$ kPa)

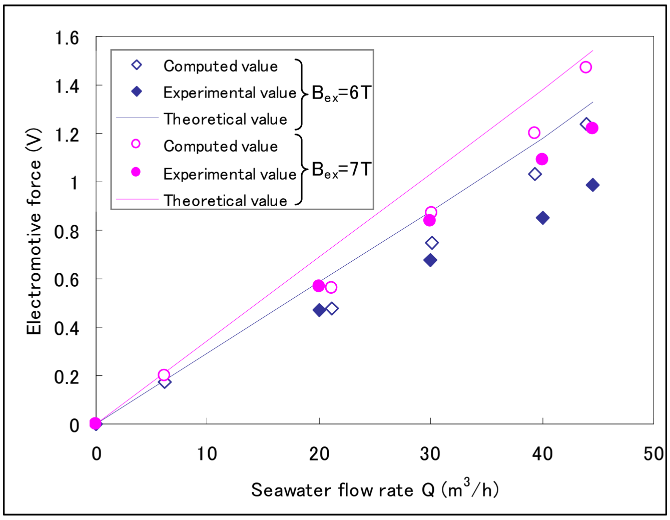

Fig. 8 Relationship between flow rate and electromotive force at B = 6 and 7 T.

rectifiers [5], which were installed in both the inlet and outlet of the generator. A photograph of a flow rectifier is shown in Fig. 9. The flow rectifier consists of a cylindrical tube 10 mm in thickness and six vanes 5 mm in thickness. The rectifier is made of polyvinyl-chloride-coated urethane foam and is 101.9 mm in diameter and 157.7 mm long. Fig. 10 shows the relationship between electromotive force and average flow velocity for the helical-type generator with flow rectifiers. The maximum value of the electromotive force was 1.35 V, which was about 10% larger than that without flow rectifiers, as expected from the decrease in flow loss of about 20% with the flow rectifiers.

Effects of Configuration of Helical Wall. To construct a calculation model of flow loss, the effects of the rotation number (3, 5, 7), pitch length (30, 37.5, 45 mm) and the inner diameter (10, 20, 30 mm) of the helical wall on flow loss were studied [6]. The experimental values for rotation numbers of 3 and 5 were in good agreement with the computed values at flow rates of 40 m^3/h or less. The experimental values for a rotation number of 7 were in good agreement with the computed values at flow rates of 20 m^3/h or less. However, the experimental values were about 17% larger than the computed values at flow rates from 30 to 40 m^3/h.

The experimental values for pitch lengths of 37.5 mm and 45 mm were in good agreement with the computed values at flow rates of 38 and 34 m^3/h or less, respectively, whereas the experimental values for a pitch length of 30 mm were about 1.5-2 times larger than the computed values at flow rates from 10 to 28 m^3/h.

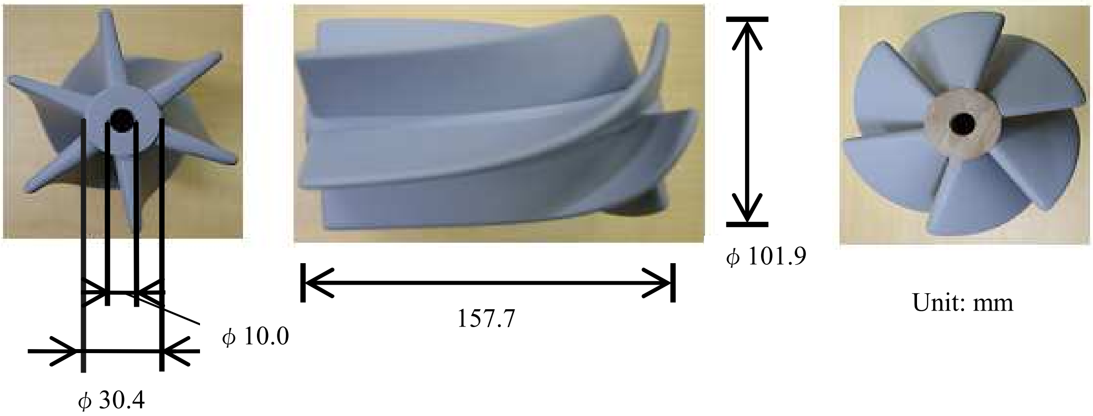

Fig. 9 Photograph of a flow rectifier.

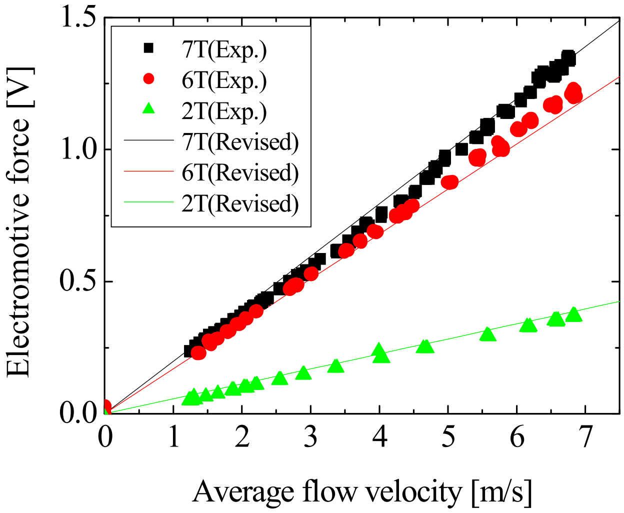

Fig. 10 Relationship between electromotive force and average flow velocity in comparison with revised theoretical values.

The experimental values for diameters of 10, 20 and 30 mm were in good agreement with the computed values at flow rates of 38, 30 and 16 m^3/h or less, respectively. However, for the diameter of 30 mm the computed values were about 20-23% larger than the experimental values at flow rates from 18 to 36 m^3/h.

Estimate of Performance. On the basis of a simple model, the performance of the helical-type generator was estimated using the experimental data for the hydraulic characteristics. The analysis of the output characteristics of the helical-type generator has been made continuously from the viewpoint of optimizing the configuration of the helical wall. We intend to carry out a test to evaluate the performance of the helical-type generator with the optimized configuration of the helical wall.

Summary

Experimental and computational results for the helical-type MHD power generator / hydrogen generator, which was designed as a new seawater MHD generator, have been discussed. On the basis of analytic results for the output characteristics, a helical-type generator with the optimized configuration of the helical wall will be constructed and tested in the near future.

Acknowledgments

The author would like to thank his research colleagues at Kobe University, Dr. T. Kiyoshi and Dr. X. Liu of National Institute for Materials Science, Japan. This work was supported by KAKENHI (18560767, 21360429), Hyogo Science and Technology Association, Kansai Research Foundation for Technology Promotion and NYK-Heyerdahl Projects, Japan.

References

[1] A. Iwata and Y. Saji: TEION KOGAKU (J. Cryo. Soc. Jpn.) Vol. 15 (1980) p. 317.

[2] K. Nishigaki, C. Sha, M. Takeda, Y. Peng, K. Zhou, A. Yang, D. Suyama, Q. J. Qing, L. Yan, T. Kiyoshi and H. Wada: Cryogenics Vol. 40 (2000) p. 353.

[3] M. Takeda, Y. Okuji, T. Akazawa, X. Liu and T. Kiyoshi: IEEE Trans. Appl. Supercond. Vol. 15 (2005) p. 2170.

[4] X. Liu, T. Kiyoshi and M. Takeda: Cryogenics Vol. 46 (2006) p. 362.

[5] M. Takeda, Y. Iwamoto, T. Akazawa, K. A. Bui, T. Kida, X. Liu and T. Kiyoshi: J. Jpn. Inst. Marine Eng. Vol. 43 (2008) p. 130.

[6] K. A. Bui, M. Takeda, and T. Kiyoshi: submitted to J. Jpn. Inst. Marine Eng.

doi:10.4028/www.scientific.net/AST.75.215

Radar Absorbing Materials Based on Metamaterials

LAGARKOV Andrey Nikolayevich[a], KISEL Vladimir Nikolayevich[b] and SEMENENKO Vladimir Nikolayevich[c]

Institute for Theoretical and Applied Electromagnetics, Russian Academy of Sciences,
Izhorskaya, 13, Moscow, 125412, Russia

[a]itae@dol.ru, [b,c]kis_v@mail.ru

Keywords: Metamaterial, radar absorbing material, double negative medium

Abstract. The use of metamaterial for design of radar absorbing material (RAM) is discussed. The typical features of the frequency dependencies of ε', ε'', μ', μ'' of composites manufactured of different types of resonant inclusions are given as an example. The RAM characteristics obtained by the use of the composites are given. It is shown that it is possible to use for RAM design the metamaterials with both the positive values of ε', μ' and negative ones. Making use of the frequency band with negative ε and μ it is possible to create a RAM with low reflection coefficient in a wide range of the angles of electromagnetic wave incidence.

Introduction

The recently developed materials with negative values of permeability and permittivity have raised a huge amount of publications devoted to research of those materials in radio-, microwave, infrared and optical ranges of electromagnetic spectrum; they have also led to design of devices that promise remarkable applications. These so called metamaterials are featured by the inclusions that interact in a resonant manner with the electromagnetic wave propagating in the metamaterial. The metamaterials intended for functioning in the acoustic range have become the subject of the investigation recently [1, 2]. The metamaterials of that type should be composed of resonant inclusions, and thus all metamaterials should possess a strong frequency dispersion of material parameters and a resonant energy absorption. The considerable losses inherent to metamaterials hinder the realization of many attractive ideas relevant to their application. The realization of superresolution [3], the solution of cloaking problem [4], the creation of open resonators [5], omnidirectional antennas [6], etc. are restrained by principal limits due to unavoidable energy losses in metamaterials (see the discussion in [7-11]). However there are applications that imply a certain level of losses, e.g. creation of radar absorbing materials. Metamaterial with magnetic losses could be used for, so called, Salisbury screen [12], and a combination of proper values of ε and μ could result in a Dallenbach layer [12].

It should be noted that composites with negative ε and μ were created and used long before the appearance of the term “metamaterial”. Yet in 1952 a section was published in a widely known book [13], it dealt with the design of composites to enhance the operation of antennas. To create artificial magnetic permeability, it was suggested to use split-ring or horseshoe shaped inclusions, and the formulas given in [13] showed the typical resonance behavior with negative value of μ at high frequencies. In 1990 a book [10] was published in Russia which summarized some of the complex materials investigations. Partly the results contained there were published in English journals [15-18]. In 1997 both the theoretical and experimental data were published [19] for composites with inclusions in the shape of bifilar helixes, where negative values of μ and ε were obtained and formulas were given which well corresponded to experimental data. At zero pitch value and number of turns equal to one they turn into expressions for well-known split-ring resonators. The mentioned investigations were not aimed to study negative refraction but rather comprised a systematic work in order to obtain any desired values of permittivity and permeability in the scope of restrictions imposed by Kramers-Kronig relations. One of their possible applications is the creation of radar absorbing materials (RAM).

Typical frequency dispersions of metamaterials used to create RAM

Composites filled with the inclusions shown in Fig.1 were used in RAM design. The composites were characterized by the volume fraction of inclusions and by different shapes of inclusions.

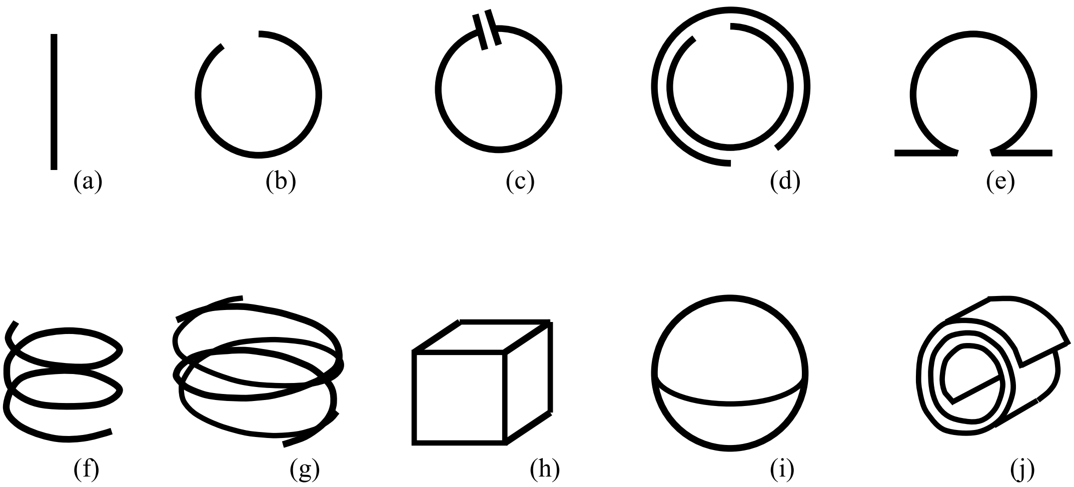

Fig. 1. Inclusions for RAM fabrication: wire (a), split ring (b), loaded ring (c), double split ring (d), Ω-inclusion (e), helix (f), bifilar helix (g), ferroelectric cube (h) and sphere (i), swiss roll (j)

The use of wires enables to create the required frequency dispersion of a composite permittivity and to get negative values of ε at above resonance frequencies. Split rings, loaded rings, double split rings, helixes, bi-helixes were used for creation of effective permeability. The same could be said with regards to swiss rolls inclusions [20].

Note that the use of helixes could result in negative values of ε thanks to the appearance of the dipole moment at the LC-resonance-causing lengths of the helix wire, where L is the helix inductance, C is the capacitance. Ferroelectric inclusions can be also used to achieve an artificial high-frequency magnetism. The appearance of the magnetic moment in particles with high values of ε at frequencies corresponding to magnetic mode resonance is rather known [21], however that phenomenon was discussed in metamaterials publications less frequently than the excitation of magnetic moment in inclusions of more common shapes, such as (b)-(e), Fig.1. The oscillations with frequencies coinciding to the eigenfrequencies of a spherical dielectric resonator can be excited in the dielectric particle of a proper radius with a high value of ε [22, 23]. The first magnetic TE-mode is a fundamental one for electromagnetic oscillations of a dielectric resonator. Note that cubes or parallelepipeds can also be used.

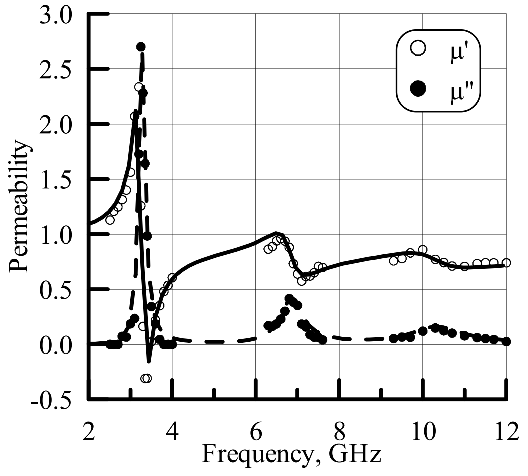

Fig.2. Effective permeability of a single-layer composite with ferroelectric inclusions of cubic shape

In Fig.2 the experimental results can be seen which obtained for the composite made of the $Ba_{i-x}Sr_xTiO_3$ ferroelectric cubes with $\varepsilon' \approx 3000$ and $\varepsilon'' / \varepsilon' \leq 0.05$. The cube edge size is 1.5 mm, the inclusion volume fraction is 68%. Here and below in the material parameter graphs the measured results are given by circle marks, the curves correspond to their analytical approximations resulted from electromagnetic modeling [23], [19]. The resonant behavior of μ′ and μ″ is perfectly seen. Note that with the help of inclusions of different sizes a magnetic mode can be excited in some of them, and the electric mode in others, as suggested in [24]. A metamaterial with negative values of ε and μ could be thus created. This is one of rather rare possibilities to obtain an isotropic metamaterial.

By applying an electric field we can control its resonant frequency. RAM made of that material is rather complex to produce despite the apparent simplicity, because it is necessary to manufacture inclusions of precise geometrical sizes of rigid ceramics; besides, that material could be too heavy. Composites made of single and bifilar helixes seem rather simple in manufacturing and light in weight. For the first time the information about such a RAM was published in [25]. It described the device for mass production of helix inclusions and the results of measuring the reflection coefficient of Dallenbach screen made of them.

We will now treat in more detail the properties of a composite filled with right- and left-handed wire helixes arranged in a certain order in the form of a single layer of inclusions (Fig. 3).

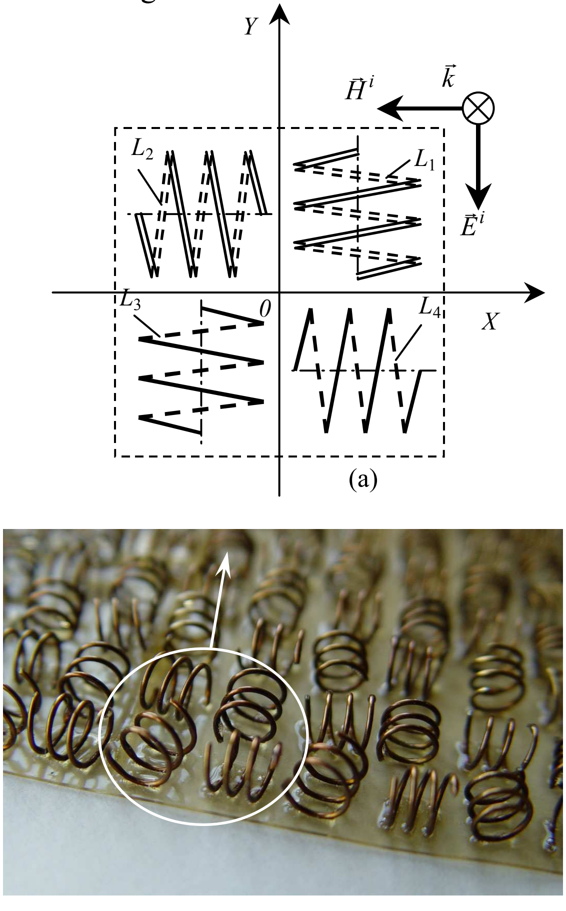

(b)

Fig. 3. Unit cell (a) and an experimental sample (b) of a composite made of wire helixes

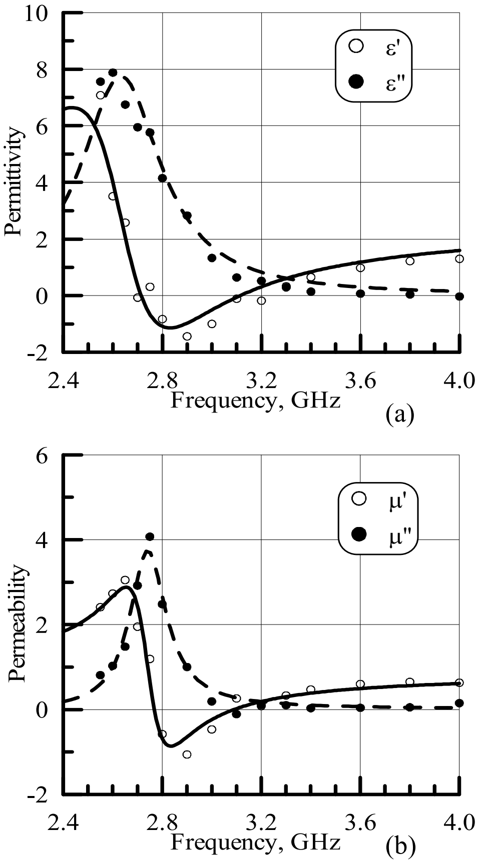

Fig. 4. Effective permittivity (a) and permeability (b) of an experimental sample of a composite made of wire helixes, each helix has three turns, the pitch of 2 mm and the diameter of 5 mm.

Each inclusion may be related to vectors of electric and magnetic moments. The components of these moments interact with the external electromagnetic field such that the macroscopic properties of the sample may be interpreted as the emergence of the effective permittivity and permeability of the composite. The results of measurements of the effective parameters of such a composite, given in Fig. 4, prove this inference.

The helixes are made of a high-resistance Nichrome wire 0.4 mm in diameter (because the composite was developed for the purpose of absorbing electromagnetic waves). The resonant electromagnetic properties of this composite show up fairly clearly. A singular feature of this material is that ε′ and μ′ reach their negative values simultaneously in one and the same frequency band. If a layer of the material is applied onto the metal the RAM the features presented in Fig. 5 will be obtained in an experiment. Naturally, the material is rather narrow-band, though it manifests the property which traditional RAMs do not possess. At low frequencies the dielectric and magnetic losses of the material are negligibly low, and the material becomes transparent for any low-frequency application. It makes the material highly promising for solving numerous electromagnetic compatibility problems.

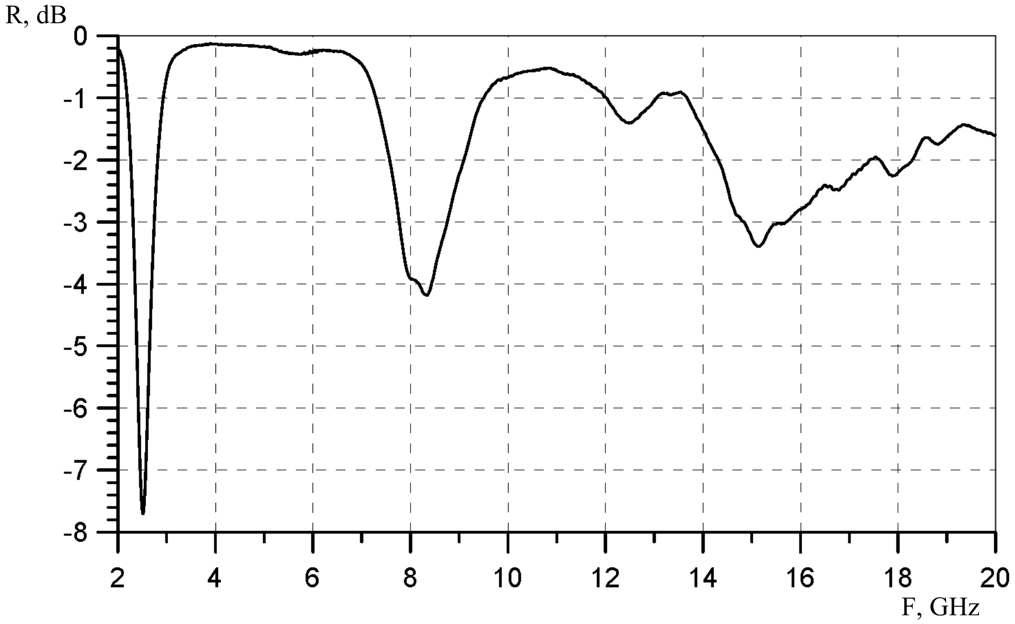

Fig. 5. Frequency dependence of the reflection coefficient of the helix-based coating

Trying to compare the measured and calculated reflection coefficient of a conducting plate coated with metamaterial we shall find that these quantities do not match each other if the calculations are performed by the use of the ε and μ values of the metamaterial layer derived from the free-space measurements. The reason for this is a change in the effective properties of the layer when a conducting substrate is placed nearby, thus invoking a strong interaction between each helix of the composite and its mirror counterpart. As a consequence, the resonant frequency is shifted and several new resonances may happen to appear. It is clearly demonstrated in Fig. 6, where the effective properties were extracted from the measurements of magnitude and phase of a flat electromagnetic wave reflected, firstly, from the layer placed in the free space and, secondly, from the same layer backed by a conducting substrate. The appearance of the extra resonances and changes in the features of the main resonance are perfectly seen (compare to Fig. 4).

Therefore the material properties of the metamaterials under discussion are of rather conditional. Here we will give effective parameters obtained by processing the values of complex reflection and transmission coefficients of the flat layers of the material while measured in

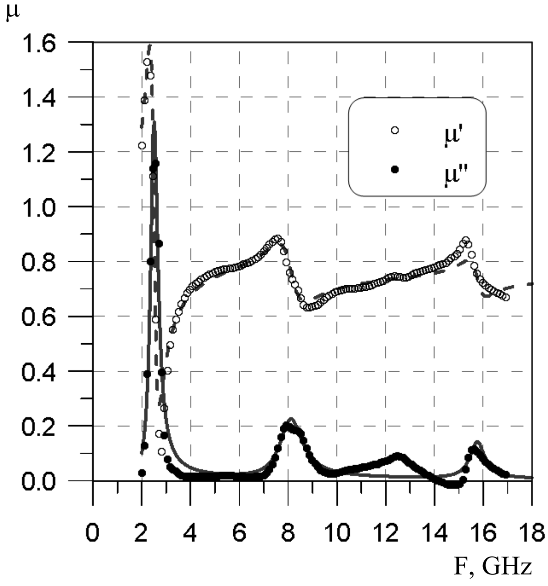

Fig. 6. Effective permeability of the helix-filled composite layer backed by a conducting substrate

the free space. Mind, that the flat electromagnetic wave incident onto the measured sample surface is distorted over specific scales that can exceed the sample layer thickness considerably [26]. Thus when the material plate is placed onto a metal surface or is applied to another similar plate to form a single sample it often causes some changes in effective parameters of the resulting layer. Therefore the precise computer RAM simulation becomes difficult.

By combining helixes of different sizes we can get rather interesting frequency features of values of ε′, ε″, μ′, μ″. They can differ in the position of minima and maxima of ε′, ε″, μ′, μ″ within a frequency band and in a great variety of metal-applied RAM reflection coefficient spectra. As an example the Fig. 7 shows the frequency dependencies of the material parameters of the sample consisting of the combination of bifilar helixes (bi-helixes) of different diameters, namely, 2 and 3 mm.

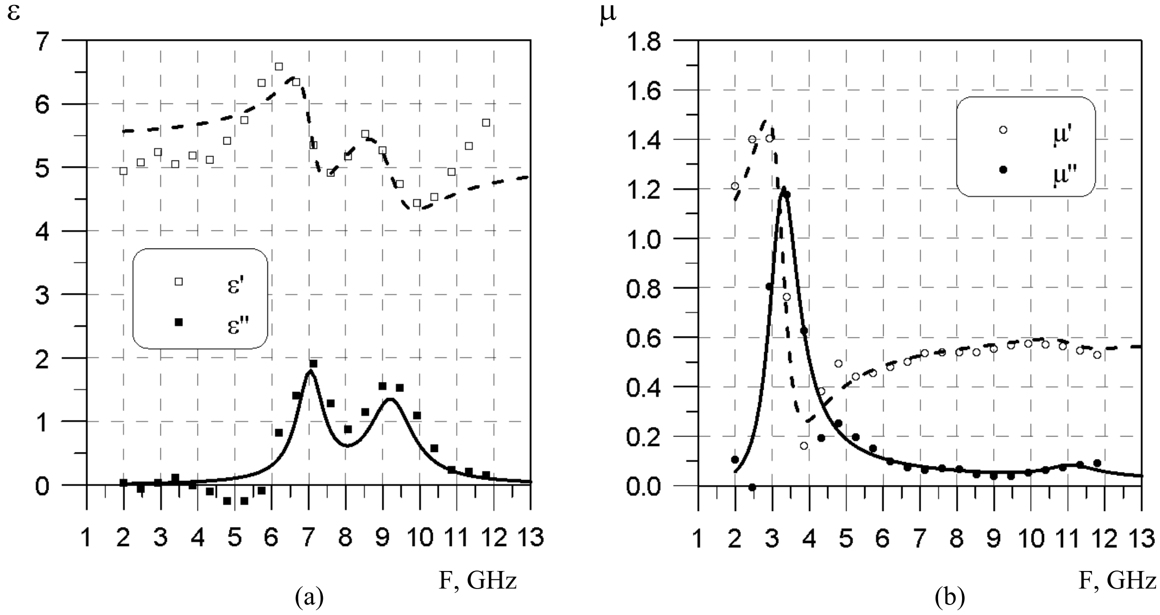

(a) (b)

Fig. 7. Frequency dependencies of the permittivity (a) and permeability (b) of a composite sample consisting of combined helixes of different diameters

The inclusions were made of 50 micrometers diameter manganin wire. The bi-helix with smaller diameter was inserted into the bigger one with their axes directed orthogonal to each other. Outer bi-helix consisted of two turns with the pitch of 1 mm. Inner bi-helix had 2.5 turns with 0.8 mm pitch. The inclusions made in that way were densely packed to form a one-layer coating. Fig. 8 shows the reflection coefficient of the coating applied onto metal. Each of the extrema is related to the specific extremum of the frequency dependence of material parameters. Note that in combining the layers prepared of helixes of different sizes we can get a coating with good wideband features.

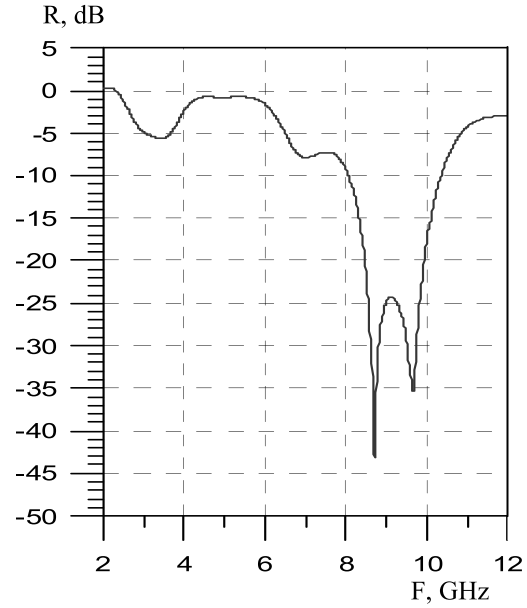

Fig. 8. Frequency dependence of the reflection coefficient of a composite sample consisting of combined helixes of different diameters

Wide angular band of the backward wave RAM

In the previous examples of RAM design no special attention was paid to the frequency region where the negative refraction manifests itself. Though, RAM can acquire absolutely remarkable properties in this specific region of negative values of ε and μ [5, 27]. Look at the Fig. 9*a*. The picture gives a schematic description of the functioning of an ordinary interference coating with $\varepsilon > 1$ and $\mu > 1$.

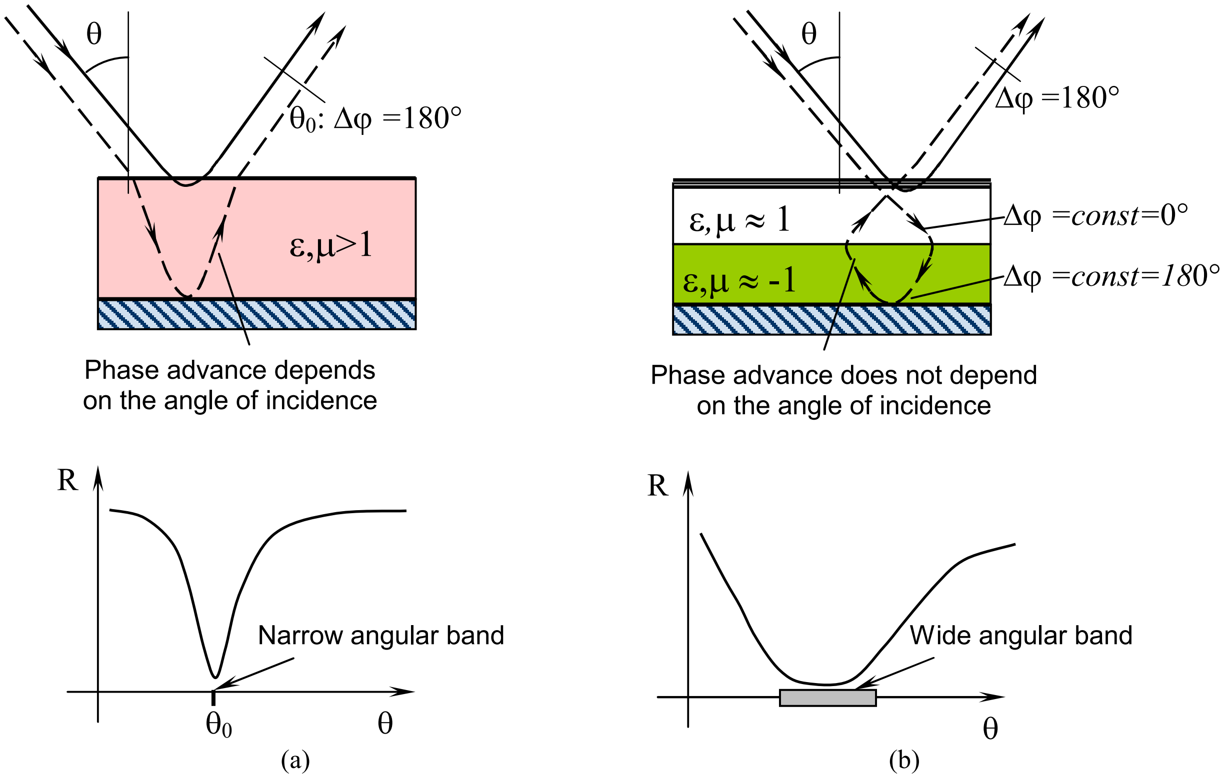

(a) (b)

Fig. 9. Schematic description of the functioning of an ordinary (a) and metamaterial-based (b) radar absorbing coatings of interference type

The thickness of the coating should be chosen as to provide the 180° phase difference of the wave reflected from the outer surface (solid line) and the wave that passed through the layer and reflected from the metal, the magnitudes should be close to each other to insure the minimum of the reflection coefficient. Let an incident wave frequency be constant. If the incident angle varies, the phase advance depends on the angle of the wave incidence provided the conventional coating is used. Correspondingly, angular dependencies are rather narrow. Let us consider the diagram shown in Fig. 9*b*. The coating consists of a thin semi-transparent magnetic film and two layers of equal thicknesses with ε, $\mu \approx 1$ and ε, $\mu \approx -1$. In this case the total phase advance inside the layer does not depend on the incident angle due to mutual compensation caused by the negative phase velocity of the backward wave travelling in the metamaterial layer. Correspondingly, the reflection coefficient weakly depends on the incident angle, at least while the necessary magnitude relations are maintained. As there are no fundamental physical restrictions on the thickness of the described absorber, it can be made electrically thin at least, in principle, like the previously suggested system of complementary metamaterials [28].

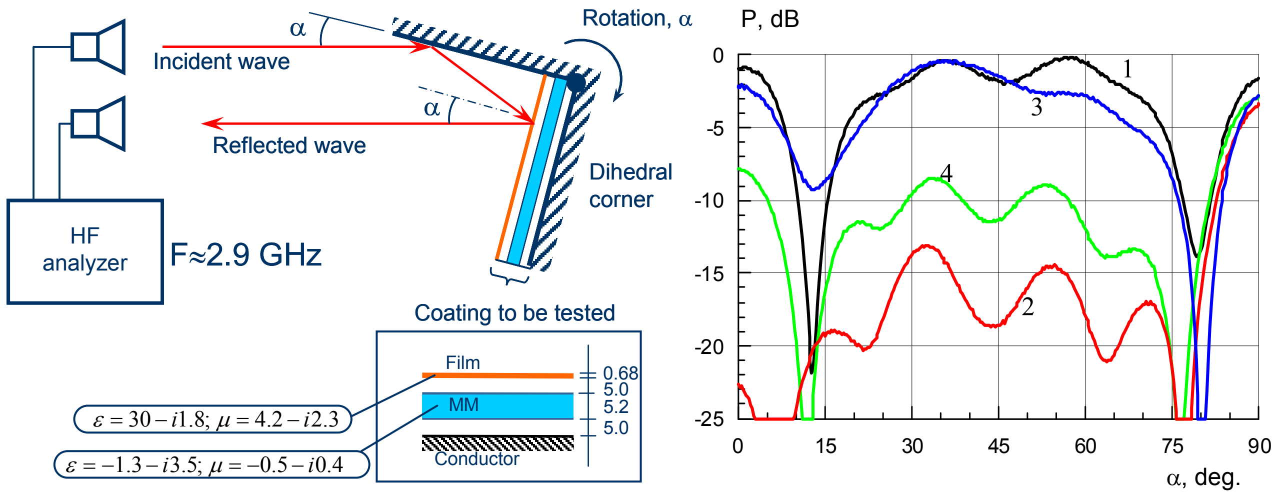

(a) (b)

Fig. 10. Experimental setup (a) and the measured angular dependencies of the reflected power when different coatings are applied to the face of a dihedral corner

Our experimental investigations (Fig. 10) support these theoretical suggestions. The experimental setup is schematically shown in Fig. 10*a*. The angular dependency of the reflection coefficient of a coating can be measured via registering the power of the reflected wave in the course of the rotation of a dihedral corner one face of which is lined with a tested coating. An example of the measured reflected power (in dB) is depicted in Fig. 10*b*, curve 1 corresponds to the uncoated corner, curve 2: metamaterial-based multilayer coating is arranged as suggested above, curve 3: only semi-transparent film is placed parallel to the corner face, curve 4: only metamaterial layer is present on the face. The metamaterial sample was prepared using right- and left-handed helixes as shown in Fig. 3 and Fig. 4. The superiority of the sandwiched structure (curve 2) is clearly seen, one can observe a broad angular range of the efficient absorption. Note, the value of operational frequency (F=2.89 GHz) was chosen as to secure the negative phase advance of the wave penetrated into the metamaterial. The observed high performance of the coating significantly degraded when frequency was changed to the values (not far from the resonance) where the metamaterial reveals the properties of ordinary matter, i.e. ε, $\mu \geq 1$.

Conclusion

Thus, the possible application of the metamaterials is the creation of effective RAMs. The discussed results demonstrate that RAM of this type may exhibit a number of advantages over conventional materials, including the extensive design flexibility. In particular, one can create artificial composite materials with good absorption due to reasonably high dielectric and magnetic losses; besides, the materials can secure low reflection provided the input impedance of the coating is close to that of the free space owing to the proper ε and μ choice.

A novel approach to design radar absorbing coatings of interference type is introduced. The use of metamaterials enables one to obtain some specific features, e.g., wide angular operational range at small electrical thickness. The latter becomes possible because the required phase relationships for mutual compensation of waves reflected from the media interfaces can be achieved by the application of a backward wave medium rather than by increasing the thickness of the coating layers. Finally, a technique to achieve a weak angular dependency of the wave reflection from a RAM coating is shown and experimentally tested.

References

[1] Z. Yang, J. Mei, M. Yang, N.H. Chan and P. Sheng: Phys. Rev. Lett. Vol. 101 (2008), p. 20431

[2] Z. Yang, H.M. Dai, N.H. Chan, G.C. Ma and P. Sheng: Appl. Phys. Lett. Vol. 96 (2010), p. 041906

[3] J.B. Pendry: Phys. Rev. Lett. Vol. 85 (2000), p. 3966

[4] J. Pendry: Physics Vol. 2 (2009), p. 95

[5] V.N. Kisel and A.N. Lagarkov: Phys. Rev. E Vol. 76 (2007), p. 065601

[6] A.N. Lagarkov and V.N. Kisel: Dokl. Phys. Vol. 46 (2001), p. 163

[7] N. Fang and X. Zhang: Appl. Phys. Lett. Vol. 82 (2003), p. 161

[8] D.R. Smith, D. Schurig, M. Rosenbluth, S. Schultz, S.A. Ramakrishna and J.B. Pendry: Appl. Phys. Lett. Vol. 82 (2003), p. 1506

[9] V.N. Kissel and A.N. Lagarkov, in: *Proc. of the 2nd Int. Conf. on Materials for Advanced Technologies, Symposium F: Electromagnetic Materials*, Singapore, 2003, edited by Lim Hock, Ong Chong Kim, Serguei Matitsine and Gan Yeow Beng (World Scientific, Singapore, 2003), p. 145

[10] A.N. Lagar'kov and V.N. Kisel': Dokl. Phys. Vol. 49 (2004), p. 5

[11] M.I. Stockman: Phys. Rev. Lett. Vol. 98 (2007), p. 177404

[12] K.J. Vinoy and R.M. Jha: *Radar absorbing materials* (Boston, Kluwer. Academic 1996) pp. 98-116.

[13] S.A. Schelkunoff and H.T. Friis: *Antennas: Theory and Practice* (New York. Wiley 1952).

[14] A. S. Antonov, V. M. Batenin, A. P. Vinogradov, A. A. Kalachev, A. V. Kulakov, A. N. Lagarkov, S. M. Matitzin, L. V. Panina, K. N. Rozanov, A. K. Sarychev and Yu. R. Smichkovich, in: *Electrophysical Properties of Percolation Systems*, edited by A. N. Lagarkov, Institute for High Temperatures, Russian Academy of Sciences (1990), in Russian.

[15] A. N. Lagarkov, L. V. Panina, A. K. Sarychev and Y. R. Smychkovich, in: *MRS Spring Meeting* (1990), paper S 9.3.

[16] A. I. Kolesnikov, A. N. Lagarkov, S. M. Matytsin, L. N. Novogrudskiy, K. N. Rozanov and A. K. Sarychev, in: *Optical and Electrical Properties of Polymers* No. 214, edited by J. A. Emerson and J. M. Torkelson/Materials Research Society (1991).

[17] A. N. Lagarkov, A. K. Sarychev, Y. R. Smychkovich and A.P. Vinogradov: J. Electromagn. Waves Appl. Vol. 6 (1992), p. 1159

[18] A. N. Lagarkov and A. K. Sarychev: Phys. Rev. B Vol. 53 (1996), p. 6318

[19] A. N. Lagarkov, V. N. Semenenko, V. A. Chistyaev, D. E. Ryabov, S. A. Tretyakov and C. R. Simovski: Electromagnetics Vol. 17 (1997), p. 213.

[20] V.N. Semenenko, V.A. Chistyaev and D.E. Ryabov, in: *Proc. of the Bianisotropics'98 7th Int. Conf. on Complex Media*, June 3-6, Braunschweig, Germany (1998), p. 313

[21] L. D. Landau and E. M. Lifshitz: *Electrodynamics of Continuous Media* (Pergamon, Oxford, 1960).

[22] V.N. Semenenko, V.A. Chistyarv and D.E. Ryabov, in: *Proc. Of the 7th Int. Crimean Conf. "Microwave and Telecommunication Technology"*, Sept. 15-18, Crimea, Ukraine (1997), p. 113

[23] A.N. Lagarkov, V.N. Semenenko, V.N. Kisel and V.A. Chistyaev: J. Magn. Magn. Mater. Vol. 238-239 (2003), p. 161

[24] I.B. Vendik, O.G. Vendik and M.A. Odit: Physics of the Solid State Vol. 51 (2009), p. 1590

[25] S.A. Kuehl, S.S. Grove, A.G. Smith and I.P. Theron, in: *Proc. Of the CHIRAL'95 Int. Conf.*, edited by A. Sihvola, S. Tretyakov, U. Unrau, V. Varadan, V. Varadan, K. Whites/The Pennsylvania State University State College, USA, Oct. 11-14 (1995)

[26] A. P. Vinogradov, D. P. Makhnovskii and K. N. Rozanov: J. Commun. Technol. Electron. Vol. 44 (1999), p. 317

[27] A.N. Lagarkov, V.N. Kisel and V.N. Semenenko: Progress in Electromagnetics Research Lett. Vol 1 (2008), p. 35

[28] A. Alu, F. Bilotti, N. Engheta and L. Vegni, in: *Proc. of the Joint Ninth International Conference on Electromagnetics in Advanced Applications (ICEAA 2005) and the Eleventh European Electromagnetic Structures Conference (EESC 2005),* edited by Roberto D. Graglia/ Torino, Italy (2005), p. 229

doi:10.4028/www.scientific.net/AST.75.224

Microwave Metamaterials Containing Magnetically Soft Microwires

M. Ipatov[1,a], V. Zhukova[1,3,b], and A. Zhukov[1,3,c] L. V. Panina1[1,2,d]

[1]Departamento de Física de Materiales, Universidad del Pais Vasco, 20009 San Sebastian, Spain,
[2]School of Computing& Mathematics, Univ. of Plymouth, Drake Circus, PL4 AA, Plymouth,UK

[3]TAMAG Ibérica S.L., Parque Tecnológico de Miramón, Paseo Mikeletegi 52, 20009
San Sebastián, Spain

[a]mihail.ipatov@ehu.es, [b]sckzhzhv@ehu.es, [c]arkadi.joukov@ehu.es, [d]L.Panina@plymouth.ac.uk,

Keywords: glass coated microwires, induced magnetic anisotropy, tuneable composite materials

Abstract. In this paper we discuss the development of metamaterials containing ferromagnetic microwires which makes it possible to tune the electromagnetic response in the microwave frequency band. Metallic wire media are known to demonstrate very strong dispersion of the effective permittivity at GHz frequencies. At certain conditions, the magnetic properties of constituent wires may strongly contribute to the system losses owing to the magnetoimpedance effect, resulting in unusual dependence of the permittivity on the external magnetic or mechanical stimuli. We also demonstrate the possibility to design the wire media with a negative index of refraction utilizing natural magnetic properties of wires. The results involve theoretical modeling and measurements of the reflection/transmission spectra by free-space methods. A reasonable agreement between theoretical and experimental data is demonstrated.

Introduction

Metamaterials containing embedded metallic wires may demonstrate a strong dispersion of the effective permittivity ε_{ef} in the microwave range [1,2]. The use of ferromagnetic wires makes it possible to sensitively tune this dispersion by changing the magnetic structure of the wire with external magnetic field, mechanical stress or temperature. The possibility to control or monitor the electromagnetic parameters (and therefore scattering and absorption) of composite metamaterials is of great interest for large-scale applications such as remote non-destructive testing, structural health monitoring, tuneable coatings and absorbers. The magnetic tunability of microwave response was reported in a number of works for different types of wire media demonstrating that underlying physics is related with the magnetoimpedance (MI) effect in wires [3-5]. In diluted structures with thin metallic wires, the constrained current resonances result in strong dispersion of the effective dielectric function which could be of a resonant or plasmonic type. Using magnetic wires, it is possible to change the system losses in the microwave range by changing the wire magnetic structure. Then, the dispersion of the permittivity can be broadened (or sharpened) by applying, for example, a moderate magnetic field or stress. Alternatively, the microwave response from the magnetic wire composites may depend on the internal stress/strain conditions, therefore, can provide information on the structural state.

In this paper, we consider different types of magnetic wire composites utilizing arrays of continuous wires or short-cut wires (as shown in Figs. 1 a,b). Diluted arrays of continuous wires are characterized by an effective permittivity of a plasmonic type with the plasma frequency of few GH for lattice spacing b=0.5-1 cm, where as short –cut wire arrays have a resonant dispersion of the permittivity with the resonant frequency determined by the half-wavelength condition which is also in the same frequency band for wire length of 2-3 cm. These diluted wire arrays could be combined with arrays of closely spaced continuous wires in perpendicular direction to add magnetic properties (Fig. 1c).

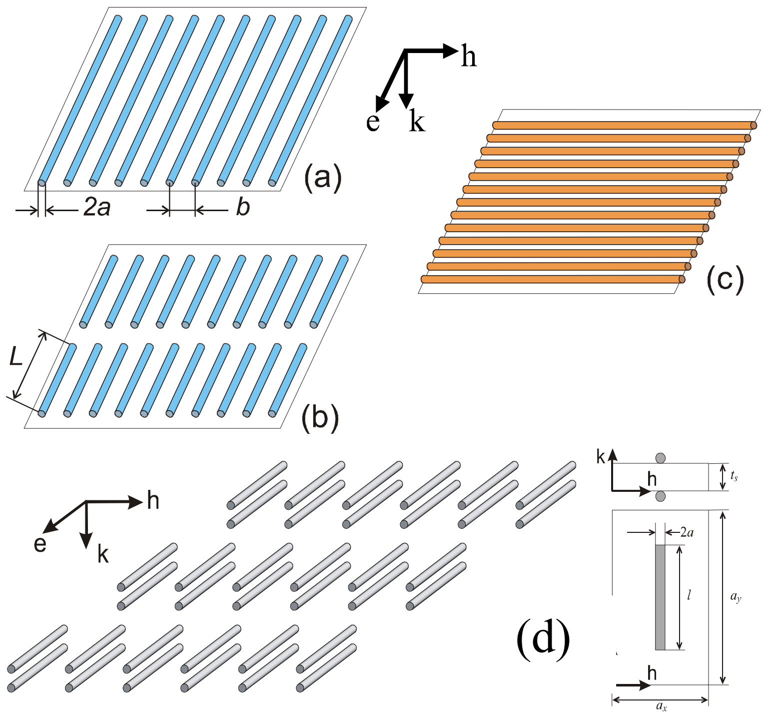

Fig.1. Schematic representation of wire-arrays: a) continuous wires,b) short-cut wires, c) contineous wires for magnetic sub-system, d)cut-wire pairs for artificial magnetism

These systems will require special polarization of the incident wave with the electric field along wires in a diluted subsystem and the magnetic field along the wires in dense (magnetic) subsystem. We also investigated the possibility to create an artificial magnetic properties using two layers of short-cut wires (Fig. 1d) [8]. We demonstrate that in all the cases the application of a magnetic field applied along the wires in the electric subsystem (meaning along the electric field in the incident wave) strongly increases the dielectric losses, which affects the effective parameters and reflection/transmission spectra.

The underlying physical mechanism of the permittivity dependence on the wire magnetic structure is based on the magnetoimpedance (MI) effect [6-8]. The high frequency impedance of a soft magnetic conductor may experience giant changes when its static magnetic structure undergoes transformation due to application of a magnetic field, stress or temperature. The nominal ratio of the impedance change, called the MI ratio, reaches several hundred percents at MHz frequencies and more than 50% at GHz frequencies in amorphous microwires with circumferential (or helical) anisotropy for characteristic magnetic field of the order of the anisotropy field, which could be as small as few Oe [6-8].

Permittivity spectra in wire-composites

Composites containing long parallel wires can be characterized by plasma-like dispersion of ε_{ef} [1-2] with a negative value of the real part of the permittivity below the characteristic plasma frequency, f_p:

$$\varepsilon_{ef}^2 = 1 - \frac{\omega_p^2}{\omega^2(1+i\gamma)}, \quad \omega_p = 2\pi f_p, \quad f_P^2 = \frac{c^2}{2\pi b^2 \ln(b/a)} \tag{2}$$

Here, γ is the relaxation parameter and c is the velocity of light. For wire radius a in the micron range and spacing b between them of about 1cm the characteristic plasma frequency is about 4 GHz. A number of experimental studies confirmed a negative permittivity in the GHz region for wire media. We have demonstrated that in general γ is defined by the wire surface impedance ς_{zz}:

$$\gamma = \frac{c\varsigma_{zz}}{\omega a \ln(b/a)} \tag{3}$$

This parameter may change under applied magnetic field, H_{ex}, as a result of the MI effect. Then, the permittivity spectra will depend on H_{ex} (see Fig. 2a). The composites with short-cut wire inclusions are characterized by a resonance type of ε_{ef} where wires behave as dipole antennas with the resonance at half wave length condition: $F_{res} = c/2l\sqrt{\varepsilon_d}$, where ε_d - permittivity of the matrix. If the interaction between the wires is small, ε_{ef} is composed of the averaged dipole polarization χ and may be expressed analytically for the case of not very strong skin effect [4]:

$$\varepsilon_{eff} = \varepsilon + 4\pi p\chi \,,\ \chi = \frac{1}{2\pi \ln(l/a)(\tilde{k}a)^2}\left(\frac{2}{\tilde{k}l}\tan(\tilde{k}l/2)-1\right), \quad (4)$$

$$\tilde{k} = k\left(1+\frac{ic\varsigma_{zz}}{\omega a \ln(l/a)}\right)^{1/2}, \ k = \omega\sqrt{\varepsilon}/c \quad (5)$$

Here p is the wire volume concentration and, $\tilde{k}$ is the renormalized wave number. Comparing equations (3) and (5) it is seen, that in both cases the dependence on the wire surface impedance occurs in a similar way, controlling the dielectric losses in the case of a moderate skin effect. The permittivity spectra for short-cut wire composites are given in Fig. 2b. It is seen that applying a magnetic field which increases the wire impedance suppresses the resonance behaviour due to increased losses.

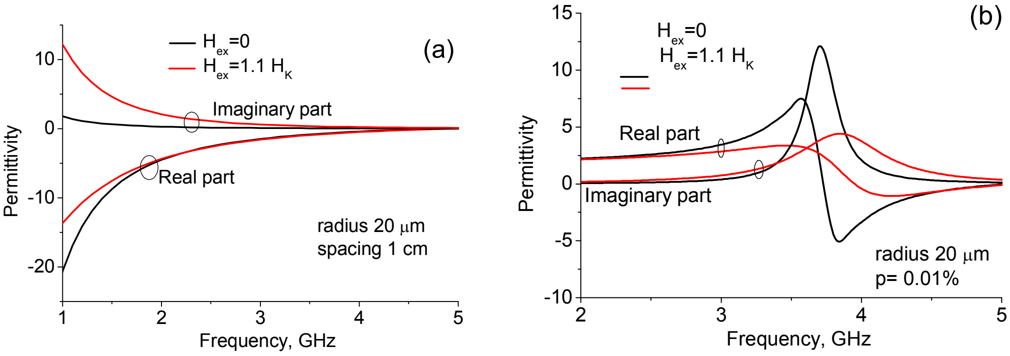

Fig. 2. Effective permittivity spectra in composites depicted in Figs.1a,b, respectively, with H_{ex} as a parameter. Modelling is performed for wires with a circumferential anisotropy (anisotropy field H_K=500A/m). The other parameters are: resistivity 130μΩcm, magnetisation 0.05T, wire radius 20 μm. For (a), b=1cm. For (b), l=4cm, p=0.01%.

The considered wire arrays can be combined with a more dense wire array in perpendicular direction to add natural magnetic properties of wires. In this case, for wires with a circumferential anisotropy the magnetic field in the incident way along the wires will generate high frequency permeability. For the parameter used, the real part of this permeability will be negative in the GHz frequency band. For the volume concentration in the range of 0.05 the effective permeability will be still negative and it is possible to design a material with a negative refraction index, as shown in Fig. 3.

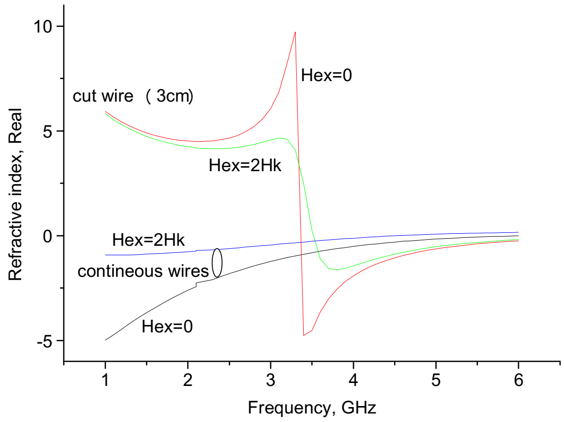

Fig. 3. Spectra of the refractive index in wire arrays (continuous wires or cut-wires) combined with dense magnetic layers with a demonstration of the effect of a magnetic field applied along the electric field in the incident wave.

Experimental method and samples. Thin magnetic glass-coated microwires based on Co, Fe and Ni (with additions of Cr to decrease the Curie temperature) were fabricated by the Taylor-Ulitovsky method. The modern Taylor-Ulitovsky process described elsewhere [6-8] is based on direct casting from the melt and allows wires of different composition and diameter to be produced. The magnetic properties of individual wires were defined from measurements of dc magnetisation loops and MI in the frequency range up to 500MHz.

The microwave properties of wire composites were investigated by free space method requiring large samples. The continuous wire-lattices of 50x50 cm^2 were produced by glowing the wires in paper. The separation varied between 0.5-1.5 cm. The magnetic subsystem will require rather dense placement of wires and it was considered theoretically only. Such samples could be cut in stripes (10-40 mm wide) to form the composites with short wires. Using two layers of cut-wire arrays separated by few mm it is possible to generate an artificial magnetic activity. Unfortunately, the frequency shift between magnetic and electrical resonances is very small and it was difficult to separate them experimentally. The S-parameters were measured in the frequency range of 0.9-17 GHz in the presence of external field ranging up to 3000A/m applied through a plane coil with turns perpendicular to the electrical field in the incident wave. The effective permittivity spectra were deduced from S-parameters with the help of Reflection/Transmission Epsilon Fast Model.

Magnetic properties of glass coated microwires. Typical hysteresis loops of glass-coated microwires with the magnetostriction constant (associated with the alloy composition) as a parameter ($Fe_{70}B_{15}Si_{10}C_5$ ($\lambda_S >0$), $Co_{75}Si_{10}B_{15}$ ($\lambda_S <0$) and $Co_{68}Mn_7Si_{10}B_{15}$($\lambda_S \approx 0$)) are shown in Fig.4. As can be observed, the hysteresis loops are strongly dependent on to the magnetostriction constant: Co-rich wires with negative λ_s show an inclined hysteresis loop, Fe-rich wires with $\lambda_s >0$ exhibit a perfectly rectangular hysteresis loop, and the best magnetic softness corresponds to the composition with vanishing λ_s. This behavior is closely related with the contribution of the magnetostrictive anisotropy into the total effective anisotropy:

$$K_{me} \approx 3/2\ \lambda_s \sigma_i, \qquad (1)$$

where σ_i is the internal stress. The magnetostriction constant depends on the chemical composition and nearly vanishes in amorphous Fe-Co based alloys with Co/Fe ≈70/5 [6-8]. Nearly-zero magnetostrictive microwires show best soft magnetic properties and GMI effect. In wires of this alloy the magnetostrictive anisotropy aligns the magnetization along the circular direction and the external axial field tries to set the magnetization along the wire, resulting in very sensitive MI. The impedance plots vs. field seen in Fig. 5 have two symmetrical peaks at a characteristic anisotropy field, which is typical of a circumferential anisotropy and the impedance change ratio is larger than 300% at 500 MHz.

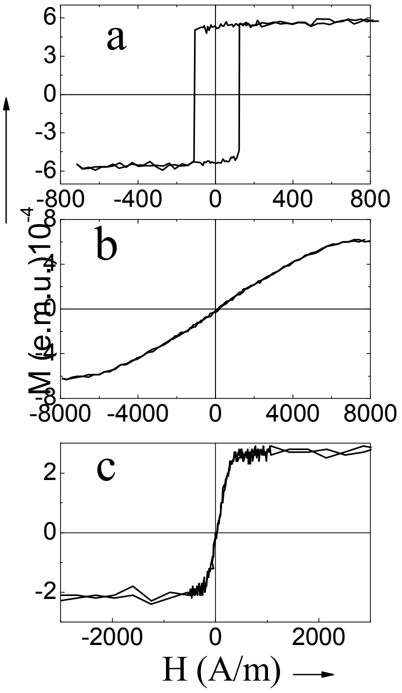

Fig.4. Hysteresis loops of (a) - $Fe_{70}B_{15}Si_{10}C_5$ ($\lambda_S >0$), (b) -$Co_{75}Si_{10}B_{15}$ ($\lambda_S <0$) and (c) - $Co_{68}Mn_7Si_{10}B_{15}$ ($\lambda_S \approx 0$)

Experimental scattering spectra. The reflection *R* and transmission *T* spectra of continuous wire array are shown in Fig. 6. It is seen that the relative change in *R* and *T* could be about 10% at lower frequencies while the phase of transmission shifts about 40 degrees at 1 GHz with the change of the field. The permittivity spectra deduced from *R* and *T* plots are consistent with the theoretical plots seen in Fig. 2a. The effective thickness was taken equal to the lattice period of 1 cm. The imaginary part of the permittivity increases with the field due to the increase in the wire impedance resulting in decrease in the transmission amplitude (although the reflection amplitude also decreases). Figure 7 shows the spectra for cut-wire composites with different wire length of 40, 20 and 10 mm and with the field as a parameter. The transmission spectra have a deep minimum near a resonance demonstrating a stop filter behaviour. The magnitude of this minimum depends strongly on the field for longer wires with lower resonance frequency, F_{res}. For shorter wires the field dependence is not noticeable since the wire ac permeability is nearly unity and the impedance becomes insensitive to the magnetic properties. The phase of the transmitted wave shows reversal behaviour near F_{res} which sensitively shifts with the field. Fig. 8 shows the $F_{res}(H_{ex})$ dependence of the resonance frequency F_r on magnetic field for composite with 40 mm inclusions. The similar form has the minimum of transmission magnitude T_{min} that is a

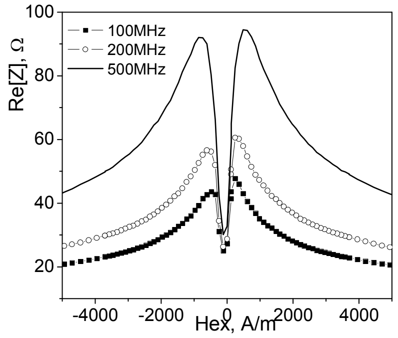

Fig.5. Wire impedance vs. field for different frequencies

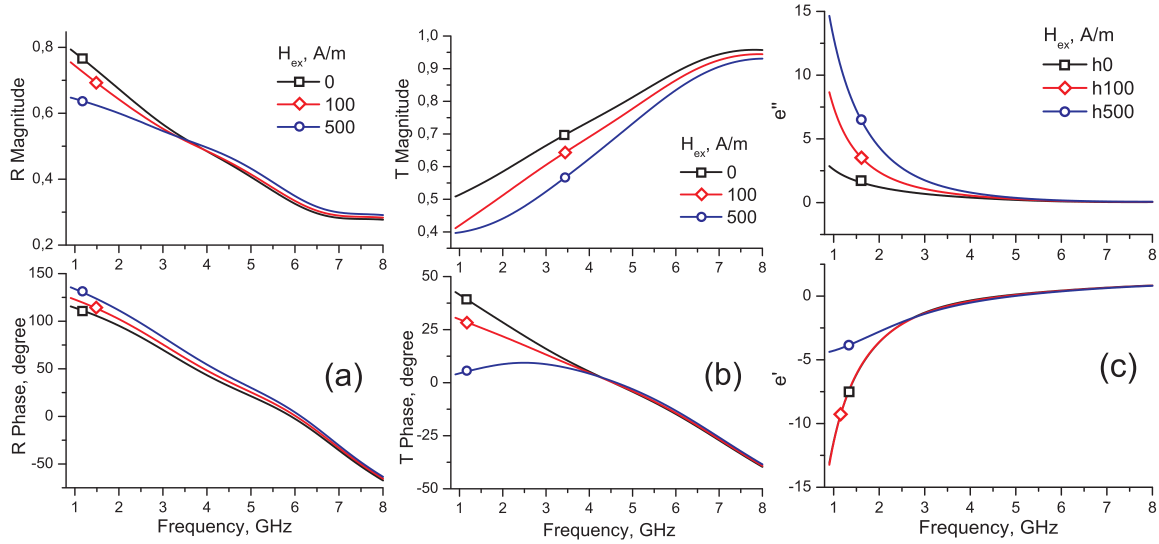

Figure 6. Spectra of *R*, *T* and ε_{ef} for composites with long wires with H_{ex} as a parameter (H_{ex}=0,100, 500A/m).

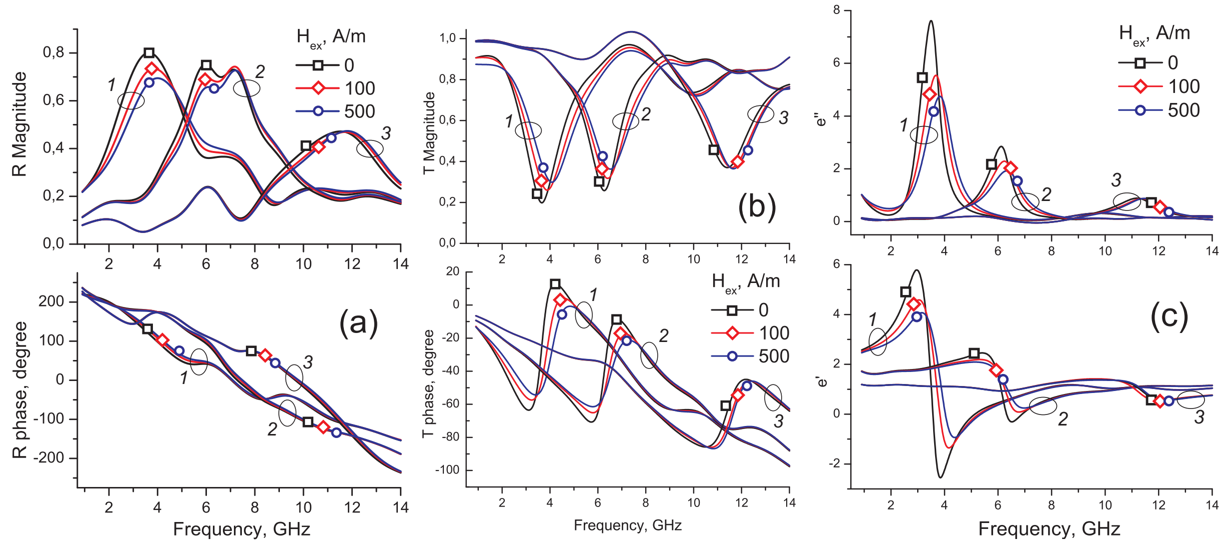

Figure 7. Spectra of *R*, *T* and ε_{ef} of composites with cut wires of length 40 (1), 20 (2) and 10 (3) mm with the field as a parameter.

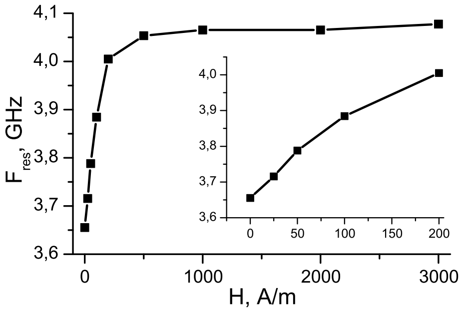

Figure 8. $F_{res}(H_{ex})$ dependence for composite with 40 mm long wires.

result of a dumping increasing with the field. For the case of cut-microwire pairs (Fig.1d) the experimental reflection/transmission spectra are show in Fig. 9. The results reveal low and higher frequencies resonance modes but it was not possible to distinguish between the electric and magnetic resonances. The effect of the external field is evident for the lower frequency resonance mode.

5. CONCLUSIONS

We report on magnetic field dependence of the dielectric response in composites with arrays of magnetic wires: continuous, short-cut and cut-wire pairs, in the frequency region of 0.9-17 GHz. Both the real and imaginary parts of ε_{ef} show strong variations in the presence of a small magnetic field owing to the MI effect which controls the losses in the dielectric response. Continuous wire composites have a plasmonic type dispersion of ε_{ef} with negative values of its real part below the plasma frequency (GHz range) the absolute value of which strongly reduced in the presence of the field. For cut-wire composites we confirmed a a broadening of the resonance dispersion of ε_{ef} in the presence of the field. We also predicted the possibility to create wire-materials with tunable negative refractive index utilizing either natural magnetic properties of wires or artificial magnetism due to currents in cut-wire pairs. For the case of cut-microwire pairs the experiments reveal low and higher frequencies resonance modes but it was not possible to distinguish between the electric and magnetic resonances. Consequently, all types of wire composites exhibit strong ε_{ef} (H_{ex}) dependence suitable for applications.

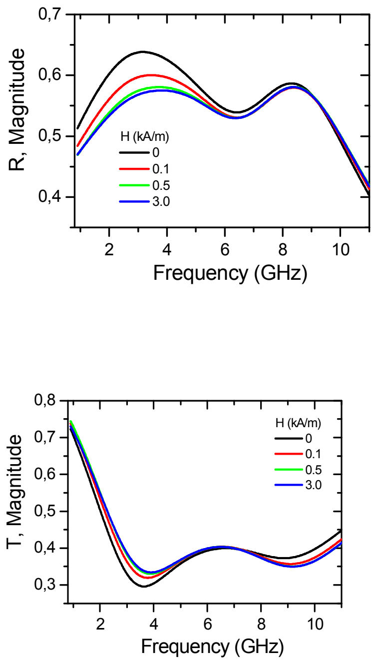

Figure 9. Experimental reflection/transmission spectra of two-layer cut magnetic wire arrays.

We acknowledge support under projects MAT2007-66798-CO3-01 (MEC), Saiotek 08 METAMAT (SPRI), DEVMAGMIWIRTEC (MANUNET-2007-Basque-3). Some of the authors, A. Zh. and V.Zh. wish to acknowledge support of the Basque Government under Program of Mobility of the Investigating Personnel of the Department of Education, Universities and Investigation for stay in Moscow (grants MV-2009-2-21 and MV-2009-2-24). L.V.P acknowledges support from the Ikerbasque Foundation

References

[1] Rotman W., “Plasma simulation by artificial dielectrics and parallel plate media,” *IRE Trans. Antennas Propagat.*, vol. 10, 82–95, 1962.

[2] Pendry, J. B., A. J. Holden, W. J. Stewart, and I. Youngs, “Extremely Low Frequency Plasmons in Metallic Mesostructures,” *Phys. Rev. Lett.*, Vol. 76, No. 25, 4773-4776, 1996.

[3] Reynet O., A.-L. Adent, S. Deprot, O. Acher, M. Latrach, “Effect of the magnetic properties of the inclusions on the high-frequency dielectric response of diluted composites,” *Phys. Rev. B* 66**,** 94412, 2002.

[4] Makhnovskiy D. P., L. V. Panina, “Field dependent permittivity of composite materials containing ferromagnetic wires,” *J. Appl. Phys*. **93** 4120, 2003.

[5] Makhnovskiy D.P., L. V. Panina, C. Garcia, A. P. Zhukov, and J. Gonzalez “Experimental demonstration of tunable scattering spectra at microwave frequencies in composite media containing CoFeCrSiB glass-coated amorphous ferromagnetic wires and comparison with theory,” *Phys. Rev. B*, Vol. 74, 064205-1–064205-11, 2006.

[6] Zhukova, V, Chizhik, A., Zhukov, A., Torcunov, A., Larin, V., and Gonzalez, J. “Optimization of giant magneto-impedance in Co-rich amorphous microwires”, *IEEE Trans. Magn*. Vol. 38, 3090-92, 2002

[7] García,C., Zhukov, A., Zhukova,V., Ipatov,M., Blanco, J.M., and Gonzalez, J. "Effect of Tensile Stresses on GMI of Co-rich Amorphous Microwires " , *IEEE Trans Magn*. Vol. 41, 3688-3690, 2005

[8] V. Zhukova, M. Ipatov and A. Zhukov, “Thin Magnetically Soft Wires for Magnetic Microsensors“ *Sensors 9*(2009) pp. 9216-9240

[9]Smith, D. R., Padilla, W. J. , Vier, D. C. , Nemat-Nasser, S. C., and Schultz , S. “ Composite Medium with Simultaneously Negative Permeability and Permittivity”, Phys. Rev. B, VOL., N0 18, 4184-87, 2000.

[10] Panina, L. V., Sandacci, S.I, and Makhnovskiy, D.P. “Stress effect on magnetoimpedance in amorphous wires at gigahertz frequencies and application to stress-tunable microwave composite materials”, *J. Appl. Phys*., Vol. 97, 013701-07, 2005.

[11]Makhnovskiy, D.P., Panina, L. V., Garcia, C. , Zhukov, A. P. , and Gonzalez J. “Experimental demonstration of tunable scattering spectra at microwave frequencies in composite media containing CoFeCrSiB glass-coated amorphous ferromagnetic wires and comparison with theory”, *Phys. Rev. B*., **74**, 064205-15, 2006.

doi:10.4028/www.scientific.net/AST.75.230

Manufacturing metamaterials using synchrotron lithography

Herbert O. Moser[1,2, a], Linke Jian[1, b], Shenbaga M.P. Kalaiselvi[1, c],
Selven Virasawmy[1, d], Sivakumar M. Maniam[1, e], Agnieszka Banas[1, f],
Krzysztof Banas[1, g], Sascha P. Heussler[1, h], Bernard Didier F. Casse[3, i],
Markus Moos[4, j], Heinz Kohler[4, k]

[1]Singapore Synchrotron Light Source (SSLS), National University of Singapore (NUS), 5 Research Link, Singapore 117603, Singapore

[2]Department of Physics, National University of Singapore, 2 Science Drive 3, Singapore 117542, Singapore

[3] Department of Physics and Electronic Materials Research Institute, Northeastern University, Boston, Massachusetts 02115, USA

[4]Institute for Sensors and Information Systems, Karlsruhe University of Applied Sciences, Moltkestr. 30, D-76133 Karlsruhe, Germany

[a]moser@nus.edu.sg, [b]slsjl@nus.edu.sg, [c]slssmk@nus.edu.sg, [d]slsvs@nus.edu.sg,
[e]slssiva@nus.edu.sg, [f]slsba@nus.edu.sg, [g]slskb@nus.edu.sg, [h]slshsp@nus.edu.sg,
[i]d.casse@neu.edu, [j]Markus.Moos@gmx.de, [k]heinz.kohler@hs-karlsruhe.de

Keywords: Metamaterials, meta-foil, synchrotron radiation, multilevel lithography, plastic moulding

Abstract. The function of metamaterials relies on their resonant response to electromagnetic waves in characteristic spectral bands. To make metamaterials homogeneous, the size of the basic resonant element should be less than 10% of the wavelength. For the THz range up to the visible, structure details of 50 nm to 30 μm are required as are high aspect ratios, tall heights, and large areas. For such specifications, lithography, in particular, synchrotron radiation deep X-ray lithography, is the method of choice. X-ray masks are made via primary pattern generation by means of electron or laser writing. Several different X-ray masks and accurate mask-substrate alignment are necessary for architectures requiring multi-level lithography. Lithography is commonly followed by electroplating of metallic replica. The process can also yield mould inserts for cost-effective manufacture by plastic moulding. We made metamaterials based on rod-split-rings, split-cylinders, S-string bi-layer chips, and S-string meta-foils. Left-handed resonance bands range from 2.4 to 216 THz. Latest is the all-metal self-supported flexible meta-foil with pass-bands of 45% up to 70% transmission at 3.4 to 4.5 THz depending on geometrical parameters.

Introduction

X-ray deep lithography with synchrotron radiation has been used for the manufacturing of tall high-aspect-ratio microstructures since the late 1970s [1]. Originally developed for the manufacturing of uranium isotope separation nozzles [2], the scope was quickly broadened to all kinds of mechanical, electromechanical, fluidic, and optical devices including acceleration sensors, electromotors, spinneret plates, micropumps, blazed stepped grating spectrometers, and more [3]. Detailed accounts are available in the Status Reports of Program Microsystems Technology at Forschungszentrum Karlsruhe, now Karlsruhe Institute of Technology (KIT) [4].

More recently, we have applied this manufacturing technique to metamaterials starting with rod-split-rings [5] and split cylinders [6] over assembled S-string bi-layer chips [7, 8] to interconnected S-string meta-foils [9, 10]. The manufacturing processes need to satisfy specifications and boundary conditions including geometrical tolerances, cost-effectiveness, and the availability of a variety of materials, over size scales extending from about 30 nm up to the mm range. Lithography followed by electroplating and plastic moulding (LIGA process) is a way to achieve that. Synchrotron radiation lithography is particularly suited for precise, small critical dimension, high-aspect-ratio, and tall structures, thus providing a rather wide parameter space for the design of structures. In the following, we shall describe the main manufacturing issues and processes as well as the metamaterials architectures achieved, and shall briefly mention some of the potential applications.

Manufacturing

Starting in 2002, we have developed the split ring approach proposed by Pendry [11] together with distributed in-plane rods to achieve the first micromanufactured THz functional metamaterial at 2.4 THz [5] (Fig. 1 (a, b)). Size reduction down to the nanoscale led to resonance frequencies of 186 THz (Fig. 1 (c)) and 216 THz. To facilitate building volume metamaterials by stacking, we made split cylinders [6] which can work in side-on incidence (Fig. 1 (d-f)). Such studies included "amorphous" split-cylinder metamaterials to make optical elements such as prisms with regularly structured surfaces by letting the defects that unavoidably develop in the bulk of a regular structure relax by some amorphisation that maintains an average value of the density of split-cylinders.

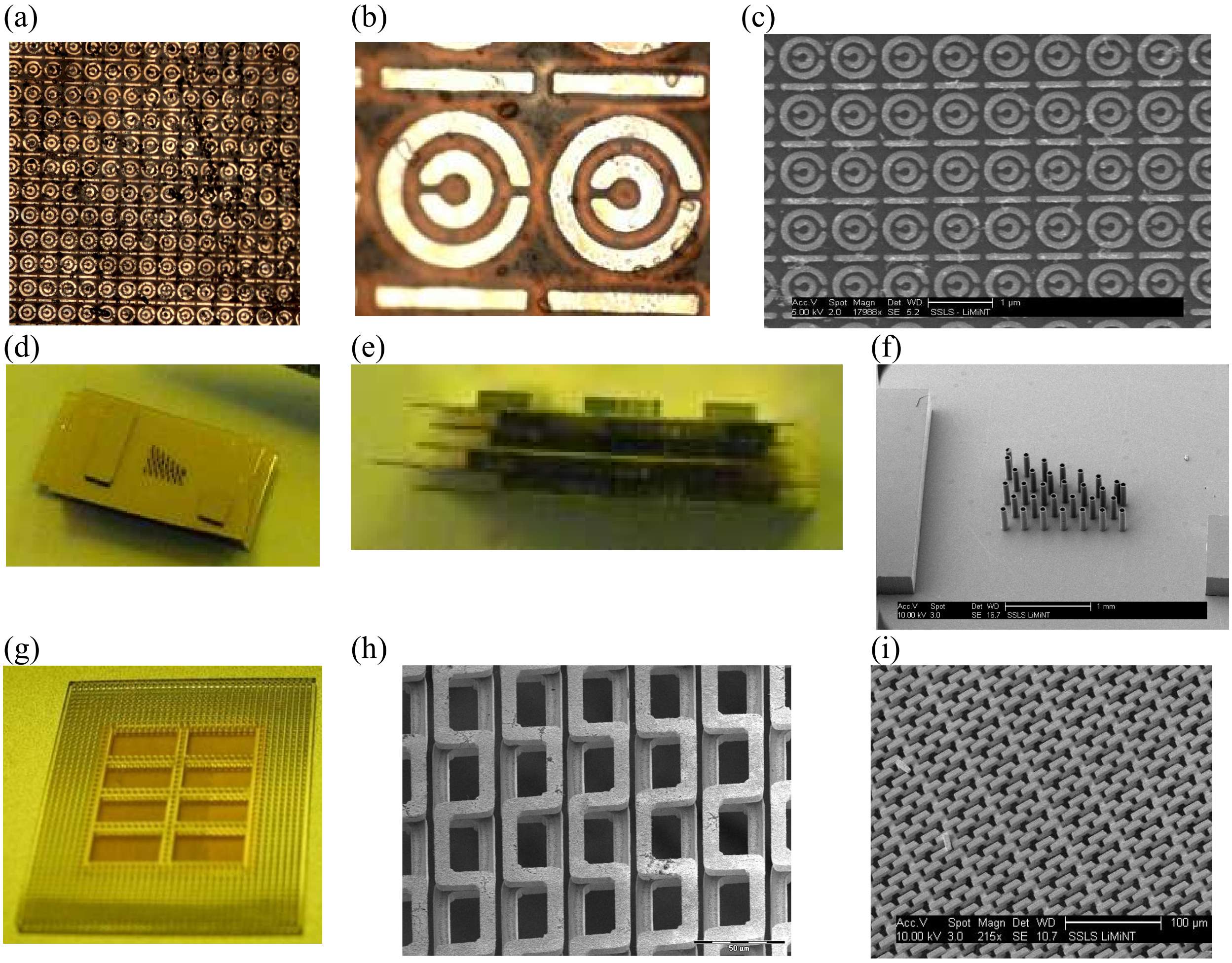

Fig. 1: Various metamaterials' architectures manufactured by SSLS. (a) Flat rod-split-ring resonators (RSRR) 2.4 THz, 73 µm outer Ø. (b) Close-up. (c) RSRR 186 THz, 710 nm outer Ø, scale bar 1 µm. (d), (e) Stack of five layers of Au split cylinders for side-on incidence arranged in a prism. (f) Prism of split cylinders in which the surfaces are formed by rows of regularly spaced cylinders while the bulk is arranged in an amorphous way to maintain a certain average density, scale bar 1 mm. (g) Window-frame bi-layer chip with a window size of 8.1×6.9 mm^2. (h) Close-up of bi-layer chip showing mutually opposite positioning of S-strings, scale bar 50 µm. (i) All-metal self-supported meta-foil featuring upright S-strings and interconnecting lines, scale bar 100 µm.

However, both rod-split-rings as well as split cylinders, needed a dielectric such as a resist or a wafer for holding the structures. Obviously, such dielectric materials introduced a basically unwanted shift and reduction of the resonance peaks of the metallic structures besides other constraints concerning thermal, chemical and radiation effects [10]. To avoid such limitations, we adopted the S-string architecture [12] and anchored such S-strings solely in a window-frame, thus getting rid of any embedding plastic matrix. To arrange string arrays parallel and opposite to each other for creating magnetic resonators, two window-frame chips were assembled to a bi-layer chip (Fig. 1 (g, h)). A breakthrough was achieved by putting S-strings upright next to each other and introducing interconnecting lines that run transversely to the S-strings and hold them together, thus forming a space grid that is locally stiff and globally flexible. This latest all-metal version of the interconnected S-string architecture is called the meta-foil (Fig. 1 (i)) [10].

The dimensions of the structures determine the resonance frequency, the smaller the structure, the higher the frequency, in general. This is illustrated in Fig. 2 for the example of the split ring by rewriting Pendry's formula [11] for the frequency versus radius r and annular gap d as

$$r = \frac{c}{2\pi^2}\sqrt{\frac{3d}{r}}\frac{1}{\nu_{res}} \qquad (1)$$

with c the speed of light *in vacuo* and ν_{res} the resonance frequency. For a fixed value of d/r, the formula can be directly evaluated. We see that it describes experimental results over more than four orders of magnitude. Obviously, aiming at the visible needs dimensions in the sub-100 nm range.

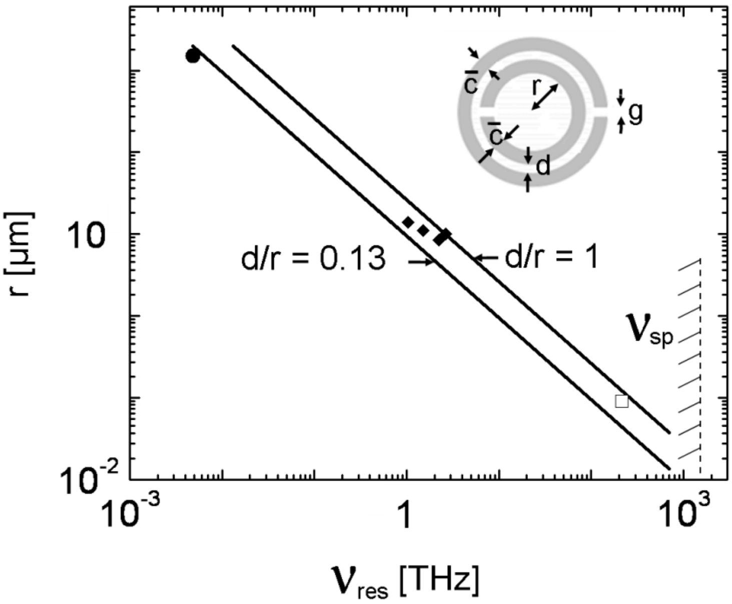

Fig. 2: Inner radius r versus resonance frequency ν_{res} for nested split-rings showing that the scale from 10 nm to mm is needed to cover the spectral range from 10 GHz to 1 PHz. Straight lines for r hold for different values of the ratio d/r of annular gap d to radius r, namely 0.13 and 1.0. Measured values reported in literature represent: ● [13] with d/r=0.13, ♦ [5] with 0.3<d/r<1, □ [14]. The saturation surface plasmon frequency ν_{sp} for Au is also indicated as derived from the bulk plasmon frequency divided by $\sqrt{2}$ [15, 16].

For the S-string architecture, the relevant geometrical parameters are provided in Fig. 3 which shows a structure that we denote 2SP because the periodicity of the interconnecting lines is 2 and the gap d_p is larger than d which results in having pairs of S-strings spaced further apart than their internal gap. The resonance frequency of S-strings depends among other parameters on the length of the S-motif. In Fig. 4, the spectral transmission is plotted with the clear width of the resonance loop w as a parameter defined by w=(a-3h)/2. It can be seen that the peak around 4 THz is the magnetic resonance that responds to the change of w and of the inductance. Accordingly, w scales as $1/\nu^2$.

The manufacturing of such meta-foil structures depends critically on micro/nanotechnology. A typical process chain is illustrated in Figs. 5-8. For either standard UV or deep X-ray lithography, a 4 inch Si wafer is used as a substrate. The manufacturing process starts with writing the primary pattern onto a mask by either laser direct writing or electron beam writing. Ion beam writing could also be used. The layout of a mask for a 4 inch substrate is shown in Fig. 5 (a). A total of 12 chips is routinely produced from one wafer (Fig. 5 (b)). The important aspect of the fabrication of the metafoils is the multi-level lithography that enables the formation of 3D resonator structures with a large extent of design freedom. The composition of the meta-foil from three distinct lithography layers is shown as explosion view in Fig. 5 (d). In the middle level, the distinction between interconnecting bars (left) and vias (three rows of three metal cubes each) becomes obvious.

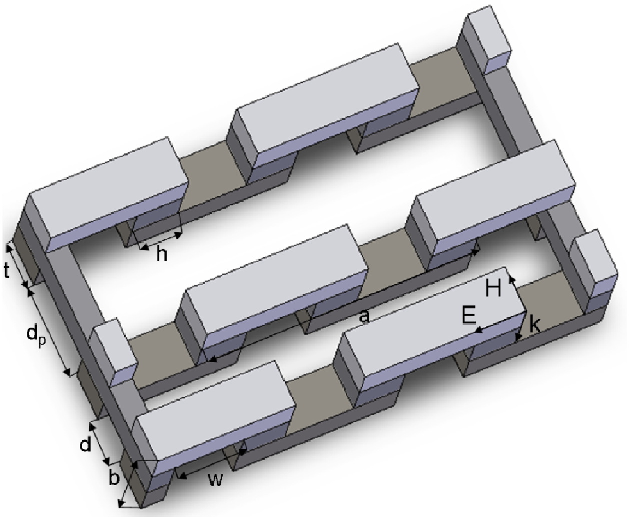

Fig. 3: Geometric parameters of a 2SP structure.

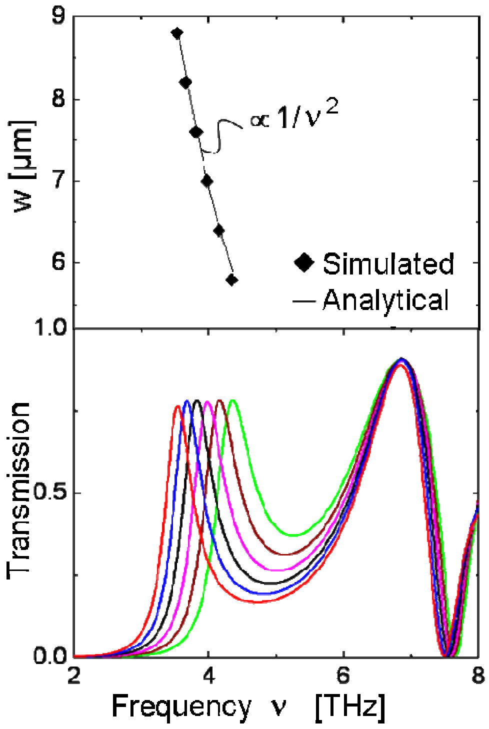

Fig. 4: Spectral transmission of the 2SP meta-foil with the clear width w of the resonance loop as a parameter (bottom) and the clear width of the magnetic resonance loop versus frequency (top). Simulated values calculated by means of MWS [17], analytical curve assuming the width w entering the inductance L linearly while L scales as $1/\nu^2$.

To manufacture the meta-foil along the process schematic shown in Fig. 6, three masks are needed with different patterns as shown in Fig. 5 (c). They also include alignment marks (not shown) to ease subsequent multi-layer lithography. Upon exposure and development of one layer, the metallic structure is made by electroplating of gold under accurate thickness control. On top of layers one and two, a thin auxiliary Au plating base is deposited without any spatial pattern to enable electroplating in the next layer (Fig. 6). After dissolving the unexposed resist and wet-etching the thin gold plating base, layer by layer, the meta-foils are released from the substrate by wet-etching of Cr. Fig. 7 shows photographs and scanning electron microscope close-up views of the so-manufactured meta-foils. The useful area of these standard samples is 7×8 mm^2.

While both lithography and subsequent electroplating are parallel-processing techniques as far as all the structures combined on one wafer are concerned and are thus already cost-saving compared to primary pattern generation such as laser or electron beam writing, an even larger cost reduction is expected from plastic moulding. In this case, a metal mould of Ni or its alloys NiFe or NiCo is produced by similar lithography and electroforming steps as described above. Then, a meta-foil made of a suitable polymer can be produced by injection moulding or hot embossing (Fig. 8). This plastic meta-foil is then metal-coated by sputter deposition or electroplating with a suitable metal. This part of the process chain is likely to lead to a final comparably low-cost product [9].

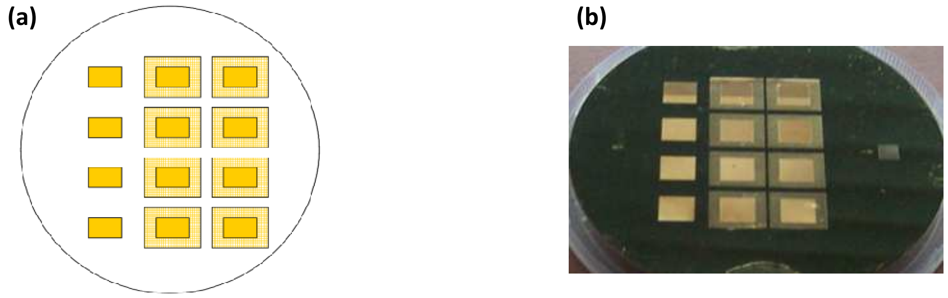

Mask layout for meta-foil

Completed meta-foils on wafer before release

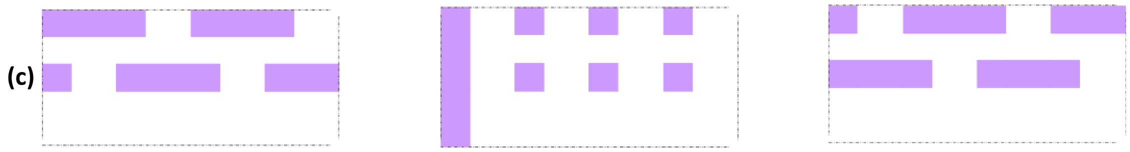

Pattern on mask 1

Pattern on mask 2

Pattern on mask 3

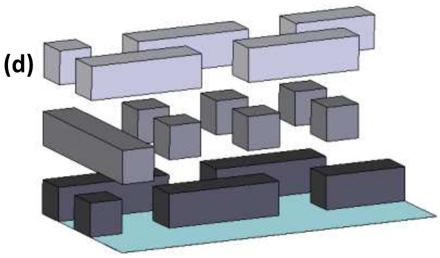

Fig. 5: (a) Mask layout including eight meta-foils with window-frame and four meta-foils without. (b) Wafer with completed meta-foils before release. (c) Absorber patterns on the three masks for a 2SP structure per unit cell. The dashed lines indicate the boundaries of the unit cell. (d) Exploded view of unit cells illustrating the arrangement of the three mask levels with respect to each other.

Fig. 6: Fabrication of the meta-foil by means of multilayer lithography with precise alignment and gold electroplating with accurate thickness control.

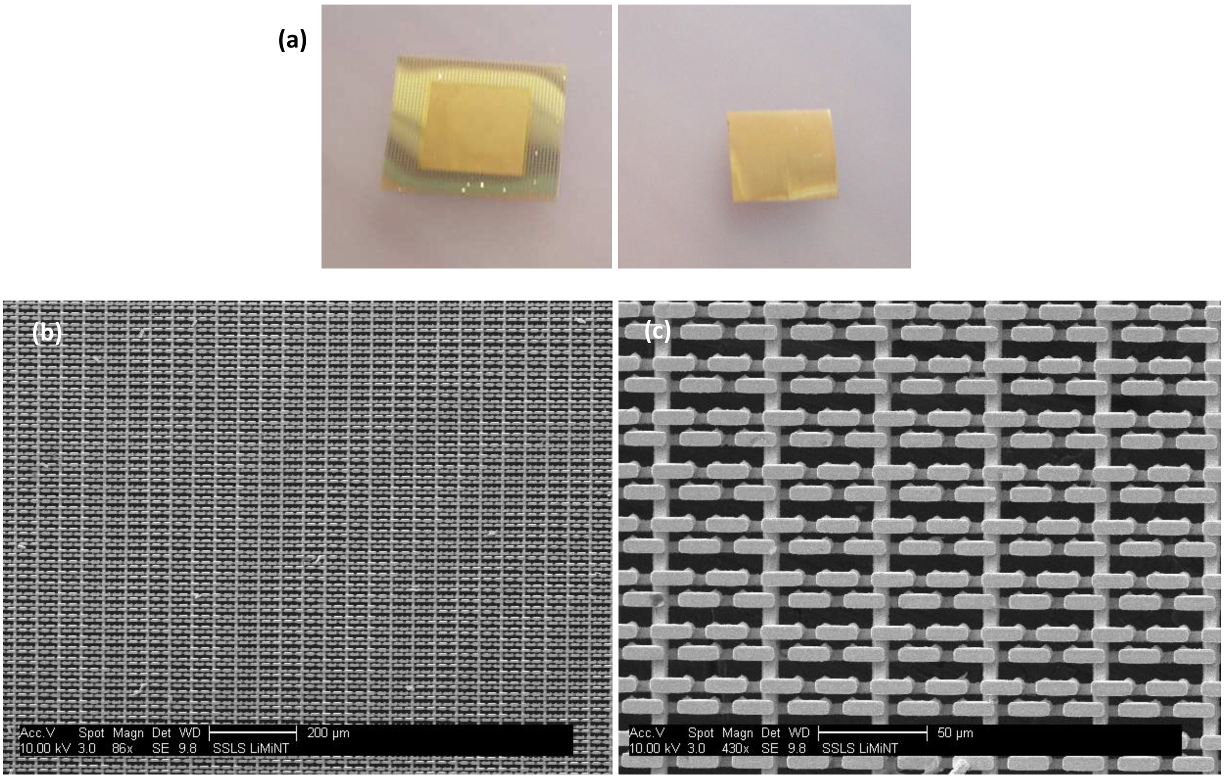

Fig. 7: Meta-foils after release from the wafer. (a) Photos of meta-foils with and without frame. (b) Scanning electron microscope (SEM) bird's eye view of a 2SP meta-foil. Scale bar 200 µm. (c) SEM close-up showing clearly the 2SP structure. Scale bar 50 µm.

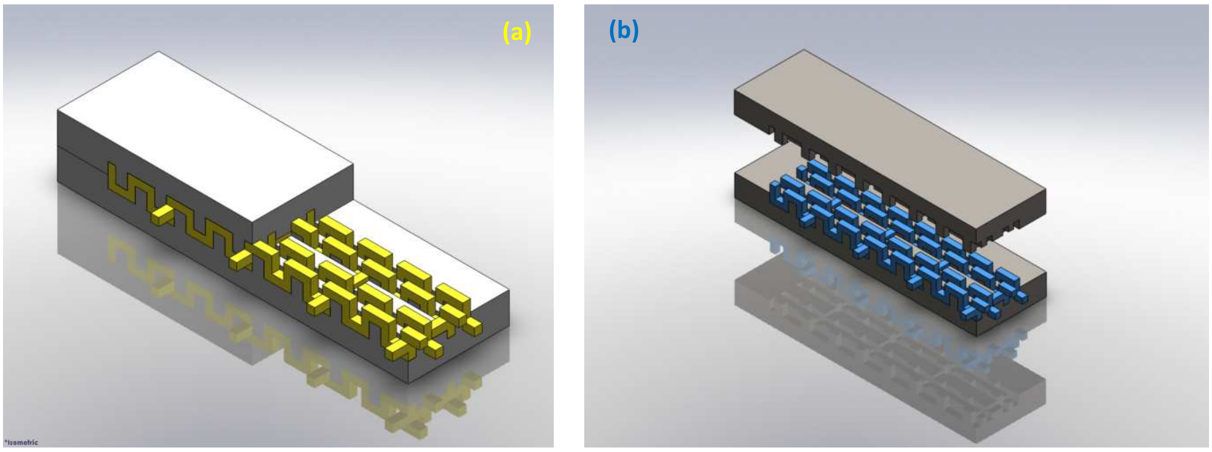

Fig. 8: Large volume production of the meta-foil by plastic molding. (a) Schematic of plastic meta-foil inside the mould. (b) Two-part mould retracted for demoulding.

Structures manufactured and their spectral performance

In the following, we present results of various metamaterials manufactured on the basis of the techniques described. No plastic moulding has been done yet. Fig. 9 shows a spectrum of one of the original nano rod-split-ring resonators with r=90 nm and d=80 nm. The record frequency measured, 216 THz, corresponds to the near infrared telecommunication wavelength of 1.39 µm [14]. With electron beam writing, resist structures can be made so small that their resonance would fall into the visible. Fig. 10 shows a case which has a calculated resonance frequency of about 700 THz [14]. However, the lift-off process to obtain clear metal structures was not successful. More studies would be needed to solve the underlying problem by undercutting the resist structures such as to prevent damage of the deposited metal while lifting off the resist.

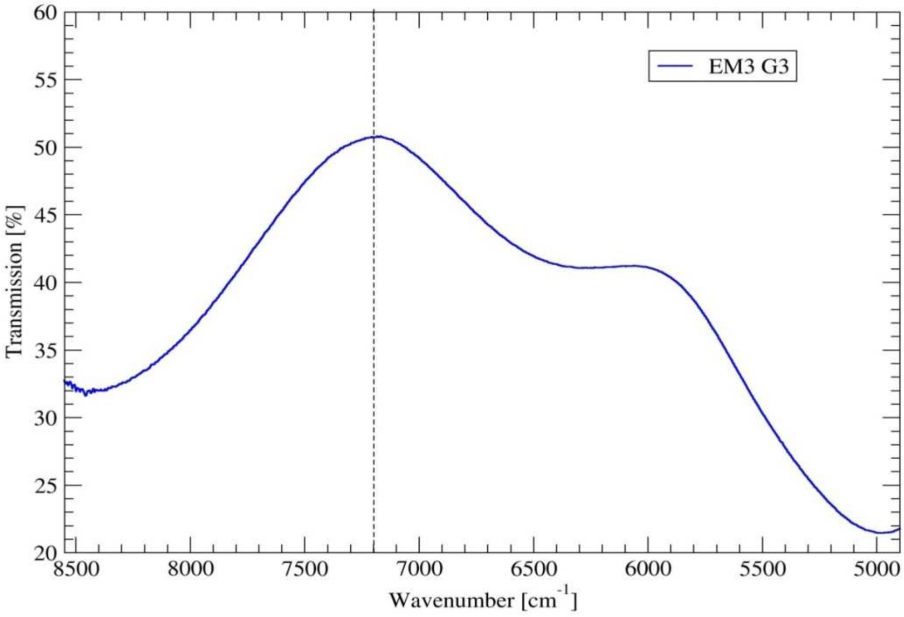

Fig. 9: Record high frequency rod-split-ring spectrum in the telecommunication near infrared. Dimensions of the nested split rings were r=90 nm and d=80 nm [14].

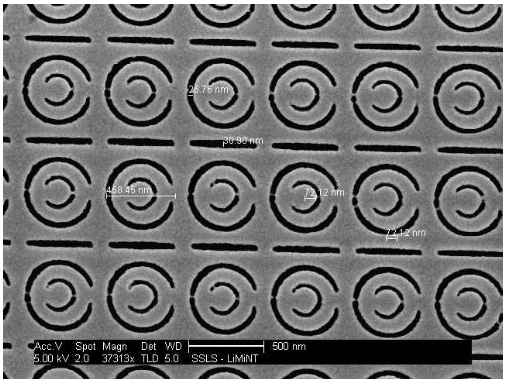

Fig. 10: Smallest RSRR structure made of PMMA resist [14]. Outer diameter 460 nm, critical feature 25 nm, estimated expected frequency of corresponding metal structure 700 THz ignoring possible plasmonic response at 1538 THz and below (see Fig. 2).

For split cylinders, side-on incidence is required because any inclination leads to a phase shift of the wave incident on various parts of the split cylinder and to subsequent mutual cancellation of induced currents (Fig. 11). The end-to-end phase difference of a split cylinder of length l is

$$\Delta\varphi(l) = 2\pi(l/\lambda)\sin\alpha. \tag{2}$$

Depending on length l and incidence angle α, parts of the cylinder are excited with opposite phase. The full quench, i.e., every phase finds its opposite phase on the split cylinder, is reached for $l = \lambda/\sin\alpha$. Then, voltages and currents representing the magnetic excitation as well as the whole signal are reduced by currents flowing between places of opposite phase.

The S-string architecture is radically different from split rings in as much as it enables to remove embedding matrices or supporting substrates by fixing the ends of the strings in a window-frame, thus leaving the S-string array free-standing without any dielectric material [7, 8]. S-string arrays have been fabricated by lithography. When two such single-layer chips are assembled together, accurately aligned and separated by a thin film that sets the gap width, the geometric arrangement of S-strings is inverted, thus creating magnetic resonance loops (Fig. 12).

As coupling of a normally incident wave to the bi-layer chip is not ideal, the geometry was changed by turning S-strings upright in their plane. In addition, metallic interconnecting lines were introduced that run transversely and hold the individual strings together (Fig. 13 and above). In this way, an all-metal self-supported meta-foil was achieved that had maximum response under normal incidence of an electromagnetic wave.

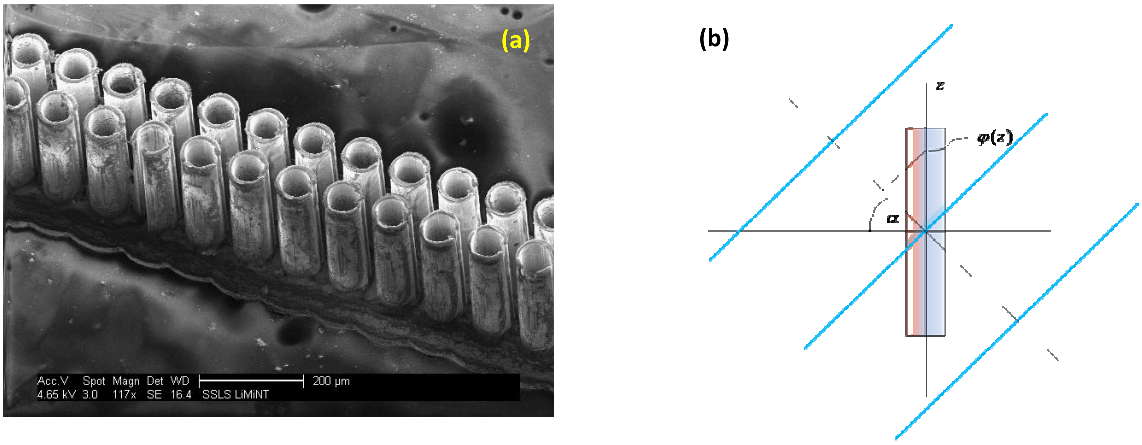

Fig. 11: (a) Double row of Ni split cylinders. Scale bar 200 µm. (b) Partial signal cancellation at oblique incidence.

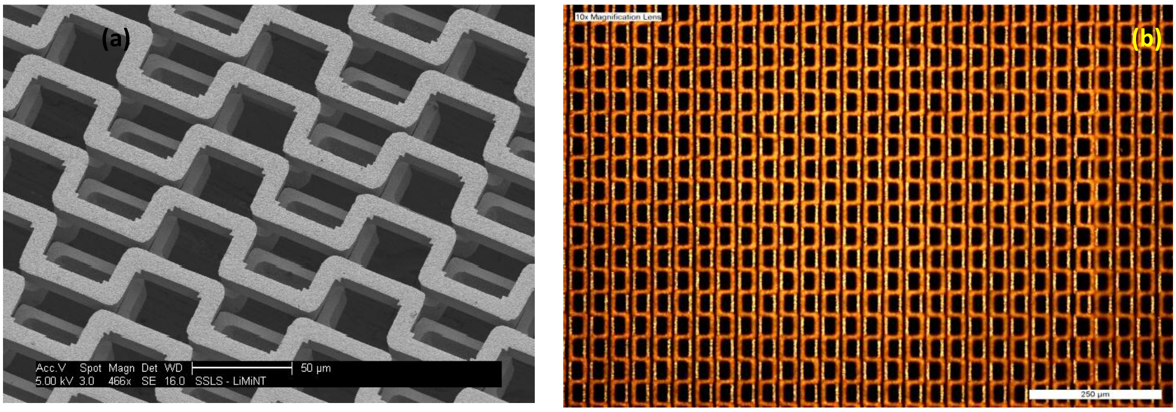

Fig. 12: (a) SEM image of a bi-layer chip showing inverted accurately aligned top and bottom layers. Scale bar 50 µm. (b) Photo of a bird's eye view of about 1.2×0.9 mm^2 of a bi-layer chip, scale bar 250 µm. A slight displacement defect can be seen between bottom and top string in column 5 from the right.

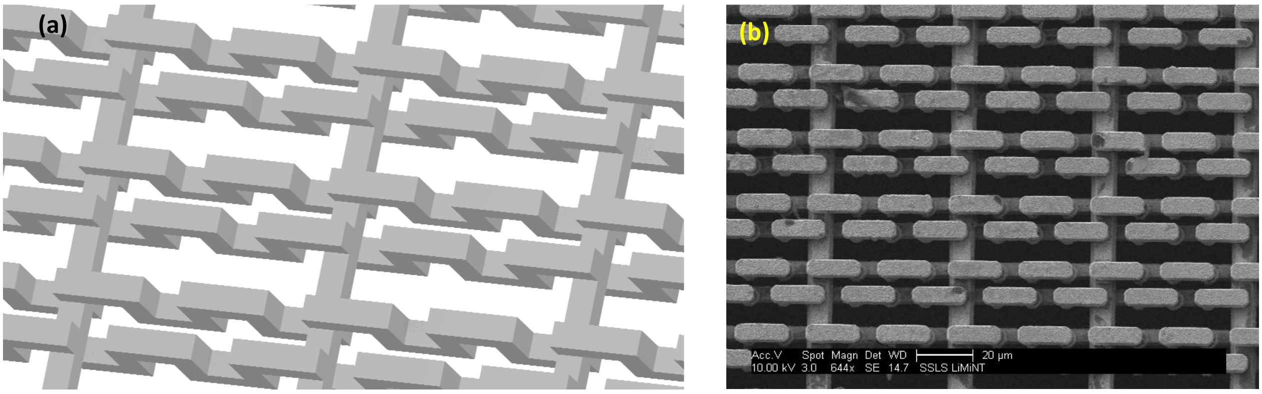

Fig. 13: (a) Schematic of 2SP meta-foil. (b) SEM image of 2SP meta-foil fabricated in Au by means of three-level lithography. The alignment between various mask levels is crucial. Scale bar 20 µm.

Finally, Fig. 14 displays a spectrum of a 2SP meta-foil between 3-6.5 THz. The peak at about 4.3 THz is the magnetically excited resonance corresponding to the peak around 4 THz in Fig. 4. It has a transmission of about 0.7. The peak at 5.7 THz is the electrically excited resonance. The two colours indicate spectra taken at different times at the same spot on the sample.

With regard to applications, meta-foils represent a technology platform on which various devices may be realized [18]. They may serve as narrow-band filters, selective high-reflectance mirrors, and focusing elements in THz optical systems for various purposes including security inspection to detect plastic materials such as explosives in the 1-10 THz range, or high bit-rate data transfer links and telecommunication. Owing to the mechanical flexibility of meta-foils, the concept of a cylindrical hyperlens made from bent meta-foils is being pursued [19]. Such hyperlenses could be used in THz microscopy systems and for infrared spectro/microscopy in the fingerprint region to obtain sub-wavelength spatial resolution. Furthermore, their small size and capability to adapt to surface shapes imposed by other design considerations make meta-foils good candidates for conformal antenna architectures of interest for automotive transportation [20]. As meta-foils are sensitive to their dielectric environment, they may also serve as sensors for dielectrics [18] in which both peak shift and amplitude reduction might be used for detection and sensing.

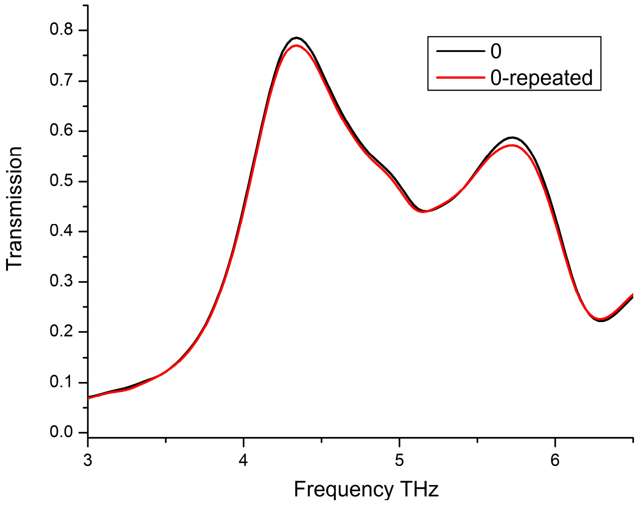

Fig. 14: Transmission spectrum of a 2SP meta-foil

Conclusion

Synchrotron radiation lithography in combination with electroplating and plastic moulding – the LIGA process - can play an important role in the manufacturing of metamaterials for the THz spectral range up to the visible because it enables the fabrication of tall high-aspect-ratio structures on the micro and nanoscale at process costs that are reduced by the parallel processing of the lithography step and by the large-volume process steps of electroplating/forming and plastic moulding. Depending on the geometric structure of the metamaterial such as split-cylinders and the meta-foil, the full LIGA process can be applied such that a cost-effective manufacturing of metamaterials by plastic moulding and metallisation in substantial quantities can be envisaged.

Acknowledgment

Work partly performed at SSLS under NUS Core Support C-380-003-003-001, A*STAR/MOE RP 979908M and A*STAR 12 105 0038 grants.

References

[1] E.W. Becker, W. Ehrfeld, P. Hagmann, A. Maner, and D. Muenchmeyer: Microelectron. Eng. Vol. 4 (1986), p. 35.

[2] E.W. Becker, W. Ehrfeld, D. Muenchmeyer, H. Betz, A. Heuberger, S. Pongratz, W. Glashauser, H.J. Michel, R. v. Siemens: Naturwissenschaften Vol. 69 (1982), pp. 520-523.

[3] W. Ehrfeld, P. Bley, F. Götz, P. Hagmann, A. Maner, J. Mohr, H.O. Moser, D. Münchmeyer, W. Schelb, D. Schmidt, E.W. Becker, in: *An investigation of Micromechanical Structures,*

Actuators and Sensors, Proc. IEEE Micro Robots and Teleoperators Workshop, Nov. 9-11, 1987, Hyannis, Massachussetts, IEEE Catalog Number 87TH0204-8, Library of Congress Number 87-82657.

[4] *2. Statuskolloquium des Projektes Mikrosystemtechnik*, Wissenschaftliche Berichte FZKA 5670, Forschungszentrum Karlsruhe, Germany, Nov. 1995 (available from KIT library)

[5] H.O. Moser, B.D.F. Casse, O. Wilhelmi, B.T. Saw: Phys. Rev. Lett. Vol. 94 (2005), p. 063901.

[6] B.D.F. Casse, H.O. Moser, J.W. Lee, M. Bahou, S. Inglis, L.K. Jian: Appl. Phys. Lett. Vol. 90 (2007), p. 254106.

[7] H.O. Moser, M. Bahou, B.D.F. Casse, A. Chen, S.P. Heussler, L.K. Jian, S.M.P. Kalaiselvi, G. Liu, S.M. Maniam, P.D. Gu, Shahrain bin Mahmood, L. Wen, J.A. Kong, H.S. Chen, B.I. Wu, X.X. Cheng: Proc. SPIE Vol. 7029 (2008), pp. 70290E1-12.

[8] H.O. Moser, J.A. Kong, L.K. Jian, H.S. Chen, G. Liu, M. Bahou, S.M.P. Kalaiselvi, S.M. Maniam, X.X. Cheng, B.I. Wu, P.D. Gu, A. Chen, S.P. Heussler, Shahrain bin Mahmood, L. Wen: Opt. Express Vol. 16 (2008), p. 13773.

[9] H.O. Moser, L. K. Jian, G. Liu, S. M. P. Kalaiselvi, S. M. Maniam, S. P. Heussler, J. A. Kong, H. S. Chen, B. I. Wu: PCT/SG2009/000098, 19 March 2009.

[10] H.O. Moser, L.K. Jian, H.S. Chen, M. Bahou, S.M.P. Kalaiselvi, S. Virasawmy, S.M. Maniam, X.X. Cheng, S.P. Heussler, Shahrain bin Mahmood, B.-I. Wu: Opt. Express Vol. 17 (2009), pp. 23914-23919(2009)

[11] J.B. Pendry, A.J. Holden, D.J. Robbins, W.J. Stewart: IEEE Trans. Microwave Theory Tech. Vol. 47 (1999), pp. 2075-2084.

[12] Hongsheng Chen, Lixin Ran, Jiangtao Huangfu, Xianmin Zhang, Kangsheng Chen, Tomasz M. Grzegorczyk, and Jin Au Kong: Phys. Rev. E Vol. 70 (2004), p. 057605.

[13] D.R. Smith, Willie J. Padilla, D.C. Vier, S.C. Nemat-Nasser, S. Schultz: Phys. Rev. Lett. Vol. 84 (2000), p. 4184.

[14] B.D.F. Casse: *Fabrication and Characterisation of Micro- and Nanostructured Electromagnetic Metamaterials for the THz Spectral Range up to the Near Infrared*, PhD Thesis, National University of Singapore, unpublished (2007).

[15] Stefan Linden, Christian Enkrich, Martin Wegener, Jiangfeng Zhou, Thomas Koschny, Costas M. Soukoulis: Science Vol. 306 (2004), pp. 1351-1353.

[16] S. Anantha Ramakrishna: Rep. Prog. Phys. Vol. 68 (2005), pp. 449-521.

[17] Microwave Studio (MWS) is a registered trademark of CST GmbH, Darmstadt, Germany.

[18] H.O. Moser, L.K. Jian, H.S. Chen, M. Bahou, S.M.P. Kalaiselvi, S. Virasawmy, X.X. Cheng, A. Banas, K. Banas, S.P. Heussler, B.-I. Wu, S.M. Maniam, Wei Hua: submitted to Journal of Modern Optics (2010).

[19] H.O. Moser, L.K. Jian, H.S. Chen, S.M.P. Kalaiselvi, S. Virasawmy, X.X. Cheng, A. Banas, K. Banas, S.P. Heussler, M. Bahou, B.-I. Wu, Wei Hua, Zhu Yi, in: *Metamaterials*, edited by N.P. Johnson, E. Özbay, R.W. Ziolkowski, N.I. Zheludev, Proc. SPIE Vol. 7711, in press, (2010).

[20] H.O. Moser, H.S. Chen, L.K. Jian, M. Bahou, S.M.P. Kalaiselvi, S. Virasawmy, S.M. Maniam, X.X. Cheng, S.P. Heussler, Shahrain bin Mahmood, B.-I. Wu, in: *Photonics in the Transportation Industry: Auto to Aerospace II*, edited by Alex A. Kazemi, Bernard C. Kress, Proc. SPIE Vol. 7314 (2009), p. 73140G.

© (2010) Trans Tech Publications, Switzerland
doi:10.4028/www.scientific.net/AST.75.240

Full Optical Scatter Analysis for Novel Photonic and Infrared Metamaterials

Thomas M. Fitzgerald[1] and Michael A. Marciniak, Ph.D.[2]

Department of Engineering Physics
Air Force Institute of Technology
Wright-Patterson AFB OH, USA
[1]thomas.fitzgerald@afit.edu
[2]michael.marciniak@afit.edu

ABSTRACT

Artificial structures with sub-optical wavelength features are engineered to feature non-conventional values for material properties such as optical and infrared permeability and permittivity. Such artificial structures are referred to as optical and infrared metamaterials.[1] The application space of electromagnetic metamaterials includes novel sub-wavelength waveguides and antennas, true time delay devices, optical filters, and plasmonic electronic-optical interfaces.[2]

In this paper presents an optical diagnostic technique adapted for measuring and analyzing bidirectional polarimetric scatter from novel photonic and infrared metamaterials of interest. This optical diagnostic technique is also broadly applicable to other optical/infrared metamaterial structures that are proposed or developed in the future.

The specific project goals are

a) Demonstrate a novel metamaterial characterization full-polarimetric diffuse ellipsometry technique suitable to measure desired material properties with stated uncertainty limits for novel photonic and infrared metamaterials of interest.

b) Demonstrate incorporation of predictive computational codes that estimate the electro-magnetic property values for metamaterial designs and concepts of interest.

I. INTRODUCTION

Artificial structures with sub-optical wavelength features can have engineered non-conventional values for material properties such as optical and infrared permeability and permittivity. Such artificial structures are referred to as optical metamaterials.[1] The application space of engineered metamaterials includes sub-wavelength waveguides and antennas, true time delay devices, optical filters, and Plasmonic electronic-optical interfaces.[2]

This research effort focuses on the development of a novel optical diagnostic technique for measuring and analyzing full-angle full-polarimetric scatter from metamaterials of interest. The approach is an evolutionary continuation of the work by Germer et al at NIST. Germer has published significant work on the employment of the model based SCATMECH scatter library for characterization of surface roughness. This research extends the previous body of work to metamaterials. Appropriate numerical scatter models are incorporated for the as built optical metamaterial architecture to include the effects of fabrication defects. The goal is to bridge the gap between metamaterial design performance and metamaterial "as-built" performance.

Metamaterial property values for permittivity and permeability are used to derive macro property values such as impedance and index of refraction. Full scatter angle Mueller Matrix measurements capture the complete interaction of a material with incident energy. The measured Mueller matrix stores the degree of attenuation, de-polarization, and retardance for all angles of interest. The currently accepted technique for measuring metamaterial permittivity and permeability uses normal incidence polarized light to determine the reflection and transmission coefficients of the metamaterial. Then the permittivity and permeability are estimated.[3] [4]

Mueller Matrix Ellipsometry requires strong predictive models in order to properly interpret the results. The DDSCAT Direct Dipole Approximation (DDA) based computational model is incorporated to develop scatter predictions for the metamaterial geometry of interest. These models provide an understanding of the CASI-DRR measured perturbations and deficiencies in material properties due to imperfect fabrication and layer defects. The finite element model provides absorption and scattering coefficients for the desired geometry based on a selected input E(k,λ) where k gives the incident k-vector and λ is the optical wavelength in air. Permittivity and permeability can then be derived from the calculated reflection and transmission coefficients.[3] [4]

This approach to metamaterials property prediction, structure fabrication, and optical measurement will be broadly applicable to other optical/infrared metamaterial structures that are proposed or developed in the future.

II. DESCRIPTION OF THE APPROACH

a. DESCRIPTION OF THE CASI-DRR INSTRUMENT

An available in-house Schmitt Complete Angle Scatter Instrument (CASI) Bi-directional Reflectance Distribution Function (BRDF) measurement system was modified to the Dual Rotating Retarder (DRR) configuration proposed by Azzam and developed by Chipman.[5, 6] Four additional motion control channels were added to the CASI instrument to achieve DRR configuration. These channels automate the rotational motion of two linear polarizers and two quarter wave plates. The representative optical layout for the instrument is shown in Figure 1.

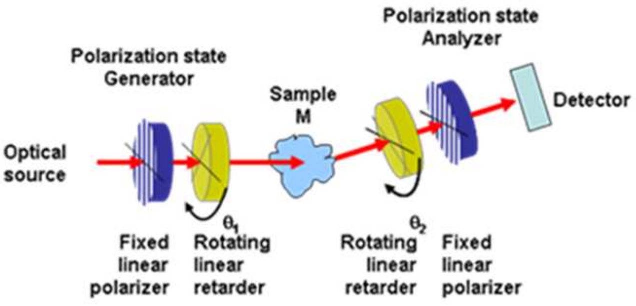

Figure 1. Optical configuration for AFIT DRR

The DRR addition consists of an input Polarization State Generator and an output Polarization State Analyzer. The Generator and Analyzer stages each feature a linear polarizer and a linear retarder. The linear retarders are rotated to produce and analyze complete polarization states. The Analyzer stage features rotational motion in a horizontal plane about the sample. Sample M has the full six degrees of freedom (DOF) necessary for full scatter characterization.

The condition number DRR instrument analysis approach proposed by Smith was applied to determine instrument operating mode.[7] In the Mueller algebra, a DRR instrument can be described by

$$I = \left(1\,0\,0\,0\right)\Pi_a(\theta_a)\Delta_a(\delta_a)M_s\Delta_g(\delta_g)\Pi_g(\theta_g)S^T \qquad (1)$$

where I is the measured intensity or Stokes S_0 parameter of the output polarization state mathematically selected by $\left(1\ 0\ 0\ 0\right)$, Π is the Mueller representation for a polarizer at angle θ with respect to the polarization axis of interest, Δ is the Mueller representation for a waveplate with δ

phase retardation, subscripts a and g refer to analyzer and generator elements, respectively, M is the sample of interest and S is the Stokes vector of the input light. Equation 1 can be recast into the W-Matrix form as

$$I = W(\theta_a, \delta_a, \delta_g, \theta_g) M_s \tag{2}$$

where W is an [N x16] matrix that fully describes the instrument configuration for any desired Generator-retarder/Analyzer retarder combination. N is the number of independent measurements necessary to return a full Mueller matrix. Smith's condition number approach to W-Matrix analysis allows determination of both N and suitable angle-increment pairs for rotation of the linear retarders. By searching the entire space of possible angle pairs, Smith determined that 34^o and 26^o increments for the Generator and Analyzer retarders respectively are optimal for inversion of the W-matrix.

$$M_s = \left(W^T W\right)^{-1} W^T I \tag{3}$$

Smith's W-Matrix analysis did not include the effects of instrument scatter or optical component misalignment. These are areas of active research and discussion for the team. Applying the Compain DRR instrument characterization and error correction technique helps correct for systematic alignment errors in the instrument.[8] Finally, the optical component characterization technique described by Chenault is used to determine diattenuation and retardance values for all of the optical components.[9] Chenault's technique is particularly well suited as it features rotating the item to be characterized between fixed linear polarizers. This technique exploits the layout of the existing DRR configuration.

b. DESCRIPTION OF THE DDSCAT MODEL

The method proposed for use in this research is the DDA as developed by Purcell and implemented by Draine as DDSCAT.[10, 11] DDSCAT uses a hybrid finite-element/coupled dipole method (FE/CDM) approach. The finite elements are point polarized dipoles on a cubic lattice. The geometry and material-dependent spectral scatter and absorption coefficients are calculated.[12]

DDSCAT has been successfully applied to determining localized surface plasmon resonance for nano-particle bio- and chem-sensor development, interstellar spectroscopy of microscopic graphite, and is starting to be used for optical metamaterial design and analysis. [13-25] DDSCAT takes into account much higher localized field strengths due to near-field interactions, local surface plasmon resonances, and interaction between the incident field and the structure geometry.[26-29] DDSCAT is used to determine the extinction (scattering and absorption) coefficients for arbitrarily shaped nano-particles. The nano-particles can either be free or placed on or in a substrate.

III. CHARACTERIZATION

The AFIT CASI-DRR instrument was initially assembled in March 2010 and is now going through characterization trials and optical alignment in order to optimize the performance of the device. A strong DRR Mueller Calculus model was developed in the Python language to facilitate modeling a measurement and to compare the measurement to the ideal. The residual difference between the measurement and ideal states the sensitivity of the instrument. The residual is given by

$$\varepsilon = \frac{I_{Ideal} - I_{Meas}}{I_{Ideal}} \tag{4}$$

where I is intensity as given in equations (1) and (2). The Mueller distance between Mueller matrices M_1 and M_2 is another useful tool for measurement analysis. The Mueller difference is given by

$$\varepsilon_{1,2} = \sqrt{\frac{\sum_{i,j}^{4,4}\left(M_{1_{i,j}} - M_{2_{i,j}}\right)^2}{16}} \qquad (5)$$

The typical Mueller distance between current measurement result and the desired Identity matrix is 0.064.[30] For comparison, the calculated Mueller distance for the NIST team led by Dr. Germer is 0.0006. [31] We are improving fast and working with the NIST team to improve our measurement.

IV. INITIAL MEASUREMENTS AND PRELIMINARY RESULTS

An initial application of our technique is to the characterization of a layer of 50nm silver nanocubes on an ITO coated glass slide [32]. The nanocubes are randomly oriented in rotation but are well aligned to the substrate face. An SEM photograph of the nanocubes is shown in Figure 4(a) with the DDSCAT-derived spectral extinction coefficients of the nanocubes shown in Figure 4(b).

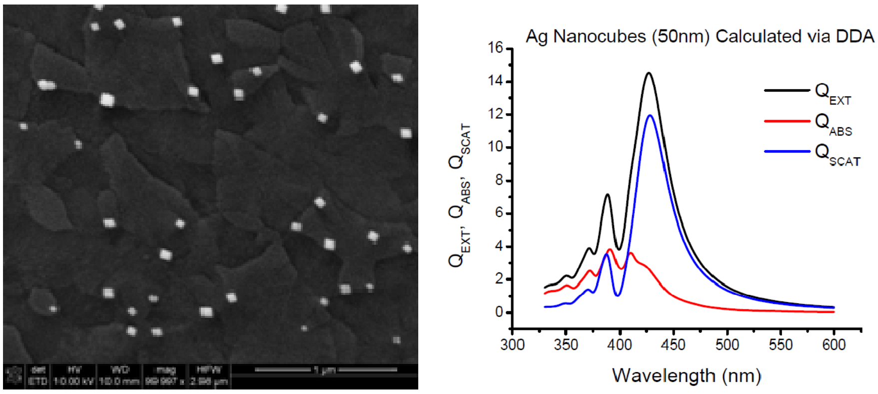

Figure 2. ((left) Silver nanocubes on glass substrate. (right) DDSCAT scattering coefficients for silver nanocubes.

Figure 3 shows full-angle Mueller Matrix for the silver nanocubes on an ITO coated glass slide. There is a rapid and clear decrease in polarization with increasing angle away from the center peak for the silver nanocube covered slide.. This is shown by the decline in the diagonal components with increasing angle in Figure 3. This feature is not present in the ITO slide with no nanocubes present We attribute the distinctive up-down pattern between -1 and +1 deg to systematic scatter in the instrument. We are working to decrease this effect.

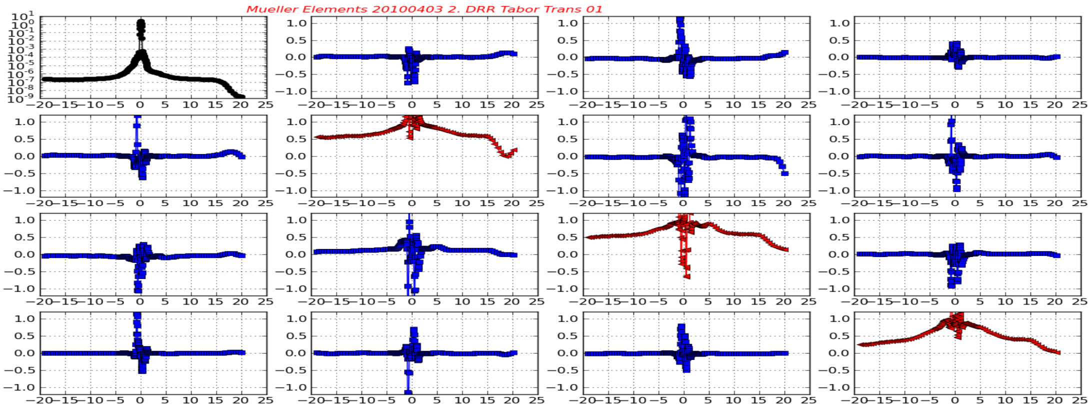

Figure 3. Full Mueller Matrix versus angle for silver nanocubes on ITO coated glass slide.

V. CONCLUSION

We have completed initial development of a full-scatter dual rotating retarder ellipsometer suitable for novel metamaterial characterization. The technique is well suited to measure desired material properties with stated uncertainty limits for novel optical and infrared metamaterials of interest. Incorporating predictive computational codes allows estimating the electro-magnetic property values for metamaterial designs and concepts of interest. We are anxious to apply our resources and instruments to targets of interest to the community.

ACKNOWLEDGMENTS

Chris Tabor AFRL/RXBN for the samples. Stephen Nauyoks for assistance with collection. Dom Maga for assistance with instrumentation development.

References

1. R. M. Walser, "Electromagnetic metamaterials," Proceedings of SPIE **4467,** 1 (2001).
2. E. Ozbay, "Plasmonics: Merging Photonics and Electronics at Nanoscale Dimensions," Science **311,** 189-193 (2006).
3. D. R. Smith, S. Schultz, P. Markoš, and C. M. Soukoulis, "Determination of effective permittivity and permeability of metamaterials from reflection and transmission coefficients," Physical Review B **65,** 195104 (2002).
4. C. Menzel, C. Rockstuhl, T. Paul, F. Lederer, and T. Pertsch, "Retrieving effective parameters for metamaterials at oblique incidence," Physical Review B **77,** 195328 (2008).
5. R. M. A. Azzam and N. M. Bashara, *Ellipsometry and polarized light* (North-Holland, 1977).
6. D. H. Goldstein and R. A. Chipman, "Error analysis of a Mueller matrix polarimeter," Journal of the Optical Society of America A **7,** 693-700 (1990).
7. M. H. Smith, "Optimization of a dual-rotating-retarder Mueller matrix polarimeter," Appl. Opt. **41,** 2488-2493 (2002).
8. E. Compain, S. Poirier, and B. Drevillon, "General and self-consistent method for the calibration of polarization modulators, polarimeters, and Mueller-matrix ellipsometers," Appl. Opt. **38,** 3490-3502 (1999).
9. D. B. Chenault and R. A. Chipman, "Measurements of linear diattenuation and linear retardance spectra with a rotating sample spectropolarimeter," Appl. Opt. **32,** 3513-3519 (1993).
10. B. T. Draine, "The discrete-dipole approximation and its application to interstellar graphite grains," Astrophys. J. **333,** (1988).
11. B. T. Draine and P. J. Flatau, "Discrete-dipole approximation for scattering calculations," JOURNAL-OPTICAL SOCIETY OF AMERICA A **11,** 1491-1491 (1994).
12. B. T. Draine and P. Flatau, "User Guide for the Discrete Dipole Approximation Code DDSCAT 7.0," eprint arXiv: 0809.0337 (2008).
13. C. Noguez, "Surface plasmons on metal nanoparticles: the influence of shape and physical environment," J.Phys.Chem.C **111,** 3806-3819 (2007).
14. C. Noguez, C. E. Roman-Velazquez, R. Esquivel-Sirvent, and C. Villarreal, "High-multipolar effects on the Casimir force: The non-retarded limit," Europhys. Lett. **67,** 191-197 (2004).
15. C. Noguez, I. O. Sosa, R. G. Barrera, and M. DF, "Light Scattering by Isolated Nanoparticles With Arbitrary Shapes," in *MATERIALS RESEARCH SOCIETY SYMPOSIUM PROCEEDINGS,* Anonymous (Warrendale, Pa.; Materials Research Society; 1999, 2001), pp. 275-280.
16. I. O. Sosa, C. Noguez, and R. G. Barrera, "Optical Properties of Metal Nanoparticles with Arbitrary Shapes," J Phys Chem B **107,** 6269-6275 (2003).
17. D. Cho, F. Wang, X. Zhang, and Y. R. Shen, "Contribution of electric quadrupole resonance in optical metamaterials," in *American Physical Society, 2008 APS March Meeting, March 10-14, 2008, abstract# D35. 012,* Anonymous (, 2008).
18. W. Cai, U. K. Chettiar, A. V. Kildishev, and V. M. Shalaev, "Optical Cloaking with Non-Magnetic Metamaterials," Arxiv preprint physics/0611242 (2006).

19. W. Cai, U. K. Chettiar, A. V. Kildishev, and V. M. Shalaev, "Optical cloaking with metamaterials," Nature Photonics **1,** 224–226 (2007).
20. U. K. Chettiar, A. V. Kildishev, H. K. Yuan, W. Cai, S. Xiao, V. P. Drachev, and V. M. Shalaev, "Dual-Band Negative Index Metamaterial: Double-Negative at 813 nm and Single-Negative at 772 nm," (2008).
21. E. M. Hicks, O. Lyandres, W. P. Hall, S. Zou, M. R. Glucksberg, and R. P. Van Duyne, "Plasmonic Properties of Anchored Nanoparticles Fabricated by Reactive Ion Etching and Nanosphere Lithography," Journal of physical chemistry.C **111,** 4116-4124 (2007).
22. A. Penttilä, E. Zubko, K. Lumme, K. Muinonen, M. A. Yurkin, B. Draine, J. Rahola, A. G. Hoekstra, and Y. Shkuratov, "Comparison between discrete dipole implementations and exact techniques," Journal of Quantitative Spectroscopy and Radiative Transfer **106,** 417-436 (2007).
23. F. S. Diana, A. David, I. Meinel, R. Sharma, C. Weisbuch, S. Nakamura, and P. M. Petroff, "Photonic crystal-assisted light extraction from a colloidal quantum Dot/GaN hybrid structure," Nano Letters **6,** 1116-1120 (2006).
24. L. J. Sherry, R. Jin, C. A. Mirkin, G. C. Schatz, and R. P. Van Duyne, "Localized surface plasmon resonance spectroscopy of single silver triangular nanoprisms," Nano Lett **6,** 2061 (2006).
25. L. J. Sherry, S. H. Chang, G. C. Schatz, R. P. Van Duyne, B. J. Wiley, and Y. Xia, "Localized surface plasmon resonance spectroscopy of single silver nanocubes," Nano Lett **5,** 2034–2038 (2005).
26. K. Byun, S. Kim, and D. Kim, "Design study of highly sensitive nanowire-enhanced surface plasmon resonance biosensors using rigorous coupled wave analysis," Optics Express **13,** 3737-3742 (2005).
27. J. Lu, C. Petre, E. Yablonovitch, and J. Conway, "Numerical optimization of a grating coupler for the efficient excitation of surface plasmons at an Ag-SiO_2 interface," Journal of the Optical Society of America B **24,** 2268-2272 (2007).
28. M. G. Moharam and T. K. Gaylord, *Rigorous Coupled-Wave Analysis of Planar-Grating Diffraction* (OSA, 1980).
29. J. Spiegel, J. de la Torre, M. Darques, L. Piraux, and I. Huynen, "Permittivity Model for Ferromagnetic Nanowired Substrates," IEEE Microwave and Wireless Components Letters **17,** 492 (2007).
30. R. A. Chipman, "Handbook of Optics, vol. II, ch. 22," Optical Society of America, (2000).
31. T. A. Germer and C. C. Asmail, "Goniometric optical scatter instrument for out-of-plane ellipsometry measurements," Rev. Sci. Instrum. **70,** 3688 (1999).
32. M. A. Mahmoud, C. E. Tabor, and M. A. El-Sayed, "Surface-Enhanced Raman Scattering Enhancement by Aggregated Silver Nanocube Monolayers Assembled by the Langmuir-Blodgett Technique at Different Surface Pressures," J. Phys. Chem. C **113,** 5493 (2009).

doi:10.4028/www.scientific.net/AST.75.246

Selected Applications of Transformation Electromagnetics

Ilaria Gallina[1,a], Giuseppe Castaldi[1,b], Vincenzo Galdi[1,c], Andrea Alù[2,d] and Nader Engheta [3,e]

[1]Waves Group, Department of Engineering, University of Sannio, Corso Garibaldi 107, I-82100 Benevento, Italy

[2]Department of Electrical and Computer Engineering, The University of Texas at Austin, 1 University Station C0803, Austin TX 78712, USA

[3] Department of Electrical and Systems Engineering, University of Pennsylvania, 200 South 33rd Street, Room 215, Moore Building, Philadelphia, PA 19104-6314, USA

[a]ilaria.gallina@unisannio.it, [b]castaldi@unisannio.it, [c]vgaldi@unisannio.it, [d]alu@mail.utexas.edu, [e]engheta@ee.upenn.edu

Keywords: Transformation electromagnetics, metamaterials, cloaking, anti-cloaking, tunneling, image displacing, image reconstruction.

Abstract. In this paper, we present a concise summary of selected results from our recent and ongoing studies on transformation electromagnetics. Specifically, we focus on cloak/anti-cloak interactions (with possible application to sensor invisibility), and on some general classes of metamaterial slabs (made of double positive, double negative or single negative media) with interesting image displacing/reconstruction capabilities.

Introduction

During the last few years, "transformation electromagnetics" [1-4] has emerged as one of the most promising approaches to the systematic design of application-oriented metamaterials, with the perspective of offering unprecedented control in the electromagnetic (EM) response of devices and components.

This approach exploits the formal invariance of Maxwell equations with respect to coordinate transformations for the design of the desired response in a fictitious auxiliary space characterized by curved metric and suitable topology, and its subsequent interpretation in a conventional Cartesian space filled up with a suitable *anisotropic* and *inhomogenous* "transformation medium."

As a sparse sample of the available application examples, besides the celebrated invisibility "cloaking" [5], it is worth recalling those pertaining to super/hyper-lensing [6,7], field concentrators [8] and rotators [9], conformal sources [10], retroreflectors [11], EM analogous of relativistic effects [12] and celestial-mechanical phenomena [13,14], as well as the broad framework of "illusion optics" [15].

In this paper, we report an overview of selected results from our ongoing investigations within this subject area, with special emphasis on invisibility cloaking/anti-cloaking effects, as well as image displacing and reconstruction.

Cloak/Anti-Cloak Interactions

In transformation-coordinate-based approaches to invisibility cloaking, the impinging energy is rerouted around the object to conceal, thanks to the refracting properties of a suitable transformation medium which embeds the coordinate-mapping effects of a curved-coordinate space containing a "hole" [5].

It has been shown analytically [16] that, in the limit of an "ideal" cloaking, the field *cannot* generally penetrate from outside to inside, and vice-versa [17]. A notable exception to the above picture, however, was recently pointed out in [18], where it was shown that a suitable transformation medium with *double-negative* (DNG) constitutive parameters may be designed so as to (partially or totally) restore the object visibility when paired to the cloak shell, thereby acting as an "anti-cloak."

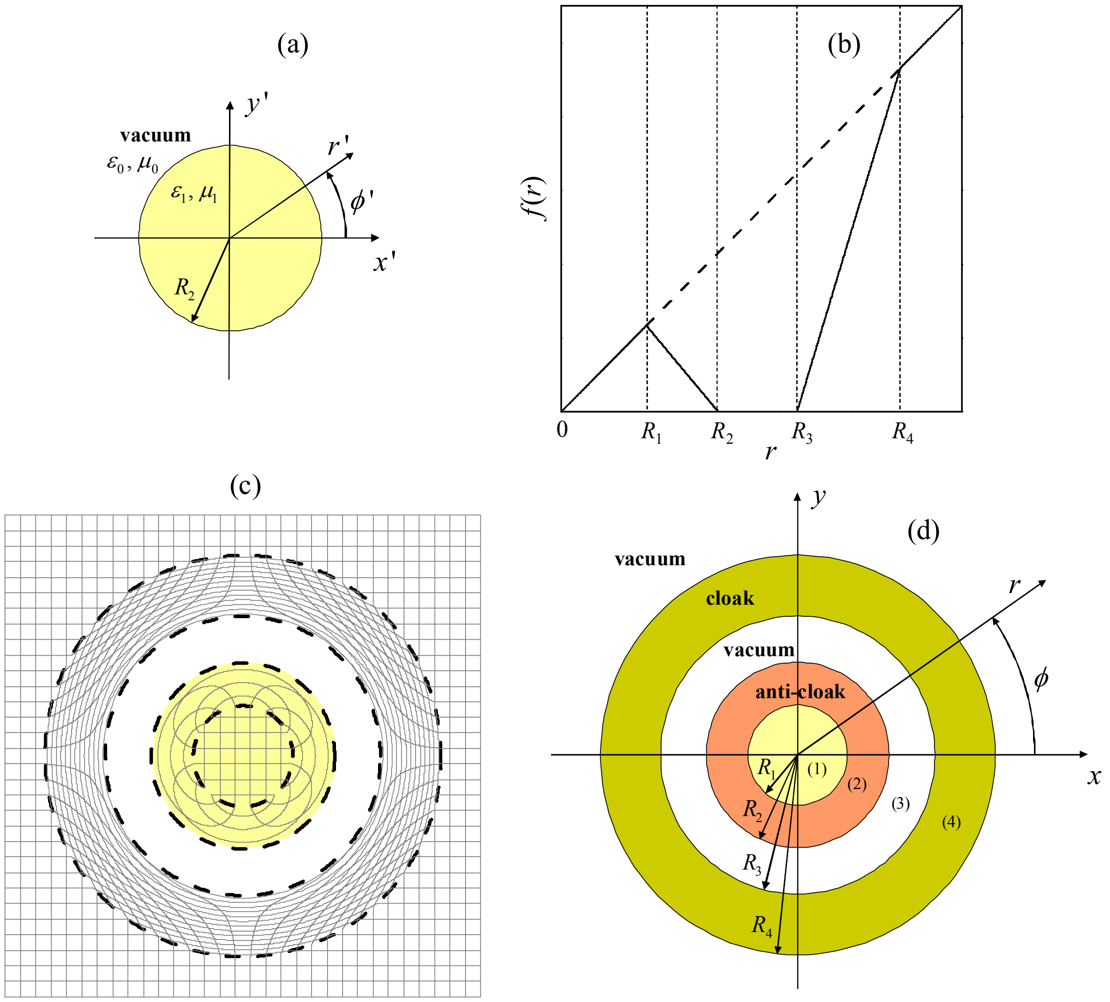

Fig. 1. From [19]. Cloak/anti-cloak scenario (details explained in the text). (a) Homogeneous circular cylinder in the auxiliary space. (b) Radial coordinate transformation in Eq. 1. (c) Topological interpretation of the mapping. (d) Alternative interpretation of the mapping in a globally flat, Cartesian space, with cloak- and anti-cloak-type transformation media.

In [19], we extended these results to a more general scenario, showing that the anti-cloak-type effect may also be achieved with *double-positive* (DPS) or *single-negative* (SNG) transformation media, and even in the presence of a vacuum shell separating the cloak and anti-cloak. Our studies consider a two-dimensional (2-D) formulation, involving an isotropic, homogeneous circular cylinder of radius R_2 with dielectric permittivity ε_1 and magnetic permeability μ_1, immersed in vacuum in the auxiliary space $\left(x', y', z'\right)$ [Fig. 1(a)], which is mapped into the actual physical space $\left(x, y, z\right)$ via the piecewise linear radial coordinate transformation [in the associated $\left(r, \phi, z\right)$ cylindrical reference system, cf. Fig. 1(b)]:

$$r' = f(r) = \begin{cases} r, & r < R_1, \quad r > R_4, \\ R_1 \left(\dfrac{R_2 + \Delta_2 - r}{R_2 + \Delta_2 - R_1} \right), & R_1 < r < R_2, \\ R_4 \left(\dfrac{r - R_3 + \Delta_3}{R_4 - R_3 + \Delta_3} \right), & R_3 < r < R_4. \end{cases} \tag{1}$$

When the (negligibly small) parameters Δ_2 and Δ_3 tend to zero, the outermost layer $R_3 < r < R_4$ corresponds to a standard invisibility cloak [5], whereas the internal layer $R_1 < r < R_2$ corresponds to the anti-cloak in [18]. Their combination yields the four-layer cylindrical configuration of radii $R_\nu, \nu = 1,...,4$ shown in Fig. 1(c), where the transformed regions are characterized by *curved* coordinates, while the separating layer $R_2 < r < R_3$ does not admit any physical image in the auxiliary (x', y', z') space, thereby constituting a "cloaked" region *inaccessible* to the EM fields. Within the framework of transformation EM, the above behavior can be translated in a *globally flat* space by filling up the transformed regions with anisotropic, spatially inhomogeneous transformation media [Fig. 1(d)], whose permittivity and permeability relevant tensor components (assuming transverse-magnetic polarization) may be expressed in cylindrical coordinates as:

$$\varepsilon_r(r) = \frac{\varepsilon'(r')}{\dot{f}(r)} \left(\frac{r'}{r} \right), \quad \varepsilon_\phi(r) = \varepsilon'(r') \left(\frac{r}{r'} \right) \dot{f}(r), \quad \mu_z(r) = \mu'(r') \left(\frac{r'}{r} \right) \dot{f}(r), \tag{2}$$

where the "overdot" denotes differentiation with respect to the argument.

Note that the constitutive parameters of the transformation medium in Eq. 2 are opposite in sign to those of the inner cylinder (ε_1, μ_1), in view of the negative slope of the transformation in the anti-cloak layer $R_1 < r < R_2$. This suggests *four* possible configurations of interest, which involve the possible combinations of DPS and DNG, or alternatively epsilon-negative (ENG) and mu-negative (MNG), media.

By extending the Fourier-Bessel-based analytical approach in [16], we have studied the time-harmonic $[\exp(-i\omega t)]$ plane-wave scattering from the four-layer configuration depicted in Fig. 1(d). Results from this study (see [19] for details) indicate that letting $\Delta_2, \Delta_3 \to 0$, while keeping their ratio *finite*, would tailor the two competing cloak/anti-cloak effects so as to create an *effectively cloaked* region in the vacuum gap, while still being able to restore a non-negligible field in the (lossless) inner cylinder.

Figure 2 shows a representative field map pertaining to a configuration with a DNG inner cylinder $(\varepsilon_1 = -\varepsilon_0, \mu_1 = -\mu_0)$ and a DPS anti-cloak, with $R_1 = 0.4\lambda_0$, $R_2 = 0.75\lambda_0$, $R_3 = 1.7\lambda_0$, $R_4 = 2.5\lambda_0$, slight losses ($\tan\delta = 10^{-4}$), and $\Delta_2/R_2 = \Delta_3/R_3 = 5 \cdot 10^{-3}$. Outside the cloak, the picture resembles that of the standard cloak. Inside the cloak, the anti-cloak and the inner cylinder form a "resonating cavity" which, via the vanishingly small coupling through the cloaked layer, is able to restore a modal field. Similar results may be observed for the other three possible combinations (DPS-DNG, ENG-MNG, MNG-ENG) of cloak and anti-cloak parameters (see [19] for details).

The above results indicate possible application scenarios for which a region of space may be cloaked, while maintaining the capability of somehow "sensing" the outside field from the inside.

A similar idea was recently explored in [20-22] within the suggestive framework of "sensor invisibility." In order to explore to what extent such effects may be used for sensing purposes, we studied the power absorption vs. scattering tradeoff of the above configuration in the presence of a *slightly lossy* object inside the inner region ($r < R_1$).

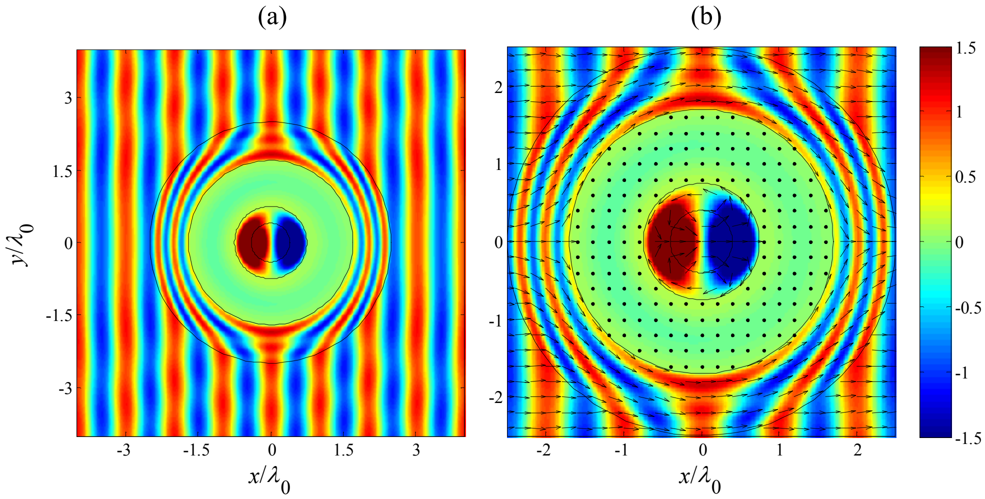

Fig. 2. From [19]. (a) Magnetic field (real part) map for a configuration featuring a DNG $(\varepsilon_1 = -\varepsilon_0, \mu_1 = -\mu_0)$ inner cylinder and a DPS anti-cloak, with $R_1 = 0.4\lambda_0$, $R_2 = 0.75\lambda_0, R_3 = 1.7\lambda_0$, $R_4 = 2.5\lambda_0, \Delta_2/R_2 = \Delta_3/R_3 = 5\cdot 10^{-3}$, and tanδ=$10^{-4}$. (b) Magnified view with a superimposed map of the real part of the Poynting vector (normalized in the uncloaked regions).

First, starting from the original cloak/anti-cloak configuration in Eqs. 1 and 2 (with *real-valued* ε_1 and μ_1), we studied *perturbatively* the effects of a slightly mismatched electrical permittivity,

$$\bar{\varepsilon}_1 = \left(1+\Delta_\varepsilon\right)^2 \varepsilon_1, \tag{3}$$

of the target, with the vanishingly small term Δ_ε parameterizing this mismatch. Referring to [23] for more details, we found that the presence of a slightly mismatched target does not affect the cloaking function, but it does affect the anti-cloaking capability of restoring a field in the target region. In a sensor-cloaking perspective, the vacuum gap $R_2 < r < R_3$ is no longer functional to creating a cloaked region, but it constitutes an additional degree of freedom to tailor the cloak/anti-cloak interactions. In this framework, we studied the limiting case,

$$R_3 = \left(1+\Delta_G\right) R_2, \tag{4}$$

with the vanishingly small term Δ_G parameterizing the gap. Proceeding as in [19], we found that, in the sensor-cloaking scenario of interest, the vanishing-gap configuration is particularly well suited, since it allows the recovery of the (otherwise logarithmically vanishing) zeroth-order terms in the Fourier-Bessel expansion of the transmitted field (and thus, in principle, a more effective power absorption), while keeping the scattered field vanishingly small. Moreover, as in the original scenario presented in [18], we found that, for the (trivial) case of a vacuum target ($\varepsilon_1 = \varepsilon_0$, $\mu_1 = \mu_0$), the anti-cloak *perfectly compensates* the cloak, restoring the impinging plane-wave. However, for materials other than vacuum, the field transmitted in the target is a distorted version of the incident one.

We also carried out a comprehensive parametric study (within and beyond the asymptotic limits $\Delta_{2,3,G,\varepsilon} \to 0$) in order to identify the "optimal" parameter configurations and possible tradeoffs, also in the more realistic case of slightly lossy cloak and anti-cloak. As a compact parameterization of the overall scattering and absorption responses of a given configuration, we considered the total scattering and absorption cross-sectional width per unit length [21] ($\overline{Q}_s$ and $\overline{Q}_a$, respectively) normalized to their reference values pertaining to the target alone (free standing in vacuum). For the more realistic case of slightly lossy cloak and anti-cloak, instead of the absorption cross-section (no longer representative of the target/sensor only), we considered the time-averaged power $\overline{P}_a$ (per unit length along the *z*-axis) in the target region, normalized to its vacuum reference value.

Results are compactly summarized via the tradeoff curves in Fig. 3, which, for a given value of the (normalized) scattering response yield the largest (normalized) absorption response attainable. In particular, they illustrate how, in the absence of the gap and varying Δ_2 and Δ_3, it is possible to span the entire range of cloak/anti-cloak interactions, going from a regime featuring weak scattering and weak absorption (i.e., cloak-prevailing) to one featuring scattering and absorption levels comparable with those in vacuum (i.e., anti-cloak compensating the cloak). In between, there is a regime where one can attain weak (though not weakest) scattering accompanied by sensible (though weaker than in vacuum) absorption. Thus, for instance, considering the lossless cloak/anti-cloak case, and accepting a scattering reduction of about 20 dB, one may achieve an absorption response nearly 7 dB below the reference case in vacuum. Qualitatively similar results are observed for the case of slightly lossy (loss-tangent=10^{-3}) cloak and anti-cloak shells with an expectable loss-induced moderate deterioration in the performance (nearly 10 dB increase in the minimum scattering response).

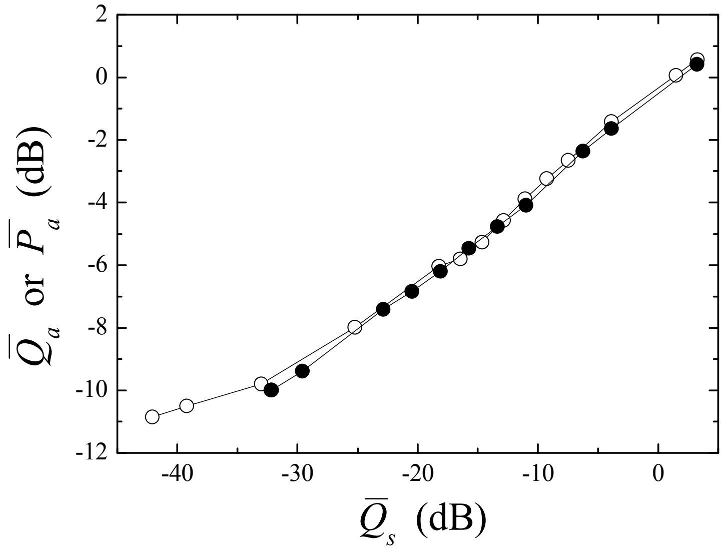

Fig. 3. From [23]. Tradeoff curves for the lossless (white markers) and slightly lossy (loss-tangent=10^{-3}, black markers) cloak/anti-cloak configurations, yielding, for a given normalized scattering cross-sectional width response, the largest normalized absorption (cross-sectional width or power, for the lossless and lossy case, respectively) attainable.

Transformation Slabs

In an ongoing series of investigations [24,25], we have been studying some general classes of transformation-EM-inspired metamaterial slabs, involving DPS, DNG or SNG transformation media, which exhibit interesting image displacing/reconstruction properties. In what follows, we provide a concise summary of the salient results from these studies.

Starting from the DPS/DNG case, the transformation slab of interest occupies the region $|x|<d$ in a physical space (x,y,z), and is characterized by the relative permittivity and permeability tensors

$$\underline{\underline{\varepsilon}}_r(x,y)=\underline{\underline{\mu}}_r(x,y)=\det\left[\underline{\underline{J}}(x,y)\right]\underline{\underline{J}}^{-1}(x,y)\cdot\left[\underline{\underline{J}}^{-1}(x,y)\right]^T, \tag{5}$$

where the superscript ^{T} denotes matrix transposition, and $\underline{\underline{J}}(x,y)=\partial(x',y',z')/\partial(x,y,z)$ is the Jacobian matrix of the 2-D coordinate transformation

$$\begin{cases} x'=au(x), \\ y'=\dfrac{y}{\dot{u}(x)}+v(x), \\ z'=z, \end{cases} \tag{6}$$

from a fictitious (vacuum) space (x',y',z'). In Eq. 6, a is a real scaling parameter, and $u(x)$ and $v(x)$ are arbitrary continuous real functions, with the derivative $\dot{u}(x)$ assumed to be continuous and nonvanishing within the slab region, so as to ensure the continuity of the coordinate transformation.

It can be shown (see [24] for details) that the transformation medium in Eq. 5 is DPS for $a>0$, and DNG for $a<0$. Moreover, for $a=1$, the medium is effectively *non-magnetic* $(\mu_{rz}=1)$ for transverse-magnetic (TM) polarization (*z*-directed magnetic field), and non-electric $(\varepsilon_{rz}=1)$ for transverse-electric (TE) polarization (*z*-directed electric field).

In [24], we showed that by enforcing $\dot{u}(\pm d)=1$, it is possible to obtain *total-transmission* for a plane wave impinging from *any* direction. Under such condition, for an observer located beyond the slab $(x>d)$, an arbitrary field distribution at a source plane $x=x_s$ would be ideally imaged at the plane $x=x_i\equiv x_s+2d-a\left[u(d)-u(-d)\right]$, with a possible rigid translation of $y_0=v(-d)-v(d)$ along the y-axis.

Moreover, we envisaged and explored a variety of interesting applications of such anisotropic and inhomogeneous slabs, including radomes, anti-cloaking, and lensing/focusing effects (see [24] for details). In particular, we showed how certain effects could be attained by using only DPS (possibly non-magnetic) transformation media [24], so as to mitigate the technological challenges involved in their fabrication. For instance, the general class of transparent slabs characterized by

$$a=1, \quad u(x)=x, \quad v(d)=v(-d), \tag{7}$$

for which the image displacement is zero $(x_i=x_s,\, y_0=0)$, exhibits the same EM response of a slab of vacuum of same thickness, and can therefore be viewed as DPS *nonmagnetic* "perfect radomes." The possibly simplest conceivable realization can be obtained by choosing

$$v(x)=\alpha|x|, \tag{8}$$

which is readily recognized to involve a "twin-crystal" configuration, similar to that (involving halfspaces instead of slabs) studied in [26] in connection with total *amphoteric* refraction. Figure 4 clearly illustrates its EM response (computed via a finite-element commercial software package [27]), which is identical to that of a vacuum slab of same size, and is attributable to two compensating beam-shift effects. Note that the constitutive properties of this configuration are particularly simple, involving only piecewise anisotropic, homogeneous media, with everywhere finite parameters.

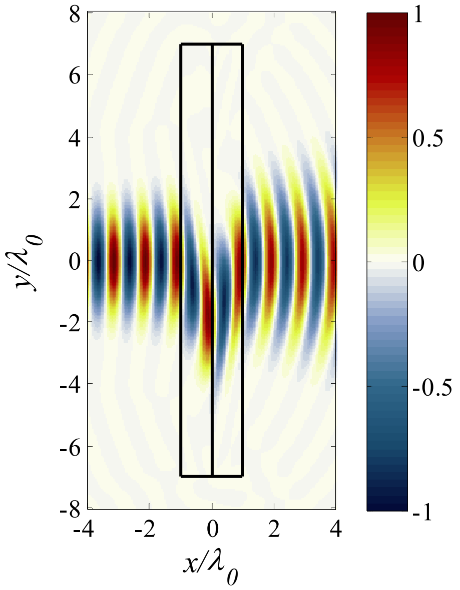

Fig. 4. From [24]. Magnetic field (real-part) map pertaining to a transformation slab with $d=\lambda_0$ (but truncated along the y-axis to an aperture of $14\lambda_0$), for the perfect-radome (twin-crystal) configuration in Eq. 8, with $\alpha=2$, assuming a loss-tangent of 10^{-3}, and a normally-incident collimated Gaussian beam (with waist of size $\sqrt{2}\lambda_0$, located at $x_s=-4\lambda_0$, i.e., $3\lambda_0$ away from the slab interface).

Another interesting class is obtained by choosing $a=1$, $v(x)=0$, and

$$u(x)=\pm\left(\frac{1}{d+D}\right)\sqrt{\left[(\pm x+D)^2-D^2+\Delta^2\right]\left[(d+D)^2-D^2+\Delta^2\right]},\quad x\gtrless 0, \tag{9}$$

where $D\geq 0$ is an offset parameter, while Δ is a small parameter that is eventually let tend to zero. Note that for $D=0$ (and $\Delta\to 0$) the transformation trivially reduces to the identity, while for $D>0$ (and $\Delta\to 0$) it vanishes at the $x=0$ plane, and the constitutive parameters tend to exhibit extreme values at the $x=0$ plane as well as for $|y|\to\infty$. Unlike the previous example, the above configuration, while still being ideally totally-transmitting, induces a nonzero image displacement along the x-axis,

$$x_i-x_s=2d-\left(\frac{2}{d+D}\right)\left[(d+D)^2-D^2\right]. \tag{10}$$

The last example is particularly interesting because the underlying transformations in Eq. 9 (intended for each of the half slabs) are directly related to that used in [8] for designing an invisibility cloak with *square* shape. The above results therefore seem to provide the building block for an “anti-cloaking” device based *only* on DPS media, thereby removing the most significant technological limitations that prevent their practical realization and that would cause significant bandwidth restrictions and loss mechanism.

As an illustrative example, the configuration in Fig. 5(a) features four modified (trapezoidal-shaped, translated and possibly rotated) versions of the transformation slab in Eq. 9, juxtaposed so as to form a square shell. The EM response for oblique plane-wave incidence in the presence of the outer (cloak) shell only is shown in Fig. 5(b). As shown in Fig. 5(c), the addition of the inner (anti-cloak) shell renders field penetration possible, with the restoration of a modal field inside the inner square region, in a fashion that closely resembles the previously described interactions involving a SNG or DNG anti-cloak.

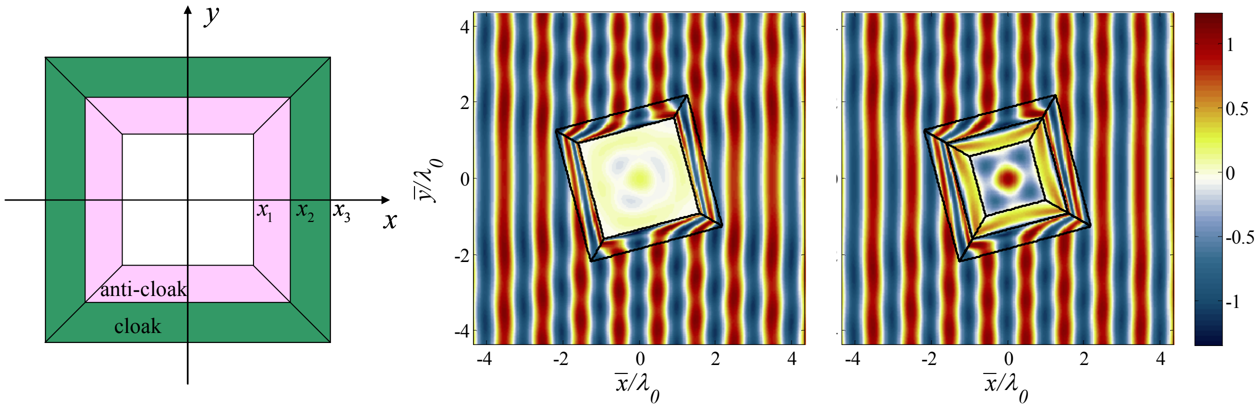

(a) (b) (c)

Fig. 5. From [24]. Square cloak/anti-cloak geometry. (b), (c) Magnetic field maps pertaining to oblique (15°) plane-wave excitation in the presence and absence, respectively, of the anti-cloak shell. Note that, for computational convenience, the oblique incidence is simulated using a 15°-rotated ($\bar{x}, \bar{y}$) coordinate system, where the illuminating wave impinges along the $\bar{x}$-axis (see [24] for more detail on the parameters).

We point out that the transformation media generated by the *real-valued* coordinate mapping in Eq. 6 are either DPS or DNG. Nevertheless, we showed in [24] that SNG transformation media could be obtained via suitable analytic continuation of the coordinate transformation in the complex plane. From a physical viewpoint, in order to map a propagating field solution in the (vacuum) fictitious space into an evanescent one in the transformed (SNG) domain, one intuitively expects the coordinate transformation parameters to exhibit a *purely imaginary* in-plane character. In this framework, it is particularly insightful to study *paired* configurations, characterized by the coordinate transformation

$$\begin{cases} x' = i a_\alpha u_\alpha(x), \\ y' = i\dfrac{y}{\dot{u}_\alpha(x)} + i v_\alpha(x), \\ z' = z, \end{cases} \tag{11}$$

where a_α are real scaling parameters, $u_\alpha(x) > 0$ and $v_\alpha(x)$ are arbitrary continuous real functions (with $\alpha = 1$ for $-d < x < 0$, $\alpha = 2$ for $0 < x < d$). Note that, unlike its counterpart in Eq. 6, the transformation in Eq. 11 is generally *discontinuous* at the interfaces $x=0, x=\pm d$, and thus special care is needed when mapping the field solutions from the fictitious space into the physical one. Depending on the sign of the parameters $a_{1,2}$ and on the field polarization, the resulting transformation media (cf. Eq. 5) are either ENG or MNG. Also in this case, some general total-transmission conditions can be derived analytically (as detailed in a forthcoming paper [25]), yielding:

$$\begin{cases} \dot{u}_2(0)\dot{u}_1(-d)=\dot{u}_2(d)\dot{u}_1(0), \\ a_2\left[u_2(d)-u_2(0)\right]=-a_1\left[u_1(0)-u_1(-d)\right], \\ \dot{u}_2(0)=\dot{u}_1(0). \end{cases} \tag{12}$$

In this case, a field distribution at a source plane $x=x_s$ would form a *virtual* image at the plane $x=x_i\equiv x_s+2d,$ with a possible rigid translation of $y_0=\dot{u}_1(-d)\left[-v_1(0)+v_1(-d)-v_2(0)+v_2(d)\right]$ along the y-axis. Note that the conditions in Eq. 12 imply that $\operatorname{sgn}(a_1)=-\operatorname{sgn}(a_2)$, and thus the two possible solutions correspond to the ENG-MNG and MNG-ENG pairings.

The class of transparent SNG transformation-media bi-layers identified by the above conditions is rather general, and includes the homogeneous, isotropic ENG-MNG bi-layers investigated in [28], and their further (inhomogeneous, anisotropic) generalizations within the framework on complementary media [29]. In particular, the complementary-media case in [29] corresponds to

$$\begin{cases} a_2=-a_1, \\ u_2(x)=-u_1(-x), \\ v_2(x)=v_1(-x), \end{cases} \tag{13}$$

which, in turn, yields the homogeneous, isotropic case in [28] for $u_2(x)=x$ and $v_2(x)=0$.

Conclusions

In this paper, we have summarized and briefly reviewed selected results from our recent and ongoing studies on transformation EM, with special emphasis on cloak/anti-cloak interactions and sensor invisibility, as well as on some general classes of (DPS, DNG and SNG) metamaterial slabs.

Current and future investigations are aimed at the exploration of different geometries (e.g., spherical cloak/anti-cloak) and configuration scenarios (e.g., SNG-DPS pairs).

References

[1] U. Leonhardt: Science Vol. 312 (2006), p. 1777.

[2] J. B. Pendry, D. Schurig, and D.R. Smith: Science Vol. 312 (2006), p. 1780.

[3] U. Leonhardt and T.G. Philbin: New J. Phys. Vol. 8 (2006), paper 247.

[4] V.M. Shalaev: Science Vol. 322 (2008), p. 384.

[5] D. Schurig, J.J. Mock, B.J. Justice, S.A. Cummer, J.B. Pendry, A.F. Starr, and D.R. Smith: Science Vol. 314 (2006), p. 977.

[6] M. Tsang and D. Psaltis: Phys. Rev. B Vol. 77 (2008), paper 035122.

[7] A. V. Kildishev and E.E. Narimanov: Opt. Lett. Vol. 32 (2007), p. 3432.

[8] M. Rahm, D. Schurig, D.A. Roberts, S.A. Cummer, D.R. Smith, and J.B. Pendry: Photonics and Nanostructures - Fundamentals and Applications Vol. 6 (2008), p. 87.

[9] H. Chen, B. Hou, S. Chen, X. Ao, W. Wen, and C.T. Chan: Phys. Rev. Lett. Vol. 102 (2009), paper 183903.

[10] N. Kundtz, D. A. Roberts, J. Allen, S. Cummer, and D.R. Smith: Opt. Express Vol. 16 (2008), p. 21215.

[11] I. Gallina, G. Castaldi, and V. Galdi: IEEE Antennas Wireless Propagat. Lett. Vol. 7 (2008), p. 603.

[12] A. Greenleaf, Y. Kurylev, M. Lassas, and U. Uhlmann: Phys. Rev. Lett. Vol. 99 (2007), paper 183901.

[13] D.A. Genov, S. Zhang, and X. Zhang: Nature Physics Vol. 5 (2009), p. 687.

[14] E.E. Narimanov and A.V. Kildishev: Appl. Phys. Lett. Vol. 95 (2009), paper 041106.

[15] Y. Lai, J. Ng, H.-Y. Chen, D. Han, J. Xiao, Z.-Q. Zhang, and C.T. Chan: Phys. Rev. Lett. Vol. 102 (2009), p. 253902.

[16] B. Zhang, H. S. Chen, B.I. Wu, Y. Luo, L.X. Ran, and J.A. Kong: Phys. Rev. B Vol. 76 (2007), paper 121101.

[17] B. Zhang, H. Chen, B.I. Wu, and J.A. Kong: Phys. Rev. Lett. Vol. 100 (2008), paper 063904.

[18] H. Chen, X. Luo, H. Ma, and C.T. Chan: Opt. Express Vol. 16 (2008), p. 14603.

[19] G. Castaldi, I. Gallina, V. Galdi, A. Alù, and N. Engheta: Opt. Express Vol. 17 (2009), p. 3101.

[20] A. Alù and N. Engheta: Phys. Rev. Lett. Vol. 102 (2009), paper 233901.

[21] Z. Ruan and S. Fan: preprint arXiv:0909.3323v1 [physics.optics] (2009).

[22] A. Greenleaf, Y. Kurylev, M. Lassas, and G. Uhlmann: preprint arXiv:0912.1872v1 [physics.optics] (2009).

[23] G. Castaldi, I. Gallina, V. Galdi, A. Alù, and N. Engheta: preprint arXiv:1001.3000v1 [physics.optics] (2010).

[24] I. Gallina, G. Castaldi, V. Galdi, A. Alù, and N. Engheta: Phys. Rev. B Vol. 81 (2010), paper 125124.

[25] G. Castaldi, I. Gallina, V. Galdi, A. Alù, and N. Engheta: under review (2010).

[26] Y. Zhang, B. Fluegel, and A. Mascarenhas: Phys. Rev. Lett. Vol. 91 (2003), paper 157404.

[27] *COMSOL MULTIPHYSICS – User's Guide* (COMSOL AB, Stockholm, 2007).

[28] A. Alù and N. Engheta: IEEE Trans. Antennas Propagat. Vol. 51 (2003), p. 2558.

[29] J. B. Pendry and S.A. Ramakrishna: J. Physics: Cond. Matter Vol. 15 (2003), p. 6345.

doi:10.4028/www.scientific.net/AST.75.256

Trapped Rainbow Storage of Light in Metamaterials

Ortwin Hess[1,a] and Kosmas L. Tsakmakidis[1,b]

[1]Advanced Technology Institute and Department of Physics, Faculty of Engineering and Physical Sciences, University of Surrey, Guildford, GU2 7XH, United Kingdom

[a]o.hess@surrey.ac.uk, [b]K.Tsakmakidis@surrey.ac.uk

Keywords: Slow light, metamaterials, negative refractive index, plasmonics, waveguides, adiabatic variation.

Abstract. We review recent theoretical and experimental breakthroughs in the realm of slow and stopped light in structured photonic media featuring negative electromagnetic parameters (permittivity/permeability and/or refractive index). We explain how and why these structures can enable complete stopping of light even in the presence of disorder *and*, simultaneously, dissipative losses. Using full-wave numerical simulations we show that the incorporation of thin layers made of an active medium adjacently to the core layer of a negative-refractive-index waveguide can completely remove dissipative losses – in a slow-light regime where the effective index of the guided wave is negative.

Introduction

Metamaterials (MMs) [1-3] and 'slow light' (SL) [4,5] have, in the last decade, evolved to two of the largest and most exciting realms of contemporary science, enabling a wealth of useful applications, such as *sub*-diffraction-limited lenses, ultra-compact photonic devices and, even, invisibility cloaks.

Recently it has been theoretically demonstrated [6] that these two highly technologically important areas of research, which were until now following separate/parallel tracks, could in fact be combined, with the potential of leading to novel metamaterial-enabled slow-light structures that can improve on existing slow-light designs and structures (in terms of the degree to which light can be decelerated, as well as of performance, functionality and efficiency); see Fig. 1.

Indeed, some of the most successful slow-light designs at present, based on photonic-crystals (PhCs) [7] or coupled-resonator optical waveguides (CROWs) [8], can so far efficiently slow down light by a factor of only 40 – otherwise, large group-velocity-dispersion *and* attenuation-dispersion occur, i.e. the guided light pulses broaden and the attainable bandwidth is severely restricted. Unfortunately, this limitation directly imposes an *upper limit* on the degree to which one can shrink the area of the corresponding slow-light devices (compactness), as well as reduce the driving electrical power. This is simply because the less a guided slow-light pulse is decelerated inside a waveguide, the less it is spatially compressed; thereby, the less is the reduction that can be achieved to the length (or area) occupied by the slow-light device. In addition to the aforementioned issues, it has by now also been realised that such positive-index slow-light structures are, unfortunately, *extremely* sensitive to the presence of (even *weak*) fabrication disorder [9] – to the point that a disorder of only 5-10 nm (at a wavelength of 1550 nm) leads to group velocities that can never, *even in the presence of dispersion*, be smaller than approximately $c/300$ [4,10].

By contrast, it has been theoretically and experimentally established that metamaterials are almost completely insensitive to the presence of *even a high degree* of fabrication disorder [11,12], since their properties arise from an averaged/effective response of their constituent 'meta-molecules', without necessarily requiring a 'perfect' lattice crystal – a situation which is similar to, e.g., crystalline or amorphous silicon, where the presence or not of a periodic atomic lattice does not, of course, preclude the attainment of an effective refractive index. This ability of metamaterial-based heterostructures to dramatically decelerated or even *completely* stop [6] light under realistic experimental conditions, has recently led to a series of experimental works [13,14] that have provided spectroscopic evidence (but not yet an unambiguous proof) for the observation of 'trapped rainbow' light-stopping in metamaterial waveguides – to our knowledge, the first experimental works to provide a telltale spectroscopic fingerprint of 'true' light-stopping in solid-state structures.

Moreover, as will be explained in the following, it can be shown (based on analytic theory and computational simulations) that negative-refraction (or negative-refractive-index) metamaterial-enabled slow-light structures enable efficient deceleration of light by factors of, *at least*, *tens of thousands without* suffering from the aforementioned group-velocity- and attenuation-dispersion limitations.

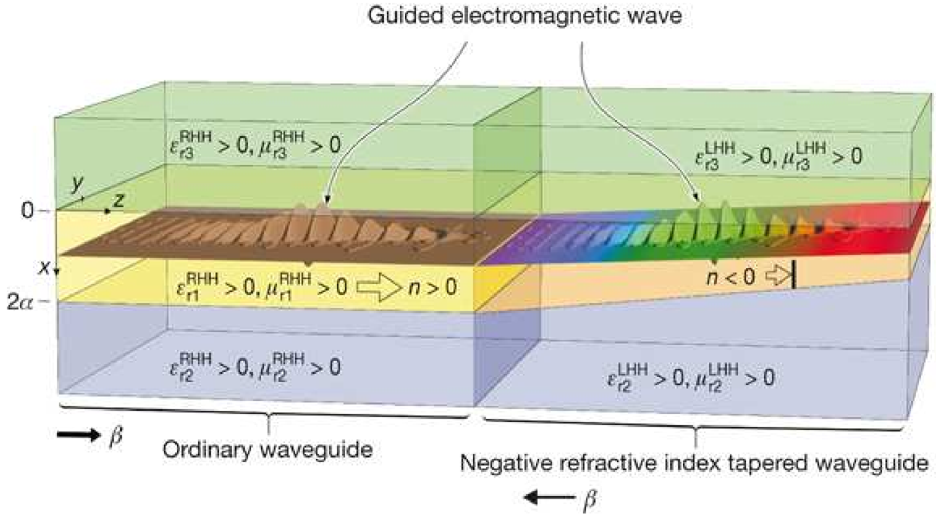

Fig. 1. The 'trapped rainbow' principle [source: K.L. Tsakmakidis, A.D. Boardman and O. Hess: "'Trapped rainbow' storage of light in metamaterials," Nature Vol. 450 (2007), p. 397]. Owing to negative Goos-Haenchen shifts, light is slowed and eventually stopped/stored in an adiabatically tapered negative-refractive-index waveguide – with each frequency 'stopping' at a different point in space.

Thus, these structures are, upon judicious construction and optimization, expected to lead to reductions in the size of and power consumption in photonic devices and systems that are considerably greater compared to what can be achieved with other technologies (based on, e.g., PhCs and/or CROWs). For instance, recent theoretical studies and computational simulations (see also below) suggest that *dispersionless* slow group velocities of light pulses in multilayer negative-refraction MM waveguides can dramatically increase the induced phase shifts in Mach-Zehnder modulators, to the point of reducing the length of the modulator's arms from a typical (present) value of a few mm down to only a few tens of microns (see, also, e.g.: Ref. [15]) – a result far better than what has been achieved with the best present, e.g., PhC based designs. Similarly promising results can also be achieved for a number of other photonic components, such as switches, buffers, filters, dispersion compensators, and so forth.

By deploying suitably designed *all-semiconductor based* [16,17] (i.e., not metallic) metamaterial waveguides that include active/gain layers, we can engineer practical slow-light structures wherein the optical (dissipative) losses of the guided slow-light pulses are reduced by orders of magnitude – or completely eliminated – compared to their metallic counterparts; a further key requirement for any useful slow-light structure. Moreover, in such structures light can be in-/out-coupled much more efficiently compared to, e.g., their PhC counterparts [6], and can be *completely* stopped even when large material losses are present. For these reasons, 'slow-light' designs based on metamaterials may conceivably lead to novel and practical designs for ultra-compact and ultralow-power photonic components, devices and systems.

In what follows, we begin by concisely reviewing the basic premises of (dispersionless) slow/stopped light in negative-constitutive-parameters metamaterial and plasmonic waveguides. We proceed by studying the waveguide dispersion equations in the presence of disorder and/or dissipative losses, and show that the zero-group- and zero-energy-velocity points are preserved; hence, a guided light pulse can still be dramatically decelerated and stopped inside these lossy structures. Next, we show how the incorporation of thin layers made of an active/gain medium placed adjacently to the core of a negative-index metamaterial waveguide can lead to a complete elimination of the dissipative losses experienced by a guided, slow-light pulse.

Main features of 'trapped rainbow' light-stopping in metamaterial and plasmonic waveguides

As was mentioned above, while recent scientific breakthroughs within the optical engineering community have proved that it is indeed possible to dramatically decelerate or 'store' light by resorting to a variety of physical effects [electromagnetically induced transparency (EIT), coherent population oscillations (CPO), stimulated Brillouin scattering (SBS), photonic crystals (PhCs) and surface plasmon polaritons (SPPs) in metallodielectric waveguides (MDWs)], such approaches nonetheless normally bear inherent weaknesses that may hinder their practical applications. For instance, so far EIT uses ultracold or hot gases and not solid-state materials, CPO and SBS are very narrowband (typically, several kHz or MHz) owing to the narrow transparency window of the former and the narrow Brillouin gain bandwidth of the latter, SPPs in MDWs are very sensitive to small variations of the media interfaces and are relatively difficult to excite, while PhCs are prone to tiny fabrication imperfections (nm-scale disorder) [18,19] that can considerably modify (shift) the photonic bandgaps. Furthermore, approaches based on PhCs or CROWs can efficiently slow down light typically by a factor of around 40 – otherwise, large group-velocity-dispersion *and* attenuation-dispersion occur [7,8]. For these reasons, so far it has only been possible to obtain stored (i.e., not – strictly speaking – stopped) light, wherein slowed-down photons were converted to (stored in the form of) metastable atomic or acoustic states (coherences) and subsequently revived/released by the action (turning 'on') of a coupling field. An unambiguous experimental demonstration of 'true' stopping of light, involving the attainment of a divergence in the group index of a light pulse (with its photons continuously preserving their identity, i.e. without being converted to a polariton) has, so far, remained elusive.

In an effort to overcome the above intrinsic limitations of positive-index slow-light schemes, a fundamentally new approach has been recently proposed [6,20,21]. This method relies on the use of negative-refractive-index, NRI, (or negative-refraction) waveguides, wherein the power-flow direction inside the NRI regions is opposite to the one in the positive-index regions, resulting in a pronounced deceleration of the guided electromagnetic energy (see Fig. 2). The scheme uses efficiently excitable waveguide oscillatory modes and is remarkably simple, since the slowing of the guided modes is performed *solely* by adiabatic decrease of the core thickness. The scheme is, also, resilient to fabrication disorder/imperfections because it does not rely on the use of stringent conditions (such as a 'perfect' photonic-crystal lattice or attainment of ultralow temperatures, etc) for decelerating and stopping light, but rather on the deployment of *negative* bulk/effective electromagnetic parameters (such as, e.g., negative refractive index or, simply, negative permittivity) that can readily be realised by even *amorphous* and *highly disordered* metamaterials [11,12]. Furthermore, these metamaterial heterostructures can be designed in such a way that they exhibit *zero* group-velocity-dispersion *and* attenuation-dispersion, even in the 'stopped-light' regime [22] (see also Fig. 3). In doing so, we are able to allow for extremely large bandwidths over

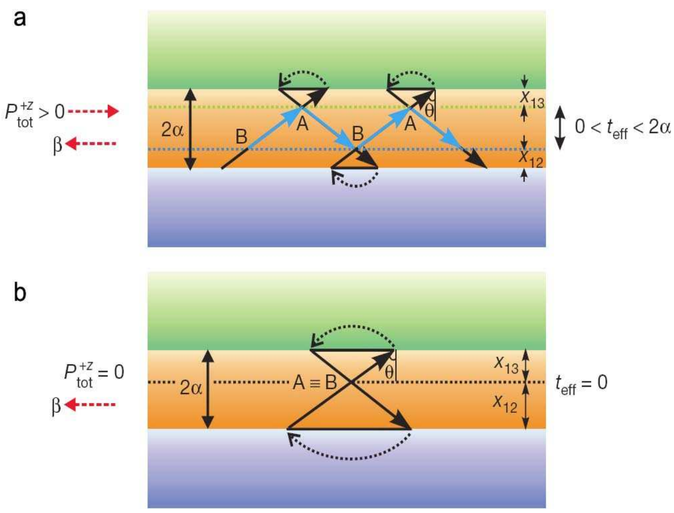

Fig. 2. Slow and stopped light in negative-refractive-index hetero- structures. (a) Slow zigzag ray propagation along a NRI hetero- structure**.** (b) Here, the ray returns exactly to its original point; the ray, thus, becomes permanently trapped (zero group velocity, $v_g = 0$) and an 'optical clepsydra' is formed.

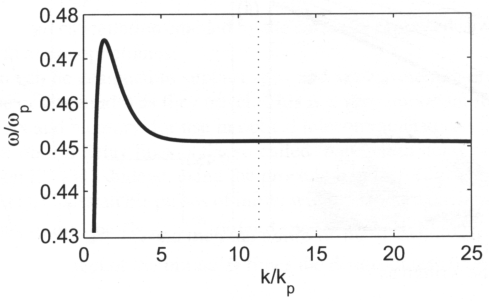

Fig. 3. An example of a dispersion diagram in a suitably designed multilayer metamaterial heterostructure in which, both, zero group velocity and *zero group-velocity dispersion* are simultaneously achieved. Note how from the negative-refraction region ($d\omega/dk < 0$) one enters the region (highlighted by the dotted line) where the group velocity *and* the group-velocity dispersion become simultaneously zero. [source: A. Karalis, *et al.*: "Tailoring and cancelling dispersion of slow or stopped and subwavelength surface-plasmonodielectric-polaritonic light," Proc. SPIE Vol. 7226 (2009), p. 72260I].

which the slowing [23] or stopping [22] of the incoming optical signals can be achieved, as well as for ultrashort device lengths. This approach also has the important advantage that it can facilitate very efficient butt-coupling, directly to a slow mode alone because: i) It supports *single-mode* operation in the slow-light regime [21]; ii) The characteristic impedance of the NRI waveguide can be appropriately adjusted by varying the core thickness [6]; and iii) The spatial distribution of the slow mode closely matches that of a single-mode dielectric waveguide [6]. These conclusions have been drawn following *exact* manipulations of Maxwell's equations, without invoking paraxial, heuristic or other approximations.

It is interesting to point out that, in addition to metallic (metallodielectric) metamaterial or plasmonic slow-light structures, we can also deploy *all-semiconductor* based, negative-refraction, heterostructures to realise 'trapped rainbow' slowing or stopping of light. Such semiconductor-heterostructure designs have recently been experimentally shown [16,17] to enable negative refraction at infrared wavelengths (8.4 µm to 13.3 µm), and (upon heavy doping) they can indeed be extended to the telecommunication – or even the ultraviolet [24] – regime. Owing to their negative-refraction property, these structures can facilitate slow-light propagation, and would be particularly well-suited for the compensation of optical losses by means of active semiconductor cladding layers, as well as for a variety of slow-light devices, such as, e.g., (ultra-compact) modulators [15].

Light stopping in the presence of metamaterial losses and fabrication disorder

An important consideration in assessing the potential of metamaterial heterostructures for ‘stopping’ light pulses ($\upsilon_g = 0$) is the degree to which such a feat can be achieved in the presence of realistic (residual) losses and/or fabrication disorder. Already our theoretical studies [6,21,25] have shown (see also Figs. 1 and 2 above) that very large light-decelerations can be achieved in metamaterial waveguides – even when dissipative (Ohmic) losses are present [26]. More recently, we have ascertained [27] that complete ‘stopping’ of light inside negative-index metamaterial waveguides is, also, possible when dissipative losses remain in the structure. This realisation stems from the fact that light *pulses* (i.e. not sinusoidal, single-frequency waves) are, in the presence of losses, characterised by a *complex frequency* and a *real* wavenumber [26] (see also Fig. 6 below) – in contrast to sinusoidal waves, which are characterised by a *complex* frequency when dissipative losses remain in the structure. This feature becomes even more prominent in the stopped-light regime, where (owing to the fact that light does *not* propagate any more) a consideration of *spatial* losses (*complex* wavenumber) lacks any appreciable physical meaning [22,28], and one should instead consider *temporal* losses (complex *frequency*).

Our analytic studies reveal that a zero group velocity ($\mathrm{Re}\{\mathrm{d}\omega/\mathrm{d}\beta\} = 0$), i.e. complete adiabatic stopping of light pulses, can indeed be achieved even when residual dissipative losses remain in the metamaterial waveguides (see Fig. 6 below). In fact, it turns out that the overall optical losses of a light *pulse* in the ‘stopped’-light regime are orders of magnitude *smaller* compared to the losses that a ‘stopped’ sinusoidal wave experiences [cf. Fig. 5(b) and Fig. 6(b)]. Thus, bringing a guided light pulse to a complete halt inside metamaterial waveguides results in, amongst others, a substantial *minimisation* of the overall optical losses – since the pulse, being ‘stopped’, does not experience propagation losses anymore, but only temporal losses [22,26,28] at the location where it is ‘stopped’/stored.

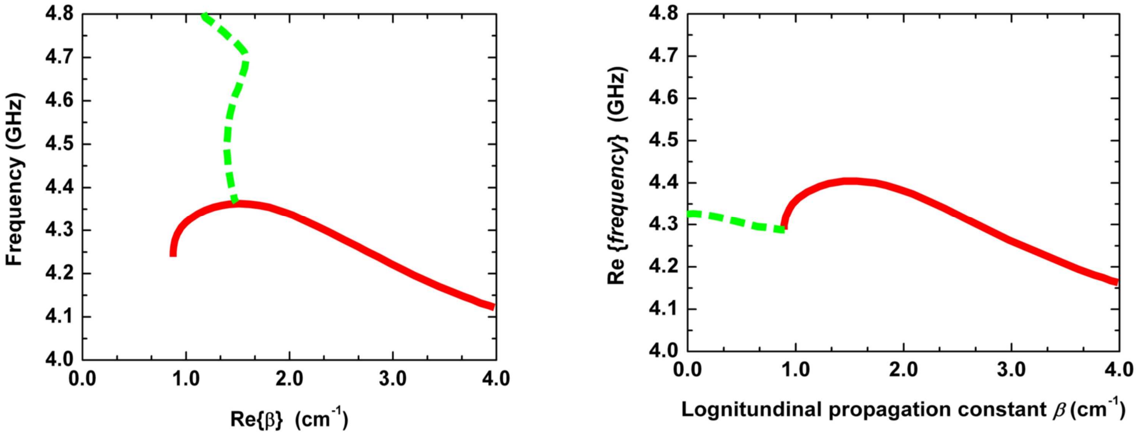

(a) (b)

Fig. 4. (a) Real-frequency/complex-wavenumber dispersion diagram of a *lossless* negative-index waveguide. (b) *Complex*-frequency/*real*-wavenumber dispersion diagram of the same waveguide as in (a).

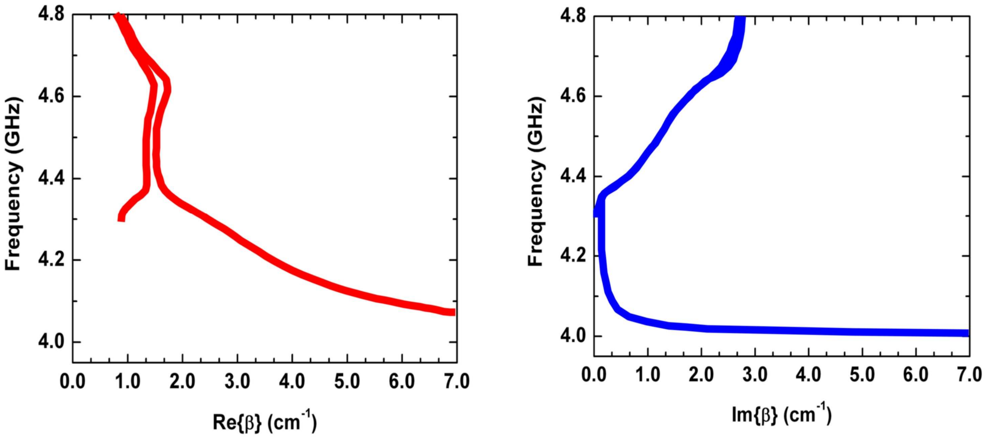

(a) (b)

Fig. 5. Variation of the frequency versus (a) the real part and (b) the imaginary part of the *complex* wavenumber in the waveguide of Fig. 4(a) when dissipative losses are, now, present.

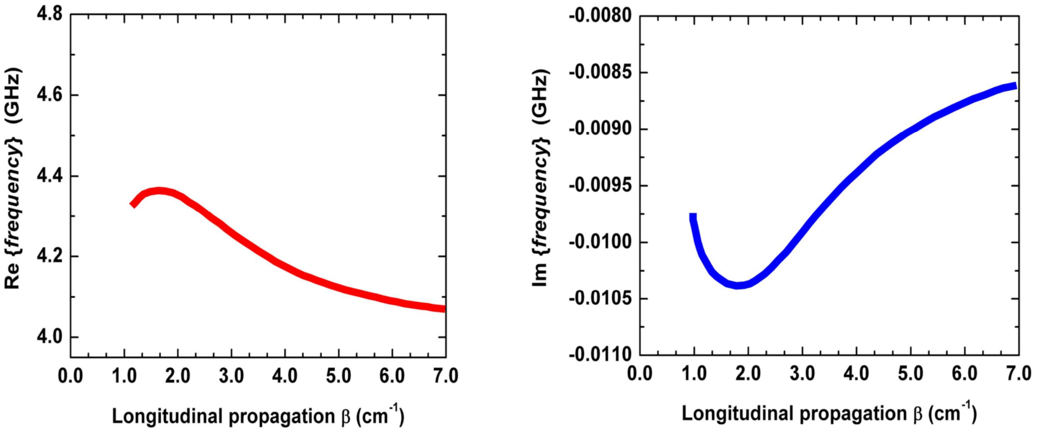

(a) (b)

Fig. 6. Variation of (a) the real part of the frequency and (b) the *imaginary part of the frequency* versus the *real* wavenumber in the waveguide of Fig. 4(b) when dissipative losses are, now, present.

Furthermore, a series of recent works [11,12,29] have conclusively shown that metamaterials can, when judiciously designed, be completely insensitive to *even high degrees* of fabrication disorder. This is simply because metamaterials owe their effective properties to an *averaged* electromagnetic response of their constituent meta-molecules, without necessarily requiring a ‘perfect’ lattice to achieve negative electromagnetic responses. Semiconductor-based metamaterial heterostructures are, also, expected to exhibit minimal sensitivity to fabrication disorder, since therein we do not make use of plasmonic meta-molecules, but planar semiconductor layers – one or more of which exhibit a negative electric permittivity below its plasma frequency. Current molecular beam epitaxy (MBE) facilities are indeed capable of growing high-quality semiconductor superlattices owing to mature, optimised growth-temperature, composition and doping-profile techniques.

Compensation of optical losses by use of gain

Although, as we saw in the previous section, a light pulse can be stopped inside a lossy metamaterial waveguide, the pulse still experiences considerable (temporal) losses. In this section, we show how, in a suitably designed metamaterial heterostructure, the losses that a slow-light pulse experiences can be completely removed by using gain (stimulated emission). An example of such a structure is schematically illustrated in Fig. 7, where we note that gain media/layers are placed adjacently to the negative-refraction semiconductor-heterostructure core layer. Similar loss-compensation configurations have recently been shown to work remarkably well [30], to the point of even allowing for *lasing* [31] in hybrid plasmonic-dielectric configurations. It turns out that by properly adjusting the 'pump' laser intensity, the (negative) imaginary part of the refractive index of the gain medium can become equal (in magnitude) to the (positive) imaginary part of the effective refractive index of the metamaterial heterostructure, so that losses can be *altogether* eliminated.

Indeed, in Fig. 8 below we are presenting numerical results (confirming the aforementioned conclusions) that were obtained using full-wave, finite-difference time- domain (FDTD) simulations of pulse propagation in the metamaterial waveguide structures of the type shown in Fig. 7. Four simulations were run, and in each simulation an oscillatory mode pulse was injected into the waveguide. The simulations examined the effect on the pulse when: only gain is present (the metamaterial is modelled as being lossless); only losses are present (the gain material is removed); neither losses nor gain are present; and both gain and losses are present. A NRI material was used for the core layer, which had a width of $0.4\lambda_0$ (λ_0 being the free-space wavelength of the pulse's central frequency). The gain layers were positioned immediately adjacent to the core layer, and extended outwards into the cladding for a distance of $0.25\lambda_0$. The rest of the cladding (shown in yellow color in Fig. 7) was assumed to be a non-dispersive material with a refractive index of 1 (air).

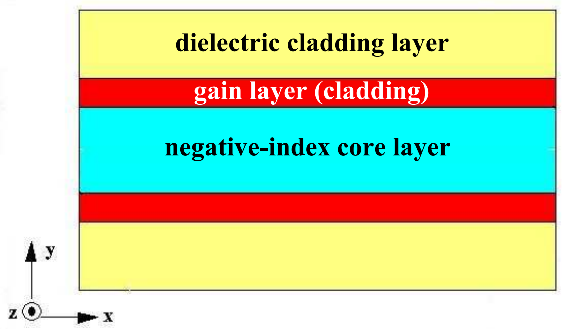

Fig. 7. Schematic illustration of the metamaterial-waveguide configuration for the (complete) compensation of the dissipative losses arising from the negative-index core layer.

For simplicity, both the permittivity and permeability response of the NRI material are simulated using the same Drude model. Thus, the refractive index of the NRI material is given by: $n(\omega) = 1 - \omega_p^2/(\omega^2 + i\omega\Gamma)$, where $\omega_p = \sqrt{5}\omega_0$ is the plasma frequency and Γ is the collision frequency, which is set at: $0.002\omega_0/(2\pi)$. This gives the metamaterial a refractive index of: $n(\omega_0) = -4 + i0.0016$.

In our simulations, the response of the gain material is simulated using a Lorentz material model: $\varepsilon(\omega) = \varepsilon_\infty + \Delta\varepsilon\,\omega_L^2/(\omega_L^2 - i2\delta\omega - \omega^2)$, with: $\varepsilon_\infty = 0.9946$, the Lorentz resonance frequency $\omega_L = 0.6\omega_0$, the damping coefficient $\delta = 20\omega_0/(2\pi)$, and $\Delta\varepsilon = -1$.

The effective refractive index of the waveguide is extracted from the simulation by recording over time the H_z-field amplitude of the pulse at two points along the waveguide's central axis. Using the Fourier transforms of these results, the change in phase and amplitude undergone by each frequency between the two points can be calculated, from where the real and imaginary parts of the effective refractive index can then be obtained. An exemplary plot of the so-extracted imaginary part of the effective index of the guided light pulse is shown in Fig. 8. We note that when gain layers are placed adjacently to the negative-index core layer, the loss experienced by the guided light pulse is (at a given frequency) completely removed (red crosses in Fig. 8). For higher frequencies, this slow-light, negative-phase-velocity pulse is *amplified* while propagating inside the negative-index waveguide. Further evidence for the removal of losses is shown in Fig. 9, from where it can be directly seen that the incorporation of gain layers restores completely the amplitude of the slow-light, negative-phase-velocity pulse.

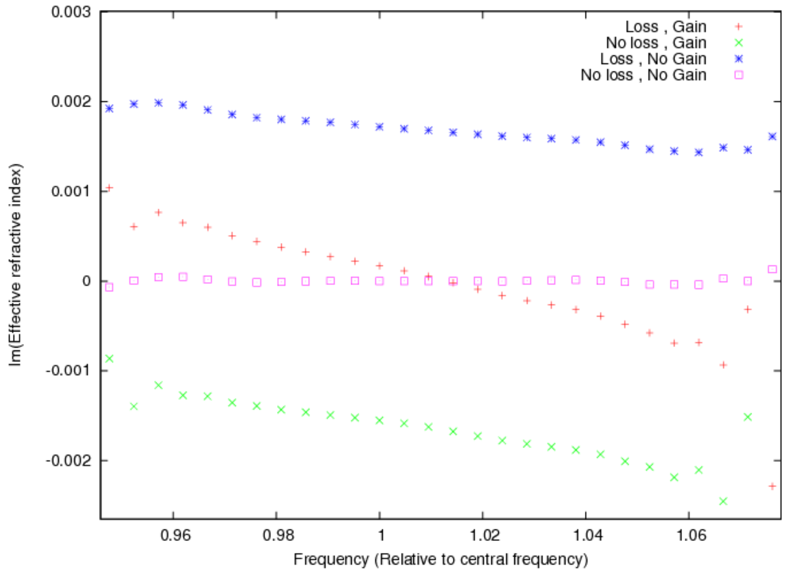

Fig. 8. Variation with frequency of the imaginary part of the effective index of a guided pulse in a negative-refractive-index waveguide for the cases where the NRI core layer is: lossless (pink square symbols); lossy (blue, tilted double-cross symbols in the upper part of the graph); lossy and gain cladding layers are used (red crosses); lossless and gain cladding layers are used (green tilted crosses in the bottom part of the graph).

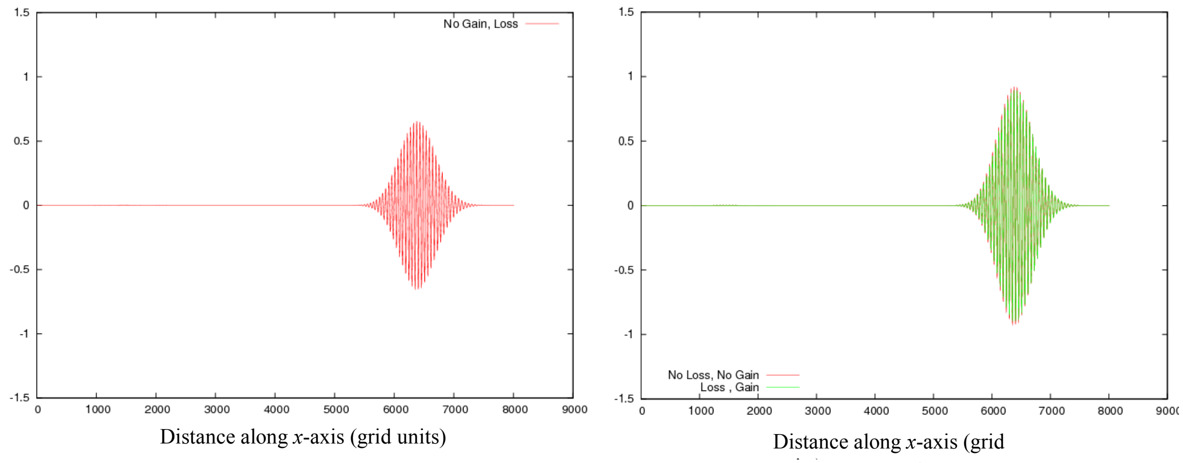

(a) (b)

Fig. 9. Pulse propagation along the waveguide of Fig. 7 in the case where: (a) The core-layer is lossy. (b) The core-layer is lossy and gain is used in the adjacent cladding-layers.

Conclusions

In summary, we have shown that metamaterial waveguides with negative electromagnetic parameters (permittivity, permeability, refractive index) can enable complete stopping of light under realistic experimental conditions [6,13,14]. This attribute is underpinned by the resilience of the deceleration mechanism in these structures to fabrication imperfections (e.g., disorder) and dissipative losses. By nature, these schemes invoke solid-state materials and, as such, are not subject to low-temperature or atomic coherence limitations. The NRI-based scheme, in particular, inherently allows for high in-coupling efficiencies, polarization-independent operation, and broadband function, since the deceleration of light does not rely on refractive index resonances. This versatile method for trapping photons opens the way to a multitude of hybrid, optoelectronic devices to be used in 'quantum information' processing, communication networks and signal processors, and conceivably heralds a new realm of combined metamaterials and slow light research.

References

[1] P. Markoš and C.M. Soukoulis: *Wave Propagation: From Electrons to Photonic Crystals and Left-Handed Materials* (Princeton University Press, Princeton & Oxford 2008).

[2] V.M. Shalaev and A.K. Sarychev: *Electrodynamics of Metamaterials* (World Scientific Publishing, New Jersey 2007).

[3] N. Engheta and R.W. Ziolkowski (eds): *Electromagnetic Metamaterials: Physics and Engineering Explorations* (Wiley-IEEE Press, New York 2006).

[4] J.B. Khurgin and R.S. Tucker (eds): *Slow Light: Science and Applications* (Taylor & Francis, New York 2009).

[5] P.W. Milonni: Fast Light, *Slow Light and Left-Handed Light* (Taylor & Francis, New Work 2005).

[6] K.L. Tsakmakidis, A.D. Boardman and O. Hess: Nature Vol. 450 (2007), p. 397.

[7] B. Corcoran, *et al.*: Nature Photonics Vol. 3 (2009), p. 206.

[8] F. Xia, *et al.*: Nature Photonics Vol. 1 (2006), p. 65.

[9] A. Petrov, *et al.*: Opt. Express Vol. 17 (2009), p. 8676.

[10] D.P. Fussell, *et al.*: Phys. Rev. B Vol. 78 (2008), p. 144201.

[11] C. Helgert, *et al.*: Phys. Rev. B Vol. 79 (2009), p. 233107.

[12] N. Papasimakis, *et al.*: Phys. Rev. B Vol. 80 (2009), p. 041102(R).

[13] V. N. Smolyaninova, *et al.*: arXiv:0911.4464v1 [physics.optics] (2009).

[14] Q. Gan, *et al.*: arXiv:1003.4060v1 [physics.optics] (2010).

[15] J.-S. Li: Opt. Laser Technol. Vol. 41 (2009), p. 627.

[16] A.J. Hoffman, *et al.*: Nature Materials Vol. 6 (2007), p. 946.

[17] A.J. Hoffman, *et al.*: J. Appl. Phys. Vol. 105 (2009), p. 122411.

[18] Z.V. Vardeny and A. Nahata: Nature Photonics Vol. 2 (2008), p. 75.

[19] S. Mookherjea, *et al.*: Nature Photonics Vol. 2 (2008), p. 90.

[20] O. Hess and K.L. Tsakmakidis: SPIE Newsroom (Nanotechnology), doi:10.1117/2.120086.1163 (2008).

[21] K.L. Tsakmakidis, *et al.*: Appl. Phys. Lett. Vol. 89 (2006) p. 201103.

[22] A. Karalis, *et al.*: Phys. Rev. Lett. Vol. 103 (2009), p. 043906.

[23] J.W. Dong and H.Z. Wang: Appl. Phys. Lett. Vol. 91 (2007), p. 111909.

[24] M.A. Vincenti, *et al.*: J. Appl. Phys. Vol. 105 (2009), p. 103103.

[25] E.I. Kirby, *et al.*: J. Opt. A: Pure Appl. Opt. Vol. 11 (2009), p. 114027.

[26] A. Archambault, *et al.*: Phys. Rev. B Vol. 79 (2009), p. 195414.

[27] K.L. Tsakmakidis and O. Hess, “Slow and stopped light in metamaterials,” J. Opt. (invited) (2010).

[28] K.C. Huang, *et al.*: Phys. Rev. B Vol. 69 (2004), p. 195111.

[29] J.J. Cook, *et al.*: J. Opt. A.: Pure Appl. Opt. Vol. 11 (2009), p. 114026.

[30] M.A. Noginov, *et al.*: Phys. Rev. Lett. Vol. 101 (2006), p. 226806.

[31] R.F. Oulton, *et al.*: Nature Vol. 461 (2009), p. 629.

Keywords Index

Authors Index